SpringerWienNewYork

CISM COURSES AND LECTURES

The series presents lecture notes, monographs, edited works and proceedings in the field of Mechanics, Engineering, Computer Science and Applied Mathematics.
Purpose of the series is to make known in the international scientific and technical community results obtained in some of the activities organized by CISM, the International Centre for Mechanical Sciences.

INTERNATIONAL CENTRE FOR MECHANICAL SCIENCES

COURSES AND LECTURES - No. 510

ANALYSIS AND CONTROL OF MIXING WITH AN APPLICATION TO MICRO AND MACRO FLOW PROCESSES

EDITED BY

LUCA CORTELEZZI
MCGILL UNIVERSITY, MONTREAL, CANADA

IGOR MEZIĆ
UNIVERSITY OF CALIFORNIA, SANTA BARBARA

SpringerWienNewYork

This volume contains 176 illustrations

Printed in Italy
SPIN 12688142

All contributions have been typeset by the authors.

ISBN 978-3-211-99345-3 SpringerWienNewYork

PREFACE

The present monograph takes inspiration from the Advanced School on "Analysis and Control of Mixing with Application to Micro and Macro Flow Processes" held in Udine, Italy, (June 1-5, 2005) at the International Center for Mechanical Sciences (CISM). The Advanced School was made possible by the financial and logistic support of CISM and by the financial support of the Marie Curie Program of the European Atelier for Engineering and Computational Sciences (EUA4X). The Advanced School was complemented by a workshop. The workshop provided a fertile environment for discussions where participants in the Advance School, as well as academic and industry experts from fluids, combustion and control disciplines, presented their most recent results. The Advanced School and the workshop attracted a wide range of scientists and practitioners: postgraduates, postdoctoral researchers, mechanical, chemical and aeronautical engineers, and applied mathematicians in universities and industries.

The study of mixing two or more fluids with or without chemical reactions is of great practical relevance to both engineering applications and natural phenomena. The analysis and control of mixing at macro and micro scales is receiving great attention because of the potential for optimizing the performance of many flow processes. In modern and futuristic industrial applications, the time allowed to find the appropriate mixing action is becoming increasingly shorter while the demands are increasingly more severe. A better understanding of mixing is crucial for improving old and designing new mixing devices that are able to reduce the residence mixing time, improve mixing homogeneity and allow the process of new materials highly sensitive to the presence of concentration and temperature gradients. In spite of much advancement, the understanding of mixing is still somewhat limited in three-dimensional flows. In particular optimization and feedback control of mixing are still in their infancy. Consequently, mixing continues to represent a rich and appealing research field for both the fundamental and the application oriented scientists.

The Advanced School provided an overview of the physics, mathematics and state-of-the-art theoretical/numerical modeling and experimental investigations of mixing in laminar and turbulent flows at macro and micro scales. This monograph follows the footsteps of

the Advanced School and contains the following contributions: Anthony Leonard presents an "Overview of Turbulent and Laminar Diffusion and Mixing", Igor Mezić discusses "Mixing and Dynamical Systems", Stefano Cerbelli presents the "Hyperbolic Behavior of Laminar Chaotic Flows", Massimiliano Giona discusses "Advection-diffusion in Chaotic Flows", Emmanuel Villermaux elaborates on "Random Mixing", Fotis Sotiropoulos presents an "Experimental Visualization of Lagrangian Coherent Structures Using Eulerian Averaging", Tatyana Krasnopolskaya discusses "Quality Measures and Transport Properties" of mixing, Tamás Tel discusses some aspects of "Reactions in Chaotic Flows", Mark A. Stremler elaborates on "Fluid Mixing, Chaotic Advection, and Microarray Analysis", Jean-Luc Thiffeault presents "The Size of Ghost Rods", Bartosz Protas discusses the utility of "Nonlinear Preconditioning in Problems of Optimal Control for Fluid Systems" and, finally, Luca Cortelezzi elaborates on the "Sensitivity of Mixing Optimization to the Geometry of the Initial Scalar Field".

We would like to thank all the contributors for their scholarly dedication in making this volume a reality. We would also like to thank all members of CISM for their help in making the Advanced School and this monograph a success. In particular, we would like to thank the Secretary General, Prof. Bernhard A. Schrefler, for encouraging and supporting our Advanced School, Dr. Sara Guttilla, for her dedicated help in all stages of our Advanced School and, finally, the Executive Editor Prof. Paolo Serafini for his precious assistance during the editing of this monograph.

Luca Cortelezzi and Igor Mezić

CONTENTS

Photo Partecipants

Overview of Turbulent and Laminar Diffusion and Mixing

A. Leonard

Graduate Aeronautical Laboratories
California Institute of Technology
Pasadena, California, USA

1 Introduction

The theme of this short course is mixing. My task is to present some basic material on convective-diffusive processes that should be useful in understanding, e.g., control of mixing and various flow processes that might be employed to enhance or delay mixing. These latter topics will be discussed in other chapters.

For our purposes, we shall be interested in characterizing the evolution in time of a passive scalar distribution function $\phi(\boldsymbol{x}, t)$ that satisfies the convection-diffusion equation,

$$\frac{\partial \phi}{\partial t} + \boldsymbol{u} \cdot \nabla \phi = D \nabla^2 \phi, \tag{1.1}$$

with appropriate initial and boundary conditions. Here $\boldsymbol{u}(\boldsymbol{x}, t)$ is a specified velocity field, or one that is computed separately, and D is the diffusion coefficient for ϕ. The velocity field can come in many different varieties, 2D or 3D, time-independent or time-dependent. The distributions of spatial scales and of time scales can be important factors also. If U and L are characteristic velocity and length scales of the flow $\boldsymbol{u}$ then an important nondimensional parameter is the Peclet number, $Pe = UL/D$.

We will see that much depends on the character of passive particle paths $\boldsymbol{x}(t)$ given as the solution to

$$\frac{d\boldsymbol{x}}{dt} = \boldsymbol{u}(\boldsymbol{x}(t), t) \tag{1.2}$$

with $\boldsymbol{x}(0) = \boldsymbol{x}_0$. If these paths have a sensitive dependence on the initial location, i.e., initially nearby trajectories diverge exponentially, one has so-called lagrangian chaos. The convective-diffusive behavior of a passive scalar

depends critically on whether the flow exhibits lagrangian chaos, especially for high Pe. Steady 2D flows do not produce chaotic particle paths, while unsteady 2D flows and steady 3D flows may have lagrangian chaos.

2 Laminar Diffusion

2.1 Case $\boldsymbol{u} = 0$

For this simple case (1.1) reduces to

$$\frac{\partial \phi}{\partial t} = D\nabla^2 \phi, \tag{2.1}$$

We consider the infinite domain with $\phi(\boldsymbol{x}, 0) = \phi_0(\boldsymbol{x})$.

Multiplying (2.1) by 1, $\boldsymbol{x}$, and $|\boldsymbol{x}|^2$ and integrating over all space we obtain, respectively,

$$\frac{d}{dt}\int \phi(\boldsymbol{x}, t) d\boldsymbol{x} = 0, \tag{2.2}$$

$$\frac{d}{dt}\int \boldsymbol{x}\phi(\boldsymbol{x}, t) d\boldsymbol{x} = 0, \tag{2.3}$$

and

$$\frac{d}{dt}\int |\boldsymbol{x}|^2 \phi(\boldsymbol{x}, t) d\boldsymbol{x} = 2dD\int \phi(\boldsymbol{x}, t) d\boldsymbol{x}, \tag{2.4}$$

where d is the number of spatial dimensions. We will use the above results subsequently.

One can easily show by substitution that the Gaussian distribution

$$\tilde{\phi}(\boldsymbol{x}, t) = \Phi_0 \frac{e^{-|\boldsymbol{x}-\boldsymbol{x}_0|^2/\sigma^2(t)}}{(\pi\sigma^2(t))^{d/2}} \tag{2.5}$$

and

$$\frac{d\sigma^2}{dt} = 4D \tag{2.6}$$

satisfies (2.1). In fact, as we show below, for a compact initial distribution $\phi_0(\boldsymbol{x})$,

$$\phi(\boldsymbol{x}, t) \to \tilde{\phi}(\boldsymbol{x}, t) \; as \; t \to \infty, \tag{2.7}$$

and, from (2.2) and (2.3), we find that

$$\Phi_0 = \int \phi_0(\boldsymbol{x}) d\boldsymbol{x}, \tag{2.8}$$

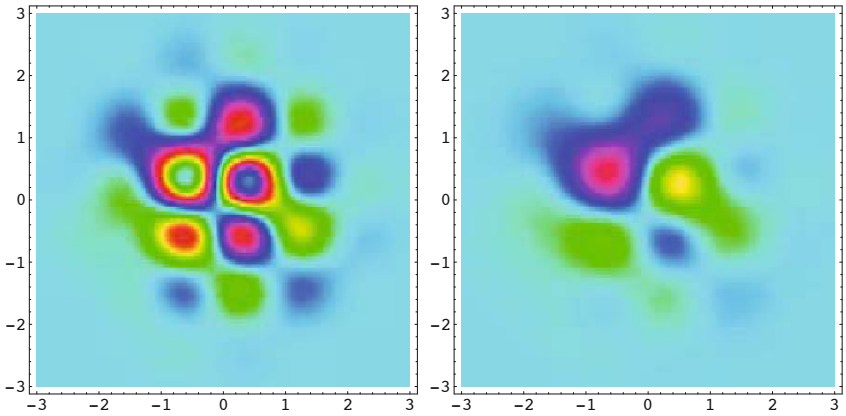

Figure 1. $\phi(x, y, t)$, random initial field, $\sigma_{0x}^2 = \sigma_{0y}^2 = 1$. Left: $t = 0$, Right: $1/(1 + 4Dt) = 0.81$.

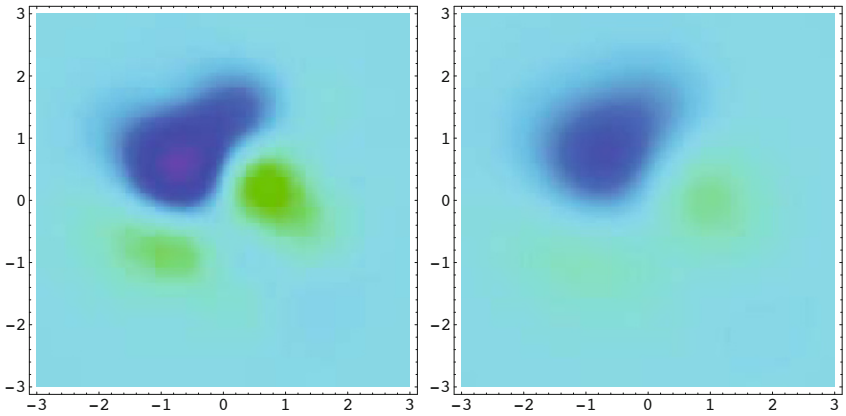

Figure 2. $\phi(x, y, t)$ random initial field, $\sigma_{0x}^2 = \sigma_{0y}^2 = 1$. Left: $1/(1+4Dt) = 0.64$, Right: $1/(1 + 4Dt) = 0.49$. Same initial field as in Fig. 1.

$$\boldsymbol{x}_0\Phi_0 = \int \boldsymbol{x}\phi_0(\boldsymbol{x})d\boldsymbol{x}, \tag{2.9}$$

and (2.6) follows from (2.4).

To determine a general solution the problem with $\boldsymbol{u} = 0$ note that

$$\psi_n(x,t) = \frac{\partial^n}{\partial x^n}\frac{\exp[-x^2/(\sigma_0^2+4Dt)]}{\sqrt{\sigma_0^2+4Dt}} \tag{2.10}$$

also satisfies (2.1) in 1D. But the $\psi_n(x,t)$ are related to the Hermite polynomials $H_n(x)$ because

$$\frac{\partial^n}{\partial x^n}\exp[-x^2] = (-1)^n H_n(x)\exp[-x^2]. \tag{2.11}$$

Thus, in 2D for example, we have the following general solution for a compact initial distribution $\phi_0(\boldsymbol{x})$,

$$\phi(\boldsymbol{x},t) = \sum_{m,n=0}^{\infty} \frac{\phi_{m,n}H_m(x/\sqrt{\sigma_{0x}^2+4Dt})H_n(y/\sqrt{\sigma_{0y}^2+4Dt})}{\pi(\sigma_{0x}^2+4Dt)^{\frac{m+1}{2}}(\sigma_{0y}^2+4Dt)^{\frac{n+1}{2}}} \times \exp[-\tfrac{x^2}{\sigma_{0x}^2+4Dt} - \tfrac{y^2}{\sigma_{0y}^2+4Dt}] \tag{2.12}$$

Note that the term $m = n = 0$ dominates as $t \to \infty$ proving the claim (2.7). The coefficients $\phi_{m,n}$ may be determined from $\phi_0(\boldsymbol{x})$ using the orthogonality of the $H_n's$:

$$\int_{-\infty}^{\infty} e^{-x^2}H_m(x)H_n(x)dx = \sqrt{\pi}2^n n!\delta_{m,n}. \tag{2.13}$$

It is a simple matter to generalize (2.12) to 3D. See Figs. 1 & 2 for an example solution. Here $0 \le m,n \le 5$ with the $\phi_{m,n}$ chosen randomly from $[-1,1]$ and weighted by $1/[(m+1)(n+1)]^2$.

2.2 Case of constant strainrate

Here $u(x,y,t) = \epsilon x$ and $v(x,y,t) = -\epsilon y$ where $\epsilon = \epsilon(t) > 0, \boldsymbol{u} = (u,v)$, and $\boldsymbol{x} = (x,y)$, i.e., the flow is expanding in the x-direction and contracting in the y-direction. In this case (1.1) becomes

$$\frac{\partial\phi}{\partial t} + \epsilon x\frac{\partial\phi}{\partial x} - \epsilon y\frac{\partial\phi}{\partial y} = D\nabla^2\phi. \tag{2.14}$$

Now it is advantageous to transform to material coordinates

$$\bar{x} = S^{-1}(t)x,\ \bar{y} = S(t)y, \tag{2.15}$$

where $S(t) = \exp[\int_0^t \epsilon(t')dt']$, and to change to a new time variable τ,

$$\tau = \int_0^t S^2(t')dt'. \tag{2.16}$$

The result is that (2.14) becomes

$$\frac{\partial \phi}{\partial \tau} = D\frac{\partial^2 \phi}{\partial \bar{y}^2} + \frac{D}{S^4(t)}\frac{\partial^2 \phi}{\partial \bar{x}^2}. \tag{2.17}$$

Notice that diffusion in the $\bar{x}$-direction is greatly reduced by the factor $1/S^4$. If we introduce an additional time variable $\hat{\tau}$ for the $\bar{x}$-direction,

$$d\hat{\tau} = \frac{d\tau}{S^4}, \tag{2.18}$$

Then we can use the solutions we generated for (2.1) above just remembering to use τ for the time variable for y and $\hat{\tau}$ for x. In particular for a gaussian initial condition, we have

$$\phi(\bar{x}, \bar{y}, \tau, \hat{\tau}) = \Phi_0 \frac{\exp[-\frac{(\bar{x}-\bar{x}_0)^2}{\sigma^2+4D\hat{\tau}} - \frac{(\bar{y}-\bar{y}_0)^2}{\sigma^2+4D\tau}]}{\pi\sqrt{\sigma^2+4D\hat{\tau}}\sqrt{\sigma^2+4D\tau}} \tag{2.19}$$

So what does this solution look like in x, y, and t? If the strainrate ϵ is independent of t then

$$\tau = \frac{1}{2\epsilon}(e^{2\epsilon t} - 1) = \frac{1}{2\epsilon}(S^2 - 1) \tag{2.20}$$

and so

$$\frac{(\bar{y} - \bar{y}_0)^2}{\sigma^2 + 4D\tau} \to \frac{\epsilon(y - y_0)^2}{2D} \tag{2.21}$$

for $\epsilon t >> 1$.. That is diffusion comes into equilibrium with compression at a lengthscale $\sim \sqrt{D/\epsilon}$. However, the prefactor

$$\frac{1}{\sqrt{\sigma^2 + 4D\tau}} \to \sqrt{\frac{\epsilon}{2D}}e^{-\epsilon t} \tag{2.22}$$

is becoming exponentially small because of the flux of ϕ in the x-direction due to straining.

For the $\bar{x}, \hat{\tau}$ behavior, we use (2.20) in (2.18) to find

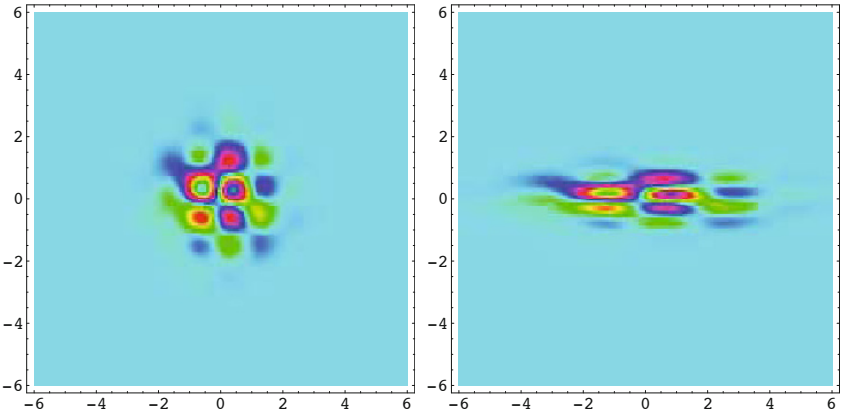

Figure 3. $\phi(x, y, t)$, random initial field with constant strainrate, $D/\epsilon = 0.01$, $\sigma_{0x}^2 = \sigma_{0y}^2 = 1$. Left: $t = 0$, Right: $e^{\epsilon t} = 2$.

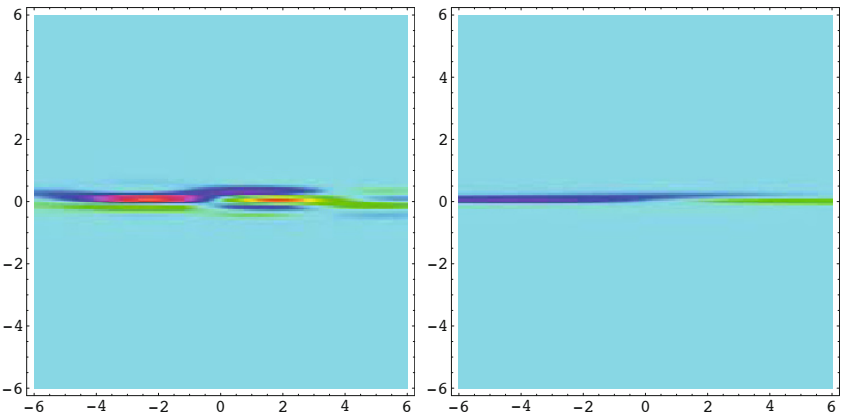

Figure 4. $\phi(x, y, t)$ random initial field with constant strainrate, $D/\epsilon = 0.01$, $\sigma_{0x}^2 = \sigma_{0y}^2 = 1$. Left: $e^{\epsilon t} = 4$, Right: $e^{\epsilon t} = 8$.

$$\hat{\tau} = \frac{\tau}{1 + 2\epsilon\tau} \tag{2.23}$$

so that

$$\hat{\tau} \to \frac{1}{2\epsilon} \tag{2.24}$$

and

$$\frac{(\bar{x} - \bar{x}_0)^2}{\sigma^2 + 4D\hat{\tau}} \to \frac{(x - x_0)^2}{e^{2\epsilon t}(\sigma^2 + 2D/\epsilon)}. \tag{2.25}$$

Thus, the "effective" diffusion coefficient in the x-direction is increasing at an exponential rate in time due to a positive strainrate or expansion in that direction. See Figs. 3 & 4 for an example of this effect. The initial field is the same as that in the pure diffusion example of Figs. 1 & 2.

2.3 Standard Diffusion in Steady Velocity Fields

We consider now a typical case of advection-diffusion in a steady velocity field with nonchaotic particle motions[1]. The flow is a model for Rayleigh-Bénard convection and is simply

$$\boldsymbol{u} = U(\cos y, -\sin x) \tag{2.26}$$

The flow takes place within square cells with cell width $L = \sqrt{2}\pi$ bounded by separatrices. See Fig. 5a. If $D = 0$ an initial distribution ϕ_0 confined to a cell will remain in the same cell for all time.

For high Pe (D small) diffusion from one cell to the next will take place within a thin layer of thickness δ near a separatrix. On each pass a particle spends time $\tau \sim L/U$ moving along next to a separatrix thus $\delta^2 \sim D\tau$. On the other hand, the effective diffusion coefficient, $\mathcal{D}$, (for $\boldsymbol{u} = 0$) would be $\sim L^2/\tau$ if an $O(1)$ fraction of the material in a cell diffused out of the cell in time τ. However, as discussed above, only a fraction , δ/L, diffuses to the next cell time τ. Thus,

$$\mathcal{D} \sim \frac{L^2}{\tau}\frac{\delta}{L} \sim \sqrt{Pe}D \sim D^{1/2}. \tag{2.27}$$

Note that $\mathcal{D}$ is much larger than D as $D \to 0$ or $Pe \to \infty$.

For the case

[1] This lecture is based on material in "Dynamical Systems Approach to Turbulence", Chap. 9, by Bohr, Jensen, Paladin & Vulpiani, Cambridge Press 1998

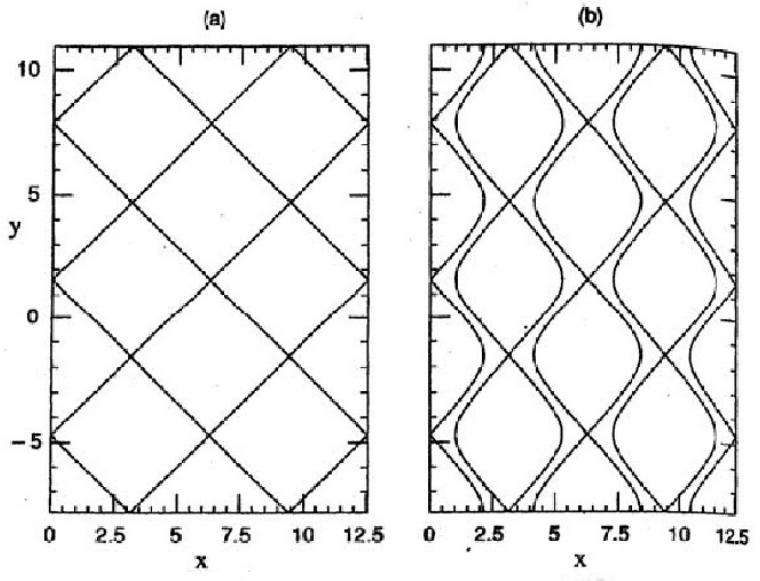

Figure 5. Structure of the separatrices for the flow of (a) Eq. (2.26) and (b) Eq. (2.28) with $\Delta = 0.3$. [3]

$$\boldsymbol{u} = U(\cos y, -(1+\Delta)\sin x) \quad \Delta \neq 0 \tag{2.28}$$

one obtains effective diffusion that is strongly anisotropic. This is because channels of width $\approx \Delta$ appear where the motion is ballistic in the y-direction. See Fig. 5b. Thus, for small D a diffusive element can travel a long distance in the y-direction before leaving the channel by diffusion. Fig. 6 depicts the motion of a diffusive particle in this flow field. In this case the particle motion is represented by trajectories given by (1.2) plus a random component,

$$\frac{d\boldsymbol{x}}{dt} = \boldsymbol{u}(\boldsymbol{x}(t), t) + \boldsymbol{\eta}(t), \tag{2.29}$$

where $\boldsymbol{\eta}$ is a gaussian process with zero mean and variance given by

$$< \eta_i(t)\eta_j(t') >= 2D\delta_{i,j}\delta(t-t'). \tag{2.30}$$

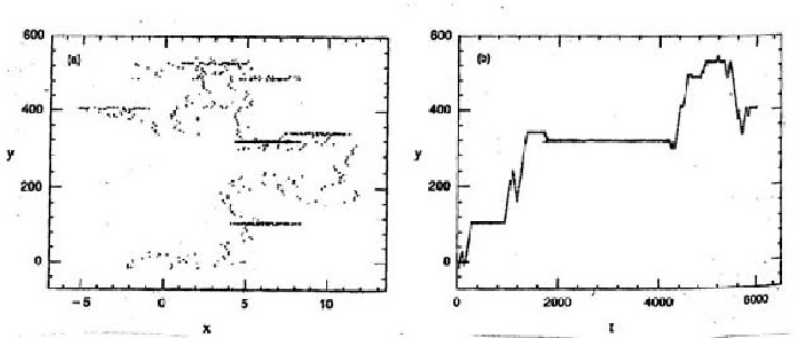

Figure 6. (a) 1000 positions (recorded every 6 units of time) of one particle evolving according to Eq. (2.29) with the velocity field of Fig. 5b and $D = 0.001$. (b) y vs. t for the same particle. [3]

The length of travel in y of a typical flight is $\ell_{\|} = Ut_{\|}$ where $t_{\|} \sim \Delta^2/D$. Thus, the effective diffusion coefficient in the channel or longitudinal direction $\mathcal{D}_{\|}$ is

$$\mathcal{D}_{\|} \sim \frac{\Delta}{L}\frac{\ell_{\|}^2}{t_{\|}} \sim Pe^2\frac{\Delta^3 D}{L^3} \sim \frac{\Delta^3}{D} \tag{2.31}$$

where the factor Δ/L is the probability of finding an element within the channel. Thus, we have an interesting example where the longitudinal dispersion is actually inversely proportional to the molecular diffusivity. Another example of this type is dispersion along the flow direction for laminar pipe flow or channel flow (see Taylor (1953)[1], Taylor (1954) [2]). Taylor showed for pipe flow that the longitudinal diffusivity is given by

$$\mathcal{D}_{\|} = \frac{R^2V^2}{48D} + D, \tag{2.32}$$

where R is the pipe radius and V is the average velocity.

Note that if Pe is fixed and $\Delta/L \to 0$ then the effective diffusion coefficient will revert to that given by (2.27). Another way to view this competition is to compare the channel width Δ to the layer thickness $\delta = \sqrt{DL/U}$ discussed in the square-cell case. If $\delta > \Delta$ then the diffusion mechanism in the square-cell case will dominate and replacing Δ by δ in (2.31) indeed gives the result (2.27). This effect is shown nicely in the numerical experiments of Crisanti et al.(1990) [3]. See Fig. 7. Note in that figure that $\mathcal{D}_{\|} \sim 1/D$

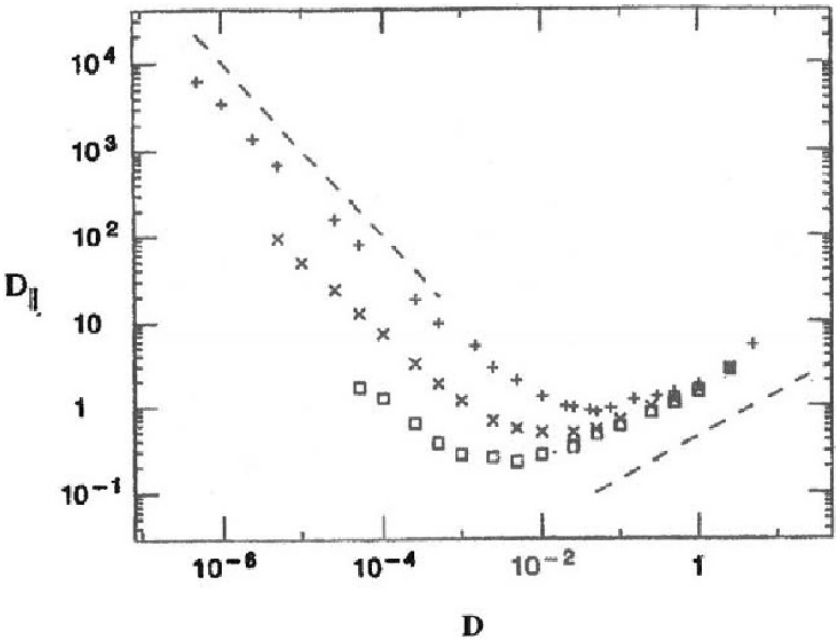

Figure 7. The longitudinal diffusion coefficient vs. molecular diffusion D for the velocity field of Eq. (2.28) and $\Delta = 0.30$ (+), 0.15 (×), 0.075 (□). The broken lines have slopes -1 and 1/2. [3]

for small D and $\mathcal{D}_\parallel \sim D^{1/2}$ for large D with the transition taking place at $\delta \approx \Delta$.

For diffusion in the transverse direction, a diffusive element in the channel only travels an effective distance L in time $t_\parallel$. Thus

$$\mathcal{D}_\perp \sim \frac{\Delta}{L}\frac{L^2}{t_\parallel} \sim \frac{L}{\Delta}D. \tag{2.33}$$

Again (2.33) will apply as long as $\Delta > \delta$. If $\delta > \Delta$ we replace Δ with δ in (2.33) giving the result (2.27) as expected. In Fig. 8 we show the results of numerical experiments confirming the prediction (2.33) (Fig. 8b) as well as the prediction (2.31) (Fig. 8a).

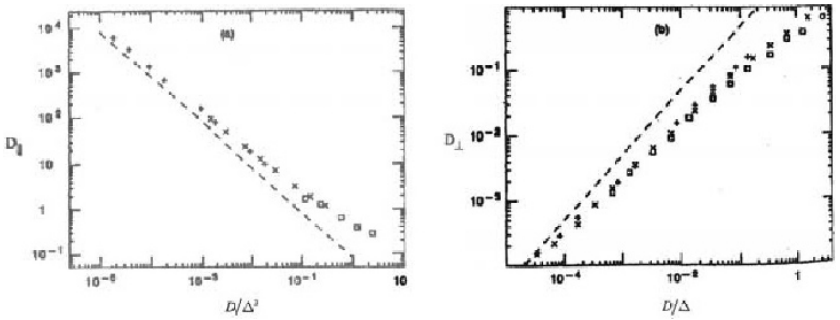

Figure 8. (a) The longitudinal diffusion coefficient vs. D/Δ^3 and a dashed line with slope -1. (b) The transverse diffusion coefficient vs. D/Δ (shown as χ/δ in the figure) and a dashed line of slope 1. The symbols correspond to $\Delta = 0.30$ (+), 0.15 (×), 0.075 (□). [3]

2.4 Anomalous Diffusion

Although in the above examples, the effective diffusion coefficient can be proportional to various powers of Pe and depend on other parameters, such as Δ/L, the diffusion is *standard*, i.e., the mean square distance traveled by a diffusive element is asymptotically linear in time, i.e.,

$$< |\boldsymbol{x}(t) - \boldsymbol{x}(0)|^2 > \sim t^{2\nu}, \tag{2.34}$$

with $\nu = 1/2$. In other example flows we might observe *anomalous* diffusion: *subdiffusion* if $\nu < 1/2$ or *superdiffusion* if $\nu > 1/2$.

For example, consider advection-diffusion in the simple shear flow

$$\boldsymbol{u} = (u(y), 0), \tag{2.35}$$

where $u(y)$ is a random periodic function which is given in terms of its Fourier transform $\hat{u}(k)$ as

$$u(y) = \sum_{k=-\infty}^{\infty} e^{i2\pi ky/\Lambda} \hat{u}(k) dk. \tag{2.36}$$

where Λ is the period. The mean-square velocity is

$$u_{rms} = \sum_{k} < |\hat{u}(k)|^2 > \approx \int_{-\infty}^{\infty} S(k) dk, \tag{2.37}$$

where $dk = 2\pi/\Lambda$ and the velocity spectrum is

$$S(k) = \frac{\Lambda}{2\pi} < |\hat{u}(k)|^2 > . \tag{2.38}$$

It has been shown (Young & Jones (1992)[4]) that the diffusion is standard and

$$\mathcal{D}_{xx} \sim \frac{1}{D} \int_0^\infty \frac{S(k)}{k^2} dk \tag{2.39}$$

as long as the integral in (2.39) is bounded. In this case, we obtain a result similar to the result (2.31) when D is small diffusive elements will travel long distances in x in one direction before diffusing to an oppositely moving shear flow. In fact,

$$\int_0^\infty \frac{S(k)}{k^2} dk \sim < u^2 > \lambda^2, \tag{2.40}$$

where λ is a typical length of the velocity field $u(y)$, e.g., the typical distance between two zeros of $u(y)$. Thus $\mathcal{D}_{xx} \sim \lambda^2/D$ rather than the cubic power of the lengthscale in (2.31) because the total width λ contributes to the diffusion process rather than a fraction $\sim \Delta/L$ in the case of (2.31).

If, on the other hand, if $S(k)$ does not go to zero fast enough as $k \to 0$ then we obtain superdiffusion. In particular if we assume that

$$S(k) \sim k^\gamma \tag{2.41}$$

as $k \to 0$ then standard diffusion occurs if $\gamma > 1$. However, if $-1 \leq \gamma \leq 1$ then we obtain superdiffusion with the exponent ν (see (2.34)) given by

$$\nu = \frac{3-\gamma}{4} > \frac{1}{2} \tag{2.42}$$

if $\gamma < 1$. For $\gamma = 1$, $< |x(t) - x(0)|^2 > \sim t \log t$.

3 Averaged diffusion equation

The effective diffusion coefficients discussed in Section 2 are special cases of a more general averaging procedure applied to (1.1). If we average (1.1) locally over a volume of linear dimensions much larger than the typical length L of the velocity field then we obtain approximately

$$\frac{\partial < \phi >}{\partial t} = \mathcal{D}_{i,j} \frac{\partial^2 < \phi >}{\partial x_i \partial x_j} \tag{3.1}$$

where $< \phi >$ is the averaged ϕ. The diffusion coefficients measure the spreading of a spot of tracer particles over very long times as follows:

$$\mathcal{D}_{i,j} = \lim_{t\to\infty} \frac{1}{2t} < (x_i(t) - < x_i >)(x_j(t) - < x_j >) > \quad i,j = 1,..,d \quad (3.2)$$

where the average is taken over the initial positions or over an ensemble of test particles. If such a covariance tensor exists, solutions to (3.1) would then asymptote to an anisotropic Gaussian distribution as discussed in Section 2.

In some cases, we can compute the covariance tensor in (3.2) in terms of the lagrangian velocity covariance tensor as follows. Note that

$$x_i(t) - x_i(0) = \int_0^t v_i(t')dt' \quad (3.3)$$

where $\boldsymbol{v}(t) = \boldsymbol{u}(\boldsymbol{x}(t), t)$ is the lagrangian velocity for the particular element being tracked in (3.3). Assuming we have factored out any net drift, i.e. $< \boldsymbol{v}(t) >= 0$, then

$$< (x_i(t) - < x_i >)(x_j(t) - < x_j >) >= \int_0^t \int_0^t < v_i(t')v_j(t'') > dt'dt''. \quad (3.4)$$

For a stationary process $< v_i(t')v_j(t' + \tau) >$ only depends on τ. Letting $t'' = t' + \tau$ in (3.4) and changing the order of integration we find for the case $i = j$, for example, that

$$< (x_i(t) - < x_i >)^2 >= \int_{-t}^t (t - |\tau|)C_{ii}(\tau)d\tau \quad (3.5)$$

where $C_{ii}(\tau) =< v_i(t)v_j(t + \tau) >$. Thus

$$< (x_i(t) - < x_i >)^2 > \to 2t \int_0^\infty C_{ii}(\tau)d\tau \quad (3.6)$$

and referring to (3.2) we see that

$$\mathcal{D}_{ii} = \int_0^\infty C_{ii}(\tau)d\tau \quad (3.7)$$

assuming the integral is bounded. The result (3.7) was first derived by Taylor(1921)[5].

4 Turbulent diffusion

Another example of superdiffusion dates back 80 years. In 1926, L. F. Richardson [6] postulated that a cloud of points in a turbulent fluid would

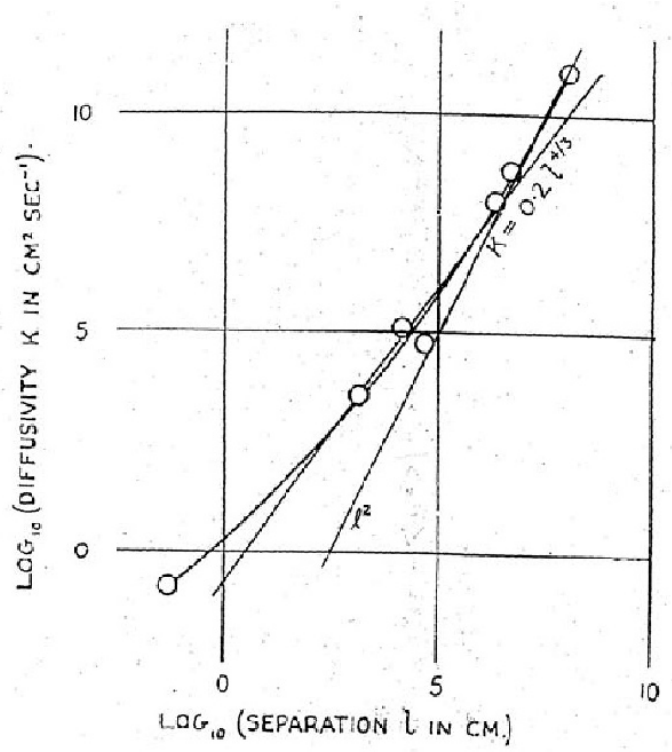

Figure 9. Log $\mathcal{D}$ vs. Log ℓ from [6]. Also shown is Richardson's fit, $\mathcal{D} = 0.2\ell^{4/3}$, and a line $\sim \ell^2$.

be dispersed with an effective diffusion coefficient that depended on the size of the cloud itself. Specifically, he proposed that $\mathcal{D} \sim \ell^{4/3}$ where ℓ is the lengthscale of the cloud. Because $\ell^2 \sim \mathcal{D}t$ then $\ell^2 \sim \ell^{4/3}t$ so we have $\ell^2 \sim t^3$ and hence superdiffusion with $\nu = 3/2$. To understand this result we can use Kolmogorov type arguments for inertial range scaling of turbulence to derive this result. Assuming that only the energy cascade rate ϵ and the lengthscale ℓ are the important parameters for turbulent diffusion and using dimensional analysis we find

$$\mathcal{D}(\ell) \sim \epsilon^{1/3}\ell^{4/3}. \tag{4.1}$$

Richardson [6] found that for the global atmosphere

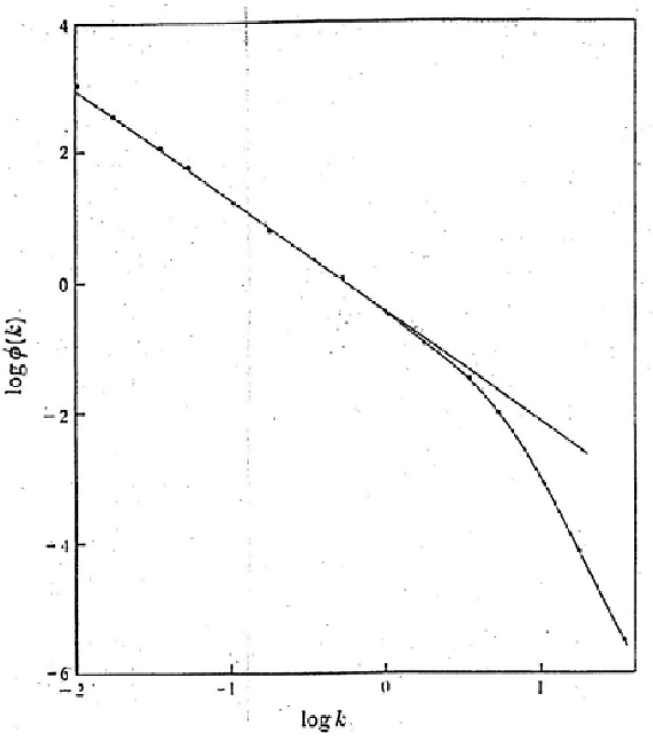

Figure 10. Energy spectrum ($\phi(k) = E(k)$) from the measurements of [8]. The straight line has slope -5/3.

$$\mathcal{D}(\ell) = 0.2\ell^{4/3} \tag{4.2}$$

with ℓ measured in cm and D in cm^2/sec (See Fig. 9). Note that the growth rate $\ell^2 \sim t^3$, is even faster as than the "ballistic" case $\ell^2 \sim (vt)^2$. This is a result of the fact that as the cloud grows in size, larger more energetic eddies participate in the dispersion and this effect will continue as long as ℓ remains within the inertial range of 3D turbulence where the energy sprectrum $E(k) \sim k^{-5/3} \sim \ell^{5/3}$. See Fig. 10.

As discussed by C. E. Leith (private communication 1999), Richardson's data for the larger lengthscales seems better fitted by $\mathcal{D} \sim \ell^2$ (Fig. 9). This result is consistent with the notion that the largescale global atmospheric motions fall with the inertial range for 2D turbulence. In this case, the

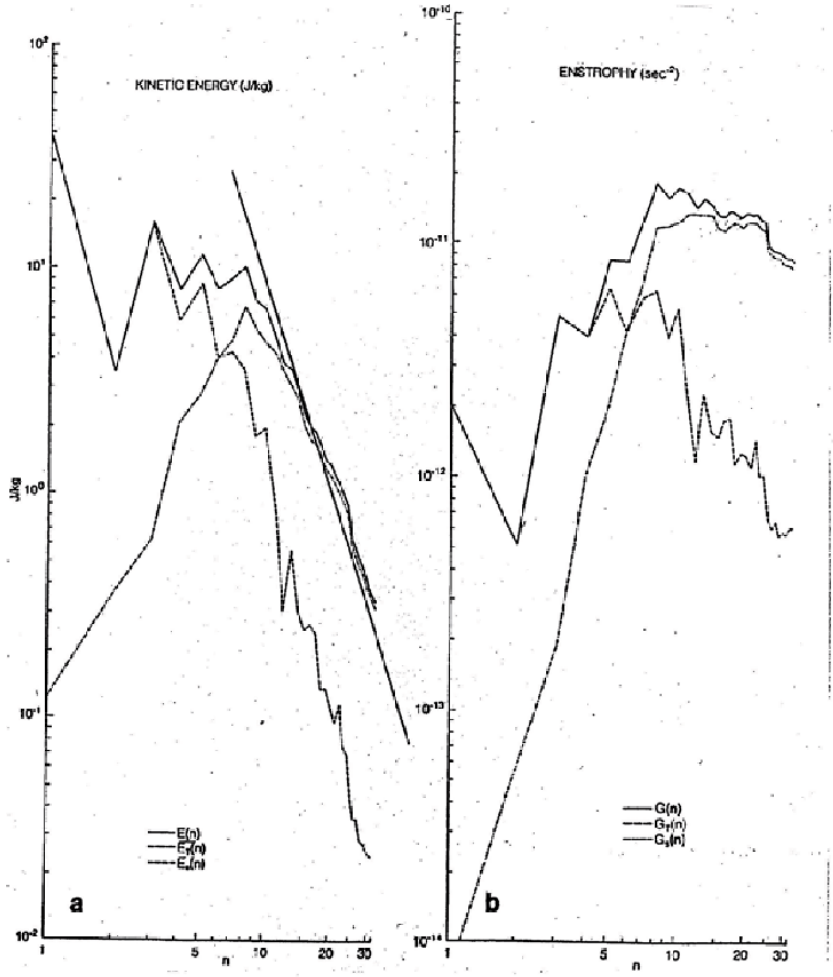

Figure 11. Spectra of largescale motions in the atmosphere ([9]) (a) kinetic energy (b) enstrophy.

enstrophy cascade rate, η, with dimension $[T^{-3}]$ combines with ℓ to yield

$$\mathcal{D}_{2D} \sim \eta^{1/3}\ell^2 \tag{4.3}$$

so that we have superdiffusion with $\nu \to \infty$ within the enstrophy cascade range. For this range $E(k)_{2D} \sim k^{-3} \sim \ell^3$ (see Fig. 11) so evidently the eddy energies grow so fast with increasing ℓ to give this curious result.

However, a more careful dimensional analysis for the case of dispersion within the enstrophy cascade range of 2D turbulence gives

$$\frac{d\ell}{dt} \sim \eta^{1/3}\ell \tag{4.4}$$

so that ℓ is exponential in time $\ell = \ell_0 \exp(C\eta^{1/3}t)$. Thus, we can write

$$\ell^2 \sim \frac{\eta^{1/3}\ell^2 t}{\log(\ell/\ell_0)} \tag{4.5}$$

giving us a log correction to (4.3),

$$\mathcal{D}_{2D} \sim \frac{\eta^{1/3}\ell^2}{\log(\ell/\ell_0)}. \tag{4.6}$$

In Pasmanter (1988)[7] anomalous diffusion is discussed for various types of flow. In this article results for the growth of pollutant clouds in the sea are reproduced and are shown in Fig. 12. Here $\sigma_{xy}^2 \sim \ell^2$ is plotted vs. t on a log-log scale for seven different types of sea flows. Note that case A, dispersion in shallows seas, shows nearly regular diffusion ($\ell^2 \sim t^{0.96}$) while case C, dispersion in the open sea, shows a result close to Richardson diffusion ($\ell^2 \sim t^{2.87}$). Other cases fall between these two.

5 Convection-diffusion with lagrangian chaos

In this Section, we investigate convection-diffusion in the presence of lagrangian chaos. In such flows, some particle paths are unstable in the sense that two nondiffusing particles, initially separated by an infinitesmial distance δ_0, will separate exponentially in time, i.e. $\delta(t) = \delta_0 e^{\lambda t}$. As we shall see, such chaos can have a dramatic effect on the convective transport with or without diffusion.

5.1 Time-dependent Rayleigh-Bénard convection

We illustrate the effect of lagrangian chaos with the example flow of time-dependent Rayleigh-Bénard convection (Camassa & Wiggins (1991) [10]).

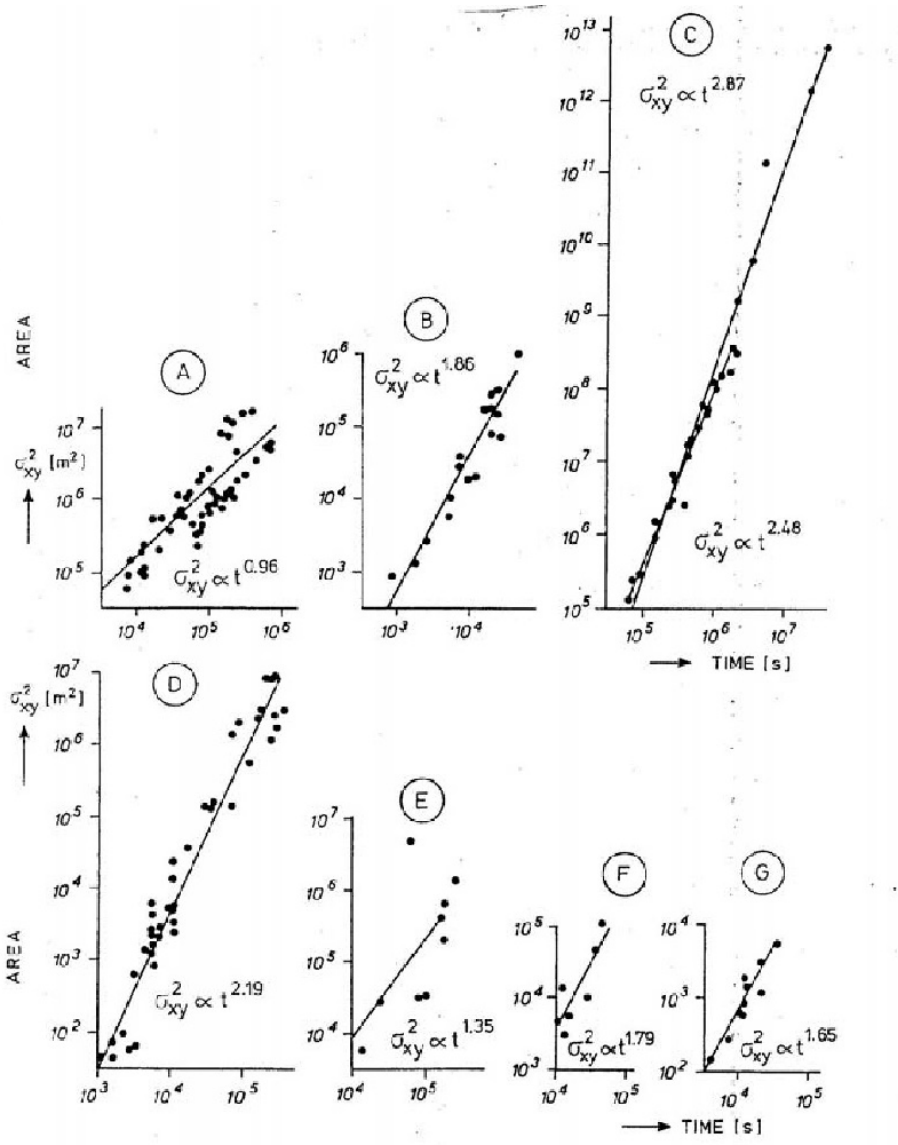

Figure 12. Average square size of pollutant clouds in the sea as a function of time: (A) shallow seas, (B) English estuaries, (C) open sea, (D) American coastal waters, (E) American estuaries, (F) Baltic coast, (G) fjords. [7]

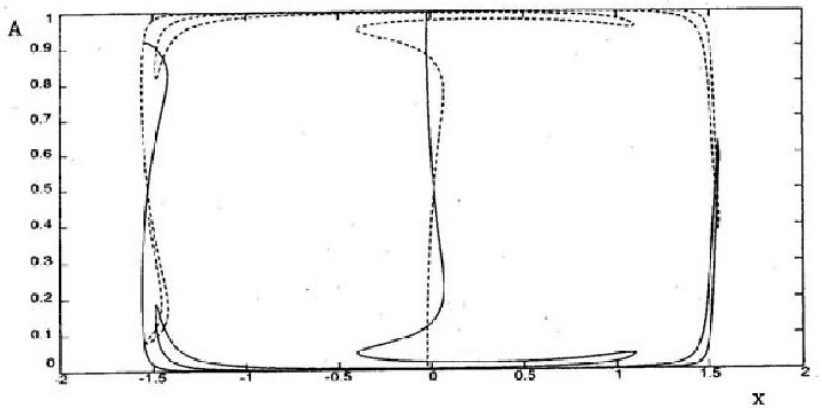

Figure 13. Stable (solid) and unstable (dashed) manifolds close to the line $x = 0$ with $\epsilon = 0.1$, $\omega = 0.6$, $U = 0.1$. [10]

If the temperature difference between the top and bottom of an array of convection cells is increased past a critical value, a time-periodic instability occurs. A model for this flow is (Solomon & Gollub (1988) [11])

$$u(x, y, t) = -\frac{U\pi}{k} \cos \pi y (\sin kx + \epsilon k \cos \omega t \cos kx) \quad (5.1)$$

$$v(x, y, t) = U \sin \pi y (\cos kx - \epsilon k \cos \omega t \sin kx) \quad (5.2)$$

where U is a typical vertical velocity and k is a wavenumber in x. The small parameter ϵ is proportional to $(R - R_c)^{1/2}$ where R is the Rayleigh number and R_c is the critical Rayleigh number.

If $\epsilon = 0$ we have steady 2D cellular flow similar to the model flow of Section 2. In the present case, vertical separatrices occur at locations $x = 0, \pm\pi/k, \pm 2\pi/k, ...$ Nondiffusive particles would orbit within two consecutive vertical separatrices and never escape. If such a particle is on the separatrix, say at x = 0, then, in infinite time, it will reach the hyperbolic stagnation point at $(0, 1)$. Thus the vertical line $x = 0$ is both a segment of the stable manifold of the stagnation point $(0, 1)$ and the unstable manifold of the stagnation point $(0, 0)$. If diffusive effects at high Pe are included then elements within a thin layer next to a separatrix have a chance to escape to the next cell as discussed in Section 2.

To consider the time-dependent case, $\epsilon \neq 0$, it is useful to consider the Poincaré map, $\mathcal{F}$, for this time-periodic flow. The Poincaré map displays the

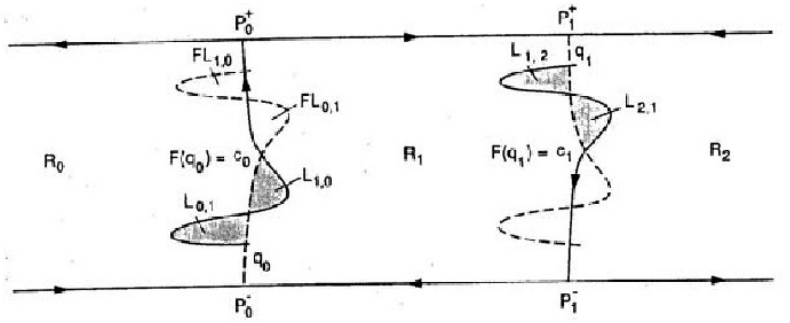

Figure 14. Turnstile lobes between cells R_1 and R_0. [10]

locations of particles at periodic intervals in time, $T = 2\pi/\omega$, corresponding to the period of the velocity field. It is particularly useful for our purposes to display all such positions for particles lying on the unstable and stable manifolds of hyperbolic stagnation points in the Poincaré map. In Fig. 13 we show parts of two such manifolds for the present case. Note, for example, that the unstable manifold shown emanates smoothly from its hyperbolic point near $(0, 0)$ but oscillates wildly near the point $(0, 1)$. The stable manifold for the point near $(0, 1)$ acts in similar fashion with respect to the critical point near $(0, 0)$.

Consider two sequential points where the unstable and stable manifolds intersect. It is clear that such pairs will map to another such pair under the action of the map $\mathcal{F}$. Thus, the segment of the unstable manifold and the segment of the stable manifold that connects these points define a "lobe" of material that is mapped in corresponding fashion (see Fig. 14). For example the lobe $L_{0,1}$ in cell R_0 is mapped to lobe $\mathcal{F}L_{0,1}$ which may be defined to be in cell R_1. On the other hand, as seen in Fig.14, $L_{1,0}$ of cell R_1, is mapped to $\mathcal{F}L_{1,0}$ in cell R_0. Corresponding transfers between cells R_1 and R_2 are also shown. For this incompressible flow all lobe areas are equal.

Higher iterates of such "turnstile" lobes become very elongated, filamentary structures. See $\mathcal{F}^k L_{1,0}$ in Fig. 15 for $k = 0, 1, 2, 3$. Observing the intersection of such lobes with other turnstile lobes reveals how transfer from cell to cell takes place. For example, note that $\mathcal{F}L_{1,0}$ resides completely in within cell R_0 being transferred from cell R_1. However, a portion L_f of $\mathcal{F}L_{1,0}$ is within the turnstile lobe $L_{1,0}$ and therefore, will be transferred to cell R_{-1} at the next iterate. A detailed account of this lobe transport process for this application is given in Camassa & Wiggins (1991)

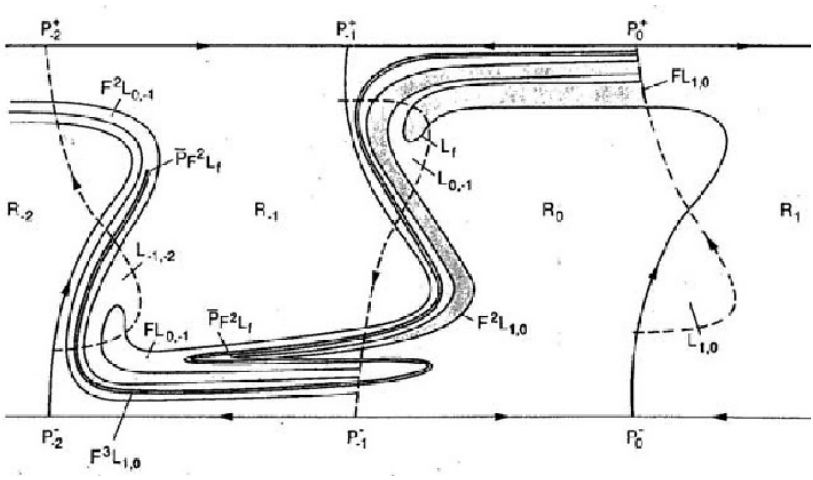

Figure 15. Iterates of the lobe $L_{1,0}$. [10]

[10]. (Hereafter referred to as CW.) A more general theoretical development appears in Rom-Kedar & Wiggins (1990) [12].

Particle motions within these lobes are clearly chaotic given the exponential rate of elongation of their boundaries. See Fig. 15. Thus, we might expect to model the lobe transport in this application by an effective diffusion process with diffusion coefficient

$$\mathcal{D} \sim \frac{\mathcal{A}_L}{T} \tag{5.3}$$

where $\mathcal{A}_L$ is the lobe area. CW compute the lobe area using Melnikov theory. They find that (converting to dimensional units)

$$\mathcal{A}_L = 2\epsilon H^2 sech \frac{\omega H}{2U} \tag{5.4}$$

where H is the cell height. Using values roughly corresponding to Solomon & Gollub's experiment [11]: $\epsilon = 0.1$, $\omega = 0.6 sec^{-1}$, $U = 0.1 cm/sec$, and $H = 1cm$, we find $\mathcal{A}_L \approx 0.02 cm^2$. With $T = 2\pi/\omega \approx 10 sec$ we have $\mathcal{D} \approx 0.002 cm^2/sec$. The molecular diffusion coefficient D for Solomon & Gollub's experiment[11] is $D \approx 5 \times 10^{-6} cm^2/sec$. The ratio is $\mathcal{D}/D \approx 400$. Thus, we expect, on short timescales, that the addition of molecular diffusion to the lobe transport mechanism would have little effect. However, if we consider a diffusion timescale, T_{diff}, defined by D and maximum lobe width $d(\epsilon)$ then

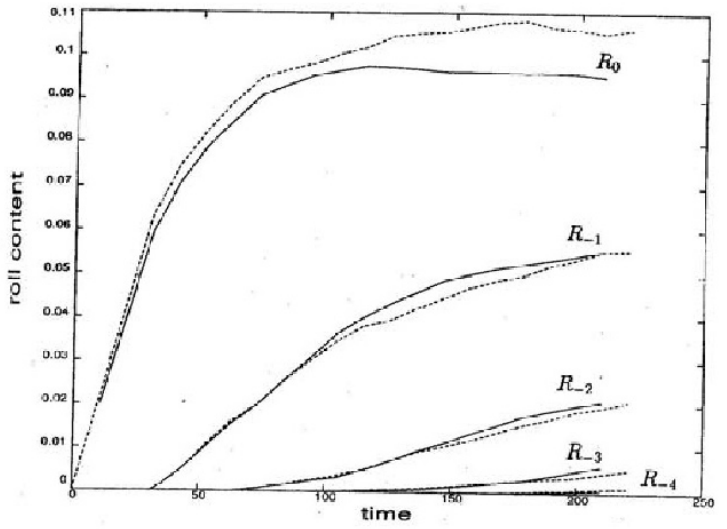

Figure 16. Results for no molecular diffusion (solid) and with molecular diffusion (dashed), $\epsilon = 0.1$, time in number of periods. [10]

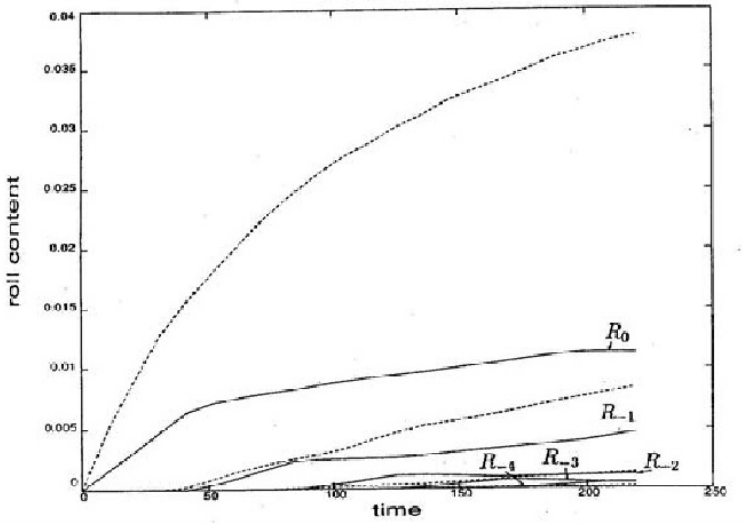

Figure 17. Results for no molecular diffusion (solid) and with molecular diffusion (dashed), $\epsilon = 0.01$, time in number of periods. [10]

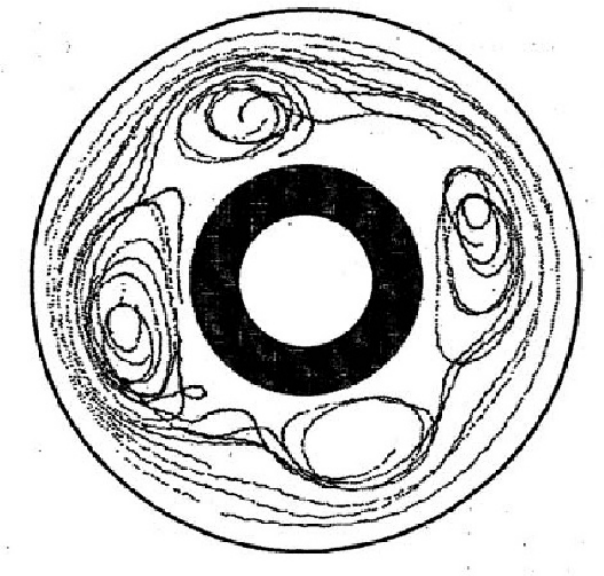

Figure 18. Paths of 100 sec long trajectories of 12 particles. [13]

$$T_{diff} = \frac{d(\epsilon)^2}{D} \approx 2000 sec, \tag{5.5}$$

where we have used the result $d(\epsilon) = \epsilon\omega H/U sech(\omega H/2U)\cosh(\pi^2 U/2\omega H)$ as computed by CW. Hence we would expect to see a significant effect of the addition of molecular diffusion at this longer timescale. Because T = 10 sec., we expect to see the effect at 200 periods. Results of corresponding numerical experiments by CW are shown in Fig. 16. We see that this estimate is roughly correct. In Fig. 17 computations for the case $\epsilon = 0.01$ are shown. All other parameters are the same as the previous case. Here $T_{diff} \approx 20 sec.$ Thus, diffusion effects should become apparent at approximately 2 periods. This estimate seems to work for cell R_0 but is too low for cell R_{-1}.

5.2 Lévy flights

In some applications, a diffusive particle can escape after being stuck in one cell and then make a long ballistic flight to another cell or, perhaps, back to the same cell. In Fig.18 such flights are depicted from the experiments of

H. Swinney's group (Weeks et al. (1996) [13]). They found that flight time and sticking time probability distribution functions (PDFs) have power law decays: $P(t) \sim t^{-\mu}$ and $t^{-\nu}$, respectively. If the flight time PDF decays slowly such that $\mu < 3$ then one obtains superdiffusion and the distribution function for $|\boldsymbol{r}(t)|^2$ is a Lévy distribution. For a slowly decaying sticking time PDF ($\nu < 3$) either subdiffusion or superdiffusion can occur. For $\mu > 3$ and $\nu > 3$ normal diffusion is recovered.

6 Numerical simulation techniques and applications

In this Section we discuss various approaches to simulate numerically the advection-diffusion equation. The approach taken will usually depend on: (1) if the Peclet number is large and (2) if the velocity field must be simulated simultaneously.

6.1 Methods for Large Pe

In the case of large Pe, significant gradients in the scalar field ϕ will typically be confined to thin sheets that move with the fluid. If F is the strain tensor for a particle located on the sheet then the axes of maximum and intermediate principal strains will (nearly) lie in the plane of the sheet. The local sheet area will have expanded by a factor $e^{(\lambda_1+\lambda_2)t}$ where λ_1 and λ_2 are the first and second finite-time Lyapunov exponents of the local strain tensor. Gradients along axes of positive strain are greatly reduced as discussed in Section 2. Perpendicular to the sheet, gradients will be greatly enhanced by the compressive effect. As discussed in Section 2, the layer thickness δ will scale as $\delta \sim \sqrt{D/\epsilon_\perp}$ where

$$\epsilon_\perp \approx \frac{1}{t}\int_0^t -\lambda_3(t')dt' = \frac{1}{t}\int_0^t (\lambda_1(t') + \lambda_2(t'))dt'. \tag{6.1}$$

For small D, or large Pe, it is not usually practical to capture the behavior of such thin moving surfaces with a fixed grid system. The total number of grid points must be $O((\mathcal{L}/\delta)^d)$ where d is the number of dimensions and $\mathcal{L}$ is the scale of the computational domain. An exception to this requirement is a grid method employing adaptive mesh refinement or AMR. Here sharp interfaces are "detected" or tracked and temporary localized blocks of fine meshes are embedded in the basic coarse mesh encompassing the interface.

The use of lagrangian methods can eliminate the use of a mesh system altogether. For example diffusive elements can tracked by Eq (2.29) with diffusive effects modeled by Brownian motion as illustrated in Sections 2 and 5. However, if accurate results are required, an extremely large number

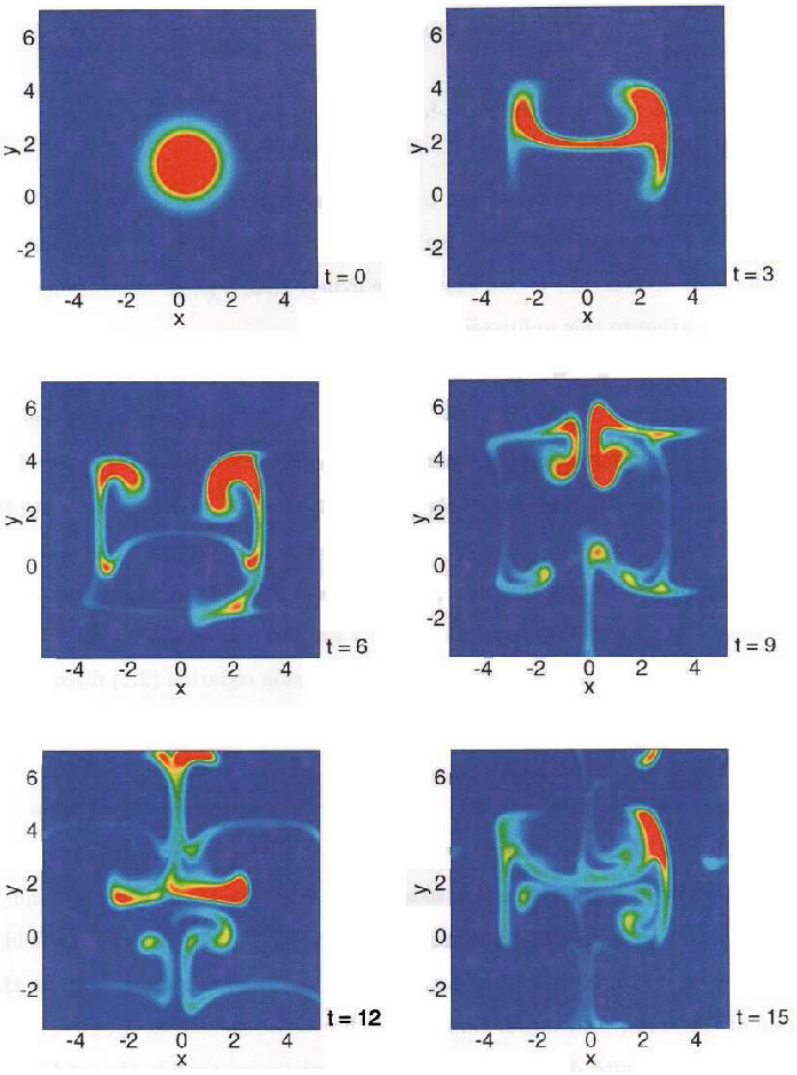

Figure 19. Convection-diffusion simulation using a particle method. Unsteady cellular flow.[14]

N of particles would be required because the error is proportional to $1/\sqrt{N}$, i.e., convergence is very slow with increasing N.

A typical deterministic lagrangian particle method of interest consists of representing the scalar field as sum of scalar blobs:

$$\phi(\boldsymbol{x},t) = \sum_i \frac{a_i e^{|\boldsymbol{x}-\boldsymbol{x}_i(t)|^2/\sigma^2(t)}}{(\sqrt{\pi}\sigma)^d}. \tag{6.2}$$

Here the blobs move with the fluid

$$\frac{d\boldsymbol{x}_i}{dt} = \boldsymbol{u}(\boldsymbol{x}_i(t),t), \tag{6.3}$$

and the core diameter satisfies

$$\frac{d\sigma^2}{dt} = 4D. \tag{6.4}$$

As discussed in Section 2, (6.4) satisfies the diffusive effects exactly in a deterministic fashion. Unless $\sigma^2 \to 0$ there is a convective error involved in the use of (6.3) which is zero only for a point particle. This error is $O(\sigma^2(\partial u_i/\partial x_j)\partial^2\phi/\partial x_i\partial x_j)$. In addition, the particles must, periodically, be redistributed onto a regular array of particles with $\sigma^2 = \sigma_0^2$ for one or both of the following reasons: (1) The $\sigma^2(t)$ become too large because of (6.4), (2) because of the accumulated strain the particles become stretched apart in some directions and with further stretching (6.2) would no longer be an accurate representation of ϕ.

Figure 19 (Moeleker & Leonard, (2001) [14]) shows a typical computation using the above deterministic particle method. The flow is similar to the oscillating Rayleigh-Bénard flow of Section 5 except that chaotic transport takes place vertically instead of horizontally. Here $D = 0.001$ and $Pe = \pi/D \approx 3,000$. A similar such flow was benchmarked by a second-order finite-difference method and required an 800x800 mesh (640,000 pts.). In the lagrangian simulation 6000 particles were used at t = 0 and that number grew to about 25,000 due to the redistribution process. The finite-difference computation took about 150 times longer in cputime.

6.2 Flame sheet problem

In some applications it may be advantageous to track surfaces of interest by lagrangian methods. Figure 20 depicts a simplified flame sheet problem. The sheet separates two reactants A and B. The stoichiometry of the reaction is such that equal masses of each reactant are consumed at the infinitely thin reaction zone on the flame sheet. A material point $\boldsymbol{p}$ on

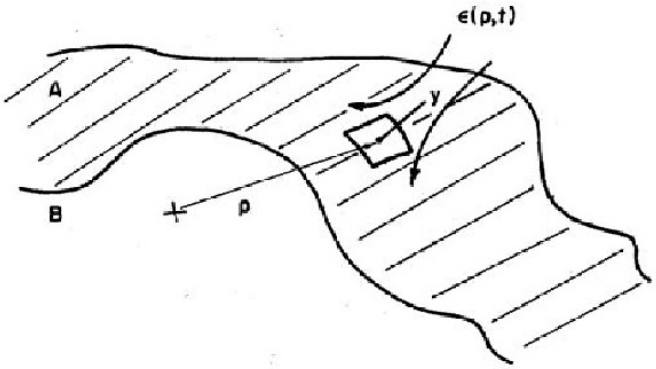

Figure 20. Flame sheet geometry. [15]

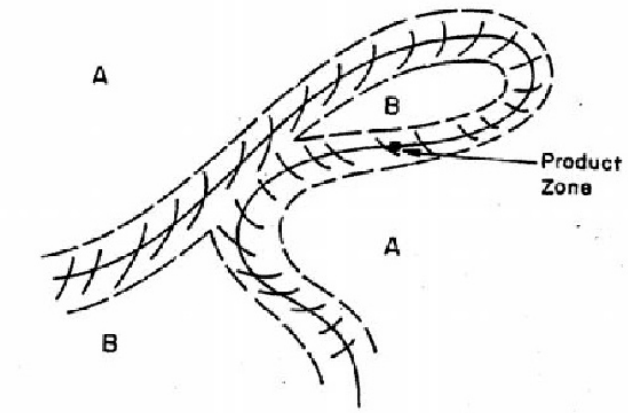

Figure 21. Overlapping of product zones. [15]

the sheet moves with velocity of the flow. Let y be a relative coordinate normal to the sheet at $\boldsymbol{p}$ into the space containing A. See Fig. 20 taken from Leonard et al. (1987) [15]. For a thin flame we require only the first term in the Taylor series for the relative convection velocity in the direction normal to the flame sheet. Thus the conservative equation for the mass fraction of reactant A, Φ_A, is

$$\frac{\partial \Phi_A}{\partial t} - \epsilon y \frac{\partial \Phi_A}{\partial y} = D \frac{\partial^2 \Phi_A}{\partial y^2} \tag{6.5}$$

where D is the diffusion coefficient and $\epsilon(t)$ is the stretching rate of the sheet at $\boldsymbol{p}$. This problem may be transformed into the familiar diffusion equation using the methods of Section 2. We find that

$$\Phi_A(\boldsymbol{p}, y, t) = erf[\frac{S(t)y}{\sqrt{4D\tau}}] \tag{6.6}$$

where S and τ are defined in terms of $\epsilon(t)$ as in Section 2. Thus, except for the important proviso to be discussed below, the reactant consumption rate per unit initial area and the volume of reactant consumed per unit initial area at $\boldsymbol{p}$ can easily be computed from (6.6) [15].

The results given above, however, are only valid up to the point when the zone of the product at $\boldsymbol{p}$ "collides" with the product zone of another point on the sheet. See Fig. 21. Thus one must factor in this sort of information for a general result.

Figure 22 shows the result of such a model computation in 2D with finite-reaction-rate chemistry (Chang et al. (1991) [16]). The model uses the assumption of self-similar internal structure within the thin reaction zone to compute the evolution of reactant, product, reaction rate, and temperature locally along each point on the sheet. Comparisons with full 2D time-grid simulations are good. See Fig. 23.

6.3 Turbulent Diffusion at Moderate Re and Pe

If one is simulating a turbulent flow including all the important scales of motion, then using the same grid system one can simultaneously directly simulate turbulent diffusion of a passive scalar if the Prandtl number, Pr, or Schmidt number $= \nu/D$, is somewhat less than unity. In other words, the scalar field has stronger gradients than the velocity field when Pr = 1. Alternatively one could lower the Re of the turbulence and study turbulent diffusion at $Pr > 1$.

The results of one such study are shown in Figs. 24 and 25 (Bogucki et al. (1997) [16]). The flow is homogeneous turbulence at $Re_\lambda = 25, 36,$

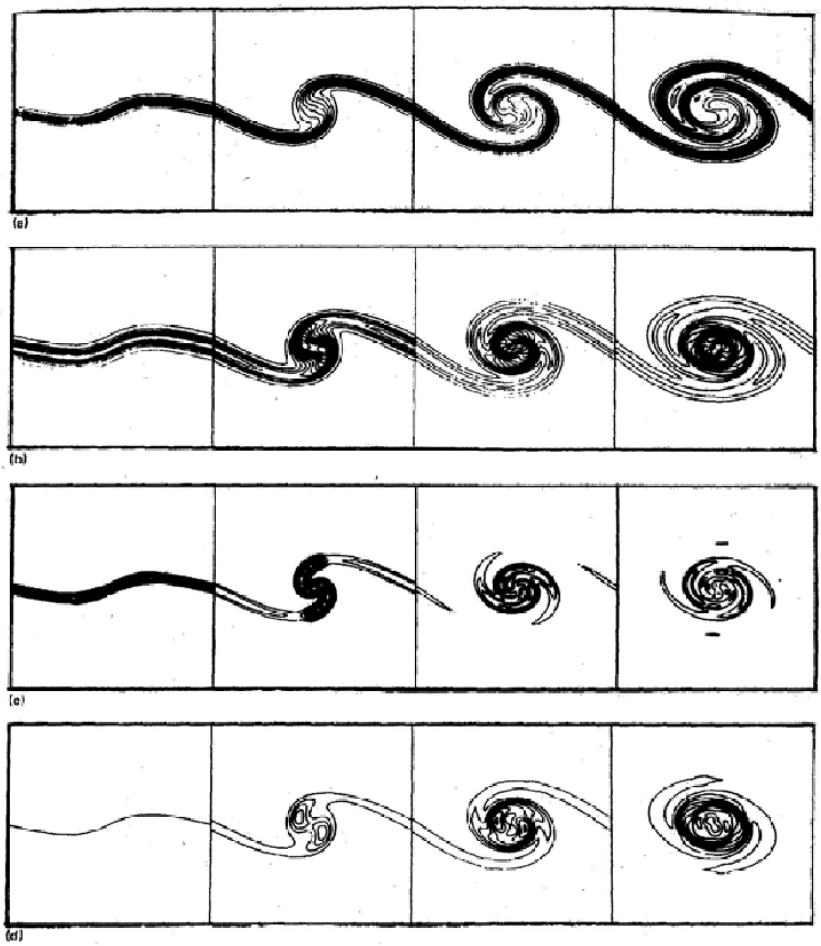

Figure 22. Model results for (a) reactant field, (b) temperature rise field, (c) reaction rate field, (d) product concentration field. [16]

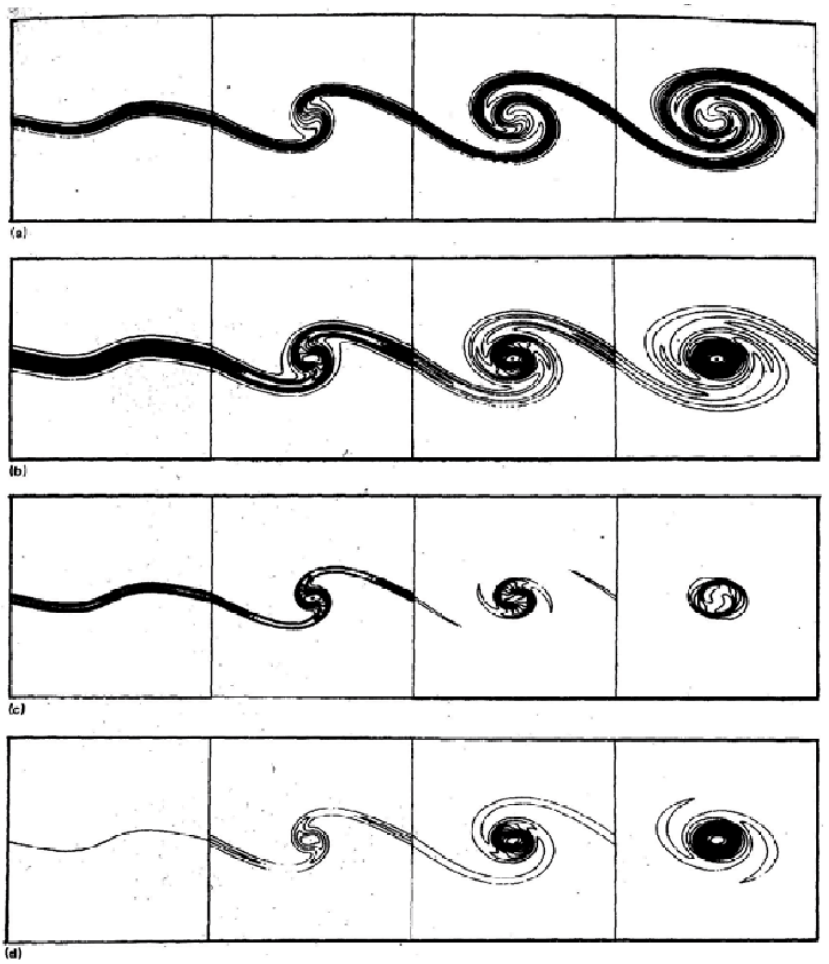

Figure 23. Full finite-difference results for (a) reactant field, (b) temperature rise field, (c) reaction rate field, (d) product concentration field. [16]

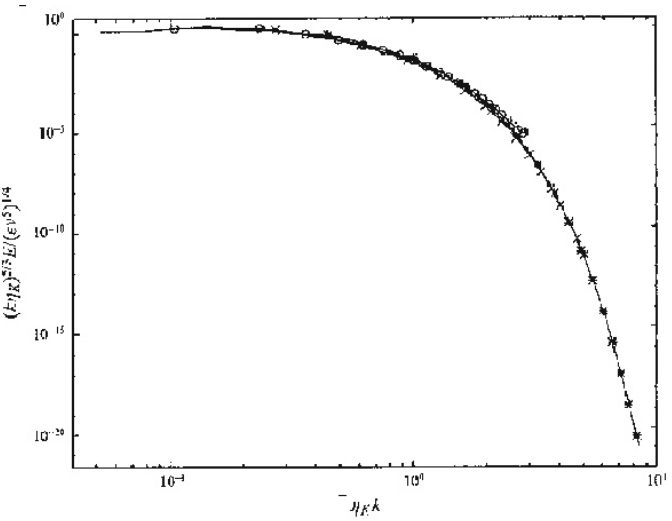

Figure 24. Normalized energy spectra. [16]

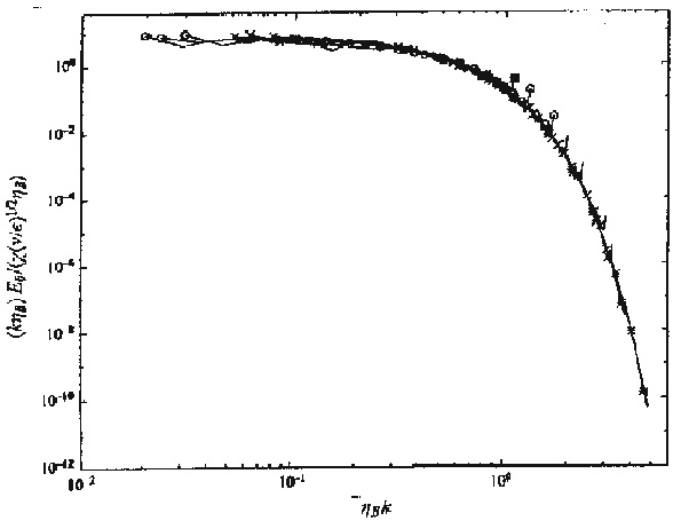

Figure 25. Normalized scalar spectra. [16]

and 77 with $Pr = 3, 5$, and 7. Forcing is applied at low wavenumbers to maintain the turbulence and scalar variance. In Fig. 24 we note that the velocity spectra have a short inertial range (especially visible for the 240^3 simulations in x's) followed by long exponential tail, i.e. the flow is over resolved. Fig. 25 shows all the scalar spectra. They all show a Batchelor spectrum $E_\theta \sim k^{-1}$ of a decade or more followed by an exponential tail.

Bibliography

[1] G. I. Taylor, *Dispersion of Soluble Matter in Solvent Flowing Slowly through a Tube*, In *P*roc. Roy. Soc. A 219, No. 1137, pages 186-203, 1953.

[2] G. I. Taylor, *The Dispersion of Matter in Turbulent Flow through a Pipe*, In *P*roc. Roy. Soc. A 225, No. 1155, pages 446-468, 1954.

[3] A. Crisanti, M. Falcioni, G. Paladin and A. Vulpiani, *Anisotropic diffusion in fluids with steady periodic velocity fields*, In *J.* Phys. A: Math. Gen. 23, pages 3307–3315, 1990.

[4] W. R. Young and S. Jones, *Shear dispersion*, In *P*hys. Fluids A 3 (5), pages 1087–1101, 1991.

[5] G. I. Taylor, *Diffusion by discontinuous movements*, In *P*roc. Lond. Math. Soc. (2) 20, pages 196-212, 1922.

[6] L. F. Richardson, *Atmospheric diffusion shown on a distance-neighbour graph*, In *P*roc. R. Soc. Lond. A 110, pages 709-737, 1926.

[7] R. A. Pasmanter, *Anomalous diffusion and anomalous strecthing in vortical flows*, In *F*luid Dyn. Res. 3, pages 320–326, 1988.

[8] H. L. Grant, R. W. Stewart and A. Moilliet, *Turbulence spectra from a tidal channel*, In *J.* Fluid Mech. 12, pages 241-268, 1962.

[9] G. J. Boer and T. G. Shepherd, *Large-Scale Two-Dimensional Turbulence in the Atmosphere*, In *J.* Atmos. Sci. 40, pages 164-184, 1983.

[10] R. Camassa and S. Wiggins, *Transport of a passive tracer in time-dependent Rayleigh-Bénard convection*, In *P*hysica D 51, pages 472-481, 1991.

[11] T. H. Solomon and J. P.Gollub, *Chaotic particle transport in time-dependent Rayleigh-Bénard convection*, In *P*hys. Rev. A 38, No. 12, pages 6280-6286, 1988.

[12] V. Rom-Kedar and S. Wiggins, *Transport intwo-dimensional maps*, In *A*rch. Rat. Mech. Anal. 109(3), pages 239-298, 1990.

[13] E. R. Weeks, J. S. Urbach, and H. L. Swinney, *Anomalous diffusion in asymmetric random walks with a quasi-geostrophic flow example*, In *P*hysica D 97, pages 291-310, 1996 .

[14] P. Moeleker and A. Leonard, *Lagrangian Methods for the Tensor-Diffusivity Subgrd Model*, In *J.* Comput. Phys. 167, pages 1-21, 2001.

[15] A. Leonard, V. Rom-Kedar, and S. Wiggins, *Fluid Mixing and Dynamical Systems*, In *N*uclear Physics B (Proc. Suppl.) 2, pages 179-190, 1987.

[16] C. H. H. Chang, W. J. A. Dahm, and G. Tryggvason, *Lagrangian model simulations of molecular mixing, including finite rate chemical reactions, in a temporally developing shear layer*, In *P*hys. Fluids A 3 (5), pages 1300-1311, 1991.

[16] D. Bogucki, J. A. Domaradzki, and P. K. Yeung, *Direct numerical simulations of passive scalars with $Pr > 1$ advected by a turbulent flow*, In *J.* Fluid Mech. 343, pages 111-130, 1997.

Lectures on Mixing and Dynamical Systems

Igor Mezić
Department of Mechanical Engineering
University of California, Santa Barbara, CA 93105-5070.

1 Subject and purpose

The subject of fluid mixing is, from the technological perspective, an old one. It is encountered almost daily when we pour milk into coffee or try to achieve a particular paint color. The yearly output of industrial products for which fluid mixing is a part of the production process is measured in billions of dollars. If two fluids are in contact, mixing can proceed purely by molecular diffusion, but it is most commonly achieved by a combination of stretching of fluid interfaces by the macroscopic velocity field and molecular diffusion. Within the subject of fluid mechanics this process has been studied for 100 years, beginning with a paper of Osborne Reynolds. A lot of work has been devoted to non-diffusive mixing in the applied dynamical systems community in the past 20 years, after a seminal paper by Hassan Aref (1984), where he coined the term "chaotic advection" to mean *efficient non-diffusive mixing in flows with simple time-dependence*. Since the 1990's the field of chaotic advection has gained increased attention from (at least) three directions: 1) Scientific investigation of fluid processes at microscale, usually producing flows with simple time-dependence, accompanying the fast technological advances in miniaturization and applications to biology and medicine, 2) Recognition that mixing by large coherent structures can be described using the chaotic advection theory and 3) Increased interest in active control of fluid processes, including control of mixing.

This set of lectures is an attempt to describe a mathematical framework for analysis of fluid mixing for different audiences, with interest in mathematical fluid dynamics and applied dynamical systems, mostly based on directions pursued within my research group. From the perspective of applied dynamical systems, the focal point of the subject is describing mixing properties of solutions of ordinary differential equations satisfying the *incompressibility* (volume-preservation) condition in a three-dimensional space. The incompressibility condition imposes structure for this class of dynamical

systems, but less so than in Hamiltonian systems. As for the mathematical fluid dynamics, the interest mostly lies in understanding the mixing properties of fluid velocity fields satisfying (in addition to incompressibility) the *Navier-Stokes equation of fluid motion* in a bounded domain, given some *fixed boundary conditions*. The goal is a complete description of the change of mixing properties with nondimensional parameters such as the Reynolds number for incompressible, Newtonian, viscous fluids. In control theory the problem of interest is inducing *maximal mixing* by changing the boundary conditions in time or introducing additional time-varying forces e.g. in electrically conducting fluids. This problem is different from the problems of stabilization to a fixed point or some other invariant manifold of the system that are usually discussed in control theory: it is in its essence the problem of *destabilization* and will not be considered in these notes.

Chaotic advection can not exist in planar steady velocity fields - periodic time-dependence is required. In the existing books on the subject of chaotic advection, those of Ottino (1989) and Wiggins (1992) most of the analytical developments are cast in the context of geometrical theory of two dimensional time dependent area-preserving flows. These lectures present a variety of results applicable to three-dimensional flows.

The theory that we describe here is mature: it has been tested in experiments and besides the relevant mathematics we describe how it is used to predict experimental results.

This is supposed to be a set of lecture notes that joins concepts from geometrical dynamical systems theory, ergodic theory and fluid kinematics into a coherent unit. The historically inclined reader might be familiar with the treatise of Truesdell (1954) "The Kinematics of Vorticity" and ponder how are the ideas and methods here different. Firstly, differential geometry and differential topology are used here in the spirit in which they are used in dynamical systems theory. Secondly, relationship is made with the statistical theory of deterministic fluid velocity fields using ergodic theory - both features are absent from Truesdell's work. Thirdly, experimentation has reached a level at which the concepts presented here can be amply illustrated. At the time of Truesdell's writing, there was little interest in Lagrangian properties of fluid velocity fields. That situation has changed dramatically in the past 20 years.

The lectures is intended for an audience of beginning graduate students in applied mathematics or mechanics or advanced undergarduates in the same field interested in "interdisciplinary mathematics". My hope is that active researchers in fluid dynamics and dynamical systems will find the lectures interesting from the point of view of both fields.

I would like to thank the many members of my group that contributed

to various pieces of the work presented here: David Betz, Domenico D' Alessandro, Umesh Vaidya, George Mathew, Frederic Bottausci and Caroline Cardonne. I would also like to thank the collaborators with whom I worked on some of the experiments that are presented: Jerry Fountain, Devang Khakhar, Julio Ottino, Fotis Sotiropoulos and Tom Solomon. Special thanks go to Stefano Rosa who carefully read and suggested numerous improvements and corrections in the manuscript. Finaly, I have benefited from many discussions with the participants of the CISM Workshop, over many years, and with many other members of the "mixing via dynamical systems" community.

2 Geometry and Mixing

The main topic of these lectures is the description of statistical properties of fluid particle motion in terms of the underlying geometrical characteristics. It has been long recognized that fluid flow kinematics (i.e. description of the motion of fluid particles) has connections with statistical mechanics (see Gibbs motivate the ergodic hypothesis in his seminal work on statistical mechanics (Gibbs (1902)) and dynamical systems theory.

2.1 Velocity fields and maps

In dynamical systems one of the key objects of study is a system of ordinary differential equations defined on a phase space. The same holds for fluid particle kinematics, with the phase space being the physical space: if the fluid is contained in a set A which is a closure of an open subset of $\mathbb{R}^3$, motion of a fluid particle in a velocity field v defined in the set A is given by

$$\dot{x} = v(x,t), x \in A, t \in \mathbb{R}, \tag{1}$$

where $x(t)$ is the position of the particle at time t. The solutions of (1) are given by $x(t, x_0, t_0)$, which denotes the position at time t of a fluid particle starting at time t_0 from x_0. Note that this means $x(t_0, x_0, t_0) = x_0$. Equation (1) is a differential equation and thus the question of existence and uniqueness of solutions immediately arises. For example,

$$\dot{x} = x^{1/2}, x \in \mathbb{R}, \tag{2}$$

has two solutions that start at $x = 0$ at time $t = 0$. These are $x(t) = 0$ and $x(t) = (1/4)t^2$ as can be checked by direct substitution. It turns out that the key property of the right-hand side of (2) that allows it to have two solutions starting from the same initial condition is that it does not have a derivative at $x = 0$. In fact, by a standard theorem in the theory of ordinary

differential equations (Arnold (2006)) if the condition

$$|v(x,t) - v(y,t)| \leq c|x-y|, \tag{3}$$

where c is a constant independent of x and y, is satisfied in an open neighborhood of x_0, then there is a time interval I such that $t_0 \in I$ and $x(t, x_0, t_0)$ exists for $t \in I$ and is unique. The condition (3) is called the local *Lipshitz condition*. It requests that the right-hand side of equation 1 does not increase faster than linearly in a domain. The problem is, the described solution might not stay around very long, i.e. it could run off to infinity at some finite time t_c. For example,

$$\dot{x} = x^2, x \in \mathbb{R},$$

satisfies the local Lipshitz condition, but has the solution

$$x(t, x_0, 0) = \frac{1}{1/x_0 - t}.$$

Clearly, for positive x_0 the solution will go to infinity when t goes to $1/x_0$. However, if the Lipshitz condition (3) is satisfied globally (i.e. the same c can be used for all $x, y \in A$), then solutions to (1) exist for all time and are unique.

The velocity fields $v(x,t)$ encountered in theoretical fluid dynamics come from solutions of an evolution equation for $v(x,t)$ such as the incompressible Navier-Stokes equation (Chorin and Marsden (1998))

$$\rho(\frac{\partial v}{\partial t} + v \cdot \nabla v) = -\nabla p + \mu \triangle v, \tag{4}$$

$$\nabla \cdot v = 0, \tag{5}$$

$$\tag{6}$$

where ρ is the fluid density and p the pressure, supplemented by the appropriate initial and boundary conditions on p and v. The question of whether the Lipshitz condition is satisfied for these equations is not resolved in some important situations (Fefferman (2000)).

Geometrically, for fixed t_0, x_0 or for fixed x_0, t the vector $x(t, x_0, t_0)$ depending on time t is a curve in the set A (see figure 1). A vector function of time (a map from $\mathbb{R} \to \mathbb{R}^2$) $\phi_{t_0}^t(x_0) = x(t, x_0, t_0)$ (t_0, x_0 held fixed) is called a *pathline,* while the vector function of initial time $\chi_{t_0}^t(x_0)$, where t, x_0 held fixed and $t_0 \leq t$ is called a *streakline* (see figure 2). By definition

$$d\phi_{t_0}^t(x_0)/dt = v(x(t, x_0, t_0)).$$

In figure 3 a streakline visualization in a three-dimensional flow is shown in a cylindrical container containing a mixture of glycerin and water. The streakline is being visualized by releasing continuously dye particles at a fixed point in space, and physically realized by injection needles shown in yellow.

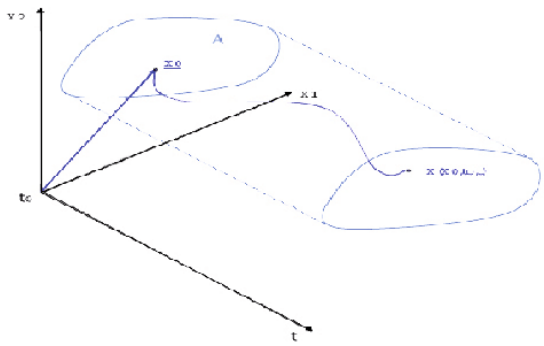

Figure 1. Trajectories starting at x_0 at time t_0 represented in space-time.

If B is a subset of A, we will denote by

$$\phi_{t_0}^t(B),$$

the collection at time t of fluid particles starting in B at time t_0 (see figure 4).

Assume that we know position of a fluid particle at time $t = 0$ and we are interested only in where it moved at time $t = 1$. In this case, the position of the fluid particle at time 1 will be described by a *map* that transforms initial positions at time 0 of points in A into their positions at time 1. This map is defined by

$$x_1 = \phi_0^1(x_0). \tag{7}$$

and transforms A into itself in a one-to-one manner if v is globally Lipshitz. Clearly, for time-dependent velocity fields the map ϕ_0^1 will in general be different from $\phi_{t_0}^{t_0+1}$ if $t_0 \neq 0$.

The dynamical systems theory studies *individual orbits.* Ergodic theory studies *collective, statistical* properties of orbits. It arose from an attempt to justify certain hypothesis necessary to obtain closed-form solutions in statistical mechanics and is thus a statistical theory.

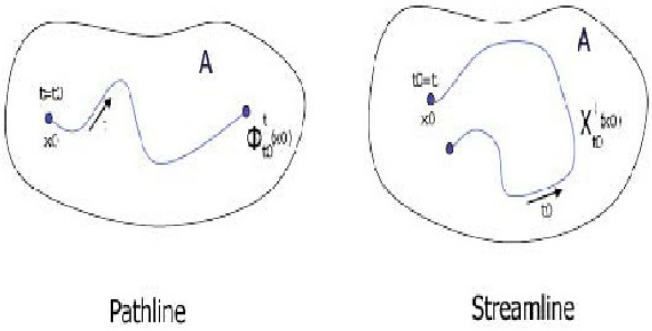

Figure 2. Pathlines and streamlines.

2.2 Incompressible velocity fields

The continuity equation for a fluid of density ρ and velocity v reads

$$\frac{\partial \rho}{\partial t} + \nabla \cdot (\rho v) = \frac{\partial \rho}{\partial t} + v \cdot \nabla \rho + \rho \nabla \cdot v = \frac{d\rho}{dt} + \rho \nabla \cdot v = 0. \tag{8}$$

The first restriction that we will put on v in (1) is the one that comes from the assumption that fluid density is conserved on particle paths, i.e. $d\rho/dt = 0$. This leads to

$$\nabla \cdot v = 0. \tag{9}$$

In fluid mechanics, flows with the Mach number $Ma = \max_{x \in A \times \mathbb{R}} |v|/a \lesssim 0.3$, where $\max_{x \in A \times \mathbb{R}} |v(x,t)|$ is the maximum value of the velocity magnitude are typically treated as "incompressible", meaning that they satisfy the equation (9). The incompressibility condition means that the volume of a moving system of fluid particles is conserved: let $V(t)$ be the volume that the fluid particles occupy as a function of time t. Let $V(t_0)$ be the volume that is occupied by that system of particles at a fixed time t_0 and $S(t_0)$ the surface that bounds that volume, with a unit normal vector field to $S(t_0)$ denoted by n (see figure 5).

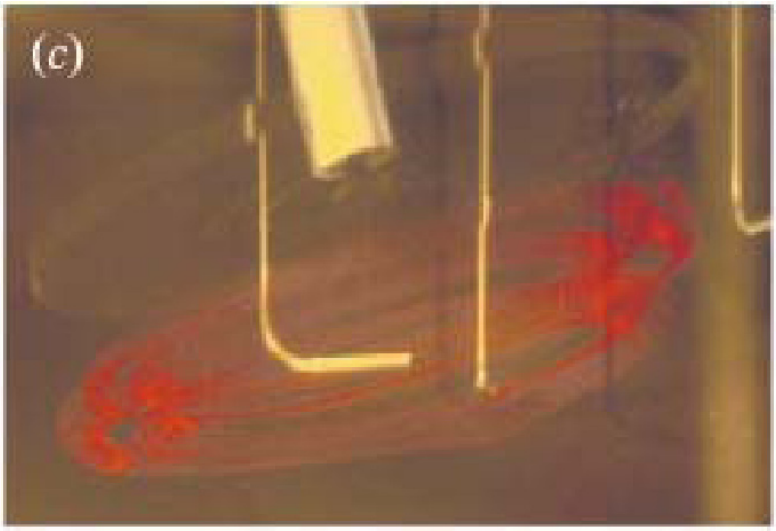

Figure 3. Dye streaklines in experiments of Fountain et al. (2000).

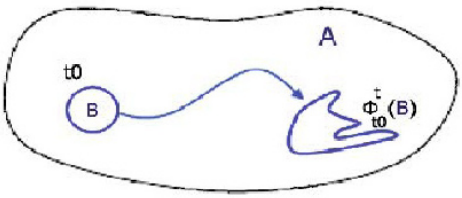

Figure 4. Transformation of a material inside set B by a flow.

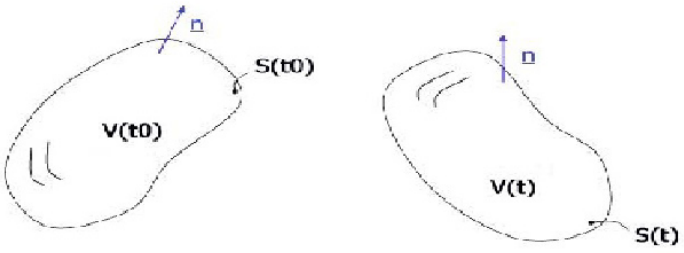

Figure 5. Control volume..

The Reynolds Transport Theorem and the Divergence Theorem (see Wikipedia) applied in the first and second line give

$$\begin{aligned}\frac{d}{dt}|_{t=t_0}\int_{V(t)} dV &= \frac{\partial}{\partial t}\int_{V(t_0)} dV + \int_{S(t_0)} v\cdot n dV \\ &= \int_{V(t_0)} (\nabla\cdot v)\, dV = 0,\end{aligned}$$

As the time t_0 is arbitrary, we have

Proposition 2.1. *Let $v(x,t)$ be a smooth velocity field of a fluid for which density is conserved on particle paths. Let $V(t_1) = \int_B dV$ be the volume of a set B of fluid particles bounded at the time $t = t_1$ by a smooth surface $S(t_0)$. Then $V(t_2) = \int_{\phi^t_{t_0}(B)} dV = V(t_1)$.*

Equation (9) has many important consequences. One of them is that two-dimensional incompressible velocity fields on contractible domains are Hamiltonian dynamical systems (Meyer and Hall (1992)). First note that it is immediate that the existence of a C^2 function $\psi(x,t)$ such that

$$\begin{aligned}\dot{x} &= \frac{\partial\psi}{\partial y}, \\ \dot{y} &= -\frac{\partial\psi}{\partial x},\end{aligned} \tag{10}$$

implies volume preservation as

$$\frac{\partial \dot{x}}{\partial x} + \frac{\partial \dot{y}}{\partial y} = 0.$$

The converse statement - that incompressibility on contractible domains implies existence of a function ψ such that (10) is satisfied is the content of the so-called Poincaré Lemma[1]. The function ψ is called a *streamfunction* and its contour levels at a fixed time t are called *streamlines*. In the case of a steady flow, the function ψ is conserved on particle paths:

$$\frac{d\psi}{dt} = \dot{x}\frac{\partial \psi}{\partial x} + \dot{y}\frac{\partial \psi}{\partial y} = 0.$$

This is the simplest case of the velocity field v being *integrable* - we found a function that is conserved on particle paths and foliates the space into 1-D trajectories.

2.3 Steady and unsteady velocity fields

Steady velocity fields

Steady velocity fields give *autonomous* dynamical systems (i.e. a system of ordinary differential equations whose right hand side is independent of time) of the form

$$\dot{x} = v(x), x \in A. \tag{11}$$

Such velocity fields have particularly nice properties. Let $x(t, x_0, t_0)$ be a solution of (11). Then

$$\frac{dx(t+s, x_0, t_0)}{dt} = v(x(t+s, x_0, t_0)).$$

so $x(t+s, x_0, t_0)$ is a solution of (11) if $x(t, x_0, t_0)$ is. Note the difference with the unsteady case, where

$$\frac{dx(t+s, x_0, t_0)}{dt} = v(x(t+s, x_0, t_0), t+s).$$

The term on the right is not necessarily equal to $v(x(t+s, x_0, t_0), t)$ and so for unsteady (or nonautonomous) velocity fields $x(t+s, x_0, t_0)$ does not have to be a solution if $x(t, x_0, t_0)$ is.

[1] see e.g. http://mathworld.wolfram.com/PoincaresLemma.html

Now $x(t, x_0, t_0)$ is a solution that for $t = t_0$ satisfies $x(t_0, x_0, t_0) = x_0$ and $x(t - t_0, x_0, 0)$ is a solution that for $t = t_0$ satisfies $x(t_0 - t_0, x_0, 0) = x(0, x_0, 0) = x_0$. By uniqueness of solutions they must be the same. More generally, adding a constant to the initial and final time in the solution does not change it: $x(t + s, x_0, t_0 + s) = x(t, x_0, t_0)$. Thus, the following *group property* holds for autonomous systems:

$$\phi_0^{t+s}(x_0) = \phi_t^{s+t}(\phi_0^t(x_0)) = \phi_0^s(\phi_0^t(x_0)) \equiv \phi_0^t \circ \phi_0^s(x_0), \tag{12}$$

for all x_0, t, s, where we have as usual used $\equiv$ to announce that we are defining a new notation. The operation $\circ$ is called the *composition* . The nice feature of (12) is that we can define a $1-$parameter family Φ^t of maps on A, $\Phi^t(x) = \phi_0^t(x)$, the parameter being t, that completely describes the motion of fluid particles under the influence of the velocity field v. In the time-dependent case in general we will be dealing with a two-parameter family, the parameters being the initial and the final time. The $1-$parameter family $\Phi^t(x)$ is called a "flow" in the dynamical systems literature while (unfortunately) "flow" is reserved for the velocity field v in the fluid dynamics literature. The family Φ^t is indeed a *group :*

1. It has an operation, the composition $\circ$ defined above, under which it is closed i.e. $\Phi^t \circ \Phi^s = \Phi^{t+s}$, which is an element of the family,
2. It has the identity element $\Phi^0 = I$, the identity map on A and
3. Every element Φ^t has an inverse Φ^{-t} such that $\Phi^t \circ \Phi^{-t} = \Phi^{-t} \circ \Phi^t = I$.

Some nice properties of solutions of (11) follow from this analysis: While time-dependent (or *nonautonomous*) velocity fields can have solutions that intersect in A - meaning that two fluid particles starting from x_0, y_0 can end up at the same point z at two different times t_0 and t_1, that is impossible for autonomous dynamical systems:

Proposition 2.2. *Let $\phi_{t_0}^t(x_0)$ and $\phi_{t_1}^t(x_1)$ be two different pathlines of (11). Further assume that $x_1 \neq \phi_u^s(x_0)$ for any $s, u \in \mathbb{R}$ i.e x_1 is not on the same pathline as x_0. Then it is impossible that $\phi_{t_0}^u(x_0) = \phi_{t_1}^s(y_0)$ for any s, u.*

Proof. We will prove this by contradiction. Assume that $\phi_{t_0}^{s_0}(x_0) = \phi_{t_1}^{s_1}(x_1)$ for some s_0, s_1. Note that $\phi_{t_1}^{s_1}(x_1) = \phi_0^{s_1 - t_1}(x_1) = \Phi^{s_1 - t_1}(x_1)$. We have (12)

$$\begin{aligned} x_1 &= \Phi^{t_1 - s_1}(\phi_{t_0}^{s_0}(x_0)) = \Phi^{t_1 - s_1}(\Phi^{s_0 - t_0}(x_0)) && (13) \\ &= \Phi^{t_1 - s_1 + s_0 - t_0}(x_0) = \phi_0^{t_1 - s_1 + s_0 - t_0}(x_0), && (14) \end{aligned}$$

which contradicts our assumption. □

Exercise 2.3. Show that if two streaklines in a steady flow that satisfy $\chi^t_{t_0}(x_0) = \chi^t_{t_1}(x_1)$ for some $t_0 \leq t_1$ then $x_1 = \chi^t_{t-(t_1-t_0)}(x_0)$. This implies that in a steady flow, a streakline passing through a point of A is unique.

The above proposition allows for a simple visualization of two-dimensional steady flows. The solution $\phi^t_{t_0}(x_0)$ defines either a curve passing through t_0, x_0 at time t_0 or a single point, if $\phi^t_{t_0}(x_0) = x_0$. Such a point is called a *stagnation point* in fluid dynamics and a *fixed point* in the dynamical sytems literature. Both of these terms carry the same meaning: the fluid particle that is at x_0 does not move from there. Fixed points of a steady velocity field v must satisfy the algebraic equation

$$v(x) = 0. \tag{15}$$

Thus, the set A is foliated into $1-$dimensional curves and points. None of these objects intersect, due to Proposition 2.2. In fact, the considerations above clarify the often-stated remark that "trajectories, pathlines and streaklines are all the same in steady flows".

Steady, two-dimensional velocity fields

In two dimensions the situation is particularly simple. We know that the streamfunction ψ is conserved on particle paths. It turns out that the level sets of ψ are composed of pathlines - we describe this in detail below. To do it, we need introduce the concept of a *manifold* -a key concept in differential topology. We do it first in the context of $1-$dimensional manifolds which will suffice for now.

1-D manifolds and their tangent spaces

Choose a basis for $\mathbb{R}$, a unit vector e such that any other vector $f \in \mathbb{R}$ is given as $f = se$,$s \in \mathbb{R}$. Also, choose an orthonormal basis for $\mathbb{R}^2$, vectors e_1 and e_2 such that any other vector $f \in \mathbb{R}^2 = xe_1 + ye_2$. Recall that C^r map means "$r-$times differentiable" map.

Definition 2.4. A set of points $M \subset \mathbb{R}^2$ is called a C^r $1-$dimensional manifold if for any point $(x, y) \in M$ there is a neighborhood U of (x, y) in M and a C^r map $\varphi : U \to V$ which has a C^r inverse $\varphi^{-1} : V \to U$.

A very important concept related to that of a manifold is its *tangent space* .

Definition 2.5. The tangent space at a point (x, y) of a $1-$dimensional manifold M in $\mathbb{R}^2$ is the line tangent to M at (x, y).

Calculating the tangent space at a point is simple if we know the map φ. As φ^{-1} is a map from $\mathbb{R}$ to $\mathbb{R}^2$ it can be represented by two components, $(\varphi_x^{-1}, \varphi_y^{-1})$. Define the derivative of the map φ^{-1} to be the vector $(\partial\varphi_x^{-1}/\partial s, \partial\varphi_y^{-1}/\partial s)$. The tangent space of M at $(x(s), y(s))$ is $d\varphi^{-1}(\mathbb{R}) = c(\partial\varphi_x^{-1}/\partial s, \partial\varphi_y^{-1}/\partial s), c \in \mathbb{R}$

A simple example of a 1-dimensional manifold in a two-dimensional space is the graph of a function. Let $f{:}\mathbb{R} \to \mathbb{R}$ be a C^r function defined on the real line. The set of points $G(f) = \{(s, f(s)) \in \mathbb{R}^2 | s \in \mathbb{R}\}$ is called the *graph* of f. Let V be any interval on $\mathbb{R}$. It is clear that $U = \{(s, f(s)) \in G(f) | s \in V\}$ is an open subset of $G(f)$, since $U = V \times \mathbb{R} \cap G(f)$, intersection of the open set $V \times \mathbb{R}$ in $\mathbb{R}^2$ with $G(f)$. Define $\varphi : G(f) \to \mathbb{R}$ by $\varphi(s, f(s)) = s$. Clearly this map is C^r and its inverse, given by $\varphi^{-1}(s) = (\varphi_x^{-1}(s), \varphi_y^{-1}(s)) = (s, f(s))$ is also C^r. The derivative $d\varphi^{-1}|_s = (\partial\varphi_x^{-1}/\partial s, \partial\varphi_y^{-1}/\partial s) = (1, df/ds|_s)$. Thus, the tangent space at a point $(s, f(s))$ is given by all the vectors of the form $(c, cdf/ds|_s), c \in \mathbb{R}$. The slope of this line is cleary $df/ds|_s$.

The concept of the manifold was invented exactly as a generalization of the above example to the case of more complicated object that can be represented as graphs of functions "locally" i.e. in a neighborhood of each of their points. General one-dimensional manifolds are grouped in two classes: those that can be smoothly transformed (meaning C^r mapped) to a circle and those that can be transformed to the real line.

Manifolds; Invariant manifolds

Let us first define an $n-$dimensional C^r manifold in analogy with previous definitions for the $1-$dimensional case:

Definition 2.6. A set of points $M \subset \mathbb{R}^m$ is called a C^r $n-$dimensional manifold if for any point $(x, y) \in M$ there is a neighborhood U of (x, y) in M and a C^r map $\varphi : U \to V \subset \mathbb{R}^n$ which has a C^r inverse $\varphi^{-1} : V \to U$.

We also define the *tangent space* of an $n-$dimensional manifold:

Definition 2.7. The tangent space at a point (x, y) of an $n-$dimensional manifold M in $\mathbb{R}^m$ is the set of all the vectors tangent to M at (x, y).

Note that the set of all the vectors tangent to a point of an $n-$dimensional manifold is an $n-$dimensional vector space and thus isomorphic to $\mathbb{R}^n$. In figure 6 the definitions are illustrated in the example of a two-dimensional surface. A single point is a $0-$dimensional manifold, as is a discrete collection of points. Compact manifolds in low dimensions are classified in simple universality classes: for example the only compact $1-$dimensional manifold without boundary is a circle (up to a mapping).

Exercise 2.8. Show that a two-dimensional sphere in $\mathbb{R}^3$ is a $2-$dimensional manifold.

The concept of an *invariant manifold* is a generalization of the pathline concept:

Definition 2.9. Let $v(x)$ be a steady velocity field in A. A C^r manifold $M \subset A$ is called an invariant manifold iff $\Phi^t(M) \subset M$ for every $t \in \mathbb{R}$.

Note that the time in the above dfinition can run both through positive and negative values and thus the fluid particle that is currently at a point $x \in M$ came from a point in M at which it was whenever the motion started and will stay in M for all the future times.

Example 2.10. Consider a steady $3-$dimensional shear flow

$$\begin{aligned} \dot{x} &= z, \\ \dot{y} &= 0, \\ \dot{z} &= 0, \end{aligned}$$

Clearly, the $2-$dimensional manifolds $z = const.$ are invariant. So are $y = const.$

Of course, the concept of a $2-$dimensional invariant manifold is the same as that of a *material surface* in classical fluid mechanics (Truesdell (1954)). $1-$dimensional invariant manifolds are unions of pathlines: It is clear that any union of pathlines is an invariant manifold Let M_1 be a $1-$dimensional manifold. Assume x, y are two points on the same pathline but $x \in M, y \notin M$. This cannot be, as $y = \Phi^s(x)$ for some $s \in \mathbb{R}$. $0-$dimensional invariant manifolds are unions of fixed points: Let M_0 be a $0-$dimensional manifold. Assume $x \in M_0$ but x is not a fixed point. Then M_0 is at least one-dimensional for $v(x) \neq 0$ which, assuming that v is continuous implies that there is an open neighborhood U of x such that $v(x) \neq 0$ on U Assuming in addition Lipshitz property for $v, \Phi^t(x), -u < t < u, u$ small enough, is a part of a unique pathline passing through x contained in U. Given $d\Phi^t(x)/dt = v(x) \neq 0$, this pathline is a C^1 $1-$dimensional manifold.

Manifolds can sometimes be defined by functions that vanish on them. The following theorem tells us when this is true:

Theorem 2.11. *Assume $f(\boldsymbol{x})$ is a differentiable function on $\mathbb{R}^n$. Assume that $\nabla f \neq 0$ on the level set $f = c$. Then the level set is an $n-1$ dimensional manifold in $\mathbb{R}^n$.*

In other words, to show that the set of points defined by $f(\mathbf{x}) = c$ is a differentiable manifold, it is enough to check that the vector of its derivatives does not vanish at every point of that set.

Streamlines, streaklines, pathlines in two-dimensional steady flows

By applying Theorem 6 from differential topology we know that the equation $\psi(x, y) = c$ defines a $1-$dimensional manifold in two dimensions if $|\partial\psi/\partial x| + |\partial\psi/\partial y| \neq 0$ for any x, y that satisfy $\psi(x, y) = c$.

Example 2.12. Take $\psi(x, y) = x^2 + y^2 = 1$ and let's pretend that we do not know this is a circle of radius 1. Note that $|\partial\psi/\partial x| + |\partial\psi/\partial y| = 2|x| + 2|y| = 2|x| + 2|\sqrt{1 - x^2}|$. The first and the second term can not be zero simultaneously, so by the preceeding criterion this equation defines a $1-$dimensional manifold. However, $\psi(x, y) = x^2 + y^2 = 0$ is satisfied only for $x = y = 0$ - not a $1-$dimensional manifold. This is the consequence of the fact that $|\partial\psi/\partial x| + |\partial\psi/\partial y| = 2|x| + 2|y| = 0$.

Streaklines and finite time ($0 \leq t_0 \leq t$) pathlines define the same curve in steady flows. This is clear from their definition: let $\chi_{t_0}^t(x_0)$ be a streakline. We have

$$\chi_{t_0}^t(x_0) = x(t, x_0, t_0) = x(t - t_0, x_0, 0) = \phi_0^{t-t_0}(x_0).$$

Conversely, let $\phi_{t_0}^t(x_0)$ be a pathline. Then

$$\phi_{t_0}^t(x_0) = x(t, x_0, t_0) = x(0, x_0, t_0 - t) = \chi_{t_0-t}^0(x_0).$$

Both pathlines and streaklines are connected sets . Recall that a set is called connected if for any two points a, b in the set there is a continuous path $z(s), s \in [0, 1]$, $z(0) = a, z(1) = b$.Although they are 1-dimensional, the level sets of ψ do not have to be connected.

Example 2.13. Let the streamfunction be given by $\psi = (1/2)y^2 + \cos(2\pi x)$. This is (with appropriate scaling and shifting of the coordinate system) the streamfunction for the so-called Kelvin's 'cat's eye' velocity field The same streamfunction is the Hamiltonian function for the mathematical pendulum. The level sets for ψ are shown in figure 7 on the domain $x \in [-1/2, 1/2), y \in (-2, 2)$.

There are four types of level sets (and thus four types of pathlines): 1) The fixed points at the origin and at $x = 0, y = 0$. 2) Pathlines in the "recirculation zone" around the origin. 3) Separating pathlines given by $y =$

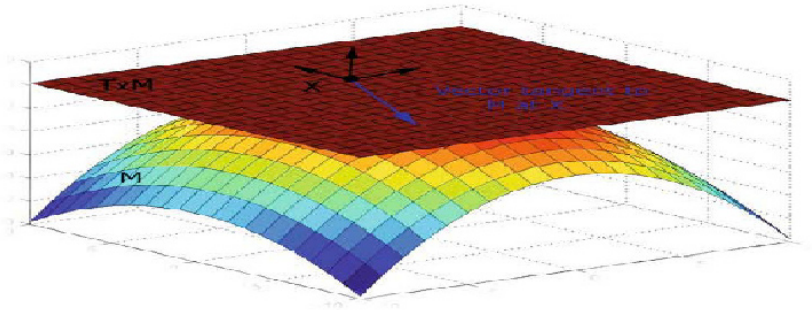

Figure 6. Tangent space to a two-dimensional manifold (a surface).

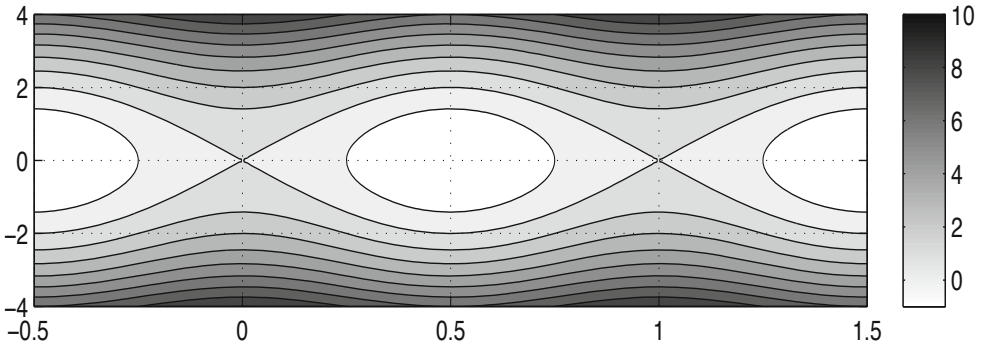

Figure 7. Kelvin's 'cat's eye'.

$\pm 2\sqrt{(1-\cos(2\pi x))}$. 4) Pathlines extending from the left edge ($x=-1/2$) of the domain to the right edge ($x=1/2$) of the domain, above the upper separating pathline and below the lower separating pathline. Note that there is no exchange of type of motion that a fluid particle can perform: if a particle is in the recirculation zone bounded by the separating pathlines (or streamlines), it will never leave that zone. Conversely, if a particle is above the upper separating streamline or below the lower separating streamline, it will never cross into the recirculation zone.

The types of pathlines introduced in the previous example are typical for two-dimensional, steady flows. In the region that contains periodic orbits we can simplify things even further introduce the so-called action-angle coordinates (Wiggins (1992)) I,θ, where $\dot{I}=0,\dot{\theta}=\omega(I)$. I is the area encircled by the periodic orbit and θ is the angular coordinate ranging from 0 to 1 on each orbit.

Because the streamfunction is conserved on particle paths, its level sets are examples of a general concept of *invariant manifolds.* We define them in full generality in the next section. The description of three dimensional incompressible steady velocity fields is more complicated that the two-dimensional case: in general there is no function that is conserved on particle paths except in the cases when the velocity field possesses some symmetry. The motion of particles is thus in general not restricted to stay on two-dimensional level sets of some functions. Given that, very complex behavior can occur. But we will first get a glimpse of complexities that await in the case of unsteady, time-periodic velocity fields.

Fixed points in 2-D steady incompressible velocity fields

Let $\overline{x}=(\overline{x}_1,\overline{x}_2)$ be a fixed point of the $2-D$ steady incompressible velocity field v i.e. $v(\overline{x})=(v_1(\overline{x}_1,\overline{x}_2),v_2(\overline{x}_1,\overline{x}_2))=(0,0)$. Let $x=\overline{x}+y$.The linearization of v around x is obtained by expanding v in Taylor series around $\overline{x}$ and reads a linear system of ordinary differential equations:

$$\dot{y_1}=\frac{\partial v_1}{\partial y_1}(\overline{x})y_1+\frac{\partial v_1}{\partial y_2}(\overline{x})y_2,$$
$$\dot{y_2}=\frac{\partial v_2}{\partial y_1}(\overline{x})y_1+\frac{\partial v_2}{\partial y_2}(\overline{x})y_2.$$

In shorthand, we write this as

$$\dot{y}=Ay, \tag{16}$$

where A stands for the matrix

$$A = \begin{bmatrix} \frac{\partial v_1}{\partial y_1}(\overline{x}) & \frac{\partial v_1}{\partial y_2}(\overline{x}) \\ \frac{\partial v_2}{\partial y_1}(\overline{x}) & \frac{\partial v_2}{\partial y_2}(\overline{x}) \end{bmatrix}.$$

The properties of the motion around $\overline{x}$ are now determined from A. Note first that the trace of A is 0 by the incompressibility of v. The determinant of A reads

$$Det(A) = -\left[\left(\frac{\partial v_1}{\partial y_1}\right)^2 + \frac{\partial v_1}{\partial y_2}\frac{\partial v_2}{\partial y_1}\right](\overline{x})$$

Thus, the eigenvalues of A are given by

$$\lambda_{1,2} = \frac{\pm\sqrt{-4Det(A)}}{2} = \pm\sqrt{\left(\frac{\partial v_1}{\partial y_1}\right)^2 + \frac{\partial v_1}{\partial y_2}\frac{\partial v_2}{\partial y_1}}. \tag{17}$$

The rate of strain tensor at $\overline{x}$ is defined by

$$e_{ij} = \frac{1}{2}\left(\frac{\partial v_i}{\partial y_j} + \frac{\partial v_j}{\partial y_i}\right)(\overline{x}),$$

while the vorticity is given by

$$\omega = \left(\frac{\partial v_2}{\partial y_1} - \frac{\partial v_1}{\partial y_2}\right)(\overline{x}).$$

Physically, it represents the local rotation rate (Aris (1962)). The eigenvalues can be written as

$$\lambda_{1,2} = \pm\sqrt{e_{11}^2 + e_{12}^2 - \frac{\omega^2}{4}}. \tag{18}$$

Irrotational velocity fields are defined by $\omega = 0$. In that case, the eigenvalues of A are given by

$$\lambda_{1,2} = \pm\sqrt{\left(\frac{\partial v_1}{\partial y_1}\right)^2 + \left(\frac{\partial v_1}{\partial y_2}\right)^2}$$

and are real. The phase portrait of 16 close to 0 is shown in figure 8. The eigenvectors of A are found by solving

$$(A - \lambda I)e = 0,$$

for $e \in \mathbb{R}^2$.

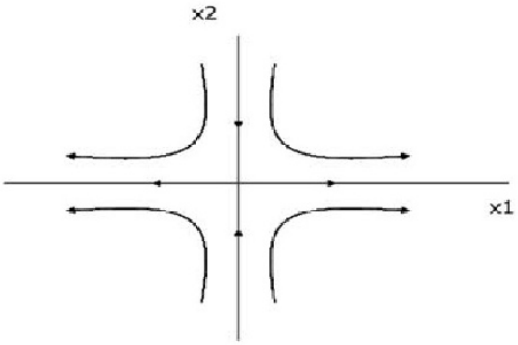

Figure 8. Fixed point with pure strain.

Example 2.14. Consider a steady velocity field

$$\dot{x_1} = \gamma x_1,$$
$$\dot{x_2} = -\gamma x_2,$$

where γ is a constant.

In the case of zero strain rate the eigenvalues are purely imaginary and the phase portrait of 16 close to 0 is shown in figure 9.

Example 2.15. Consider a steady velocity field

$$\dot{x_1} = \frac{\omega}{2} x_2,$$
$$\dot{x_2} = -\frac{\omega}{2} x_1,$$

where ω is a constant.

We found that the eigenvalues of the linearization around a fixed point in a two-dimensional steady incompressible velocity field can be either pure

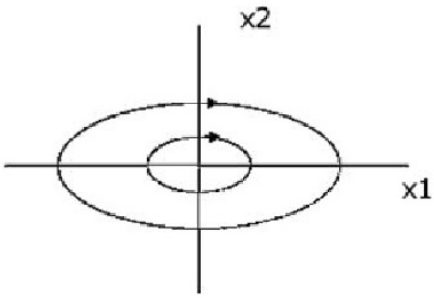

Figure 9. Phase portrait around a fixed point with no strain.

imaginary (and complex conjugate) or real and opposite in sign. This is always so for Hamiltonian systems - but here we were able to connect the phase portrait properties with physical quantities of vorticity and strain.

Steady, two-dimensional, spatially periodic velocity fields

In many situations it is interesting to consider velocity fields that are spatially periodic

$$v(x+l) = v(x), l \in \mathbb{R}^2$$

The simplest of such velocity fields is the constant velocity field

$$\begin{aligned} \dot{x_1} &= \alpha, \\ \dot{x_2} &= \beta, \end{aligned} \tag{19}$$

where $\alpha, \beta \in \mathbb{R}$.This velocity field has very simple properties when viewed on $\mathbb{R}^2$. The pathlines are given by $\phi_{t_0}^t(x_{10}, x_{20}) = (x_{10}+\alpha t-\alpha t_0, x_{20}+\beta t-\beta t_0)$. Fluid particles move along straight lines of the slope β/α. However, if we split the plane into squares of side 1, as shown in figure 10 and identify the top and bottom side and the left and right side of such a square, we obtain

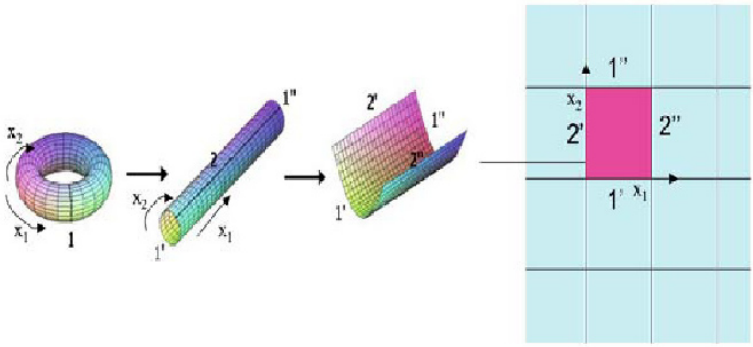

Figure 10. Representation of the torus on the plane.

a torus. Me call this operation is called "modulo 1" or "mod 1". First note that $\alpha = 0$ or $\beta = 0$ imply that all the pathlines on the torus are circles. For $\alpha = 0$, pathlines on the torus are circles $x_1 = c$. For $\beta = 0$, pathlines on the torus are circles $x_2 = d$. Now assume $\alpha \neq 0$. There are two types of motion on the torus that can be induced by the velocity field 19, depending on whether the ratio β/α is rational or irrational. To see this, consider the circle $x_1 = 0$. Point starting at $t_0 = 0$ at $(0, x_{20})$ returns to $x_1 = 0$ after the time $t = 1/\alpha$ and lands at $x_2 = x_{20} + \beta/\alpha$. Thus we can consider a *return map*

$$x_2 \to x_2 + \beta/\alpha, \tag{20}$$

defined on a circle of length 1. We can now consider two cases, the rational and irrational rotation :

1. β/α rational. In this case $\beta/\alpha = p/q$, where $p, q \in \mathbb{Z}$. The map 20 then carries an initial point at x_{20} to $x_{20}^n = x_{20} + pn/q$ in n steps. Equivalently, the velocity field 19 carries an initial point $(0, x_{20})$ to $(0, x_{20} + pn/q)$ after n rotations in the direction of x_1. Clearly, if $n = q$, $x_{20}^n = x_{20}$ as $x_{20} = x_{20} + p$ on a circle of length 1. In the context of the velocity field 19 the pathline starting at $(0, x_{20})$ returns to that point after circling q times in the direction of x_1.
2. β/α irrational. There is clearly no n such that $x_{20} + n\beta/\alpha = x_{20} + p$ as this would imply rationality of $\omega = \beta/\alpha$. Because the map is defined on a circle of length 1, it can be defined as a map $z \to \exp(i2\pi\omega)z$, where $z \in \mathbb{C}$ is a complex number of norm $|z| = 1$. Let us consider the orbit starting from $z = 1$, given by the sequence $\{z_n\}, z_n = \exp(i2\pi n\omega), n \in \mathbb{Z}$. This is a countable sequence in a compact set and thus contains a subsequence $\{z_{n_k}\}$ (where $z_{n_k} = \exp(i2\pi n_k\omega), n_k \in \mathbb{Z}$) that converges as $n_k \to \infty$. Choose $\epsilon = 1/k$ arbitrarily small (i.e. k arbitrarily large). The circle is split into k intervals I_l of length ϵ, one of them being $(1, \exp(i2\pi\epsilon)]$. It is clear then that there is an N such that for $n_{k-1} > N$ $\exp(i2\pi(n_k - n_{k-1})\omega)$ is element of $(\exp(i2\pi\epsilon), \exp(-i2\pi\epsilon))$. Without loss of generality assume $\exp(i2\pi(n_k - n_{k-1})\omega) \in (1, \exp(i2\pi\epsilon))$ for some fixed $n_k, n_{k-1} \in \mathbb{Z}$ (note that $\exp(i2\pi(n_k - n_{k-1})\omega) \neq 1$, as that would imply that the orbit is periodic). Now let $m = n_k - n_{k-1}$ and consider points $s_j = \exp(i2\pi jm\omega), j \in \mathbb{Z}$. The sequence $\{s_j\}$ is clearly a subsequence of $\{z_n\}$. As $0 < (m\omega) \bmod 1 < \epsilon$, there is an s_j inside every interval I_l. But, if we choose an arbitrary interval I on the circle, there is always a sufficiently small ϵ such that one of I_l is a subset of I. Thus, the sequence $\{z_n\}$ is dense in the circle i.e arbitrarily close to any point p on the circle there is an element of the sequence $\{z_n\}$. Clearly, if we consider any other orbit the conclusion is stil valid: an orbit of the map starting at z_0 is just a translation by z_0 of the orbit starting at 1. In terms of the pathlines of the original velocity field 19, this implies that they are dense on the two-dimensional torus: every pathline passes arbitrarily close to any chosen point on the torus.

Clearly, in the case when β/α is irrational the dynamics becomes somewhat complicated. We will se later that such dynamics possesses the property of being *ergodic :* a time average of an arbitrary integrable function f along any orbit of the map is equal to the spatial average of f on the circle. Thus, besides being able to come arbitrarily close to any point on the circle, the orbits of the map sample the circle homogeneously.

In the above considerations, we have, for the first time introduced a method that will be very useful throughout the notes: instead of studying the properties of pathlines of the velocity field, we studied properties of its

Poincaré map-map defined on the circle to which all of the pathlines return repeatedly.

Three-dimensional steady velocity fields; Poincaré maps

Two-dimensional steady incompressible velocity fields on the plane are relatively simple: the level sets of the streamfunction foliate the plane into one-dimensional or zero-dimensional manifolds. In general, there is no a priori smooth function that is conserved on particle paths for three-dimensional, steady flows, except when velocity field has a symmetry as will be described later. With no symmetry, particle motion can be chaotic in three-dimensional, steady fields.

Certainly, it would be simpler to study two-dimensional instead of three-dimensional dynamics. We can achieve this in some situations for three-dimensional velocity fields by introducing the concept of a Poincaré map . In figure 11 we show an orbit of a three-dimensional velocity field piercing through a surface S that we will call a *surface of section*

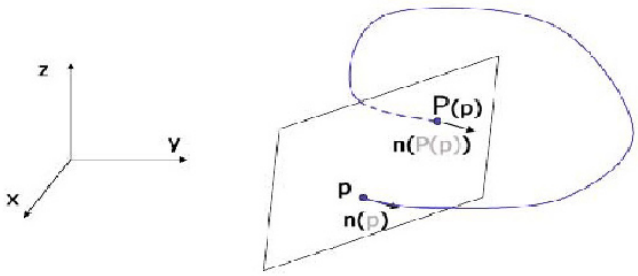

Figure 11. Schematic of the Poincaré map construction in 3D.

Let p, be the point of intersection of a pathline with S. We call the intersection of a pathline with a surface *transversal at* p if $v(p)\cdot n\neq 0$, where n is the outward normal to S at p.

Definition 2.16. A connected surface of section S in A satisfying $v(p)\cdot n\neq 0$ is a two-dimensional C^1 manifold such that every pathline intersecting S transversely at a point p intersects it again at a point that we denote $P(p)$.

Note that connectedness of S and continuity of v implies that $v(p)\cdot n$ does not change sign on S. This definition allows us to define a map $P : S \to S$ that we call a Poincaré map for the velocity field v. We would now like to show that incompressibility of v implies that the map P preserves some *area* in a generalized sense: let $\rho : S \to \mathbb{R}$ be a continuous function. We will call S *area-preserving* if there exists a function ρ such that for any open, simply-connected set $B \subset S$, with the smooth closure $B \cup \partial B$

$$\int_{BU\partial B} \rho dS = \int_{P(B\cup\partial B)} \rho dS.$$

We have

Lemma 2.17. *Let v be a three-dimensional incompressible steady velocity field and S its surface of section. Than the Poincaré map $P : S \to S$ is area-preserving with function $\rho = v \cdot n$.*

Proof. Let the volume V be defined as follows: let $Z = \bigcup_{p\in\partial B} \Phi^{0\le t\le t(p)}(p)$ where $t(p)$ is the time at which the pathline starting at p at time 0 intersects S. The surface $B \cup \partial B \cup Z \cup P(B \cup \partial B)$, bounds the volume V. Reynolds' transport theorem together with volume-preservation than gives

$$\int_{BU\partial B} v \cdot n dS = \int_{P(B\cup\partial B)} v \cdot n dS,$$

which proves the Lemma. □

An example of the surface of section for a vortex breakdown flow is shown in figure 12. A numerical simulation revealing chaotic and regular parts of the surface of section is shown in figure 13. Note that in both of these figures, strictly speaking, only half of the surface (left or right) represents the surface used in the Poincaré map construction. This is because the orientation at which the trajectory is piercing the surface has to be the same for all points on the surface of section.

Unsteady velocity fields

Unsteady velocity fields do not have the nice group property described above. However, we will now learn a useful construction from dynamical systems that will help us significantly in the study of unsteady systems: the concept of *suspension* . Let $\dot{x} = v(x,t) = v(x,t+T)$ be an unsteady, time-periodic velocity field on A with period T. It defines a nonautonomous

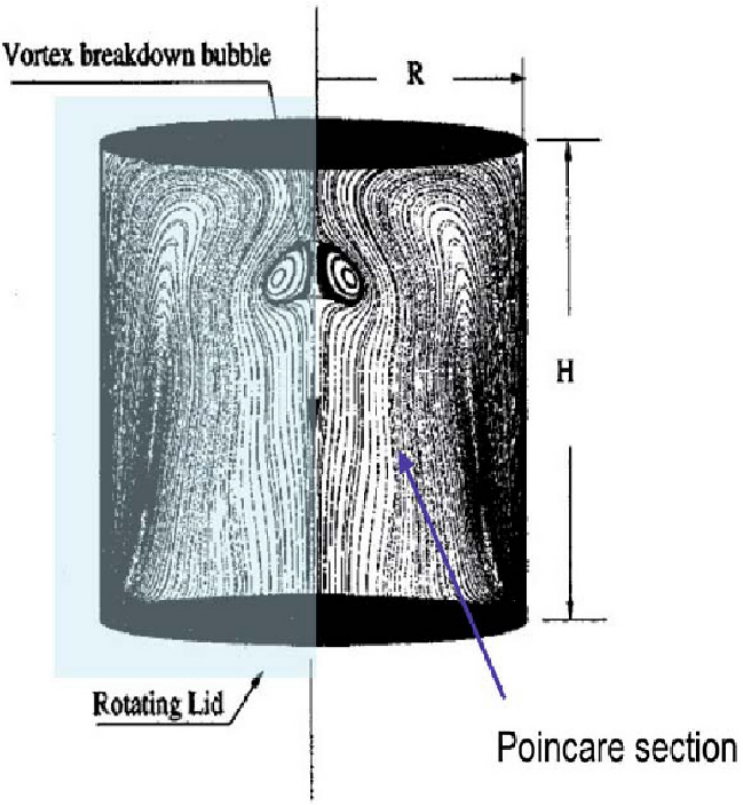

Figure 12. Surface of section in a three-dimensional vortex breakdown flow. Courtesy Fotis Sotiropoulos.

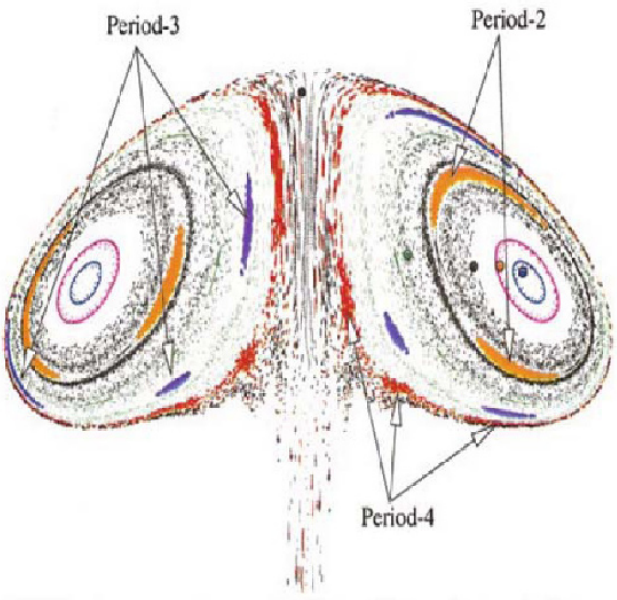

Figure 13. Chaotic surface of section in a three-dimensional vortex breakdown flow. Courtesy Fotis Sotiropoulos.

dynamical system on A. The results that were valid for steady velocity fileds on nonintersection of pathlines do not hold any more. In fact, pathlines can now intersect in general and it is not easy to understand their behavior by plotting a couple of them. The same holds for streaklines. However, at the expense of introducing another dimension, we can recover the simplicity of the steady picture we had before.

Let $x = (x_1, x_2) \in \mathbb{R}^2, \dot{x_1} = v_1(x,t) = v_1(x,t+T), \dot{x_2} = v_2(x,t) = v_2(x,t+T)$ be an unsteady velocity field on $A \subset \mathbb{R}^2$ which is time-periodic

with period T. We can instead consider a velocity field defined by

$$\begin{aligned} \dot{x_1} &= v_1(x,\theta), \\ \dot{x_2} &= v_2(x,\theta), \\ \dot{\theta} &= 1. \end{aligned} \tag{21}$$

on $A \times \mathbb{R}$, this velocity field being steady. Clearly, $\theta(t) = \theta(0) + t$. Thus, $v(x,\theta) = (v_1(x,\theta), v_2(x,\theta), 1) = v(x,\theta+T)$ and the velocity field is spatially periodic in the direction of θ with period T. In this case we can identify the planes $\theta = 0$ and $\theta = 1$ and consider our velocity field as defined on the space $A \times S^T$,where S^T is a circle of length T (see figure 14). A reader

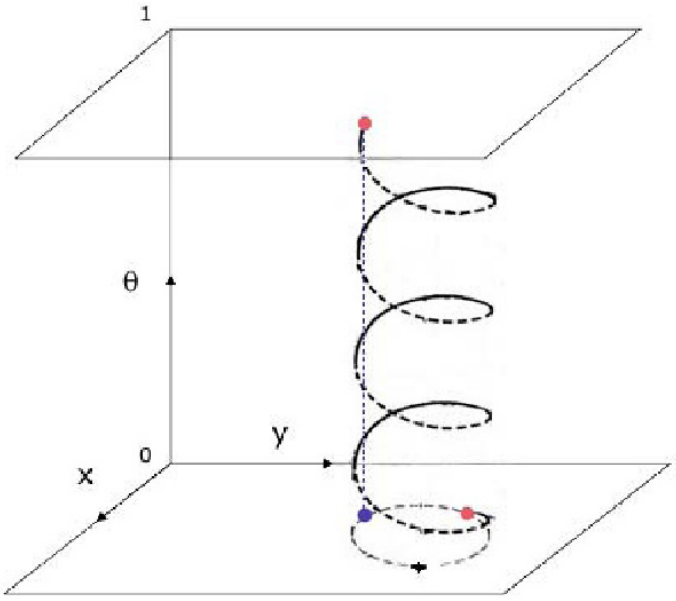

Figure 14. Suspension.

might wonder what did we achieve with this device: we have increased the dimension of the space in which the motion takes place by 1 without

apparently achieving any simplification. However, recall from our discussion of steady, three-dimensional velocity fields that the device of Poincaré maps allows us to *reduce* the dimension of the space by 1 for a properly chosen surface of section. Let the surface of section in $A \times S^T$ be defined by $S = A \times \{0\}$ (of course, any other θ besides $\theta = 0$ will do; we expand on this later). The Poincaré map $P : S \to S$ is defined by

$$x_1^{'} = x_1 + \int_0^T v_1(x(t,(x_0,0),0),t)dt = x_1 + f_1(x_1,x_2),$$
$$x_2^{'} = x_2 + \int_0^T v_2(x(t,(x_0,0),0),t)dt = x_2 + f_2(x_1,x_2),$$

where $(x(t,(x_0,0),t_0),t)$ is the solution of 21 passing through $(x_0 = (x_1,x_2) \in A = S, \theta_0 = 0)$ at $t = 0$. This solution is unique, so the suspension done previously allowed for this construction. The map P preserves the true area of the plane $S = A$ as our discussion in the previous section $\rho = v \cdot n = 1$ (see Lemma 2.17). By the change of variables theorem if P is a C^1 area-preserving transformation it must be that the Jacobian of P,

$$DP = \begin{bmatrix} 1 + \frac{\partial f_1}{\partial x_1} & \frac{\partial f_1}{\partial x_2} \\ \frac{\partial f_2}{\partial x_1} & 1 + \frac{\partial f_2}{\partial x_2} \end{bmatrix},$$

has determinant 1 :

$$1 + \frac{\partial f_1}{\partial x_1} + \frac{\partial f_2}{\partial x_2} + \frac{\partial f_1}{\partial x_1}\frac{\partial f_2}{\partial x_2} - \frac{\partial f_1}{\partial x_2}\frac{\partial f_2}{\partial x_1} = 1,$$

i.e.

$$\frac{\partial f_1}{\partial x_1} + \frac{\partial f_2}{\partial x_2} + \frac{\partial f_1}{\partial x_1}\frac{\partial f_2}{\partial x_2} - \frac{\partial f_1}{\partial x_2}\frac{\partial f_2}{\partial x_1} = 0.$$

Physically, Px_0 represents the position, after time T, of a fluid particle starting at x_0 at time 0.

Consider a two-dimensional, slightly unsteady, time-periodic (of period $T = 2\pi/\omega_T$) velocity field

$$\dot{x} = v_x(x,y) + \epsilon f_x(x,y,t),$$
$$\dot{y} = v_y(x,y) + \epsilon f_y(x,y,t),$$

If there is a region of periodic orbits for the $\epsilon = 0$ velocity field, we can simplify the representation of the velocity field in that region by introducing new, action-angle (Wiggins (1992)) variables I, θ, by

$$I = \frac{1}{2\pi}\int_{\psi} ydx \tag{22}$$

$$\theta = \frac{2\pi}{T(\psi)}t(x,y) \tag{23}$$

$$\tag{24}$$

where ψ is the streamfunction of the steady unperturbed ($\epsilon = 0$) velocity field. Note also that $\dot{\theta} = -\partial\psi/\partial I$.

Example 2.18. For flow with constant vorticity $\omega = 2$, $\dot{x} = y, \dot{y} = -x$, and $\psi = x^2/2 + y^2/2$. Thus, since I is the area under the constant streamline curve, $I = \pi(x^2 + y^2)/2\pi = 2\psi/2 = \psi$ Then, since $\psi = I$, it turns out that $\dot{\theta} = -1$. Generally $\dot{\theta} = \Omega(I)$, where $\Omega(I)$ is *n*ot constant if the system is nonlinear.

Now, in I, θ variables we have

$$\dot{I} = 0 \tag{25}$$

$$\dot{\theta} = \Omega(I) \tag{26}$$

$$\tag{27}$$

Thus, I is constant along streamlines and theta parametrizes the flow along streamlines.

$$\dot{I} = \frac{\partial I}{\partial x}\dot{x} + \frac{\partial I}{\partial y}\dot{y} = \epsilon f_I(I,\theta,t),$$
$$\dot{\theta} = \frac{\partial \theta}{\partial x}\dot{x} + \frac{\partial \theta}{\partial y}\dot{y} = \Omega(I) + \epsilon f_\theta(I,\theta,t),$$

Taking the period-T Poincaré map yields, starting at time 0 from I_0, θ_0:

$$I(T) = I(0) + \epsilon\int_0^T f_I(I(t,I_0,\theta_0),\theta(t,I_0,\theta_0),t)dt,$$
$$\theta(T) = \theta(0) + \int_0^T \Omega(t,I_0,\theta_0)dt + \epsilon\int_0^T f_\theta(I(t,I_0,\theta_0),\theta(t,I_0,\theta_0),t)dt,$$

Now for any finite time, for sufficiently small ϵ,

$$\begin{aligned} I(t, I_0, \theta_0) &= I_0 + \epsilon p_I(I_0, \theta_0), \\ \theta(t) &= \theta_0 + \epsilon p_\theta(I_0, \theta_0) \end{aligned} \tag{28}$$

for some functions p_I and p_θ, where $I(0) = I_0$ and $\theta(0) = \theta_0$. Thus, $\Omega(t, I_0, \theta_0) = \Omega(I_0) + O(\epsilon)$. In turn,

$$I(T) = I_0 + \epsilon \tilde{f}_I(I_0, \theta_0, \epsilon), \tag{29}$$

$$\theta(T) = \theta_0 + \bar{\Omega}(I_0)T + \epsilon \tilde{f}_\theta(I_0, \theta_0, \epsilon) = \theta_0 \bar{\Omega}(I_0) + \epsilon \tilde{f}_\theta(I_0, \theta_0, \epsilon), \tag{30}$$

where $\bar{\Omega} = 2\pi\Omega/\omega_T$. Thus, in the region of elliptic streamlines (periodic orbits) we have obtained the following Poincaré map:

$$I' = I + \epsilon \tilde{f}_I(I, \theta, \epsilon), \tag{31}$$

$$\theta' = \theta + \bar{\Omega}(I) + \epsilon \tilde{f}_\theta(I, \theta, \epsilon), \tag{32}$$

This map is in the class of the perturbation of the so-called "twist maps", provided $d\bar{\Omega}/dI \neq 0$. For $\epsilon = 0$ we call such a map an "integrable twist map". These are discrete dynamical systems with well-known properties. For example, any circle $I = c$ is an invariant manifold of the integrable twist map. On such a circle, rotation $\theta' = \theta + c$ is either rational, provided c is rational, or dense, provided c is irrational. There are also strong theorems describing their behavior upon perturbation. We describe the most famous such theorem next.

The Kolmogorov-Arnold-Moser (KAM) theorem (Arnold (1978)) (in Moser's version (Siegel and Moser (1971)) considers a perturbation of an integrable twist map and at least 4 times differentiable. Under the condition that the perturbed map is area-preserving (in fact that it possesses the so-called intersection property, that is implied by area-preservation which in our, incompressible fluid mechanics case is the consequence of incompressibility) KAM theorem states that, for ϵ small enough the majority of initial conditions stay on 1-dimensional invariant curves close to the unperturbed invariant curves on which $G(y)$ satisfies the so-called Diophantine condition.[2] The condition means that ω can not be approximated too rapidly by rational numbers of form p/q). It is commonly stated that unperturbed invariant curves that have sufficiently irrational dynamics "persist" under perturbation.

[2]This condition implies strong irrationality: if ω is an irrational number that satisfies the following condition:

$$|\frac{\omega}{2\pi} q - p| \geq \frac{c_0}{q^\mu} \quad \text{for} \quad q, p \in \mathbb{Z},\ \mu \geq 2$$

we say that it satisfies the Diophantine condition.

2.4 Mixing in the Standard Map

In this section we explain the phenomenology of mixing in two-dimensional maps based on the classical example of the standard map. We start with the simple shear flow:

$$\begin{aligned} v_x &= y, \\ v_y &= 0, \end{aligned} \tag{33}$$

and pulse it with a single mode perturbative flow

$$\begin{aligned} v_{x,p} &= 0, \\ v_{y,p} &= \epsilon\delta(t - nT)sin(2\pi x), \end{aligned} \tag{34}$$

where δ is the Dirac delta function and the period of the perturbation is T. Particle trajectories are thus solutions of

$$\begin{aligned} \dot{x} &= y, \\ \dot{y} &= \epsilon\delta(t - nT)sin(2\pi x), \end{aligned} \tag{35}$$

Between the pulses, a particle starting at x_0, y_0 travels acording to

$$\begin{aligned} x(t) &= x_0 + y_0 t, \\ y(t) &= y(0). \end{aligned} \tag{36}$$

Thus at $T = T^-$

$$\begin{aligned} x(T^-) &= x_0 + y_0 T^-, \\ y(T^-) &= y(0). \end{aligned} \tag{37}$$

After the pulse, at T^+,

$$\begin{aligned} x(T^+) &= x(T^-), \\ y(T^+) &= y(0) + \epsilon \sin(2\pi x(T^-)). \end{aligned} \tag{38}$$

Letting flow go for another period,

$$\begin{aligned} x(2T^-) &= x(T^-) + y(T^+)T, \\ y(2T^-) &= y(T^+) = y(T^-) + \epsilon \sin(2\pi x(T^-)). \end{aligned} \tag{39}$$

Since we can always consider the scaled coordinate Ty instead of y, there is no loss in generality in setting $T = 1$. Thus we obtained the following map

that tells us how fluid particle evolves starting at time just before one pulse and ending at the time just before the next pulse:

$$\begin{array}{rcll} x' & = & x + y + \epsilon \sin(2\pi x) & [mod\ 1] \\ y' & = & y + \epsilon \sin(2\pi x) & [mod\ 1] \end{array} \tag{40}$$

Note how the form of (40) is the same as the Poincaré map of an unsteady fluid flow in region of elliptic streamlines, (32), that we derived in the previous section. For $\epsilon = 0$, the particles are advected by the pure shear flow for period $T = 1$. This is shown in figure 15. Consider the density field shown in that figure, with no vertical variation and a step change in density at $x = 1/2$. As time goes on it will get stretched in "stripes" of width that decays algebraically, like $1/nT$. The rightmost field in that figure, however, will not get mixed at all. Generally speaking, "shear-like" flows will mix at most at an algebraic rate, and there might be density fields for such flows that do not get mixed at all.

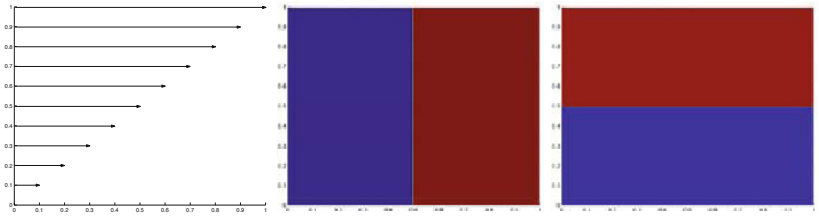

Linear Shear Flow $c_1(x, y) = f(x)$ $c_2(x, y) = g(y)$

Figure 15. The linear shear flow effects the two different density fields pictured above very differently.

Adding a small pulsed perturbation to the shear flow, as described above, leads to substantial changes in mixing behavior. For example, out of all the straight lines that are invariant under the unperturbed map, the ones for which y is strongly irrational (i.e. satisfies the Diophantine condition) persist by the KAM theorem described above. The lines for which y is rational break up. Around them, for small nonzero ϵ, small "islands" of rotational motion are formed. From one period to the other, fluid particles "jump" between such islands. Such zones are called the "resonance zones", the reason behind it being that for $y = p/q$ the period T of forcing is in rational relationship with the time it takes the shear flow to advance a particle through one periodic "cell" in x direction, $yT/T = p/q$. In other

words, since $Tp = yTq$, after p periods of forcing, the particle will traverse the basic cell in the x direction q times. For example, for $y = 1/2$ two "islands" form, shown in the middle of the figure 16. The zone outside

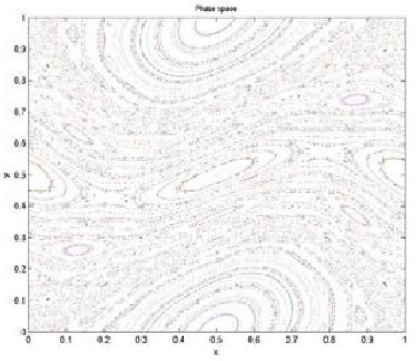

Figure 16. Phase space plot of the standard map for 10000 initial conditions on a regular 100×100 grid. The parameter $\epsilon = 0.15$.

of the "islands" contains a lot of trajectories with seemingly space-filling behavior. They uniformly fill the area they are contained in. It is believed (although not proven) that the behavior of trajectories in such zones is both ergodic (the sampling of the area within which the trajectory is contained is uniform over time) and mixing (if one would distribute dye within any small subset of such a zone, it would end up uniformly covering the zone, even if no diffusion is present). These properties are part of the ergodic theory of dynamical systems and are discussed formally later. It is interesting to consider the same density fields as those shown in figure 15 evolving under the perturbed map. It is easy to see that for the perturbed map, neither of these density fields would be thoroughly mixed over the whole phase space! In particular, whenever initially blue color covers a whole "island" that island will be covered by blue forever. Thus, although in chaotic zones mixing happens thoroughly and rapidly, in islands there is no mixing whatsoever. The perturbed map shows a somewhat mixed picture of mixing :-)

In his seminal paper, Aref (1984) has observed these properties in a map that resulted from "blinking" (time-periodic) application of point vortices. He termed the process in which good mixing is established by simple time-dependent flows "chaotic advection". The key property of chaotic advection

that is useful in applications and separates it from shear-flow type mixing processess is that it stretches and folds interfaces exponentially fast. The kinematic complexity of such motion is in a different "universality class" than pure shear. Two dimensional steady flows can not possess this property, as opposed to three-dimensional steady and unsteady flows and two-dimensional unsteady flows. In section 4 we discuss an applied area in which the above kinematic considerations are quite important - that of microfluidic mixing. Specifically, different mixer designs will be classified along the lines of kinematic complexity arguments. The key problem in design is that, just like in the case of the standard map above, a single flow can have regions of algebraic mixing and regions of exponential chaotic advection mixing. Thus optimization and control of mixing is an important topic, that we discuss briefly towards the end of this text.

3 Geometrical methods in 3-D flows

3.1 Geometrical methods in dynamical systems and mixing in 3-D flows

In two dimensional flows, it is quite useful to start from the fact that a streamfunction exist and, specifically, that for steady flows it leads to simple trajectories that are the level sets $\psi = const.$ of the streamfunction ψ. Such flows are called integrable. Perturbation theories such as KAM theory and theory of resonance zones lead to quite complete picture of fluid particle motion in such flows. Thus, it is useful to start from integrable flows to describe kinematics of three-dimensional, steady flows. But, a problem arises: except for a few well-known examples such as rotationally symmetric, axially symmetric and helically symmetric flows (Batchelor (1967)) it is not common to talk about streamfunctions in three-dimensional flows. Existence of a streamfunction in a 3-D steady flow means that fluid particles are restricted to move on a two-dimensional manifold (cf. Theorem 6). Provided this two-dimensional surface is a torus, rational or irrational windings described earlier will ensue on it. Poincaré-Bendixon theorem (Wiggins (1990)) can be used on other closed surfaces such as a sphere to show that there is no complicated motion. So steady integrable flows in three dimensions seem to be a good starting point for discussion of kinematics of integrable flows.

In 1965 Arnold published a note on the integrability of three-dimensional steady Euler flows (Arnold (1966)). In that note he asserted that three-dimensional Euler flows are integrable except in the case when vorticity and velocity are parallel -the case of Beltrami flows. In fact, even when vorticity and velocity are parallel, but the constant of proportionality varies with space, such Beltrami flows are still integrable. Both of these facts were

known to Lamb (Lamb (1932)) and the surfaces spanned by non-parallel velocity and vorticity are known as Lamb surfaces (see Sposito (1997) for a detailed discussion of these). In what follows, we connect these observations to existence of a symmetry for a flow.

Geometrical and dynamical symmetries

A sufficient condition for integrability (i.e. absence of chaotic motion) of a three-dimensional, incompressible vector field $\mathbf{v}$ is that it admits a volume-preserving symmetry (Mezić (1994); Mezić and Wiggins (1994); Haller and Mezić (1998)) i.e. that there exists another incompressible vector field $\mathbf{s}$ cuch that the Lie bracket $[\mathbf{v}, \mathbf{s}]$ is zero. In Cartesian coordinates these conditions become

$$[\mathbf{v}, \mathbf{s}] = \mathbf{v} \cdot \nabla \mathbf{s} - \mathbf{s} \cdot \nabla \mathbf{v} = 0, \tag{41}$$

$$\nabla \cdot \mathbf{s} = 0. \tag{42}$$

When general incompressible $\mathbf{v}, \mathbf{s}$ satisfy (41), a function B defined by the equation

$$\nabla B = -\mathbf{v} \times \mathbf{s} \tag{43}$$

is an integral of motion for both $\mathbf{v}, \mathbf{s}$, i.e. B is conserved on trajectories of both of these vector fields:

$$\frac{dB}{dt} = \mathbf{v} \cdot \nabla B = -\mathbf{v} \cdot \mathbf{v} \times \mathbf{s} = \mathbf{0} = -\mathbf{w} \cdot \mathbf{v} \times \mathbf{s} = \mathbf{s} \cdot \nabla B = \frac{dB}{ds},$$

where s is a time-like variable used to parametrize trajectories of the vector field $\mathbf{s}$. As an example of above general results, consider an incompressible vector field $\mathbf{v}$ which is symmetric with respect to translation along the z axis i.e. the velocity components (v_x, v_y, v_z) are independent of z. Let $\mathbf{s} = (0, 0, 1)$. Then (41,42) are clearly satisfied, as in components we have

$$\frac{\partial v_x}{\partial z} = \frac{\partial v_y}{\partial z} = \frac{\partial v_z}{\partial z} = 0,$$

$$\frac{\partial v_x}{\partial x} + \frac{\partial v_y}{\partial y} = 0,$$

and 43 becomes

$$\frac{\partial B}{\partial x} = v_y$$
$$\frac{\partial B}{\partial y} = -v_x$$

These equations clearly have a solution for B because $\mathbf{v}$ is incompressible. The cases of rotational and helical symmetry are treated similarly. These types of symmetries that result, from symmetries of the flow domain have been called geometrical symmetries in Yannacopoulos et al. (1998). In fact, in the case when a volume-preserving symmetry exists, the velocity field can be put in the form

$$\dot{z}_1 = \frac{\partial B}{\partial x}$$
$$\dot{z}_2 = -\frac{\partial B}{\partial y}$$
$$\dot{z}_3 = f(z_1, z_2).$$

for appropriately defined variables $(z_1(x, y, z), z_2(x, y, z), z_3(x, y, z))$ and some function $B(z_1, z_2, z_3)$ (see Mezić and Wiggins (1994)). Additionally, if z_3 is an angular coordinate (such as in the case of rotationally symmetric flows), this representation leads to introduction of action-action-angle coordinates I, θ, ϕ-where I, θ come from the two-dimensional portion defined by the "streamfunction" B and ϕ is a function of I, θ, and z_3 Mezić and Wiggins (1994). In these variables, the flow becomes

$$\dot{I} = 0$$
$$\dot{\theta} = \omega_1(I)$$
$$\dot{\phi} = \omega_2(I). \tag{44}$$

Another type of symmetry that can arise is induced by the evolution equations of the fluid. The most well-known such symmetry is the content of the Taylor-Proudman theorem for fast rotating flows: when the Rossby number of a flow around an axis with angular velocity $\mathbf{\Omega}$ goes to zero, the velocity field satisfies

$$\mathbf{\Omega} \cdot \nabla \mathbf{v} = 0.$$

Thus, since Ω is constant, (41,42) are satisfied and such a flow posseses an integral of motion. More generally, it is clear at once that (41,42) are satisfied by velocity $\mathbf{v}$ and vorticity $\omega = \mathbf{s}$ of an Euler flow (Mezić (1994); Mezić and Wiggins (1994); Haller and Mezić (1998)). Thus every Euler flow is integrable with the Bernoulli integral $B = (1/2)\mathbf{v}^2 + p/\rho$. The surfaces of constant B are called Lamb surfaces (see Sposito (1997)). The topology of these surfaces inside of a bounded analytical surface was shown to be toroidal or cylindrical by Arnold (1966), with the exception of separating surfaces between these tori and cylinders.

According to this analysis, a typical integrable flow in a three-dimensional closed container will look somewhat like that shown in figure 17. In region I there is a family of tori, on which the particle motion can be described by equations (44). Region II also contains invariant tori (not shown). The separating manifold between these two regions is (topologically) a sphere. There are two fixed points on the sphere. Both are of spiral-node type.

Fixed points for 3D steady flows

In fact in three-dimensional steady flows, there are only two types of fixed points provided the linearization of the flow at the fixed point is not degenerate (i.e. has no zeros among its eigenvalues). This follows from the divergence-free condition. Let $DV_{ij} = [\frac{\partial v_i}{\partial x_j}]$ be the i, j entry of the Jacobian matrix DV of the velocity field. The incompressibility condition

$$\frac{\partial v_x}{\partial x} + \frac{\partial v_y}{\partial y} + \frac{\partial v_z}{\partial z} = 0$$

implies $Trace(DV) = 0$ which in turn implies $\lambda_1 + \lambda_2 + \lambda_3 = 0$ where λ_i are eigenvalues of DV taken at some fixed point. Thus, for a three-dimensional steady flows, the eigenvalues of the linearization imply that nondegenerate fixed points (i.e. those for which no eigenvalues are 0 are of two basic types: 1) Saddle nodes, with all real eigenvalues. 2) Saddle foci, with a complex conjugate pair and a real eigenvalue. The types of fixed points that can occur - that are the same as types of periodic orbits for three-dimensional unsteady flows - are shown in figure 20.

3.2 Viscosity, Inertia and Chaotic Advection

Based on the above result on integrability of Euler flows, Arnold suggested the special solution of Euler's equation, the so-called ABC (Arnold-Beltrami-Childress) flows as possible nonintegrable flows. These are spatially periodic Euler flows for which velocity is proportional to vorticity

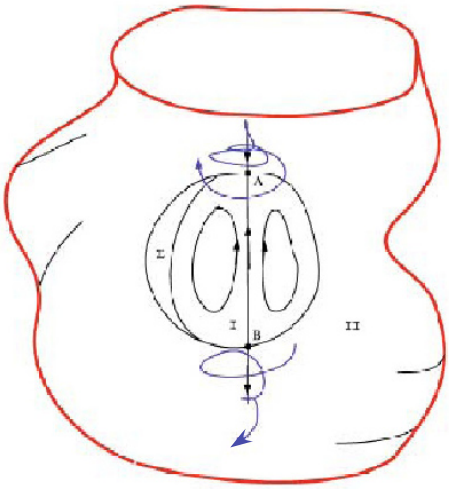

Figure 17. An integrable flow in a three-dimensional container.

(i.e. they are Beltrami flows). Hénon (1966) perfomed a numerical simulation of ABC flows and found evidence of chaotic behavior. Thus, the first results in the field of chaotic advection were based on the analysis of velocity fields that were smooth solutions of Euler equations. In contrast, the flows discussed in chaotic advection studies in the 80's and 90's were kinematic models that did not satisfy dynamical equations of fluid motion, solutions of Stokes equations, or weak solutions based on singular vortex distributions. Only recently, a few studies (Ashwin and King (1995b,a); Yannacopoulos et al. (1998); Balasuriya et al. (1997)) appeared that took account of the restrictions imposed by the fact that Newtonian fluid flows satisfy Navier-Stokes equations.

One way of interpreting Arnold's suggestion on importance of ABC flows is that viscous perturbations to Euler flows can be taken to be small away from the boundaries and, due to integrability of Euler flows that do not have velocity and vorticity proportional, chaotic motion can be only caused by an ABC-type flow. But, ABC flows are in quite special. The condition that velocity is proportional to vorticity is very hard to establish experimentally (Solomon (1998)). In fact it can be shown rigorously that - in the region of the flow where inertial forces are dominant - the assumption that the steady

flow can be split into dominant inertial part that solves Euler equation and small viscous part leads to conclusion that the Euler (inertial) part can not be a chaotic ABC flow (Mezić (2000)). In what follows, we paint quite a different picture of the physical nature of chaotic fluid particle motion in three-dimensional steady fluid flows: the cause for chaotic motion lies in viscous forces and, as Reynolds number increases to infinity, the extent of chaotic motion starts to decrease in a well-defined way. Consider now an unbounded steady incompressible Navier-Stokes flow in $\mathbb{R}^3$. It satisfies

$$\mathbf{v} \cdot \nabla\omega - \omega \cdot \nabla\mathbf{v} = \mathrm{Re}^{-1} \triangle\omega \tag{45}$$

where Re is the Reynolds number of the flow. For such flows a regular perturbation expansion at large Reynolds numbers would read

$$\mathbf{v} = \mathbf{v}_E + \mathrm{Re}^{-1}\, \mathbf{v}_1 + \mathcal{O}(\mathrm{Re}^{-2}), \tag{46}$$

where $\mathbf{v}_E$ satisfies Euler's equation of motion and is thus integrable. This flow is thus $\mathcal{O}(\mathrm{Re}^{-1})$, away from an Euler flow. That Euler flow is integrable (Mezić (2000)). Thus, the flux through any separating surfaces in this flow will be of the order $\mathcal{O}(\mathrm{Re}^{-1})$, as was pointed out in the introduction of Mezić (1994), if $\mathbf{v}_1$ does not possess any symmetries.

The case of 2-D unsteady flows, which was treated rigorously in Balasuriya et al. (1997), can be considered also within the theory outlined above (Haller and Mezić (1998)). Two-dimensional steady flows of incompressible fluid are known to be integrable (i.e. the possibility of chaotic advection is excluded) due to the existence of a streamfunction. Consider an unsteady, 2-dimensional Euler flow $\mathbf{v}$ time-periodic with period $2\pi/\Omega$. Its vorticity ω satisfies the two-dimensional Euler equation

$$\frac{\partial\omega}{\partial t} + \mathbf{v} \cdot \nabla\omega = 0.$$

which implies that ω is a quantity conserved on particle paths and thus the flow is integrable. In the terms of discussion above, $\mathbf{v}$ possesses a dynamical symmetry. Let the domain in $\mathbb{R}^2$ in which the flow takes place be denoted by $\mathcal{D}$. Then the three-dimensional steady flow $\mathbf{v}_E = (v_x, v_y, \Omega)$ is defined on $\mathcal{D}\times S^1$. For example, when $\mathcal{D}$ is a region in $\mathbb{R}^2$ whose boundary is a circle, then $\mathcal{D}\times S^1$ has the shape of a donut. The symmetry vector field $\mathbf{s}$ such that $[\mathbf{v}_E, \mathbf{s}] = 0$ is given by $\mathbf{s} = (\partial\omega/\partial y, -\partial\omega/\partial x, 0)$ (Haller and Mezić (1998)). At large Re, $\mathbf{v}_E$ serves as the first term in the expansion of a Navier-Stokes flow. If there are no solid boundaries, then this expansion is (46).

3.3 KAM theory

Kolmogorov-Arnold-Moser theorem on persistence of invariant tori in Hamiltonian systems has played a historically important role in the develoment of dynamical systems theory (see e.g. Siegel and Moser (1971)). As we saw above, the Moser version of the theorem has direct applicability to treatment of two-dimensional, unsteady (time-periodic) flows. It is bit more difficult to obtain the appropriate result for three-dimensional flows. In the context of the representation we obtained from symmetry considerations above, we can consider steady flows of the form

$$\begin{aligned}\dot{I} &= \epsilon f_1(I,\theta,\phi)\\ \dot{\theta} &= \omega_1(I) + \epsilon f_2(I,\theta,\phi)\\ \dot{\phi} &= \omega_2(I) + \epsilon f_3(I,\theta,\phi).\end{aligned}$$

where ϵ measures deviations from symmetry. Moser (1968) already proved that tori $I = const.$ that satisfy the Diophantine condition

$$n_1\omega_1(I) + n_2\omega_2(I) \geq c/(|n_1| + |n_2|)^{\mu},$$

where n_1, n_2 are integer and the constant $\mu > 1$ "persist" i.e. the perturbed ($\epsilon > 0$ sufficiently small) flow also has invariant tori that restrict fluid particle motion. In the case of a time-periodic perturbation of period T,

$$\begin{aligned}\dot{I} &= \epsilon f_1(I,\theta,\phi,t)\\ \dot{\theta} &= \omega_1(I) + \epsilon f_2(I,\theta,\phi,t)\\ \dot{\phi} &= \omega_2(I) + \epsilon f_3(I,\theta,\phi,t).\end{aligned}$$

where $f_i(I,\theta,\phi,t) = f_i(I,\theta,\phi,t+T)$, invariant tori $I = const.$ persist, provided

$$n_1\omega_1(I) + n_2\omega_2(I) + n_3\omega_3 \geq c/(|n_1| + |n_2| + |n_3|)^{\mu}$$

where $\omega_3 = 2\pi/T$, n_1, n_2, n_3 are integer and the constant $\mu > 2$. The major difference of such results with those in Hamiltonian systems is that the motion on the tori in the perturbed flow does not necessarily have the same rotational frequencies as the unperturbed ones (Cheng and Sun (1990)).

3.4 Resonances in 3-D steady flows

Given the important role that resonance zones play in two-dimensional time-periodic flows, it is important to study such effects in three-dimensional

flows. Three-dimensional steady flows behave in a similar way to two-dimensional unsteady ones. For example, tori with resonant particle motion frequencies ω_1 and ω_2 ($\omega_1(I)/\omega_2(I) = n_2/n_1$ where n_1, n_2 are integer) are typically destroyed upon ϵ perturbation and give rise to chaotic zones between KAM tori. Sometimes this kind of a phenomenon is labeled internal resonance - since it is the frequencies of motion in two different directions that are in resonance, not a motion that is inherent to the system and an external perturbing force.

Experiments by Ottino's group (Fountain et al. (2000)) confirmed the effects of resonance in three-dimensional steady flows in a spectacular manner. In the figure 18 we show a) The experimental set-up, that consists of a container and a disk positioned inside the container. The disc can be tilted, thus increasing the asymmetry. The flow is visualized by dye of various colors injected in the flow via needles and laser sheet that cross-sections the flow as shown. Any time the fluorescent dye passess through the laser sheet, it illuminates that point. When the disc is not tilted, the flow swirls around the vertical axis and also on tori caused by upwelling and downwelling due to Ekman pumping type effect. This causes a flow to be of integrable Action-Angle-Angle type, with trajectories residing on tori with either quasiperiodic motion (for the case the rotational frequencies around the z axis and cross-sectional rotation frequency are in irrational relationship) or periodic motion (for rational ratio of these frequencies of particle motion). In b) Ratios of frequencies $\Omega_\phi/\Omega_\theta$, where ϕ is the angle around the vertical axis and θ is the frequency of motion on tori is shown for the untilted disc (symmetric case). Different curves are for different speeds of rotation N. For example for $N = 30$, the curve does not cross the $1/3$ level. This means we should not see a period-3 or period-2 resonant island in the tilted disc case. This is confirmed in figure d) where we see that the lowest-order period island is that of period-4. Analogously, for $N = 60$, the frequency ratio crosses above $1/2$ and in figure c) we see that the dominant island is period-2. In figure e) numerical simulations of the Poincaré map for this flow are shown, corresponding to the physical parameters in figure d). Similarity between these is evident. The numerical simulation makes clear the existence of a persisting KAM torus (indicated in the figure) that separates the period-4 island from the domain close to the container walls. It is interesting how these invariant tori predicted by perturbation theory to exist for sufficiently small tilt angles still survive for relatively large tilt angles. In between the boundary of the container and island areas there is a chaotic zone in which trajectories fill the two-dimensional cross-section (and thus fluid trajectories fill the three-dimensional volume).

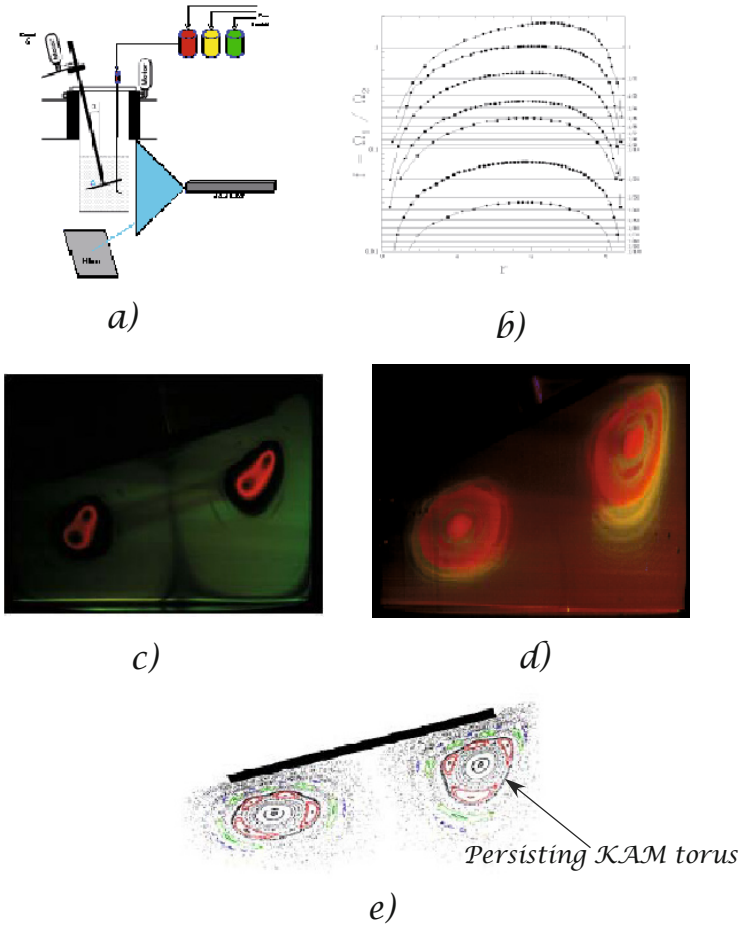

Figure 18. Experiments on a three-dimensional steady rotating flow in a cylindrical container (Fountain et al. (2000)).

3.5 Resonances in 3-D time-dependent flows.

It is evident from the previous discussion that three-dimensional flows whose unperturbed (symmetric) form is Action-Angle-Angle behave similarly to two-dimensional Action-Angle maps like the Standard Map: there are toroidal resonance zones (instead of circular resonance zones as in 2-D) and chaotic zones. The Action-Angle-Angle form arises because of existence of an integral of motion for the three-dimensional flow. If besides the invariant function, B, that arises from the symmetry we can find another function invariant on trajectories of the flow, the unperturbed flow can be

transformed to the so-called Action-Action-Angle form

$$\begin{aligned}\dot{I}_1 &= 0,\\ \dot{I}_2 &= 0,\\ \dot{\theta} &= \omega(I_1, I_2).\end{aligned}$$

This would, for example, be the case in above experiments with no disc tilt -if we switch the roles of variables θ and ϕ - if there was no Ekman pumping (i.e. very low Reynolds number flow) and all the fluid particle trajectories would reside on $z = const.$ surfaces, spinning on circles around the vertical axis. Thus $B = z$ would be an invariant function due to axial symmetry along z axis, and $B_1 = r$ would be another invariant function for this flow - that also arises due to a symmetry, this time rotational symmetry around the z axis. Such flows also commonly arise as large-scale ocean eddies that are mostly two-dimensional due to density stratification.

Now we consider the situation in which the above Action-Action-Angle flow is perturbed by a small, time-periodic (period T) perturbation. We take the period-T Poincaré map and obtain an integrable action-action-angle map, of the form

$$\begin{aligned}I_1' &= I_1,\\ I_2' &= I_2,\\ \theta' &= \theta + \Omega(I_1, I_2),\end{aligned} \tag{47}$$

where $I_1 \in \mathcal{I}_1 = [a_1, b_1] \subset \mathbb{R}, I_1 \in \mathcal{I}_2 = [a_2, b_2] \subset \mathbb{R}$ and $\theta \in S^1$. The domain of definition of I_1, I_2 is denoted by $B = \mathcal{I}_1 \times \mathcal{I}_2 \subset \mathbb{R}^2$.

Exercise 3.1. Show that the map 47 arises as period-T Poincaré map of the flow

$$\begin{aligned}\dot{I}_1 &= \epsilon f_1(I_1, I_2, \theta, t),\\ \dot{I}_2 &= \epsilon f_2(I_1, I_2, \theta, t),\\ \dot{\theta} &= \omega(I_1, I_2) + \epsilon f_3(I_1, I_2, \theta, t).\end{aligned}$$

(Mezić (1994); Mezić and Wiggins (1994)) where f_i are $T-periodic$, when $\epsilon = 0$. Such a flow for $\epsilon = 0$ and $\omega(I_1, I_2) = I_1$ is depicted in figure 19.

The equations $I_1 = c_1, I_2 = c_2$ for constant c_1, c_2 define an invariant circle γ_{c_1,c_2} for (47). If $\Omega(I_1, I_2)/2\pi = p/q,\ p, q \in \mathbb{Z}$, γ_{c_1,c_2} consists of

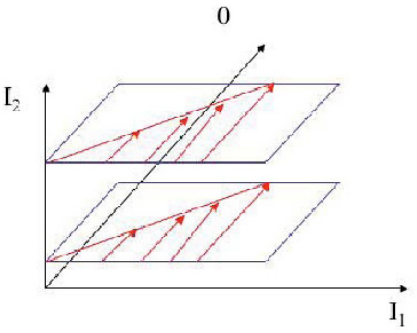

Figure 19. Schematic representation of unperturbed three-dimensional shear layer leading to the integrable action-action-angle map (47)

periodic orbits with period q. We call these p/q-orbits. Furthermore, a point belonging to a p/q orbit is called a p/q point. For $\Omega(I_1, I_2)/2\pi$ irrational, every orbit on γ_{c_1,c_2} is dense.

Let us first discuss the nature of two-dimensional invariant manifolds for maps of the type (47). Obviously, any manifold of the type $V \times S^1$ where V is a zero-, one- or two-dimensional manifold in B is invariant. Any invariant manifold that is not of type $V \times S^1$ is of *resonant type*, i.e. each point (I_1^*, I_2^*, θ^*) on it satisfies $\Omega(I_1^*, I_2^*) = 2\pi k/j$, where $j, k \in \mathbb{Z}$. For simplicity, we will show this only for manifolds that are cut out by analytic functions. If $F(I_1, I_2, \theta) = c$ describes an invariant manifold $\mathcal{M}$ of (47), with F analytic and $\partial F/\partial\theta \neq 0$ (this is equivalent to saying that F is not of the type $V \times S^1$), then

$$F(I_1, I_2, \theta + \Omega(I_1, I_2)) = F(I_1, I_2, \theta). \tag{48}$$

Assume that on $\mathcal{M}$ there is a point (I_1^*, I_2^*, θ^*) such that $\Omega(I_1^*, I_2^*) \neq 2\pi k/j$

for any $j, k \in \mathbb{Z}$. Taking the Fourier transform of (48) we obtain

$$\exp(in\theta)(\exp(in\Omega(I_1^*, I_2^*) - 1)) = 0$$

which has to be satisfied for every n for which the corresponding Fourier mode of F is non-zero, which gives us contradiction. Because the surfaces defined by the resonance condition $\Omega(I_1^*, I_2^*) = 2\pi k/j$, where $j, k \in \mathbb{Z}$ do not intersect, resonant manifolds can be zero or one-dimensional. As an example, consider the map (47) with $\Omega(I_1, I_2) = I_1$. Then a resonant manifold is defined by

$$\sin\theta = 0, I_1 = \pi.$$

3.6 Action-action-angle maps

We are going to concentrate efforts on understanding persistence under perturbation of the above described two-dimensional manifolds of the type $V \times S^1$ and zero-dimensional manifolds of resonant type (these are in fact periodic orbits). It turns out that these issues have to do the most with transport in action-action-angle maps. Thus, we consider a class of volume-preserving perturbations of action-action-angle maps of the form

$$\begin{aligned} I_1' &= I_1 + \epsilon f_1(I_1, I_2, \theta, \epsilon), \\ I_2' &= I_2 + \epsilon f_2(I_1, I_2, \theta, \epsilon), \\ \theta' &= \theta + \Omega(I_1, I_2) + \epsilon f_3(I_1, I_2, \theta, \epsilon). \end{aligned} \tag{49}$$

We assume that Ω, f_1, f_2 and f_3 are analytic functions of their variables..

Non-existence of two-dimensional invariant manifolds

Feingold, Kadanoff and Piro first performed a beautiful study of such maps in Feingold et al. (1988). They observed numerically that they behave differently from action-angle-angle maps in that they could not find any invariant surfaces persisting and pursued an analytical perturbation argument to imply this statement of non-persistence is true. Such a result would indicate that, as opposed to the KAM case, there are no surfaces bounding particle motion in the perturbed system and thus perhaps global chaos could be expected upon small perturbation. We will see here under which conditions this is true rigorously.

Consider a map given by (49). In the case $\epsilon = 0$ the phase space is foliated by circles γ_{c_1,c_2}. We denote the resonant manifold $\Omega(I_1, I_2)/2\pi = k/j$, $j, k \in \mathbb{Z}$ by $\mathcal{R}_{k,j}$. Let $V \subset B$ be a one-dimensional analytic manifold. As said before, any manifold of the type $V \times S^1$ is invariant for the unperturbed system ($\epsilon = 0$). In the following theorem we state that typically

none of such manifolds persist when $\epsilon \neq 0$ except possibly in the case similar to that of *proper degeneracy* (Arnold (1963)) in Hamiltonian systems. We will be formal here and state a theorem and then explain the result in practical terms. The germ of the proof of the theorem below (a first-order perturbation expansion) can be found in Piro and Feingold (1988).

Theorem 3.2. *Let $F^0(I_1, I_2) = 0$ define an invariant manifold $\mathcal{M}$ of the system (49) of the type $V \times S^1$. Let the Fourier expansions of $f_1|_{\epsilon=0}, f_2|_{\epsilon=0}$ be given by*

$$f_1(I_1, I_2, \theta, 0) = \sum_{j \in \mathbb{Z}} \hat{f}_1^j(I_1, I_2) \exp(ij\theta),$$
$$f_2(I_1, I_2, \theta, 0) = \sum_{j \in \mathbb{Z}} \hat{f}_2^j(I_1, I_2) \exp(ij\theta). \tag{50}$$

Assume

1. $(\hat{f}_1^0, \hat{f}_2^0) \cdot \nabla F^0 \neq 0$ *or*
2. $(\hat{f}_1^0, \hat{f}_2^0) \cdot \nabla F^0 = 0$, $(\hat{f}_1^0, \hat{f}_2^0) \cdot \nabla \Omega \neq 0$. *Moreover, for every $j \in \mathbb{Z}$ there is $m = nj$, $n \in \mathbb{Z}$ such that $(\hat{f}_1^m, \hat{f}_2^m) \nparallel (\hat{f}_1^0, \hat{f}_2^0)$. or*
3. $(\hat{f}_1^0, \hat{f}_2^0) = 0$, $\nabla F^0 \nparallel \nabla \Omega$, *and for any $p, q \in \mathbb{Z}$ there exist $m = l_1 p, n = l_2 q \in \mathbb{Z}$ such that $(\hat{f}_1^m, \hat{f}_2^m) \nparallel (\hat{f}_1^n, \hat{f}_2^n)$.*

Then there are no manifolds $\mathcal{M}^\epsilon$ defined by $F(\epsilon, I_1, I_2, \theta) = 0, F$ analytic, such that

$$\lim_{\epsilon \to 0} F(0, I_1, I_2, \theta) = F^0(I_1, I_2)$$

.

Note that $\hat{f}_i^0 = 1/(2\pi) \int_0^{2\pi} f_i(I_1, I_2, \theta) d\theta$ is the average of the perturbation part of the map. So the first condition states that if we consider manifolds F^0 to which the average of the vector field over unperturbed trajectories and time (recall that we integrated over time to obtain the Poincaré map and thus the functions f_i) projected on the normal on F^0 is nonzero (i.e. the average of the perturbation is "piercing through" the manifold F^0), then that manifold can not persist under perturbed dynamics. This is quite intuitive.

The proof of the above statement does not depend on the incompressibility of the underlying flow (and therefore volume-preservation for the map). However, for sufficiently small ϵ, $(\hat{f}_1^0, \hat{f}_2^0)$ is a Hamiltonian vector field, with the Hamiltonian function H.

Exercise 3.3. The last statement is a consequence of volume-preservation that implies that the determinant of the Jacobian of the map is 1. Prove that for small ϵ, $(\hat{f}_1^0, \hat{f}_2^0)$ is Hamiltonian by calculating the determinant of the Jacobian to $O(\epsilon)$ and finding the condition for it to be equal to 1.

Thus, looking at the first condition of the theorem, if a manifold of the type $V \times S^1$ is to persist under a perturbation, V must be composed of level sets of H (this follows from the fact that the first condition for non-existence implies $\nabla H \cdot \nabla F^0 \neq 0$).

The second condition can be interpreted as follows: even if the average of the perturbation is parallel to the manifold F^0 that we are "examining" for persistence, if Ω and F^0 do not coincide, F^0 will not persist. This is due to the fact that Ω changing value on F^0 implies there will be rational values of it and thus periodic orbits. Not all periodic orbits persist (see below) and thus the surface is broken, provided that additionally some higher terms in Fourier expansion of the perturbation are not parallel to F^0. The third condition is similar in that it implies that F^0 must intersect some resonant surface $\Omega = n/m$.

We can now examine the case in which $(\hat{f}_1^0, \hat{f}_2^0) \cdot \nabla\Omega = 0$ and $(\hat{f}_1^0, \hat{f}_2^0) \cdot \nabla F^0 = 0$, i.e. F^0 is functionally dependent on Ω and constant along the orbits of a vector field $(\hat{f}_1^0(I_1, I_2), \hat{f}_2^0(I_1, I_2))$. Clearly, if $\Omega/2\pi = k/j$ $\mathcal{M}^\epsilon$ will generally not persist. But for Diophantine Ω it could. Consider the system

$$\begin{aligned} I' &= I + \epsilon f_1(I, \theta_1, \theta_2, \epsilon), \\ \theta_1' &= \theta_1 + \epsilon\Omega_1(I) + \epsilon f_2(I, \theta_1, \theta_2, \epsilon), \\ \theta_2' &= \theta_2 + \Omega_2(I) + \epsilon f_3(I, \theta_1, \theta_2, \epsilon). \end{aligned} \tag{51}$$

Assume that $\int_0^{2\pi} f_1(I, \theta_1, \theta_2, \epsilon) d\theta_2 = 0$ and $\int_0^{2\pi} f_2(I, \theta_1, \theta_2, \epsilon) d\theta_2 = 0$. In the notation of the theorem,

$$(\hat{f}_1^0, \hat{f}_2^0) \cdot \nabla\Omega = (0, \epsilon\Omega_1(I)) \cdot (\Omega_2', 0) = 0.$$

And thus there is a possibility of persistence of $\mathcal{M}$ defined by $F_0(I) = \Omega_2(I) = const.$ where Ω_2 is Diophantine. This case is similar to the proper degeneracy case in Hamiltonian systems treated in Arnold (1963). In fact, in Vaidya and Mezić (2006), persistence of invariant tori in such a case was proven. In fluid dynamics, this case corresponds to the case of rotationally symmetric, no-swirl vortex ring perturbed by small swirl. The result in Vaidya and Mezić (2006) states that invariant tori will exist upon such perturbation (under certain additional conditions). In fluid dynamics, this

has potential relevance to the problem of "swirl stabilization" in combustion, where the anchoring of the flame is achieved by a toroidal surface "generated" by an imposed swirl in the flow.

Theorem 3 gives rigorous backing to observations of Piro and Feingold (1988) but also contains additional information: manifolds on which $\Omega(I_1, I_2)$ is constant could persist if the average of the perturbation in actions is tangent to these manifolds. In fact, in Cartwright et al. (1996), figure 7b shows surfaces that are tangent to the average of the perturbation, broken at intersections with resonant surfaces. In the following section we examine the dynamics near the resonant surfaces $\Omega(I_1, I_2) = p/q$.

Persistence of periodic orbits

Every invariant manifold $\mathcal{R}_{p,q}$ of the map (49) at $\epsilon = 0$ is filled with p/q-orbits. We call the map (49) T. Consider the q-th iterate of that map, T^q:

$$\begin{aligned} I_1^q &= I_1 + \epsilon \tilde{f}_1(I_1, I_2, \theta, \epsilon), \\ I_2^q &= I_2 + \epsilon \tilde{f}_2(I_1, I_2, \theta, \epsilon), \\ \theta^q &= \theta + q\Omega(I_1, I_2) + \epsilon \tilde{f}_3(I_1, I_2, \theta, \epsilon). \end{aligned} \tag{52}$$

For this map $\mathcal{R}_{p,q}$ is a manifold of fixed points. Let $\tilde{\Omega}(I_1, I_2) = q\Omega(I_1, I_2) - 2\pi p$ and consider the map S given by

$$\begin{aligned} I_1' &= I_1 + \epsilon \tilde{f}_1(I_1, I_2, \theta, \epsilon), \\ I_2' &= I_2 + \epsilon \tilde{f}_2(I_1, I_2, \theta, \epsilon), \\ \theta' &= \theta + \tilde{\Omega}(I_1, I_2) + \epsilon \tilde{f}_3(I_1, I_2, \theta, \epsilon). \end{aligned} \tag{53}$$

For this map $\mathcal{R}_{p,q}$ is given by $\tilde{\Omega}(I_1, I_2) = 0$. We denote the Jacobian of two functions f and g with respect to variables i, j by $\{f, g\}_{(i,j)}$ where i, j can be I_1, I_2 or θ. The following has been proven for general perturbations in Wiggins (1985); Wiggins and Holmes (1987):

Proposition 3.4. *Assume that (I_1^0, I_2^0, θ^0) is a point on the manifold $\mathcal{M}$ such that the action part of the perturbation vanishes, i.e.*

$$\tilde{f}_1(I_1^0, I_2^0, \theta^0, 0) = \tilde{f}_2(I_1^0, I_2^0, \theta^0, 0) = 0.$$

Furthermore, assume

$$[\frac{\partial \tilde{\Omega}}{\partial I_1}\{\tilde{f}_1, \tilde{f}_2\}_{(I_2,\theta)} - \frac{\partial \tilde{\Omega}}{\partial I_2}\{\tilde{f}_1, \tilde{f}_2\}_{(I_1,\theta)}]|_{(I_1^0, I_2^0, \theta^0, 0)} \neq 0. \tag{54}$$

Then, for all sufficiently small ϵ there is $p(\epsilon) = (I_1(\epsilon), I_2(\epsilon), \theta(\epsilon))$, which is a fixed point of (53).

Proof. If (I_1^0, I_2^0, θ^0) is a solution of $\tilde{f}_1|_{\epsilon=0} = 0, \tilde{f}_2|_{\epsilon=0} = 0, \tilde{\Omega} = 0$ by the implicit function theorem, there exists a solution $p(\epsilon) = (I_1(\epsilon), I_2(\epsilon), \theta(\epsilon))$ for $\tilde{f}_1 = 0, \tilde{f}_2 = 0, \tilde{\Omega} + \epsilon \tilde{f}_3 = 0$ provided the determinant of

$$\begin{bmatrix} \frac{\partial \tilde{f}_1}{\partial I_1} & \frac{\partial \tilde{f}_1}{\partial I_2} & \frac{\partial \tilde{f}_1}{\partial \theta} \\ \frac{\partial \tilde{f}_2}{\partial I_1} & \frac{\partial \tilde{f}_2}{\partial I_2} & \frac{\partial \tilde{f}_2}{\partial \theta} \\ \frac{\partial \tilde{\Omega}}{\partial I_1} & \frac{\partial \tilde{\Omega}}{\partial I_2} & 0 \end{bmatrix}$$

does not vanish at $(I_1^0, I_2^0, \theta^0, 0)$, which is exactly the condition (54). □

Note that the proof does not use the volume-preserving property of the perturbation: this condition is going to be used for stability considerations later. Under the assumptions of the above proposition, there is a finite set of p/q-orbits on the manifold $\Omega(I_1, I_2) = p/q$ that persist after the perturbation.

The stability of periodic orbits

We can now examine the stability of the fixed points that persist due to Proposition 3.4. Let

$$\begin{aligned} \mathcal{X} &= \left[\frac{\partial \tilde{f}_1}{\partial \theta} \frac{\partial \tilde{\Omega}}{\partial I_1} + \frac{\partial \tilde{f}_2}{\partial \theta} \frac{\partial \tilde{\Omega}}{\partial I_2} \right], \\ \mathcal{Y} &= \left[\frac{\partial \tilde{\Omega}}{\partial I_1} \{\tilde{f}_1, \tilde{f}_2\}_{(I_2,\theta)} - \frac{\partial \tilde{\Omega}}{\partial I_2} \{\tilde{f}_1, \tilde{f}_2\}_{(I_1,\theta)} \right]. \end{aligned} \tag{55}$$

Proposition 3.5. *If*

$$\mathcal{X}(I_1^0, I_2^0, \theta^0, 0) > 0$$

the fixed point $(I_1(\epsilon), I_2(\epsilon), \theta(\epsilon))$ is a hyperbolic saddle. If

$$\mathcal{X}(I_1^0, I_2^0, \theta^0, 0) < 0$$

the fixed point is a saddle-focus. If the fixed point is a hyperbolic saddle it has a two-dimensional stable manifold and one-dimensional unstable manifold if

$$\frac{\mathcal{Y}}{\mathcal{X}}(I_1^0, I_2^0, \theta^0, 0) > 0$$

and a two-dimensional unstable manifold and one-dimensional stable manifold if

$$\frac{\mathcal{Y}}{\mathcal{X}}(I_1^0, I_2^0, \theta^0, 0) < 0$$

If the fixed point is a saddle focus, the stable and unstable dimensions are reversed.

Different stability types of periodic orbits are shown in figure 20. The

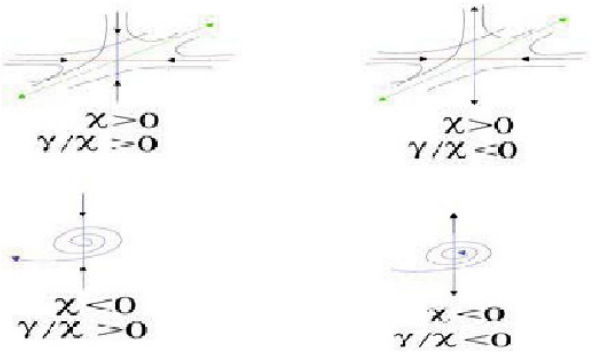

Figure 20. Stability of various types of periodic orbits persisting the perturbation in map (47)

$\mathcal{O}(\epsilon)$ polynomial that we solved in order to obtain a pair of $\mathcal{O}(\sqrt{\epsilon})$ eigen-

values is obtained from the eigenvalue problem for the matrix

$$\begin{bmatrix} 1 & 0 & \epsilon\frac{\partial f_1}{\partial\theta} \\ 0 & 1 & \epsilon\frac{\partial f_2}{\partial\theta} \\ \frac{\partial\Omega}{\partial I_1} & \frac{\partial\Omega}{\partial I_2} & 1 \end{bmatrix}$$

After a calculation we find that the eigenvectors corresponding to $1\pm\sqrt{(}\epsilon\mathcal{X})$ are

$$(\sqrt{\epsilon}(\partial f_1/\partial\theta), \sqrt{\epsilon}(\partial f_2/\partial\theta), \pm\sqrt{\mathcal{X}})$$

(of course, the real eigenvectors are obtained from real and imaginary parts in the case of $\mathcal{X}$ negative). Define again $J = \Omega(I_1, I_2)$ and consider the $J-\theta$ plane. It is easy to show that the angle of the plane spanned by these eigenvectors with the tangent space of the $J-\theta$ plane is $\mathcal{O}(1)$. For simplicity, let $\Omega(I_1, I_2) = I_1$. Then the tangent space of the $I_1-\theta$ plane is spanned by $(1,0,0)$ and $(0,0,1)$. The normal to this plane is thus given by $(0,1,0)$. The normal to the eigenvector plane is given by

$$(-\frac{\partial f_2}{\partial\theta}/\sqrt{(\frac{\partial f_2}{\partial\theta})^2+(\frac{\partial f_1}{\partial\theta})^2}, \frac{\partial f_1}{\partial\theta}/\sqrt{(\frac{\partial f_2}{\partial\theta})^2+(\frac{\partial f_1}{\partial\theta})^2}, 0).$$

Thus, the angle α between the two planes satisfies

$$\cos\alpha = \frac{\partial f_1}{\partial\theta}/\sqrt{(\frac{\partial f_2}{\partial\theta})^2+(\frac{\partial f_1}{\partial\theta})^2}$$

which is in general of $\mathcal{O}(1)$. This observation will prove quite useful in describing resonant transport later.

For use in an example treated later we record the following: consider the map

$$\begin{aligned} J_1' &= J_1 + \epsilon g_1(J_1, J_2, \phi, \epsilon) \\ J_2' &= J_2 + \epsilon g_2(J_1, J_2, \phi, \epsilon) \\ \phi' &= \phi + J_1 + \epsilon g_3(J_1, J_2, \phi, \epsilon). \end{aligned} \tag{56}$$

For the points close to $J_1 = 0$ we obtain

Corollary 3.6. *If $\partial g_1/\partial\phi > 0$ the fixed point $(J_1(\epsilon), J_2(\epsilon), \phi(\epsilon))$ is a hyperbolic saddle. If $\partial g_1/\partial\phi < 0$ the fixed point is a saddle-focus. If the fixed point is a hyperbolic saddle it has a two-dimensional stable manifold and one-dimensional unstable manifold if*

$$\frac{\{g_1, g_2\}_{(J_2,\phi)}(J_1^0, J_2^0, \phi^0, 0)}{\frac{\partial g_1}{\partial\phi}(J_1^0, J_2^0, \phi^0, 0)} > 0$$

and a two-dimensional unstable manifold and one-dimensional stable manifold if

$$\frac{\{g_1, g_2\}_{(J_2,\phi)}(J_1^0, J_2^0, \phi^0, 0)}{\frac{\partial g_1}{\partial \phi}(J_1^0, J_2^0, \phi^0, 0)} < 0$$

If the fixed point is a saddle focus, the stable and unstable dimensions are reversed.

While the maps studied up to this point of are three-dimensional perturbations of integrable two-dimensional symplectic maps, consider the case when the unperturbed dynamics is governed by time-dependent equations of motion

$$\begin{aligned}
\dot{x} &= \frac{\partial H}{\partial y}(x, y, z, t), \\
\dot{y} &= -\frac{\partial H}{\partial x}(x, y, z, t), \\
\dot{z} &= 0,
\end{aligned}$$

where H is periodic in time with period T. When the time-T Poincaré map is taken, on constant z planes we obtain an area-preserving map which is not necessarily integrable. Study of three-dimensional perturbations of such flows is important in oceanographic context (Pedlosky (1987)). We consider a perturbation of an area-preserving map of this type, given by

$$\begin{aligned}
I_1' &= I_1 + f_1(I_1, I_2, \theta) + \epsilon g_1(I_1, I_2, \theta, \epsilon), \\
I_2' &= I_2 + \epsilon g_2(I_1, I_2, \theta, \epsilon), \\
\theta' &= \theta + I_1 + f_3(I_1, I_2, \theta) + \epsilon g_3(I_1, I_2, \theta, \epsilon),
\end{aligned} \tag{57}$$

where at $\epsilon = 0$ the map is area-preserving in I_1, θ. As the consequence of area preservation, we have

$$\det \begin{bmatrix} 1 + \frac{\partial f_1}{\partial I_1} & \frac{\partial f_1}{\partial \theta} \\ 1 + \frac{\partial f_3}{\partial I_1} & 1 + \frac{\partial f_3}{\partial \theta} \end{bmatrix} = 1, \tag{58}$$

which implies .

$$\frac{\partial f_1}{\partial I_1} + \frac{\partial f_3}{\partial \theta} + \frac{\partial f_1}{\partial I_1}\frac{\partial f_3}{\partial \theta} - \frac{\partial f_1}{\partial \theta} - \frac{\partial f_3}{\partial I_1}\frac{\partial f_1}{\partial \theta} = 0. \tag{59}$$

Let

$$\Xi \equiv \frac{\partial f_1}{\partial I_1} + \frac{\partial f_3}{\partial \theta}.$$

We assume that the map (57) for $\epsilon = 0$ has a fixed point at (I_1^0, I_2^0, θ^0), i.e.

$$f_1(I_1^0, I_2^0, \theta^0) = 0,$$
$$I_1^0 + f_3(I_1^0, I_2^0, \theta^0) = 0.$$

Linearization at (I_1^0, I_2^0, θ^0) yields two eigenvalues that are real if $\Xi > 0$ and complex-conjugate if $\Xi < 0$. By the implicit function theorem, if there is a fixed point (I_1^0, θ^0) on the $I_1 - \theta$ plane for some I_2^0, then there are fixed points of the $\epsilon = 0$ map on all of the close enough I_2 planes provided that

$$\det \begin{bmatrix} \frac{\partial f_1}{\partial I_1} & \frac{\partial f_1}{\partial \theta} \\ 1 + \frac{\partial f_3}{\partial I_1} & \frac{\partial f_3}{\partial \theta} \end{bmatrix} (I_1^0, I_2^0, \theta^0) = \frac{\partial f_1}{\partial I_1}\frac{\partial f_3}{\partial \theta} - \frac{\partial f_1}{\partial \theta} - \frac{\partial f_3}{\partial I_1}\frac{\partial f_1}{\partial \theta} \neq 0, \quad (60)$$

but,

$$\frac{\partial f_1}{\partial I_1}\frac{\partial f_3}{\partial \theta} - \frac{\partial f_1}{\partial \theta} - \frac{\partial f_3}{\partial I_1}\frac{\partial f_1}{\partial \theta} = -\Xi,$$

by (59) and thus for hyperbolic saddles or elliptic fixed points a line of fixed points parametrized by I_2 is obtained in the neighborhood of (I_1^0, I_2^0, θ^0). If $|\Xi| > c > 0$ in the domain of the definition of the map, then this line of fixed points extends throughout the domain of definition of I_2 as suppose not: then there is an I_2^* such that there is a sequence I_2^n of fixed points converging to I_2^* each having a neighborhood in I_2 whose size is, by $|\Xi| > c > 0$ bounded away from zero. That leads to a contradiction.

Let us now assume that $|\Xi| > c > 0$ for some interval $\mathcal{J}_2$ in the domain of definition of I_2. Thus, there is a line of fixed points $(I_1^0(I_2), I_2, \theta^0(I_2))$ for the unperturbed map parametrized on $\mathcal{J}_2$. In the case when

$$\frac{\partial f_1}{\partial I_2} = \frac{\partial f_3}{\partial I_2} = 0,$$

we have the following result:

Proposition 3.7. *Assume that*

$$g_2(I_1^0(I_2^*), I_2^*, \theta^0(I_2^*), 0) = 0,$$

for some I_2^* *and* $\Xi(I_1^0(I_2^*), I_2^*, \theta^0(I_2^*)) \neq 0$. *In addition, let*

$$\frac{\partial g_2}{\partial I_2}(I_1^0(I_2^*), I_2^*, \theta^0(I_2^*), 0) \neq 0.$$

Then, for sufficiently small ϵ *there exists a fixed point of (57)* $\epsilon-$*close to* $(I_1^0(I_2^*), I_2^*, \theta^0(I_2^*))$. *In the case* $\Xi > 0$ *this fixed point is a hyperbolic saddle*

and in the case $\Xi < 0$ it is a saddle-focus. In the case $\Xi > 0$ the hyperbolic saddle has two unstable and one stable directions if

$$\partial g_2/\partial I_2(I_1^0(I_2^*), I_2^*, \theta^0(I_2^*), 0) > 0$$

and two stable and one unstable directions if

$$\partial g_2/\partial I_2(I_1^0(I_2^*), I_2^*, \theta^0(I_2^*), 0) < 0.$$

In the case $\Xi < 0$ the the saddle focus has one unstable and two stable directions if

$$\partial g_2/\partial I_2(I_1^0(I_2^*), I_2^*, \theta^0(I_2^*), 0) > 0,$$

and two unstable and one stable directions if

$$\partial g_2/\partial I_2(I_1^0(I_2^*), I_2^*, \theta^0(I_2^*), 0) < 0.$$

Proof. The persistence part is a straightforward application of the implicit function theorem. The stability results are obtained from considering the eigenvalues of the linearization of the map at $(I_1^0(I_2^*), I_2^*, \theta^0(I_2^*))$:

$$\det \begin{bmatrix} 1-\lambda+\frac{\partial f_1}{\partial I_1}+\epsilon\frac{\partial g_1}{\partial I_1} & \epsilon\frac{\partial g_1}{\partial I_2} & \frac{\partial f_1}{\partial \theta}+\epsilon\frac{\partial g_1}{\partial \theta} \\ \epsilon\frac{\partial g_2}{\partial I_1} & 1-\lambda+\epsilon\frac{\partial g_2}{\partial I_1} & \epsilon\frac{\partial g_2}{\partial \theta} \\ 1+\frac{\partial f_3}{\partial I_1}+\epsilon\frac{\partial g_3}{\partial I_1} & \epsilon\frac{\partial g_3}{\partial I_2} & 1-\lambda+\frac{\partial f_3}{\partial \theta}+\epsilon\frac{\partial g_3}{\partial \theta} \end{bmatrix} = 0,$$

by observing that $\lambda = 1 + \epsilon\frac{\partial g_2}{\partial I_1}$ solves this equation to $\mathcal{O}\left(\epsilon^2\right)$. □

3.7 Transport and mixing

Transport and mixing in action-action-angle maps and flows is largely determined by the nature of fixed points and periodic orbits the existence and type of which was discussed above in the perturbative case. For example, the two-dimensional stable and unstable manifolds of saddle-foci generically intersect, establishing a heteroclinic orbit between two such points. Everywhere in the phase space except in the neighborhood of these heteroclinic orbits and the fixed points themselves, the motion in I_1, I_2 directions is given by the adiabatic approximation [19] which can be obtained by noticing that $I_1' - I_0 = \epsilon f_1^0(I_1, I_2)$ is a discretization of $\dot{I}_1 = f_1(I_1, I_2, \theta)$ for small $\epsilon = \delta t$. Thus, the map in I_1, I_2 can be replaced by its flow version

$$\begin{aligned} \dot{J}_1 &= f_1^0(J_1, J_2), \\ \dot{J}_2 &= f_2^0(J_1, J_2), \end{aligned} \tag{61}$$

We know that the system (61) is Hamiltonian, with a Hamiltonian function $H(J_1, J_2)$. On the other hand, close to heteroclinic orbits and fixed points the system will have very different behavior. Thus, orbits follow the ones given by the "adiabatic" approximation (61) until they encounter one of the resonant surfaces. At these they are governed by the dynamics of heteroclinic orbits. It is important to point out that the saddle-foci complex conjugate eigenvectors, which play the biggest role in transport, do not lie in the resonance plane but at an angle to it, as we have shown earlier. Thus, when an orbit encounters the fixed point, it is displaced away from the value of the adiabatic invariant that it had when it encountered the resonant surface. Note that the right-hand side of (61) plays a prominent role in our theorem on nonexistence of invariant surfaces. In general, if the surfaces of constant Ω and adiabatic surfaces coincide and the trajectory is on a surface for which Ω is Diophantine, such surface could persist and the global transport would be prevented, as the jumping from one adiabatic surface to the other occurs at the intersection of resonant and adiabatic surfaces. For the case of flows, global transport is possible if all surfaces tangent to (f_1^0, f_2^0) intersect $\Omega = 0$ surface.

A figure that describes the nature of transport in the 3D action-angle angle maps and flows that we studied is 21a. A saddle-focus with 2 stable and 1 unstable direction is shown, directing the dynamics away from one and towards another adiabatic surface. Globally chaotic dynamics is enabled by such "hopping" from one adiabatic surface to another. A beautiful rendering of saddle foci that control transport and mixing in an apparatus of counterrotating disc from the work of Lackey and Sotiropoulos (2006) is shown in figure 21b.

3.8 Solomon experiments

In Solomon and Mezić (2003) the above ideas on resonances were tested in an experiment The flow studied in Solomon and Mezić (2003) is dominated by a horizontal chain of alternating vortices (shown in blue in figure 22) with a secondary flow due to Ekman pumping (red), a process that occurs whenever a vortical flow is bounded by a solid surface (see figure 22). Radial pressure gradients due to the no-slip boundary condition push the fluid inward just above the solid boundary and up through the vortex centers. This is a common 3D flow perturbation; we therefore expect the internal mixing properties observed with this flow to be generic to a wide variety of vortical flows; basically, laminar vortex flows in the presence of a rigid boundary, particularly vortex flows in microfluidic devices.

Time dependence takes the form of lateral oscillations of the vortex

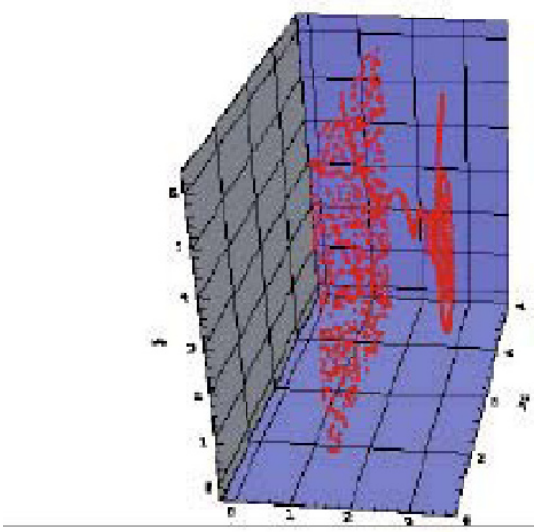

a)

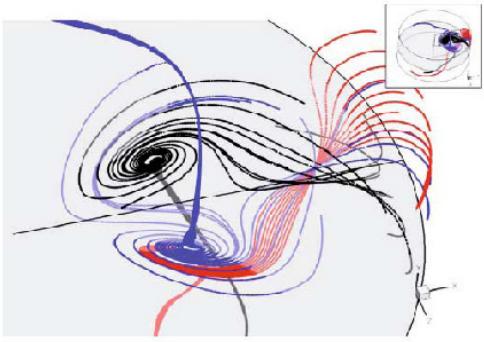

b)

Figure 21. a) A saddle-focus with 2 stable and 1 unstable direction, directing the dynamics away from one and towards another adiabatic surface b)Saddle foci that control transport and mixing in an apparatus of counterrotating disc Lackey and Sotiropoulos (2006)

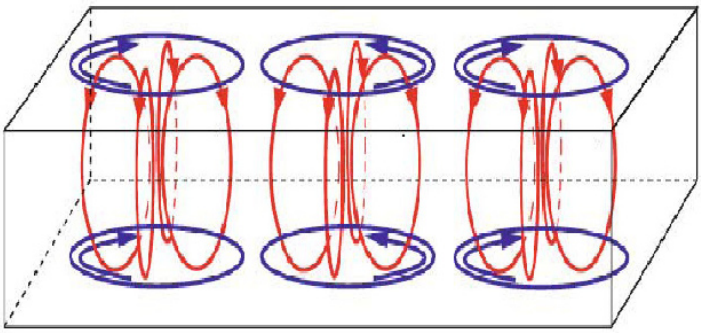

Figure 22. The physical nature of the flow in Solomon experiments. There are chains of horizontal and vertical vortices, whose centers move in a periodic fashion (see equation (62)).

chain, similar to the oscillatory instability of Rayleigh-Bénard convection. A model for the above described flow is

$$\begin{aligned}
\dot{x} &= -\cos(\pi x_s(t))\sin(\pi y) + \epsilon \sin(2\pi x_s(t))\sin(\pi z),\\
\dot{y} &= \sin(\pi x_s(t))\cos(\pi y) + \epsilon \sin(2\pi y)\sin(\pi z),\\
\dot{z} &= \epsilon \cos(\pi z)(\cos(2\pi x_s(t)) + \cos(2\pi y))
\end{aligned} \tag{62}$$

where $x_s(t) = x + b\sin(\omega t)$, where b and ω are the non-dimensionalized oscillation amplitude and frequency. Results of the model simulation are shown in figure 23. Figure 23a) shows the Poincaré section for 2D, time-periodic case ($\epsilon = 0, b = 0.01, \omega = 2.5$), determined by plotting locations of five tracers once each period, initially located on the x axis at $x = 0.49, 0.4, 0.3, 0.2$ and 0.1. Note that the time-dependence is small. As expected, we see a small chaotic zone around the separatrices for the unperturbed steady 2-dimensional flow ($b = 0$) and evidence of a big resonant island (crescent-like structure in the figure). In 23b, the trajectory of tracer in 3D, time-independent flow ($\epsilon = 0.005, b = 0$) rolls around a 2-dimensional torus, and shows no signs of chaos. In 23c, Poincaré section for a tracer near a periodic orbit for 3D, time-periodic case ($\epsilon = 0.0001, b = 0.001, \omega = 2.5$), showing the tracer spiralling off one adiabatic surface (the spiral is very tightly wound and may be difficult to resolve) and onto a different one, just as predicted in the previously described theory. In 23d, Horizontal

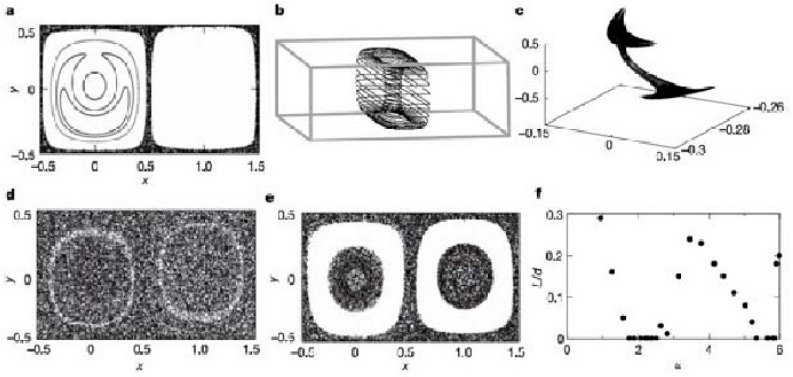

Figure 23. Results of the simulation of (62). For description, see the text.

slice ($-0.1 \leq z \leq 0.1$) of Poincare section of a single tracer for 3D, time-periodic case ($\epsilon = 0.005, b = 0.01, \omega = 2.5$); the tracer is initially located at $(x, y, z) = (0.49, 0, 0)$, and the forcing frequency is almost resonant with tracers circulating in the central crescent island shown in 23a) . In 23e, horizontal slice of Poincaré section for a non-resonant forcing frequency ($\epsilon = 0.005, b = 0.01, \omega = 4.0$) is shown. In absence of resonance, an excluded zone with poor mixing results. In 23f, the width L of the excluded region shown in e) (as a fraction of the vortex width d) is plotted versus non-dimensional driving frequency ($\epsilon = 0.005, b = 0.01$). Uniform mixing is achieved for the frequencies where the width goes to zero. These results, in summary, tell us that global mixing can be achieved in three-dimensional, time-dependent perturbations of two-dimensional flows, even if the perturbation is very small, provided that resonance conditions are met (in the case of the model just presented, the time-dependence particulary needs to be resonant with circulation times in the steady two-dimensional flow for particles close to the position of the two-dimensional crescent-like island shown in 23a)).

The conditions that, in the model, lead to global chaotic behavior in the phase space, lead to good mixing in the corresponding experimental set-up, as indicated in figure 24. The top view of the apparatus is shown. The dye is initially put in two "cells" that appear bright in the figure. From the top to the bottom, snapshots of the concentration field at 5-minutes intervals are shown. Despite the fact that the flow in the vertical direction is 1/10

of the strength of the flow in the horizontal direction, complete mixing is achieved.

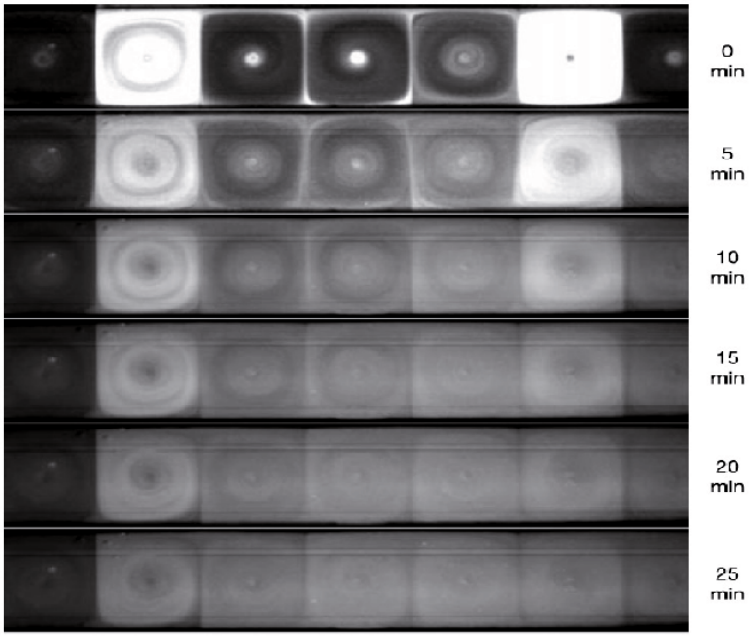

Figure 24. Experiments on resonant mixing in weakly three-dimensional time-periodic flows (Solomon and Mezić (2003))

4 Application to micromixers

Engineers would like to design and control mixing, not just analyze it - although for devices operating at large Reynolds numbers, turbulent mixing usually provides satisfactory results. Microfluidic devices typicaly have laminar flow due to low Reynolds number but require good mixing. In this section we expand on the uses, need and some designs for mixing in microfluidics, and point out where the above described geometric approach is useful and where new theory can help.

The use of integrated microelectromechanical systems (MEMS) is ex-

panding rapidly due to improvements in microfabrication technology. MEMS have applications in a variety of industries, including the automotive, aerospace, computer, and biomedical industries. Micro total analysis systems (μTAS) are being developed for drug discovery, drug delivery and chemical sensing (Chiem et al. (1997)). Technical barriers of these systems include device packaging and interfacing, chemical surface absorption, and control of fluid motion on the microscale (Karniadakis and Beskok (2001)). A recent review of flow physics, including mixing, in microscale devices is given in Squires and Quake (2005). The performance of these devices can be limited by the rate at which mixing occurs at the microscale. Mixing of two fluids is enhanced when the interface between the fluids is increased through stretching and folding (for a perspective on mixing strongly emphasizing the stretching and folding aspect, see Ottino (1989)), so that diffusion between the fluids only has to occur over a relatively small distance. At the macroscale, stretching and folding of interfaces is performed by three-dimensional turbulent eddies that contain a continuous spectrum of length scales. A turbulent flow regime in channels occurs at a relatively high Reynolds number, defined as $Re = UL/\nu$, where U is the characteristic velocity, L is the characteristic lengthscale (e.g. the width of the channel), and ν is the kinematic viscosity. A water flow through a 200 μm wide channel, with a kinematic viscosity, $\nu = 10^{-6}\ m^2/s$, and a characteristic velocity of 1 cm/s, has a Reynolds number of 2. The flow at this Reynolds number is laminar. In microdevices, fluids are often mixed through pure molecular diffusion. However, depending upon the rate at which diffusion occurs, the diffusion time scale, t_D, defined as $t_D = L^2/D$, where L is the relevant mixing length (i.e. the characteristic width of the flow channel), and D is the molecular diffusivity, may be too large. As an example, in practical BioMEMS applications (e.g. biosensors, (Vijayendran et al. (2003))), one is often interested in transporting and mixing biological molecules. The diffusion coefficient of hemoglobin in water, is $D = 70\ \mu m^2/s$, and therefore it would take up to 570 s for this molecule to diffuse over a length of $L = 200$ μm. Thus, advective stretching and folding of interfaces is still desirable in order to improve the effective diffusion coefficients. Microscale mixers that were designed to achieve such an improvement can be divided into two broad classifications: passive and active. Passive mixers rely on geometrical properties of channel shape to induce complicated fluid particle trajectories and thus mix. Examples include work in Branebjerg et al. (1994, 1996); Miyake et al. (1993); Liu et al. (2000); Yi and Bau (2000); Stroock et al. (2002).

As we explained earlier since the induced laminar flows are steady, in order to produce good (exponential in time) mixing they must rely on three-

dimensionality of the resulting particle motion. Recent passive designs e.g. in Liu et al. (2000); Stroock et al. (2002) use the concept of chaotic advection. As mentioned before, the key advantage of chaotic advection-based strategies is that exponential rate of mixing is achieved, as opposed to an algebraic rate (e.g. t^{-1}) that is achieved e.g. by inducing shearing vortical motion (besides the discussion above, see also the book Ottino (1989), and -for an example in micromixing- the paper Chou et al. (2001)). In figure 25 design of a passive micromixer along with some results from Stroock et al. (2002) are shown. The design of the through-flow micromixer shown in figure 25 consists of periodically repeated "basic cell" units. Such a basic cell unit is shown in the lower part figure 25 a). On top of that figure the cross-sectional streamlines that are induced by the patterns of grooves on the bottom of the basic cell unit are shown. Because of the low Reynolds number, the fluid tends to flow along the groove, hit the wall and upwell, to proceed towards the groove wedge plane and downwell there. Since grooves in the first part and the second part of the cell have different lengths on different sides, the vortical motions that are formed are asymmetric. The dye material that starts in one of the vortical regions will stay there (diffusion being small) over the part of the cell with the same groove pattern. When the groove pattern changes, there is also exchange between different vortical regions and exchange of dye between them as shown in figure 25 b). Even after 5 repeated cell units the layering of the fluorescent dye material and pure water (dark in the figures) is visible, and thus advection is dominant over diffusion. Thus, methods that we have discussed can be applied to study this three-dimensional flow on a periodic domain. In particular, Poincaré map can be generated by considering the surface of section at the end of the cell.

In contrast to steady designs which initially relied on laminar shear for mixing, even the first active micromixer, designed by Evans et al. in Evans et al. (1997), was based on the concept of chaotic advection. As seen on the example leading to the standard map, an essentially two-dimensional laminar flow can mix well if it is time-periodic (steady two-dimensional flows can only mix at an algebraic, not exponential rate). One example is that of a commonly used design, the *shear superposition micromixer (SSM)* that was first presented in Volpert et al. (1999), based on the prior theoretical study of optimal mixing by sequences of shear flows at different angles in D'Alessandro et al. (1999). In contrast to Evans et al. (1997) this is a continuous through-flow micromixer consisting of the main channel with three cross-flow side-channels that are capable of producing time-dependent shear flow in the direction transverse to the main stream (see figure 26). The physical mechanism of mixing in SSM is similar to that described mathematically

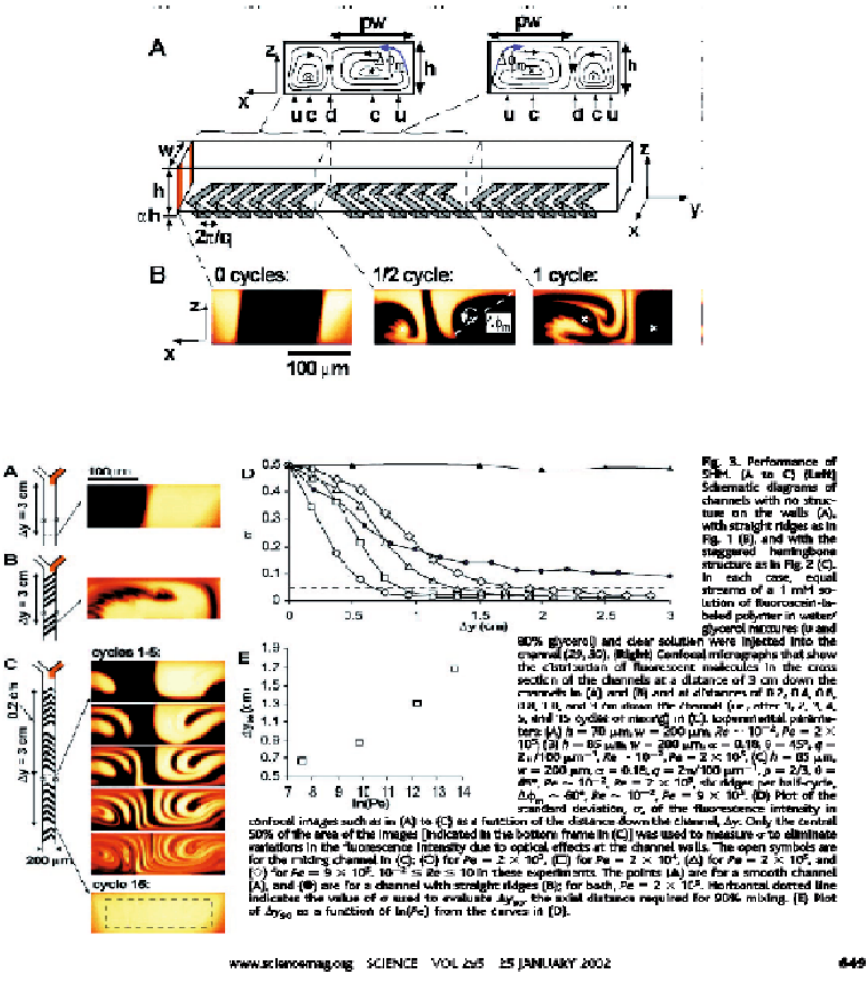

Fig. 3. Performance of SHM. (A to C) (Left) Schematic diagrams of channels with no structure on the walls (A), with straight ridges as in Fig. 1 (B), and with the staggered herringbone structure as in Fig. 2 (C). In each case, equal streams of a 1 mM solution of fluorescein-labeled polymer in water/glycerol mixtures (u and 80% glycerol) and clear solution were injected into the channel (29, 30). (Right) Confocal micrographs that show the distribution of fluorescent molecules in the cross section of the channels at a distance of 3 cm down the channels in (A) and (B) and at distances of 0.2, 0.4, 0.6, 0.8, 1.0, and 1.4 cm down the channel (or, after 1, 2, 3, 4, 5, and 16 cycles of mixing) in (C). Experimental parameters: (A) $h = 70$ μm, $w = 200$ μm, $Re \sim 10^{-4}$, $Pe = 2 \times 10^5$; (B) $h = 65$ μm, $w = 200$ μm, $\alpha = 0.16$, $\theta = 45°$, $q = 2\pi/100$ μm^{-1}, $Re \sim 10^{-3}$, $Pe = 2 \times 10^5$; (C) $h = 65$ μm, $w = 200$ μm, $\alpha = 0.15$, $q = 2\pi/100$ μm^{-1}, $\beta = 2/3$, $\theta = 45°$, $Re \sim 10^{-3}$, $Re = 2 \times 10^5$, six ridges per half-cycle, $\Delta\phi_{ch} = 60°$, $Re \sim 10^{-3}$, $Pe = 9 \times 10^5$. (D) Plot of the standard deviation, σ, of the fluorescence intensity in confocal images such as (A) to (C) as a function of the distance down the channel, Δy. Only the central 50% of the area of the images (indicated in the bottom frame in (C)) was used to measure σ to eliminate variations in the fluorescence intensity due to optical effects at the channel walls. The open symbols are for the mixing channel in (C): (○) for $Pe = 2 \times 10^5$, (□) for $Pe = 2 \times 10^4$, (△) for $Pe = 2 \times 10^3$, and (◇) for $Pe = 9 \times 10^2$. $10^{-4} \leq Re \leq 10$ in these experiments. The points (▲) are for a smooth channel (A), and (●) are for a channel with straight ridges (B); for both, $Pe = 2 \times 10^5$. Horizontal dotted line indicates the value of σ used to evaluate Δy_{90}, the axial distance required for 90% mixing. (E) Plot of Δy_{90} as a function of ln(Pe) from the curves in (D).

Figure 25. A passive micromixer.

in D'Alessandro et al. (1999) and consists of rearrangement of streamwise-oriented strips to cross-stream oriented strips and subsequent stretching by parabolic shear (somewhat similar to the tendril-whorl map introduced in Ottino (1989)), as described in Mueller et al. (2003). In the same paper, optimization of frequencies for mixing was performed on a two-dimensional model. The two-dimensional model introduced in Volpert et al. (1999) and used in Niu and Lee (2003) is kinematic and consists of a superposition of a parabolic flow profile in the main channel with the solution of Navier-Stokes equation with oscillatory pressure gradient in the side channels. It was extended to three dimensions in Bottausci et al. (2004)

This design was also considered in Lee et al. (2001), where a single side-channel configuration was presented. In Niu and Lee (2003) a study of that design with periodic repetition of spatial cells was performed using ideas from chaotic dynamics. In that study, the frequency used for actuation of every side-channel was the same. Thus, the study was performed on the periodic domain using a two-dimensional map of the type discussed in the previous sections. In Volpert et al. (1999) the frequencies of the actuation for downstream increases. This is based on the physical fact that the first side channel introduces layering of two fluid streams. Thus, the size of maximal blobs of non-mixed fluid decreases downstream, and the frequency necessary for good mixing increases. The methods that we introduced in the previous sections are applicable to closed domain (this could be either a closed container or a periodic domain as in the case of the steady mixer described above and time-periodic actuation of the active spatially periodic mixer as pursued in Niu and Lee (2003)), time-periodic or steady flows. However, when time-dependence is more complicated than periodic and/or the domain is not closed, different techniques of analysis are needed. In the rest of the lectures, we present a number such techniques, based on concepts from ergodic theory that apply in a more general context just described.

5 Ergodic theory and mixing

There are a number of problems in the theory of advective mixing that require a departure from the geometrical approach adopted above. In fact, historically the statistical approach was the one predominantly used to characterize mixing via discussion of residence times and concentration distributions Paul et al. (2004). Introduction of dynamical systems methods shed new light on these statistical issues as well. In the next several sections we concentrate on a few topics in which Ergodic Theory, a branch of mathematics closely associated with Dynamical Systems Theory is used to discuss statistical and visualization issues in mixing.

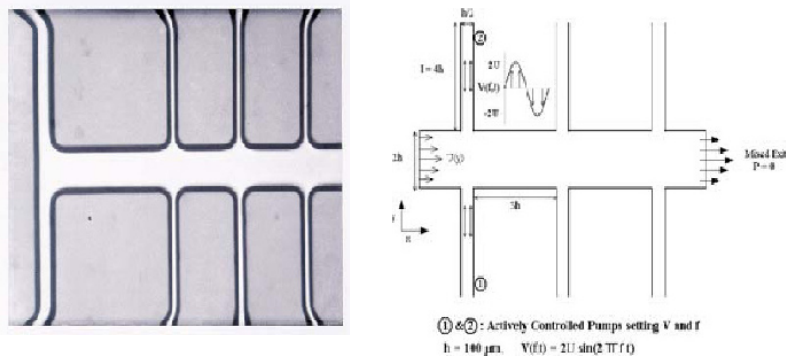

Figure 26. Left: Micrograph of the working portion of the mixing microchip. The active mixing device shown consists of a main mixing channel and three pairs of secondary channels that perturb the flow in the main channel. Two unmixed, miscible fluids enter the main channel, and are then manipulated by pressure-driven flow from the secondary channels. The flow from the secondary channels is specified to be oscillating at different frequencies, to provide enhanced mixing efficiency. Right: Schematic of the fluid flow in the channel. The mixing channel is $2h$ high and $13.5h$ long, where h is an adjustable length scale ranging from $50\mu m$ to $150\mu m$, depending on the application of the mixer. The six secondary channels (or three pairs of secondary channels) are perpendicular to the main channel, and are $h/2$ wide, $5h$ long and separated from each other by a distance of $3h$. An approximately parabolic profile develops at the entrance of the main channel. In the side channels, an oscillatory flow is induced by pumping. The channels are set to oscillate at phases $(0, \pi, 0)$, while the amplitude and frequencies are varied to achieve optimal mixing. This gives a versatile design that can mix efficiently under varying flow conditions.

5.1 Visualization

There is a variety of ways one can study dynamical systems and their trajectories besides solving them analytically or integrating them numerically. Visualization of different regular features in the phase space clearly plays a major role in this context. In particular, visualization of invariant sets is of special interest for understanding of mixing in fluids. Specifically, if the set invariant under advection does not occupy the whole space available for fluid motion, then at least two separate invariant sets exist and particles can transition from one to another only through diffusion[3]. This puts an immediate bound on how fast the uniformization of the mixture can proceed: let the diffusion coefficient be D m^2/s, and the area of the boundary of the domain occupied by dye be denoted by A. Denote the volume inside A by V. Let V be an invariant set. Then the flux across A is purely diffusive:

$$F = \int_A D\nabla c \; dA \leq D \cdot area(A) \cdot \max_A |\nabla c|.$$

The idea in Mezić (1994); Mezić and Wiggins (1999) is to compute time averages of functions on the flow domain, associate these time averages with the initial conditions and plot the contour plot of the time average function. This turns out to visualize invariant sets. To see this, consider an arbitrary continuous function $f(x, y, z)$ defined on a compact flow domain in $\mathbb{R}^3$ (note: continuous functions on compact domains have a maximum and a minimum on the domain). For simplicity we will work with steady velocity fields. A specific example is velocity component in the direction of x axis, $v_x(x, y, z)$. Starting from an initial point $\mathbf{x}_0 = (x_0, y_0, z_0)$ compute the time average

$$\frac{1}{T}\int_0^T f(\mathbf{x}(t, \mathbf{x}_0))dt.$$

Taking the limit $T \to \infty$, define

$$f^*(\mathbf{x}_0) = \lim_{T\to\infty} \frac{1}{T}\int_0^T f(\mathbf{x}(t, \mathbf{x}_0))dt.$$

This quantity does not depend on the initial point on a specific trajectory we started from: assume $\mathbf{x}_0$ and $\mathbf{x}_1$ are two points on the same trajectory. Then it must be that $\mathbf{x}_1(t_1) = \mathbf{x}(t_1, \mathbf{x}_0, 0)$, for some t_1 (see section 2.3).

[3]To be precise, we should say "measure 1 set" instead of "the whole volume" since invariant sets of zero measure, such as unstable periodic orbits, are embedded in chaotic regions.

Without loss of generality we can choose $t_1 > 0$. For any time $T > t_1$, we have

$$\int_0^T f(\mathbf{x}(t,\mathbf{x}_0))dt = \int_0^{t_1} f(\mathbf{x}(t,\mathbf{x}_0))dt + \int_{t_1}^T f(\mathbf{x}(t,\mathbf{x}_1))dt \quad (63)$$

$$= \int_0^{t_1} f(\mathbf{x}(t,\mathbf{x}_0))dt + \int_0^{T-t_1} f(\mathbf{x}(t,\mathbf{x}_1))dt. \quad (64)$$

Thus,

$$f^*(\mathbf{x}_0) = \lim_{T\to\infty} \frac{1}{T}\int_0^T f(\mathbf{x}(t,\mathbf{x}_0))dt \quad (65)$$

$$= \lim_{T\to\infty} \frac{1}{T}\int_0^{t_1} f(\mathbf{x}(t,\mathbf{x}_0))dt + \lim_{T\to\infty} \frac{1}{T}\int_0^{T-t_1} f(\mathbf{x}(t,\mathbf{x}_1))dt.$$

The first term on the right is zero since t_1 is finite and f is bounded. For the second term, we have

$$\lim_{T\to\infty} \tfrac{1}{T}\int_0^{T-t_1} f(\mathbf{x}(t,\mathbf{x}_1))dt \quad (66)$$

$$= \lim_{T\to\infty} \tfrac{1}{T}\int_0^{T} f(\mathbf{x}(t,\mathbf{x}_1))dt - \lim_{T\to\infty} \tfrac{1}{T}\int_{T-t_1}^{T} f(\mathbf{x}(t,\mathbf{x}_1))dt, \quad (67)$$

where the second term is again zero due to finiteness of f and t_1. Thus, $f^*(\mathbf{x}_0) = f^*(\mathbf{x}_1)$ and time averages of continuous functions are constant on trajectories. From this it is clear that level sets of the function f^* are in fact invariant sets. We will call the plots of time averages *Mesochronic Plots*.

Of course, in computations we are restricted to finite time. The time averages described above converge with an error of order $1/T$ in regions where particle motion is periodic or quasi-periodic in time. They converge as $1/\sqrt{T}$ where particle motion is chaotic (Mezić and Sotiropoulos (2002)).

When we have a time-periodic velocity field, we consider the Poincaré map $\mathbf{x}' = \mathbf{T}\mathbf{x}$. The time average $f^*(\mathbf{x}_0)$ under the dynamics corresponding to some initial point $\mathbf{x}_0$ is now defined as

$$f^*(\mathbf{x}_0) := \lim_{n\to\infty} \frac{1}{n}\sum_{k=0}^{n-1} f(\mathbf{T}^k\mathbf{x}_0)$$

and exists almost everywhere in the phase space (Mane (1987)). A simple observation $f^*(\mathbf{T}\mathbf{x}) = f^*(\mathbf{x})$ implies that f^* is an invariant function, meaning that two points having the same time average for some function are contained in the same invariant set.

The following computations have been done in Z. Levnajić's thesis work at UCSB (Levnajić (2006)). We will compute plots of $f^*(x_0, y_0)$ for certain

functions f for a grid of 800×800 initial points (x_0, y_0). To begin with we will set $f^*(x,y) \equiv f_N(x,y)$ for $N = 30,000$ i.e. time averages will be identified with partial time averages computed up to 30,000 iterations.

In Fig. 27a we show trajectories of the standard map for the $\epsilon = 0.17$ case. In Fig. 27b we show contour plot of Lagrangian time averages (i.e. Mesochronic Plot) of the function $f(x,y) = \sin(5\pi y + 6\pi y)$. The features of the trajectory plot are mimicked closely by the time-average plot. In figure 28 we show how Mesochronic Plots reflect changes in the phase space for increase of the parameter value of the standard map. Note that the functions whose Mesochronic Plots are shown in 28 are different than that in 27b.

In two dimensions we can plot trajectories and the comparisons above are just to show the close correspondence to the plot of trajectories. This technique is quite useful when studying three-dimensional maps, since it is difficult to analyze three-dimensional trajectory plots. Consider for example the following 3-D map defined on the three-dimensional box with periodic boundaries (i.e. a three-dimensional torus):

$$\begin{aligned} x^{'} &= x + z + \epsilon \sin(2\pi x)\sin(2\pi y) \\ y^{'} &= y + \epsilon z^2 + \epsilon \cos(2\pi x) \\ z^{'} &= z + \epsilon \sin(2\pi x)\sin(2\pi y) \end{aligned} \tag{68}$$

Note that $z = const.$ surfaces are invariant for this map at $\epsilon = 0$. The map is of degenerate action-angle-angle type (since one of the frequencies -ϵz^2 is of the same size as the perturbation). For this special class of maps, it was shown that KAM-type theorem holds (Vaidya and Mezić (2006)). Thus, we would expect to see $z = const$ tori (note: because of boundary conditions, $z = const.$ surfaces are two-dimensional tori) should persist. In the figure 29 we show Mesochronic Plots for $f = \sin 2\pi z$ function at the $y = 0.5$ plane, for $\epsilon = 0.001$ (top left), $\epsilon = 0.005$ (top right), $\epsilon = 0.1$ (bottom left) and $\epsilon = 0.2$ (bottom right). The plots were obtained by starting 500×500 initial conditions on the $y = 0.5$ plane and computing time averages of f. The interpretation of Mesochronic Plot at $y = 0.5$ is that it represents intersection of invariant sets in 3D with the $y = 0.5$ plane. The almost straight level sets in the top left figure represent a family of invariant tori that persist via KAM. In the bottom of the Mesochronic Plot, there is a zone of chaotic motion (grainy features are due to slow convergence in chaotic zones). That zone gets bigger with the increase of parameter ϵ and leads to fully chaotic Mesochronic Plot in the bottom right, for $\epsilon = 0.2$.

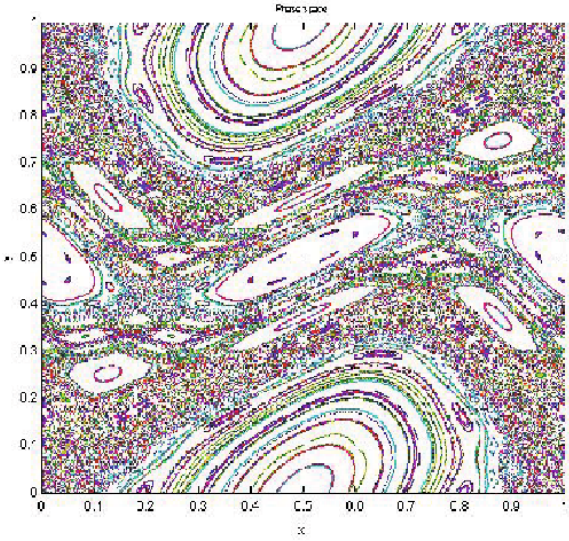

a

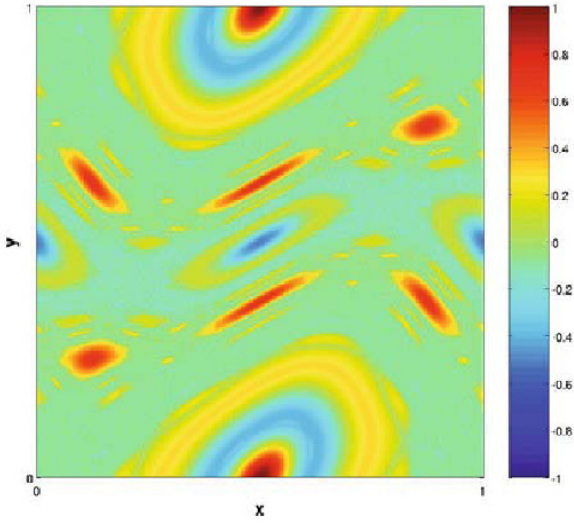

b

Figure 27. Phase portrait of the standard map at $\epsilon = 0.17$ b) time average of $f(x, y) = \sin(5\pi y + 6\pi y)$ with $\varepsilon = 0.17$ (b)

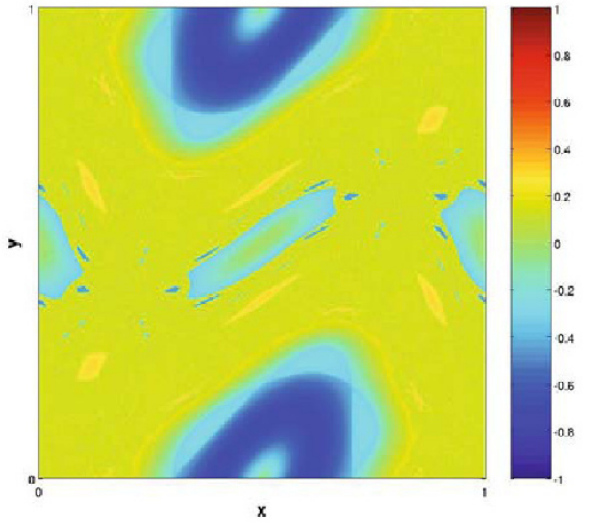

a

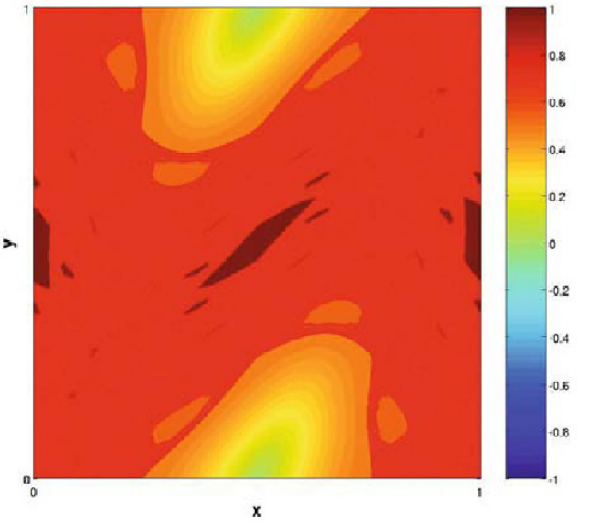

b

Figure 28. $f(x,y) = \sin(2\pi x + 3\pi y)$ with $\varepsilon = 0.21$ (a); $f(x,y) = \sin(\pi y)$ with $\varepsilon = 0.26$ (b)

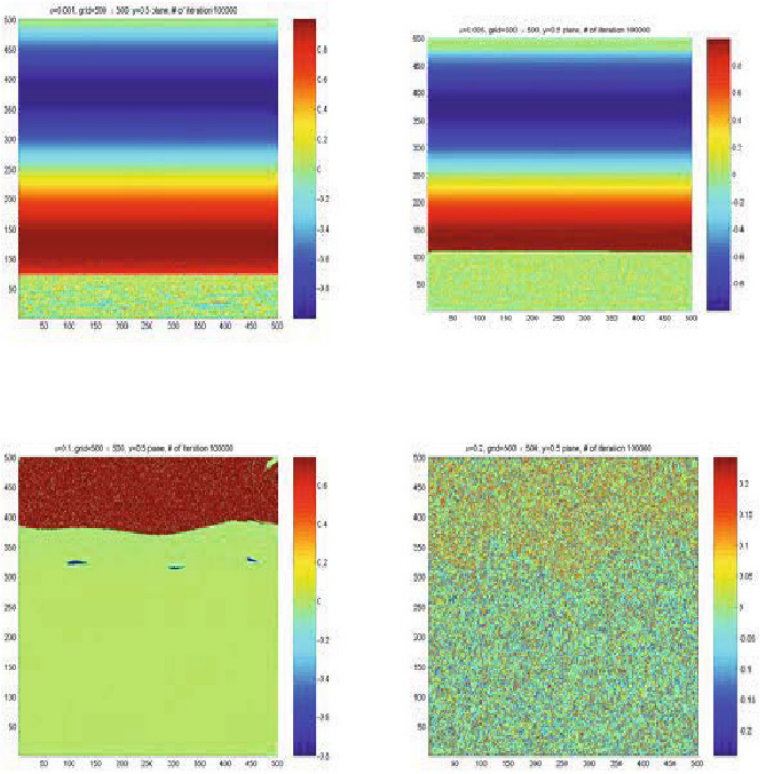

Figure 29. Mesochronic Plot at $y = 0.5$ for the map (68), and $f = \sin 2\pi z$.

6 Conclusions

Statistical description of non-diffusive mixing in fluid flows can be achieved using ergodic theory. In these lectures we use ergodic theory to provide only visualization methods, but it can be used for quite a bit more (Mathew et al. (2005)) The question of mixing is different for naturally occuring, e.g. oceanographic, fluid flows and those important in engineering applications such as microfluidics. The latter can typically be influenced via time-dependent boundary conditions or external forces. Thus, a question arises that is properly set in the context of control theory: which time-dependence, or mixing protocol (as introduced in Ottino (1989)) should be chosen to achieve maximal mixing? When molecular diffusion is present, any protocol will achieve uniform final concentration. Thus the question reduces to the question of the rate of convergence. But in the case of non-diffusive mixing, both the issue of completeness of mixing and its speed need to be considered in order to formulate the control-theoretic "cost function". Such issues have become a topic of quite a bit of interest recently, but we leave them for a discussion elsewhere.

Bibliography

H. Aref. Stirring by chaotic advection. *Journal of Fluid Mechanics*, 143: 1–21, 1984.

R. Aris. *Vectors, tensors, and the basic equations of fluid mechanics*. Prentice-Hall, Englewood Cliffs, N.J., 1962.

V. I. Arnold. Small denominators and problems of stability of motion in classical and celestial mechanics. *Russ. Math. Survey*, 18:85–192, 1963.

V. I. Arnold. Sur la géométrie differentielle des groupes de lie de dimension infinie et ses applications á l'hydrodynamique des fluides parfaits. *Ann. Inst Fourier*, 16:316–361, 1966.

V. I. Arnold. *Mathematical Methods of Classical Mechanics*. Springer-Verlag, New York, 1978.

V.I. Arnold. *Ordinary Differential Equations*. Springer Verlag, Berlin, N.Y., 2006. Theorem and remark after Theorem 17,chapter 5, Sec. 3.3.

P. Ashwin and G. P. King. Azimuthally propagating ring vortices in a model for nonaxisymmetric Taylor vortex flow. *Physical Review Letters*, 75:4610–4613, 1995a.

P. Ashwin and G. P. King. Streamline topology in eccentric Taylor vortex flow. *Journal of Fluid Mechanics*, 285:215–247, 1995b.

S. Balasuriya, C. K. R. T. Jones, and B. Sandstede. Viscous perturbations of vorticity-conserving flows and separatrix splitting. *Nonlinearity*, 11: 47–77, 1997.

G. K. Batchelor. *An Introduction to Fluid Dynamics*. Cambridge University Press, Cambridge, 1967.

F. Bottausci, I. Mezić, C. D. Meinhart, and C. Cardonne. Mixing in the shear superposition micromixer: three-dimensional analysis. *Philosophical Transactions of the Royal Society of London Series A-Mathematical Physical and Engineering Sciences*, 362:1001–1018, 2004.

J. Branebjerg, B. Fabius, and P. Gravesen. *Application of Miniature Analyzers from Microfluidic Components to μTAS*, pages 141–151. Proceedings of Micro Total Analysis System Conference, Twente, Netherlands. 1994.

J. Branebjerg, B. Fabius, and P. Gravesen. *Fast mixing by lamination*, pages 441–446. Proceedings of the 9th Annual Workshop on Micro Electro Mechanical Systems, San Diego, CA. 1996.

J. H. E. Cartwright, M. Feingold, and O. Piro. Chaotic advection in three-dimensional unsteady incompressible laminar flow. *Journal of Fluid Mechanics*, 316:259–284, 1996.

C.-Q. Cheng and Y.-S. Sun. Existence of invariant tori in three-dimensional measure-preserving mappings. *Celestial Mechanics*, 47:275–292, 1990.

N. Chiem, C. Colyer, and Harrison. *Microfluidic Systems for Clinical Diagnostics*, pages 183–186. International Conference on Solid State Sensors and Actuators, Chicago, IL, vol 1. 1997.

A.J. Chorin and J.E. Marsden. *A Mathematical Introduction to Fluid Mechanics*. Springer-Verlag, New York, 1998.

H.-P. Chou, M. A. Unger, and S. R. Quake. A microfabricated rotary pump. *Biomedical Microdevices*, 3:323–330, 2001.

D. D'Alessandro, M. Dahleh, and I. Mezić. Control of mixing in fluid flow: A maximum entropy approach. *IEEE Transactions on Automatic Control*, 44:1852–1863, 1999.

J. Evans, D. Liepmann, and A. P. Pisano. *Planar laminar mixer*, pages 96–101. 10th Annual Workshop of Micro Electro Mechanical System, Nagoya, Japan. 1997.

C.L. Fefferman. Existence & smoothness of the navierstokes equation. Description of Millenium Prize problems for Clay Mathematics Institute,, 2000.

M. Feingold, L. P. Kadanoff, and O. Piro. Passive scalars, 3-dimensional volume-preserving maps and chaos. *Journal of Statistical Physics*, 50: 529–565, 1988.

G. O. Fountain, D. V. Khakhar, I. Mezić, and J. M. Ottino. Chaotic mixing in a bounded 3-D flow. In press, Journal of Fluid Mechanics, 2000.

J. W. Gibbs. *Elementary principles in statistical mechanics: developed with special reference to the rational foundation of thermodynamics*. Yale University Press, New Haven, 1902.

G. Haller and I. Mezić. Reduction of three-dimensional, volume-preserving flows by symmetry. *Nonlinearity*, 11:319–339, 1998.

M. Hénon. Sur la topologie des lignes de courant dans un cas particulier. *C.R. Acad. Sci. Paris A*, 262:312–314, 1966.

G.E. Karniadakis and A. Beskok. *Micro Flows*. Springer-Verlag, New York, 2001.

T. C. Lackey and F. Sotiropoulos. Relationship between stirring rate and reynolds number in the chaotically advected steady flow in a container with exactly counter-rotating lids. *Physics of Fluids*, 18:053601, 2006.

H. Lamb. *Hydrodynamics*. Dover, New York, 1932.

Y. K. Lee, J. Deval, P. Tabeling, and C. M. Ho. *Chaotic mixing in electrokinetically and pressure-driven micro flows*, pages 483–486. Proceedings of the 14th IEEE Workshop on MEMS, Interlaken, Switzerland. 2001.

Z. Levnajić. Ucsb master's thesis in mechanical engineering. 2006.

R. H. Liu, K. V. Sharp, M. G. Olsen, M. A. Stremler, J. G. Santiago, R. J. Adrian, H. Aref, and D. J. Beebe. A passive micromixer: Three-dimensional serpentine microchannel. *J. of MEMS*, 9(2), 2000.

R. Mane. *Ergodic Theory and Differentiable Dynamics*. Springer-Verlag, 1987.

G. Mathew, I. Mezić, and L. Petzold. A multiscale measure for mixing. *Physica D*, 211:23–46, 2005.

K. R. Meyer and G. R. Hall. *Introduction to Hamiltonian systems and the N-body problem*. Springer-Verlag, New York, 1992.

I. Mezić. *On Geometrical and Statistical Properties of Dynamical Systems: Theory and Applications*. PhD thesis, California Institute of Technology, 1994.

I. Mezić. ABC flows as a paradigm for chaotic advection in 3-d. Preprint, 2000.

I. Mezić and F. Sotiropoulos. Ergodic theory and experimental visualization of invariant sets in chaotically advected flows. *Physics of Fluids*, 14:2235–2243, 2002.

I. Mezić and S. Wiggins. On the integrability and perturbation of three dimensional fluid flows with symmetry. *Journal of Nonlinear Science*, 4: 157–194, 1994.

I. Mezić and S. Wiggins. A method for visualization of invariant sets of dynamical systems based on the ergodic partition. *Chaos*, 9:213–218, 1999.

R. Miyake, T. S. J. Lammerink, M. Elwenspoek, and J. H. J. Fluitman. *Micro Mixer with fast diffusion*, pages 248–253. Proceedings of the IEEE Micro Electro Mechanical Workshop, Fort Lauderale, FL. 1993.

J. Moser. On the theory of quasiperiodic motion. *SIAM Review*, 8:145–172, 1968.

S. D. Mueller, I. Mezić, J. H. Walther, and P. Koumoutsakos. Transverse momentum micromixer optimization with evolution strategies. To appear in Computers and Fluids, 2003.

X. Niu and Y. K. Lee. Efficient spatio-temporal chaotic mixing in microchannels. *Journal of Micromechanics and Microengineering*, 13:454–462, 2003.

J.M. Ottino. *The Kinematics of Mixing: Stretching, Chaos and Transport*. Cambridge University Press, Cambridge, 1989.

E. L. Paul, V. A. Atiemo-Obeng, and S. M. Kresta. *Handbook of Industrial Mixing*. Wiley-Interscience, New York, 2004.

J. Pedlosky. *Geophysical Fluid Dynamics*. Springer-Verlag, New York, 1987.

O. Piro and M. Feingold. Diffusion in three-dimensional Liouvillian maps. *Physical Review Letters*, 61:1799–1802, 1988.

C. Siegel and J. Moser. *Lectures on Celestial Mechanics*. Springer Verlag, Berlin, 1971.

T. H. Solomon. *Personal communication*, 1998.

T. H. Solomon and I. Mezić. Uniform resonant chaotic mixing in fluids. *Nature*, 425:376–380, 2003.

G. Sposito. On steady flows with Lamb surfaces. *Int. J. Engng. Sci.*, 35: 197–209, 1997.

T. M. Squires and S. R. Quake. Microfluidics: Fluid physics at the nanoliter scale. *Reviews of Modern Physics*, 77:977–1026, 2005.

A. D. Stroock, S. K. W. Dertinger, A. Ajdari, I. Mezić, H. A. Stone, and G. M. Whitesides. Chaotic mixer for microchannels. *Science*, 295:647–651, 2002.

C. Truesdell. *The Kinematics of Vorticity*. Indiana University Publications, Bloomington, Indiana, 1954.

U. Vaidya and I. Mezić. Existence of invariant tori in action-angle-angle maps with degeneracy. 2006.

R. A. Vijayendran, K. M. Motsegood, D. J. Beebe, and D. E. Leckband. Evaluation of a three-dimensional micromixer in a surface-based biosensor. *Langmuir*, 19:1824–1828, 2003.

M. Volpert, I. Mezić, C. D. Meinhart, and M. Dahleh. An actively controlled micromixer. pages 483–487, 1999. Proceedings of the ASME Mechanical engineering International Congress and Exposition, MEMS, Nashville, TN.

S. Wiggins. *Slowly Varying Oscillators*. PhD thesis, Cornell University, 1985.

S. Wiggins. *Introduction to Applied Nonlinear Dynamical Systems and Chaos*. Springer-Verlag, New York, 1990.

S. Wiggins. *Chaotic Transport in Dynamical Systems*. Springer-Verlag, New York, 1992.

S. Wiggins and P. Holmes. Periodic orbits in slowly varying oscillators. *SIAM Journal of Mathematical Analysis*, 18:592–611, 1987.

T. Yannacopoulos, I. Mezić, G. King, and G. Rowlands. Eulerian diagnostics for Lagrangian chaos in three dimensional Navier-Stokes flows. *Physical Review E*, 57:482–490, 1998.

M. Yi and H. H. Bau. *The kinematics of bend-induced stirring in micro-conduits*. Proceedings of MEMS-Vol. 2, Micro-Electro-Mechanical Systems, ASME, Orlando FL. 2000.

On the Hyperbolic Behavior of Laminar Chaotic Flows

Stefano Cerbelli
Dipartimento di Ingegneria Chimica
Università di Roma "La Sapienza"
Via Eudossiana, 18 - 00184 Roma

1 Introduction. A historical perspective on laminar mixing

The subject of laminar chaotic mixing, also referred to as *Lagrangian chaos*, is a relatively new field of investigation, started about two decades ago with the publication of the article "Stirring by chaotic advection" (Aref , 1984) by Hassan Aref published in the Journal of Fluid Mechanics in 1984, which showed how it is possible to generate unexpectedly complex mixing structures through the application of a simple stirring protocol (the case of two two-dimensional ideal vortexes blinking periodically was used as a case study in the article in question). The idea underlying Aref's paper was a major breakthrough in the fluid dynamics community. Yet, a mathematician or a physicist involved in the study of Hamiltonian mechanics would have considered this idea not altogether new, since it was known since Poincaré's contribution in celestial mechanics (Diacu and Holmes, 1996) that a conservative system whose dynamics is governed by nonlinear equations is apt to display complex dynamical behavior. In point of fact, an article discussing the existence of nonintegrable Euler flows was published by Arnold almost twenty years before Aref's paper (Arnold, 1966). One may wonder why it took so many years to appreciate the analogy between a conservative mechanical system and the kinematics induced by an incompressible flow[1]. A popular answer to this question is that the connection was made when the availability of cheap computer power made it possible to carry out numerical

[1] This formal analogy holds, for instance, between a one-degree of freedom periodically perturbed Hamiltonian system and a two-dimensional time-periodic incompressible flow, with the x and y coordinates of the flow domain playing the role of position and momentum of the phase space associated with the mechanical system.

simulations of fluid particle trajectories and uncover the complex, "erratic" behavior of the dynamics. However, a more attentive analysis of this issue suggests that experimental tools to detect complex mixing structures (e.g. fluorescent dye advection, X-ray tracking of radioactive tracers) had been available long before 1984, whereas experimental results confirming the existence of physically realizable laminar chaotic flows where published only after numerical computations had unveiled such possibility (see, e.g. Leong and Ottino (1989) and therein cited references).

Another possible explanation is that before Aref's article, it was a common belief that mixing was tightly connected with velocity fluctuations associated with flow instability and turbulence, and, as such, its study could be framed in the same Eulerian reference framework used for describing the velocity field. This common belief was probably due to the fact that most of industrial as well as laboratory mixing equipment typically works in turbulent regime, which, whenever possible, was (and still is) the most efficient and direct way to blend unmixed fluids. Shifting the attention from the (possibly fluctuating) pointwise vector velocities to fluid particle trajectories was all that was needed to start a new and fruitful field of investigation. The work carried out along twenty years of research in this direction has undoubtedly contributed, either directly or indirectly, not only to the improved design of mixers that must operate under laminar conditions (e.g. those processing shear-sensitive materials or highly viscous liquids), but also to the understanding of natural phenomena such as chaotic advection within the ocean and the atmosphere (Kuznetsov et al., 2004). In the last few years, as closing a virtuous circle, the swiftly growing microfluidics technology demands a unified theoretical framework where the design of optimized micromixers can be carried out on a rational basis. In turn, this forces the people working in the field of laminar mixing to a critical analysis of the state of the art of the theory, and to lay out the research guidelines for the near future. The accomplishment of this goal cannot do away with an effort to connect the phenomenology arising from the study of laminar chaotic flows with the more recent advances of the hyperbolic theory of dynamical systems. The scope of this lecture is to explore this connection in some detail and highlight some of the issues that could be taken as common grounds for bridging the gap between theoreticians and practitioners. The lecture is (roughly) organized into two parts.

In the first part (Section2), the basic tools of the kinematic approach to mixing are presented, and the phenomenology arising from the application of this approach is discussed in the context of two-dimensional time-periodic incompressible flows. The choice of a two-dimensional setting simplifies remarkably the analysis of mixing dynamics, especially as regards the evolu-

tion of material interfaces which, in this context, are represented by plane curves. However, it is important to remark that in microfluidics three-dimensional effects can be important in that they can trigger the transition between regular and chaotic flow (see, e.g., Karniadakis et al. (2005) and references therein).

In the second part of the lecture (Section 3), the interpretation of this phenomenology is analyzed in the light of the hyperbolic theory of dynamical systems, with specific reference to Pesins's theory of nonuniformly hyperbolic behavior (Pesin and Barreira, 2002).

2 The kinematic approach to fluid mixing

2.1 Mixing mechanisms

Mixing in single phase flows, be them laminar or turbulent, takes place through two independent if cooperating mechanisms, namely convection and molecular diffusion. To refer to a concrete framework, consider a "thought experiment" where a blob of black dye is being mixed in a colorless fluid flowing with a prescribed incompressible velocity field, say $\mathbf{v}(\mathbf{x}, t)$, with $\nabla \cdot \mathbf{v} = 0$, within a certain region Ω of the ordinary space. We assume that Ω is bounded (i.e. it can be embedded in a finite-size ball of $\mathbb{R}^3$), and that the boundary $\partial\Omega$ of this region is impermeable to the flow, i.e. $\mathbf{v}\cdot\mathbf{n}|_{\partial\Omega} = 0$ at any time t, where $\mathbf{n}$ represents a unit vector normal to $\partial\Omega$ at a generic $\mathbf{x} \in \partial\Omega$. At the initial time instant, the blob is uniquely identified by its surrounding "interface", i.e. the surface separating colored and colorless fluid. Any time later, in the presence of molecular diffusion - however small - the distinction between colored and colorless becomes fuzzy, as the concentration of dye is bounded away from zero at any point of the mixing space Ω. What at the beginning was black and colorless has instantaneously become a field of black intensities. At any given point $\mathbf{x}$, and at any give instant of time, t, the intensity of black color depends upon the local concentration of dye say $c(\mathbf{x}, t)$. Quantitatively, the process is described by an evolution equation, the advection-diffusion equation,

$$\frac{\partial c}{\partial t} = -\mathbf{v} \cdot \nabla c + \mathcal{D}\nabla^2 c = \mathcal{L}_{\mathbf{v},\mathcal{D}}[c] \,, \tag{1}$$

where $\mathcal{L}_{\mathbf{v},\mathcal{D}} = -\mathbf{v} \cdot \nabla c + \mathcal{D}\nabla^2$ is the advection-diffusion operator, and $\mathcal{D}$ denotes the diffusion coefficient. As regards the boundary conditions, we ask that the normal derivative at any point of the boundary be zero at any positive time. This implies that the diffusive flux of the scalar c through the boundary is everywhere zero on $\partial\Omega$. The evolving concentration field $c(\mathbf{x}, t)$ undergoes qualitatively different behaviors according to whether $\mathcal{D}$

is equal to, or greater than, zero. In the latter case, the concentration field approaches asymptotically a constant (i.e. homogeneous) value, independently of the advecting flow[2]. In the first case, i.e. in a diffusionless flowing continuum, mixing must be given a different meaning than homogenization, as at zero diffusivity the value of the concentration at a given point $\overline{\mathbf{x}}$ and a given time $\bar{t}$ is just "brought around" by the advecting field while its value remains unaltered. Thus, *convective mixing is a process that acts only on the support of the initial datum but not on its range of values*. Formally, this concept can be expressed by saying that the trajectories of the Ordinary Differential Equation (ODE) system

$$\dot{\mathbf{x}} = \mathbf{v}(\mathbf{x}, t) \tag{2}$$

are characteristic lines of the pure advection equation

$$\frac{\partial c}{\partial t} = -\mathbf{v} \cdot \nabla c \tag{3}$$

The kinematic approach (Ottino, 1989) consists of analyzing, in a broad perspective, the dynamics induced in the phase space by the advection Eq. (2), which carries on the same information as the first-order PDE of Eq. (3). The term "broad perspective" means that we are interested not only in the trajectories of tracers (i.e. massless points that are passively carried around by flow), but also in the local deformation of line elements (and surface elements in three dimensions), as well as in the global geometric structure attained by finite-size lines and surfaces that evolve under the flow. This is because many processes that occur along with advection are more influenced by the deformation than the displacement associated with the flow. To give an example, the evolution of a magnetic field embedded within the flowing continuum can be amplified by the local deformation about the flow trajectories (in the hypothesis where the feedback of magnetic field onto the velocity field is neglected, this problem is referred to as *fast dynamo*, Childress and Gilbert (1995)). Another example of physical interest where the local deformation impacts upon the dynamics of physical processes is provided by the advection-diffusion Eq. (1) discussed above (Toussaint et al., 2000; Giona et al., 2004). In these examples, the actual influence of convection upon the process is strictly related to the kinematic motion induced by the flow, meaning that interesting effects are typically associated with a local hyperbolic structure of the deformation process (i.e. shrinking and expansion of lengths along transverse directions). Specifically, the existence

[2]The interaction between convection and diffusion determines, however, the rate at which homogenization is approached.

of a shrinking direction is responsible for the amplification of the gradient of the transported entity, be it a scalar (e.g. concentration of a chemical species or temperature), or a vector quantity (the magnetic field). This gradient amplification mechanism is exactly where convection and diffusion processes meet and interact with each other. Specifically, flows that tend to regenerate continuously gradients of the transported entity as they are being erased by diffusion are good candidates for providing short homogenization timescales. From these observations, it appears clear why, in a number of applications, one seeks flow conditions that provide sustained local hyperbolic deformation for the "largest possible" set of trajectories. It is a well established fact that this "massive" local hyperbolic dynamics is invariably associated with a complex behavior of the flow trajectories, which is generically referred to as *chaotic*.

Understanding how and why the optimal condition of maximum chaos is reached is an issue that is far from being trivial, even when very simple classes of flow protocols are considered. To date, there is no simple way of predicting the mixing performance associated with a prescribed flow protocol other than running an experiment or a direct numerical simulation. Therefore, far from being a predictive tool useful to design optimal protocols, the core of mixing theory is still at the stage of describing, and quantifying on a rational basis, the mixing performance of prescribed flow protocols. In this Section, an overview of the modern approach to characterizing mixing in incompressible flows, the so-called *kinematic approach*, is discussed.

2.2 Kinematics

The traditional approach to assess mixing performance dates back to the early 50s and was developed by Danckwerts (Danckwerts, 1952), who defined objective indexes, such as the linear scale of segregation - quantifying the average linear size of segregated regions - and the intensity of segregation - a normalized scalar variance - , to quantify the degree of mixedness associated with a given mixture. Owing to the conceptual simplicity and the experimental feasibility of Danckwerts' approach, these indexes are still largely used to characterize mixing performance, especially when complex flows are to be dealt with. However, the intrinsic limitation of this approach is that it uses no information whatsoever about the fluid dynamics and kinematics governing the evolution of the mixture, making it difficult to establish a relationship between the dynamics of the indexes and the salient features of the mixing protocol.

In 1984, starting with Aref's work (Aref , 1984), a new approach to mix-

ing spread out in the fluid dynamics community. This approach was motivated by the observation that even simple flows, e.g. possessing just a single "macroscopic" characteristic lengthscale, can generate incredibly complex mixing structures, provided they are allowed to act for a sufficiently long time. The key property that makes this possible is the nonlinear dependence of $\mathbf{v}(\mathbf{x}, t)$ on the spatial coordinates $\mathbf{x}$. In (Aref , 1984), the author showed that a time-periodic sequence of two ideal vortexes (specifically, a piecewise-steady flow) in two dimensions can define, for certain values of the geometric parameters and of the time period, an efficient stirring protocol. The importance of this observation can hardly be overestimated, as soon as one considers that until then the wording *mixing* and *turbulence* were used almost as synonymous, with the underlying understanding that the mixing action of the velocity field was to be ascribed essentially to the fluctuating components of the velocity. The fact that a deterministic (e.g. laminar) flow can provide efficient mixing changed drastically not only the realm of physical systems that were to be considered worth of investigation, but also the techniques for quantifying the mixing action of the flow system. These techniques, straightforwardly derived from dynamical systems theory, include Poincaré sections, computation of local stretch factors, finite-time Lyapunov exponents and global characteristic exponents (e.g. the topological entropy), reconstruction of global invariant manifolds and characterization of their spatial structure and dynamics. In what follows, a brief review of these techniques and of the typical phenomenology of deterministic incompressible mixing flows is discussed. The first point to be established is what category of systems, with specific reference to fluid mixing, can be approached through the dynamical system approach.

Flow systems The (classical) dynamical system theory analyzes the qualitative features of evolving deterministic systems, i.e. of systems whose past and future evolution is uniquely identified by the state of the system at a given time. Basically all of the results of the theory are applicable to *systems whose evolution law does not depend explicitly on time*, referred to as *autonomous systems*. The time variable can take values over the real line $\mathbb{R}$ (continuous systems) or on the set of relative - positive and negative - integers $\mathbb{Z}$ (discrete systems).

As regards fluid mixing systems, we assume that - (i) the flow domain Ω containing the incompressible fluid is a bounded, impermeable two- or three-dimensional domain, i.e. $\mathbf{v} \cdot \mathbf{n}|_{\partial\Omega} = 0$ at any point $\mathbf{x} \in \partial\Omega$ of the boundary, whenever it exists[3]. - (ii) the velocity field is time-periodic

[3]Many flow systems used as model of two-dimensional flows are defined on boundaryless

$\mathbf{v}(\mathbf{x},t) = \mathbf{v}(\mathbf{x},t+T)$ where the positive real number T is the flow period. This definition clearly includes autonomous flows, which can be regarded as a time-periodic flow of arbitrary period. From assumption -(i) it follows that the flow originated by the velocity field is volume-preserving, and that the dynamics of passive tracers ("fluid particles") is defined at all times. Assumption -(ii) is essential for recasting the system into an autonomous form whenever the velocity field depends explicitly on time. This can be accomplished with a construction referred to as *suspension* (Katok and Hasselblatt, 1995). The idea is quite simple and consists of regarding the time variable t just like another spatial coordinate, say $t = \xi$. From this definition it follows that $\dot{\xi} = 1$. Thus, one can consider an "enlarged" dynamical system, given by the latter equation together with the original equation $\dot{\mathbf{x}} = \mathbf{v}(\mathbf{x},t) = \mathbf{v}(\mathbf{x},\xi)$, defined on the Cartesian product $\Omega \times \mathbb{R}$, where the real axis $\xi \in \mathbb{R}$ represents all the possible times (past and future). Finally, this unbounded phase space can be transformed into a bounded one by noting that it is made of an infinite number of identical "pieces" where the velocity field possess the same structure, namely the sets $\Omega_T = \Omega \times [nT, (n+1)T]$ (see Fig. 1). Each of these pieces contains all the information about the dynamics. Thus one can to study the system within the set Ω^{per} obtained by folding Ω_l onto itself and gluing together the end surfaces, which physically represent the snapshots of the mixing space Ω at times $t = nT$ and $t = (n+1)T$. It can be readily verified that this time-continuous dynamical system, defined on a toroidal-shaped mixing space (of dimension $N+1$, if N is the dimension of the flow domain) is incompressible.

A further reduction can be obtained by considering a cross-section of this system, say $\Omega_{\overline{\xi}} = \{\mathbf{y} \in \Omega^{\text{per}} | \xi = \overline{\xi}\}$, and the correspondence $\mathbf{x} \mapsto \Phi_{\overline{\xi}}(\mathbf{x})$ between two consecutive intersections, $\mathbf{x}$ and $\Phi_{\overline{\xi}}(\mathbf{x})$, respectively, of a continuous trajectory, with the surface of section $\Omega_{\overline{\xi}}$. The surface of section $\Omega_{\overline{\xi}}$ is a global *Poincaré section* of the suspended system Physically, it represents the state of the system in a stroboscopic time-discrete framework, $t_n = \overline{\xi} + nT$

The Poincaré stroboscopic map $\Phi_{\overline{\xi}}$, henceforth simply denoted by Φ, is a volume-preserving map (or area-preserving map, in the case of a two dimensional flow domain) defined on the same domain Ω as the velocity field. Note that the area-preserving property of the Poincaré map stems form the fact that by construction of the suspended system, the normal velocity component of the flow to the surface is constant independently of the point position on the surface of section. For a generic three-dimensional

manifolds. For instance, the standard map family, used in these notes as a representative example of two-dimensional time-periodic flows, is defined on the two-dimensional torus $\mathbb{T}^2$.

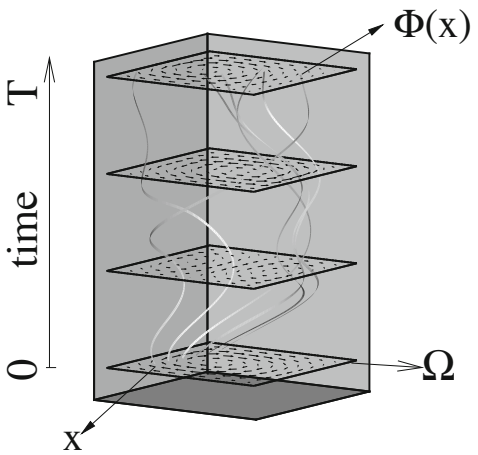

Figure 1. Schematic representation of the suspended system in the case of a two-dimensional time-periodic flow.

autonomous flow the ratio of velocity magnitudes at $\mathbf{x}$ and $\Phi(\mathbf{x})$ appears as a weighting factor in defining the invariant measure (see the lecture by I. Mezic).

The Poincaré map defines the discrete dynamical systems

$$\mathbf{x}_{n+1} = \Phi(\mathbf{x}_n) \quad . \tag{4}$$

In these notes, we investigate the dynamics associated with Eq. (4) in the case where the flow domain Ω is a two-dimensional bounded domain.

A simple model exhibiting mixed behavior In what follows, the Standard Map family (Casati and Chirikov, 1995) is chosen as a representative example of generic protocols defined by two-dimensional time-periodic velocity fields. Given that the original motivation for introducing this model comes from low-dimensional Hamiltonian mechanics, a derivation of the SM model in the context of fluid mixing is next discussed. The flow domain where the time-periodic flow is defined is the two dimensional-torus $\mathbb{T}^2$, which can be represented by the unit square domain $I^2 = \{\mathbf{x} = (x, y) \in [0, 1) \times [0, 1)\}$, equipped with periodic boundary conditions which identify opposite edges (i.e. a fluid particle that leaves the unit square crossing an edge, re-enters instantaneously the unit domain at the corresponding

point on the opposite edge). On this domain, consider the time-periodic flow generated by blinking alternately the two steady unidirectional flows $\mathbf{v}^{(1)} = (v_x^{(1)}, v_y^{(1)}) = (0, \sin(2\pi x))$, $\mathbf{v}^{(2)} = (v_x^{(2)}, v_y^{(2)}) = (y, 0)$, the first acting for a generic time τ, the second acting for a unit time as represented in Fig. 2.

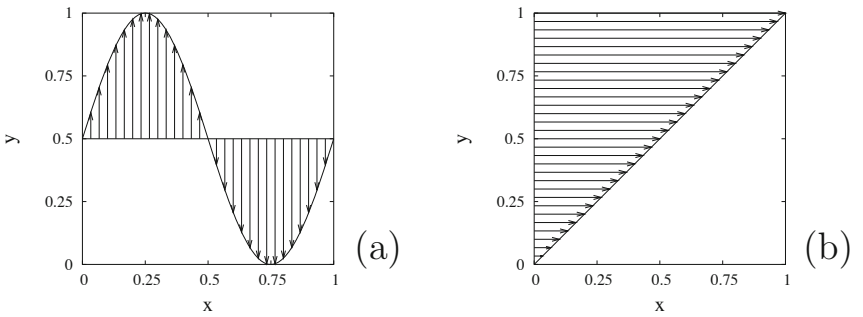

Figure 2. The two steady flows $\mathbf{v}_1$ (panel (a)), and $\mathbf{v}_2$ (panel (b)) that define the time-periodic protocol giving rise to the SM family. The flow $\mathbf{v}_1$ acts for a generic time τ, whereas the flow $\mathbf{v}_2$ acts always for a unit time. The overall protocol is periodic with period $T = \tau + 1$.

By definition of the protocol, the overall period of the flow is $T = \tau + 1$. The stroboscopic map $\Phi_T(\mathbf{x}) = \mathbf{M}(\mathbf{x})$ is then defined by

$$\mathbf{M}(\mathbf{x}) = \mathbf{M}(x, y) = (x', y') = \begin{cases} x' &= x + y + \tau \sin(2\pi x) \quad [\text{mod. } 1] \\ y' &= y + \tau \sin(2\pi x) \quad [\text{mod. } 1] \end{cases}, \tag{5}$$

and yields the new position $\mathbf{x}' = (x', y')$ after one flow period of a point originally located at $\mathbf{x} = (x, y)$. The "[mod. 1]" (modulus 1) condition appearing at the r.h.s. of Eq. (5) means that only the proper fractional part of each of the displaced coordinates (x', y') is considered, whereas the integer part is discarded (e.g. if $x' = 3/2$, then $x'[\text{mod. } 1] = 1/2$). This takes automatically into account the periodic boundary conditions imposed on the unit square domain (see Section 3 for further details). As τ varies in $[0, \infty)$, Eq. (5) defines a family of area-preserving maps which display a variety of different dynamical behaviors. These dynamical behaviors are qualitatively consistent with those observed in physically realizable two-dimensional time-periodic flows (e.g. the flow within a lid-driven cavity and the flow between eccentric cylinders, see Ottino (1989)), as well as with those arising from Poincaré sections of three-dimensional autonomous flows

(such as the Poincaré section the partitioned-pipe mixer, see Khakhar et al. (1987) and the Kenics static mixer, see Hobbs and Muzzio (1997)). Let us start to analyze these behaviors in terms of trajectories.

Trajectories and invariant sets One of the first issues is to understand the structure of the phase space associated with a prescribed mixing protocol, i.e. how many qualitatively different types of trajectories coexist within one and the same mixing domain. In the discrete setting of the Poincaré stroboscopic map, each trajectory associated with a given point $\mathbf{x}$ is composed by a countable set of points $\{\mathbf{x}_n = \mathbf{M}^n(\mathbf{x})\}$, where $n \in \mathbb{Z}$, consisting of the forward and backward iterates of $\mathbf{x}$ under the action of $\mathbf{M}$. Stemming from the geometric meaning of $\mathbf{M}$ as a Poincaré map of the associated suspended system, the plot of a sufficiently long segment of trajectory in the phase space is referred to as Poincaré section. To unveil the global structure of the dynamics, several trajectories are typically superimposed onto the same Poincaré section. Figure 3 shows the Poincaré sections associated with several initial conditions in different protocols of the SM family. Different qualitative behaviors are immediately evident, namely trajecto-

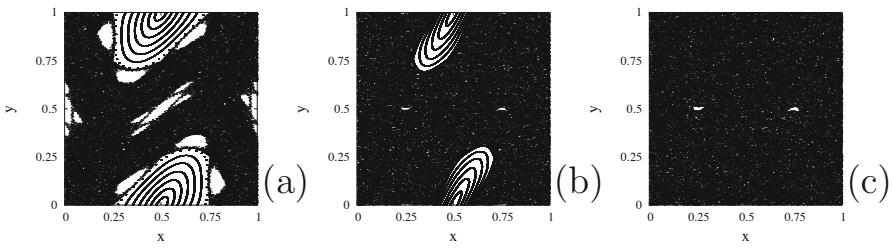

Figure 3. Poincaré section of the Standard Map $\mathbf{M}$ for three stirring protocols characterized by -(a) $\tau = 1/4$, -(b) $\tau = 1/2$, and -(c) $\tau = 1$.

ries that wander endlessly in a "massive" subregion[4] of the mixing domain, referred to as *the chaotic region*, and trajectories that are confined to a collection of closed curves, which are referred to as *quasiperiodic trajectories*. Globally, the set of all quasiperiodic trajectories is also massive, and is referred to as the *regular region* or the *island region*. As can observed in Fig. 3, the location, the shape and the relative size of the chaotic and regular regions depends strongly upon the specific protocol considered. It

[4] In these notes, the wording *massive* means "of positive Lebesgue measure" (see, e.g. Rudin (1986) for an introduction to Lebesgue measure theory).

is important to stress out that, beyond a handful of simple archetypal cases (see, e.g., Wojtkowski (1981)), there is no other way to predict the presence of islands than running a numerical simulation, or, in the case of a physically realizable flow, an appropriate experiment. Quasiperiodic and chaotic behavior are not the only possible qualitative behaviors occurring in nonlinear area-preserving maps. Other possible types of trajectories include *periodic orbits* as well as *orbits that are asymptotically attracted to periodic orbits*.

Periodic orbits are composed by all the points $\mathbf{x}_\alpha$ that verify the relationship $\mathbf{M}^l(\mathbf{x}_\alpha) = \mathbf{x}_\alpha$ for some positive integer $l \geq 1$. The smallest integer that verifies this relationship is called the *minimal period* of the orbit. A periodic orbit of minimal period l is therefore composed by exactly l points $\{\mathbf{x}_1, \mathbf{x}_2, \cdots \mathbf{x}_l\}$. It is called *hyperbolic*, *parabolic* or *elliptic* according to whether the Jacobian matrix (i.e. the matrix of the first-order partial derivatives) of the l-fold map $D\mathbf{M}^l|_{\mathbf{x}} = D\mathbf{M}|_{\mathbf{M}^{l-1}(\mathbf{x})} \cdot D\mathbf{M}|_{\mathbf{M}^{l-2}(\mathbf{x})} \cdots \cdots D\mathbf{M}|_{\mathbf{M}(\mathbf{x})} \cdots D\mathbf{M}|_{\mathbf{x}}$, where $\mathbf{x}$ is any point of the periodic orbit, is hyperbolic, parabolic or elliptic, respectively.

The existence of nonperiodic points that are asymptotically attracted to a (hyperbolic) periodic orbit is a straightforward consequence of the existence of stable and unstable manifolds associated with hyperbolic periodic points (see Section 3).

Before analyzing what types of deformation mechanisms occur along each of these qualitative types of dynamical behaviors, we observe that the sets of points composed by trajectories belonging to each of the different types of dynamics are *globally invariant*. In other words, it is impossible for given type of orbit segment to change its nature along the dynamics (e.g. a periodic orbit cannot become chaotic or quasiperiodic and viceversa).

2.3 Local deformation along trajectories

From the analysis of Poincaré section a natural question arises, namely *is there any peculiar feature associated with regular and chaotic orbits that marks the watershed between these two types of dynamics?* We have already observed that each chaotic trajectory appears to visit a massive region, whereas regular orbits are confined to sets of null measure. Yet, the existence of a massive chaotic region is a property that depends globally on the whole set of chaotic trajectories, and proving the existence of such region is typically impractical. In order to unveil the difference between regular and chaotic dynamics, an analysis of the local deformation process along the evolving orbit is necessary. The simplest approach consists of analyzing the *linear approximation* to the deformation process. Consider a point $\mathbf{X} = (X, Y)$ and its image $\mathbf{x} = (x, y) = \mathbf{M}(\mathbf{X}) = (M_x(X, Y), M_y(X, Y))$.

Consider a displaced point $\mathbf{X}+\Delta\mathbf{X}=(X+\Delta X, Y+\Delta Y)$, and denote its image by $\mathbf{x}+\Delta\mathbf{x}=(x+\Delta x, y+\Delta y)=(M_x(X+\Delta X, Y+\Delta Y), M_y(X+\Delta X, Y+\Delta Y)$ (see Fig. 4).

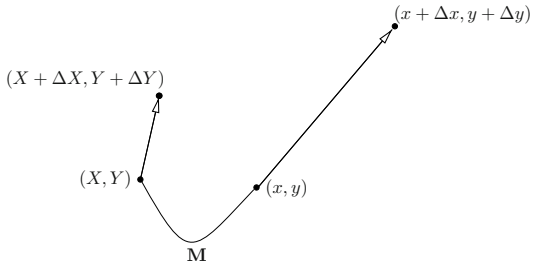

Figure 4. Evolution of a small perturbation about a point.

By expanding the image of the displaced point in Taylor series, we obtain that

$$\begin{cases} M_x(X+\Delta X, Y+\Delta Y) = M_x(X,Y) + \frac{\partial M_x}{\partial X}|_{(X,Y)}\Delta X + \frac{\partial M_x}{\partial y}|_{(X,Y)} + o(||\Delta\mathbf{X}||^2) \\ M_y(X+\Delta X, Y+\Delta Y) = M_y(X,Y) + \frac{\partial M_y}{\partial X}|_{(X,Y)}\Delta X + \frac{\partial M_y}{\partial y}|_{(X,Y)} + o(||\Delta\mathbf{X}||^2) \end{cases} \tag{6}$$

and therefore, by disregarding higher order terms, it results that the displaced segment $(\Delta x, \Delta y) = (M_x(X+\Delta X, Y+\Delta Y) - M_x(X,Y), M_y(X+\Delta X, Y+\Delta Y) - M_y(X,Y))$ is given by

$$\begin{pmatrix} \Delta x \\ \Delta y \end{pmatrix} = \begin{pmatrix} \partial M_x/\partial X & \partial M_x/\partial Y \\ \partial M_y/\partial X & \partial M_y/\partial Y \end{pmatrix}_{(X,Y)} \cdot \begin{pmatrix} \Delta X \\ \Delta Y \end{pmatrix} . \tag{7}$$

When applied recursively for n iterations, Eq. (7) writes in compact form

$$\Delta\mathbf{x}^{(n)} = D\mathbf{M}^{(n)}|_{\mathbf{X}} \cdot \Delta\mathbf{X} = \left[D\mathbf{M}|_{\mathbf{M}^{(n-1)}(\mathbf{X})} \cdots D\mathbf{M}|_{\mathbf{M}(\mathbf{X})} \cdot D\mathbf{M}|_{\mathbf{X}}\right] \cdot \Delta\mathbf{X} . \tag{8}$$

It is important to keep in mind that Eq. (8) represents *a linear approximation* to the evolution of the segment $\Delta\mathbf{X}$. This approximation becomes more and more inaccurate as time elapses (i.e. in the discrete timeframe, as the number of iterations of Eq. (8) increases), because higher order terms become more and more important. However, if a limit $\Delta\mathbf{X} \to \mathbf{0}$ is considered, then Eq. (8) is well defined at all times, and it quantifies the dynamics of an infinitesimal arc segment, say $d\mathbf{s}_n = \mathbf{M}^{(n)}(d\mathbf{S})$, attached to the evolving point $\mathbf{x}_n = \mathbf{M}^{(n)}(\mathbf{X})$. In other terms, along with Eq. (4), one considers the nonautonomous linear system

$$\mathbf{l}_{n+1} = D\mathbf{M}|_{\mathbf{x}_n} \cdot \mathbf{l}_n , \tag{9}$$

equipped with the initial condition $\mathbf{l}_0 = \mathbf{l}$, where $\mathbf{l}_n$ is a vector belonging to the tangent space (see the lecture by Mezic for a definition of the tangent space to a manifold) to the manifold Ω representing the flow domain at the point $\mathbf{x}_n$. A fundamental quantity associated with Eq. (9) is the *stretch factor* $\lambda_n(\mathbf{X}, \mathbf{l}/||\mathbf{l}||)$, defined by

$$\lambda_n(\mathbf{X}, \mathbf{l}/||\mathbf{l}||) = \frac{||\mathbf{l}_n||}{||\mathbf{l}||} , \tag{10}$$

which depends upon the initial point $\mathbf{X}$ to which the vector is attached, and on the initial orientation $\mathbf{l}/||\mathbf{l}||$ of the vector. The fact that λ_n depends only on the orientation of the initial vector, and not upon its magnitude is a consequence of the linear structure of the evolution in the tangent space. Thus, the stretch factor λ_n is numerically coincident with the norm of the image vector $\mathbf{l}_n$ associated with a unit norm initial condition $||\mathbf{l}|| = 1$. From the structure of Eq. (9), it is evident that the stretch factor after n iterations depends on the entire trajectory segment $\{\mathbf{x}_i\}_{i\in[0,n]}$ in that the Jacobian matrices $D\mathbf{M}|_{\mathbf{x}_i}$ that appear in the product yielding the Jacobian of the n-th order map are computed at each point of the orbit segment. Furthermore, *the product of Jacobian matrices is, in general, non-commutative.* This implies that the order according to which points are visited is essential in defining the overall stretch factor.

Let us next analyze what types of stretch factor dynamics can occur. Figure 5 shows the result of a numerical simulation for different initial conditions in the SM protocol defined by $\tau = 1/4$ (see Fig. 3-(a)). Three initial conditions, referred to as $\mathbf{C}_1$, $\mathbf{C}_2$, and $\mathbf{C}_3$, are considered. The initial conditions $\mathbf{C}_1$ and $\mathbf{C}_2$ refer to an initial point $\mathbf{X} = (1/10, 1/10)$ (placed in the chaotic region) and orientations of the initial vector $\mathbf{l}$ set to $(1, 0)$ and $(0, 1)$, represented by a continuous line and square symbols, respectively. For the initial condition $\mathbf{C}_3$, a point $\mathbf{X} = (1/2, 1/10)$ belonging to the main island region and an initial orientation $\mathbf{l} = (1, 0)$ was chosen. Owing to the huge range values attained by the stretch factors, the value of $\log(\lambda_n)$ of this particular initial condition (empty circles) was multiplied by a factor 10^2 for better visualizing the shape of the curve. The linear growth of $\log(\lambda_n)$ associated with the initial data attached to the chaotic orbit indicates clearly that the stretch factor increases exponentially along chaotic trajectories. As regards condition $\mathbf{C}_3$, the logarithm of the stretch factor, $\log(\lambda_n)$ settles onto an oscillating behavior whose average coincides with a logarithmic trend (i.e. the stretching increases linearly with time).

A quantitative characterization of the exponential stretching process can

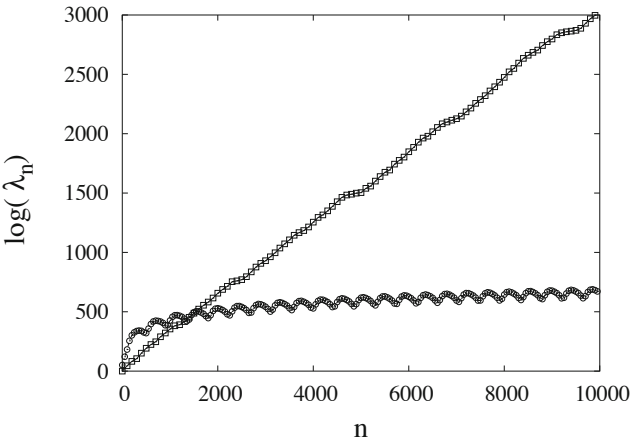

Figure 5. Stretch factor dynamics for a point belonging to the chaotic region with different initial orientations of the vector (squares and continuous line), and for a point falling in a quasiperiodic island (empty circles). The value of $\log(\lambda_n)$ associated with the quasiperiodic orbit is multiplied by a factor 10^2 to enhance visualization of stretch dynamics.

be obtained by considering the limit

$$\Lambda\left(\mathbf{X}, \mathbf{l}/||\mathbf{l}||\right) = \lim_{n\to\infty} \frac{1}{n}\log(\lambda_n)\ . \tag{11}$$

The number Λ exists for almost all points $\mathbf{X}$, and for an assigned point $\mathbf{X}$, can attain at most two different values $\{\Lambda_1, \Lambda_2\}$ (N different values for a generic N-dimensional manifold). These values are called *Lyapunov exponents* associated with the point $\mathbf{X}$ (see, e.g., Eckmann and Ruelle (1985) for a physics-oriented introduction to Lyapunov exponents. The mathematics-oriented reader is referred to Katok and Hasselblatt (1995), and to the original paper by Oseledec (1968), where the existence of Lyapunov characteristic number was proved for the first time). In the case of area-preserving nonlinear maps, the set of Lyapunov exponent must necessarily be of the form $\{-\Lambda, \Lambda\}$, where $\Lambda \geq 0$ is shortly referred to as the Lyapunov exponent associated with $\mathbf{X}$. This property stems from the fact that Lyapunov exponents verify the condition $\sum_{l=1}^{N} \Lambda_l(\mathbf{X}) = \log\left[\det\left(\sqrt[2n]{[D\mathbf{M}^n|_{\mathbf{X}}]\cdot[D\mathbf{M}^n|_{\mathbf{X}}]^*}\right)\right]$, where N is the dimension of the manifold Ω, and "$[\cdot]^*$" is the matrix transpose of '$[\cdot]$" (see, e.g., Eckmann and Ruelle (1985)). Given that the Jacobian matrix of $\mathbf{M}$ possess determinant equal to unity at every point $\mathbf{X} \in \Omega$ (the

mapping is area-preserving), then the Lyapunov exponents associated with any point must sum up to zero.

Figure 6 shows the convergence of the limit in Eq. (11) in the SM protocol $\tau = 1/4$, for the the same initial conditions used in Fig. 5. As can be

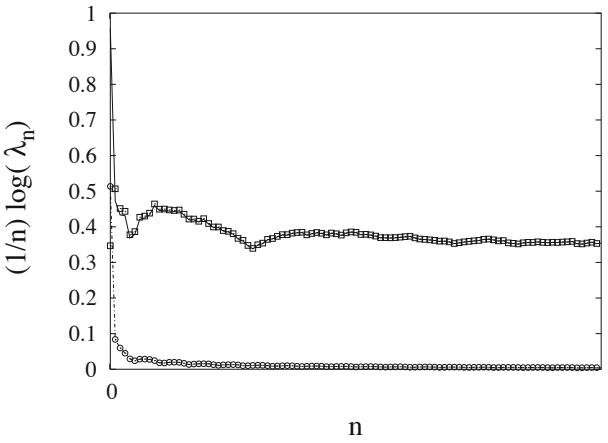

Figure 6. Convergence of the average of $\log \lambda_n$ along the orbit towards the Lyapunov exponent. Symbols are consistent with those of Fig. 5.

noted, the initial condition $\mathbf{C}_3$ associated with a point falling inside the main island quickly decays to zero. Any initial condition associated with points of the chaotic region would yield the the same value of Lyapunov exponent, regardless of the initial location $\mathbf{X}$ and of the initial orientation $\mathbf{l}/||\mathbf{l}||$. Thus, *this characteristic number can be associated with the entire chaotic region.*

Therefore, the maximal Lyapunov exponent is a characteristic number that allows to distinguish between quasiperiodic and chaotic orbits in that these different types of dynamics are characterized by zero and positive Lyapunov exponent, respectively. However, the positivity of the Lyapunov exponent, which implies the sensitive dependence of trajectories on the initial data, is not a safe criterion to establish the chaotic character of a trajectory, as by definition hyperbolic periodic orbits also possess positive Lyapunov exponent. In point of fact, chaotic behavior is result of the combination between the "erratic" (ergodic) behavior of trajectories *and* the sensitive dependence on the initial datum.

Another issue that qualifies the tangent vector dynamics in the chaotic region is that the orientation of the evolving vector displays "fading mem-

ory" with respect to the initial orientation, i.e. if one considers a stencil of vectors spanning the 2π angle and attached to the same point $\mathbf{X}$, the mapped vectors after a sufficiently long time (typically, few iterations) will be contained in a narrow cone (see Fig. 7).

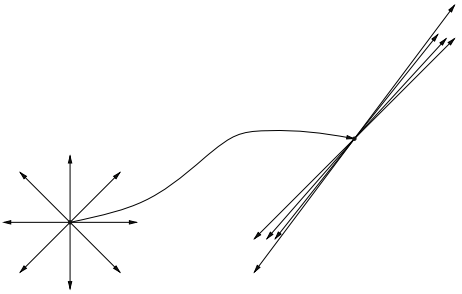

Figure 7. Orientation properties of tangent vectors in the chaotic region. After few iterations a stencil of vectors whose orientations span the 2π angle is mapped into a narrow cone (the higher the number of iterations, the narrower the cone).

This behavior finds a simple explanation in the context of the theory of hyperbolic dynamical systems, which postulates the existence of expanding and contracting directions at each point of the chaotic region (see Section 3).

By definition, the Lyapunov exponent is a measure of the *average* stretching rate (in fact, it represents the average of the logarithm of one-step stretching factors) experienced by an infinitesimal arc of a material line. Yet, the fact that all elementary arcs embedded in the chaotic region experience the same asymptotic average stretching rate does not tell a complete story about the stretching process itself.

In order to unveil differences between stretching histories experienced by arc elements associated with different points of the chaotic region, let us undertake a statistical approach. Specifically, let us compute the Probability Density Function $P\left(\log(\lambda_n)\right)$ of the logarithm of stretch factors $\log(\lambda_n)$ associated with a swarm of evolving vectors that are uniformly distributed throughout the chaotic region. Figure 8 shows the result of this computation for a swarm of 10^6 vectors stirred by the SM protocol defined by $\tau = 1$, for $n = 2, 4, \cdots, 18$. The x-axis reports $\log(\lambda_n) - \Lambda_n$, (where $\Lambda_n = \langle \log \lambda_n \rangle$ is the average value of the stretching logarithms) in place of $\log(\lambda_n)$, to enhance visualization of the PDFs evolution. As time increases (in the direction of the arrows), the PDFs undergo increasing broadening, thus

indicating a history of deformation that becomes more and more heterogeneous (e.g. the gap between the maximum and minimum value of the n-fold stretch factor increases with time).

As an overall quantification of the dispersive behavior of stretch factors, Fig. 8-(b) reports the squared variance $\sigma_n^2 = \langle(\log(\lambda_n) - \Lambda_n)^2\rangle$, which undergoes the typical linear growth observed in a large class of area-preserving nonlinear systems. In the same figure, the linear growth of $\Lambda_n = n\Lambda$, where Λ is the Lyapunov exponent associated with the chaotic region is also reported.

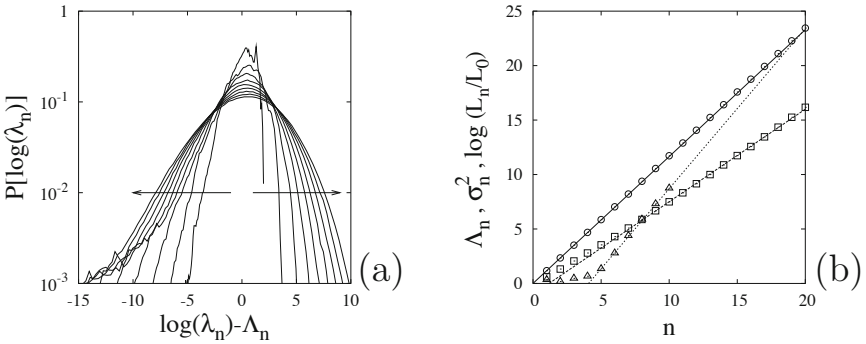

Figure 8. Dynamics of stretch factors in the SM protocol defined by $\tau = 1$. Panel (a): Probability Density Function $\mathcal{P}[\log(\lambda_n)]$. The arrows indicate increasing times. Panel (b): Average, Λ_n (circles), and squared variance, σ_n^2 (squares), of $\mathcal{P}[\log(\lambda_n)]$. The triangles depict the growth of a finite-sized line.

The analysis of local deformation can be pushed further to analyze the evolution of higher order properties. The most significant feature that depends on higher order (in fact, second-order) derivatives of the Poincaré map $\mathbf{M}$ is the local curvature. Consider a smooth - not self-intersecting - curve Γ embedded in the flow domain. Let Γ be represented by the parametric representation $\mathbf{x}(s) = (x(s), y(s))$ where the parameter $s \in [0, L_\Gamma]$ represents the arc length, and L_Γ is the overall length of the curve, i.e. the curve is parametrized with respect to its fundamental representation. In differential geometry, the curvature $\mathbf{k}$ of the plane curve Γ at a point $\mathbf{x}(\overline{s})$ is the second spatial derivative $\mathbf{k} = d^2\mathbf{x}/ds^2|_{s=\overline{s}}$. It is represented[5] by a vector

[5]More properly, curvature is a second-order, skew-symmetric tensor (see, e.g., Drummond and Munch (1991) and therein cited references). The "curvature vector" is just a geometric representation of this tensor in a fixed reference frame, with the understanding that $\mathbf{k}$ does not change as a vector quantity under coordinate transformations.

whose modulus equals the inverse radius of the best osculating circle to the curve at the specified point, and whose direction is orthogonal to the local tangent to the curve. The orientation of $\mathbf{k}$ points towards the center of the osculating circle. Dynamical equations for the evolution of the curvature $\mathbf{k}$ can be derived by considering a curve Γ and its image $\gamma = \mathbf{M}(\Gamma)$ under the transformation $\mathbf{M}$. The modulus $\kappa_{\mathbf{M}(\mathbf{X})} = ||\mathbf{k}_{\mathbf{M}(\mathbf{x})}||$ of the local curvature of the transformed curve $\gamma = \mathbf{M}(\gamma)$ at the image point $\mathbf{M}(\mathbf{X}) \in \gamma$ of a point $\mathbf{X} \in \Gamma$ is given by

$$\kappa_{\mathbf{M}(\mathbf{X})} = \frac{||(D\mathbf{M}|_{\mathbf{X}} \cdot \mathbf{T}) \times (DD\mathbf{M}|_{\mathbf{X}} : \mathbf{TT}) + (D\mathbf{M}|_{\mathbf{X}} \cdot \mathbf{T}) \times (D\mathbf{M}|_{\mathbf{X}} \cdot \mathbf{K}))||}{||D\mathbf{M}|_{\mathbf{X}} \cdot \mathbf{T}||^3}\,, \tag{12}$$

where $\mathbf{T}$ and $\mathbf{K}$ are the tangent and curvature vectors of Γ at $\mathbf{X}$, and where $DD\mathbf{M}$ is the third-order tensor of second-order spatial derivatives of $\mathbf{M}$, i.e. $DD\mathbf{M} = (((\partial^2 M_i/\partial x_l \partial x_m)))$. The double inner product $DD\mathbf{M} : \mathbf{TT}$ entering the right hand side of Eq. (12) is thus given by $DD\mathbf{M} : \mathbf{TT} = (T_l T_m \partial^2 M_i/\partial x_l \partial x_m)$, and represents a vector quantity.

The dynamics of curvature in the chaotic region possesses the same "fading memory" features as the that of tangent vectors. There is, however one important difference, namely that curvature becomes independent of the initial conditions (i.e. of the initial vectors $\mathbf{T}$ and $\mathbf{K}$) *as regards both the modulus and the orientation* of $\mathbf{k}$.

A consequence of this phenomenon is that a statistics performed over a swarm of evolving curvature "vectors" embedded in a chaotic region *yields a sequence of PDFs of curvature moduli that collapse onto an invariant master curve* (see, e.g. Cerbelli at al. (2000)). Therefore the average value and the variance of curvature PDF converge towards constant values that are specific of the deformation process inside the entire chaotic region. This invariance can be put one-to-one with the existence of invariant manifolds associated with hyperbolic trajectories. In fact, under relatively weak assumptions, it can be proved that for any point of the chaotic region, the curvature vector $\mathbf{k}_n$ converges exponentially fast to the local curvature of the unstable manifold associated with the current point $\mathbf{x}_n$ of the trajectory. However, this fact should not lead to the conclusion that the curvature field associated with the chaotic region is a "well behaved" function. This corresponds to the fact that unstable manifolds are only locally smooth, but may display singular points.

Indeed, direct numerical simulations suggest that there exists points at the boundary of the chaotic region, in the neighborhood of which the local invariant curvature attains arbitrarily large values. A way to observe this phenomenon is to track curvature dynamics along a single ergodic trajectory embedded in the chaotic region. Figure 9 shows the behavior of the function

$K_n = \max_{1 \le i \le n}\{\kappa_i\}$ (i.e. K_n is the highest value of curvature experienced along the orbit up to iteration n).

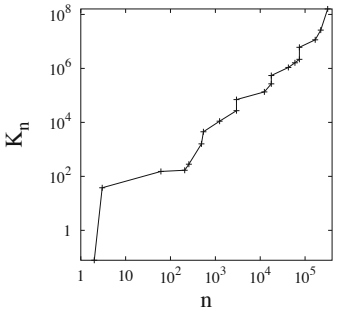

Figure 9. Supremum of the curvature modulus along a chaotic trajectory in the SM protocol ($\tau = 1$).

As can be observed, the behavior of the function suggests an unbounded growth trend, thus implying that there are points of the chaotic region where curvature "blow up" phenomena can occur. The presence of singular points for curvature can be connected with the nonuniformly hyperbolic character of the SM family, or of any other physically realistic map, for that matter (Cerbelli and Giona, 2005a).

2.4 Deformation of finite-size interfaces

The complex history of local deformation events occurring in the chaotic region find an even more complicated counterpart in the dynamics of finite-sized material interfaces, which, in two-dimensions, are represented by curves evolving under the action of **M**. Figure 10 shows the first few iterates, $n = 4$ and $n = 5$ respectively, of a small segment, say Γ, anchored at the point $(0, 0)$. The curve quickly develops into a nested folded structure that invades larger and larger portions of the chaotic region (the protocol $\tau = 1$ of the SM family is considered throughout this section, see Fig. 3). This picture suggests that eventually the curve will be present in neighborhood (however small) of any point the chaotic region.

The overall length of the curve increases exponentially, but with an exponent, say h_{line}, that is different (strictly greater than) the Lyapunov exponent. In measure preserving systems, the exponent h_{line} is equal to a global characteristic exponent, referred to as *the topological entropy of the map*, h_{top}, that is a topological invariant quantifying the "degree of orbit complexity" (Katok and Hasselblatt, 1995). Heuristically, the difference be-

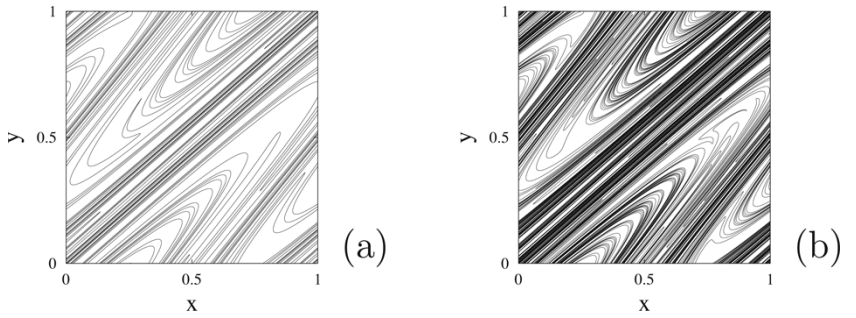

Figure 10. Evolutes of a small segment anchored at the origin after -(a) four, and -(b) five iterations of the SM protocol defined by $\tau = 1$.

tween the line stretching exponent and the Lyapunov exponent is related to the fact that, even though the curve will eventually visit densely the chaotic region, the space-invading process is such that the curve images result preferentially concentrated in certain zones, where the local stretching is higher.

The nonuniform character of the space-filling dynamics of the filament can be analyzed quantitatively by defining a box-counted measure, which we refer to as w-measure $\mu_w^{(n)}(\mathbf{x}, \Delta\mathbf{x})$, which quantifies the fraction of length of the n-th iterate of the curve that falls within a squared box of size Δx centered around a given point $\mathbf{x}$ (Giona and Adrover, 1998). As n increases, such measure converges towards an invariant measure $\mu_w(\mathcal{D})$, where $\mathcal{D}$ is a generic measurable subset of Ω. Qualitatively equivalent information can be gathered by considering the intersections of the curve with an assigned reference line. Consider, e.g., the horizontal line $r = \{(x, y)|0 \leq x \leq 1,\ y = 1/4\}$ and the intersections $\{\xi_i\}_{1 \leq i \leq N(n)}$, where $N(n)$ is the total number of intersections between γ_n and r. Let $\mu_w^{(n)}(x)$ represent the fraction of the total number of intersections falling in the interval $[0, x]$. Figure 11 shows the one-dimensional measures $\mu_w^{(n)}(x)$ for $n = 8, 10, 12$. The convergence towards and invariant curve is so fast that the difference between the approximations to the invariant measure is barely appreciable. The highly nonuniform feature of the space-filling process associated with the iterates $\gamma_n = \mathbf{M}^n(\Gamma)$ is reflected in the singular character of the invariant measure $\mu_w^{(n)}(x)$, which does not possess a density function. Let us analyze this aspect by consider-

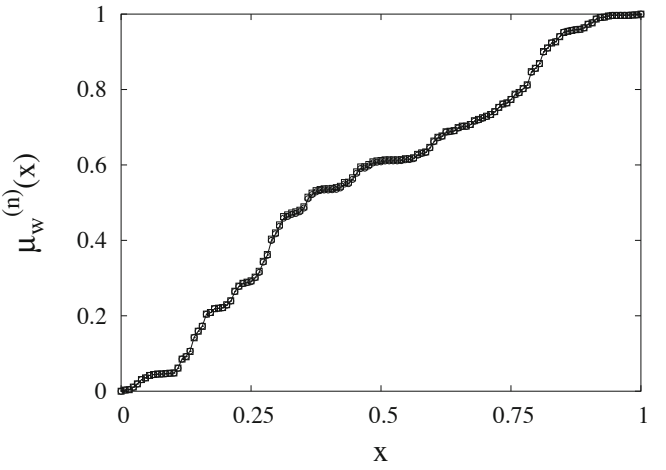

Figure 11. Convergence of the intersection measure $\mu_w^{(n)}$ towards the invariant measure μ_w. Three iterations of the filament are considered, namely $n = 8$ (squares), $n = 10$ (circles), $n = 12$ (continuous line).

ing the box-counted frequency $\rho^{(n)}(x_h, \Delta)$, where $x_h = h\Delta$ and Δ is the size of the intervals covering the reference line, and where $\rho^{(n)}(x_h, \Delta)$ is defined as the fraction of intersections falling in the interval (x_h, x_{h+1}). We want to investigate, at fixed n, the behavior of the function $\rho^{(n)}(x_h, \Delta)$ as the size Δ of the box covering decreases to zero. For this reason, we consider an iterate n large enough so that there will be a statistically significant number of intersections in each of the boxes of the smallest partition considered in the scaling analysis. Figure 12 shows the result of this computation for $n = 12$ and $\Delta = 1/N_b$ with $N_b = 128; 256; 512$ (Figure 12-(a), -(b), -(c), respectively).

As can be observed, at smaller and smaller values of Δx, the function $\rho^{(n)}(x_h, \Delta)$ becomes more and more spiky, suggesting a global diverging behavior as the norm of the box size, Δx, shrinks to zero.

Periodic points Another interesting issue of physically realistic models of chaos in two-dimensional time-periodic incompressible flows is the increasingly complicated spatial structure attained by sets of periodic points, say Per_n, whose minimal period does not exceed n. Figure 13 shows the structure of the set Per_n for a stirring protocol, referred to as the sine-flow model, which possesses qualitative features altogether similar to those of

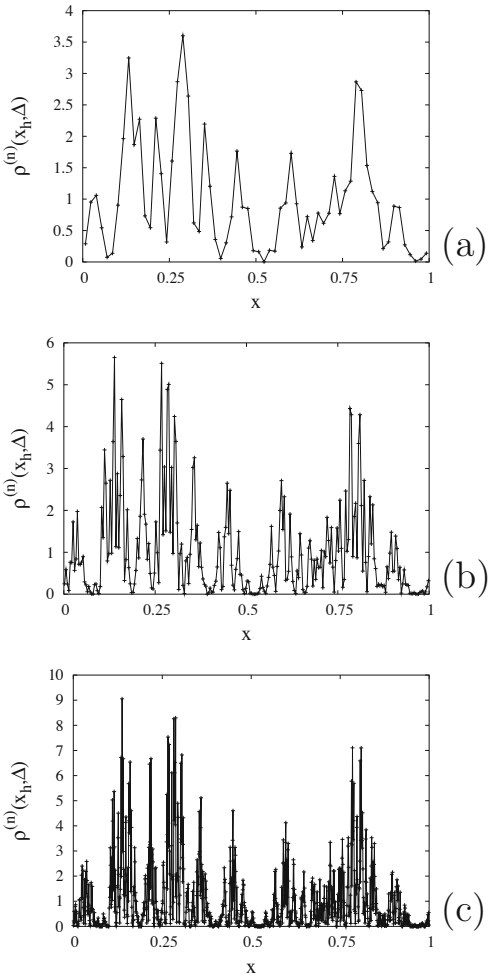

Figure 12. Singular character of the density function $\rho^{(n)}(x_h, \Delta)$. The tenth iterate of the line depicted in Fig. 10 was considered. The density functions are associated with -(a) $\Delta x = 2^{-6}$, -(b) $\Delta x = 2^{-8}$, and -(c) $\Delta x = 2^{-10}$.

the SM family[6].

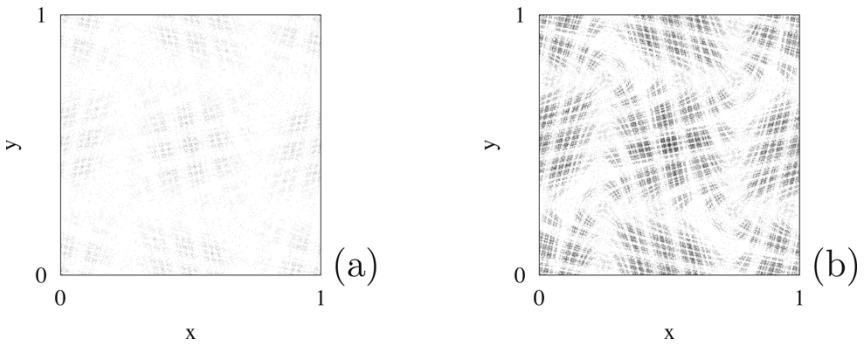

Figure 13. Spatial structure of the set Per_n for (a): $n = 4$, and (b): $n = 5$ in the Sine Flow map

The spatial distribution of Per_n is manifestly highly nonuniform. Likewise what observed for the distribution of material lines, it turns out that a measure-theoretical approach can also be used to characterize the set Per_n. Let $N_{Per}(n)$ be the cardinality of these sets for each given n (i.e. the total number of points of Per_n). Then, at each fixed n, the following measure (referred to as the *Bowen measure*) can be associated with Per_n,

$$\mu_{Bow}^{(n)} = \frac{1}{N_{Per}(n)} \sum_{i=1}^{N_{Per}(n)} \delta(\mathbf{x} - \mathbf{x}_i) \ , \tag{13}$$

where $\delta(\mathbf{x} - \mathbf{x}_i)$ denotes the Dirac's delta distribution, and $\mathbf{x}_i$ is a generic point of Per_n. The Bowen measure is a superposition of atomic measures with support on Per_n, where each point of the set is given the same weight. For specific classes of systems (expansive systems) it has been proved that the limit $\lim_{n\to\infty} = \mu_{Bow}^{(n)}$ converges towards an invariant measure, which we refer to as μ_{Bow} (Katok and Hasselblatt, 1995). Results of numerical simulations performed over physically relevant models suggest that this measure is well defined for a larger class of systems than those for which a rigorous proof of the convergence has been derived (Giona and Cerbelli, 2005).

[6]The family of sine-flow maps (Liu et al., 1994) is defined as the Poincaré map of the time periodic-flow defined by the action of two steady unidirectional blinking flows $\mathbf{v}_1 = (0, \sin(2\pi x))$, and $\mathbf{v}_2 = (\sin(2\pi y), 0)$, each acting alternately for a time $\tau = T/2$, where T is the overall period of the protocol.

2.5 Conclusions

The kinematic approach to mixing permits to classify different stirring protocols on the basis of quantities derived by the convective process, such as global characteristic exponents (Lyapunov exponent(s), topological entropy), stretch factor statistics, spatial structure of the measure, μ_w, associated with material interfaces, and of the Bowen measure associated with the set Per_n. In generic flows that depend nonlinearly on the spatial coordinates (i.e. in all the flows of physical interest), the dynamics of these quantities is characterized by universal qualitative features which can be summarized as follows

1. Coexistence of regular and chaotic behavior within one and the same phase space.
2. Dispersive behavior of stretch factors statistics.
3. Nonuniform (multifractal) character of the μ_w measure associated with material interfaces and of the Bowen measure associated with periodic points.
4. Presence of singular points in the neighborhood of which the local curvature of material interfaces advected by the stirring protocol diverges to infinity.

The impact of each of this specific phenomena on processes that occur along with stirring depends strongly on the process considered. For instance, it has been observed that the selectivity of parallel-competitive chemical reactions in partially chaotic flows is strongly influenced by the size and shape of the quasiperiodic islands (Zalc and Muzzio, 1999). As regards stretch factors, it has been argued that a dispersive dynamics of stretch factor statistics has quantitatively important consequences on the evolution of advecting-diffusing magnetic flows (Finn and Ott, 1988). Furthermore, the presence of islands and the dynamics of stretching strongly influences the homogenization timescales of advecting-diffusing scalar fields.

3 Hyperbolic theory

In this part of the lecture we are going to analyze to what extent the hyperbolic theory of dynamical systems (Katok and Hasselblatt, 1995) can be used to explain and connect to one another the different dynamical behaviors of kinematic quantities that we observed in physically interesting models of laminar chaotic mixing systems. As the kinematic approach was discussed in the specific context of two-dimensional time-periodic incompressible flows, the basic ideas of hyperbolic theory will be analyzed in the framework of a generic area-preserving transformation $\mathbf{f}$ of a bounded two-dimensional manifold $\mathcal{M}$, where bounded means that $\mathcal{M}$ can be embedded

in a finite-size ball of $\mathbb{R}^3$. The condition that the manifold $\mathcal{M}$ is bounded is essential in defining the property of the dynamics, since it influences the recurrence properties of the trajectories. In fact, Poincaré's recurrence theorem ensures that *almost all points* of a measure-preserving transformation of a bounded measurable manifold must come back arbitrarily close to their original position (see, e.g., Arnold (1989) for a proof). The wording "almost all" means that the property is true for all the points of the manifold with the possible exception of a set of points that possesses zero measure (i.e. roughly speaking, zero "area").

It is important to highlight that while Poincaré's theorem ensures that almost any orbit of a measure preserving transformation defined on a bounded measurable manifold must recur, it does not say anything about the spatial and temporal properties of such recurrence. The simplest example of recurrence is clearly represented by periodic behavior, where a point returns exactly at its original position at periodic intervals of time. In Section 2 of this lecture we have already discussed examples of nontrivial recurrence, namely quasiperiodic and chaotic behavior. Next, we choose the simplest example of hyperbolic systems to show how the boundedness of the mixing space directly impacts the property of the dynamics.

3.1 Hyperbolic dynamics in bounded and unbounded manifolds

Let us consider a hyperbolic matrix $H_1 = \left(\begin{smallmatrix} 1 & 2 \\ 1 & 3 \end{smallmatrix}\right)$ possessing integer entries and unit determinant. The most obvious way to associate a dynamical system with the matrix H_1 is to define a linear operator $\mathcal{A} : \mathbb{R}^2 \to \mathbb{R}^2$ that maps points of the xy plane onto itself as $\left(\begin{smallmatrix} \mathcal{A}_x(x,y) \\ \mathcal{A}_y(x,y) \end{smallmatrix}\right) = H_1 \cdot \left(\begin{smallmatrix} x \\ y \end{smallmatrix}\right)$. The operator $\mathcal{A}$ possesses two real eigenvalues $\lambda_u = 2 + \sqrt{3}$, $\lambda_s = 2 - \sqrt{3}$, to which two linear eigenspaces E^u, E^s can be associated, where E^u and E^s are the span spaces of the eigenvectors $\mathbf{e}^u = \left(\begin{smallmatrix} 2 \\ \lambda_u - 1 \end{smallmatrix}\right)$ and $\mathbf{e}^s = \left(\begin{smallmatrix} 2 \\ \lambda_s - 1 \end{smallmatrix}\right)$. The dynamics of points of the real plane under $\mathcal{A}$ is rather trivial. The origin of the real plane is a fixed point. The straight lines through the origin with slopes $\alpha = \lambda_u - 1/2$ and $\beta = \lambda_s - 1/2$, $y_u = \alpha x$ and $y_s = \beta x$ are invariant under $\mathcal{A}$ (unstable and stable manifold of the origin, respectively). Points of the unstable manifold are repelled away from the origin at an exponential rate, points on the stable manifold are attracted exponentially fast to the origin (see Fig. 14).

The trajectory of any other point of the plane is confined onto hyperbolas and diverges to infinity along the direction of the unstable manifolds through the origin[7]. There are no periodic points other than the origin, which is the

[7] Is is easy to show that such hyperbolas are invariant under $\mathcal{A}$.

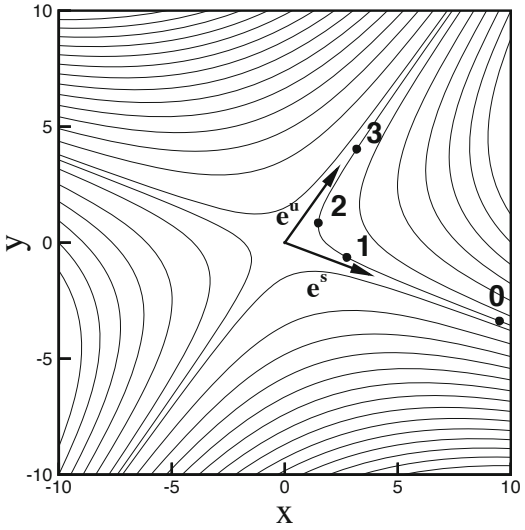

Figure 14. Dynamics induced by the linear operator $\mathcal{A}$ defined on the real plane.

only point that exhibits (trivial) recurrence. Of course there is no violation of Poincaré's theorem in that $\mathbb{R}^2$ is not a bounded manifold. Next, let us use the same hyperbolic matrix H_1 to define a dynamical system whose behavior is much less trivial than that of $\mathcal{A}$. By exploiting the fact that H_1 possesses integer entries we can define a transformation $\mathcal{H}_1 : \mathbb{I}^2 \to \mathbb{I}^2$, on the unit square domain where $\mathbb{I}^2 = (0,1] \times (0,1]$, as follows

$$\left\{ \begin{array}{lcll} \mathcal{H}_{1x}(x,y) & = & x + 2y & [\text{mod. } 1] \\ \mathcal{H}_{1y}(x,y) & = & x + 3y & [\text{mod. } 1] \end{array} \right. . \tag{14}$$

By this definition, to each point of $\mathbb{I}^2$ there corresponds one and only one image point that still belongs to $\mathbb{I}^2$. The "mod. 1" condition is automatically obtained if one identifies the opposite edges of the square, i.e. if one folds the square into a cylinder first, and then the cylinder into a two-torus (a "doughnut-shaped" surface, see Fig. 15). Any displacement of integer length along the x or y directions brings any point back to its original position.

The fact that the matrix H_1 possesses integer entries ensures that the transformation $\mathcal{H}_1$ is continuous (in fact, smooth) in the torus topology,

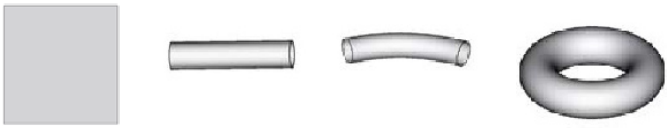

Figure 15. Folding the unit square into a two-torus.

i.e. a continuous domain is not broken into pieces when the transformation is considered defined on the two-torus. The operator $\mathcal{H}_1$ is an example of *Hyperbolic Toral Automorphism* (henceforth denoted as **HTA**).

Even though they were constructed starting from the same matrix H_1, the dynamics associated with $\mathcal{A}$ and $\mathcal{H}_1$ are altogether different, the latter being remarkably more complicated (a comprehensive discussion about the properties of hyperbolic toral automorphisms can be found in Katok and Hasselblatt (1995) or in Devaney (1986)). To begin with, there is a countable infinity of periodic points of arbitrarily large period associated with $\mathcal{H}_1$, namely all the points of the torus that possess rational coordinates (see, e.g. Devaney (1986)). Furthermore, it is possible to prove that there are uncountably many trajectories that fill densely the mixing space. In fact, the set of all of these trajectories possesses full measure. As regards the dynamics of tangent vectors, the same properties observed for the linear operator A defined on $\mathbb{R}^2$ still hold true, i.e. there exist an expanding and contracting direction defined at each point of the torus by the span spaces of the eigenvectors $\mathbf{e}^u$, $\mathbf{e}^s$, which define the dynamics of tangent vectors attached to any point of the torus. In fact, consider a point $\mathbf{x}$ and a vector $\mathbf{w}$ attached to it. It is possible to decompose $\mathbf{w}$ as the sum of two vectors $\mathbf{w}_u$ and $\mathbf{w}_s$, parallel to E^u, E^s, respectively. Each of these directions is invariant under $D\mathcal{H}_1^{(n)} = H_1^n$. The modulus of the components $\mathbf{w}_u^{(n)}$, $\mathbf{w}_s^{(n)}$ is expanded by a factor λ_u^n and contracted by a factor $\lambda_s^n = 1/\lambda_u^n$ (for $n > 0$), respectively. This causes any vector $\mathbf{w}$ whose unstable component is nonvanishing (i.e. "almost any" vector) to be stretched exponentially in the forward dynamics while being rapidly oriented along the unstable direction (the opposite is true when negative times are considered).

Let us next analyze the dynamics of finite-sized interfaces, e.g. by considering a straight initial segment of finite length.

As regards the fate of such segment under iterations of the linear opera-

tor $\mathcal{A}$ defined on the real plane, its dynamics is rather simple. The segment is stretched and rotated to become more and more parallel to the unstable direction E^u while being displaced at increasing distance from the origin. Globally, the segment is attracted closer and closer to the unstable manifold through the origin. It is worth highlighting that there is no straight invariant line other than the stable and unstable manifolds associated with the origin (even though there exists a foliated decomposition of the plane into hyperbolas. Note that the length of any finite-sized arc of such hyperbolas diverges to infinity both in the forward and backward time dynamics).

The dynamics of curves under $\mathcal{H}_1$ is instead rich and interesting. Consider first a straight segment attached to the origin aligned along the unstable direction. Figure 16 shows increasing iterates of such segment [8]. As n

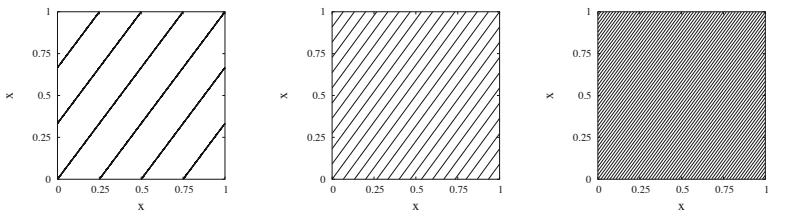

Figure 16. Increasing iterates (from left to right) of the local unstable manifold through the origin associated with the **HTA** $\mathcal{H}_1$. The segment develops towards a dense curve that wraps around the torus surface.

increases, the segment develops towards a continuous curve of exponentially increasing length that wraps densely around the torus and never intersects itself. As can be readily appreciated by the analysis of Fig. 16, the spatial distribution of the segment images within the mixing space is uniform. In fact, the same type of dynamics pertains to any segment that is aligned with the unstable direction. The same asymptotic properties will be attained in the backward time dynamics by any segment that is transverse to the stable direction E^s.

Another property associated with $\mathcal{H}_1$ which does not find counterpart in the dynamics induced by $\mathcal{A}$ is the so-called mixing property, which can be defined both in the topological and the measure-theoretical frameworks (see also the lecture by Mezic). The topological mixing property implies that

[8] Owing to the continuity of the map, the line is clearly continuous when looked at in the torus topology.

however one chooses two open sets, say U and V, there will be an integer ν such that for $n > \nu$ the intersection $\mathcal{H}_1^{(n)}(U) \cap V$ results nonempty. If one chooses $U = V$, this definition vaguely recalls the content of Poincaré's theorem. Yet, the topological mixing property is much stronger than recurrence in that it demands that the intersection between U and its images be *eventually nonempty*, whereas recurrence implies that such intersection be nonempty from time to time. The measure-theoretical counterpart of this definition considers any couple of measurable sets U and V. The transformation is mixing if $\mu(U \cap \mathcal{H}_1^{(n)}(V)) \rightarrow \mu(U)\ \mu(V)$ as $n \rightarrow \infty$. It is relatively straightforward to prove that any **HTA** possesses both of these properties. If the measure μ is regarded as a probability measure, the measure-theoretical mixing property basically means that any couple of events become asymptotically uncorrelated.

3.2 Uniformly Hyperbolic Systems on the two-torus

The **HTA** paradigm can be generalized by considering the class of (nonlinear) toral diffeomorphisms, i.e. the Hyperbolic Toral Diffeomorphisms -henceforth denoted as **HTD**- defined as the set of all toral diffeomorphisms that are topologically conjugated to a linear **HTA**. Roughly speaking, topological conjugacy between two systems, say $\mathcal{B}_1$ and $\mathcal{B}_2$, means that there exists a continuous change of coordinates that maps trajectories of one system into trajectories of the second system. In symbols, one writes $\mathcal{B}_2 = \mathcal{G}^{(-1)} \circ \mathcal{B}_1 \circ \mathcal{G}$, where $\mathcal{G}$ is a continuous mapping of the mixing space (the two-torus in the present case). An example of **HTD** is the Liverani's family of maps (Liverani, 2004) $\Phi_\varepsilon(x, y)$ given by

$$\Phi_\varepsilon(x,y) = \begin{pmatrix} x' \\ y' \end{pmatrix} = \begin{pmatrix} x + y + g_\varepsilon(x) \\ y + g_\varepsilon(x) \end{pmatrix} \ (\text{mod. } 2\pi), \tag{15}$$

where $0 \leq x, y < 2\pi$ and $g_\varepsilon(x) = x - (1 + \varepsilon \sin x)$, with $-1 \leq \varepsilon < 0$. Figure 17 shows the main kinematic properties of the mapping $\Phi_\varepsilon(x, y)$ for $\varepsilon = -0.1$. One observes the same qualitative features of kinematic quantities such as, the nonuniform distribution of advected interfaces (Figure 17-(a)), characterized by a fractal measure μ_w (Figure 17-(c) and -(d)), and the strict inequality between Lyapunov exponent and line stretching exponent (Figure 17-(b)). The example provided by Liverani's map contains in their greatest generality all the basic behaviors that define the class of *Uniformly Hyperbolic Systems*-**UH**, which we next define in general terms.

Let $\mathcal{M}$ be a bounded measurable manifold and $\mathbf{f}$ a smooth measure-preserving transformation of $\mathcal{M}$ onto itself. Let T_x be the tangent plane to $\mathcal{M}$ at the point $\mathbf{x}$, namely the plane that contains all the tangent vectors

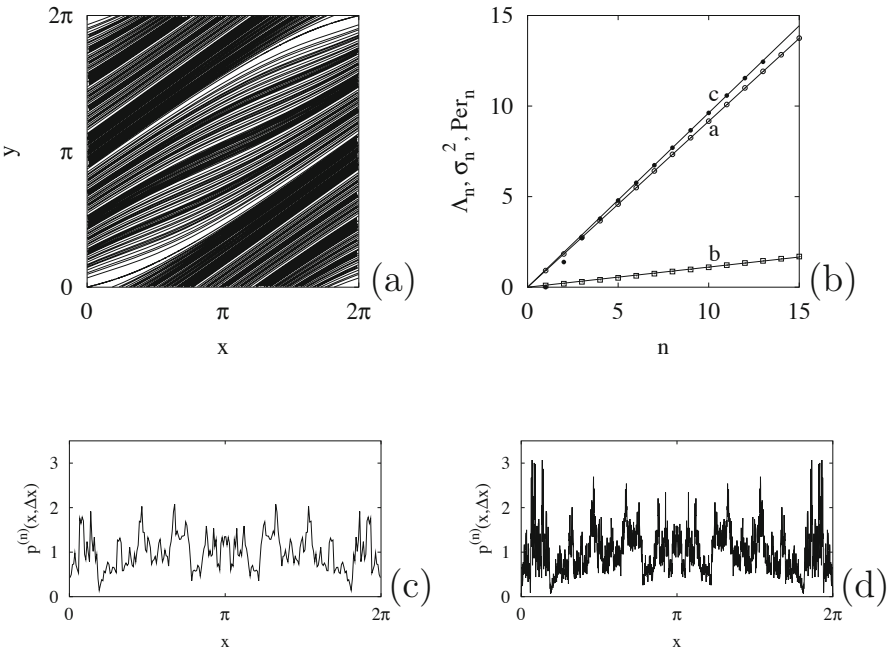

Figure 17. Geometric and statistical properties of Liverani's map. Panel (a): structure of the unstable manifold through the origin. Panel (b): statistical properties. Lines `a` and `b` depict the average value and the variance of the logarithm of the n-fold stretch factor for a swarm of 10^6 evolving vectors, respectively. Line `c` shows the growth of the set, Per_n, of periodic points of period less or equal to n. The slope of the latter curve is numerically equal to the line stretching exponent h_{top}. Panels (c) and (d): PDF of the intersections of the unstable manifold with a reference line, at increasing level of resolution Δx. The data suggest a fractal character of the corresponding w-measure (i.e. the nonexistence of a smooth density function).

to any smooth curve in $\mathcal{M}$ passing through $\mathbf{x}$, at the point $\mathbf{x}$. For instance, in the case of toral diffeomorphisms, T_x is the plane tangent to the torus surface at $\mathbf{x}$. Let $\mathcal{T}$ denote the *tangent bundle*, i.e. the collection of all tangent planes to any point of the manifold. The assumption that $\mathbf{f}$ is a smooth transformation allows one to define the linearized dynamics of $\mathbf{f}$, i.e. the dynamics of vectors in the tangent bundle $\mathcal{T}$. This can be done as follows. Let $\mathbf{v}$ be a vector belonging to the tangent plane at $\mathbf{x}$. We define a mapping that associates to the vector $\mathbf{v}$ belonging to $\mathbf{x}$, the vector $\mathbf{v}_1$ belonging to $T_{\mathbf{f}(\mathbf{x})}$ given by

$$\mathbf{v}_1 = D\mathbf{f}|_{\mathbf{x}} \cdot \mathbf{v} \quad , \tag{16}$$

where $D\mathbf{f}|_{\mathbf{x}}$ is the differential of $\mathbf{f}$, represented by its Jacobian matrix com-

puted at the point $\mathbf{x}$.

Shortly, a DS is uniformly hyperbolic if *at each point* of the manifold $\mathcal{M}$, the tangent space $T_{\mathbf{x}}$ splits into the sum of two invariant subspaces, referred to as $E^u_{\mathbf{x}}$ (unstable), $E^s_{\mathbf{x}}$ (stable), characterized by the following properties

1. if $\mathbf{v} \in E^u_{\mathbf{x}}$ then

$$\|D\mathbf{f}^{(n)}|_{\mathbf{x}} \cdot \mathbf{v}\| \leq A \exp(-\Lambda_1 |n|) \qquad \text{as } n \to -\infty \tag{17}$$

and

2. if $\mathbf{v} \in E^s_{\mathbf{x}}$ then

$$\|D\mathbf{f}^{(n)}|_{\mathbf{x}} \cdot \mathbf{v}\| \leq B \exp(-\Lambda_2\, n) \qquad \text{as } n \to \infty \tag{18}$$

The constants A, B, Λ_1, Λ_2 are all supposed positive, bounded away from zero and independent of the point $\mathbf{x}$. In fact the wording "uniformly hyperbolic" stems from the fact that the estimates on stretch factors are uniform on the entire manifold. It can be proved that if the subspaces $E^u_{\mathbf{x}}$ and $E^s_{\mathbf{x}}$ exist, then they are necessarily *unique and invariant* under DF,

$$D\mathbf{f}|_{\mathbf{x}}(E^u_{\mathbf{x}}) = E^u_{\mathbf{f}(\mathbf{x})} \qquad \text{and} \qquad D\mathbf{f}|_{\mathbf{x}}(E^s_{\mathbf{x}}) = E^s_{\mathbf{f}(\mathbf{x})} \quad . \tag{19}$$

The mapping $\Phi_\varepsilon(x, y)$ defined by Eq. (15) is an example of a uniformly hyperbolic system on the torus (see Liverani (2004)). It can be noted that, unlike the linear case (**HTA**), the stable and unstable invariant directions are different at different points of the manifold. This can be directly observed by the structure of the piece of unstable manifold depicted in Fig. 17-(a), which results tangent at each of its points to the local unstable direction. Another interesting geometric aspect associated with uniformly hyperbolic systems is that the angle between the stable and unstable subspaces $E^u_{\mathbf{x}}$ and $E^s_{\mathbf{x}}$ is bounded away from zero over the entire manifold $\mathcal{M}$.

The presence of a field of dilating and contracting invariant directions allows to link the orientation and the stretching properties associated with the evolution of tangent vectors that where observed in the SM model. In fact, the asymptotic directionality property, by which a stencil of initial vectors associated with a hyperbolic trajectory is swiftly aligned along a prescribed invariant direction at each point of the trajectory, is readily explained by the existence of invariant expanding and contracting directions. Each vector of the stencil possesses a nonvanishing component along the unstable direction that expands exponentially, whereas all the components along the stable direction are shrunk to vanishing norm.

The qualitative agreement between some of the kinematic features associated with **UH** systems and those associated with physically interesting models of chaos (such as the Standard Map) raises the question as to

whether the **UH** paradigm is well suited for representing mixing in incompressible flows as well as chaotic behavior in Hamiltonian systems. Unfortunately, the answer to this question is negative, as there are some qualitative features of physically interesting models that find no counterpart in Anosov systems. The first obvious inadequacy is that, by definition, a **UH** system does not possess nonhyperbolic points, whereas the presence of such points in physical models of conservative chaos appears somehow unavoidable (a macroscopic example of nonhyperbolic region is given by the quasiperiodic islands). Furthermore, nonhyperbolic points strongly influence the dynamics even inside the chaotic region. For instance, the direct comparison between the structure of unstable manifold in the SM model (Fig. 10) and Liverani's map (Fig. 17-(a)) suggests that, however rich, the invariant geometric properties associated with uniform hyperbolicity are yet too simple to represent the nature of the stretching and folding process that occurs in physically relevant chaotic systems. The case of the two-torus is an important benchmark test in this analysis, since we know by Manning's and Frank's theorems (Manning, 1974) that the even the most general Anosov (i.e. uniformly hyperbolic) system must be topologically conjugated to a "linear" **HTA**. From this property, it follows that every invariant stable or unstable manifold of a **UH** toral diffeomorphism must be topologically conjugated to a straight line (i.e. a line of constant -irrational- slope that winds densely around the torus surface). This is a strong geometric constraint for the structure of invariant manifolds, and a natural question arises as to whether the invariant manifolds associated with a physically interesting model such as the SM discussed before share the same property of topological conjugacy with the linear case. In trying to answer this question, let us consider again the structure of an invariant leave of the SM model. We have already observed heuristically that this curve undergoes "wild bends" at certain locations of the chaotic region. This concept can be made formally precise by introducing the notion of *recursively folding* property, which turns out to be one of the characteristic fingerprints of mixed behavior (i.e. of coexistence of regular and chaotic behavior).

Let us first define this property in the general context of a continuous transformation $\mathbf{f}$ of a smooth two-dimensional (orientable) manifold $\mathcal{M}$.

3.3 Recursive folding in physical models of chaotic mixing

Let $\mathcal{W}$ be a $\mathbf{f}$-invariant manifold (be it a global stable or unstable manifold) that is dense in a chaotic region $\mathcal{P} \in \mathcal{M}$. Let an orientation along $\mathcal{W}$ be established (e.g. by introducing the natural parametrization in terms of the arc length s from an arbitrary point $\mathbf{x}_0 \in \mathcal{W}$ and by considering

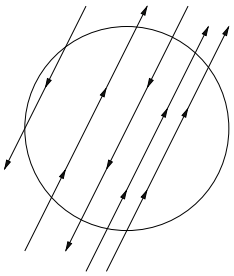

Figure 18. Sketch of the recursive folding property. There are nearby arcs of any given invariant manifold that are traveled in opposite directions by a representative point on the manifold that follows a prescribed orientation.

increasing values of s). By the fact that $\mathcal{W}$ is dense in $\mathcal{P}$, it will intersect the boundary ∂B_ε of any ε-ball embedded in the chaotic region at infinitely many points $\mathbf{x}_l \in \partial B_\varepsilon$. At each point $\mathbf{x}_l$, it is well defined whether, following the assigned orientation along the curve, the crossing occurs while entering or leaving B_ε. We say that the map is recursively folding if for each crossing point $\mathbf{x}_l$ where $\mathcal{W}$ enters B_ε there is a crossing point $\mathbf{x}_m$ arbitrarily close to it where $\mathcal{W}$ leaves B_ε (see Fig. 18).

The property of recursive folding is the geometric watershed between the **UH** paradigm and the behavior of physically relevant models of conservative chaos. As a confirmation of this statement, let us consider the SM model $\mathbf{M}$ discussed in Section 1, and follow the intersections of the unstable manifold of the origin $\mathcal{W}^u_{\mathbf{0}}$ with a reference line, say the horizontal segment $\{0 \leq x < 1,\ y = 1/4\}$, which represents a circumference in the torus topology. Figure 19-(a) shows the signed intersections of $\mathcal{W}^u_{\mathbf{0}}$ with this circumference.

The sign associated with the intersection is taken as positive or negative according to whether the crossing of the reference line along $\mathcal{W}^u_{\mathbf{0}}$ occurs upwards or downwards (i.e. while increasing or decreasing the value of the y-coordinate), respectively. As can be noted, there are oppositely signed intersections arbitrarily close to each other. Figure 19-(b) shows the result of the same computation for a **UH** system $\mathbf{g}(\mathbf{x})$, constructed by using the SM $\mathbf{M}(\mathbf{x})$ as a change of coordinates of an Anosov toral homeomorphism $\mathbf{a}(\mathbf{x}) = \mathbf{a}(x, y) = (x + y, x + 2y)$ [mod. 1], i.e. $\mathbf{g}(\mathbf{x}) = \mathbf{M}^{-1} \circ \mathbf{a} \circ \mathbf{M}(\mathbf{x}) = \mathbf{M}^{-1}(\mathbf{a}[\mathbf{M}(\mathbf{x})])$, $\mathbf{M}^{-1}$ being the inverse of the map $\mathbf{M}$. This example clearly indicates that recursive folding does not occur in a uniformly hyperbolic system on the two-torus. Thus, the presence of recursive folding must be strictly related to that of nonhyperbolic trajectories.

From these considerations, one gathers that in physically relevant sys-

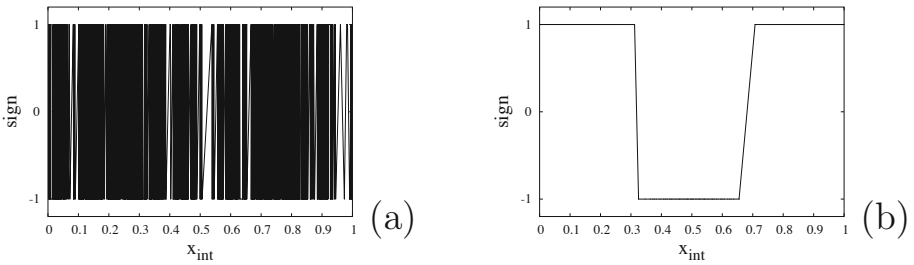

Figure 19. Signed intersections of an unstable manifold with a reference line for (a) the SM model, and (b) a **UH** system.

tems chaos is typically "massive but not ubiquitous", and that the presence of nohyperbolic points embedded in, or laying at the boundary of, the chaotic region has a dramatic impact on the structure of invariant manifolds within the chaotic region. Specifically, the recursive folding property is the fingerprint of other "pathological issues" of invariant manifolds, such as the presence of points of the chaotic region where the local curvature of these manifolds can attain arbitrarily large values (due to space limitation we refrain from discussing this issue in this lecture. We refer the interested reader to Cerbelli and Giona (2005a)).

It can be observed that the notion of massively chaotic systems that are not uniformly chaotic has been given a rigorous mathematical framework by Pesin in the mid 70's (Pesin, 1976a,b), is a series of papers (substantially ignored by the physics and engineering communities) in which the author introduced the category of *nonuniformly hyperbolic systems*.

In a two-dimensional phase space, nonuniformly hyperbolic systems are defined as those systems for which the set of all hyperbolic trajectories (referred to as *t*he Pesin set, say $\mathcal{P}$) has positive measure. The presence of nonhyperbolic orbits can influence geometric and statistical properties associated with points of the Pesin set $\mathcal{P}$. For instance, the existence of a strictly positive constant entering the bounds of vectors norm dynamics is granted only pointwise (i.e. one cannot find a constant that works for the entire set $\mathcal{P}$), and so is the lowerbound for the angle between stable and unstable invariant directions. The latter property implies that in the Pesin region of a nonuniformly hyperbolic system, it is possible to find points at which the angle between stable and unstable directions becomes arbitrarily small, i.e. the stable and unstable manifolds become almost tangent to each other. The question of how this tangency condition is related to recur-

sive folding and curvature singularity of invariant manifolds is a subject of ongoing research (Cerbelli and Giona, 2005a).

In closing this lecture we provide a succinct description of a recently proposed topological model of conservative chaotic systems whose properties can be derived analytically to a large extent (Cerbelli and Giona, 2005b). We expect that this model can provide a starting point for bridging the gap between the physical and mathematical approach to two-dimensional area-preserving systems.

3.4 A topological archetype of the Standard map

Next, we describe an archetypal model, the toral homeomorphism $\mathcal{H}$, which, as regards the geometric picture discussed above, can be envisioned as a topological analogous of the SM $\mathcal{M}$. A detailed account of all the statistical and geometric properties of $\mathcal{H}$ (most of which can be derived analytically) can be found in (Cerbelli and Giona, 2005b). Here, we describe the geometric aspects of the transformation that are strictly pertinent to the focus of the present discussion. The homeomorphism $\mathcal{H}(\mathbf{x}) = = \mathcal{H}(x, y) = (x', y')$ is a piecewise linear, globally continuous transformation of the two-torus defined by

$$\left\{ \begin{array}{lcl} x' & = & x + f(y) \\ y' & = & x + y + f(y) \end{array} \right. \quad \text{(mod. 1)}, \tag{20}$$

where (x, y), $(x', y') \in [0, 1) \times [0, 1)$ are coordinates on the two-torus, and $f(\xi) : [0, 1] \to [0, 1]$ is the tent map defined by $f(\xi) = 2\xi$ for $0 \leq \xi < 1/2$, and $f(\xi) = 2 - 2\xi$ whenever $1/2 \leq \xi < 1$. In (Cerbelli and Giona, 2005b), it is shown that one can break down the torus into two disjoint subsets say Σ_1 and Σ_2 (see Fig. 20), where the invariant stable and unstable directions, $E^s_{\mathbf{x}}$ and $E^s_{\mathbf{x}}$ respectively, are constant.

For $\mathbf{x} \in \Sigma_1$, these directions, say E^s_1 and E^u_1, are given by the contracting and expanding eigenspace associated with the hyperbolic matrix $H_1 = \left(\begin{smallmatrix} 1 & 2 \\ 1 & 3 \end{smallmatrix}\right)$, i.e. $E^s_1 = \mathtt{span}(\mathbf{s}_1)$, and $E^u_1 = \mathtt{span}(\mathbf{u}_1)$, where $\mathbf{u}_1 = (2, 1+\sqrt{3})$, and $\mathbf{s}_1 = (2, 1 - \sqrt{3})$. The invariant directions E^s_2 and E^u_2 at points $\mathbf{x} \in \Sigma_2$ are given by the images of the eigenspaces associated with points of Σ_1 through the matrix $H_0 = \left(\begin{smallmatrix} 1 & -2 \\ 1 & -1 \end{smallmatrix}\right)$, i.e. $E^s_2 = \mathtt{span}\,(H_0 \cdot \mathbf{s}_1)$, and $E^u_2 = \mathtt{span}\,(H_0 \cdot \mathbf{u}_1)$. Figure 21 shows the structure of the stable and unstable manifold of the origin $\mathbf{0}$, $\mathcal{W}^s_{\mathbf{0}}$ and $\mathcal{W}^u_{\mathbf{0}}$, respectively.

These curves are globally continuous, piecewise-smooth, $\mathcal{H}$-invariant, and everywhere dense on the torus. They are nonsmooth only at the boundary $\partial\Sigma_2$ of the set Σ_2.

The relatively simple structure of the fields of invariant dilating and contracting directions defined by the linearized dynamics associated with

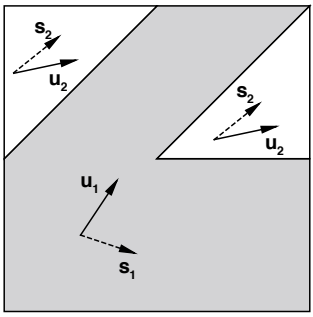

Figure 20. Structure of the stable and unstable subspaces for the map $\mathcal{H}$.

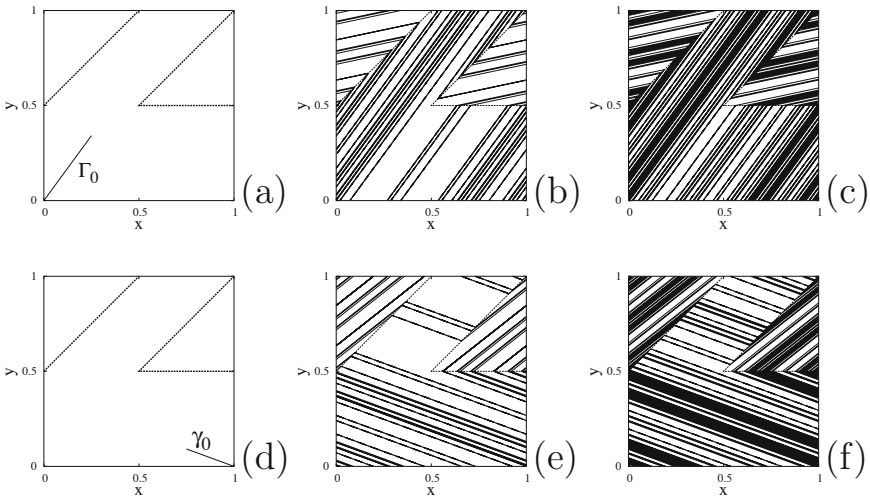

Figure 21. Panels (a), (b), (c): forward evolutes of the local unstable manifold through the origin for (a): $n = 0$, (b): $n = 5$, (c): $n = 7$. Panels (d), (e), (f): backward evolutes of a local stable manifold at the origin for (d): $n = 0$, (e): $n = -5$, and (f): $n = -7$. The thick dashed lines represent the set of points where the curves are not differentiable.

$\mathcal{H}$ allows to prove analytically a number of typical properties of hyperbolic systems, and some peculiar features that characterize nonuniformly chaotic systems, e.g. the strict inequality between the line stretching exponent (which equals the topological entropy) and the positivity Lyapunov exponent and the sign-alternating property (Cerbelli and Giona, 2005b). An analysis of the structure of the stable and unstable manifolds in the neighborhood of the points $\mathbf{x}_1 = (1, 1/2)$ and $\mathbf{x}_2 = (1, 1)$ provides one with a direct perception of why the latter property holds true in the $\mathcal{H}$ model. In fact, visual inspection of these structures shows that near $\mathbf{x}_1$ the stable and unstable manifolds undergo a (nonsmooth) bend enclosing $\mathbf{x}_1$, as depicted in Fig. 22. Next, consider any point $\mathbf{y}_1$ of the segment belonging to the parallel to the local unstable direction in the lower half-square domain and therein embedded. Let $\mathbf{y}_1$ be such that its forward orbit is dense in the mixing space (one can show that there is abundance of such points on the segment considered). Consider a small segment, say σ_s passing through $\mathbf{y}_1$ and parallel to the local stable direction and define as $\mathcal{L}$ the simply connected domain formed by σ_s and the continuous arc of the unstable manifold enclosing the point $\mathbf{x}_1$. Let $\mathbf{y}_2$ be the second intersection point of σ_s with the arc of unstable manifold. The domain $\mathcal{L}$ is referred to as a (generalized) lobe (Cerbelli and Giona, 2005a). As lengths on σ_s are exponentially shrunk, the images of the lobe under iterations of $\mathcal{H}$ will be such that the mapped points $\mathcal{H}^{(n)}(\mathbf{y}_1)$ and $\mathcal{H}^{(n)}(\mathbf{y}_2)$ will collapse onto each other. Besides, since the image of the lobe region is still a simply connected domain, the local arcs of the unstable manifold at the points $\mathcal{H}^{(n)}(\mathbf{y}_1)$ and $\mathcal{H}^{(n)}(\mathbf{y}_2)$ will be still oppositely oriented. but as $\mathcal{H}^{(n)}(\mathbf{y}_1)$ traces a dense orbit, this means that there are oppositely oriented arcs of the unstable manifold in the neighborhood of any point of the mixing space.

Another interesting feature of the model is that it can be straightforwardly associated with a symbolic system evolving in the space of (one-sided) sequences of two symbols (e.g. "0" and "1") obtained by considering the binary representation of the coordinates and expressing the action of the map in this sequence space. This allows to to compute the trajectories of the system with arbitrary precision.

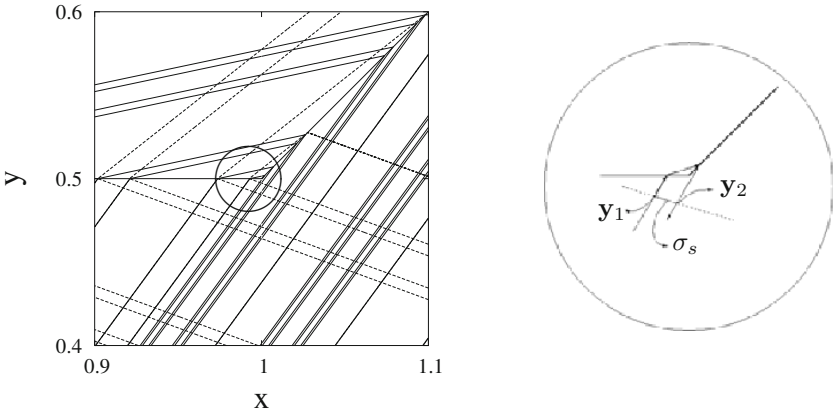

Figure 22. Left panel: Structure of the invariant manifolds associated with the $\mathcal{H}$ model near the parabolic-like critical point $\mathbf{x}_1 = (1, 1/2)$ originating the recursive folding property (a different projection chart of the torus is used in this figure for rendering the continuity of the invariant manifolds). Both the stable (dashed line) and unstable manifold (continuous line) undergo a sharp bend enclosing the point $\mathbf{x}_1$. Right Panel: Zoom in of the circled region of left panel showing the existence of a lobe (gray shaded area) formed by two continuous arcs of a stable and an unstable manifold that intersect only at two points, thus defining a simply connected region. The existence of the lobe, together with the existence of a dense orbit (topological transitivity), implies the recursive folding property of $\mathcal{H}$.

Bibliography

H. Aref. Stirring by Chaotic Advection, *J.* Fluid Mech., 143:1-21, 1984.

V.I. Arnold, Sur La geometrie differentielle des groupes de Lie de dimension infinie et ses applications a l'hydrodynamique des fluides parfaits. *A*nn. Inst. Fourier 16:316-361, 1966.

V.I. Arnold, *M*athematical methods of classical mechanics. Springer, New York, 1989.

L. Barreira and Y.B. Pesin, *L*yapunov exponents and smooth ergodic theory. University Lecture Series, 23, American Mathematical Society, Providence, RI, 2002.

G. Casati and B.V. Chirikov, editors. *Q*uantum Chaos, Cambridge University Press, Cambridge, 1995.

S. Cerbelli, J.M. Zalc and F.J.Muzzio. The evolution of material line curvature in deterministic chaotic flows. *Chem. Eng. Sci.*, 55:363-371, 2000.

S. Cerbelli, and M. Giona. One-sided invariant manifolds, recursive folding, and curvature singularity in area-preserving nonlinear maps with nonuniform hyperbolic behavior. *Chaos, Solitons & Fractals*, 29:36-47, 2005a.

S. Cerbelli, and M Giona. A continuous archetype of nonuniform chaos in area-preserving dynamical systems. *Jou. Nonl. Sci.*, 15:387-421, 2005b.

S. Childress and A.D. Gilbert. *S*tretch, Twist and Fold: The Fast Dynamo, Springer, New York, 1995.

P.V. Dankwerts. The definition and measurment of some characteristics of mixtures. *Appl. Sci. Res. A*, 3:279-296, 1952.

L.R. Devaney. *An introduction to chaotic dynamical systems.* Addison-Wesley Advanced Book Program, Redwood City, CA, 1986.

F. Diacu and P. Holmes. *Celestial Encounters. The origin of chaos and stability.* Princeton University Press, Princeton, NJ, 1996.

I.T. Drummond and W. Munch. Distortion of line and surface element in model turbulent flows. *J. Fluid Mech.*, 225:529-543, 1991.

J.P. Eckmann and D. Ruelle. Ergodic theory of chaos and strange attractors. *Rev. Mod. Phys.*, 57:617-656, 1985.

J.M. Finn and E. Ott. Chaotic flows and magnetic dynamos. *P*hys. Fluids, 31:2992-3011, 1988.

M. Giona and A. Adrover. Nonuniform stationary measure of the invariant unstable foliation in Hamiltonian and fluid mixing systems. *P*hys. Rev. Lett., 81:3864-3867, 1998.

M. Giona, A. Adrover, S. Cerbelli and V. Vitacolonna. Spectral properties and transport mechanisms of partially chaotic bounded flows in the presence of diffusion. *P*hys. Rev. Lett. , 92:114101, 2004.

M. Giona and S. Cerbelli. Connecting the spatial structure of periodic orbits and invariant manifolds in hyperbolic area-preserving systems. *P*hysics Letters A, 347:200-207, 2005.

D.M. Hobbs and F.J. Muzzio. The Kenics Static Mixer: a three-dimensional chaotic flow. *C*hem. Eng. J. , 67:153-166, 1997.

G. Karniadakis, A. Beskok, N. Aluru. *Microflows and nanoflows*, Springer, New York, 2000.

A. Katok and B. Hasselblatt. *Introduction to the modern theory of dynamical systems*. Encyclopedia of mathemathics, Cambridge University Press, Cambridge, 1995.

D.V. Khakhar, J.G. Franjione and J.M. Ottino. A case study of chaotic mixing in deterministic flows: the partitioned-pipe mixer. *Chem. Eng. Sci.*, 42:2909-2926, 1987.

L. Kuznetsov, C.K.R.T. Jones. M. Toner, A.D. Kirwan Jr. Assessing coherent feature kinematics in ocean models. *Physica D*, 191:81-105, 2004.

C. W. Leong and J.M. Ottino. Experiments on mixing due to chaotic advection. *J.* Fluid Mech. 209:463-499, 1989.

M. Liu, F.J. Muzzio, F. and R.L. Peskin. Quantification of mixing in aperiodic chaotic flows. *Chaos Solitons and Fractals* 4:869-893, 1994.

C. Liverani. Birth of an elliptic island in a chaotic sea. *Math. Phys. Electron. J.*. 10:paper 1, 2004.

A. Manning. There are no new Anosov diffeomorphisms on tori. *Am. J. Math.*, 96:422-429, 1974.

V.I. Oseledec. A multiplicative ergodic theorem. Lyapunov characteristic numbers for dynamical systems. *Trans. Moscow Math. Soc*, 19:197-231, 1968.

J.M. Ottino. *T*he Kinematics of Mixing. Stretching, Chaos and Transport. Cambridge University Press, Cambridge, 1989.

Ya. B. Pesin. Families of invariant manifolds corresponding to nonzero characteristic exponents *Izv. Akad. Nauk. SSSR Ser. Mat.*, 40:1332-1379, 1976a.

Ya. B. Pesin. Characteristic Lyapunov exponents and smooth ergodic theory. *Russian Math. Surveys*, 32:55-112, 1976b.

W. Rudin *R*eal and complex analysis. McGraw-Hill, Singapore (1986).

V. Toussaint, P. Carriere, J. Scott and J.N. Gence. Spectral decay of a passive scalar in chaotic mixing. *P*hys. Fluids, 12:2834-2844, 2000.

M. Wojtkowski. A model problem with coexistence of stochastic and integrable behavior. *C*omm. Math. Phys, 80:453-464, 1981.

J.M. Zalc and F.J. Muzzio. Parallel-competitive reactions in a two-dimensional chaotic flow. *C*hem. Eng. Sci. , 54:1053-1069, 1999.

Advection-diffusion in chaotic flows

Massimiliano Giona
Dipartimento di Ingegneria Chimica Università di Roma "La Sapienza",
Via Eudossiana 18 00184 Roma, Italy
E-mail: max@giona.ing.uniroma1.it

1 Introduction

The aim of these notes is to provide an overview of the different approaches used to address the advection-diffusion equation, viewed as the mathematical setting for studying mixing in laminar incompressible flows. In its beginnigs[1], i.e. starting from the paper by Aref (1984), the field of laminar mixing was essentially a new playground for physicists, fluid dynamicists and engineers, where the tools of dynamical system theory could be applied.

In the last few years, laminar mixing is experiencing a second youth. This is essentially due to the impulse given by miniaturization of mechanical and chemical equipment, a new research subject which is imposing itself as a fundamental piece of knowledge in the development of tools such as the "lab-on-a-chip" or microplants (Ehrfeld et al., 2004; Nguyen and Zu, 2005; Hessel et al., 2005; Stroock et al., 2002). The perception of this radical change in the expectations, and in fund raising, connected with laminar mixing is readily evident from the *incipit* of a recent article on micromixers: "Microfluidics is now part of big science and big business ..." Ottino and Wiggins (2004). The connection with laminar mixing is provided by the fact that at such small spatial scales, as those involved in microflow devices, the Reynolds number is tipically well below the turbulent threshold.

Aside from specific microfluidic applications (biomedicals, sensors), a change of *weltanschauung* in the approach to industrial production (at least for the most advanced products) is becoming appreciable as engineers are beginning to question the classical paradigm towards the scale-up of large

[1] In a historical perspective, it should be mentioned that the first contributions of methods of chaotic dynamics in laminar flows are Arnold (1965); Henon (1966). For further discussion see Mezic (2001).

industrial plants, and are re-orienting reseach-and-development efforts towards a different approach (more respectful for the enviroment, more lucrative for the companies) based on plant miniaturization (Nguyen and Zu, 2005; Hessel et al., 2005, 2004; Squires and Quake, 2005). Programs like *scaling-down* and *numbering-up* are becoming part of the emerging manifesto for the new industrial century. Among the various fields of application of this new approach, it is sensible to expect a potentially high impact related to the advances of molecular biology and genetics.

If this scenario will prove a reasonable picture of what will become the driving force of technological development in the near future, the theoretical modelling of fluid-flow phenomena at micro and nano scales will necessarily become one of the founding cornerstones of such development.

The scale of the characteristic lengths involved in microdevices simplifies the fluid-dynamic analysis and the computation of velocity fields inside micro-flow equipment in that the laminar character of the flow makes it unnecessary to investigate and model the impact of turbulent fluctuations. On the other hand, mixing theory (i.e. the characterization of the "mixedness" of a fluid mixture and the optimization of the flow protocol) becomes a crucial and challenging issue.

A mature and critical analysis of all the technical, formal and computational tools associated with the description of dispersion and homogenization of a fluid phase becomes urgent[2], also in connection with concrete practical applications of the theory. These notes attempt to provide an insight of what might be relevant in this analysis. This attempt is unavoidably influenced by the personal research experience of this author in the field.

These notes are organized as follows. In the first part (Sections 2 and 3), a brief description is presented of what "mixing" means and of the conceptual paradigms for approaching it. Section 4 addresses some basic functional-theoretical tools useful in the mathematical setting of the problem. Sections 5 describes some spectral results and the properties of the advection-diffusion equation in bounded domains. Section 6 develops a critical analysis of some "controversial issues", while Section 7 addresses some current open problems in the theory of mixing. While most of the analysis, especially as it regards the interplay between advection and diffusion is of general validity, the numerical examples refer to two-dimensional flows for which the velocity field is given. The inertial effects on mixing induced e.g. by the increase of the Reynolds number are not considered.

[2] In the epistemological approach developed by Imre Lakatos, this critical analysis may correspond to the conflict between different and competing "research programs".

2 Paradigms and approaches

More than half a century of investigation on the theory of fluid mixing can be outlined by describing the main conceptual paradigms that have organized and oriented the research in this field, especially as it regards the definition of what mixing is and how it can be characterized objectively and quantitatively.

By making a rather brutal simplification, fluid mixing theory can be subdivided into three main eras and paradigms: (I) the Danckwerts' era, (II) the kinematic (Lagrangian) paradigm, (III) and the functional-theoretical paradigm. As in any scientific activity, no sharp boundaries can be drawn between these three paradigms, and a certain degree of "interdiffusion" exists between these three approaches.

The Danckwerts' era corresponds to the investigation on mixing initiated in the mid of the last century by P. V. Danckwerts (1952, 1953, 1958). It is reasonable to argue that the research on mixing at that time was triggered by the practical need of the growing chemical industry to obtain reliable quantitative information on the efficiency of mechanical stirring in chemical reactors and process units. In the 50's, the chemical industry was essentially concerned in fluid-phase processing, and the need of quantifying the degree of mixing was urgent for plant optimization, and cost reduction (nowadays, solid particle processing associated with pharmaceutical and electronic industries has shifted the focus on mixing mainly towards particle processing and granular materials).

The mixing theory proposed by Danckwerts was essentially based on a *black-box* statistical approach aimed at providing a set of diagnostic parameters to quantify the degree of mixedness, independently of the specific physico-chemical processes occurring within the mixture. At any time $\bar{t}$, the mixture was viewed as a function $\phi(\mathbf{x})$ defined over the points $\mathbf{x}$ of the mixing space Ω. By considering $\phi(\mathbf{x})$ as the description of a mixture of two immiscible liquids A and B (and by indicating with the same symbols A and B the regions of the mixing space occupied by the two liquids), the function $\phi(\mathbf{x})$ can be expressed as: $\phi(\mathbf{x}) = 1$ if $\mathbf{x} \in A$, and $\phi(\mathbf{x}) = 0$ if $\mathbf{x} \in B$.

In the Danckwerts' formulation, mixedness is represented by the spreading of A in B (or viceversa), and consequently it can be described by means of the squared variance of the representative function $\phi(\mathbf{x})$,

$$I = \int_{\Omega} (\phi(\mathbf{x}) - \overline{\phi})^2 \, d\mathbf{x} = \langle (\phi - \overline{\phi})^2 \rangle_{\Omega} \,, \tag{1}$$

where $\overline{\phi} = \int_{\Omega} \phi(\mathbf{x}) \, d\mathbf{x}$, referred to as the *intensity of segregation*.

The quantity I was not sufficient in the Danckwerts' formulation for

providing an exhaustive account for the structure of a mixture. The information on the intensity of segregation had to be complemented with the information on the characteristic linear size of the complex convoluted structures created within a fluid phase under stirring. The knowledge of the characteristic linear size S of partially mixed structures was finalized at obtaining an order-of-magnitude estimate of the characteristic time scales for homogenization due to the effect of diffusion, $t_{dif} = S^2/D$ (where D is a characteristic diffusivity). For this reason, Danckwerts introduced the concept of *linear scale of segregation* S, which can be estimated starting from the decay of the autocorrelation function of $\phi(\mathbf{x})$ (Danckwerts, 1952).

The Danckwerts's approach is still adopted in solving practical mixing problems due to its simplicity. However, it suffers from some conceptual weak points. Consider a fluid mixture under stirring and assume the effects of diffusion are negligible. Let $\phi(\mathbf{x}, t)$ be the concentration of a dye, initially located in a bounded domain of the mixing space. It follows from Eq. (1) that $I(t) = I(0) =$ constant (see Section 4). This means that the Danckwerts' intensity of segregation remains constant in the absence of diffusion no matter how the mixture is stirred, although it is evident that the action of a stirring protocol improves the degree of mixedness. For instance, compare Fig. 1 (A), corresponding to the initial condition of a blob of dye, and Fig. 1 (B) depicting dye distribution after the action of a stirring protocol of a model flow.

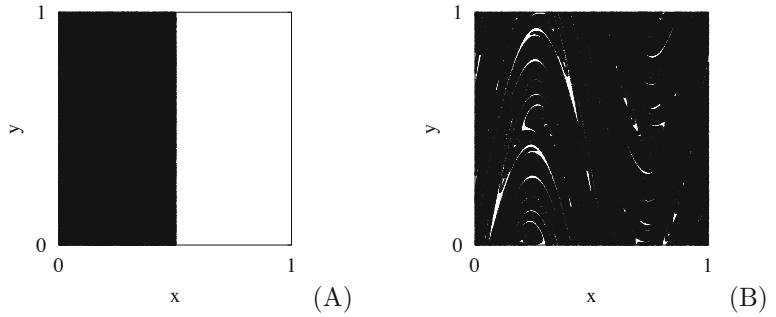

Figure 1. Action of a stirring protocol on an initial blob of dye. The flow protocol is a model flow on the 2-torus, the time-periodic Sine Flow at $T = 1.6$. (A) Initial blob of dye. (B) Blob after three periods of the stirring protocol.

Subsequent elaborations of the Danckwerts' approach have characterized

other research directions. One of them, referred to as *lamellar model*, was very popular 20-30 years ago (Ranz, 1979; Ottino et al., 1979; Ottino, 1989; Muzzio and Ottino, 1989). In the lamellar model - essentially applied to describe (bimolecular) reactions in stirring flows - the mixture is regarded as a superposition of a system of lamellae (strips) each of which initially composed by either one or the other reactant. Theoretical models (*the warped time approach*) were elaborated by simplifying the stirring action of an advecting flow as a hypothetical stretching flow near a hyperbolic stagnation point (Batchelor, 1959; Ottino et al., 1979). The major drawback of the lamellar approach is that it is unable to capture the essential effects of folding and spatial nonlocality induced by the action of a flow in a bounded domain. As result, the practical utility of these models is limited.

In the spirit of the early works by Danckwerts, several other global quantities have been introduced, such as the concept of *mixedness* and *unmixedness* by Dimotakis and Miller (1990), see also (Smith et al., 1997), which is related to the statistical properties (variance) of the probability density function $p_\phi(\phi)$ of the concentration intensity. Given any scalar field ϕ, let $p_\phi(\phi)$ the probability density function associated with the concentration intesities of ϕ within the mixing space, and let ϕ_m and ϕ_M the minimum and maximum values attained by ϕ within the mixing space (or the interrogation area considered, such as a mixing layer), respectively. A measure U of mixedness according to Dimotakis and Miller is given by (Dimotakis and Miller, 1990; Smith et al., 1997)

$$U = \frac{1}{(\phi_M - \overline{\phi})(\overline{\phi} - \phi_m)} \int_{\phi_m}^{\phi_M} (\phi - \overline{\phi})^2 \, p_\phi(\phi) \, d\phi \,, \qquad \overline{\phi} = \int_{\phi_m}^{\phi_M} \phi \, p_\phi(\phi) \, d\phi \,. \tag{2}$$

However, this quantity does not provide any objective description of mixing, as can be argued by the simple observation that the two concentration fields $\phi_1(x)$ and $\phi_2(x)$ depicted in Fig. 2 (A)-(B) possess the same degree of mixedness according to (Dimotakis and Miller (1990)), although visual inspection and the intuitive perception of what mixing means, suggest the opposite. The above criticism on the definition of the degree of mixedness U Eq. (2), as a reliable measure of the state of a mixture, applies to any global quantity constructed starting from the probability density function of intensities of any scalar field, since in this way the spatial structure of the scalar field distribution within the mixing space is neglected.

The Lagrangian (kinematic) approach spread out starting from the celebrated paper by Aref (1984). Retrospectively, the interest raised by this approach can be considered a fall-out of the emerging interest in nonlinear dynamics and chaos that has characterized the scientific community starting

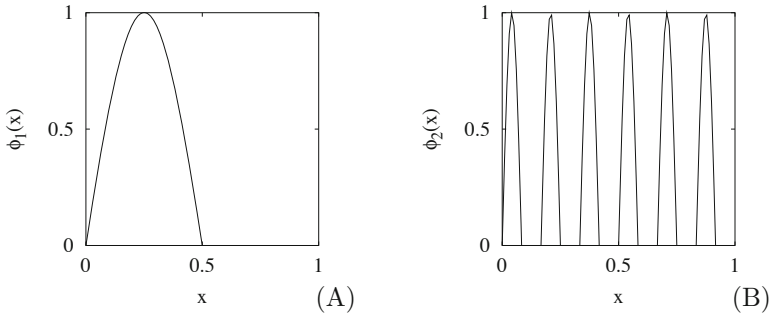

Figure 2. Two concentration function $\phi_1(x)$, $\phi_2(x)$ on $[0,1]$ possessing the same *unmixedness* according to Dimotakis and Miller (1990).

from the seventies of the last century.

The starting point in the Lagrangian analysis is the kinematic equation of motion of fluid particles which are passively advected in a stirred continuum by the velocity field $\mathbf{v}(\mathbf{x},t)$

$$\frac{d\mathbf{x}}{dt} = \mathbf{v}(\mathbf{x},t) \qquad \mathbf{x} \in \Omega\,. \tag{3}$$

The paradigm of this approach is simple and evocative, also in view of the fact that it has implied a radical change of attitude with respect to dynamic phenomena within the engineering communities (and particularly amongst chemical engineers), rooted in a static description of processes and phenomena. Simply, the Lagrangian approach dictates that good mixing performance can be achieved solely if the kinematic equations of motion exhibit chaotic behavior (i.e. a sensitive dependence on the initial conditions). The *degree of chaos* was *ipso facto* a measure of the mixing efficiency.

The 1984-paper by Aref was a kind of magic box. It gave a simple recipe to tackle fluid mixing starting from the analysis of the low dimensional, apparently simple, dynamical system Eq. (3). Once this box was opened, all the tools of nonlinear dynamical system theory (Eckmann and Ruelle, 1985) were ready and available for a quantitative description of mixing.

Within this paradigm, it was immediately clear that two-dimensional autonomous flows (such that $\mathbf{v} = \mathbf{v}(\mathbf{x})$ is independent of time) could not produce efficient mixing, since for these systems, fluid particle dynamics cannot be chaotic, as each particle orbit is confined on a streamline of $\mathbf{v}$. Conversely, two-dimensional time-periodic flow protocols, which induce a

crossing between instantaneous streamlines at different time instants, could become candidates for efficient mixing, and could be used as standard prototypes of a mixing system. Poincaré maps and stroboscopic sections were used as a first, global visual indicator of the goodness of a stirring protocol. The statistical apparatus (Lyapunov exponents, topological and metric entropies, statistics of stretching and curvature) was borrowed from dynamical system theory and applied for characterizing mixing, viewed as the outcome of pure stirring (Ottino, 1989; Muzzio et al., 1991; D'Alessandro et al., 1999). The role of the unstable manifolds was thoroughly investigated as the basic template for the evolution of material lines which are boundary of finite-sized fluid elements in two-dimensional systems (Beigie et al., 1994; Giona and Adrover, 1998).

After more than two decades of research activity along this track, a critical examination of the results achieved suggests that the Lagrangian approach cannot produce a complete and application-oriented quantitative description of mixing. This observation should not induce to underestimate the role of Lagrangian analysis. To begin with, the Lagrangian analysis has contributed to clarify the role of stretching and folding as a basic mechanism of mixing protocols (Smale, 1967; Childress and Gilbert, 1995). Furthermore, it has provided a connection between the geometric features of mixing (i.e. the spatial structure and the dynamics of mixing patterns) and the statistical properties associated with the local deformation process occurring along a typical (i.e. "chaotic") orbit (Beigie et al., 1994).

In the light of concrete applications to microdevices, the Lagrangian approach suffers some intrinsic conceptual drawbacks, the most significant of which is that it does not account for diffusion, which is, ultimately, the only mechanism that ensures that spatial homogeneity within the mixture will be eventually reached. Also, even though the Lagrangian approach defines objective indexes assessing the quality of the mixing process within each of the invariant sets associated with the kinematic equations of motion, it does not provide any information about how these region-dependent indexes should be combined together to construct a global measure of mixing in the flow domain as a whole. This last issue is clearly connected with the first in that the only flux exchange of a scalar entity (be it a chemical species or energy) that is being transported between kinematically invariant sets relies exclusively on the presence of the diffusion mechanism.

This problem can be clearly appreciated by considering a typical Poincaré section of a chaotic flow (specifically, the partitioned pipe mixer analyzed by Khakhar et al. (1987)), depicted in Fig. 3. For generic flows, and specifically for physically realizable velocity fields (which are solution of the Navier-Stokes equation in the domain Ω), the global orbit structure within

the phase space Ω shows the simultaneous occurrence of regions of regular (periodic/quasiperiodic) motion intermingled with regions characterized by chaotic kinematics. Each of these regions is invariant for the Lagrangian dynamics, and is characterized by a specific set of Lyapunov numbers, entropies, etc. The Lagrangian description captures separately the properties of each of these invariant regions. This observation suggests that the Lagrangian approach provides a global description of mixing solely for globally chaotic flows, i.e. for flows exhibiting a single full-measure chaotic region, such that its closure coincides with the mixing space Ω itself. Apart from archetypical examples, the occurrence of global chaos has been (numerically) observed solely in very simple model flows on the torus, i.e. on boundaryless manifolds. Indeed, to the best of this author's knowledge there is no example of a globally chaotic flow defined in a closed and bounded set Ω of $\mathbb{R}^2$ or $\mathbb{R}^3$. This raises doubts whether globally chaotic flows may exist on manifolds with boundaries and, most importantly, whether such flows may be associated with velocity fields that are solutions of the Navier-Stokes equation in closed and bounded domains.

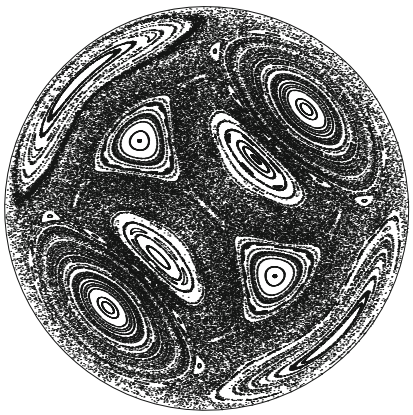

Figure 3. Poincaré section of a model flow (the partitioned pipe).

It is worth observing that some of the limitations of the Lagrangian approach can be overcome even within a purely kinematic (i.e. diffusionless) setting. In point of fact, instead of a Lagrangian description of fluid particle motion, one can consider the evolution of ensemble of particles, and

ultimately of particle densities (Lasota and Mackey, 1994). This can be regarded as the *kinematic density approach* to fluid mixing.

In the absence of diffusion, the kinematic density approach analyzes the operator $F_t : L^1(\Omega) \to L^1(\Omega)$, ($L^1(\Omega)$ is the space of integrable functions in Ω), which maps a density $\phi(\mathbf{x}, t_1)$ at the time instant t_1 ($\phi(\mathbf{x}, t_1) \geq 0$, $\int_\Omega \phi(\mathbf{x}, t_1)\, d\mathbf{x} = 1$), into the density $\phi(\mathbf{x}, t_1 + t)$ at time $t_2 = t_1 + t$, according to the kinematic protocol expressed by Eq. (3). This operator, mapping densities into densities, is referred to as the *Frobenius-Perron operator* (Lasota and Mackey, 1994).

For flows generated by the velocity field $\mathbf{v}(\mathbf{x}, t)$, the evolution of the density is described by the continuity equation for ϕ

$$\partial_t \phi + \nabla \cdot (\mathbf{v}\, \phi) = 0\,. \tag{4}$$

Throughout these notes incompressible flows are considered, so that $\nabla \cdot \mathbf{v} = 0$.

If the kinematics of a time-periodic velocity field $\mathbf{v}(\mathbf{x}, t + T) = \mathbf{v}(\mathbf{x}, t)$ is expressed by means of the Poincaré map Φ, i.e. $\mathbf{x}_{n+1} = \Phi(\mathbf{x}_n)$ where $\mathbf{x}_n = \mathbf{x}(nT)$ (by incompressibility $|\det(\Phi^*(\mathbf{x}))| = 1$, where $\Phi^*(\mathbf{x}) = \partial\Phi(\mathbf{x})/\partial\mathbf{x}$), the Frobenius-Perron operator $F = F_T$ can be explicited. Letting $\phi^{(n)}(\mathbf{x}) = \phi(\mathbf{x}, nT)$, the stroboscopic evolution equation for the density reads

$$\phi^{(n+1)}(\mathbf{x}) = F[\phi^{(n)}(\mathbf{x})] = \phi^{(n)}(\Phi^{-1}(\mathbf{x}))\,, \tag{5}$$

where $\phi^{(n)}(\mathbf{x}) = \phi(\mathbf{x}, nT)$.

The application of the density description is motivated by the need of overcoming the shortcomings of the Lagrangian analysis discussed above. Within the kinematic density approach, the paradigm of good mixing is derived from ergodic theory (Arnold and Avez, 1989; Walters, 1982). A good mixing protocol corresponds to a Frobenius-Perron operator which is a *mixing transformation* in the measure-theoretical sense. Let μ be the normalized Lebesgue measure in Ω, $\mu(\Omega) = 1$. The map F is *mixing*, if for any pair of measurable sets $A, B \subseteq \Omega$

$$\lim_{n\to\infty} \mu(A \cap \Phi^{-n}(B)) = \mu(A)\,\mu(B)\,. \tag{6}$$

The kinematic density approach can be viewed as a functional approach since it involves the analysis of an operator, the Frobenius-Perron operator, which is defined in a suitable metric space of functions, typically $L^1(\Omega)$. The Lagrangian analysis and the kinematic density approach are closely related, since the characteristic lines for the continuity Eq. (4) are the kinematic equations Eq. (1). However, there is a profound conceptual shift in these

two approaches, since the former is oriented towards a trajectory-based description of mixing, while the latter focuses on the collective motion of measurable ensembles of orbits.

A further generalization is represented by the advection-diffusion approach, which considers mixing processes as the result of the interplay between a stirring field $\mathbf{v}(\mathbf{x}, t)$ and diffusion, that, in its simplest formulation, can be modelled by means of a Fickian term. The starting point is the Advection-Diffusion Equation (ADE), which in dimensionless form reads

$$\partial_t \phi + \nabla \cdot (\mathbf{v}\, \phi) = \varepsilon \nabla^2 \phi \,, \tag{7}$$

where ϕ is the dimensionless concentration of a chemical species, ε the reciprocal of the Peclet number, $\varepsilon = 1/Pe$, where $Pe = VL/D$ is the ratio of the characteristic time for diffusion $t_{dif} = L^2/D$ to the characteristic time for advection $t_{adv} = L/V$, and L, V, D are a characteristic lengthscale, a characteristic velocity intensity and the diffusivity, respectively. In deriving Eq. (7), the time is made dimensionless with respect to the advection time scale $t \to tV/L$.

The functional approach shifts the focus of mixing theory from the investigation of a low-dimensional ordinary diffential equation to the analysis of an infinite-dimensional dynamical system expressed by the parabolic equation Eq. (7). However, this apparent increase in model complexity is compensated by the fact the while Eq. (1) is intrinsically nonlinear, Eq. (7) is linear, and many robust results of the theory of linear operators (Reed and Simon, 1980; Kato, 1980) provide tools and suggestions to set and tackle mixing problems.

This change of paradigm (from ODE to PDE) shows some similarities with the transition from the (nonlinear) Newtonian dynamics to the (linear) quantum mechanical formulation expressed by means of the Schrödinger equation (in the non-relativistic case). This analogy is even more strict, by further considering that the spectral theory of operators, (essential in quantum theory), is equally important in the quantification of mixing (this claim is explained in the remainder of these notes). Unfortunately, while in the quantum mechanical case, the relevant operators are Hermitian (self-adjoint), the advection-diffusion operator does not possess this property, and the lack of self-adjointness makes the analysis more complex.

In other words, *nonlinear vs linear*, opposed to *finite-dimensional vs infinite-dimensional* is the trade-off associated with the transition from the Lagrangian to the ADE and the Frobenius-Perron formulations.

The kinematic density approach, i.e. Eq. (4), can be viewed as a particular case of Eq. (7) for $\varepsilon = 0$. However, the physical advantage of Eq. (7) is that the two main and opposite contributions governing mixing, namely

Paradigms of mixing	Formal setting
Danckwerts' approach	Statistical description based on I and S
Lagrangian theory	Dynamic and statistical properties associated with $\dot{\mathbf{x}} = \mathbf{v}(\mathbf{x}, t)$
Functional approach (kinematic density approach)	Functional properties of the FP operator $\partial_t \phi + \nabla \cdot (\mathbf{v}\, \nabla \phi) = 0$
Functional approach (advection-diffusion approach)	Asymptotic/spectral properties of the ADE $\partial_t \phi + \nabla \cdot (\mathbf{v}\, \phi) = \varepsilon \nabla^2 \phi \ , \quad \varepsilon > 0$

Table 1. Schematic review of the paradigms of mixing discussed in Section 2.

advection and diffusion are included in the evolution equation. In many pratical applications, the inclusion of diffusional effects is strictly necessary for a correct physical formulation of the problem.

The concept of good mixing within the advection-diffusion formalism is addressed in the next two Sections, after describing the role of the boundary conditions and some elementary properties of Eq. (7).

Table 1 reviews the main mixing paradigms discussed throughout this Section. In an epistemological perspective, it would be interesting to compare and contrast these paradigms by focusing on their reciprocal *incommensurabilities* (Feyerabend, 1975).

3 Dispersion vs homogenization

The ADE Eq. (7) is a parabolic differential equation. In order to set properly a mixing problem, the boundary conditions should be specified. This is a rather obvious observation that sometimes is forgotten in practice.[3] Quoting Roache (1972):

> "A first-order *ordinary* differential equation such as $df/dx = 0$ specifies the solution of the problem up to an additive constant; the boundary condition determines the value of the constant. A

[3] For example, the Batchelor approach (Batchelor, 1959), and the warped-time approach developed by Ranz and Ottino (Ranz, 1979; Ottino et al., 1979) refer to a hypothetical shear flow around a hyperbolic stagnation point in an infinitely extended continuum with no boundaries. The results obtained under these conditions do not apply to the phenomenology observed in bounded closed flows, especially as it regards the long-time (asymptotic) properties.

first-order *partial* differential equation such as $\partial f(x,y)/\partial x = 0$ specifies very little of the solution; any function $g(y)$ satisfies the PDE, and the boundary conditions must specify the *function*. A PDE such as $\nabla^2\psi = \zeta$ really contains very little information on ψ. All the fantastic flow patterns of common gases and liquids are solutions of the same PDE's, the Navier-Stokes equations. The flows (solutions) are distinguished only by boundary and initial conditions, and by the flow parameters such as *Re*."

There are three main geometrical configurations of the mixing space Ω corresponding to three different formulations of the boundary conditions:

1. Unbounded domains, such as the entire space $\mathbb{R}^2$ or $\mathbb{R}^3$, or infinitely extended strips $\{\ (x,y)\ |\ 0 \le y \le 1,\ x \in \mathbb{R}\ \}$, which are infinitely extended along one direction.
2. Bounded closed domains, which e.g. represent the mixing space within a chemical reactor operating under batch condition.
3. Bounded open domains, which e.g. describe channel flows on finite structures, T-junctions, or static mixers.

Let us review the boundary conditions in these three situations. Let us consider first unbounded domains, such as $\mathbb{R}^2$ or $\mathbb{R}^3$. In the open space, no boundary conditions apply besides the regularity condition at infinity.

In bounded closed domains, the boundary $\partial\Omega$ is impermeable to mass transfer. Both the normal component of the velocity field, $v_n|_{\partial\Omega} = \mathbf{v}\cdot\mathbf{n}|_{\partial\Omega} = 0$ ($\mathbf{n}$ is the normal unit vector pointing outward), and the normal component of the diffusive flux

$$\left.\frac{\partial\phi}{\partial n}\right|_{\partial\Omega} = \nabla\phi\cdot\mathbf{n}|_{\partial\Omega} = 0 \tag{8}$$

vanish at the boundary of Ω. Therefore, the boundary conditions on ϕ are of Neumann type Eq. (8).

In modelling bounded closed flows, boundaryless compact manifolds, such as the two- and the three-dimensional unit tori, T^2 and T^3, are frequently considered. Boundaryless manifolds simplify the analytical manipulations associated with the solution of the ADE. Let us consider T^2. A projection chart for T^2 is given by the unit square $I^2 = [0,1]\times[0,1]$ with opposite edges identified. Consequently, the boundary conditions to be imposed on ϕ are periodic boundary conditions. This simply implies that the solution of the ADE on T^2 can be expressed in a Fourier series $\phi(\mathbf{x},t) = \sum_{h,k}\phi_{h,k}\mathrm{e}^{i2\pi(hx+ky)}$, where $i = \sqrt{-1}$. For example, the Sine Flow (see Appendix B), and the flow associated with the Standard Map (see Section 7) are defined on T^2, while the ABC flow, a classical three-dimensional autonomous model flow (Dombre et al., 1986), is defined on T^3.

In bounded open flows, the boundary of the flow domain can be decomposed into three different parts

$$\partial\Omega = \partial\Omega_0 \cup S_{in} \cup S_{out}\,, \tag{9}$$

i.e. into solid walls $\partial\Omega_0$, on which impermeability to mass transfer should be enforced, an inlet and an outlet section S_{in} and S_{out}, respectively. The distinction between S_{in} and S_{out} depends on the direction of the velocity field, which points inward on S_{in}, and outward on S_{out}. The behavior of the normal velocity component (pointing outward), and the boundary conditions on ϕ read

$$\begin{cases} v_n = 0 & \text{on } \partial\Omega_0 \\ v_n \le 0 & \text{on } S_{in} \\ v_n \ge 0 & \text{on } S_{out} \end{cases} \qquad \begin{cases} \partial\phi/\partial n = 0 & \text{on } \partial\Omega_0 \\ \phi = \phi_{in} & \text{on } S_{in} \\ \partial\phi/\partial n = 0 & \text{on } S_{out}\,. \end{cases} \tag{10}$$

Specifically, it is reasonable to assume that the value of the concentration is specified on S_{in} and equal to $\phi_0(\mathbf{x})$, while at the outlet section Danckwerts' boundary conditions may be applied (Froment and Bischoff, 1979), dictating that the normal derivative of ϕ vanishes on S_{out}.

The assessment of the inlet and outlet boundary conditions have been subject of intense debate in the past (Wehner and Wilhelm, 1956; Pearson, 1959; Bischoff, 1961). As it regards outlet flow, the Danckwerts boundary condition $\partial\phi/\partial n|_{S_{out}} = 0$ is a simple and widely used choice, although there is no rigorous derivation of it. The Danckwerts setting of the outlet condition has been criticized by some researchers, e.g. (Smith, 1988). However, the attempts made to improve it, such as those reported in (Smith, 1988) apply to a limited number of cases (specifically one-dimensional models of channel flows) and cannot be extended to generic flow geometries. This is the reason why, notwithstanding its limitations, the Danckwerts outlet condition still remains the most widely used in applications.

Instead of

$$\phi = \phi_{in} \qquad \text{on } S_{in}\,, \tag{11}$$

introduced in Eq. (10), an alternative choice for the inlet condition, due to Danckwerts is of mixed type, namely

$$v_n\phi_{in} = v_n\phi - \varepsilon\frac{\partial\phi}{\partial n} \qquad \text{on } S_{in}\,. \tag{12}$$

In the case of Eq. (11) the continuity of ϕ at the inlet boundary is ensured, and moreover the flux of ϕ can be extended continuously to S_{in}. Conversely, the inlet condition Eq. (12) implies a discontinuity of the concentration ϕ

at the inlet boundary. In point of fact, for high Peclet values ($Pe \geq 10^2$) the differences between Eq. (11) and Eq. (12) become immaterial.

The nature of the mixing domain Ω, and the setting of three different boundary value problems on Eq. (7) in bounded/unbounded, open/closed flows specify the physical meaning of the mixing problem, and the mathematical techniques to be used to tackle it. Indeed, the bounded vs unbounded nature of the flow domain corresponds at least to two different physical problems, namely *homogenization* and *dispersion*.

In unbounded flow domains[4], the relevant phenomenology relies on the dispersion properties of the concentration field, in a long-time long-distance perspective. This typically occurs in pollutant dispersion in the environment, in large-scale oceonographic analysis of dispersion, in the analysis of the effects of fluid streams on the stability of an ecosystem. The hypothesis that the flow domain is unbounded implies that the long-time long-distance properties of the solutions of Eq. (7) are given by the solution of a pure diffusion equation with constant tensor diffusivities $\mathcal{D}_{h,k}$. The estimate of $\mathcal{D}_{h,k}$ depends on the properties of the velocity field, and can be obtained through the application of homogenization theory (Bensoussan et al., 1978).

In homogenization theory, it is convenient to express the advection-diffusion equation in dimensionless form with respect to the characteristic diffusional time scale $t \to tD/L^2$, so that Eq. (7) becomes (for $\nabla \cdot \mathbf{v} = 0$)

$$\partial_t \phi + Pe\, \mathbf{v} \cdot \nabla \phi = \nabla^2 \phi \,. \tag{13}$$

Consider the typical case of a periodic (cellular) flow possessing zero mean. In the analysis of the long-time long-distance properties of the solution of Eq. (13), it is natural to assume that the ratio δ between the velocity and the concentration lengthscale becomes very small. It is therefore useful to rescale time and space as $\mathbf{x} \to \delta \mathbf{x}$, $t \to \delta^2 t$, and the concentration ϕ as

$$\phi_\delta(\mathbf{x}, t) = \delta^{-d} \phi(\delta \mathbf{x}, \delta^2 t) \,, \tag{14}$$

where d is the dimension of the flow domain ($d = 2, 3$). In the long-time, long-distance limit, the rescaled concentration $\phi_\delta(\mathbf{x}, t)$ Eq. (14) approaches a limit function $\overline{\phi}(\mathbf{x}, t)$, i.e. $\lim_{\delta \to 0} \phi_\delta(\mathbf{x}, t) = \overline{\phi}(\mathbf{x}, t)$, which satisfies an

[4]To avoid misunderstanding it is useful to point out that analytical results derived for unbounded domain can be applied, under certain conditions, to finite geometries. For instance, the classical work by Taylor (1953) and Aris (1956) on dispersion in laminar channel flows can be applied to finite length geometries, such as chromatographic columns. However, its proper formal setting implies the unboundedness of the channel along its axial direction. See e.g. the original paper by Aris (1956).

effective diffusion equation

$$\frac{\partial \overline{\phi}}{\partial t} = \sum_{h,k=1}^{d} \frac{\partial}{\partial x_h} \left(\overline{\mathcal{D}}_{h,k} \frac{\partial \overline{\phi}}{\partial x_k} \right) , \tag{15}$$

where x_h, $h = 1, \ldots, d$ are the spatial coordinates. The tensor diffusivity decomposes into an isotropic contribution and a convection-enhanced diffusivity tensor $\mathcal{D}_{h,k}$, $\overline{\mathcal{D}}_{h,k} = \delta_{h,k} + \mathcal{D}_{h,k}$, where $\delta_{h,k}$ is the Kronecker symbol. The tensor diffusivities $\mathcal{D}_{h,k}$ are determined by the equation

$$\mathcal{D}_{h,k} = \langle \nabla \zeta_h \cdot \nabla \zeta_k \rangle_{cell} , \qquad h, k = 1, \ldots, d , \tag{16}$$

where the average $\langle \cdot \rangle_{cell}$ is performed on the unit cell of the flow, and the vector-valued function $\boldsymbol{\zeta} = \{\zeta_h\}_{h=1}^{d}$ is the solution of a partial differential equation. Specifically, for steady cellular flow, $\boldsymbol{\zeta}$ is the unique zero-mean periodic solution of the elliptic equation

$$\nabla \zeta_h - Pe \mathbf{v} \cdot \nabla \zeta_h = Pe v_h , \qquad h = 1, \ldots, d . \tag{17}$$

For further details on homogenization techniques and on dispersion properties of more complex flows see (Bensoussan et al., 1978; Majda and Kramer, 1999; Fannjang and Papanicolau, 1994).

In the case of unbounded flows, stochastic approaches based on the analogy between Eq. (7) and a Langevin equation driven by a Wiener process proves very useful (Chandrasekhar, 1943). Information on the asymptotic properties can be inferred from the scaling of the mean square displacement of tracer particles, or from other, conceptually analogous, stochastic indicators.

The situation is completely different, in the case of bounded flows, for which the analysis of stochastic parameters such as the scaling of the mean square displacement is of very limited use due to the boundedness of the domain.

Apart from specific applications to stirred tanks and batch mixing systems (i.e. to systems of chemical engineering interest), there is however, another, more deep reason why bounded flow models are of valuable theoretical interest. Advection of passive particles (especially in those cases in which the kinematics gives rise to some form of partial or global chaos) is essentially related to the stretching and folding action imposed by the stirring field. In unbounded domains, the effects of folding is made immaterial by the infinite extent of the flow domain. The complex kinematic features (expressed by the Poincaré sections) of partially chaotic flows, resulting in the coexistence of regions of mixing (chaos) intertwined with regions of

quasiperiodic motion, loose their clear dynamic meaning in unbounded domains, although a Lagrangian description of mixing in open flows have been suggested by several Authors (Pentek et al., 1999; Tel et al., 2000).

For the reasons outlined above, bounded flows provide the most intriguing setting for analyzing how the stretching and folding action of a given flow field interacts with diffusion, and how this interaction determines the long-term (asymptotic properties) associated with the evolution of concentration fields driven by Eq. (7).

In bounded and closed domains, the problem of mixing corresponds *sensu stricto* to a homogenization problem, i.e. to the relaxation of the concentration field $\phi(\mathbf{x},t)$ towards the uniform distribution $\overline{\phi} = \int_\Omega \phi(\mathbf{x},t)\, d\mathbf{x}$. Given an initial condition $\phi_0(\mathbf{x})$, the main issue is to determine the characteristic time scale t_{mix} (the mixing time) for achieving a prescribed homogenization, i.e. such that, fixing $\eta > 0$, $\int_\Omega (\phi(\mathbf{x},t) - \overline{\phi})^2\, d\mathbf{x} < \eta$ for $t > t_{mix}$. The characterization of the mixing efficiency in bounded and closed domains implies the estimate of the mixing time t_{mix}, and in a design perspective its optimization. This is the first and foremost piece of information requested by mixing practitioners for a short-cut design of the equipment (Biggs, 1963; Nienow, 1997) (in industrial equipment also power-consumption properties are relevant), and this is exactly the result coming out from functional analysis of the ADE (see Section 5).

For second-order linear operators in bounded domain, the strategy for achieving a complete characterization of their action is to consider their spectral (eigenvalues/eigenvector) properties. In point of fact, spectral characterization, i.e. the distribution of the energy content amongst spatial wavelengths, provides the appropriate setting to define what mixing is, and to obtain quantitative indicators of the degree of mixedness (Giona et al., 2002, 2004a,b; Mathew et al., 2005). This is discussed in Sections 4 and 5.

To conclude this Section, let us consider the case of bounded open flows. For simplicity, let us assume that the inlet function $\phi_0(\mathbf{x})$ does not depend on time. Let $\chi_\Omega(\mathbf{x})$ be a generic, sufficiently smooth function in the weak sense (Robinson, 2001) such that

$$\begin{cases} \chi_\Omega(\mathbf{x}) = 1 & \text{on } S_{in} \\ \chi_\Omega(\mathbf{x}) = \partial\chi_\Omega(\mathbf{x})/\partial n = 0 & \text{on } \partial\Omega_0 \cup S_{out}\,. \end{cases} \tag{18}$$

The use of the auxiliary function $\widetilde{\phi}(\mathbf{x},t) = \phi(\mathbf{x},t) - \phi_{in}(\mathbf{x})\,\chi_\Omega(\mathbf{x})$ permits to homogenize the boundary conditions, since the auxiliary function $\widetilde{\phi}(\mathbf{x},t)$ is the solution of the equation

$$\partial_t\widetilde{\phi} + \mathbf{v}\cdot\nabla\widetilde{\phi} = \varepsilon\nabla^2\widetilde{\phi} + G \tag{19}$$

where the forcing term is

$$G(\mathbf{x}) = \varepsilon\nabla^2(\phi_{in}(\mathbf{x})\chi_\Omega(\mathbf{x})) - \mathbf{v}(\mathbf{x})\cdot\nabla(\phi_{in}(\mathbf{x})\chi_\Omega(\mathbf{x})) = T[\phi_{in}(\mathbf{x});\chi_\Omega(\mathbf{x})]\,, \tag{20}$$

equipped with the boundary conditions $\widetilde{\phi}|_{S_{in}} = 0$, $\partial\widetilde{\phi}/\partial n|_{\partial\Omega_0\cup S_{out}} = 0$, and with the initial condition $\widetilde{\phi}(\mathbf{x},0) = \phi_0(\mathbf{x}) - \phi_{in}(\mathbf{x})\chi_\Omega(\mathbf{x})$. We have assumed for simplicity that the velocity field is autonomous. At steady state, Eq. (19) reduces to an elliptic problem

$$\mathcal{L}[\widetilde{\phi}] = \varepsilon\nabla^2\widetilde{\phi} - \mathbf{v}\cdot\nabla\widetilde{\phi} = -G\,, \tag{21}$$

the solution of which can be formally expressed as

$$\widetilde{\phi} = -\mathcal{L}^{-1}[G] = -\mathcal{L}^{-1}\circ T[\phi_{in};\chi_\Omega]\,, \tag{22}$$

and therefore,

$$\phi = \phi_{in}\chi_\Omega - \mathcal{L}^{-1}\circ T[\phi_{in};\chi_\Omega] = Z[\phi_{in}]\,. \tag{23}$$

The mapping Z is independent of χ_Ω and its restriction to S_{out}, $Z_{out} = Z|_{S_{out}}$, specifies completely the input-output properties of an open-flow device (such as a static mixer).

Albeit, the spectral approach could be equally well applied to an open-flow system, it is clear that a quantitative characterization of the homogenization induced by open-flow devices on the outlet concentration is contained within the functional properties of the operator $Z|_{S_{out}}$, defined by Eq. (23).

In the remainder of these notes, attention is focused on closed and bounded flows. The case of open-flow devices is touched in passing in the open-problem Section 7.

3.1 Infinitely fast reactions

Apart from tracer dispersion and homogenization experiments, the ADE describes the evolution of a bimolecular chemical reacting system in the limit of infinitely fast chemical reactions (Sokolov and Blumen, 1991).

Consider a bimolecular reaction

$$A + B \rightarrow \text{Products}\,, \tag{24}$$

and let c_A, c_B be the concentrations of the two reactants. Moreover, let us assume that the diffusivities of the reacting species are equal $D_A = D_B = D$. The balance equations for c_A and c_B in a stirred incompressible mixture read

$$\begin{aligned} \partial_t c_A + \mathbf{v}\cdot\nabla c_A &= \varepsilon\nabla^2 c_A - r(c_A,c_B) \\ \partial_t c_B + \mathbf{v}\cdot\nabla c_B &= \varepsilon\nabla^2 c_B - r(c_A,c_B)\,, \end{aligned} \tag{25}$$

where $r(c_A, c_B)$ is the dimensionless reaction rate. By defining $\phi = c_A - c_B$, it follows readily that ϕ satisfies the ADE Eq. (7). The most interesting situation occurs when the reaction rate is arbitrarily large, which is referred to as the *infinitely fast reaction-rate limit*. In this case, if A and B are initially segregated, they remain segregated at all the time, due to the assumption of instantaneous reaction. For infinitely fast reactions, the difference function ϕ completely specifies the reaction evolution, since

$$c_A = \frac{\phi + |\phi|}{2} \qquad c_B = \frac{-\phi + |\phi|}{2} \,. \tag{26}$$

In the case of stoichiometric initial loading, which corresponds to equal masses of the two reactants (the stoichiometric coefficients are assumed to be equal), $\phi(\mathbf{x}, 0)$ possesses zero mean, and so does the solution of Eq. (7) for $t > 0$.

In the case of infinitely fast reactions, the zero-level set $\Gamma_0(t)$ of the concentration difference ϕ

$$\Gamma_0(t) = \{\mathbf{x} \mid \phi(\mathbf{x}, t) = 0 \} \tag{27}$$

is the separation manifold between the two reactants, thus defining the *reaction interface*. This is the simplest way of defining a physically significant geometric interface associated with the evolution of the ADE (Giona et al., 2002).

4 Functional setting of the ADE and norm inequalities

This Section addresses the functional setting and some functional-theoretical properties of the ADE in bounded-closed flows. In closed flows, the ADE is equipped with Neumann boundary condition Eq. (8). At the end of this Section, a formulation of mixing processes within the paradigm of the functional analytical approach is addressed.

We assume that the flow is incompressible and that the domain is sufficiently "regular". Mathematically this means that the boundary $\partial\Omega$ is the union of a finite number of Lipschitz curve arcs.

In the dynamical system framework, the ADE Eq. (7) can be envisioned as an evolution equation

$$\frac{\partial \phi}{\partial t} = \mathcal{L}[\phi; t] \,, \tag{28}$$

defined in a suitable functional space, where $\mathcal{L}$ is the differential operator:

$$\mathcal{L}[\phi; t] = -\mathbf{v}(\mathbf{x}, t) \cdot \nabla \phi + \varepsilon \nabla^2 \phi \,. \tag{29}$$

A first property stemming from mass conservation is that the solution of the ADE possesses a constant mean $\overline{\phi}(\mathbf{x},t) = \overline{\phi}(\mathbf{x},0) = \overline{\phi}_0$ for any $t \geq 0$. This observation has a straightforward consequence. The ADE leaves invariant two subspaces: the subspace of constant functions, and the subspace of nonconstant functions possessing vanishing mean. The practical implication of this elementary observation is discussed in the remainder of this Section, in connection with a definition of mixing in bounded and closed flows.

4.1 Functional setting

As for many parabolic problems, the most simple and convenient functional setting for the ADE Eq. (7) is to regard its solutions as elements of the functional space $L^2(\Omega)$ of the square summable functions in Ω

$$L^2(\Omega) = \left\{ f \;\middle|\; \int_\Omega |f(\mathbf{x})|^2 \, d\mathbf{x} < \infty \right\} . \tag{30}$$

Indeed, the functional space $L^2(\Omega)$ can be viewed as the direct sum of two orthogonal subspaces $L^2(\Omega) = c(\Omega) \oplus \dot{L}^2(\Omega)$, where $c(\Omega)$ is the space of constant functions in Ω and $\dot{L}^2(\Omega)$ is the subspace of square summable functions possessing zero mean (i.e. such that if $f \in \dot{L}^2(\Omega)$, then $\int_\Omega f(\mathbf{x}) \, d\mathbf{x} = 0$). From what stated above, it is sufficient to consider the ADE within $\dot{L}^2(\Omega)$, since constant functions are left invariant under the advection-diffusion evolution.

The functional spaces $L^2(\Omega)$ and $\dot{L}^2(\Omega)$ are Hilbert spaces, equipped with the inner product $(\cdot,\cdot)_{L^2}$ and the norm $||\cdot||_{L^2}$, defined as

$$(f,g)_{L^2} = \int_\Omega f(\mathbf{x}) \, g^*(\mathbf{x}) \, d\mathbf{x} \, , \qquad ||f||_{L^2} = \sqrt{(f,f)_{L^2}} \, , \tag{31}$$

$f, g \in L^2(\Omega)$, where g^* is the complex conjugate of g.

In point of fact, the space $\dot{L}^2(\Omega)$ is a too general functional space for a convenient setting of Eq. (7), since the differential nature of the operator $\mathcal{L}$ requires that any solution of this equation should possess stronger regularity (differentiability) properties, than solely bounded L^2-norm. Such regularity properties are accounted for by considering the Sobolev space $\dot{H}^1(\Omega) \subset \dot{L}^2(\Omega)$, which is the space of zero-mean square summable functions, possessing square summable first-order generalized derivatives (Robinson, 2001)

$$\dot{H}^1(\Omega) = \left\{ f \;\middle|\; f \in \dot{L}^2(\Omega) \, , \quad \int_\Omega |\nabla f(\mathbf{x})|^2 \, d\mathbf{x} < \infty \right\} . \tag{32}$$

The Sobolev space $\dot{H}^1(\Omega)$ is a Hilbert space equipped with the inner product

$$(f,g)_{H^1} = \int_\Omega \left[f\, g^* + \sum_{h=1}^{d} \frac{\partial f}{\partial x_h} \frac{\partial g^*}{\partial x_h} \right] d\mathbf{x}\,. \tag{33}$$

Consequently the H^1-norm is given by

$$||f||_{H^1} = \left[(f,f)_{H^1}\right]^{1/2} = \left[||f||^2_{L^2} + ||\nabla f||^2_{L^2}\right]^{1/2}\,. \tag{34}$$

In the functional space $\dot{L}^2(\Omega)$ a Poincaré inequality applies (Temam, 1997; Robinson, 2001), and this means that

$$||f||_{L^2} \leq c_0 ||\nabla f||_{L^2} \qquad \forall f \in \dot{L}^2(\Omega)\,, \tag{35}$$

where $c_0 = c_0(\Omega)$ is a positive constant depending exclusively on the geometry of the mixing space Ω but not on f. The Poincaré inequality is a useful tool for proving functional-theoretical properties of the solutions of the ADE.

A first consequence of Eq. (35) is that an equivalent norm for $\dot{H}^1(\Omega)$ is given by

$$||f||_{H^1} = ||\nabla f||_{L^2}\,, \tag{36}$$

and this norm is adopted henceforth.

A solution of Eq. (7), starting from a zero-mean initial condition can be viewed as an element of $\dot{H}^1(\Omega)$ for any $t > 0$. Theorems of existence and uniqueness for the solution of the ADE can be found elsewhere (Temam, 1997; Sell and You, 2002), under mild hypotheses on the regularity of $\mathbf{v}(\mathbf{x},t)$, such as piecewise continuity with respect to $\mathbf{x}$.

For autonomous flows $\mathbf{v} = \mathbf{v}(\mathbf{x})$, the formal solution of Eq. (7), starting from the initial condition $\phi(\mathbf{x},0) = \phi_0(\mathbf{x})$ can be expressed in the operatorial form

$$\phi(\mathbf{x},t) = \exp(\mathcal{L}t)\,\phi_0(\mathbf{x})\,. \tag{37}$$

For non-autonomous flows, the formal solution of Eq (7) attains the form

$$\phi(\mathbf{x},t) = \exp(\mathcal{W}(t))\phi_0(\mathbf{x})\,. \tag{38}$$

where the operator $\mathcal{W}(t)$ can be expressed via a Magnus expansion (Kowalski, 1994; Iserles et al., 1999).

In the time-periodic case, $\mathbf{v}(\mathbf{x}, t+T) = \mathbf{v}(\mathbf{x},t)$ with $T > 0$, one can define an autonomous operator $\mathcal{P}$, referred to as the Poincaré (or Floquet) operator associated with Eq. (7) by considering the evolution of the concentration field sampled at periodic instant of time with the period of the flow.

Therefore, $\mathcal{P}$ maps the function $\phi(\mathbf{x}, nT)$, $n = 0, 1, \ldots$, into the function $\phi(\mathbf{x}, (n+1)T)$, solution of Eq. (7) after one period of motion. By making use of Eq. (38), the Poincaré operator can be formally expressed as

$$\mathcal{P} = \exp(\mathcal{W}(T)) \,. \tag{39}$$

A particular case of time-periodic flows is given by *blinking steady flows* (also referred to as piecewise steady time-periodic flows), for which the time-periodic flow protocol is obtained by blinking alternately two steady flows $\mathbf{v}_1(\mathbf{x})$ and $\mathbf{v}_2(\mathbf{x})$, each of which for time intervals T_1 and T_2, respectively, where $T_1 + T_2 = T$.

For piecewise steady time-periodic flows, the operator $\mathcal{L}$ Eq. (29) reduces to two distinct autonomous operators

$$\mathcal{L}_i = -\mathbf{v}_i(\mathbf{x}) \cdot \nabla + \varepsilon \nabla^2 \,, \qquad i = 1, 2 \,, \tag{40}$$

which act for time intervals T_1 and T_2, respectively. For this class of flows, the Poincaré operator can be expressed as

$$\mathcal{P}[\phi] = \mathrm{e}^{\mathcal{L}_2 T_2} \circ \mathrm{e}^{\mathcal{L}_1 T_1} \, \phi \,. \tag{41}$$

where "$\circ$" indicates operator composition.

4.2 Norm evolution

Many useful properties of the solutions of Eq. (7) can be inferred from the analysis of the time evolution of the norms of the scalar field ϕ.

Consider a real solution ϕ of Eq. (7). Multiplying Eq. (7) by ϕ and integrating over Ω, it follows that

$$\frac{d||\phi||^2_{L^2}}{dt} = -2\varepsilon ||\nabla\phi||^2_{L^2} \,. \tag{42}$$

Eq. (42) states the dissipative nature of the ADE for any $\varepsilon > 0$, since the L^2-norm of any solution of Eq. (7) with vanishing initial mean (i.e. belonging to $\dot{L}^2(\Omega)$) is a strictly decreasing function of time. The strict decreasing of $||\phi||^2_{L^2}$ stems from the fact that any function $\phi \in \dot{L}^2(\Omega)$, different from the zero function, possesses a non vanishing $||\nabla\phi||_{L^2}$, since constant functions do not belong to $\dot{L}^2(\Omega)$.

Eq. (42) indicates that the decreasing of the L^2-norm of the solutions of the ADE is controlled by the L^2-norm of its gradient. For this reason, it is useful to express the evolution equation for $||\nabla\phi||^2_{L^2}$. By putting $\mathbf{g} = \nabla\phi$, it follows that

$$\frac{d||\mathbf{g}||^2_{L^2}}{dt} = -2 \int_\Omega (\nabla \mathbf{v}) : \mathbf{g}\,\mathbf{g} \, d\mathbf{x} - 2\varepsilon \sum_{i=1}^{d} \int_\Omega \nabla g_i \cdot \nabla g_i \, d\mathbf{x} \,, \tag{43}$$

where g_i are the entries of $\mathbf{g}$, and the diadic term at the rhs of Eq. (43) has the meaning

$$\nabla \mathbf{v} : \mathbf{g}\,\mathbf{g} = \sum_{i,j=1}^{d} \frac{\partial v_i}{\partial x_j}\, g_i\, g_j \ . \tag{44}$$

Eq. (43) indicates that the evolution of the gradient norm is the outcome of two conflicting actions: (i) the stretching effects due of the velocity field (first term at the rhs of Eq. (43)), which tends to increase the gradient norm, and (ii) the smoothing action of diffusion (second term at the rhs of Eq. (44)), which opposes to it and relaxes the gradient.

The proof of Eqs. (42) and (43) is just a matter of simple manipulations based on the divergence theorem. In order to obtain Eq. (42), multiply Eq. (7) by ϕ and integrate over the flow domain Ω:

$$\int_\Omega \phi \frac{\partial \phi}{\partial t}\, d\mathbf{x} = -\int_\Omega \phi\, \mathbf{v}\cdot\nabla\phi\, d\mathbf{x} \ + \varepsilon \int_\Omega \phi \nabla^2 \phi\, d\mathbf{x}$$

By enforcing the zero-flux boundary conditions, the incompressibility of $\mathbf{v}$, and the vanishing of the normal component of the velocity at $\partial\Omega$, the three terms appearing in the above equation can be expressed as:

$$\begin{aligned}
\int_\Omega \phi \frac{\partial \phi}{\partial t}\, d\mathbf{x} &= \frac{1}{2}\int_\Omega \frac{\partial \phi^2}{\partial t}\, d\mathbf{x} = \frac{1}{2}\frac{d}{dt}\int_\Omega \phi^2\, d\mathbf{x} \\
\int_\Omega \phi\, \mathbf{v}\cdot\nabla\phi\, d\mathbf{x} &= \int_\Omega \mathbf{v}\cdot(\phi\nabla\phi)\, d\mathbf{x} = \frac{1}{2}\int_\Omega \mathbf{v}\cdot\nabla\phi^2\, d\mathbf{x} \\
&= \frac{1}{2}\int_\Omega \nabla\cdot(\mathbf{v}\phi^2)\, d\mathbf{x} = \frac{1}{2}\int_{\partial\Omega} \phi^2 \mathbf{v}\cdot\mathbf{n}\, d\sigma = 0 \\
\int_\Omega \phi\nabla^2\phi\, d\mathbf{x} &= \int_\Omega \nabla\cdot(\phi\nabla\phi)\, d\mathbf{x} - \int_\Omega \nabla\phi\cdot\nabla\phi\, d\mathbf{x} \\
&= \int_{\partial\Omega} \phi\nabla\phi\cdot\mathbf{n}\, d\mathbf{x} - \int_\Omega \nabla\phi\cdot\nabla\phi\, d\mathbf{x} = -\int_\Omega \nabla\phi\cdot\nabla\phi\, d\mathbf{x}\,.
\end{aligned}$$

In a similar way, Eq. (44) can be proved (hint: take the gradient of lhs and rhs of Eq. (7), multiply by $\nabla\phi$, and integrate over the mixing space Ω).

4.3 Some functional observations

Before addressing the properties of the solutions of the ADE, some elementary observations on linear operators in infinite-dimensional spaces may be useful. This is because new phenomena arise in infinite-dimensional spaces that find no counterpart in the finite-dimensional case. For a thorough analysis of the content of this Section, see e.g. (Reed and Simon, 1980; Kato, 1980), or any reference textbook in functional analysis.

Let $\mathcal{C}$ be an infinite-dimensional vector space (e.g. $\mathcal{C} = \dot{L}^2(\Omega)$) and $A : \mathcal{C} \to \mathcal{C}$ a linear operator acting on it. Let us assume that $\mathcal{C}$ is a Hilbert space equipped with the inner product $(\cdot, \cdot)$, the norm $||\cdot||$ and the distance function $d(\cdot, \cdot)$, inherited by the definition of the inner product. Let us further assume that $\mathcal{C}$ is *separable*, i.e. it admits a countable basis.

A linear operator $A : \mathcal{C} \to \mathcal{C}$ is *bounded* if for any $y \in \mathcal{C}$, there exists a constant $k > 0$ such that $||A[y]|| \leq k||y||$. By definition, linear bounded operators are also continuous.

A linear operator $A : \mathcal{C} \to \mathcal{C}$ is *compact* if it maps bounded sets of $\mathcal{C}$ into *precompact* sets. The notion of compactness is crucial, and needs a further discussion, since it is one of the "tricky" features that differentiate infinite-dimensional spaces from finite-dimensional ones.

Let us recall the definition of compact and precompact sets. Given a complete metric space $\mathcal{C}$, a subset $\mathcal{B} \subseteq \mathcal{C}$ is compact if for any sequence of elements $\{y_h\}_{h=1}^{\infty}$ belonging to $\mathcal{B}$, it is always possible to extract a convergent subsequence. A subset $\mathcal{B} \subseteq \mathcal{C}$ is precompact if its closure is compact.

In finite-dimensional spaces, any bounded set is also precompact (and this is the essence of the Weierstrass theorem in $\mathbb{R}^d$). This property does not hold in infinite-dimensional spaces. For example, consider the functional space $L^2_{per}([0,1])$ of square summable functions of unit period, and the bounded set $\mathcal{B} = \{\ \phi \mid ||\phi||_{L^2} = 1\ \}$, i.e. the unit ball in $L^2_{per}([0,1])$. It is straightforward to observe that $\mathcal{B}$ is not compact, simply by considering that from the sequence of functions $\{y_h = \mathrm{e}^{i2\pi hx}\}_{h=1}^{\infty} \subset \mathcal{B}$ it is not possible to extract any converging subsequence. In this case, the infinite dimensionality of the space provides an escaping way for the elements y_h of this sequence.

Compact sets in a infinite-dimensional Hilbert spaces can be viewed as *almost finite-dimensional sets*. More precisely, let Π_n be a projection operator, mapping $\mathcal{C}$ onto a n-dimensional subspace E_n, spanned by the basis $\{e_1, \ldots, e_n\}$. Let $\Pi_n^c = Id - \Pi_n$, the complementary projection operator in $\mathcal{C}$, where Id is the identity operator. For any $y \in \mathcal{C}$, $y = \Pi_n[y] + \Pi_n^c[y]$, and moreover $||y||^2 = ||\Pi_n[y]||^2 + ||\Pi_n^c[y]||^2$. The following proposition holds: *a necessary and sufficient condition ensuring that a subset $\mathcal{B} \subset \mathcal{C}$ is compact is that $\mathcal{B}$ is bounded, and for any $\eta > 0$, there exists a finite integer $n = n(\eta)$, such that $||\Pi_n^c[y]|| \leq \eta$ for any $y \in \mathcal{B}$.*

To make the story short, depending on the nature of the functional space considered, bounded sets may or may not be precompact. For future developments, it is important to register that bounded sets of $L^2(\Omega)$ are not precompact, while bounded sets in $H^1(\Omega)$ are precompact. Observe that for a bounded set in $H^1(\Omega)$, both the norm an the gradient norm of its elements f should be bounded.

The interest in bounded and compact operators lies in their spectral properties.

Spectral properties of linear operators in infinite-dimensional spaces are not as simple as their finite-dimensional counterparts. For a linear operator $\mathcal{A}$ in a n-dimensional vector space E_n, the spectral characterization is exhaustive: any finite-dimensional linear operator possesses exactly n eigenvalues (counted with their algebraic multiplicities), and the system of the generalized eigenvectors of $\mathcal{A}$ is a basis for E_n.

The spectral theory of operators is fairly more complicated in infinite-dimensional spaces. Boundedness of the operator tells us very little about its spectral properties, and it is possible to exhibit simple examples of bounded operators which does not possess any eigenvalue at all. A typical example is the Frobenius-Perron operator associated with a mixing transformation, defined in the space of square summable functions possessing zero mean. Conversely, it is possible to give elementary examples of Frobenius-Perron operators associated with autonomous flows, which possess a continuous spectrum of eigenfunctions.

More definite are the properties of linear compact operators, which are specified by the Theorem by Riesz and Schauder. *The eigenvalue spectrum of a compact operator is discrete (i.e. finite or countable) and does not possess any accumulation point except $\lambda = 0$. Moreover, any nonzero eigenvalue possesses finite multiplicity (which means that the corresponding space of eigenfunctions is finite-dimensional).*

In the next Section, we show that the evolution operator associated with an ADE with $\varepsilon > 0$ is compact (under mild assumptions on the velocity field). This property can be proved by showing that the H^1-norm of the solutions is bounded. The technique for proving this property makes use of two useful tools of applied functional analysis: the Young inequality, and the uniform Grönwall lemma (Temam, 1997; Robinson, 2001).

The Young inequality is a classical inequality for real numbers, stating that for any a, b, $\eta > 0$ and for any p, q, such that $1 < p < \infty$ and $1/p + 1/q = 1$, it results that

$$ab \leq \frac{\eta}{p} a^p + \frac{\eta^{-q/p}}{q} b^q \,. \tag{45}$$

The uniform Grönwall Lemma, derived by Foias and Prodi (1967) can be stated as follows. *Let $g(t)$, $h(t)$, $y(t)$, be three positive localy integrable functions on (t_0, ∞), such that $dy(t)/dt$ is locally integrable on (t_0, ∞), and which satisfy:*

$$\frac{dy(t)}{dt} \leq g(t)\, y(t) + h(t)\,, \qquad \textit{for } t > t_0 \tag{46}$$

and

$$\int_t^{t+\tau} g(\sigma)\, d\sigma \leq A_1\,, \qquad \int_t^{t+\tau} h(\sigma)\, d\sigma \leq A_2\,, \qquad \int_t^{t+\tau} y(\sigma)\, d\sigma \leq A_3\,, \tag{47}$$

for $t > t_0$, where A_1, A_2, A_3, τ are positive constants. Then:

$$y(t+\tau) \leq \left(\frac{A_3}{\tau} + A_2\right) \exp(A_1) \qquad t > t_o\,. \tag{48}$$

It is possible to derive a slight modification of this Lemma. Let us suppose that

$$\int_t^{t+\tau} g(\sigma)\, d\sigma \leq A_1\,, \qquad h(t) = 0\,, \qquad \int_t^{t+\tau} y(\sigma)\, d\sigma \leq m(t)\,, \tag{49}$$

where $m(t) \geq 0$ and $\tau > 0$. Then, for $t > t_0$, the following inequality holds:

$$y(t+\tau) \leq \frac{m(t)}{\tau} \exp(A_1)\,. \tag{50}$$

4.4 Compactness and exponential decay

This Section addresses the compactness of the evolution operator associated with the ADE, and the exponential bounds for the solutions. By the term *evolution operator* associated with Eq. (7), we mean the linear operator $\mathcal{T}(t) : L^2(\Omega) \to L^2(\Omega)$, such that the solution $\phi(\mathbf{x}, t)$ of Eq. (7) in a bounded and closed domain at time $t > 0$ can be expressed as $\phi(\mathbf{x}, t) = \mathcal{T}(t)[\phi_0(\mathbf{x})]$. Since initial conditions $\phi_0(\mathbf{x})$ possessing zero mean are considered below, the solution $\phi(\mathbf{x}, t)$ of Eq. (7) belongs to $\dot{L}^2(\Omega)$ for any $t > 0$.

Throughout this Section, we assume that the velocity field is incompressible and uniformly bounded, i.e. there exists a positive constant V_m such that

$$|\mathbf{v}(\mathbf{x}, t)|^2 \leq V_m^2\,. \tag{51}$$

This assumption implies that for any t, $\mathbf{v} \in L^2(\Omega)$.

Below, the statements of the main results are reported. The proofs of these propositions can be found in Appendix A.

Theorem 4.1. *The L^2-norm of the solution of Eq. (7) satisfies the inequality*

$$||\phi||_{L^2}(t) \leq ||\phi||_{L^2}(0) \exp(-t\varepsilon/c_0^2)\,. \tag{52}$$

This theorem provides an upper bound for the exponential decay of the solutions, which corresponds to the diffusional exponential decay. The exponent of this decay is inversely proportional to the Peclet number (recall that $\varepsilon = 1/Pe$), and depends on the Poincaré constant c_0 of the mixing domain Ω.

Next theorem expresses a stronger property of the solutions, namely that the H^1-norm of the solution of Eq. (7) is eventually bounded.

Theorem 4.2. *If $\varepsilon > 0$ then,*

$$||\phi||^2_{H^1}(t) = ||\nabla\phi||^2_{L^2}(t) \leq C(\varepsilon, ||\phi||_{L^2}(0), ||\nabla\phi||_{L^2}(0)), \tag{53}$$

where the upper bound $C(\varepsilon, ||\phi||_{L^2}(0), ||\nabla\phi||_{L^2}(0)) > 0$ depends on ε, $||\phi||_{L^2}(0)$, and $||\nabla\phi||_{L^2}(0)$. Moreover, for $t > 2\varepsilon/V_m^2$, independently of $||\nabla\phi(0)||_{L^2}$, the following inequality holds

$$||\nabla\phi||^2_{L^2}(t) \leq \frac{eV_m^2}{4\varepsilon^2} \, . \tag{54}$$

In Eq. (54), $e = 2.718281\ldots$ is the Napier number. The main implication of Eq. (53) is the compactness of the evolution operator associated with the ADE Eq. (7), since it maps bounded sets of $\dot{L}^2_0(\Omega)$ into precompact sets of $\dot{L}^2_0(\Omega)$. The latter property stems from the fact that bounded sets of $\dot{H}^1_0(\Omega)$ are precompact.

While the existence of an upper exponential bound for the decay of the L^2-norm of the solutions of Eq. (7) (Theorem 4.1), follows straightforwardly as a consequence of the Poincaré inequality, the assessment of a lower exponential bound for suitable initial conditions, requires further elaborations.

Theorem 4.3. *The function*

$$Q(t) = ||\nabla\phi||^2_{L^2}(t) + \frac{V_m^2}{4\varepsilon^2}||\phi||^2_{L^2}(t) \tag{55}$$

is non-increasing. Moreover,

$$||\nabla\phi||^2_{L^2}(t) \to 0 \, , \quad \textit{for } t \to \infty. \tag{56}$$

In order to prove some strict inequality for the asymptotic behavior of $||\phi||^2_{L^2}(t)$, consider the quantity $||\nabla\phi||^2_{L^2}(t)/||\phi||^2_{L^2}(t)$, since

$$\frac{d||\phi||^2_{L^2}}{dt} = -2\varepsilon \left(\frac{||\nabla\phi||^2_{L^2}(t)}{||\phi||^2_{L^2}(t)} \right) ||\phi||^2_{L^2} \, . \tag{57}$$

Eq. (123) (in Appendix A) shows that the quantity $||\nabla\phi||^2_{L^2}(t+\tau)/||\phi||^2_{L^2}(t)$ is bounded, but this is not sufficient for inferring an exponential decay for $||\phi||^2_{L^2}(t)$, since $\tau > 0$.

This problem can be circumvented in the following way. Consider an initial condition $\phi(\mathbf{x}, 0) \in \dot{H}^1(\Omega)$ (i.e. $||\nabla\phi||^2_{L^2}(0) < \infty$), and let

$$||\phi||^2_{L^2}(t) = ||\phi||^2_{L^2}(0) \exp(-2\nu(t)) \,, \tag{58}$$

where

$$\nu(t) = \varepsilon \int_0^t \frac{||\nabla\phi||^2_{L^2}(\theta)}{||\phi||^2_{L^2}(\theta)} \, d\theta \,. \tag{59}$$

Owing to the Poincaré inequality, the function $\nu(t)$ is monotonically increasing. From Eq. (42), it follows that

$$||\nabla\phi||^2_{L^2}(t) = \frac{2||\phi||^2_{L^2}(0)}{Pe} \, \dot{\nu}(t) \exp(-\nu(t)) \,, \tag{60}$$

where $\dot{\nu}(t)$ indicates the time derivative.

We want to show that the function $\nu(t)$ cannot eventually increase faster than a linear function, and consequently that $||\phi||^2_{L^2}(t)$ possesses an *exponential decay.*

Theorem 4.4. *The solutions of the ADE in the presence of uniformly bounded velocity fields possess a lower bound which decays exponentially.*

As consequence of Theorem 4.4, there exists a positive constant K^* such that

$$\lim_{t\to\infty} \frac{\nu(t)}{t} \leq K^* \,, \tag{61}$$

for any (autonomous, time-periodic, aperiodic) flow, the velocity field $\mathbf{v}(\mathbf{x}, t)$ of which is uniformly bounded. This completes the analysis of the properties of the ADE that can be obtained by enforcing elementary functional analysis.

4.5 Spectral theory of ADE and the definition of mixing

In closed and bounded domains, the functional characterization of compact operators can be grounded on spectral (eigenvalue/eigenfunction) analysis (Reed and Simon, 1980). Therefore, it is natural to consider the eigenvalue/eigenfunction spectra of the ADE operator (for autonomous flows) and of the Poincaré operator (for time-periodic flows) as the quantities yielding an exhaustive description of the dynamics of homogenization (mixing).

First, consider autonomous flows. It has been shown by several Authors (Agmon, 1962, 1965; Faierman, 1995) under slightly different assumptions on the velocity field (a safe assumption is to suppose that $\mathbf{v}(\mathbf{x})$ is uniformly bounded), and on the geometry of the mixing space (a safe assumption is to suppose that Ω is connected and possesses a Lipschitz boundary) that the eigenvalue spectrum $\{\lambda_h\}_{h=0}^{\infty}$ of the advection-diffusion operator with $\varepsilon > 0$,

$$\mathcal{L}[\psi] = -\mathbf{v}(\mathbf{x}) \cdot \nabla\psi + \varepsilon\nabla^2\psi = \lambda\psi \,, \tag{62}$$

is countable and that the (generalized) eigenfunctions $\{\psi(\mathbf{x})\}_{h=0}^{\infty}$ form a basis for $L^2(\Omega)$. The eigenvalues λ_h are in general complex numbers (since the ADE operator is not Hermitian), and possess non positive real part.

The eigenvalues $\lambda_h = \lambda_h^R + i\lambda_h^I$ can be ordered with respect to the real part, $\lambda_h^R \geq \lambda_{h+1}^R$. Due to mass conservation, there exists the eigenvalue $\lambda_0 = 0$, associated with the constant eigenfunction $\phi_0(\mathbf{x}) = 1$, while all the other eigenvalues possess negative real part $\lambda_h^R < 0$, $h = 1, 2, \ldots$.

The spectral characterization is slighly more complex for time-periodic velocity fields, and involves the eigenvalues/eigenfunctions of the Poincaré operator $\mathcal{P}$. Albeit the completeness of the eigenfunctions has not been proved, strong results have been obtained by Liu and Haller (2004b), who showed that under mild hypotheses (such as the uniform boundedness of the velocity field), the ADE possesses an exponentially attracting finite-dimensional inertial manifold (Temam, 1997), and, restricted to it, the eigenfunctions of the Poincaré operator form a basis for this manifold. This result is closely connected with the compactness of the evolution operator associated with the ADE (Theorem 4.1), and with the exponential lower-bound for the solutions of the ADE (Theorem 4.4).

However, it is reasonable to conjecture that for typical model flows and for physically realizable velocity fields, the eigenvalue spectrum of $\mathcal{P}$ is countable, and the eigenfunctions form a basis for $L^2(\Omega)$.

In the case of aperiodic velocity fields, the spectral characterization looses its meaning. However, Theorems 4.1 and 4.4 indicate that the solutions of the ADE are always upper- and lower-bounded by an exponential decay, also in the presence of aperiodic flows for which the velocity is uniformly bounded.

The completeness of the eigenfunctions provides an exhaustive characterization of homogenization dynamics. For autonomous flows, any solution $\phi(\mathbf{x}, t) \in \dot{L}^2(\Omega)$ can be expressed as

$$\phi(\mathbf{x}, t) = \sum_{h=1}^{\infty} \phi_{h,0} \mathrm{e}^{\lambda_h t} \psi_h(\mathbf{x}) \,, \tag{63}$$

where $\psi_h(\mathbf{x})$ are the complex-valued eigenfunctions, and the coefficients $\phi_{h,0}$ characterize the initial condition.

For generic initial conditions, the norm decay is controlled by the non-vanishing eigenvalue λ_1 possessing the largest real part,

$$C_1 \mathrm{e}^{\lambda_1^R t} \leq ||\phi||_{L^2}(t) \leq C_2 \mathrm{e}^{\lambda_1^R t} \qquad t \to \infty \,, \tag{64}$$

where $0 < C_1 < C_2$. The real part of λ_1 with reversed sign is referred to as the dominant decay rate $\Lambda = -\lambda_1^R$ of the ADE, and Eq. (64) can be rewritten as a scaling law

$$||\phi||_{L^2}(t) \sim \mathrm{e}^{-\Lambda t} \qquad \text{for large } t \,. \tag{65}$$

The exponent Λ corresponds to the slowest decay rate attainable during the homogenization dynamics.

An analogous approach applies for time-periodic velocity fields. Let $\{\mu_h\}_{h=0}^{\infty}$ be the eigenvalue spectrum of the Poincaré operator. All the eigenvalues possess a modulus smaller than or equal to 1. The eigenvalue spectrum can be ordered in a nonincreasing way with respect to the modulus, i.e. $|\mu_h| \geq |\mu_{h+1}|$. Mass conservation implies that $\mu_0 = 1$ (the associated eigenfunction is $\psi_0(\mathbf{x}) = 1$), while $|\mu_h| < 1$ for $h = 1, 2, \ldots$. Apart from $\mu_0 = 1$, the eigenvalue μ_1 controls the decay rate for generic initial conditions. For time-periodic flows, the dominant decay rate entering Eq. (65) is given by

$$\Lambda = \frac{-\log |\mu_1|}{T} \,, \tag{66}$$

where T is the period of the flow protocol.

The description of the spectral properties for typical model flows is developed in the next Section.

For the time being, it is important to address how the spectral characterization provides the most simple and efficient way to describe homogenization dynamics in bounded closed flows, and how mixing can be defined in these systems.

First of all, the spectral characterization is intimately associated with the practical (engineering) description of mixing, since it readily yields the values of the decay rates controlling the relaxation towards the perfectly mixed state. The structure of the eigenfunctions is equally important, since it provides the spatial structure of the characteristic patterns attained by the scalar field $\phi(\mathbf{x}, t)$ during the relaxation process towards perfectly mixed conditions (the partially mixed structures).

For any finite value of the Peclet number, the optimal time-periodic flow protocol corresponds to a velocity field yielding the largest value of the

dominant rate exponent Eq. (66). This condition, is a kind of normative (generic) formulation, as it does not account for the properties of the initial condition $\phi_0(\mathbf{x})$, i.e. the fact that the optimal flow protocol up to time t should be tuned-up in order to minimize the mixing time *starting from the given initial condition* $\phi_0(\mathbf{x})$. The effect of the initial condition can be easily accounted for within the functional characterization of mixing, by observing from Eqs. (58)-(59) that the instantaneous homogenization decay rate $\Gamma(t,\varepsilon)$ at time t,

$$||\phi||_{L^2}(t) = ||\phi||_{L^2}(0)\mathrm{e}^{-t\,\Gamma(t;\varepsilon)}\,, \tag{67}$$

is given by the average over the mixing history, i.e. over the interval $[0,t)$, of the ratio of the square H^1-norm to the square L^2-norm of ϕ times ε

$$\Gamma(t;\varepsilon) = \frac{1}{t}\int_0^t \frac{\varepsilon\,||\nabla\phi||^2_{L^2}(\theta)}{||\phi||^2_{L^2}(\theta)}\,d\theta\,. \tag{68}$$

The quantity $\Gamma(t,\varepsilon)$ provides for fixed t the most natural and physically meaningful objective function to be used for flow-protocol optimization in bounded and closed domains (in open domains the situation is different, see Section 7). This optimization criterion can be roughly expressed as: *optimal mixing performances correspond to flow protocols which maximize the time-average of the L^2-norm of the normalized gradient.*

It is useful to observe that the concept of *optimal mixing conditions* has a dichotomic meaning, and a distinction should be drawn between *perfectly mixed conditions* as a status of a fluid continuum, and *good mixedness* as a dynamic process. In a static perspective, perfectly mixed conditions correspond to the occurrence of a constant concentration field throughout the mixing space. Once this condition is achieved in a closed system, neither diffusion nor advection can perturb or modify it. Although perfectly mixed conditions are the ultimate goal of any mixing equipment, the characterization of these conditions is trivial, and moreover it is uninteresting in mixing theory, which is focused on the description and optimization of the evolution of a fluid mixture as a dynamic process towards the best attainable mixedness. Good mixedness corresponds to the situation for which the relaxation towards perfectly mixed conditions proceeeds at a sufficiently fast rate. In fact, optimization of mixing in a closed domain implies the finding of the stirring protocol yielding the minimum possible time to reach the prescribed homogenization conditions, as stated above.

It is possible to frame these observations on mixedness with the spectral formulation (Mathew et al., 2005). Since dynamic mixing conditions are controlled by the norm of the gradient of ϕ, it is natural to express the

functional properties of $\phi(\mathbf{x},t)$ with respect to a functional basis which is harmonically ordered.

Let us define an *ordered H^1-basis*, as an orthonormal set of functions $\{f_k(\mathbf{x})\}_{k=1}^{\infty}$,

$$||f_k||_{L^2} = 1\,, \qquad (f_k, f_h)_{L^2} = \delta_{k,h} \tag{69}$$

which is a basis of $\dot{L}(\Omega)$, and such that the sequence of their H^1-norms is nondecreasing, and diverging to infinity

$$||\nabla f_{k+1}||_{L^2} \geq ||f_k||_{L^2} \qquad \lim_{k\to\infty} ||\nabla f_k||_{L^2} \to \infty\,. \tag{70}$$

A H^1-ordered basis can be referred to as a *harmonic basis*.

The typical harmonic basis in a closed domain Ω is given by the eigensystem of the Laplacian operator in Ω, equipped with the Neumann boundary conditions on $\partial\Omega$. Let $\{\ell_k(\mathbf{x})\}_{k=1}^{\infty}$ be such eigensystem. The eigenfunction $\ell_0(\mathbf{x}) = 1$ is not considered since it does not belong to $\dot{L}^2(\Omega)$.

The system $\{\ell_k(\mathbf{x})\}_{k=1}^{\infty}$ forms a basis for $\dot{L}^2(\Omega)$, and the eigenvalues $-\nu_k$, $\nabla^2\ell_k(\mathbf{x}) = -\nu_k\ell_k(\mathbf{x})$, are negative and form a sequence of real numbers diverging to $-\infty$. Moreover, the eigenvalues $-\nu_k$ are related to the structure of the corresponding eigenfunction by the equation

$$\nu_k = \frac{||\nabla\ell_k||_{L^2}^2}{||\ell_k||_{L^2}^2}\,. \tag{71}$$

Essentially, the concept of harmonic basis provides a way to define an ordering within the spatial harmonics, so that low values of k correspond to low-frequency spatial harmonics, and large k-values to high frequency spatial components. The integer k plays the role of a wavenumber. Therefore, the distinction between static perfectly mixed conditions and dynamically perfect mixedness can be viewed in a wavenumber graph as the difference between the point $k = 0$ at the origin of this graph and the point at infinity of the wavenumber-axis (see Fig. 4).

Given a harmonic basis, the concentration field $\phi(\mathbf{x},t) \in \dot{L}^2(\Omega)$ can be expressed with respect to this basis as

$$\phi(\mathbf{x},t) = \sum_{k=1}^{\infty} \phi_k(t)\,\ell_k(\mathbf{x})\,, \qquad \phi_k(t) = (\phi,\ell_k)_{L^2}\,. \tag{72}$$

Spectral measures[5] can be defined starting from the decomposition Eq.

[5]This analysis of spectral measures is an elaboration of the spectral theory developed by Mathew et al. (2005).

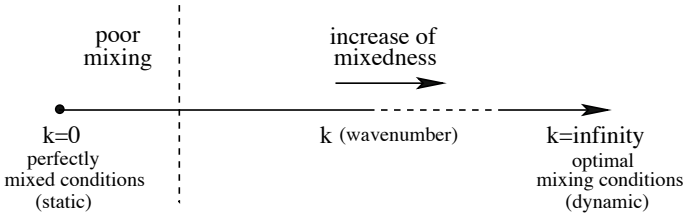

Figure 4. Difference between static and dynamic perfectly mixed conditions on the wavenumber axis.

(72). For example,

$$\frac{||\nabla\phi||^2_{L^2}(t)}{||\phi||^2_{L^2}(t)} = \frac{\sum_{k=1}^{\infty}\nu_k|\phi_k(t)|^2}{\sum_{k=1}^{\infty}|\phi_k(t)|^2}\,. \tag{73}$$

The spectral representation provides a formal way to define powers of a positive operator such as $-\nabla^2$ (Robinson, 2001). For any real α, the action of the α-th power of $-\nabla^2$ on $\phi(\mathbf{x},t)$ can be defined as:

$$(-\nabla^2)^{\alpha}\phi(\mathbf{x},t) = \sum_{k=1}^{\infty}\nu_k^{\alpha}\,(\phi,\ell_k)_{L^2}\,\ell_k(\mathbf{x})\,, \tag{74}$$

and consequently the following family of spectral measures $\sigma_\alpha(\phi)$ can be defined for ϕ:

$$\sigma_\alpha(\phi) = ((-\nabla^2)^{\alpha}\phi,\phi)_{L^2} = ||(-\nabla^2)^{\alpha/2}\phi||^2_{L^2} = \sum_{k=1}^{\infty}\nu_k^{\alpha}|\phi_k|^2\,. \tag{75}$$

For example, the mixnorm introduced by Mathew et al. (2005) on S^1 (the unit circumference) is equivalent for $\phi\in\dot{L}^2(S^1)$ to the square root of $\sigma_\alpha(\phi)$ with $\alpha=-1/2$.

In principle, any spectral measure, such as $\sigma_\alpha(\phi)$, grounded on the expansion of the scalar field ϕ with respect to a harmonic basis, is a useful measure for the degree of mixedness, although specific values of α may be more significant (e.g. $\alpha=1$ or $\alpha=-1/2$), for highlighting the dynamic properties of homogenization. It is advisable to consider normalized spectral measures $\widehat{\sigma}_\alpha(\phi)$, obtained by rescaling Eq. (75) by the square of the L^2-norm:

$$\widehat{\sigma}_\alpha(\phi) = \frac{\sigma_\alpha(\phi)}{||\phi||^2_{L^2}}\,. \tag{76}$$

To conclude, the spectral expansion provides also a convenient way to simulate the ADE. By expanding $\phi(\mathbf{x}, t)$ with respect to the eigensystem of the Laplacian operator, and by enforcing the orthonormality of the basis $\{\ell_k(\mathbf{x})\}$, the evolution equation for the spectral coefficients $\phi_k(t)$ reads:

$$\frac{d\phi_k(t)}{dt} = \sum_h A_{k,h}(t)\phi_h(t) - \varepsilon\nu_k\phi_k(t)\,, \tag{77}$$

where

$$A_{k,h}(t) = -\int_\Omega \ell_k^*(\mathbf{x})\,\mathbf{v}(\mathbf{x}, t)\cdot\nabla\ell_h(\mathbf{x})\,d\mathbf{x}\,. \tag{78}$$

Eqs. (77)-(78) are the classical expressions for the Galerkin expansion of the ADE Eq. (7) with respect to the eigensystem of the Laplacian operator, that can be fruitfully applied in order to simulate numerically the outcome of a homogenization experiment.

It is useful to point out that the (spectral) Galerkin simulation of the ADE is completely divorced from the spectral analysis of homogenization described above. More precisely, the spectral characterization via the spectral measures $\sigma_\alpha(\phi)$ can be applied to any flow system for which the numerical simulations of the corresponding ADE have been performed by using any of the classical numerical tools of computational fluid dynamics (finite differences, finite volumes, finite elements). This means that spectral analysis can be applied also to complex geometries of the mixing domain Ω, for which the Galerkin expansion is not the optimal way to solve numerically the ADE.

By truncating the number of spectral coefficient up to a finite value N, and by defining a "vector of coefficients" $\mathbf{c}(t) = (\phi_1(t), \ldots, \phi_N(t))^T$, Eq. (77) can be expressed in matrix form as

$$\frac{d\mathbf{c}}{dt} = \mathbf{A}\,\mathbf{c} - \varepsilon\mathbf{D}\mathbf{c}\,, \tag{79}$$

where $\mathbf{D} = \mathrm{diag}(\nu_1, \ldots \nu_N)$ is the diagional matrix accounting from diffusion. The truncation order N should be sufficiently large to ensure numerical accuracy. In point of fact, the compactness of the evolution operator for the ADE ensures that a finite truncation can be arbitrarily accurate for N sufficiently large. In practice, the trade-off for N between accuracy and computational efficiency depends on ε, i.e. on the Peclet number. A save "rule-of-thumb" is the higher Pe, the larger should be the number of modes considered.

For autonomous flows, Eq. (79) is a linear system of ODE with constant coefficients, and the evolution operator can be formally expressed as the

exponential of the coefficient matrix:

$$\mathbf{c}(t) = \mathrm{e}^{(\mathbf{A}-\varepsilon\mathbf{D})\,t}\mathbf{c}(0)\,. \tag{80}$$

For time-periodic blinking flows, a truncated approximation of the Poincaré operator reads:

$$\mathcal{P}(T) = \mathrm{e}^{(\mathbf{A}_2-\varepsilon\mathbf{D})\,T_2}\,\mathrm{e}^{(\mathbf{A}_1-\varepsilon\mathbf{D})\,T_1} \tag{81}$$

i.e. the truncated Poincaré operator is the matrix composition of the two operators Eq. (80) associated with the two steady blinking flows acting over the time spans T_1 and T_2, respectively.

5 Spectral properties of ADE equation in closed flows

In this Section some results in the scaling theory of ADE operators are described (Adrover et al., 2001; Cerbelli et al., 2003, 2004; Giona et al., 2004a; Toussaint et al., 1995, 2000). Specifically, the case of parallel flow is considered, leading to the concept of universal scaling (Giona et al., 2004b). The implications of this property in connection with physically realizable flows is also discussed. Numerical simulations are presented for the spectral properties of the ADE in chaotic flows by considering the Sine-Flow (TPSP) as a prototype flow system (see Appendix B).

5.1 Universality

Consider the ADE for the Autonomomous Sine-Flow (ASF). For ASF, the advection-diffusion operator becomes

$$\mathcal{L}[\phi] = -\sin(2\pi x)\,\frac{\partial\phi}{\partial y} + \varepsilon\left(\frac{\partial^2\phi}{\partial x^2} + \frac{\partial^2\phi}{\partial y^2}\right), \tag{82}$$

equipped with periodic boundary conditions on the edges of the unit square domain.

The salient spectral feature of the Sine Flow is the occurrence of two spectral branches (Cerbelli et al., 2004; Giona et al., 2004a): (i) a diffusive branch, the eigenvalues $\{\lambda_n\}$ of which are real and scale linearly with ε, $\lambda_{n,dif} \sim \varepsilon$, and (ii) a convective branch, the eigenvalues of which are complex and possess a real part which scales as $\lambda^R_{n,con} \sim \sqrt{\varepsilon}$ (Fig. 5). The latter branch possesses qualitatively the same scaling behavior observed in unbounded cellular flows (Fannjang and Papanicolau, 1994), and referred to as *Convection-Enhanced Diffusion* (CoED).

The occurrence of two different spectral branches, as well as other properties of the advection-diffusion equation, can be explained by introducing

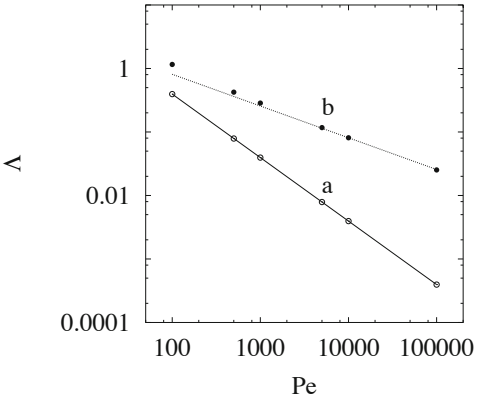

Figure 5. Dominant decay rate Λ vs the Peclet number for the diffusive branch ($\circ$) and the CoED branch ($\bullet$) for the ASF. The solid lines are the scaling laws $\Lambda \sim Pe^{-1}$ (curve a) and $\Lambda \sim Pe^{-1/2}$ (curve b).

the following representation

$$\phi(x, y) = \mathrm{e}^{-i2\pi m y}\psi(x) \;, \tag{83}$$

where m is an integer. By substituting Eq. (83) into Eq. (82), the ADE splits into a countable family of 1-d problems associated with the operators:

$$\mathcal{L}[\psi](x) = \varepsilon\frac{d^2\psi(x)}{dx^2} - 4\pi^2 m^2 \varepsilon\psi(x) + i2\pi m \sin(2\pi x)\psi(x) \;. \tag{84}$$

For $m = 0$, the eigenvalues of $\mathcal{L}$ scale diffusively, while for $m \neq 0$ an effective coupling between advection and diffusion takes place.

Eq. (84) indicates that $\mathcal{L}[\phi]$ is the linear combination of two operators: a diagonal operator $-4\pi m^2\varepsilon\psi$, and the second-order complex-valued operator $\mathcal{A}[\psi]$, defined by:

$$\mathcal{A}[\psi](x) = \varepsilon\frac{d^2\psi(x)}{dx^2} + iV_m(x)\psi(x) \;, \tag{85}$$

where $V_m(x) = 2\pi m \sin(2\pi x)$. The operator $\mathcal{A}$ can be viewed as a Schrödinger operator in the presence of an imaginary potential $iV_m(x)$ defined on the unit circumference.

Consider the case $m = 1$, dropping the subscript m, i.e. defining $V(x) = V_1(x)$. Let $\mu = \mu_R + \mathrm{i}\omega$ be an eigenvalue of $\mathcal{A}$, and ψ the corresponding eigenfunction:

$$\varepsilon \frac{d^2\psi(x)}{dx^2} + iV(x)\psi(x) = \mu\,\psi(x)\ . \tag{86}$$

The real and imaginary part of the eigenvalues is related to the spatial structure of the corresponding eigenfunction ψ by the equations (Giona et al., 2004b):

$$\mu_R = -\frac{\varepsilon\,||D\psi||^2_{L^2}}{||\psi||^2_{L^2}}\ , \qquad \omega = \frac{(V\psi,\psi)_{L^2}}{||\psi||^2_{L^2}}\ . \tag{87}$$

where $D\psi(x) = d\psi(x)/dx$. Since $\psi(x) =$ constant is not an eigenfunction of $\mathcal{A}$ unless $V(x) =$ constant, the latter expression for μ_R indicates that the eigenvalues of $\mathcal{A}$ possess a strictly negative real part that ensures dissipativity.

Another useful expression for the eigenvalues of $\mathcal{A}$ is:

$$\mu \int_0^1 \psi(x)\,dx = i\int_0^1 V(x)\,\psi(x)\,dx\ , \tag{88}$$

which can be expressed as $\mu(\psi,1)_{L^2} = i(\psi,V)_{L^2}$.

In order to characterize the dispersion properties of the ADE, the most important spectral feature of the operator $\mathcal{A}$ is the localization of the eigenfunctions belonging to the complex conjugate arms of the spectrum. Figure 6 (A) depicts the modulus $|\psi(x)|$ of the dominant eigenfunction for several values of the Peclet number, and shows that the eigenfunctions are strongly localized around the critical point $x_c = 1/4$ of the potential. In fact, the dominant eigenfunctions $\psi_\varepsilon(x)$ for different $\varepsilon \to 0$ can be rescaled into a single master curve $g(\xi)$ (see Figure 6 B):

$$\psi_\varepsilon(x) = A^{-1}(\varepsilon)\,g(\xi)|_{\xi=(x-x_c)/\beta(\varepsilon)} \tag{89}$$

where $A(\varepsilon)$ is a normalization constant, and the scaling function $\beta(\varepsilon) > 0$ is proportional to $\varepsilon^{1/4}$.

The localization property of the eigenfunctions for the second-order operator $\mathcal{A}$ in the presence of an imaginary potential is the indicator of a universal scaling characterizing the advection-diffusion equation.

Consider a particular class of periodic potentials defined by the properties that: (i) $V(x)$ possesses a single local maximum at $x = 0$, and a single local minimum at $x = x_m > 0$, such that $V(0) = -V(x_m)$, and

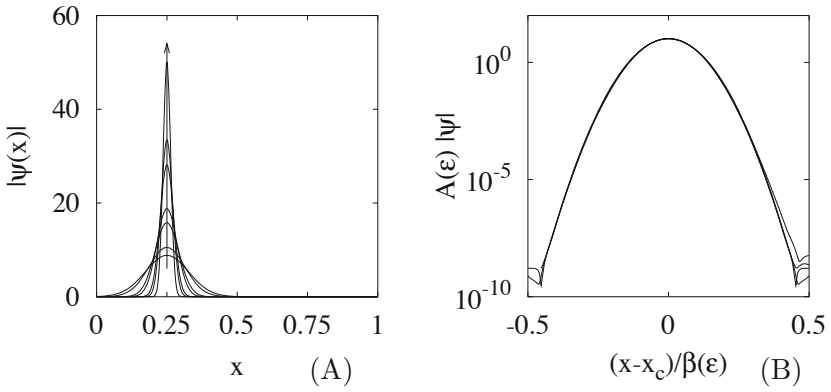

Figure 6. Dominant eigenfunction of the operator $\mathcal{A}$ for different values of the Peclet number ($\varepsilon = Pe^{-1}$). (A) $|\psi(x)|$ vs x. The arrow indicates increasing values of Pe, $Pe = 5\,10^2$, 10^3, $5\,10^3$, 10^4, $5\,10^4, 10^5, 5\,10^5$. (B) Validity of Eq. (89) for rescaling the eigenfunction: $A(\varepsilon)|\psi|$ vs $(x-x_c)/\beta(\varepsilon)$, for different values of $Pe = 10^3$, 10^4, 10^5, 10^6.

that (ii) $V(x)$ near $x = 0$ and $x = x_m$ attains the same nonlinear behavior characterized by the same exponent γ:

$$\begin{aligned} V(x) &= V_M - V_1|x|^\gamma + o(|x|^\gamma) && \text{for } |x| < \eta \\ V(x) &= -V_M + V_1|x - x_m|^\gamma + o(|x - x_m|^\gamma) && \text{for } |x - x_m| < \eta\,, \end{aligned} \tag{90}$$

where $\eta > 0$. For example the sine flow model falls into this class by considering the translation $x' = x - 1/4$, and is a quadratic potential i.e. $\gamma = 2$. In the "pathological" case of a potential $V(x)$ which possesses maxima and minima, in the neighborhood of which $V(x)$ is constant (flat critical points), the value $\gamma = \infty$ can be assigned to these critical points, since $\gamma = \infty$ can be viewed as the limit value for the exponents γ_n $n = 1, 2, ..$ associated with an analytic sequences of potentials $V_n(x)$ converging to $V(x)$.

Since we are considering the behavior of the eigenvalues and eigenfunctions as $\varepsilon \to 0$, we will indicate explicitly their dependence on ε as $\mu = \mu(\varepsilon)$ and $\psi = \psi_\varepsilon(x)$.

Let us assume Eq. (89), i.e. $\psi_\varepsilon(x) = A^{-1}(\varepsilon)\, g(x/\beta(\varepsilon))$. By substituting this expression into Eq. (86), and performing the change of variable $\xi =$

$x/\beta(\varepsilon)$ it follows that:

$$-\mu_R(\varepsilon) = \frac{\varepsilon}{\beta^2(\varepsilon)} \frac{\int_{-1/2\beta(\varepsilon)}^{1/2\beta(\varepsilon)} |Dg(\xi)|^2 \, d\xi}{\int_{-1/2\beta(\varepsilon)}^{1/2\beta(\varepsilon)} |g(\xi)|^2 \, d\xi} \, , \tag{91}$$

where $Dg(\xi) = dg(\xi)/d\xi$. Since the master function $g(\xi)$ is vanishingly small outside a narrow interval centered around $\xi = 0$ and since, for $\varepsilon \to 0$, the integration limits approach $\pm\infty$, Eq. (91) implies

$$-\mu_R(\varepsilon) \simeq C \frac{\varepsilon}{\beta^2(\varepsilon)} \, , \tag{92}$$

where $C = \int_{-\infty}^{\infty} |Dg(\xi)|^2 \, d\xi / \int_{-\infty}^{\infty} |g(\xi)|^2 \, d\xi$.

Let us now consider Eq. (87). By applying the scaling assumption for $\psi_\varepsilon(x)$, and by making the same approximation regarding the integration limits, one obtains:

$$\mu \int_{-\infty}^{\infty} g(\xi) \, d\xi = i \int_{-\infty}^{\infty} V(\beta(\varepsilon)\xi) \, g(\xi) \, d\xi \, . \tag{93}$$

Owing to the fact that $g(\xi)$ is localized around $\xi = 0$, the integral at the r.h.s. of Eq. (93) depends on the local behavior of $V(\beta(\varepsilon)\xi)$ near $\xi = 0$. Therefore, we can apply the local expansion Eq. (90), thus obtaining a linear system for the two unknowns $\mu_R(\varepsilon)$ and $\omega(\varepsilon)$:

$$\begin{bmatrix} A_{0,R} & -A_{0,I} \\ A_{0,I} & A_{0,R} \end{bmatrix} \begin{bmatrix} \mu_R(\varepsilon) \\ \omega(\varepsilon) \end{bmatrix} = \begin{bmatrix} -V_M A_{0,I} + V_1 \beta^\gamma(\varepsilon) A_{1,I} \\ V_M A_{0,R} - V_1 \beta^\gamma(\varepsilon) A_{1,R} \end{bmatrix} \tag{94}$$

where:

$$A_{0,k} = \int_{-\infty}^{\infty} g_k(\xi) \, d\xi \qquad A_{1,k} = \int_{-\infty}^{\infty} |\xi|^\gamma \, g_k(\xi) \, d\xi \qquad k = R, I \tag{95}$$

and $g(\xi) = g_R(\xi) + \mathrm{i} g_I(\xi)$. The solution of the linear system (94) is:

$$-\mu_R(\varepsilon) = \beta^\gamma(\varepsilon) \frac{V_1(A_{0,I}A_{1,R} - A_{0,R}A_{1,I})}{A_{0,R}^2 + A_{0,I}^2} \, , \tag{96}$$

$$-\mu_R(\varepsilon) = \beta^\gamma(\varepsilon) \frac{V_1(A_{0,I}A_{1,R} - A_{0,R}A_{1,I})}{A_{0,R}^2 + A_{0,I}^2} \, . \tag{97}$$

Let us first consider the scaling behavior of the real part of the eigenvalues with ε. By equating Eqs. (92) and (96) it follows that:

$$\beta(\varepsilon) = B\varepsilon^{1/(2+\gamma)} \, , \tag{98}$$

where B is a positive constant, and therefore from Eq. (92) one obtains

$$-\mu_R(\varepsilon) \sim \varepsilon^{\alpha} , \tag{99}$$

where the exponent α is given by

$$\alpha = \frac{\gamma}{2+\gamma} . \tag{100}$$

Eq. (100) is the main result regarding universality, since it expresses the scaling behavior of the dominant eigenvalue as a function of the local behavior near the critical point. In the case of quadratic potentials (as for the sine-flow) $\gamma = 2$, and therefore $\alpha = 1/2$ as observed numerically. The formal analogy with the Feigenbaum universality (Feigenbaum, 1979) for the period-doubling cascade of unimodular maps on the interval is evident, since in both cases the scaling exponents depend exclusively on the local behavior near the critical point.

5.2 Implications for physically realizable flows

The scaling behavior predicted by the universal theory, finds application in the analysis of physically realizable flows, such as the cavity flow (see Appendix B).

For the cavity flow, the structure of the flow domain indicates that the velocity component along the streamlines possesses a quadratic behavior, so that it is reasonable to expect a classical COeD scaling for one of the spectral branches characterized by an exponent $\alpha = 1/2$.

Figure 7 shows the behavior of the dominant scaling exponent Λ for the autonomous cavity flow. The eigenvalue spectrum can be decomposed into several distinct eigenvalue branches, each of which characterized by a different scaling behavior with the Peclet number (for $Pe \to \infty$). For the autonomous cavity flow, two distinct branches can be observed, corresponding respectively to real and complex conjugate eigenvalues, the dominant exponents of which are depicted in Fig. 7 (dotted lines (a) and (b), respectively). At large Pe, the real branch is characterized by a diffusive scaling $\Lambda \sim 1/Pe$, inversely proportional to the Peclet number, while the complex conjugate branch displays a convection-enhanced scaling $\Lambda \sim Pe^{-1/2}$, as predicted by the universal theory.

It is interesting to analyze further the spatial structure of the eigenfunctions of the cavity flow. Figure 8 (A)-(B) shows the spatial structure of the eigenfunction $\gamma_r^{(1)}(\mathbf{x})$ (throughout this Section, all of the eigenfunctions considered are normalized to unit L^2-norm) and of the modulus of the eigenfunction $\gamma_{cc}^{(1)}$ associated with the dominant eigenvalues of the real

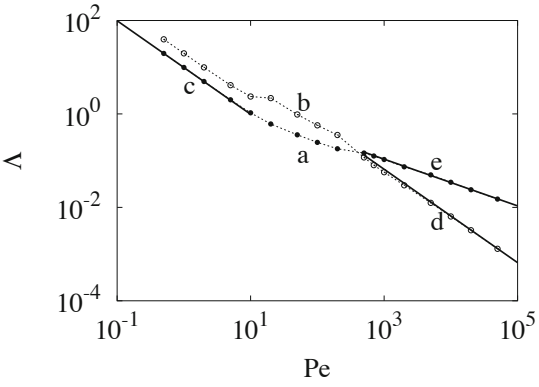

Figure 7. Autonomous cavity flow. Dominant scaling exponent Λ vs Pe. Dotted line (a) and (•) refer to the complex conjugate branch of the spectrum, dotted line (b) and (○) to the real branch. Lines (c) and (d) represent the diffusive scaling $\Lambda \sim Pe^{-1}$, line (e) the convection-enhanced scaling $\Lambda \sim Pe^{-1/2}$.

and complex-conjugate branch for $Pe = 10^3$. The real eigenfunction (associated with the diffusive eigenvalue scaling) resembles the structure of the stream function. Conversely, the dominant eigenfunction of the complex conjugate branch displays, (as expected), higher gradients, localized near the walls. As Pe increases, the dominant eigenfunctions of the diffusive branch (the real branch) converges towards an invariant shape the contour plot of which corresponds to that of the streamfucntion. This is depicted in Fig. 8 (C) showing the dominant real eigenfunction $\gamma_r^{(1)}(\mathbf{x})$ at $Pe = 10^4$. This result is not surprising, since the family the dominant eigenfunctions of the diffusive branch are characterized by the property $\lim_{Pe\to\infty} ||\nabla\gamma_r(\mathbf{x})||_{L^2} = C =$ constant, i.e. their gradients converge towards a constant quantity. The higher-order eigenfunctions of the diffusive branch of the spectrum can be viewed as higher-order modulations of a fundamental shape possessing as level sets the streamlines of the stirring flow. For example, Fig. 8 (D) shows the second dominant eigenfunction $\gamma_r^{(2)}(\mathbf{x})$ at $Pe = 10^4$.

The case of the flow between concentric cylinders can be also tackled within the universal theory. It gives a COeD exponent $\alpha = 1/3$, confirmed by numerical simulations. For details see (Giona et al., 2004b,c).

5.3 ADE in chaotic flows

In this Section, we consider the spectral properties of the ADE in chaotic flows by taking the Sine-Flow as a prototype. Indeed, the Sine-Flow is particularly handy for spectral analysis, since the evolution of the Fourier coefficients of the scalar field ϕ reduces in the first half-period of motion $T_1 = T/2$ to a system of ODE, the coefficient matrix of which is tridiagonal:

$$\frac{d\phi_{r,s}(t)}{dt} = -4\,\varepsilon\pi^2(r^2+s^2)\;\phi_{r,s}(t) - \pi r(\phi_{r,s-1}(t) - \phi_{r,s+1}(t))\,. \qquad (101)$$

Analogous expression holds for the second half-period with indexes r and s reversed. Let $\psi_{r,s} = \psi^R_{r,s} + i\psi^I_{r,s}$. A general property of the Time-Periodic Sine Flow (TPSF) is the occurrence of two spectral branches, referred to as the C (for cosine) and S (for sine) branches, respectively. The C branch is formed by those eigenvalues for which the spectral coefficient of the associated eigenfunctions admit vanishing imaginary part ($\psi^I_{r,s} = 0$, for all r, s), and consequently, the eigenfunctions of this branch can be expressed as a cosine series. Conversely, the S branch is characterized by the eigenfunction property $\psi^I_{r,s} = 0$ for all r, s.

The aim of the spectral analysis is to describe the properties of the spectral branches characterizing the Poincaré operator associated with the ADE, the spatial structure of the associated eigenfunction, and how this properties are related to the global kinematic properties of the flow.

Figure 9 (A)-(B) shows the structure of the Poincaré section of the TPSF for several values of the period T. In general, the simultaneous occurrence of regular and chaotic regions characterizes these flows. For $T = 1.6$, a single massive chaotic region invades the mixing space Ω, and numerical simulations suggest that this region possesses full measure. This claim is based exclusively on numerical simulations and does not stem from any analytical results. The case $T = 1.6$ is a candidate for studying the spectral properties in (almost) globally chaotic conditions.

Figure 10 shows the dominant scaling exponents associated with the eigenvalues of the two spectral branches C and S. For large Peclet numbers, the dominant eigenvalue which is real and belongs to the S branch, turns out to be independent of Pe, i.e.

$$\Lambda \sim \text{constant} \qquad \text{for } Pe \to \infty\,, \qquad (102)$$

which can be referred to as *Chaos Enhanced Diffusion* (ChED). It is interesting to observe that not only the dominant eigenvalue of this branch, but

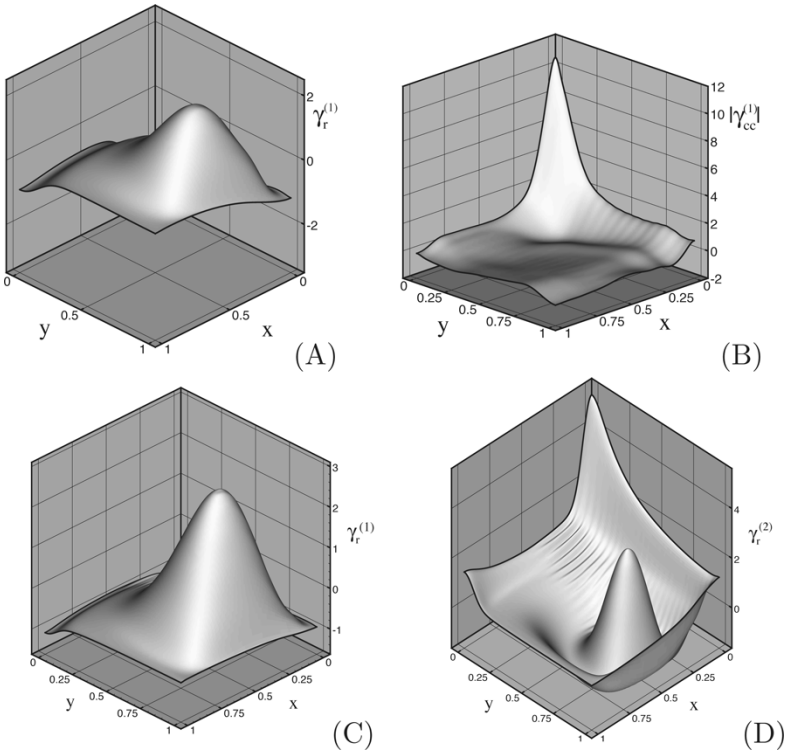

Figure 8. Three-dimensional plots of the eigenfunctions of advection-diffusion operator for the autonomous cavity flow. (A) Dominant eigenfunction $\gamma_r^{(1)}$ of the diffusion-controlled branch for $Pe = 10^3$. (B) Modulus of the dominant eigenfunction $\gamma_{cc}^{(1)}$ of the convection-enhanced branch for $Pe = 10^3$. (C) Dominant eigenfunction $\gamma_r^{(1)}$ of the diffusion-controlled branch for $Pe = 10^4$. (D) Second dominant eigenfunction $\gamma_r^{(2)}$ of the diffusion-controlled branch for $Pe = 10^4$.

also the second, the third eigenvalue as so forth possess the same scaling Eq. (102). For this reason, ChED regime may be referred to as a *homogeneous coupling* between convection and diffusion. It is worth mentioning that Eq. (102) has been obtained by other Authors (Toroczkai et al., 2001; Fereday et al., 2002; Pikovsky and Popovych, 2003; Sukhatme and Pierrehumbert, 2002; Thiffeault and Childress, 2003), not for the real advection-diffusion equation, but for the simplified pulsed-system model, which is obtained

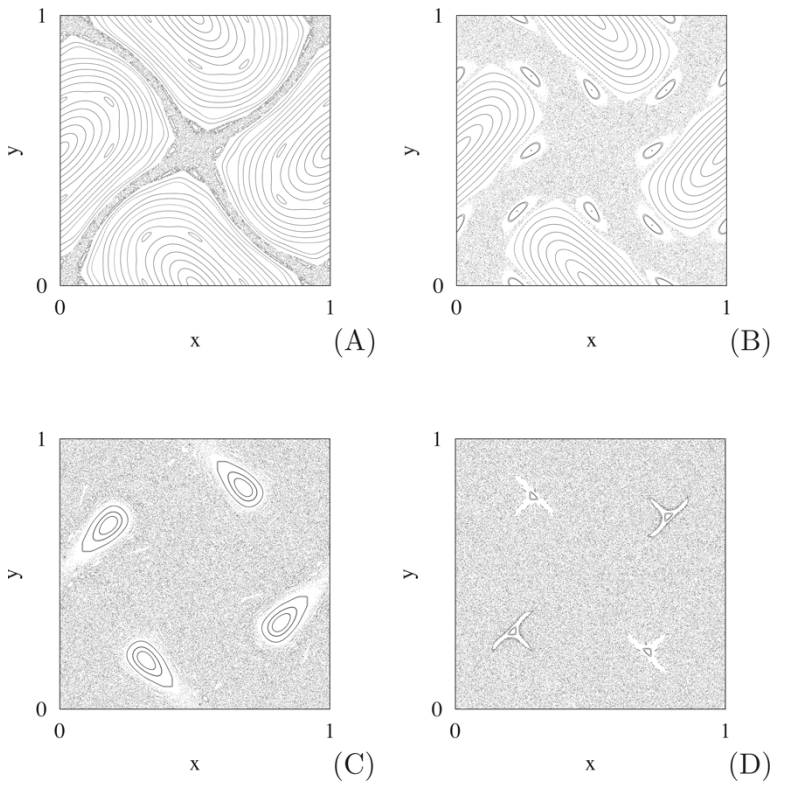

Figure 9. Poincaré sections of the time-periodic Sine Flow. (A) $T = 0.4$. (B) $T = 0.56$. (C) $T = 0.8$. (D) $T = 1.18$.

by splitting the interplay between advection and diffusion in two separate steps: a first step in which advection is active and no diffusion occurs, a second step without advection, in which diffusion smoothes the gradients (see Section 6).

Figure 11 (A) shows the contour plot of the normalized dominant eigenfunction for $Pe = 10^5$, and Fig. 11 (B) the contour plot of the norm of its gradient. It can be observed that the spatial region characterized by high values of the gradient tends to invade the entire mixing region, and that the contour plot (or the reaction interface associated with the dominant eigenfunction) closely resembles the structure of the leaves of the unstable

foliation.

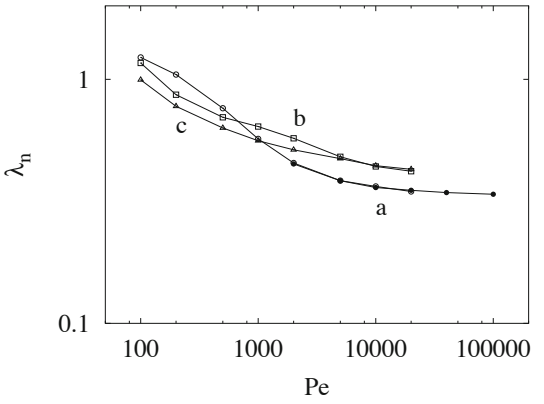

Figure 10. Dominant scaling exponents for the two spectral branches C ($\circ$) and S the TPSF at $T = 1.6$ vs the Peclet number. Empty ($\circ$) and filled ($\bullet$) circles refer to the dominant eigenvalues of the S branch estimated by the eigenvalue spectrum and by means of the power method, respectively. Triangles ($\triangle$) refer to the first complex eigenvalue of the C branch, and boxes ($\square$) to the first real eigenvalue of the C branch. Solid lines are simply interpolating curves, depicted for visual aid.

Consider the behavior of the TPSF at lower values of T, in the case of partially chaotic flows. The review of the scaling behavior of the dominant decay rate Λ for these flow protocols is depicted in Fig. 12. The dominant decay exponent Λ display for large Peclet a power-law scaling

$$\Lambda \sim Pe^{-\alpha} = \varepsilon^{\alpha}\,, \qquad \text{for large } Pe \text{ values}\,, \tag{103}$$

where the exponent α attains values between 0 (ChED) and 1 (diffusive scaling). Table 2 summarizes the values of the exponent α vs the flow period T. The occurrence of the scaling behavior expressed by Eq. (103) with $\alpha < 1$ (strictly) for the dominant decay rate (or for the dominant decay rate associated with a secondary, faster branch of the spectrum), is connected with the phenomenon referred to as the occurrence of *strange eigenfunctions* by some authors Liu and Haller (2004a). Indeed, if $\alpha < 1$, the family of eigenfunctions $\psi_\varepsilon(\mathbf{x})$ associated with the dominant eigenvalue and parametrized with respect to the Peclet number, displays the property

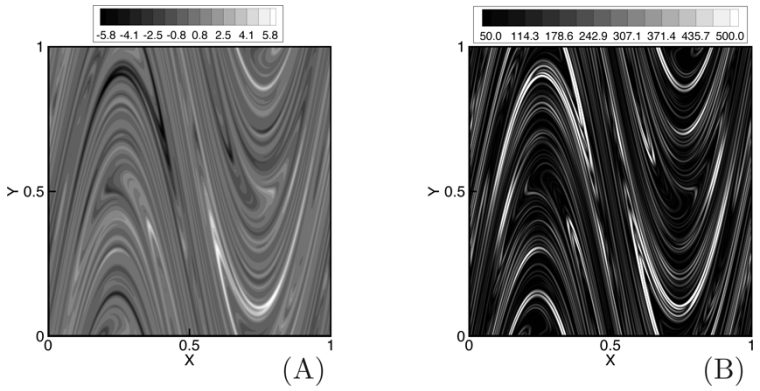

Figure 11. Contour plot of the dominant eigenfunction and of its gradient for the TPSF at $T = 1.6$, $Pe = 10^5$.

$\lim_{\varepsilon \to 0} ||\nabla \psi_\varepsilon||^2_{L^2} / ||\psi_\varepsilon||^2_{L^2} = \infty$, i.e. their normalized gradient norms diverge as $Pe \to \infty$.

Due to space limitations, solely the case $T = 0.8$ is discussed below in some detail.

In the analysis of spectral structure, it is useful to register the analogy betwen the ADE and bimolecular infinitely fast reactions (Section 3). Keeping in mind this analogy, positive and negative regions of the eigenfunctions can be viewed as the portion of the mixing space within which the two reactants are localized. While discussing the case of $T = 0.8$, this analogy is frequently used.

The case $T = 0.8$ is particularly interesting in order to highlight the complex role of the quasiperiodic islands in the interplay between diffusion and advection, and the role of symmetry. Figure 13 shows the scaling of the dominant decay rates of the C and S branches. In this case, both these eigenvalues are real, but their scaling is different. The smallest C eigenvalue, which is dominant in the Peclet range $[10^2, 10^6]$, follows Eq. (103) with $\alpha = 0.745$, while the S dominant eigenvalue scales diffusively, i.e. proportional to $1/Pe$. The functional decoupling between C and S branches, which is typical of the SF system, indicates that for very large Peclet values (approximatively of the order of 2×10^6), a crossing will occur between these two branches, and the S-branch diffusive eigenvalue will eventually dominate the asymptotic scaling. The physical nature of this phenomenon can be fully appreciated by the analysis of the eigenfunctions associated

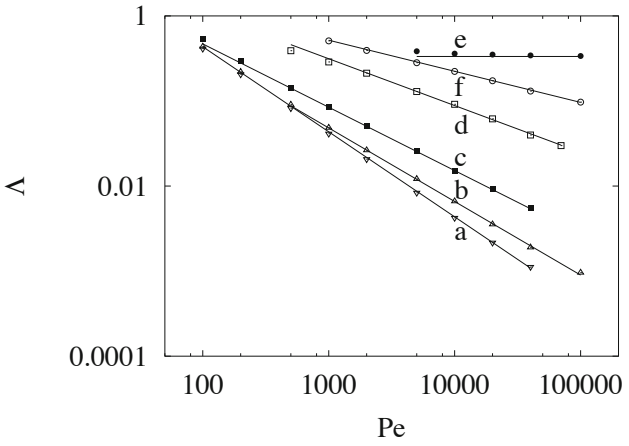

Figure 12. Dominant decay exponent Λ vs Pe for the TPSF system. The dominant eigenvalues follows the scaling Eq. (103). (a) $T = 0.4$, $\alpha = 1.0$; (b) $T = 0.56$, $\alpha = 0.865$; (c) $T = 0.8$, $\alpha = 0.745$; (d) $T = 1.18$, $\alpha = 0.55$; (e) $T = 1.6$, $\alpha = 0.0$ (f) $T = 2.0$, $\alpha = 0.37$.

Period T	α	Observations
0.4	1	-
0.56	0.865	-
0.8	0.745	for $Pe < 10^6$
”	1	for $Pe > 2\,10^6$ (extrapolated)
1.18	0.55	-
1.6	0	ChED
2.0	0.37	-
∞ (Aut.)	1	CoED may occur with $\alpha = 1/2$

Table 2. Review of the scaling exponent α for the TPSF at different periods T of the flow protocol.

with these two branches. Figures 14, 15, 16 show, respectively, the shapes (Fig. 14), the contour plots (Fig. 15) of the dominant eigenfunctions of the two branches, and the contour plots of their normalized gradient norm (Fig. 16). Essentially, the two different scalings associated with the C and S branches correspond to two different mixing conditions and to two different geometric localization properties of the eigenfunctions within the quasiperiodic islands.

In the case of the C branch, the two reacting species in a hypothetical infinitely fast bimolecular reaction (which correspond respectively to positive and negative values of the eigenfunction) are localized within the two different super-islands separated by the main chaotic region (see Fig. 14, 15 A). (In order to avoid ambiguity the four main egg-like islands appearing in the Poincaré section of the SF system at $T = 0.8$, can be regarded as organized in two main super-islands, since each couple of nearby islands is connected to each other via a chain of smaller islets, see Fig. 9 (C).

As a consequence, transport is mediated by the action of advection within the chaotic region, and this transfer mechanism can be appreciated by the inspection of the gradient norm (Fig. 16 A), the contour plot of which shows the occurrence of typical flamelets embedded within the chaotic region. This situation can be described as an inter-island transfer (i.e. between different islands) mediated by chaotic advection, thus quantitatively resulting in a dominant exponent possessing an intermediate scaling law between purely diffusive regime and CoED.

The structure of the dominant eigenfunction of the S branch displays a completely different transfer mechanism. Both the reactants are present within each of the two main super-islands, as can be observed by the localization of the plus and minuses of the dominant eigenfunction (Fig. 14 B) and by the distribution of white and black spots in its contour plot (Fig. 15 B). It results an intra-island transfer (i.e. within the same island), fully localized within each super-island, and in which the role of advection, acting in the main chaotic region, is immaterial. This phenomenon can be clearly observed by the inspection of the contour plot of the gradient modulus of the S-branch dominant eigenfunction (Fig. 16 B), showing that the gradient is completely localized within the quasiperiodic islands, without smearing the chaotic region, and without "interacting" with it.

6 Conjectures and refutations

This Section is named after the title of one of the most widely known work by Karl Popper (1969). Although the Popperian theory of the scientific method is essentially normative, the falsification principle, which charac-

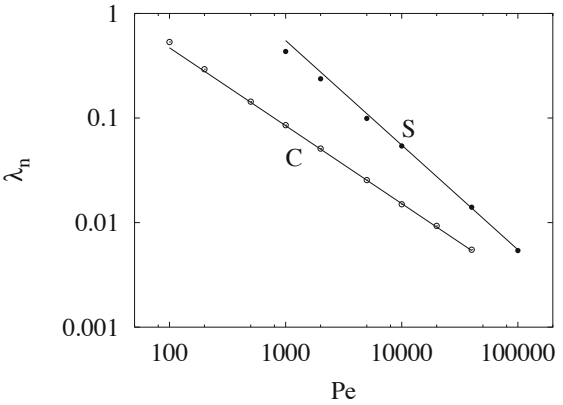

Figure 13. Dominant decay exponents for the two spectral branches (C and S) of the sine flow at $T = 0.8$ vs the Peclet number. The solid lines represent the scalings $\lambda_n = APe^{-\alpha}$ (C branch) with $\alpha = 0.745$, and $\lambda_n = B/Pe$ (S branch) respectively. A and B are two positive constants.

terizes his epistemological approach, can be a useful guideline particularly in connection with applied mathematical research linked to a robust physical phenomenology. For this branch of the scientific investigation, models, theories and paradigms can be checked and falsified by means of sound numerical simulations, and simple analytical counterexamples.

In this Section, few conjectures and claims are briefly addressed in the light of the falsificationism, gently observing that it is sufficient to provide and exhibit a clear and well-posed example of the lack of validity of a specific conjecture (or claim) to undermine its validity.

6.1 Pulsed systems

Pulsed-system modelling has become a popular tool for approaching mixing problems, in which a temporal splitting of the action of advection from that of diffusion is performed (Childress and Gilbert, 1995; Toroczkai et al., 2001; Fereday et al., 2002; Pikovsky and Popovych, 2003).

Restricting the analysis to time-periodic flows, the pulsed system approach consists in substituting the Poincaré operator $\mathcal{P}(T)$ Eq. (81),

$$\mathcal{P}(T) = \mathrm{e}^{(\mathbf{A}_2 - \varepsilon\mathbf{D})\,T_2}\,\mathrm{e}^{(\mathbf{A}_1 - \varepsilon\mathbf{D})\,T_1}$$

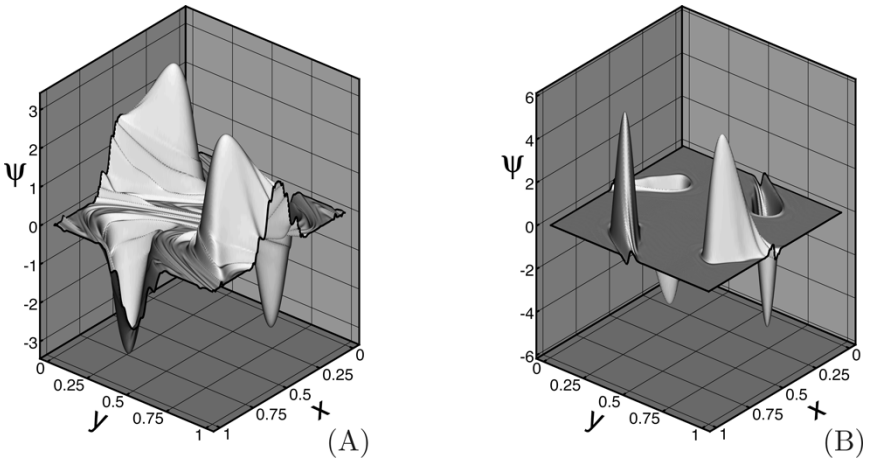

Figure 14. Profiles of the dominant eigenfunctions of the TPSF system at $T = 0.8$ for $Pe = 4 \times 10^4$. (A) C branch. (B) S branch.

where $T_1 + T_2 = T$, with the "pulsed operator"

$$\mathcal{P}_{pulsed}(T) = \mathrm{e}^{-\varepsilon \mathbf{D} T} \mathrm{e}^{\mathbf{A}_2 T_2} \mathrm{e}^{\mathbf{A}_1 T_1} = \mathrm{e}^{-\varepsilon \mathbf{D} T} F \tag{104}$$

where F is the Frobenius-Perron operator associated with a purely kinematic motion.

Apart from typical and striking situations, for which the pulsed-system approach gives completely unphysical anwsers (such as for uniformly hyperbolic toral automorphisms), since it predicts a decay of the L^2-norm which is faster than any exponential (actually a decay which behaves as the exponential of an exponential), it is important to observe that any pulsed operator is to some extent arbitrary and divorced from a specific flow protocol.

In order to investigate this issue, this Section analyzes the behavior of a pulsed system, arising from a nonlinear map - the Standard Map - and compares quantitatively its asymptotic behavior with that of the solutions of the advection-diffusion equation associated with a flow, the stroboscopic representation of which coincides with the Standard Map.

The Standard Map is defined by the equation $\mathbf{x}_{n+1} = \Phi(\mathbf{x}_n)$, where

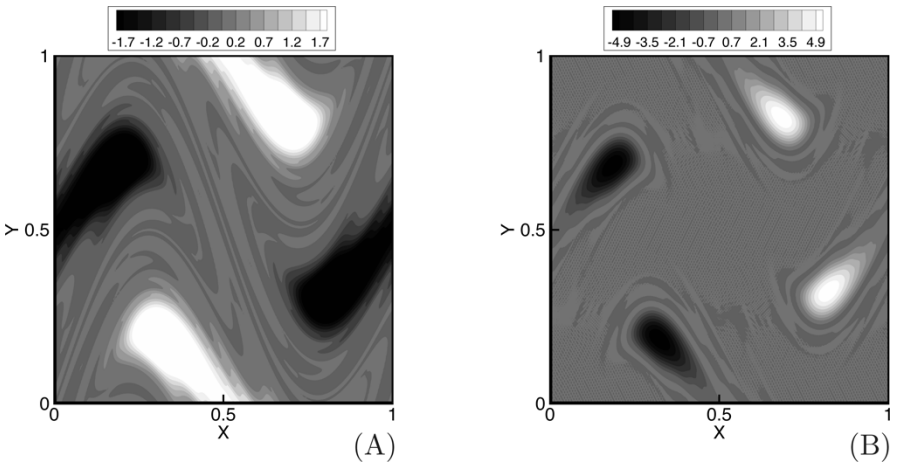

Figure 15. Contour plots of the dominant eigenfunctions for the TPSF system at $T = 0.8$ for $Pe = 4 \times 10^4$. (A) C branch. (B) S branch.

$\mathbf{x}_n = (x_n, y_n)$, and

$$\begin{aligned} x_{n+1} &= x_n + \frac{p}{2\pi}\sin(2\pi y_n) \qquad \text{mod. } 1 \\ y_{n+1} &= x_n + y_n + \frac{p}{2\pi}\sin(2\pi y_n) \qquad \text{mod. } 1 \end{aligned} \tag{105}$$

defined on the two-torus (i.e. on the unit square with opposite edges identified). We consider the case $p = 9.5$. A family of incompressible time-periodic flows can be defined by blinking in a periodic way two steady parallel flows $\mathbf{v}_1(\mathbf{x})$, $\mathbf{v}_2(\mathbf{x})$, which within a period are defined as $\mathbf{v}_1(\mathbf{x}) = (v_{o2}\sin(2\pi y), 0)$ for $0 \le t < T_1$, and $\mathbf{v}_1(\mathbf{x}) = (0, v_{o2}x)$ for $T_1 \le t < T_1 + T_2$. where v_{o1}, v_{o2}, T_1, T_2 are real parameters. The stroboscopic representation of this flow after a period $T = T_1 + T_2$ coincides with the Standard Map Eq. (105) provided that $v_{o1}T_1 = p/2\pi$ and $v_{o2}T_2 = 1$. We consider the case $T_1 = T_2 = T_c$, $v_{p1} = p/(2\pi T_c)$ and $v_{o2} = 1/T_c$. These flows, parametrized with respect to T_c, are referred to as the family of Standard-Map flows. A first, preliminary, observation follows immediately from the definition of Standard-Map flows: *the definition of a pulsed system is not one-to-one with a continuous time-period flow, which admits the same map as its stroboscopic representation.* In general, given an assigned pulsed system, an uncountable family of different flow protocols may be defined, all of which can be viewed as its time-continuous counterparts.

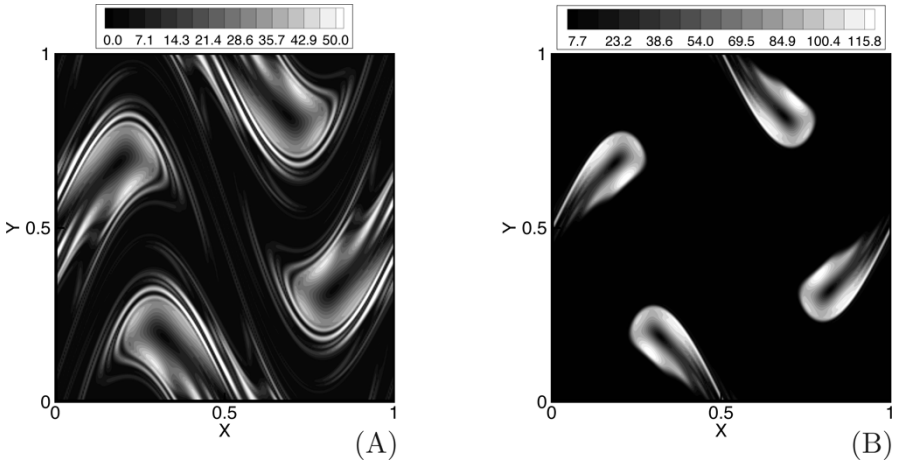

Figure 16. Contour plots of gradient modulus of the dominant eigenfunctions for the TPSF system at $T = 0.8$ for $Pe = 4 \times 10^4$. (A) C branch. (B) S branch.

This formal ambiguity reflects itself into a quantitative disagreement between the prediction of a pulsed system, and of any of its associated advection-diffusion equations. This phenomenon is depicted in Fig. 17 (A)-(B), which shows the L^2-norm decay for the pulsed system associated with the Standard Map (driven by the pulsed system operator), compared to the decay of the solutions of the ADE driven by the Standard-Map flows, for several values of the parameter T_c, at two different values of the Peclet number $Pe = 10^3$, 10^4. In order to make a "fair" comparison, the pulsed system is defined over a unit period, while the results of the numerical simulation of the advection-diffusion equation are rescaled to unit period (by defining the dimensionless time t/T). This implies that, if $\Lambda(Pe)$ is the dominant scaling exponent of the advection-diffusion equation for the Standard-Map flow possessing period T, the effective scaling exponent to be compared with the predictions of the pulsed system model is $\Lambda_{eff}(Pe) = \Lambda(Pe)T$.

For the solutions of the advection-diffusion equations and of the corresponding pulsed-system model, the decay of the L^2-norm is exponential, but the actual decay exponents $\Lambda_{eff}(Pe)$, corresponding to the slopes of the curves depicted in Fig. 17 (A)-(B) in a log-normal plot, are completely different. More precisely, for high Peclet values (such as $Pe = 10^4$, Fig.

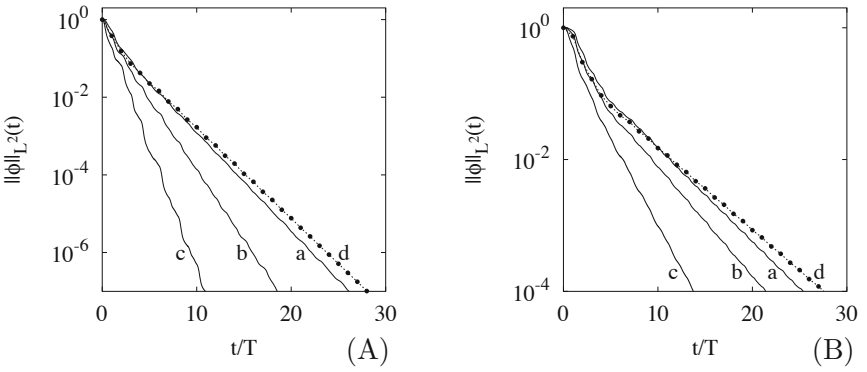

Figure 17. $||\phi||_{L^2}(t)$ vs t/T for the advection-diffusion equation driven by the family of Standard-Map flows compared with the pulsed Standard Map. (A) $Pe = 10^3$, (B) $Pe = 10^4$. Lines (a)-(c) refer to the Standard-Map flow with $T_c = 0.4, 1, 4$, respectively. The period is $T = 2\,T_c$. Dotted line (d) and (•) refer to the pulsed Standard Map.

17 (B)), the initial (transient) behavior (up to $t/T \leq 4$ in Fig. 17 (B)) of the solutions of the advection-diffusion equations (approximatively for any value of T_c) and of the pulsed system model is similar. This is physically reasonable, since in the initial transient, homogenization is dominated by the advecting term, and the influence of diffusion is negligible.

This phenomenon is further highlighted in Fig. 18, which depicts the behavior of $\Lambda_{eff}(Pe)$ for the advection-diffusion equation associated with Standard-Map flows as a function of T, for several values of $Pe = 10^2$, 10^3, 10^4. The dotted horizontal lines correspond to the values of the decay exponent for the three different values of Pe considered pertaining to the pulsed system model. It can be observed that for any value of T, i.e. for any Standard-Map flow, the scaling exponents associated with asymptotic decay are intrinsically different from that associated with the pulsed model.

As stated at the beginning of this Section, there is an intrinsic ambiguity in associating a pulsed system with a flow model, which makes practically useless the application of pulsed system approach to derive quantitative predictions on a specific advection-diffusion problem. This ambiguity is unavoidably associated with the time-discrete parametrization of the advection kinematics, through the use of a stroboscopic map in the pulsed system approach, decoupled from diffusive dynamics.

The analysis of the data depicted in Fig. 18 enables us to derive an-

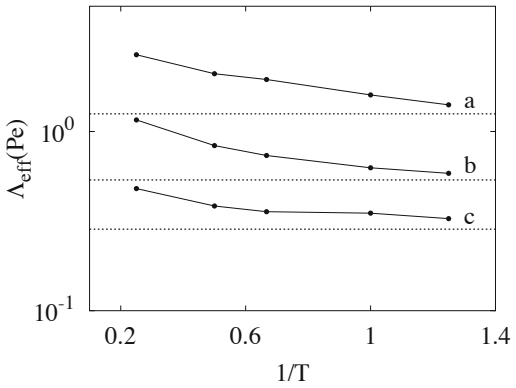

Figure 18. Dominant decay rate $\Lambda_{eff}(Pe)$ vs T^{-1} for the family of Standard-Map flows. Solid lines and (•) refer to $Pe = 10^2$ (a), $Pe = 10^3$ (b), $Pe = 10^4$ (c). Dotted horizontal lines correspond to the value of the dominant eigenvalue for the pulsed Standard Map at $Pe = 10^2$, 10^3 and 10^4, respectively.

other interesting result: the scaling exponent of the pulsed model coincides with that of advection-diffusion in the limit for $T \to 0$, i.e. if the period of the advecting action tends to zero. Although, formally interesting, this result is again of very little use in practice, since it narrows the application of pulsed models to a very limited class of flow systems (substantially, of limited physical and practical interest in many applications). This result is consistent with the original formulation due to Backus (1958) of the "*jerky approximation*" for the action of an advecting velocity field. This approximation is a computational technique (similar to time-splitting algorithms), in which a velocity field is η-closely approximated by means of a series of summable flow "jerks", over time scales of order $\mathcal{O}(\eta)$.

The divorce from physical reality of the pulsed system approach makes this author wonder why this technique has become so popular and widespread. This question is even more justified if one considers that, apart from simple toy models, the numerical simulation of pure advection (in the absence of diffusion) is computationally more complex than the simulation of the corresponding ADE (the smoothing action of diffusion helps the numerics, and makes it more stable). The above observations do not imply that pulsed systems are completely divorced from any physically relevant problem. What is reasonable to argue is that pulsed systems can be fruit-

fully viewed as a *mollification* of the Frobenius-Perron operator associated with a given flow for $\varepsilon = Pe^{-1} \to 0$, which simplifies its analysis due to compactness of the pulsed system operator. Consequently, the proper realm for the use of pulsed models is the study of pure advection (i.e. in the absence of diffusion), which can be viewed, through the use of the Frobenius-Perron operator, as a linear problem in an infinite-dimensional functional space.

7 Open problems

The aim of this Section is to highlight some open problems that are still awaiting a conclusive answer. This author considers that the answer to these problems could be significant for the advancement of laminar mixing theory.

7.1 Spectral and global characterization of mixing

The "holy Graal" of mixing theory and practice is the definition of mixing indexes. A mixing index is any functional $M : L^2(\Omega) \to \mathbb{R}$, which specifies the mixedness status of a fluid continuum. The intensity of segregation I and the scale of segregation S in Danckwerts' theory are the mixing indexes associated with this approach.

The spectral analysis carries along its own indexes. Given a concentration field $\phi(\mathbf{x}, t)$ in a closed and bounded mixing space Ω, the instantenous rate $r(\phi)$,

$$r(\phi) = \frac{||\nabla\phi||^2_{L^2}}{||\phi||^2_{L^2}}\,, \tag{106}$$

is a measure of mixedness (the larger $r(\phi)$, the better mixing efficiency), since its integral is proportional to the decay rate $\Gamma(t;\varepsilon)$ Eq. (68).

In general, any normalized spectral measure $\widehat{\sigma}_\alpha(\phi)$ defined by Eq. (76) can be viewed as a mixing index. This is also the case of the mixnorm M_{MN} (Mathew et al., 2005), which admits a simple geometric meaning as the average with respect to the mixing space and to the lengthscale of the square of the local concentration averages. The maximum mixedness corresponds to $M_{MN}[\phi] = 0$, while high values of $M_{MN}[\phi]$ ($M_{MN}[\phi] \leq 1$) correspond to poor mixing conditions.

The mixnorm is closely connected with the spectral characterization, and can be viewed as a kind of spectral measure Eq. (75), i.e. as the norm of ϕ in the Sobolev space $H^{-1/2}(\Omega)$.

The choice and the tuning of mixing indexes derived from spectral analysis is certainly bound to be considered an important issue in the near future, with practical implications in the design of microdevices.

Whatever mixing index $M[\phi]$ is considered, its functional form should satisfy some elementary constraints. Consider the hypothetical profiles depicted in Fig. 19: $\phi_1(x) = \sin(2\pi x)+1$, $\phi_2(x) = \phi_1(x)-\overline{\phi}_1$, $\phi_3(x) = \lambda\phi_1(x)$, with $\lambda = 5$.

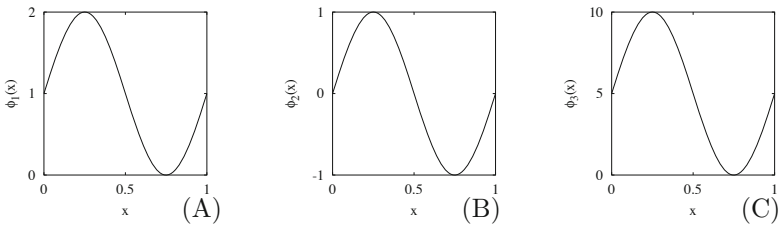

Figure 19. Three model functions that should possess the same "mixing index". (A) $\phi_1(x)$. (B) $\phi_2(x) = \phi_1(x) - \overline{\phi}_1$. (C) $\phi_3(x) = \lambda\phi_1(x)$.

It is intuitive to claim that the "mixedness" associated with these three profiles is the same. Consequently, whatever the functional form of the mixing index $M[\phi]$ is, it should satisfy the constraints

$$\begin{array}{ll} M[\phi + c] = M[\phi] & \text{for any } c \in \mathbb{R} \\ M[c\phi] = M[\phi] & \text{for any } c \in \mathbb{R}\,, \end{array} \tag{107}$$

i.e. it should be invariant for summation and multiplication by a constant. Specifically, Eqs. (107) imply that for any $\phi \in L^2(\Omega)$

$$M[\phi] = M\left[\frac{\phi - \overline{\phi}}{||\phi - \overline{\phi}||_{L^2}}\right]. \tag{108}$$

The first condition Eq. (107) is associated with the analysis developed in Section 4 on the difference between perfectly mixed conditions as a static property, and mixedness as a dynamic quantity.

7.2 Kinematics and global behavior

Beside the intrinsic relevance of Lagrangian and kinematic analysis of mixing as a tool for understanding the connections between topological, geometrical and dynamical properties associated with the evolution of passive fluid particles driven by a velocity field, a crucial point to be addressed is the real impact of these approaches in the quantification and optimization of mixing equipment. This means essentially the possibility of extracting

reliable mixing indexes from the kinematic (trajectory-based or density-based) description, to be applied in physical problems where diffusion is unavoidably present.

Even though this author suspects that the answer to this question is in general negative, (e.g. there are paradigmatic cases for which the kinematic approach fails in assessing practical design criteria), it is instructive to consider a further example of the interplay between advection and diffusion in the Time-Periodic (TP) cavity flow (see Appendix B).

Fig. 20 depicts the Poincaré sections of the kinematics for different periods of the flow protocol. The situation is similar to what already observed for the TPSF, i.e. the simultaneous presence of regions of chaotic motion and quasiperiodic islands, for all the flow periods considered.

The analysis of the solutions of the ADE reveals interesting and seemingly unexpected phenomena. Consider the TP cavity flow for $T = 1$, 1.5, 2, 4 (the Poincaré sections associated with these protocols are depicted in Fig. 20), and the time-behavior of the homogenization dynamics at $Pe = 10^3$, starting from a segregated initial condition $\phi_0(\mathbf{x}) = \sqrt{2}$ for $x < 1/2$, and $\phi_0(\mathbf{x}) = -\sqrt{2}$. This initial profile can be viewed as the representation of two completely segregated reacting species A and B.

Fig. 21 (A) shows the decay of the L^2-norm of $\phi(\mathbf{x}, t)$ for several TP protocols, compared to the corresponding decay observed in the autonomous cavity flow. The behavior of the quantity $||\nabla\phi||^2_{L^2}/(Pe||\phi||^2_{L^2})$ (which is the integrand of the function $\Gamma(t;\varepsilon)$ Eq. (68)) for the same numerical experiments is depicted in Fig. 21 (B). An interesting phenomenon may be observed: time-periodic protocols (curves (b)-(d) in Fig. 21 (A)), which give rise to Lagrangian chaos (at least in some regions of the mixing space) behave significantly worse, as it regards mixing performance (viewed as the timescale to achieve a certain degree of homogenization) than the corresponding autonomous flow protocol (Fig. 21 line (a)). For example, the TP cavity flow protocol at $T = 2.0$, which possesses a massive central chaotic region, shows a significantly slower decay rate in the relaxation towards homogenization than the autonomous cavity flow. This phenomenon does not refer exclusively to the asymptotic behavior (when the L^2-norm is small), but can be significant even in the early stages of the homogenization process (i.e. for time-scales for which $||\phi||_{L^2}(t)/||\phi||_{L^2}(0) > 5 \times 10^{-2}$). This seemingly unexpected phenomenon occurs for a broad range of Pe values ranging from 500 up to 5000. To complete the analysis, for $T = 4.0$, better mixing performance is achieved than in the autonomous case (see Fig. 21 (A), line (e)).

This is just a simple example how things can get complicated when diffusion enters the scenes, disrupting the invariant kinematic structure and

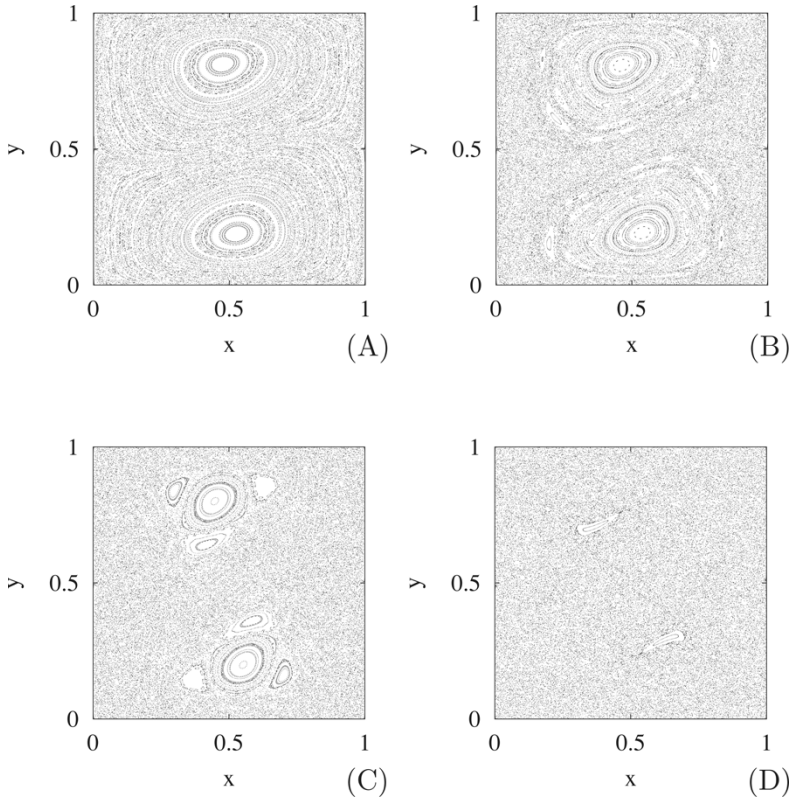

Figure 20. Poincaré sections of TP cavity flows. (A) $T = 1$. (B) $T = 1.5$. (C) $T = 2$. (D) $T = 4$.

forcing an "information exchange" (actually a mass exchange) between the otherwise not interacting kinematically segregated (invariant) regions.

The situation is even more complex, by further considering that initial concentration profiles that possess qualitatively similar kinematic behavior (viewed through the kinematic density approach, i.e. making use of the evolution equation for densities) may excite different spectral branches, or different eigenmodes within the same branch, leading to completely different homogenization dynamics in the presence of small but non-vanishing diffusivities.

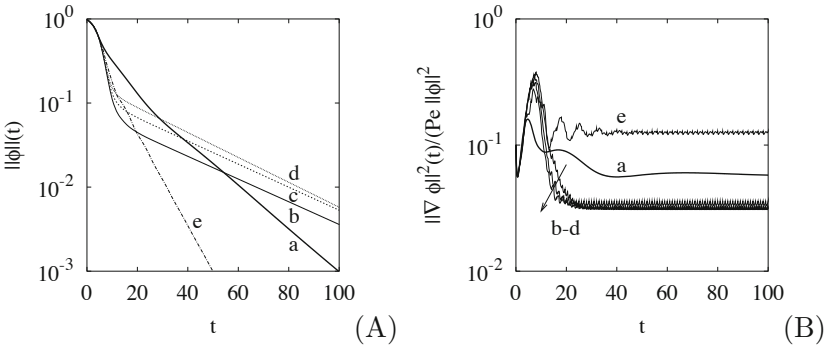

Figure 21. TP and autonomous cavity flows at $Pe = 10^3$. (A) $||\phi||_{L^2}(t)$ vs t. (B) $||\nabla\phi||^2_{L^2}/(Pe||\phi||^2_{L^2})$ vs t. The thicker line (a) refers to the autonomous cavity flow, line (b) to TP cavity flow at $T = 1$, line (c) to TP cavity flow at $T = 1.5$, line (d) to TP cavity flow at $T = 2$, line (e) to TP cavity flow at $T = 4$.

7.3 Partially chaotic flows

The analysis of the spectral properties of the ADE in chaotic flows (Section 5) has highlighted the occurrence of different mixing regimes, which correspond to different values of the scaling exponent α entering Eq. (103). Two cases give rise to well-defined values of this exponent, namely diffusive scaling, $\Lambda \sim Pe^{-1}$, and ChED, $\Lambda \sim$ constant, which represent the extremes in the range of variability of α, namely $\alpha = 1$ in pure diffusion and $\alpha = 0$ in globally chaotic advection (ChED). The latter situation may occur either in two- and three-dimensional time-periodic flows, and even in three-dimensional autonomous stirring protocols.

The other broad class of mixing regimes may be referred to as *mixed-mode regimes*. This class encompasses autonomous 2-*d* stirring protocols, and time-periodic protocols giving rise to partially chaotic Lagrangian kinematics. The main phenomenological properties of this class of mixing regimes are the following: (i) occurrence of different eigenvalue branches possessing different scaling laws Eq. (103), i.e. different exponents α; (ii) values of α in the range (0,1); (iii) localization of the dominant eigenfunctions around the poorly mixed regions (quasiperiodic islands). Therefore, both spectral and spatial heterogeneities characterize this class of flows.

To date, no theory is available for predicting the mixing regimes and the value of the scaling exponent α entering the scaling equation Eq. (103)

for flow systems, the kinematic Poincaré sections of which exhibit regions of chaotic motions and regions of periodic/quasiperiodic behavior. This issue is tricky, as the exponent α does not depend in a simple way on the "size" of the regular islands, but it is influenced also by their location and symmetries.

Any advancement in this direction is certainly significant at least for two main reasons: (i) it would give a conclusive setting to the theory of mixing in bounded closed flows and, more importantly for practical applications, (ii) it would provide a way for predicting *a-priori* the behavior of real mixing systems, since it is almost unaivoidable to observe invariant regions of regular kinematics in physically realizable flows.

7.4 Open flows

The core of these notes is centered around bounded and closed flows. The case of bounded open flows, which is even more important in microfluidic applications, deserves some specific observations.

While it is certainly true that the functional setting is an appropriate approach to tackle even open flows, spectral analysis grounded on the eigenvalues/eigenfunctions of the advection-diffusion operator (central in the analysis of bounded and closed flows) is probably the less convenient answer. This is essentially due to the following reasons: (i) the eigenvalues of the advection-diffusion operator are the characteristic time scales of the homogenization process, but are of limited use in devices in which the characteristic processing time t_{proc} is controlled by the global axial velocity V and by the linear size of the system L, $t_{proc} = L/V$, i.e. the mixing process within the device is characterized by its own timescale t_{proc}, (ii) open flow devices behave as input-output systems, and the input-output characterization is the core of their use in flow circuits.

For these reasons, a convenient and practical quantification of the mixing properties of an open-flow device should be grounded on spectral measures of the scalar field restricted to the outlet, compared to the corresponding properties of the concentration field entering the device, i.e. at the inlet section. If M is such a mixing index, attaining the value 1 for the worst possible mixing conditions, and the value 0 for the optimal ones, the mixing efficiency η_{mix} of an open flow device can be measured by any quantity of the form

$$\eta_{mix} = 1 - \frac{2\, M[\phi|_{S_{out}}]}{1 + M[\phi|_{S_{in}}]} \tag{109}$$

where $\phi|_{S_{out}}$ and $\phi|_{S_{in}}$ are the concentrations at the outlet and inlet section respectively. In fact, $\eta_{mix} = 0$ for a non-mixing flow unit ($M[\phi|_{S_{out}}] = 1$)

and $\eta_{mix} = 0$ for a perfectly mixing open-flow device ($M[\phi|_{S_{out}}] = 0$, $M[\phi|_{S_{in}}] > 0$). It is worth pointing out that the definition of η_{mix} is purely indicative of what can be regarded as a performance index for mixing in open-flow systems. Specific theoretical efforts aimed at these devices will certainly result in the definition of more appropriate mixing indexes.

8 Appendix A

Proof of Theorem 4.1 - Consider Eq. (42). Poincaré inequality applied to $||\nabla\phi||^2_{L^2}$ gives:

$$\frac{d||\phi||^2_{L^2}}{dt} = -2\varepsilon||\nabla\phi||^2_{L^2} \leq -\frac{2\varepsilon}{c_0^2}\,||\phi||^2_{L^2}\,. \tag{110}$$

The application of the classical Grönwall lemma to Eq. (110) yields Eq. (52). $\diamond$.

Proof of Theorem 4.2 - Multiply Eq. (7) by $-\nabla^2\phi$ and integrate ove Ω. By enforcing the Neumann boundary conditions, it follows that

$$-\int_\Omega \nabla^2\phi\,\frac{\partial\phi}{\partial t}\,d\mathbf{x} = \frac{1}{2}\frac{d||\nabla\phi||^2_{L^2}}{dt}\,. \tag{111}$$

Therefore,

$$\frac{1}{2}\frac{d||\nabla\phi||^2_{L^2}}{dt} = -\varepsilon\,||\nabla^2\phi||^2_{L^2} + \int_\Omega \nabla^2\phi\,\mathbf{v}\cdot\nabla\phi\,d\mathbf{x}\,, \tag{112}$$

and

$$\begin{aligned}\int_\Omega \nabla^2\phi\,\mathbf{v}\cdot\nabla\phi\,d\mathbf{x} &\leq \int_\Omega |\nabla^2\phi|\,|\mathbf{v}\cdot\nabla\phi|\,d\mathbf{x} \leq V_m\int_\Omega |\nabla^2\phi|\,|\nabla\phi|\,d\mathbf{x} = \\ &= V_m\,(|\nabla^2\phi|,|\nabla\phi|)_{L^2}\,.\end{aligned} \tag{113}$$

(The symbol $|\cdot|$ indicates both the absolute value of a scalar and the modulus of a vector quantity. This does not induce confusion, since the scalar/vector nature of a quantity can be inferred from the context). The use of the Cauchy inequality $|(f,g)_{L^2}| \leq ||f||_{L^2}||g||_{L^2}$), and the application of the Young inequality Eq. (45) (with $p = q = 2$, $a = ||\nabla^2\phi||_{L^2}$, $b = ||\nabla\phi||_{L^2}$) yields

$$(|\nabla^2\phi|,|\nabla\phi|)_{L^2} \leq ||\nabla^2\phi||_{L^2}\,||\nabla\phi||_{L^2} \leq \frac{\eta}{2}||\nabla^2\phi||^2_{L^2} + \frac{1}{2\eta}||\nabla\phi||^2_{L^2}\,, \tag{114}$$

where $\eta > 0$ is an arbitrary positive constant. By making use of Eqs. (113)-(114), Eq. (112) becomes

$$\frac{1}{2}\frac{d||\nabla\phi||^2_{L^2}}{dt} \leq -\left(\varepsilon - \frac{V_m\eta}{2}\right)||\nabla^2\phi||^2_{L^2} + \frac{V_m}{2\eta}||\nabla\phi||^2_{L^2}\,. \tag{115}$$

By setting $\eta = 2\varepsilon/V_m$, the first term at the right-hand side of Eq. (115) vanishes so that

$$\frac{d||\nabla\phi||^2_{L^2}}{dt} \leq \frac{V_m^2}{2\varepsilon}||\nabla\phi||^2_{L^2}\,, \tag{116}$$

and therefore,

$$||\nabla\phi||^2_{L^2}(t) \leq ||\nabla\phi||^2_{L^2}(0)\exp(tV_m^2/2\varepsilon)\,, \qquad t \geq 0\,. \tag{117}$$

In order to prove the boundness of the H^1-norm it is useful to recall Eq. (42). By integrating this equation between t and $t+\tau$, where $\tau > 0$ it follows that

$$\int_t^{t+\tau} ||\nabla\phi||^2_{L^2}(\theta)\,d\theta = \frac{1}{2\varepsilon}\left(||\phi||^2_{L^2}(t) - ||\phi||^2_{L^2}(t+\tau)\right) \leq \frac{||\phi||^2_{L^2}(0)}{2\varepsilon}\,, \tag{118}$$

since $||\phi||^2_{L^2}(t)$ is a monotonically decreasing function of t. Eq. (116) and the inequality Eq. (118) are the two fundamental conditions for the application of the uniform Grönwall lemma. By using the same notation as in Section 4, i.e. setting $y(t) = ||\nabla\phi||^2_{L^2}(t)$, $g(t) = V_m^2/(2\varepsilon)$, $h(t) = 0$, $A_1 = \tau V_m^2/2\varepsilon$, $A_2 = 0$, $A_3 = ||\phi||^2_{L^2}(0)/2\varepsilon$, it follows, for any $\tau > 0$ and $t > 0$, that

$$||\nabla\phi||^2_{L^2}(t+\tau) \leq \frac{||\phi||^2_{L^2}(0)}{2\varepsilon\tau}\exp(\tau V_m^2/2\varepsilon)\,. \tag{119}$$

Gathering together Eqs. (117) and (119), it follows that $||\nabla\phi||^2(t) \leq C$, where the constant C is given by:

$$C = \inf_\tau \max\left\{||\nabla\phi||^2_{L^2}(0)\exp(\tau V_m^2/2\varepsilon)\,, \frac{||\phi||^2_{L^2}(0)}{2\varepsilon\tau}\exp(\tau V_m^2/2\varepsilon)\right\}\,. \tag{120}$$

which proves Eq. (53). The second part of the theorem, Eq. (54), follows from Eq. (119) by taking the local minimum of $||\nabla\phi||^2_{L^2}(t+\tau)$ as a function of τ, which occurs for $\tau = 2\varepsilon/V_m^2$. $\diamond$

Proof of Theorem 4.3 - From Eqs. (42),(117), it follows that

$$\frac{dQ(t)}{dt} = \frac{d||\nabla\phi||^2_{L^2}(t)}{dt} + \frac{V_m^2}{4\varepsilon^2}\frac{d||\phi||^2_{L^2}(t)}{dt} \leq ||\nabla\phi||^2_{L^2}(t)\left(\frac{V_m^2}{2\varepsilon} - \frac{V_m^2}{2\varepsilon}\right) = 0 \tag{121}$$

which proves the first part of the Theorem. In order to prove Eq. (56), consider Eq. (118). The following, more strict inequality can be applied

$$\int_t^{t+\tau} ||\nabla\phi||^2_{L^2}(\theta)\, d\theta \leq \frac{1}{2\varepsilon}\, ||\phi||^2_{L^2}(t)\,. \tag{122}$$

The modified formulation of the uniform Grönwall lemma can be thus applied to yield

$$||\nabla\phi||^2_{L^2}(t+\tau) \leq \frac{||\phi||^2_{L^2}(t)}{2\varepsilon\tau}\ \exp\left(\frac{V_m^2\tau}{2\varepsilon}\right)\,, \tag{123}$$

for $t>0$ and $\tau>0$. Since $||\phi||^2_{L^2}(t)\to 0$ for $t\to\infty$, Eq. (56) follows. $\diamond$

Proof of Theorem 4.4 - Let us suppose that $||\phi||_{L^2}(t)$ decays faster than any exponential. This means that for any $k>0$

$$\lim_{t\to\infty} \mathrm{e}^{2kt}||\phi||^2_{L^2}(t)=0 \qquad \lim_{t\to\infty} \mathrm{e}^{2kt}||\nabla\phi||^2_{L^2}(t)=0\,. \tag{124}$$

Consider the auxiliary scalar field $u(\mathbf{x},t)=\mathrm{e}^{kt}\phi(\mathbf{x},t)$, which satisfies the equation

$$\frac{d||u||^2_{L^2}(t)}{dt} = 2k||u||^2_{L^2} - 2\varepsilon||\nabla u||^2_{L^2}\,. \tag{125}$$

Eq. (124) imples that for any $\eta>0$, there exists a time instant t^* such that $||\nabla u||^2_{L^2}(t)<\eta$ for $t>t^*$. From Eq. (125), it follows that for $t>t^*$

$$\frac{d}{dt}\left(\mathrm{e}^{-2kt}||u||^2_{L^2}(t)\right) = -2\varepsilon\mathrm{e}^{-2kt}||\nabla u||^2_{L^2}(t) \geq -2\varepsilon\eta\mathrm{e}^{-2kt} \tag{126}$$

and therefore

$$||u||^2_{L^2}(t) \geq \mathrm{e}^{2k(t-t^*)}\left[||u||^2_{L^2}(t^*) - \frac{\varepsilon\eta}{k}\right] + \frac{\varepsilon\eta}{k}\,. \tag{127}$$

By chosing k such that $k>\varepsilon\eta/||u||^2_{L^2}(t^*)$, it follows from Eq. (127) that

$$||u||^2_{L^2}(t) \geq \frac{\varepsilon\eta}{k}\,. \tag{128}$$

But this contradicts that starting assumption of a decay faster than exponential, and the theorem is proved. Indeed, it is convenient to proceed further. By enforcing the Poincaré inequality Eq. (35) applied to u, and considering Eq. (128) one obtains

$$||\nabla u||^2_{L^2}(t) \geq \frac{1}{c_0^2}||u||^2_{L^2}(t) \geq \frac{\varepsilon\eta}{c_0^2 k}\,. \tag{129}$$

Therefore,

$$||\nabla\phi||^2_{L^2}(t) \geq \frac{\varepsilon\eta}{c_0^2 k}\mathrm{e}^{-2kt}\,. \tag{130}$$

Since $||\nabla\phi||^2_{L^2}(t+\tau) \leq G(\tau)||\phi||^2_{L^2}(t)$, where the function $G(\tau)$ is defined by Eq. (123), it follows that

$$||\phi||^2_{L^2}(t) \geq \frac{\varepsilon\eta\mathrm{e}^{-2k\tau}}{c_0^2 k G(\tau)}\mathrm{e}^{-2kt}\,, \tag{131}$$

from which the exponential lower bound for the solutions of the ADE Eq. (7) follows. $\diamond$

9 Appendix B

Throughout these notes, two model flows are mainly considered: the Sine-Flow (SF) (Liu et al., 1994a), and the Cavity Flow.

The SF system is defined on the two-dimensional torus T^2 as the periodic sequence of two steady sinusoidal flows, $\mathbf{v}_1(\mathbf{x}) = (v_{1,x}, v_{1,y}) = (\sin(2\pi y), 0)$, and $\mathbf{v}_2(\mathbf{x}) = (0, \sin(2\pi x))$, acting alternately for a time $T/2$ on points of the two-dimensional torus, or equivalently, on the points $\mathbf{x} = (x, y)$ of the unit square with opposite edges identified. In particular, we refer to such protocols as TPSF (Time-Periodic Sine Flow), as opposed to the stationary flow defined by the velocity field $\mathbf{v}_1(\mathbf{x})$ acting for an infinite time (ASF - Autonomous Sine Flow).

Since in the SF case the stirring protocol is generated by periodically blinking each $T/2$ time units the two steady flows $\mathbf{v}_1(\mathbf{x})$ and $\mathbf{v}_2(\mathbf{x})$, the Poincaré map Φ can be obtained explicitly:

$$\Phi(\mathbf{x}) = \begin{pmatrix} x + (T/2)\,\sin(2\pi y) \\ y + (T/2)\,\sin[2\pi(x + (T/2)\,\sin(2\pi y))] \end{pmatrix} \qquad \text{mod. } 1 \tag{132}$$

where the "mod. 1" condition accounts for the spatial periodicity of the flow domain. The fact that the flow is divergence-free ($\nabla \cdot \mathbf{v} = 0$) reflects into the area-preserving property of Φ.

The other model flow which is physically realizable, is the two-dimensional cavity flow under creeping flow conditions, defined on the two-dimensional unit square $\Omega = \{(x, y) \mid 0 \leq x, y \leq 1\}$. The cavity flow derives from a streamfunction $\Psi(x, y)$, and the components of the velocity field $\mathbf{v} = (v_1, v_2)$ are given by

$$v_1 = \frac{\partial\Psi}{\partial y}\,, \qquad v_2 = -\frac{\partial\Psi}{\partial x}\,. \tag{133}$$

Under creeping flow conditions, the streamfunction Ψ is the solution of the biharmonic equation $\nabla^4\Psi = 0$, equipped with vanishing boundary conditions on Ψ and $\partial\Psi/\partial n$ all over the boundary except on $y = 1$, for which $v_1|_{y=1} = \partial\Psi/\partial y|_{y=1} = 1$.

An approximation for the streamfunction is considered, which derives from a first-order expansion of the solution of the biharmonic equation obtained by applying the method of weighted residuals. Within this approximation, the streamfunction $\Psi(x, y)$ reads as (Chella and Ottino, 1985)

$$\Psi(x, y) = Cx^2(1 - x)^2 k_0(y)\,, \tag{134}$$

where $C = 21$, $k_0(y) = A_2\cosh(\delta_1 y)\sin(\delta_2 y) + \sinh(\delta_1 y)[B_1\sin(\delta_2 y) + B_2\cos(d_2 y)]$, where $\delta_1 = 4.1503$, $\delta_2 = 2.28582$, and the coefficients A_2, B_1, and B_2 are given by:

$$\begin{aligned} A_2 &= \frac{\delta_1\sinh(\delta_1)\sin(\delta_2)}{(\delta_2\sinh(\delta_1))^2 - (\delta_1\sin(\delta_2))^2} \\ B_1 &= -\frac{\delta_1\cosh(\delta_1)\sin(\delta_2) - \delta_2\sinh(\delta_1)\cos(\delta_2)}{(\delta_2\sinh(\delta_1))^2 - (\delta_1\sin(\delta_2))^2} \\ B_2 &= -\frac{A_2\delta_2}{\delta_1}\,. \end{aligned} \tag{135}$$

Within this approximation, the velocity at the moving boundary is given by $v_1|_{y=1} = Cx^2(1 - x)^2$.

A time-periodic flow protocol can be obtained by blinking alternately the two steady flows associated with the streamfunctions $\Psi^{(1)}(x, y) = \Psi(x, y)$ (giving rise to the velocity field $\mathbf{v}^{(1)}$) for the first half period $T/2$, and $\Psi^{(2)}(x, y) = -\Psi(x, 1 - y)$ (velocity field $\mathbf{v}^{(2)}$) for the second half period, where T is the period of the flow protocol. The TP cavity flow defined above originates from the instantaneous switching of the upper ($y = 1$) and lower ($y = 0$) wall motion, with a wall velocity oriented in positive x-direction, i.e. $v_1^{(1)}|_{y=1} = v_1^{(2)}|_{y=0} = x^2(1 - x)^2$. The assumption of instantaneous switching between the two steady flows is an approximation. As discussed by Liu et al. (1994b), this approximation is reasonably accurate at low Reynolds numbers such as $Re < 1$.

Bibliography

A. Adrover, S. Cerbelli, and M. Giona. On the interplay between advection and diffusion in closed laminar chaotic flows. *J. Phys. Chem.*, 105: 4908–4916, 2001.

S. Agmon. On the eigenfunctions and on the eigenvalues of general elliptic boundary value problems. *Comm. Pure Appl. Math.*, XV: 110-147, 1962.

S. Agmon. *Lectures on elliptic boundary value problems*. Van Nostrand, Princeton, 1965.
H. Aref. Stirring by chaotic advection. *J. Fluid Mech.*, 143: 1–21, 1984.
R. Aris, On the dispersion of a solute in a fluid flowing through a tube. *Proc. Roy. Soc. A*, 235, 67–77, 1956.
V.I. Arnold, Sur la topologie des écoulements stationnaires des fluides parfaits. *C.R. Acad. Sci. Paris*, 261: 17–20, 1965.
V. I. Arnold and A. Avez. *Ergodic Problems of Classical Mechanics*. Addison-Wesley, Redwood City, 1989.
G. Backus. A class of self-sustaining dissipative spherical dynamos. *Annals Phys.*, 4: 372–447, 1958.
G. K. Batchelor. Small-scale variation of convected quantities like temperature in turbulent fluid. Part 1 General discussion and the case of small conductivity. *J. Fluid Mech.*, 5: 113–133, 1959.
D. Beigie, A. Leonard, and S. Wiggins. Invariant manifold templates for chaotic advection. *Chaos, Solitons & Fractals*, 4: 749–868, 1994.
A. Bensoussan, J.-L. Lions, and G. Papanicolau. *Asymptotic Analysis for Periodic Structures*. North-Holland, Amsterdam, 1978.
R.D. Biggs. Mixing rates in stirred tanks. *AIChE J.*, 9: 636–640, 1963.
K.B. Bischoff. A note on boundary conditions for flow reactors. *Chem. Eng. Sci.*, 16: 131–133, 1961.
S. Cerbelli, A. Adrover, and M. Giona. Enhanced diffusion regimes in bounded chaotic flows. *Phys. Lett. A*, 312: 355–362, 2003.
S. Cerbelli, V. Vitacolonna, A. Adrover, and M. Giona. Eigenvalue-eigenfunction analysis of infinitely fast reactions and micromixing regimes in regular and chaotic bounded flows. *Chem. Eng. Sci.*, 59: 2125–2144, 2004.
S. Chandrasekhar. Stochastic problems in physics and astronomy. *Rev. Mod. Phys.*, 15: 1–89, 1943.
R. Chella and J. M. Ottino. Fluid Mechanics of Mixing in a Single-Screw Extruder. *Ind. End. Chem. Fundam.*, 24: 170–180, 1985.
S. Childress and A.D. Gilbert. *Stretch, Twist, Fold: the Fast Dynamo*. Springer Verlag, Berlin, 1995.
P. V. Danckwerts. The definition and measurement of some characteristics of mixtures. *Appl. Sci. Res. A*, 3: 279–296, 1952.
P. V. Danckwerts. Continuous flow system-distribution of residence times. *Chem. Eng. Sci.*, 2: 1–13, 1953.
P. V. Danckwerts. The effect of incomplete mixing on homogeneous reactions. *Chem. Eng. Sci.*, 8: 93–99, 1958.
D. D'Alessandro, M. Dahleh and I. Mezic. Control of mixing in fluid flow: A maximum entropy approach. *IEEE Trans. Aut. Control*, 44: 1852–1863, 1999.

P. E. Dimotakis and P.L. Miller. Some consequences of boundedness of scalar fluctuations. *Phys. Fluids A*, 2: 1919–1920, 1990.

T. Dombre, U. Frisch, J.M. Greene, M. Henon, A. Mehr, and A.M. Soward. Chaotic streamlines in the ABC flows. *J. Fluid Mech.*, 167: 353–391, 1986.

J.-P. Eckmann and D. Ruelle. Ergodic theory of chaos and strange attractors. *Rev. Mod. Phys.*, 57: 617–655, 1985.

W. Ehrfeld, V. Hessel, and H. Löwe. *Microreactors*. Wiley-VCH, Weinheim, 2004.

M. Faierman. On the spectral theory of an elliptic boundary value problem involving an indefinite weight. In I. Gohberg and H. Langer, editors, *Operator Theory and Boundary Eigenvalue Problems*. Birkhäuser Verlag, Basel, pages 137–154, 1995.

A. Fannjang and G. Papanicolau. Convection enhanced diffusion for periodic flows. *SIAM J. Appl. Math.*, 54: 333–408, 1994.

M. J. Feigenbaum. The universal metric properties of nonlinear transformations. *J. Stat. Phys.*, 21: 669–706, 1979.

D. R. Fereday, P.H. Haynes, A. Wonhas, and J. C. Vassilicos. Scalar variance decay in chaotic advection and Batchelor-regime turbulence. *Phys. Rev. E*, 65: 035301 I–IV, 2002.

P.K. Feyerabend. *Against method*, NBL, New York, 1975.

C. Foias and G. Prodi. Sur le comportement global des solutions non stationnaires des equations de Navier-Stokes en dimension 2. *Rend. Sem. Mat. Univ. Padova*, 3: 1–34, 1967.

G. F. Froment and K. B. Bischoff. *Chemical Reactor Analysis and Design*. John Wiley & Sons, New York, 1979.

M. Giona and A. Adrover. Nonuniform Stationary Measure of the Invariant Unstable Foliation in Hamiltonian and Fluid Mixing Systems. *Phys. Rev. Lett.*, 81. 3864–3867, 1998.

M. Giona, S. Cerbelli, and A. Adrover. Geometry of reaction interfaces in chaotic flows. *Phys. Rev. Lett.*, 88: 024501 I-IV, 2002.

M. Giona, A. Adrover, S. Cerbelli, and V. Vitacolonna. Spectral properties and transport mechanisms of partially chaotic bounded flows in the presence of diffusion. *Phys. Rev. Lett.*, 92: 114101 I–IV, 2004a.

M. Giona, S. Cerbelli, and V. Vitacolonna. Universality and imaginary potentials in advection-diffusion equations in closed flows. *J. Fluid Mech.*, 513: 221–237, 2004b.

M. Giona, V. Vitacolonna, S. Cerbelli, and A. Adrover. Advection-diffusion in non-chaotic closed flows: non-Hermitian operators, universality and localization. *Phys. Rev. E*, 70: 046224 I–XII, 2004c.

M. Hénon. Aur la topologie des lignes de courant das un cas particulier. *C.R. Acad. Sci. Paris*, 262, 314–316, 1966,

V. Hessel, S. Hardt, and H. Löwe. *Chemical Micro Process Engineering*. Wiley-VCH, Weinheim, 2004.

V. Hessel, H. Löwe, and F. Schönfeld. Micromixers - a review on passive and active mixing principles. *Chem. Eng. Sci.*, 60: 2479–2501, 2005.

A. Iserles, A. Marthinsen, and S.P. Norsett. On the implementation of the method of Magnus series for linear differential equations. *BIT Num. Math*, 39: 281–304, 1999.

T. Kato. *Perturbation Theory for Linear Operators*. Springer-Verlag, Berlin, 1980.

D. V. Khakhar, J. G. Franjione, and J. M. Ottino. A case study of chaotic mixing in deterministic flows: the partitioned-pipe mixer, *Chem. Eng. Sci.*, 42: 2909–2926, 1987.

K. Kowalski. *Methods of Hilbert spaces in the theory of nonlinear dynamical systems*. World Scientific, Singapore, 1994.

A. Lasota and M. C. Mackey. *Chaos, Fractals and Noise*. Springer Verlag, New York, 1994.

W. Liu and G. Haller. Strange eigenmodes and decay of variance in the mixing of diffusive tracers. *Physica D*, 188: 1–39, 2004a.

W. Liu and G. Haller. Inertial manifolds and completeness of eigenmodes for unsteady magnetic dynamos. *Physica D*, 194: 297–319, 2004b.

M. Liu, F.J. Muzzio, and R.L. Peskin. Quantification of mixing in aperiodic flows. *Chaos, Solitons & Fractals*, 4: 869–893, 1994a.

M. Liu, R. L. Peskin, F. J. Muzzio, and C. W. Leong. Structure of the Stretching Field in Chaotic Cavity Flows. *AIChE J.*, 40: 1273–1286, 1994b.

A.J. Majda and P. R. Kramer. Simplified models for turbulent diffusion: Theory, numerical modelling, and physical phenomena. *Phys. Rep.* 314: 237–574, 1999.

G. Mathew, I. Mezic, and L. Petzold. A multiscale measure for mixing. *Physica D*, 211: 23–46, 2005.

I. Mezic. Chaotic advection in bounded Navier-Stokes flows. *J. Fluid Mech.*, 431: 347–370, 2001.

F.J. Muzzio and J.M. Ottino. Evolution of a lamellar system with diffusion and reaction. *Phys. Rev. Lett.*, 63: 47–50, 1989.

F.J. Muzzio, P.D. Swanson, and J.M. Ottino. The statistics of stretching and stirring in chaotic flows. *Phys. Fluid A*, 3: 1039–1050, 1991.

N.-T. Nguyen and Z. Wu. Micromixers - a review. *J. Micromech Microeng.*, 15: R1–R16, 2005.

A.W. Nienow. On impeller circulation and mixing effectiveness in the turbulent flow regime. *Chem. Eng. Sci.*, 52: 2557–2565, 1997.

J.M. Ottino. *The kinematics of mixing, stretching, chaos and transport*. Cambridge University Press, Cambridge, 1989.

J.M. Ottino, W.E. Ranz, and C. W. Macosko. A lamellar model for the analysis of liquid-liquid mixing. *Chem. Eng. Sci.*, 34: 877–890, 1979.

J. M. Ottino and S. Wiggins. Designing Optimal Micromixers. *Science*, 305: 485–486, 2004.

J.R.A. Pearson. A note on the "Danckwerts" boundary conditions for continuous flow reactors. *Chem. Eng. Sci.*, 19: 281–284, 1959.

A. Pentek, G. Karolyi I. Scheuring, T. Tel, Z. Toroczkai, J. Kadtke, and C. Grebogi. Fractality, chaos and reactions in imperfectly mixed open hydrodynamical flows. *Physica A*, 274: 120–131, 1999.

A. Pikovsky and O. Popovych. Persistent patterns in determinstic mixing flows. *Europhys. Lett.*, 61: 625–631, 2003.

K. R. Popper. *Conjectures and refutations*. Routledge and Kegan Paul, London, 1969.

W. E. Ranz. Application of a stretch model to mixing, diffusion and reaction in laminar and turbulent flows. *AIChE J.*, 25: 41–47, 1979.

M. Reed and B. Simon. *Methods of Modern Mathematical Physics I Functional Analysis*, Academic Press, Orlando, 1980.

P. J. Roache. *Computational Fluid Dynamics*. Hermosa Publishers, Albuquerque, 1972.

J. C. Robinson. *Infinite-Dimensional Dynamical Systems*. Cambridge University Press, Cambridge, 2001.

G.R. Sell and Y. You. *Dynamics of evolutionary equations*. Springer-Verlag, New York, 2002.

S. Smale. Differentiable dynamical systems. *Bull. Amer. Math. Soc.*, 73: 747–817, 1967.

R. Smith. Entry and exit conditions for flow reactors. *IMA J. Appl. Math.*, 41: 1–20, 1988.

L. L. Smith, A. J. Majamaki, I. T. Lam, O. Delabroy, A. R. Karagozian, F. E. Marble, and O. I. Smith. Mixing enhancement in a lobed injector. *Phys. Fluids*, 9: 667–678, 1997.

I.M. Sokolov and A. Blumen. Mixing in reaction-diffusion problems. *Int. J. Mod. Phys. B*, 5: 3127–3164, 1991.

T.M. Squires and S.R. Quake. Microfluidics: Fluid physics at the nanoliter scale. *Rev. Mod. Phys.*, 77: 977–1026, 1995.

A.D. Stroock, S.K.W. Dertinger, A. Ajdari, I. Mezic, H.A. Stone and G.M. Whitesides. Chaotic Mixers for Microchannels. *Science*, 295, 648–651, 2002.

J. Sukhatme and R. T. Pierrehumbert. Decay of passive scalars under the action of single scale smooth velocity fields in bounded two-dimensional domains: from non-self-similar probability distribution functions to self-similar eigenmodes. *Phys. Rev. E*, 66: 056302 I–XI, 2002.

G. Taylor. Dispersion of soluble matter in a solvent flowing slowly through a tube. *Proc. Roy. Soc. A*, 219: 186–203, 1953.

T. Tel, G. Karolyi, A. Pentek, I. Scheuring, Z. Toroczkai, C. Grebogi, and J. Kadtke. Chaotic advection, diffusion and reactions in open flows. *Chaos*, 10: 89–98, 2000.

R. Temam. *Infinite-dimensional dynamical systems in mechanics and physics*. Springer-Verlag, New York, 1997.

J.-L. Thiffeault and S. Childress. Chaotic mixing in a torus map. *Chaos*, 13: 502–507, 2003.

Z. Toroczkai, G. Karolyi, A. Pentek, and T. Tel. Autocatalytic reactions in systems with hyperbolic mixing: exact results for the active Baker map. *J. Phys. A*, 34: 5215–5235, 2001.

V. Toussaint, P. Carriere, and F. Raynal. A numerical Eulerian approach to mixing by chaotic advection. *Phys. Fluids*, 7: 2587–2600, 1995.

V.Toussaint, P. Carriere, J. Scott, and J.-N. Gence. Spectral decay of a passive scalar in chaotic mixing. *Phys. Fluids*, 12: 2834–2844, 2000.

P. Walters. *An Introduction to Ergodic Theory*. Springer Verlag, New York, 1982.

J.F. Wehner and R.H. Wilhelm. Boundary conditions of flow reactors. *Chem. Eng. Sci.*, 6: 89–93, 1956.

On Random Mixing

J. Duplat*, C. Innocenti† and E. Villermaux‡

* Aix-Marseille Université, IUSTI, 13453 Marseille Cedex 13, France
† University of Florence, Department of Physics, Florence, 50019, Italy
‡ Aix-Marseille Université, IRPHE, 13384 Marseille Cedex 13, France
and Institut Universitaire de France

Abstract We study the relaxation of initially segregated scalar mixtures in randomly stirred media, aiming at describing the overall concentration distribution of the mixture, its shape, and rate of deformation as it evolves towards uniformity. Two distinct experiments, one involving an ever dispersing mixture, the other a mixture confined in a channel, both in high Reynolds, three dimensional flows, behave very differently. We show how these differences are reminiscent of two concomitant aspects of the process of mixing, namely the distribution of individual histories on one hand examined in the present review, and the interaction between the fluid particles on the other, examined separately in Duplat and Villermaux [2008]. The particles are stretched sheets whose rates of diffusive smoothing and coalescence build up the overall mixture concentration distribution. The randomness of the particle's net elongation at a given instant of time induces a distribution of the mixing time from which molecular diffusion becomes effective in erasing the concentration differences. This ingredient is shown to rule the composition of an ever dispersing mixture, providing a detailed analytic description of the overall concentration distribution. It compares favorably with experiments using three different passive scalars suggesting that the mixture composition results from a one step lengthening process distributed among the sheets. Consequences of these processes on the spectral, and some geometrical facets of random mixtures are also examined.

1 Introduction

A mixture is a transient state between the initial segregation of the constituents, and their ultimate homogeneity. The constituents are segregated as long as they stand at distinct spatial locations at the molecular level; homogeneity is an appreciation of the residual concentration fluctuations of

the constituents in the mixture compared to their mean. The omnipresence across spatial scales in the physical world of the process consisting in following how initially segregated phases put together on a, either spontaneously or externally stirred substrate, interpenetrate and mix, from micro-fluidic devices or living organisms, industrial stirred tanks, the earth's mantle and atmospheric or ocean circulation to interstellar accretion disks, is enough to introduce the subject as a fundamental topic with dendritic relations with geometry, kinetics and structures (Ottino [1990], Villermaux et al. [1999]).

Among the basic issues, making mixing a paradigm for irreversible phenomena (see Chapter XII of Gibbs [1901]), is the problem of the decay of passive scalar concentration fluctuations on a permanently, randomly stirred substrate. As noted by Dimotakis [2005], this is only one of the many facets of the problem as a whole, but this apparently simple question, in spite of efforts coming from several schools of thought and recent important progresses, has resisted a detailed physical description.

The overall mixing process of say, a drop of colored particles in the same colorless medium, as illustrated on figure 1, involves two concomitant phenomena : a process of dispersion of the particles constitutive of the drop by which the phases interpenetrate, and a process of interaction between the particles from which homogeneity arises. While it is usually believed that the dispersion aspects mainly rely on kinematics in random media (Welander [1955]), the role of molecular diffusion is confined to the last stage for erasing the concentration differences (Eckart [1948]). These two processes, however, occur simultaneously in a stirred medium and have no reason to be independent. Moreover, we will illustrate in the present work how, depending on the dispersion properties of the underlying stirring field and the boundary conditions of the flow domain, a mixture may evolve quite differently. In order to address this question, we will discuss how the normalized histogram $P(C,t)$ of the concentration content of the mixture deforms throughout the stirring process, aiming at describing the fraction of the fluid particles in the mixture $P(C,t)\mathrm{d}C$ which bear a concentration level between C and $C+\mathrm{d}C$ at time t. To this respect, the literature is rich of a number of interestingly convergent observations, albeit made in quite different systems. The concentration distribution $P(C,t)$ presents in general a bell-shape centered around its average, except for extreme cases including one discussed here (see also Villermaux et al. [1998]); it is usually skewed, and presents broad, exponential-like tails. These observations are common place in various instances including turbulent convection (Castaing et al. [1989]), grid turbulence (Warhaft [1991], Jayesh and Warhaft [1991, 1992], Thoroddsen and Van Atta [1992]), shear layers, jets (Villermaux and Rehab [2000]), randomly stirred two dimensional flows (Holzer and Siggia [1994],

Figure 1. A drop a colored fluid deposed in a layer of the same viscous fluid is stirred according to a two-dimensional protocol. The mixture evolves towards uniformity as the number of stirring cycles increases from left to right (after Villermaux and Duplat [2003])

Williams et al. [1997], Jullien et al. [1980]), polymer solutions (Groisman and Steinberg [2001]), microfluidic devices (Simonet and Groisman [2005], Villermaux et al. [2008]) to quote a few among many examples.

The very nature of the route to uniformity which leaves, however, room for large fluctuations has prompted a number of interpretations belonging essentially to two main categories:

1.1 Particle interaction

It has been thought that the crucial ingredient to account for is the interaction of fluid particles in the mixture. The interaction has been devised in a such a way that, by accumulation, all the concentration levels tend to be alike. This evolution process was first proposed in a detailed manner by R. L. Curl (Curl [1963]) and is since then referred to as the celebrated *coalescence–redispersion* model: particles meet at random, coalesce in equalizing their concentration levels before breaking up to meet other particles in a sequential fashion. A very similar construction was imagined by von Smoluchowski [1917] to represent the kinetic aggregation of colloidal particles and the distribution of the particles clusters sizes. Pumir et al. [1991] have, in a sligtly different context, developed the same idea which leads to an evolution principle for $P(C,t)$ based on its convolution with itself, reflecting the random addition of the scalar levels C in the mixture. Pope [1985], Dopazo [1994] and Fox [2004] give a general exposition of this and others stochastic models of mixing aiming at deriving an evolution equation for $P(C,t)$.

1.2 Distributed histories

Recent developments on scalar turbulence disregard the interaction between the particles in itself, but rather focus on the distribution of histories among the particles in the mixture. In particular, (see e.g. Shraiman and Siggia [1994], Chertkov et al. [1995], Balkovsky and Fouxon [1999], Son [1999], Kalda [2000], Fereday and Haynes [2004], Sukhatme and Pierrehumbert [2002]) these exponentials tails are interpreted as reflecting the fluctuations in the stretching induced elongation of the fluid particles along their path in the fluid, thus giving rise to a distribution of the time when molecular diffusion is effective, and therefore to a distribution of concentration. In this vision, the probability that a fluid element has not been stretched enough to mix is a Poisson process with a decaying exponential distribution of life, or mixing times, from which the exponential distribution of concentration follows. The same lines of thought relating the Lagrangian trajectories of particles in the flow and global statistics have succeeded in describing the statistics of concentration *differences* in the medium (Shraiman and Siggia [2000], Falkovich et al. [2001]).

Both of these point of views happen to have some relevance, one or the other being the dominant effect depending on the precise situation in the experiments we discuss below. The two set of experiments are very simple and both consist in injecting a colored stream of diffusive substances in a colorless sustained turbulent medium. In one set of experiments, the injected stream is free to disperse at will in the medium as it mixes and is the subject of the present paper. In the other set of experiments presented in Duplat and Villermaux [2008], the mixture is confined in a channel and evolves keeping its average concentration constant.

2 Setup and methods

2.1 Flow configurations

The present experiments aim at understanding the shape of the concentration distribution $P(C,t)$ and its rate of deformation as the mixture progresses towards uniformity in stirred, turbulent media. We therefore choose flow configurations with a mean advection velocity where space can be easily converted to time, and for which the development of the turbulent velocity field is decoupled from the process of mixing itself.

In a first set of experiments, the scalar is injected in a sustained, large scale turbulent flow in which it is free to disperses while it mixes (Villermaux and Innocenti [1999], Villermaux et al. [2001]). As shown on figure 2, the scalar is injected continuously in the far field and on the axis of a turbulent

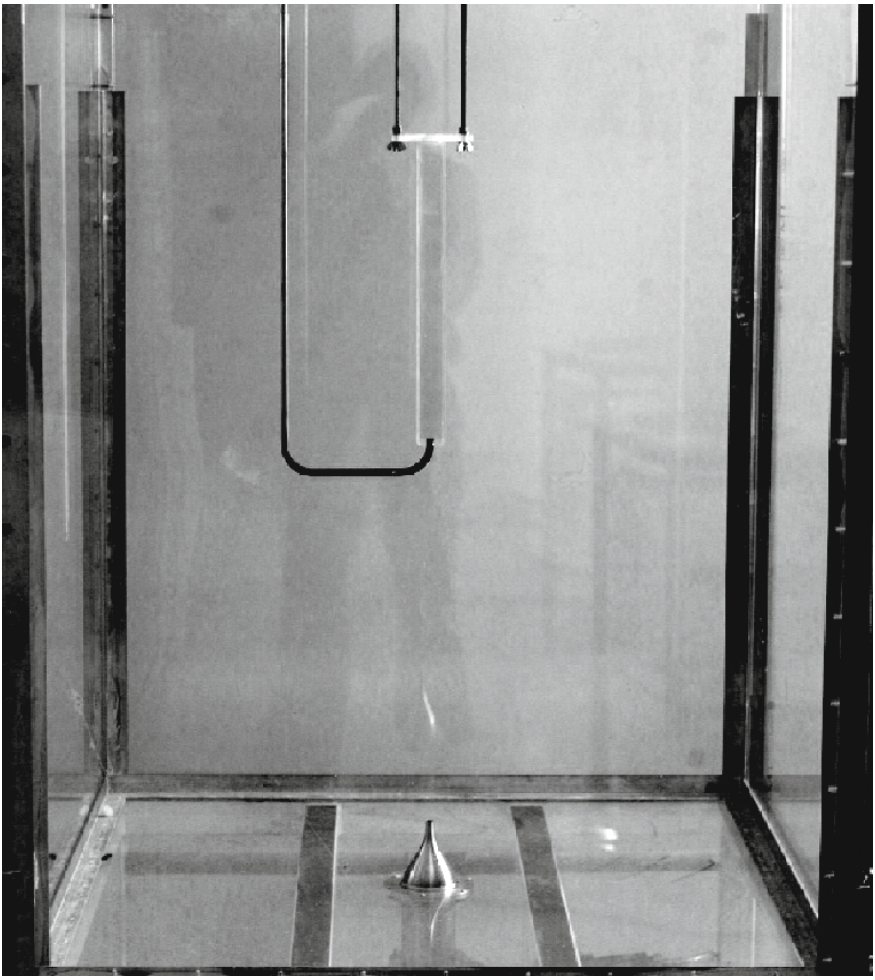

Figure 2. Experimental set-up. The tank is 1m×1m wide and 1.2 m tall. It is entirely filled with water. The orifice of the main turbulent jet is seen on the bottom and at the center of the tank. The exit of the scalar injection tube is placed at the entrance of the confinement channel. The channel can be removed to study the ever dispersing mixture.

jet via a small tube whose diameter d is smaller than the local integral scale L. We have mainly used three tube such that $d/L = 0.05$, 0.1 and 0.16. The injection tube is placed 30 to 50 diameters downstream of the turbulence generator jet exit. The local integral scale is of the order of $L = 6$ cm to 8 cm and the root mean square (r.m.s.) velocity u' is about 25 percent of the mean velocity u, giving a turbulent Reynolds number $Re = u'L/\nu = 6000$ for $u = 0.4$ m/s, and $Re = u'L/\nu = 12000$ for $u = 0.8$ m/s where ν denotes the fluid kinematic viscosity. The injection point behaves neither as a source, nor as a sink of momentum, in the mean, since the injection velocity u_{inj} through the injection tube is set equal to the average flow velocity u. The properties of the flow (stirring scale L, r.m.s. velocity u') are constant during the uniformization period of the scalar. The presence of the injection tube was checked to perturb a region of not more than 2 diameters (Villermaux et al. [2001]).

These experiments have been repeated with three types of scalars aiming at varying the intrinsic diffusive properties of the scalar being mixed and quantify its impact on the process, by varying the Schmidt number $Sc = \nu/D$ where D is the scalar diffusivity. The scalars were temperature in air ($Sc = 0.7$), temperature in water ($Sc = 7$) and the concentration of disodium fluorescein in water ($Sc = 2000$).

A second set of experiments allows to follow the mixture in a confined space. A turbulent jet of water plus diluted fluorecein discharges in a square, transparent, long duct. The jet and the duct are immersed in a large tank filled with transparent water at rest. The jet exit velocity u is such that $Re = ud/\nu \simeq 10^4$ with a turbulence intensity u'/u about 8 percent in that case (Schlichting [1987]). For a given duct cross section, the injection diameter d and the velocity of the co-flow at the entrance of the duct can be varied so that the average concentration of the dye in the channel can be set at will. Since the cross-section of the duct and the average velocity of the mixture in the downstream direction are constant, the average concentration is conserved. The experiments presented here have been done with $d = 8$ mm and a square ($L \times L$ with L= 3 cm) duct.

Some experiments at very high Reynolds number ($Re = u'L/\nu \simeq 10^7$) have been made in the in the return vein of ONERA Modane wind tunnel, 16 meters in diameter and where the air flows at typically 30 m/s with u'/u about 10 percent, at an average temperature of about 50 degrees Celsius. The measurements were made downstream of side entries at the wall of the tunnel through which cold air was engulfed from outside in the main vein. These entries have the form high slots, 70 cm wide. The different flows and conditions are summarized on Table 1.

Flow type:	Dispersing	Confined	Modane
u (m/s)	0.2–0.8	0.2–0.4	30
u'/u	0.25	0.08	0.1
L (cm)	6–8	3	70
$Re = u'L/\nu$	6000–45000	10^3–10^4	10^7
d (mm)	3–10	8	700
$Sc = \nu/D$	0.7, 7 and 2000	2000	0.7

Table 1. Summary of the types of flows and corresponding range of variables.

2.2 Measurement methods

Point measurements of the concentration and temperature are made by a fiber optics probe, a cold film thermometer and a cold wire thermometer constructed at the laboratory, respectively. The optical probe is made of two 100 μm optical fibers positionned at right angle. One fiber illuminates the medium seeded with dye, and the other collects the fluorescence signal whose intensity is measured by a photodiode. The overall signal to noise ratio is over 50. Temperature in water was measured by a 250 μm TSI cold film providing an overall signal to noise ratio about 100. Temperature in air was measured by a 1 μm in diameter and 200 μm in length cold wire with a signal to noise ratio larger than 100. The signals were further amplified and digitized by a 16 bits A/D converter. The resolution of the probes matches the Kolmogorov scale, in all cases.

Planar measurements of the fluorescent scalar field were done by shining a plane, monomode (488 nm) argon laser sheet through the water tank in a plane containing the axis of the mean flow. The images were recorded by a cooled, 12 bits, 1280×1024 pixels wide CCD camera. All these experiments are made using low concentration levels of dye (C_0=10^{-4} mol.l^{-1}) with no appreciable attenuation on the corresponding optical path, and weak temperature differences so that the scalars are always passively advected by the flow. The relative density differences $\alpha = \Delta\rho/\rho$ due to the presence of dye, or heated fluid particles are such that the associated buoyancy effects are sensitive on a lengthscale $\ell_B = u\sqrt{L/\alpha g}$ of the order of 10 meters, much larger that the set-up typical size. In the following, distances are counted in the direction downstream from the scalar injection location, and we relate space to time by

$$x = ut \tag{1}$$

where u is the mean flow convection velocity, and we convert frequencies f

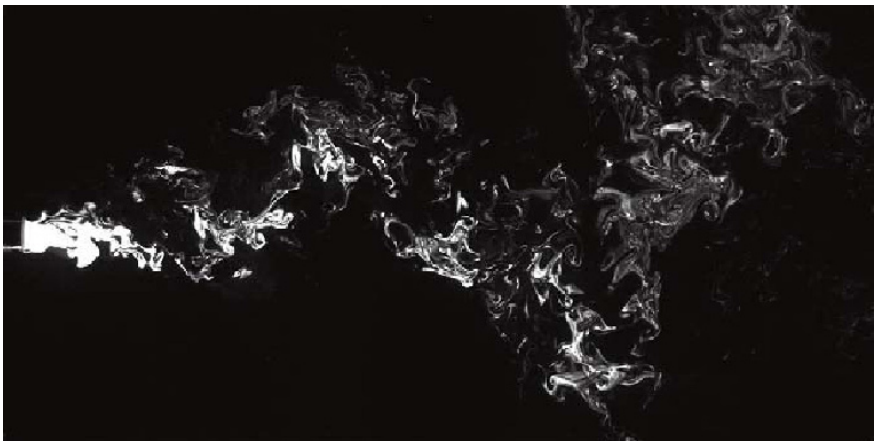

Figure 3. A snapshot of a dispersing plume made by the injection of a dye through a small tube of $d = 8$ mm in diameter on the axis of a larger turbulent jet whose integral scale is $L = 8$ cm at the injection location. $Re = u'L/\nu = 10^4$.

into wavenumbers k via Taylor hypothesis i.e. $2\pi f = ku$. Concentrations are normalized by the injection concentration so that C stands for C/C_0.

3 Mixtures: limit cases

A mixture may evolve by ever dispersing in an ocean of diluting medium, or may be confined in a closed volume. In the latter case, its average concentration $\langle C \rangle$ is a constant of time, while in the first case, the average concentration diminishes gradually in time. The comparison between these extreme cases is of interest.

3.1 The ever dispersing mixture

A plume of scalar is released in a large scale, sustained turbulent medium on the axis and in the far field of a turbulent jet. The scalar is initially seggregated from the environment in which it is free to disperse while it mixes. As it is seen on figure 3, which displays an instantaneous planar cut through the field, the support of the scalar rapidly takes the form of an intermittent set of stretched sheets separated by larger and larger voids, some of the sheets possibly coalescing as they spread out and fade away. Figure 3 also illustrates that at a given location in the flow and even far

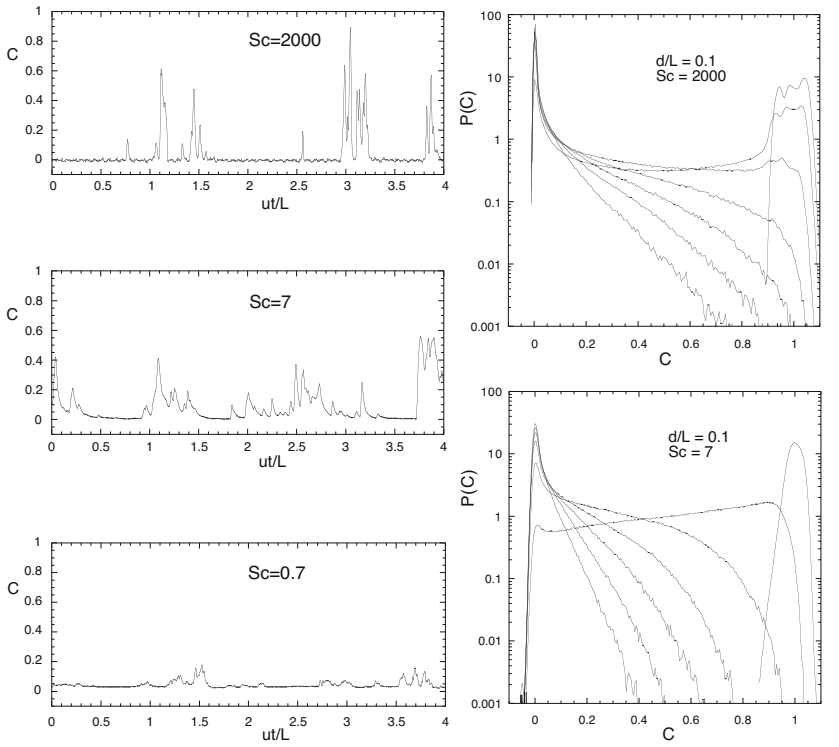

Figure 4. Left: Temporal traces of the concentration signal recorded at $x/d = 10$ and converted, with Taylor hypothesis, to instantaneous one dimensional cuts of the concentration field, for three different Schmidt numbers $Sc = 2000, 7$ and 0.7 with $d/L = 0.05$. Right: Evolution of the concentration distribution $P(C)$ of the ever dispersing shown in figure 3 for increasing distances from the injection point $x/d = 0, 2.5, 5, 7.5, 10, 12.5, 15$, and two distinct Schmidt numbers and $Re = 10^4$.

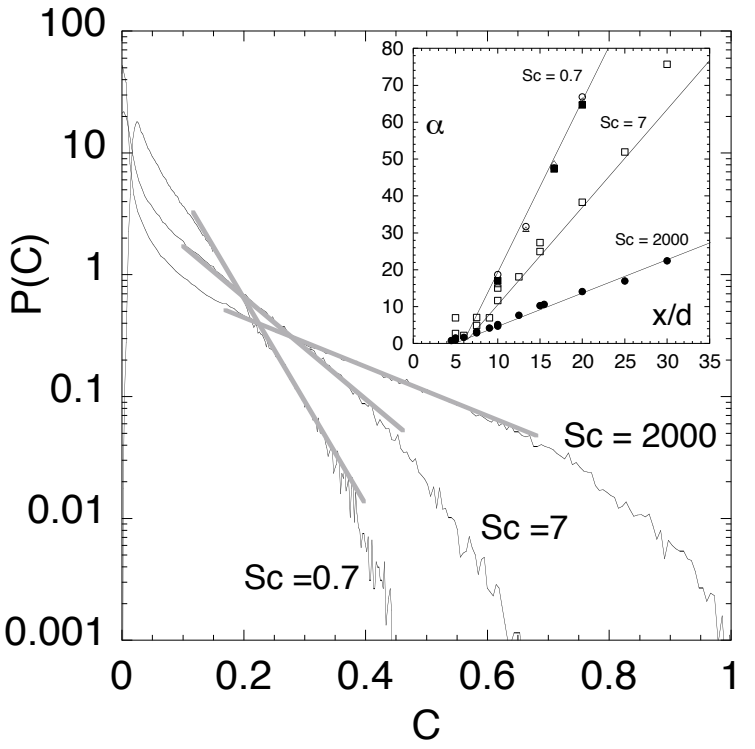

Figure 5. Concentration distributions $P(C)$ of the ever dispersing mixture of figure 3 recorded at $x/d = 10$ for three different Schmidt numbers. The shape of the distributions is exponential near the gray shades regions like $P(C) \sim \exp(-\alpha C)$. *Insert*: The argument α for different downstream locations x/d, Reynolds numbers and three Schmidt numbers. • : $Sc = 2000, Re = 6000$ and $12000, d/L = 0.05, 0.1, 0.6$. □ : $Sc = 7, Re = 6000, d/L = 0.05, 0.1, 0.16$. ■ : $Sc = 0.7, d/L = 0.08, Re = 23000$; ◯, △ : $Sc = 0.7, d/L = 0.08, Re = 45000$.

from the injection exit coexist sheets which bear a concentration close to the injection concentration and sheets which are almost fading away in the diluting medium.

The distribution of concentration $P(C)$ is measured on the centerline of the main turbulent jet at various downstream distances. Since the scalar plume meanders in the radial direction, these measurements made at locations fixed in space probe the entire concentration levels available in the distribution $P(C)$ at each position. The traces of the concentration signal recorded in three distinct experiments with $Sc = 2000$, 7 and 0.7 at $x/d = 10$ display the expected trend that the concentration fluctuations are weaker when the dye is more diffusive (figure 4).

The distributions $P(C)$ exhibit a cusped shape at the origin close to the concentration at the diluting concentration $C = 0$. That cusp is followed by an exponential-like behavior around an inflexion point (figure 5) which itself precedes a rapid fall-off for larger values of C at the tail of the distribution. Lavertu and Mydlarski [2005] make the same qualitative observation downstream of a line source in grid turbulence. The argument of the exponential tangent at the inflexion point steepens with downstream distance as

$$P(C) \sim \exp(-\alpha C) \quad \text{with} \quad \alpha = \frac{x}{d}\,\mathrm{f}(Sc) \tag{2}$$

where $\mathrm{f}(Sc)$ is a slowly increasing function of the Schmidt number. Indeed, as also shown on figure 5, the slopes of these exponentials tangent to $P(C)$ at the inflexion point depend, for a given value of x/d, on the dye diffusivity; a fit consistent with the data is a weak power-law $\mathrm{f}(Sc) \sim Sc^{1/5}$ although a logarithmic dependence $\mathrm{f}(Sc) \sim \ln(Sc)$, is not inconsistent as well. The use of three different injection diameters indicates that d is actually the relevant lengthscale which sets the argument of the exponential decrease, and of the overall shape of the distribution. This is apparent as well on the first moment of $P(C)$, namely the average concentration

$$\langle C \rangle = \int C P(C) \mathrm{d}C \tag{3}$$

whose downstream evolution is shown on figure 6 in the scaled coordinates x/d for three different injection diameters. The asymptotic trend is consistent with

$$\langle C \rangle \sim \left(\frac{x}{d}\right)^{-2} \tag{4}$$

independently of the Schmidt number. This relation is an immediate consequence of mass conservation and of the continuity of the scalar flux, advected at a mean velocity u and issuing in the medium from a section of diameter

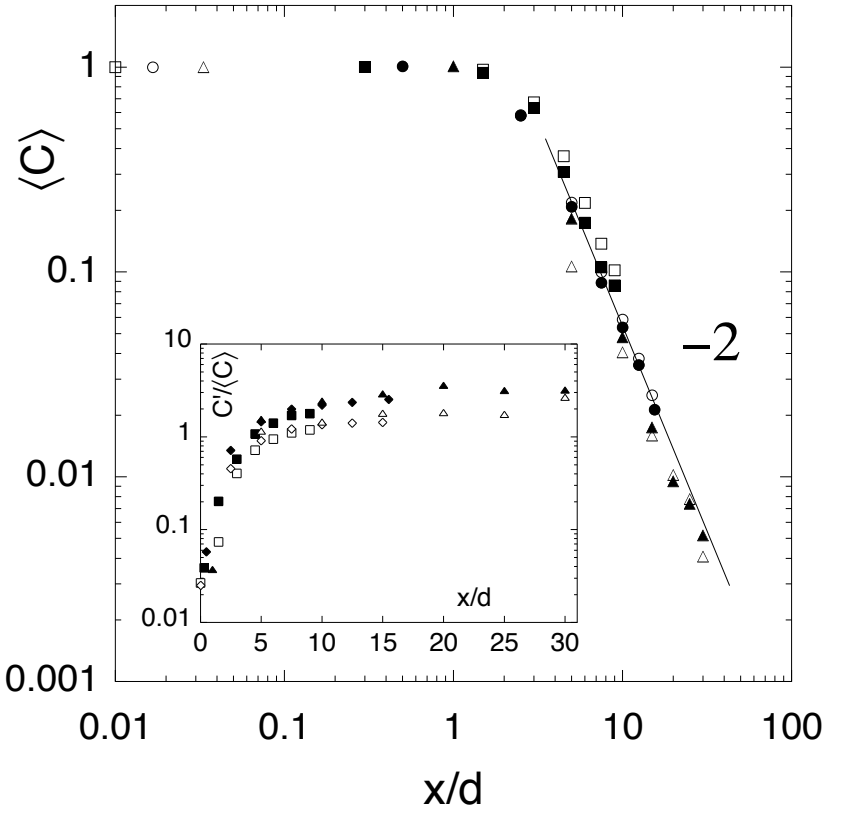

Figure 6. Downstream evolution of the average concentration $\langle C \rangle$ in the ever dispersing mixture of figure 3 for three different injection diameters and two Schmidt numbers. Insert: Downstream evolution of the fluctuations $C'/\langle C \rangle = \sqrt{\langle C^2 \rangle / \langle C \rangle^2 - 1}$. $Re = 6000.d/L = 0.05(\blacktriangle), 0.1(\blacksquare), 0.16, (\bullet), Sc = 2000$. For $Sc = 7$, same opened symbols.

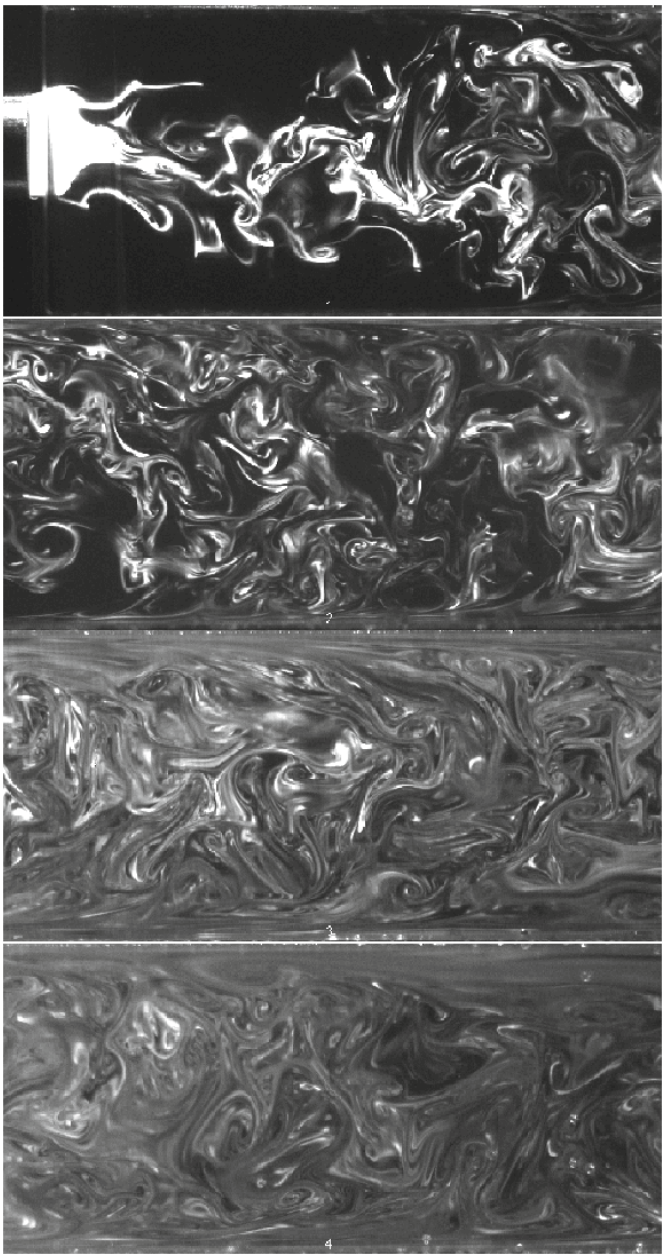

Figure 7. Mixing of a dye discharging from a jet of diameter $d = 8$ mm in a square ($L \times L$ with L= 3 cm) duct. From 1 to 4, successive instantaneous planar cuts of the scalar field at increasing downstream locations in the duct showing the progressive uniformization of the dye concentration.

d. The radius of exploration of the plume downstream of the tube exit increases in proportion to distance x for $x < L$ as a result of the persistent ballistic motion within one integral turnover time (Taylor [1921]), hence providing the equation above (see also Villermaux and Innocenti [1999]). In particular, the exponent -2 has a purely geometrical origin. It would be -1 immediately downstream of a line source for $x < L$ and $-1/2$ for $x \gg L$ in the normal diffusive regime (see e.g. the measurements of Lavertu and Mydlarski [2005]). Because of this geometrical constraint, it is thus not surprising that the downstream evolution of the mean concentration in equation (4) is independent of the Schmidt number.

3.2 The confined mixture

The scalar plume is now released at the entrance of a square, transparent, long duct by means of a tube. The jet and the duct are immersed in a large tank filled with transparent water at rest. The jet exit velocity u is such that $Re = ud/\nu \simeq 10^4$.

The flow is made visual by means of a plane Argon laser sheet slicing the duct along its axis, and the evolution of the mixture from the entrance of the duct to farther downstream is followed by computing the concentration fluctutations in each section. For a given duct cross section, the injection diameter d and the velocity of the co-flow at the entrance of the duct can be varied so that the average concentration of the dye in the channel $\langle C \rangle$ can be set at will. Since the cross-section of the duct and the average velocity of the mixture in the downstream direction are constant, the average concentration is conserved in that case.

As can be seen on figure 7, the dye rapidly invades the whole duct cross section and the concentration differences are progressively erased as it travels downstream to relax towards a more or less uniform mixture. After the dye has filled the channel cross section and evolves around a constant average concentration, the distribution $P(C)$ presents a skewed, bell shape which gets narrower around $\langle C \rangle$ in time. Axial distances are converted to time through the average axial velocity with confidence as it is known that radial velocity profiles in a turbulent duct are flat ($u'/u \approx 0.08$ see Schlichting [1987]). As shown on figure 8, the shape of $P(C)$ is very well described by a family of one parameter distributions, namely Gamma distributions of the form

$$P(X = C/\langle C \rangle) = \frac{n^n}{\Gamma(n)}\, X^{n-1}\, e^{-nX}. \tag{5}$$

The parameter n is adjusted at each downstream location for the Gamma distribution of equation (5) to fit the experimental one. It is seen on figure

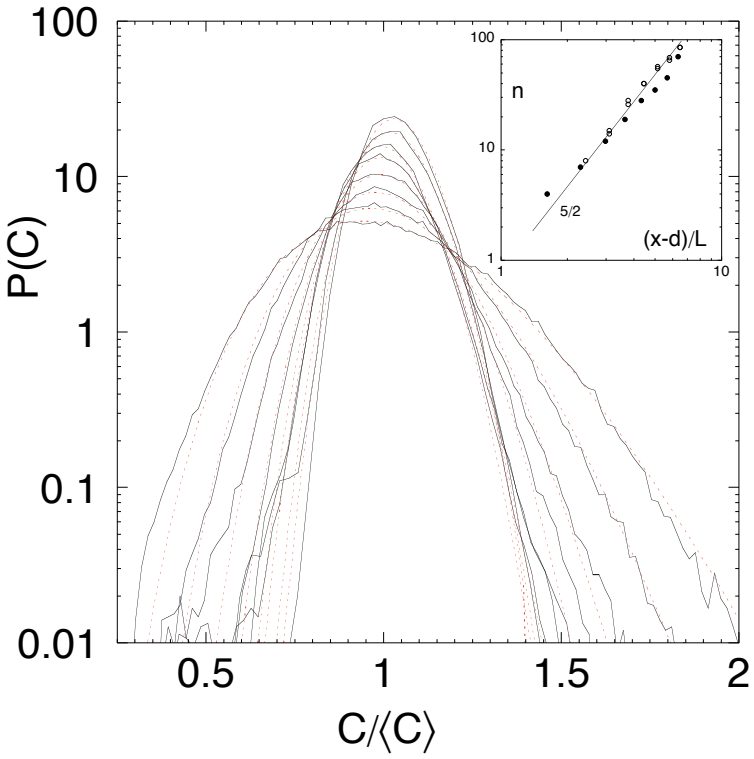

Figure 8. Downstream evolution of the concentration distribution $P(C)$ as the dye progresses along the duct as shown on figure 7. The concentration distribution of the evolving mixture gets narrower around the average concentration $\langle C \rangle = 0.3$. Solid line: experimental distributions, dashed line: distributions given by equation (5). Insert: Fitting parameter n of the distributions 5 as a function of the downstream distance $(x - d)/L$. $\circ$: $Re = 10^4$, $\bullet$: $Re = 5 \times 10^3$.

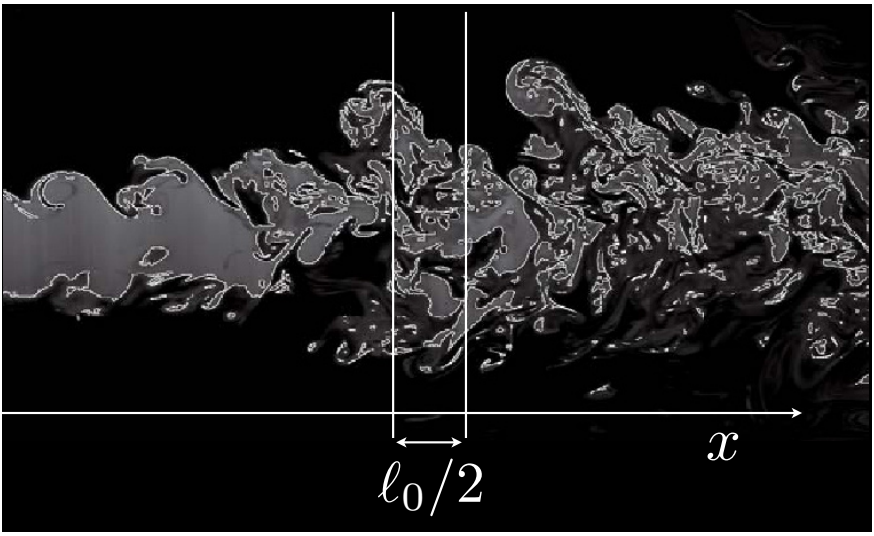

Figure 9. An example of contour length extraction when the threshold concentration $C_s(x)$ is adjusted for the contour to concern a fixed fraction of the fluid particles in the mixture at each location x, namely $\int_0^{C_s(x)} P(C,x)\mathrm{d}C = 0.93$.

8 that the fairness of the fit holds for the whole concentration range, down to low probability levels, and accounts for the downstream deformation of $P(C)$ through the single parameter n, whose dependence on the downstream location is quite strong: figure 8 suggests a power-law type of dependence with an exponent between 2 and 3; the line drawn has a slope 5/2. The dependence of n on the jet Reynolds number is, if noticeable, very weak when Re is varied by a factor 2.

4 Material contours

Stirring motions increase the length of material lines. We quantify the increase of the scalar support contour length from the two-dimensional slices through the field by a procedure illustrated on figure 9, which holds for both the dispersing, and confined mixtures.

From a large number of images of the field like the one on figure 9, we compute the amount of contour area $\ell(x)$ within a window of width ℓ_0 around each downstream location x when the field has been thresholded

at a given concentration C_s. The threshold concentration C_s may be kept constant for all downstream locations, or may be adjusted such that the contour contains a given fraction of the whole field. Specifically, the contour may be defined at each x location such that

$$C_s(x) = \mathrm{C}^{\mathrm{st}} \quad \text{or} \quad \int_0^{C_s(x)} P(C,x)\mathrm{d}C = \mathrm{C}^{\mathrm{st}}, \tag{6}$$

the constants being equal to a fraction determined a-priori. The evolution of contour lengths according to the first rule ($C_s(x) = \mathrm{C}^{\mathrm{st}}$) were studied by Villermaux and Innocenti [1999] in the ever dispersing mixture. In that case, the length first increases as a consequence of the motions in the flow, and then, as the concentration levels diminish, decreases. The fraction of the fluid particle in the mixture whose concentration has remained above the threshold at a given location x diminishes as well with x. The trend is independent of the choice of C_s, only the chronology is (figure 10).

We have here also examined the case when the threshold concentration is adjusted for the contour to concern a fixed fraction of the fluid particles in the mixture. We find that the early increase of the amount of contour within ℓ_0 is superimposed on that of the fixed threshold rule, and that the increase goes on in a linear fashion with downstream distance.

A direct way to understand this trend is to consider the separation velocity (or pair dispersion) $\Delta r/\Delta t$ between two material points separated by r, that we take for simplicity here as

$$\left\langle \frac{\Delta r}{\Delta t} \right\rangle = \gamma(t) r \tag{7}$$

on ensemble average, where $\gamma(t)$ is a –possibly time-dependent– stretching rate.

Let $N(r,t)$ be the number of segments of length r needed to cover the contour of a material element at time t. The element current length viewed at scale r is thus $\ell(r,t) = rN(r,t)$. Conservation of the number of segments stretched by the base flow writes $N(r+\Delta r, t+\Delta t) = N(r,t)$ and gives

$$\frac{\partial N}{\partial t} + \left\langle \frac{\Delta r}{\Delta t} \right\rangle \frac{\partial N}{\partial r} = 0. \tag{8}$$

With $\tau(t) = \int_0^t \gamma(t')\mathrm{d}t'$, equations (8) and (7) amount to

$$\frac{\partial N}{\partial \tau} + \frac{\partial N}{\partial \ln(r)} = 0 \tag{9}$$

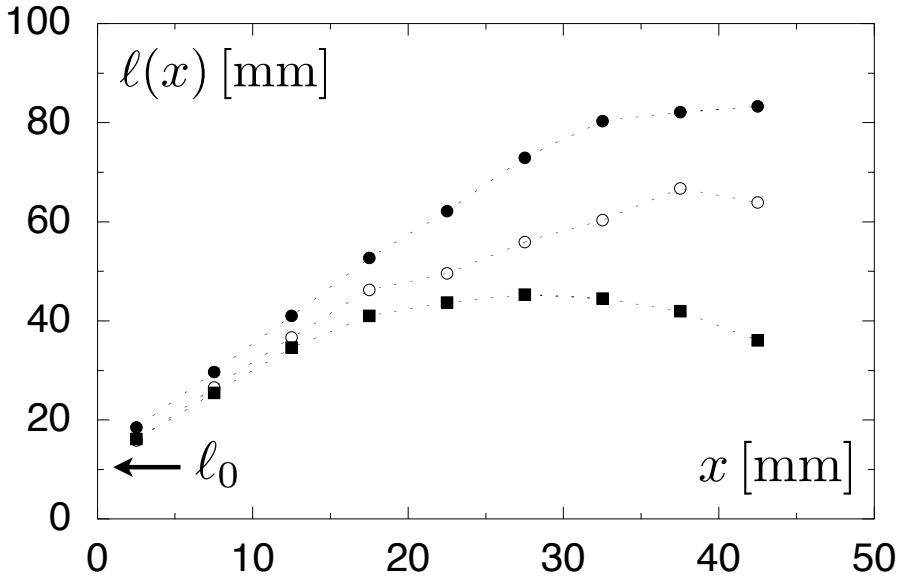

Figure 10. Downstream increase of contour lengths $\ell(x)$ measured in a window of width $\ell_0/2 = 5$ mm and averaged over many realizations, represented versus downstream distance x, for three different injection diameters: •, $d = 10$ mm, ∘, $d = 6$ mm, ■, $d = 3$ mm. The contours are extracted with a constant concentration threshold $C_s \approx 0.9$.

indicating that $N(r,t)$ propagates at speed unity in the $\{\ln(r), \tau\}$ space. Solutions are thus of the form $N(r,t) = f[\ln(r) - \tau]$. For an initially smooth contour

$$N(r, t = 0) = \frac{\ell_0}{r} \tag{10}$$

one has at any posterior time t

$$N(r,t) = \frac{\ell_0}{r} \exp\left(\int_0^t \gamma(t')\mathrm{d}t'\right) \tag{11}$$

A more refined scale dependence in equation (7) would in addition account for the *fractal* character of the contour (Sreenivasan [1991]), with a dimension $-\mathrm{d}\ln N(r,t)/\mathrm{d}r$ depending on scale r (Catrakis and Dimotakis [1996]) and increasing as time elapses (Villermaux and Innocenti [1999]).

The increase of the net material blob contour length therefore defines the effective stretching rate $\gamma(t)$. A constant stretching rate $\gamma(t) \equiv \gamma$ will

obviously lead to exponential growth. Let $\gamma(t) = \alpha\sigma/(1+\sigma t)$ where σ is some elongation rate, one expects in that case

$$\ell(t) = \lim_{r\to 0}\{rN(r,t)\} = \ell_0(1+\sigma t)^{\alpha} \tag{12}$$

The observations reported on figure 10 indicate that

$$\ell(x) - \ell_0 \sim x \tag{13}$$

independently of the injection diameter d. Therefore, one has from equation (12), $\alpha = 1$ and, with $x = ut$, the effective stretching rate

$$\gamma(t) = \frac{\sigma}{1+\sigma t} \tag{14}$$

and elongation rate

$$\sigma = \frac{u}{d} \tag{15}$$

As the mixture disperses and mix, the length of a contour bordering a fixed fraction of the mixture increases in proportion of time. Conversely, since these measurements have been done on two-dimensional slices through a three dimensional field, it is believable, that surfaces of material elements increase like $\ell(t)^2 \sim t^2$. This observation holds for both the dispersing mixture, and for the confined mixture.

5 Stretching enhanced diffusion

Consider the dispersing mixture of figure 3 and focus at the scale of the elementary scalar sheets visible from the intercept with the visualization plane. It is known that a succession of random stretching motions applied to passive objects form sheets (Betchov [1956], Girimaji and Pope [1990], Duplat and Villermaux [2000]). Due to possible folding motions in the flow, those are brought close to each other. Before we analyze the overall scalar composition of any complex configuration, it is useful to consider the elementary interaction between two scalar lamellae, as shown on figure 11.

Two pieces of a folded sheet embedded in a saddle point of the underlying displacement field are brought close to each other. The two pieces bear a slightly different concentration of scalar and at one point, the diffusive boundaries of the concentration profiles across the sheets interpenetrate to give rise to a single sheet, whose concentration profile is the *addition* of the concentration profiles of each individual sheet. This elementary interaction rule is a consequence of the linearity of the Fourier diffusion equation (Fourier [1822]).

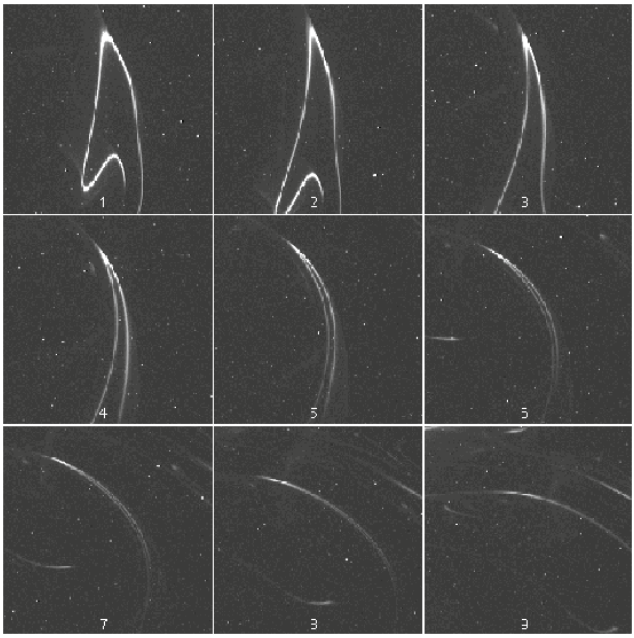

Figure 11. A folded sheet seen at consecutive instants of time embedded in a three-dimensional, turbulent flow and undergoing coalescence. The sheet is made visual by a planar two-dimensional cut through the medium. Length and time scales are given in figure 18.

Let us consider a *single* sheet first, and let C be the scalar concentration in the vicinity of the sheet and z a coordinate in the direction normal to the isoconcentration surface C (figure 12). The diffusive uniformisation of the dye is enhanced by the stretching of the underlying motions. The convection-diffusion transport equation for C reduces (see e.g. Levèque [1928], Mohr et al. [1957], Marble and Broadwell [1977], Ranz [1979], Allègre and Turcotte [1986], Marble [1988], Ottino [1989], Beigie et al. [1991], Meunier and Villermaux [2003], Fannjiang et al. [2004]) to a one dimensional problem when the radius of curvature of the isoconcentration surface is large compared to the lamellae thickness (Dimotakis and Catrakis [1999]). Let $s(t)$ be the distance between two material particles in the direction z perpendicular to a sheet, and

$$\frac{\mathrm{d}\ln\{s(t)\}}{\mathrm{d}t} \tag{16}$$

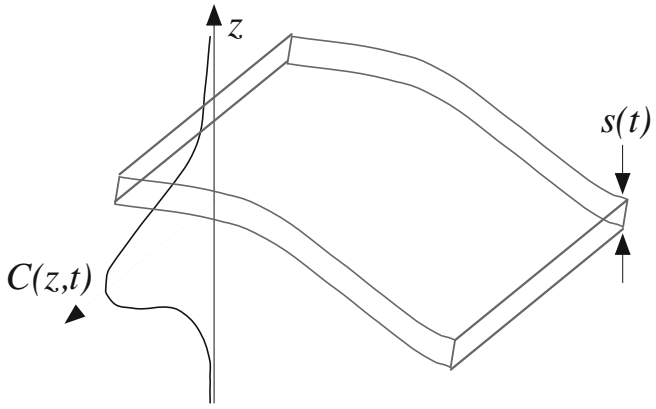

Figure 12. Sketch of an isolated stretched scalar lamellae being compressed in its transverse direction, and associated concentration profile.

its rate of compression. The mass conservation equation of a species with diffusion coefficient D then writes

$$\frac{\partial C}{\partial t} + \frac{\mathrm{d}\ln\{s(t)\}}{\mathrm{d}t} z \frac{\partial C}{\partial z} = D \frac{\partial^2 C}{\partial z^2}. \tag{17}$$

By the change of variables

$$\tau = D \int_0^t \frac{\mathrm{d}t'}{s(t')^2} \quad \textit{and} \quad \xi = \frac{z}{s(t)}, \tag{18}$$

equation (17) is reduced to a simple diffusion equation

$$\frac{\partial C}{\partial \tau} = \frac{\partial^2 C}{\partial \xi^2}. \tag{19}$$

Suppose that the lamellae has an initial width s_0, and uniform concentration C_0 so that its concentration profile is a "top hat". At any later time, its concentration profile writes, in the scaled coordinates of equation (18)

$$C(\xi, \tau) = \frac{1}{2}\left[\mathrm{erf}\left(\frac{\xi + 1/2}{2\sqrt{\tau}}\right) - \mathrm{erf}\left(\frac{\xi - 1/2}{2\sqrt{\tau}}\right)\right]. \tag{20}$$

The evolution of this profile is ruled by two antagonist phenomena: substrate compression opposes to diffusive spreading. The sheet thickness reduction process goes on until the rate of diffusive spreading of the concentration profile across the lamellae balances the rate of compression of the

concentration gradient transverse to the lamellae. This instant defines the *mixing time* t_s after which the maximal concentration in the lamellae

$$C(0,t) = \mathrm{erf}\left(\frac{1}{4\sqrt{\tau}}\right) \tag{21}$$

starts to decay. The lamellae has reduced to a sheet which vanishes in the diluting medium. The time t_s is readily estimated by noticing that the maximal concentration $C(0,t)$ decays as soon as $1/4\sqrt{\tau}$ is of order unity, the warped time τ being itself a function of the real time t throught equation (18). This time depends a-priori on the lamellae initial thickness s_0, the diffusion coefficient D and on an elongation rate σ setting the compression rate which itself reflects the strength of the stirring field; those quantities define a dimensionless parameter

$$Pe = \frac{\sigma s_0^2}{D} \tag{22}$$

known as a Péclet number. Non-trivial i.e. non purely diffusion dominated problems are such that $s_0^2/D > \sigma^{-1}$, and are thus such that $Pe > 1$. The formulation of equations (18) to (20) is general and can be adapted to any particular situation where the rate of increase of material line length, conversely the rate compression between adjacent points, is known. Its interest is to map a convection–diffusion problem onto a pure diffusion problem in suitably chosen variables, for which all the solutions are known. We describe below several generic examples:

The simple shear with one direction of elongation We consider incompressible flows in two dimensions which increase the length of material lines in proportion to time as σt. Many flows in two dimensions present a persistent shear with this property (see e.g. Ranz [1979], Marble [1988], Meunier and Villermaux [2003] and figure 13). The mean transverse thickness of the scalar filaments decrease as

$$s(t) = \frac{s_0}{\sqrt{1+(\sigma t)^2}} \tag{23}$$

and thus

$$\tau = \frac{Dt}{s_0^2}\left(1 + \frac{(\sigma t)^2}{3}\right), \tag{24}$$

providing

$$C(0,t) \sim \left(\frac{t}{t_s}\right)^{-3/2} \quad \text{for} \quad t > t_s \quad \text{with} \quad t_s \sim \frac{1}{\sigma} Pe^{1/3}. \tag{25}$$

where the condition $\tau = \mathcal{O}(1)$ has been used to compute t_s.

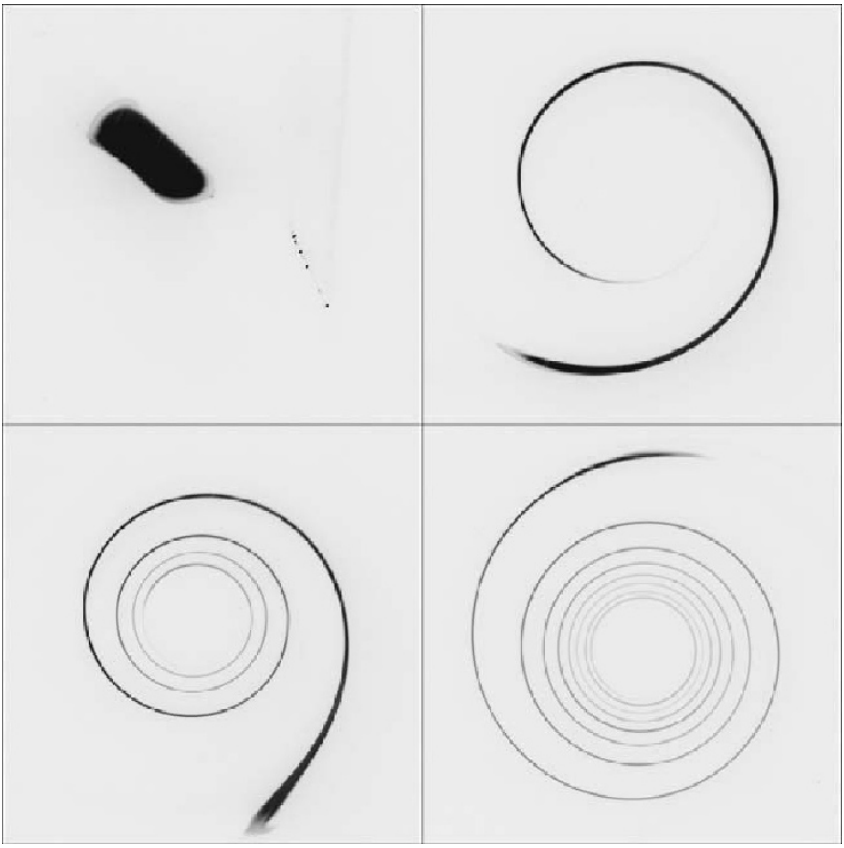

Figure 13. Roll-up of a blob of fluorescent dye in a point vortex at $t = 0$ (upper left), $t = 2\,\text{sec}$ (upper right), $t = 5\,\text{sec}$ (lower left) and $t = 10\,\text{sec}$ (lower right). Each picture covers a field $4.8 \times 4.8\,\text{cm}^2$ wide and the circulation of the vortex is $14.2\,\text{cm}^2/\text{s}$. Adapted from Meunier and Villermaux [2003].

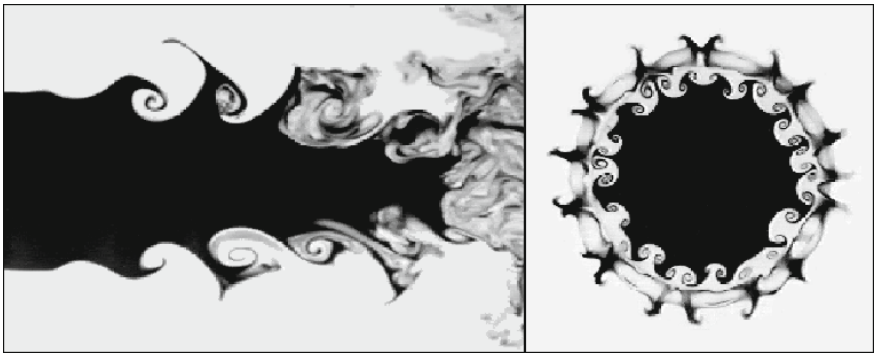

Figure 14. Snapshots of the destabilization of an inner round seeded jet by a fast annular jet. Left: Planar cut containing the jet axis. Right: Transverse cut at one inner diameter downstream. Adapted from Villermaux and Rehab [2000].

The simple shear with two directions of elongation We consider an incompressible flow in three dimensions which increases isotropically the length of material lines in proportion to time as σt. The rate of increase of surfaces is thus proportional to $(\sigma t)^2$. An example of such a flow is an unstable shear layer which rolls-up in the spanwise direction and produces concomitantly longitudinal vortices in the axial direction (see e.g. Villermaux and Rehab [2000] and figure 14).

The transverse size of a blob is in that case given by

$$s(t) = \frac{s_0}{1 + (\sigma t)^2} \tag{26}$$

and, from equation (18),

$$\tau = \frac{Dt}{s_0^2}\left(1 + \frac{2}{3}(\sigma t)^2 + \frac{1}{5}(\sigma t)^4\right), \tag{27}$$

thus

$$t_s \sim \frac{1}{\sigma} Pe^{1/5} \quad \textit{and} \quad C(0,t) \sim \left(\frac{t}{t_s}\right)^{-5/2} \quad \textit{for} \quad t > t_s. \tag{28}$$

On figure 16 are plotted various quantities such as the sheet thickness σ_C defined from the variance of the concentration profile

$$\sigma_C^2 = \frac{\int_{-\infty}^{\infty} z^2 C(z,t)}{\int_{-\infty}^{\infty} C(z,t)} \tag{29}$$

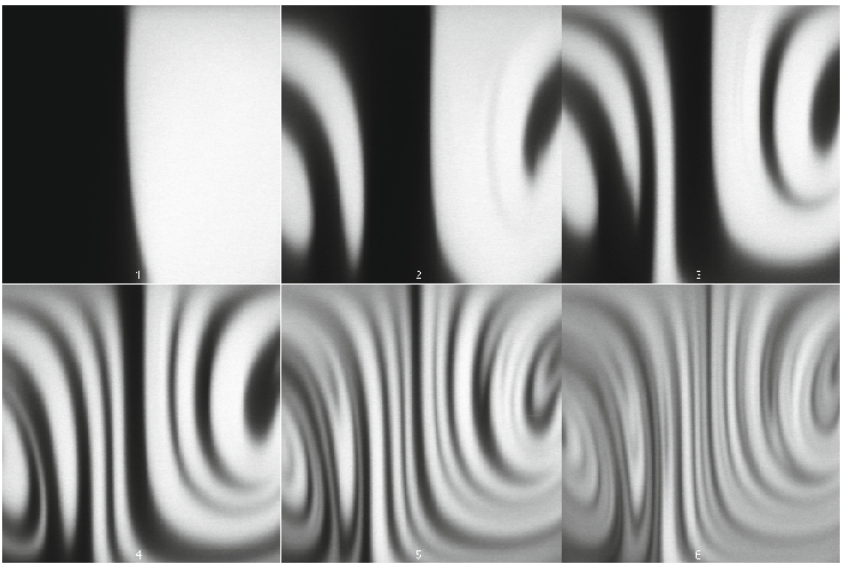

Figure 15. Mixing states at successive downstream positions in a microchannel fitted with bas-relief structures inducing transverse motions which stretch and fold the fluid. The width of the channel is of the order of 100μm and the Péclet number is $Pe = 2 \times 10^5$. Adapted from Stroock et al. [2002] (see also Villermaux et al. [2008]).

and the maximal concentration in the course of time (see also Villermaux and Rehab [2000]). It is seen that the thickness of the diffusion profile follows the decrease imposed by the kinematics of the flow up to the mixing time. At that moment, the lamellae has reduced to a sheet which is aligned parallel to the streamlines of the flow after what, for $t \gg t_s$, the maximal concentration $C(0,t)$ decays as $(\sigma t)^{-5/2}$ and the sheet thickness re–increases diffusively like $(Dt)^{1/2}$ (the rate of compression $\mathrm{d}\ln s(t)/\mathrm{d}t$ decays like $1/t$ so that molecular diffusion becomes finally dominant).

Exponential stretching We consider incompressible flows in which the length of a material line increases exponentially in time as $e^{\sigma t}$ or, in other words, whose rate of stretch is independent of its length. This kind of stretching is for instance achieved in the vicinity of a permanent saddle point flow. It is in practice realized by a succession of stretching and folding

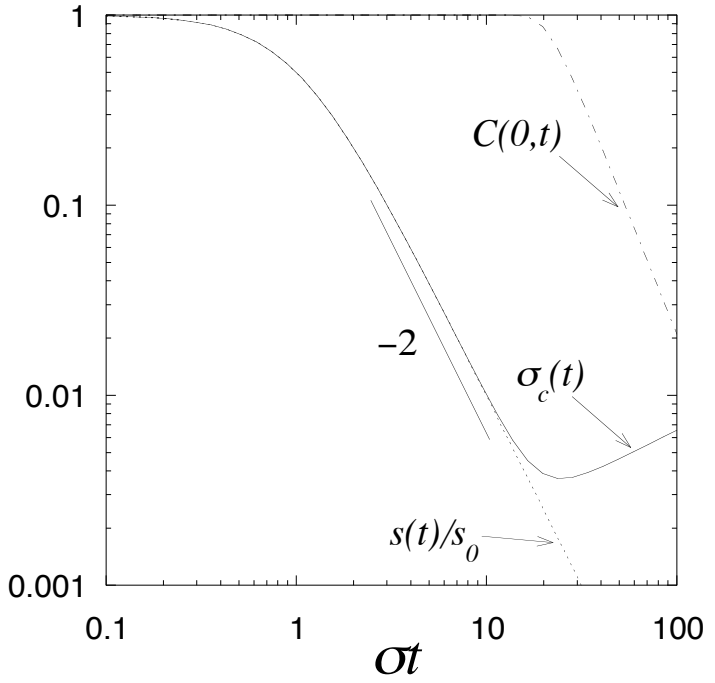

Figure 16. Evolutions as a function of σt and for $Pe = \sigma s_0^2/D = 10^7$ of: *dotted line*, thickness $s(t)/s_0$ given by equation (26); *continuous line*, standard deviation σ_C of the concentration profile across the lamellae given by equation (20) normalized by s_0; *dashed line*, maximal concentration $C(0,t)$ at the center of the sheet given by equation (21).

motions, at a scale which compares with the scalar blob being mixed, a procedure sometimes referred to as the "baker transform" (see figure 15 for an example in the microfluidics context Stroock et al. [2002]).

It is also usually admitted that disordered, turbulent flows have the property of increasing material lines exponentially (see e.g. Kida and Goto [2002]), although laboratory measurements, like those reported here on figure 10, often suggest a weaker (closer to a power-law) time dependence (see also Villermaux and Gagne [1994], Villermaux and Innocenti [1999] and figure 17). There is no fundamental reason dictating that the length of a line with macroscopic dimensions should increase exponentially. We will not

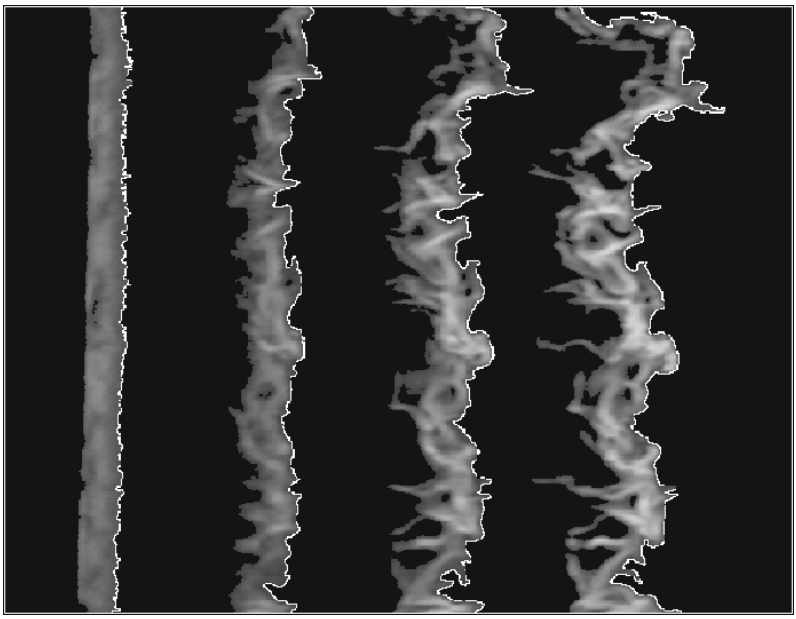

Figure 17. Snapshots of the evolution of a passive smoke ribbon immersed in a grid-generated turbulence. Adapted from Villermaux and Gagne [1994].

discuss here these subtle differences which rely on the interplay between the particle pair dispersion properties of the flows (Richardson dispersion, after Richardson [1926]), and the geometry of material contours (see a discussion in Cocke [1971]). We rather consider as an illustration a two-dimensional flow in which a simple linear shear as in section 5 is successively applied to a blob in alternated perpendicular directions (Hinch [1999]). For a time lapse Δt, the blob elongates in one direction up to $s_0\sqrt{1+(\sigma\Delta t)^2} \approx s_0\sigma\Delta t$ if $\sigma\Delta t \gg 1$, and is then submitted to a perpendicular shear σ' applied for a duration $\Delta t'$. The blob length is thus given in course of time by

$$s_0(\sigma\Delta t\sigma'\Delta t')^{t/(\Delta t+\Delta t')} \tag{30}$$

For a symmetric cycle such that $\sigma = \sigma'$ and $\Delta t = \Delta t'$, one sees that the blob length will increase like $s_0 e^{\gamma t}$ with

$$\gamma = \sigma\frac{\ln(\sigma\Delta t)}{\sigma\Delta t}. \tag{31}$$

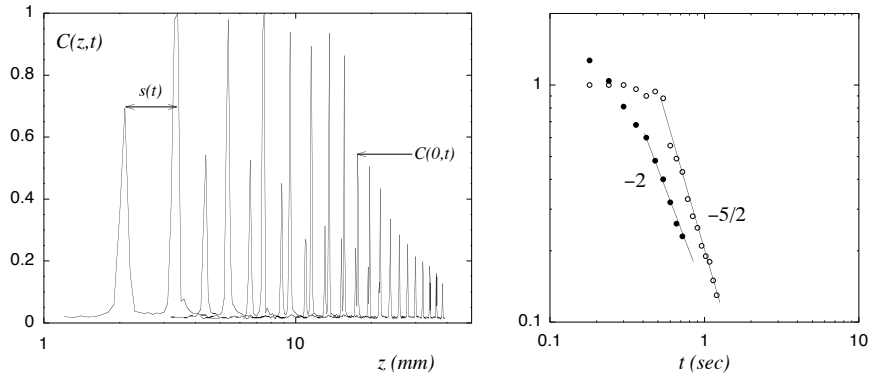

Figure 18. Left: Spatial concentration profiles $C(z,t)$ of the folded coalescing sheet shown on figure 11, superimposed for successive instants of time. The sheet moves perpendicular to itself as its two pieces gets closer; the figure shows the concentration profiles resulting from the intersection of the sheet on figure 11 with a line fixed in space. Right: The distance $s(t)$ between the maxima of concentration of the profiles ($\bullet$), and the evolution of the maximal concentration $C(0,t)$ of the overall profile ($\circ$) as a function of time.

Conversely, the transverse size of the blob is given, in two dimensions, by

$$s(t) = s_0 e^{-\gamma t} \tag{32}$$

and, from equation (18),

$$\tau = \frac{D}{2\gamma s_0^2}\left(e^{2\gamma t} - 1\right), \tag{33}$$

thus

$$t_s \sim \frac{1}{2\gamma}\ln Pe \quad \textit{and} \quad C(0,t) \sim e^{-\gamma t} \quad \textit{for} \quad t > t_s. \tag{34}$$

For that type of exponential deformation, the thickness of the sheet, as it vanishes in the diluting medium, remains equal to

$$s(t_s) = \sqrt{\frac{D}{\gamma}} \quad \textit{for} \quad t > t_s. \tag{35}$$

sometimes called the Batchelor scale, after Batchelor [1959].

The times t_s given in equations (25), (28) and (34) are the relevant mixing times of a scalar blob as soon as the inverse of the elongation rate σ^{-1} is smaller than the diffusive time of the blob constructed on its initial size s_0^2/D, that is for $Pe > 1$. In this limit, t_s is essentially given by the time needed to deform the blob σ^{-1} and molecular diffusion, although a crucial step in the ultimate uniformization, plays only a weak correction role in the kinetics of the process; a fact known in the engineering practice for a long time (Nagata [1975]).

5.1 Rules of thumb

Qualitatively, the mixing time can be estimated in any concrete situation from the knowledge of the rate of compression of two material points due to stretching, and the diffusional properties of the scalar. Let $s(t)$ be the distance between two material points near a scalar sheet. The reduction of the concentration profile width in the sheet goes on until the rate of compression $\mathrm{d}\ln s(t)/\mathrm{d}t$ balances the rate diffusive broadening on its current size $D/s(t)^2$ that is

$$\frac{D}{s^2} \sim -\frac{1}{s}\frac{\mathrm{d}s}{\mathrm{d}t} \tag{36}$$

and this balance defines the *mixing time* t_s of the sheet. Taking for instance the generic form

$$s(t) = s_0(1+\sigma t)^{-\beta} \tag{37}$$

where σ is a rate of elongation, then the balance condition writes

$$\sigma t_s \sim \left(\frac{\sigma s_0^2}{D}\right)^{\frac{1}{2\beta+1}} \tag{38}$$

From this characteristic time, the maximal concentration in the sheet $C(0,t)$ which is such that $C(0,t)(Dt)^{1/2}/s(t)$ is, by mass conservation, constant, decreases like

$$C(0,t) \sim (t/t_s)^{-\beta-1/2} \tag{39}$$

The value of the exponent $5/2$ is now transparent: the surface of the sheet increases like t^2 and the width of the diffusion profile like $t^{1/2}$; the concentration in the sheet is thus such that $C(0,t)\times t^2 \times t^{1/2}$ is, by mass conservation, constant. The same argument obviuously applies to the previous case in two dimensions where $3/2$ actually means $1{+}1/2$.

6 Distributed individual trajectories

Our reasoning has up to now involved a single elongation rate σ and therefore a single mixing time t_s. We now consider possible fluctuations in the

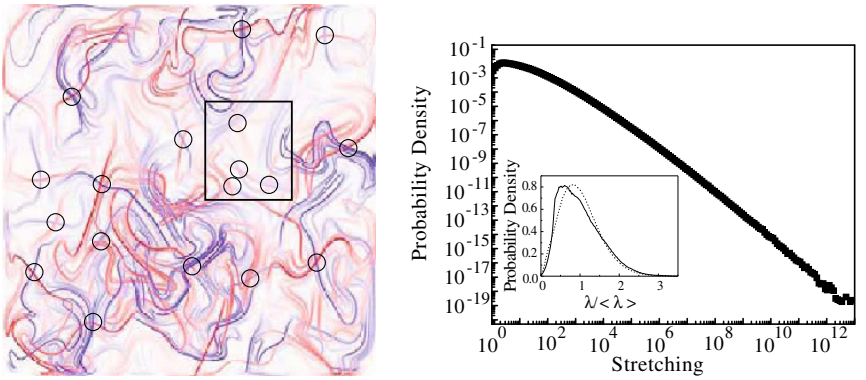

Figure 19. Stretching field in a two-dimensional experiment (adapted from Voth et al. [2002]) for two consecutive instants of time (marked in red, and blue), and corresponding stretching intensity distribution.

net elongation along the path of the fluid particles in the medium, fluctuations whose natural consequence is the *distribution of the mixing times* themselves. This phenomenon is evident from figure 3, or looking at the more familiar smoke puff shown on figure 20 (see also Voth et al. [2002] and figure 19): at a given location in the flow coexist sheets which still bear the injection concentration and sheets which are almost fading away in the diluting medium. Another example is the mixing properties of a point vortex considered by Meunier and Villermaux [2003]: fluid particles close to the vortex center are more elongated, at a given instant of time, than those initially located farther from the center, giving rize to a *distribution of mixing times*, itself inducing the concentration distribution of the scalar wrapped around the vortex.

6.1 Distribution of elongations

We now envisage this ingredient and examine its consequences on the shape of $P(C)$. Regarding turbulent, random flows, the fundamental question to ask is whether the distribution of elongation among fluid particles at a *fixed time* results from a *sequential process* with many independent steps, or from a *single event* distributed in intensity. Another, less important aspect, is whether the flow is of a *stretching* type, that is if material lengths increase exponentially in time, or of a *lengthening* type, that is if material lengths grow algebraically. Starting with a collection of identical particles of size ℓ_0, they will fall in a distribution of elongation $\mathcal{P}(\ell, t)$ an instant of

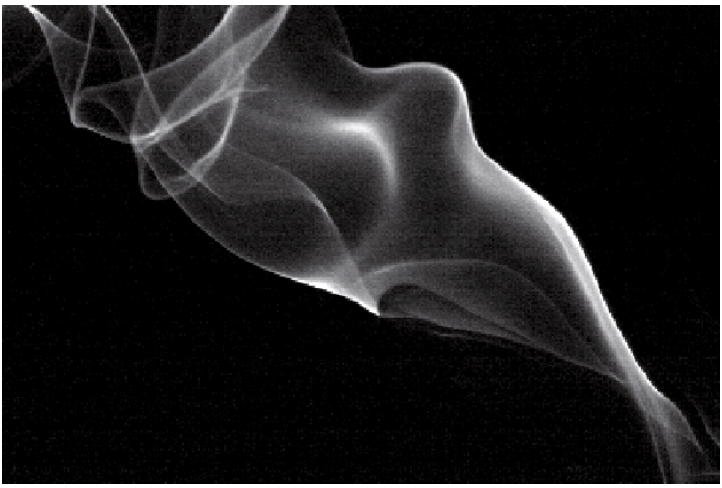

Figure 20. A smoke plume forming a folded ascending curtain from a cigarette, illuminated by a uniform white light. The distributed stretching histories is obvious from the different optical depths of the smoke (whose diffusivity is essentially zero) through the curtain.

time t later whose two first moments, either on a linear scale

$$\langle \ell \rangle = \int \ell \mathcal{P}(\ell, t) \mathrm{d}\ell \quad \text{and} \quad \sigma_\ell^2 = \langle \ell^2 \rangle - \langle \ell \rangle^2 \tag{40}$$

or on a logarithmic scale

$$\langle \ln \ell \rangle = \int \ln(\ell) \mathcal{P}(\ell, t) \mathrm{d}\ell \quad \text{and} \quad \sigma_{\ln \ell}^2 = \langle \ln(\ell)^2 \rangle - \langle \ln(\ell) \rangle^2 \tag{41}$$

define its width relative to its mean. Several scenarii may arise. We describe some of them, explore the consequences on the evolution of material lengths, and compare with our experimental findings.

1. **One step lengthening**
   Let $\ell = \ell_0 + \sigma t$, with the elongation rate σ distributed (different particles are lengthened at different rates, but for each fluid particle the elongation rate is constant). The distribution of length $\mathcal{P}(\ell, t) = 1/t P_\sigma((\ell - \ell_0)/t)$ is given by the distribution of σ. Consequently, $\mathcal{P}(\ell, t)$ is self-similar in ℓ as time t is varied, and the moments grow in time as $\langle \ell \rangle \sim t$, $\sigma_\ell \sim t$, $\langle \ln \ell \rangle \sim \ln t$, and $\sigma_{\ln \ell} \sim C^{te}$.

Measurements and numerical simulations in various chaotic flows by Muzzio and Ottino (see e.g. Szalai and Muzzio [2003] and references therein) indicate that the distribution of the elongation ℓ/ℓ_0 does tend asymptotically, in this context, towards a bell-shape curve translated self-similarly in log–log coordinates.

2. **One step stretching**

   Let $\ell = \ell_0 \exp(\gamma t)$, with the streching rate γ fixed but distributed among the different particles. The distribution of length $\mathcal{P}(\ell, t) = 1/(\ell t) P_\gamma(\ln(\ell/\ell_0)/t)$ gets broader with time. The distribution of $\ln(\ell)$ is similar to P_γ, and one has $\langle \ln(\ell) \rangle \sim t$ and $\sigma_{\ln(\ell)} \sim t$. The mean length $\langle \ell \rangle$ grows faster than exponentially, as is more and more impacted by higher stretching rates : for instance, with P_γ gaussian with mean $\langle \gamma \rangle$, and variance σ_γ^2, one has $\langle \ell \rangle \sim \int d\gamma \exp(\gamma t) \exp(-(\gamma - \langle \gamma \rangle)^2/2\sigma_\gamma^2)$, i.e. $\langle \ell \rangle \sim \exp(\langle \gamma \rangle t + \sigma_\gamma^2 t^2/2)$ and $\sigma_\ell \sim \exp(\langle \gamma \rangle t + \sigma_\gamma^2 t^2)$.

3. **Multistep lengthening with steps defined on determined time intervals, and stationary elongation distribution**

   Let $d\ell/dt = \sigma_i$ with the elongation σ_i fixed for one particle during the time interval $[t_i \ t_{i+1}]$. This is a typical case for application of the Central Limit Theorem : If the distribution of elongation is independent on time, and the time intervals have a constant duration, the distribution $\mathcal{P}(\ell, t)$ at large t is nearly gaussian with $\langle \ell \rangle \sim t$ and $\langle \sigma_\ell \rangle \sim \sqrt{t}$.

4. **Multistep stretching with steps defined on determined time intervals, and stationary stretching distribution**

   Let $d\ell/dt = \gamma_i \ell$ with the stretching γ_i fixed for one particle during the time interval $[t_i \ t_{i+1}]$. This is another typical case of application of the Central Limit Theorem, applied for $\ln(\ell)$. If the distribution of stretching rates is independent on time, the distribution $\mathcal{P}(\ell, t)$ at large t is nearly lognormal with $\langle \ln(\ell) \rangle \sim t$ and $\langle \sigma_{ln(\ell)} \rangle \sim \sqrt{t}$. Taking $\mathcal{P}(\ell, t)$ as an exact lognormal distribution (i.e. if the stretching rates γ_i are gaussians) leads to $\langle \ell \rangle \sim \exp(\langle \ln(\ell) + \sigma_{\ln(\ell)}^2/2) \sim \exp(\alpha t)$ and $\sigma_l \sim \exp(\langle \ln(\ell) \rangle + \sigma_{\ln(\ell)}) \sim \exp(\beta t)$ with $0 < \alpha < \beta$ two positive constants.

5. **Multistep stretching with steps defined on constant time intervals, and decaying stretching rates**

   Let $d\ell/dt = \gamma_i \ell$ with the stretching γ_i fixed for one particle during the time interval $[t_i \ t_{i+1}]$, and let the self-similar distribution of γ_i be given by $1/\langle \gamma_i \rangle P(\gamma_i/\langle \gamma_i \rangle)$. Let $\langle \gamma_i \rangle \sim t^{-\alpha}$ be a decaying function of time. $\ln(\ell)$ is a sum of random variables with mean $\langle \ln(\ell) \rangle \sim \int t'^{-\alpha} dt'$

and variance $\sigma^2_{\ln(\ell)} \sim \int dt' t'^{-2\alpha}$. Then for $1/2 < \alpha \leq 1$ the variance of the sum tends to a finite limit as time tends to infinity, whereas its mean diverges. The variance –and the shape– of the distribution of $\ln(\ell)$ is mostly determined by the first steps, and there is no convergence toward a gaussian; besides, the mean $\langle \ln(\ell) \rangle$ may tend to infinity. In such decaying stretching process, the shape of the distribution $\mathcal{P}(\ell, t)$ is essentially fixed by the first steps. The subsequent events induce a narrowing of the distribution of stretchings.

The distribution $\mathcal{P}(\ell, t)$ is nearly self similar in ℓ as time t is varied, and completely determined by the value of $\langle \ell(t) \rangle$. We can now exhibit two particular cases : If $\langle \gamma(t) \rangle = 1/t$, then $\langle \ell \rangle \sim t$ and one recovers case (1) above, whereas if $\langle \gamma(t) \rangle = 3/2t$, then $\langle \ell \rangle \sim t^{3/2}$, which is the classical Richardson dispersion.

This latter scenario is however very unlikely for turbulent flows : the particular behavior of $\mathcal{P}$ is not only due to the decay of the stretching rate, but also to a specific choice for the temporal auto-correlation of the stretching: the correlation time of the stretching in this scenario is constant, and independent on the stretching rate.

6. **Multistep stretching with decaying stretching rates, but a fixed persistency**

Stretching rates are broadly distributed in random flows (Voth et al. [2002]). However what matters as far as material length growth is concerned is the *product* of the rate of stretch by its correlation time τ, which defines the *persistency*. The stretching of a material element in turbulent flows is likely to persist for a time inversely proportional to its intensity : most likely the stretching rate γ_i at the i^{th} step is constant for a time τ_i such that $\gamma_i \tau_i \approx 1$ (Duplat and Villermaux [2000]). In this scenario, the length attained after n steps is independent of the individual trajectory ($\ell_n = \exp(n)\ell_0$), but the time t_n spent to reach this length is distributed among the particles. It is then useful to introduce the probability $\mathcal{T}(\ell, t)$ as the distribution of time t needed to reach the length ℓ. This probability is unambiguously defined as soon as we consider that ℓ is a strictly increasing function of time, so that for each trajectory there exist a unique correspondence between ℓ and t.

The relation between $\mathcal{T}$ and $\mathcal{P}$ can be obtained as follows : Let us consider a particular time t^* and a particular length ℓ^*. A certain proportion of fluid particles have a length larger than ℓ^*, at time t^* which, by definition of $\mathcal{P}$ is

$$\int_{\ell^*}^{\infty} \mathcal{P}(\ell, t^*) d\ell.$$

For these particles, the length ℓ^* was reached before the time t^*, so that this proportion is also

$$\int_0^{t^*} \mathcal{T}(\ell^*, t)dt.$$

and thus

$$\mathcal{P}(\ell^*, t^*) = -\frac{d}{d\ell}\left(\int_0^{t^*} \mathcal{T}(\ell, t)dt\right)\Bigg|_{\ell=\ell^*}. \tag{42}$$

The distribution of time $\mathcal{T}(\ell, t)$ is determined by the self similar distribution of time τ_i associated with each steps $P_{\tau,i}(\tau_i) = 1/\langle\tau_i\rangle P(\tau/\langle\tau_i\rangle)$. The decrease of the stretching rate implies that $\langle\tau\rangle \sim l^\alpha$ with $\alpha > 0$. As $\ell_i \sim \ell_0 \exp(i)$, we have $\tau_i \sim \tau_0 \exp(\alpha i)$. After n steps, the average time is $\langle t\rangle \sim \tau_0(\exp(\alpha n) - 1)/(\exp(\alpha) - 1)$. The last step lasts for a proportion $(1 - \exp(-\alpha))$ of the total duration. The variance for time after n steps is $\sigma_t^2 \sim \tau_0^2(\exp(2\alpha n) - 1)/(\exp(2\alpha) - 1)$, is also mostly given by the last step, for sufficient large α.

Then, for a stretching decaying sufficiently fast (i.e. for α sufficiently large) the distribution $\mathcal{T}(\ell, t)$ is nearly equal to the distribution for the last step. It is then characterized by a single time scale $\langle t_\ell\rangle$:

$$\mathcal{T}(\ell, t) = 1/\langle t_\ell\rangle P(t/\langle t_\ell\rangle),$$

consequently

$$\mathcal{P}(\ell, t) = \frac{d\langle t_\ell\rangle}{d\ell}\frac{1}{\langle t_\ell\rangle^2} P(t/\langle t_\ell\rangle). \tag{43}$$

The case $\alpha = 1$ corresponds to a linear growth of material lengths with time, whereas $\alpha = 2/3$ corresponds to a Richardson-like expansion ($\langle\ell^2\rangle \sim t^3$).

The scenarii described above do not cover all the possibilities but represent several relevant cases and limits. The experimental facts in section 3.1 actually suggest that the overall statistical content of the ever dispersing mixture depends solely on a single, Schmidt dependent timescale since the distributions shapes are identical, albeit a rescaling involving Sc only (see figure 5), at a given location from the source. The width of the distribution is proportional to its mean. This self-similarity property rules out cases (2) and (3) listed above and since material lines grow linearly in time, only cases (1) and (6) remain as compatible candidates to represent $\mathcal{P}(\ell, t)$. We do not consider case (5) because of the varying persistency, which is unlikely in stationary flows.

These two cases (1 and 6) lead to similar behaviors for $\mathcal{P}(\ell,t)$ and $\mathcal{T}(\ell,t)$. The latter is fully determined by the mean time $\langle t_\ell\rangle$ that grows like ℓ/u for a linear growth of material line with time. In that case, an obvious assumption is to postulate that the distribution of times to reach a length ℓ is such that

$$\int_T^\infty \mathcal{T}(\ell,t)\mathrm{d}t = \lim_{\delta t\to 0}\left(1-\frac{\delta t}{\ell/u}\right)^{T/\delta t} = e^{-uT/\ell} \tag{44}$$

according to the usual Poisson estimate, so that

$$\mathcal{T}(\ell,t) = \frac{u}{\ell}e^{-ut/\ell} \tag{45}$$

and equivalently, owing to equation (43) giving the distribution of elongations ℓ at time t as an *Inverted Gamma* distribution

$$P(\ell,t) = \frac{ut}{\ell^2}e^{-ut/\ell} \tag{46}$$

sometimes encountered in other contexts (Bouchaud and Potters [2003]).

6.2 Distribution of mixing times

Associated to the distribution of the elongation ℓ is a distribution of the mixing times t_s. Indeed, $\mathcal{T}(\ell,t)$ is defined for all length ℓ, and in particular for $\ell_s = u\langle t_s\rangle$ the elongation of the particle at the mixing time. As $\mathcal{T}(\ell,t)$ is self similar in time as ℓ is varied, $\mathcal{T}_s(t_s) = \mathcal{T}(\ell_s,t_s) = \langle t_s\rangle/\langle t_\ell\rangle\mathcal{T}(\ell,t_s\langle t_\ell\rangle/\langle t_s\rangle)$.

At a given instant of time, particles have been more elongated than others, because ℓ is distributed. As a result, some particle have not yet reached their mixing time because they have not been elongated enough and still bear the initial concentration, while some other which are more elongated have a concentration which has already started to decay.

The construction and meaning of $\mathcal{T}_s(t_s)$ is very similar to the "distribution of doubling-times" (Boffetta and Sokolov [2002], Rivera and Ecke [2005]), that is the time it takes to increase the distance between two particles by a prescribed amount. This distribution is also encountered in other contexts (Coppersmith et al. [1996]). It is found to have an exponential tail directly associated to the fact that the elongation events are Poisson distributed.

From equation (45), we thus have the distribution of mixing times as

$$\mathcal{T}_s(t_s) = \frac{1}{\langle t_s\rangle}\exp\left(-\frac{t_s}{\langle t_s\rangle}\right) \tag{47}$$

over the whole range of t_s, a distribution which was already obtained from similar arguments (Shraiman and Siggia [1994], Villermaux et al. [1998])

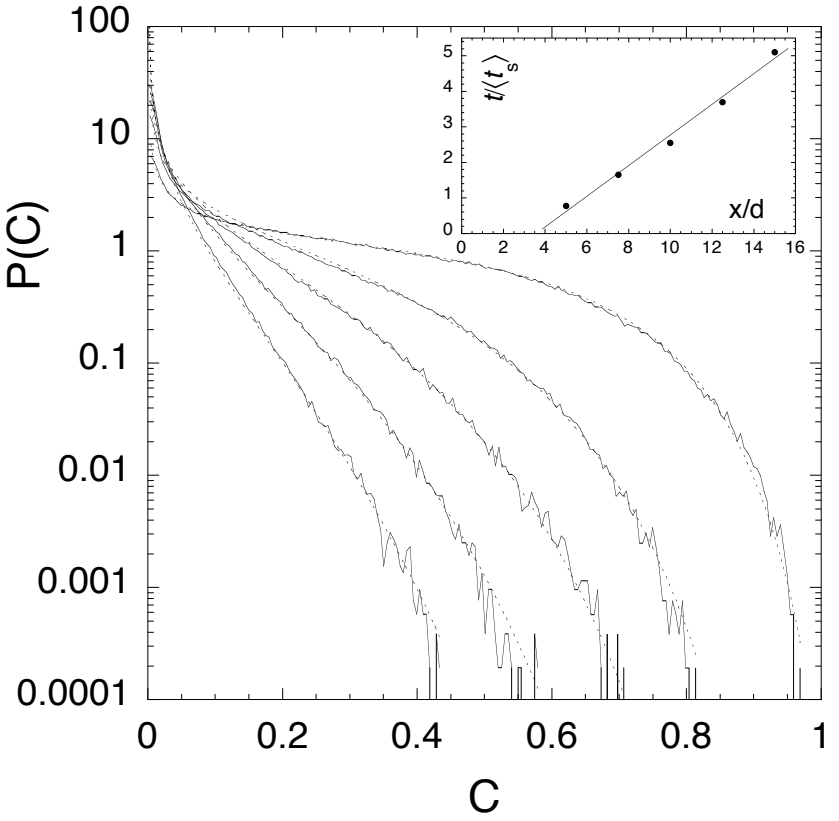

Figure 21. Concentration distributions of the ever dispersing mixture recorded at $x/d = 5, 7.5, 10, 12.5$ and 15 with $d = 0.6$ cm that is $d/L = 0.1$ and $Sc = 7$. Superimposed as a dashed line is the distribution given in equation with the reduced times $t/\langle t_s \rangle$ reported in the insert for each downstream location.

or in the short time-correlation limit (Balkovsky and Fouxon [1999]). This expression for the distribution of mixing time is consistent with any one-step scenario (i.e. case 1, 2, 5 and 6). However this particular distribution implies a particular distribution of elongation rate (case 1) and of stretching rate (case 2, 5 and 6) :

- In case (1), $\sigma = \ell_s/t_s$ so that σ is distributed as

$$P_\sigma(\sigma) = \frac{\ell_s}{\sigma^2\langle t_s\rangle}\exp\left(-\frac{\ell_s}{\sigma\langle t_s\rangle}\right).$$

- For case (2) one as $\gamma = \ln(\ell_s/\ell_0)/t_s$, so that γ is distributed as

$$P_\gamma(\gamma) = \frac{\ln(\ell_s/\ell_0)}{\gamma^2\langle t_s\rangle}\exp\left(-\frac{\ln(\ell_s/\ell_0)}{\gamma\langle t_s\rangle}\right).$$

- In case (5), the dispersion of stretching rates is due to the first step only, and one has $\ell \approx \ell_0\exp(\gamma_1\tau_1 + \int_{\tau_1}^{t} dt'\langle\gamma\rangle)$. To reach the mixing length ℓ_s the cumulative stretching of any element is fixed, so that

$$\gamma_1 = (1/\tau_1)(\ln(\ell_s/\ell_0) - \int_{\tau_1}^{t_s} dt'\langle\gamma(t')\rangle)$$

  With $\langle\gamma(t)\rangle \propto t^{-\alpha}$, $\gamma_1 = A - Bt_s^{1-\alpha}$ with A and B two positive constants. Since t_s is exponentially distributed, so that, for $t_s > \tau_1$, i.e. $\gamma_1 < \ln(\ell_s/\ell_0)/\tau_1$, one has

$$P_\gamma(\gamma_1) = \frac{1}{\langle t_s\rangle(1-\alpha)B}\left(\frac{A-\gamma_1}{B}\right)^{\frac{\alpha}{1-\alpha}}\exp\left[-\left(\frac{A-\gamma_1}{B}\right)^{\frac{1}{1-\alpha}}/\langle t_s\rangle\right].$$

- For case (6), $t_s \approx \tau_n\langle t_s\rangle/\langle\tau_n\rangle = \tau_n\ln(\ell_s/\ell_0)/\ln(\ell_n/\ell_{n-1})$ is approximately proportionnal to τ_n the duration of the last step. Since $\ell_n = \ell_{n-1}\exp(\gamma_n\tau_n)$,

$$P_\gamma(\gamma) = \frac{\ln(\ell_n/\ell_{n-1})}{\gamma^2\langle t_1\rangle}\exp\left(-\frac{\ln(\ell_n/\ell_{n-1})}{\gamma\langle\tau_n\rangle}\right),$$

  which is the same distribution as in case (2). Another way of finding the same result is to note that since the persistency of a stretching event $\gamma\tau = 1$ is fixed, the distribution of mixing times is dominated by the distribution of the last event, which lasts for a time τ. With τ distributed exponentially, the stretching rate is distributed like

$$P_\gamma(\gamma) = \frac{1}{\gamma^2\langle\tau\rangle}\exp\left(-\frac{1}{\gamma\langle\tau\rangle}\right).$$

6.3 Concentration distribution

Finally, the distribution of concentration $P(C,t)$ derives from similar arguments. Similarly as the way $\mathcal{P}(\ell,t)$ is deduced from $\mathcal{T}(\ell,t)$, one may define $\mathcal{T}(C,t)$ the distribution of time at which a certain level of concentration C is reached. Since C is a decreasing function of time

$$P(C^*,t^*) = + \frac{d}{dC}\left(\int_0^{t^*} \mathcal{T}(C,t)dt\right)\Bigg|_{C=C^*}. \tag{48}$$

$\mathcal{T}(C,t)$ results of a one dominating step process, and is therefore a self-similar function of time, as the concentration C is varied. It is completely defined by the distribution of mixing time $\mathcal{T}_s(t_s)$ (see equation (47)) and the average time associated to each concentration level $\langle t_C\rangle$. The latter is given by the time dependence of the concentration $C(t)$ of a fluid particle before, and after the mixing time given by the microscopic convection–diffusion problem. We have showed in section 5 that $C(t)$ remains close to 1 for $t \ll t_s$ and that $C(t) = (\sigma s_0^2/D)^{1/2}(\sigma t)^{-\nu}$ with $\nu = 5/2$ for $t \gg t_s$. A convenient (but not restrictive) crossover function bridging these two extremes is

$$C(t) = \left(1 + \frac{t}{t_s}\right)^{-\nu} \tag{49}$$

leading to

$$\langle t_C\rangle = \langle t_s\rangle \left(C^{-1/\nu} - 1\right), \tag{50}$$

and providing finally the concentration distribution $P(C,t)$ as a function of time

$$P(C,t) = \frac{\tilde{t}}{\nu}\frac{C^{-\frac{1+\nu}{\nu}}}{(C^{-\frac{1}{\nu}}-1)^2}\exp\left(-\frac{\tilde{t}}{C^{-\frac{1}{\nu}}-1}\right) \tag{51}$$

where $\tilde{t} \equiv t/\langle t_s\rangle$.

The change of variables $c = C^{-1/\nu} - 1$ allows to compute all the moments $\langle C^q\rangle$ of $P(C)$ as

$$\langle C^q\rangle = \int_0^1 C^q P(C)\mathrm{d}C = \tilde{t}\int_0^\infty \frac{(1+c)^{\nu q}}{c^2} e^{-\frac{\tilde{t}}{c}}\mathrm{d}c \tag{52}$$

which are given by

$$\langle C^q\rangle = \Gamma(1+\nu q)U(\nu q, 0, \tilde{t}) \tag{53}$$

where Γ and U are the Gamma and the Confluent Hypergeometric functions, respectively. The asymptotic behavior in time is $\langle C^q\rangle \xrightarrow{t\to\infty} \Gamma(1+\nu q)t^{-\nu q}$

(Abramowitz and Stegun [1964]) so that the width of the distribution becomes of the order of the mean

$$\frac{\langle C^2\rangle}{\langle C\rangle^2} \sim \frac{\Gamma(1+2\nu)}{\Gamma(1+\nu)^2} \xrightarrow{\nu=5/2} \frac{512}{15\pi} \tag{54}$$

As can be seen on figure 21 where equation (51) fits the experimental distributions over the entire concentration range. The slight mismatch at large excursion reflects the fact that sheets do slightly interact in this flow, and aggregate in a way discussed in Duplat and Villermaux [2008], but in an extent that does not alter much $P(C,t)$. Signs of aggregation between the sheets will be further given section 8.

Of particular interest is the behavior of the distribution of equation (51) around its inflection point as this makes contact with the direct measurements presented in section 3.1. The local slope at that point was found to steepen linearly in time, with a prefactor depending on the scalar diffusivity (figure 5). The shape of $P(C)$ about its inflection point (in log–lin scales) is essentially dominated by the exponential factor $\exp(-\tilde{t}/(C^{-\frac{1}{\nu}}-1))$ so that $\partial^2 \ln P(C)/\partial C^2 = 0$ for

$$C^* = \left(\frac{\nu-1}{\nu+1}\right)^{\nu} \tag{55}$$

and that

$$\left.\frac{\partial \ln P}{\partial C}\right|_{C^*} = -\frac{(\nu-1)^2}{4\nu}\left(\frac{\nu+1}{\nu-1}\right)^{\nu+1}\tilde{t} \tag{56}$$

which actually represents precisely the observed trends for $P(C)$, an exponential shape with an argument increasing in proportion of time like $t/\langle t_s\rangle$, as seen on figure 5.

The agreement of this prediction with the experimental measurements indicates a posteriori the relevant limits and mechanisms involved in the process :

- Individual trajectories result from a complex, time dependent, possibly sequential stirring process, however the effective stretching rate is dominated by the last step sampled in the distribution, consistent with an effective one step lengthening process (scenario (1)): the standard deviation of $P(\ell,t)$ is proportional to its mean.
- Consequently, the distribution of mixing times has a single characteristic timescale $\langle t_s\rangle$. It is exponential, as for a Poisson process.
- The average growth of material lines is linear, which implies an algebraic decay of the individual concentration levels $C(t)$ with $\nu = 5/2$.

7 Kinetics

The rate of deformation in time of the distributions $P(C)$ is prescribed by a characteristic time, i.e. the mixing time t_s. For the particular flows we have in the present experiments, where material lines grow linearly in time like σt, in three dimensions, we have shown in section 5 that this time writes

$$t_s \sim \frac{1}{\sigma}\left(\frac{\sigma s_0^2}{D}\right)^{1/5} \tag{57}$$

where s_0 is the initial size of the scalar blobs subsequently stretched into sheets. The composition of the medium solely depends on $x/d = ut/d \sim t/t_s$ in the dispersing mixture suggesting that the mixing time t_s scales like $\sigma^{-1} \sim d/u$ in that case. The mixture composition depends on x/L in the confined case, where L is the channel width, suggesting that $t_s \sim L/u$ in this other situation (see also Duplat and Villermaux [2008]).

The fair *independence* of both the shape of $P(C)$, and of its rate of deformation with the flow Reynolds number (see figures 5 and 8) suggests that this characteristic time is itself independent of Re. That independence is recovered if the size s_0 is itself a function of the elongation rate. The typical scale of the velocity gradient in a turbulent flow is given by the balance between the stretching time σ^{-1}, and the time of diffusion of vorticity s_0^2/ν with ν the kinematic viscosity of the fluid. This defines

$$s_0 \sim \sqrt{\frac{\nu}{\sigma}} \tag{58}$$

as an analogous to the Taylor microscale of the flow (Taylor [1935], Pope [2000]). This scale represents the transverse size of the sheets initially "peeled-off" from the source by the (unsteady) relative motions in the flow. This observation is consistent with the one step lengthening process of scenario (1) in section 6 (see also Villermaux et al. [1998], and Villermaux and Rehab [2000] for an example with a sustained shear). With this estimate, the mixing time above becomes

$$t_s \sim \frac{1}{\sigma} Sc^{1/5} \tag{59}$$

where $Sc = \nu/D$ is the Schmidt number, and is indeed independent of the Reynolds number. The quantitative comparison on figure 21 indicates that $t_s \approx 2d/u$ for $Sc = 7$ in the dispersing mixture with r.m.s. velocity such that $u'/u \approx 0.25$, so that $t_s \approx 1.35(d/u)Sc^{1/5}$ or $t_s \approx 0.4(d/u')Sc^{1/5}$. A fluid particle emanating from a source of size d such that, say, $d/L \approx 0.1$

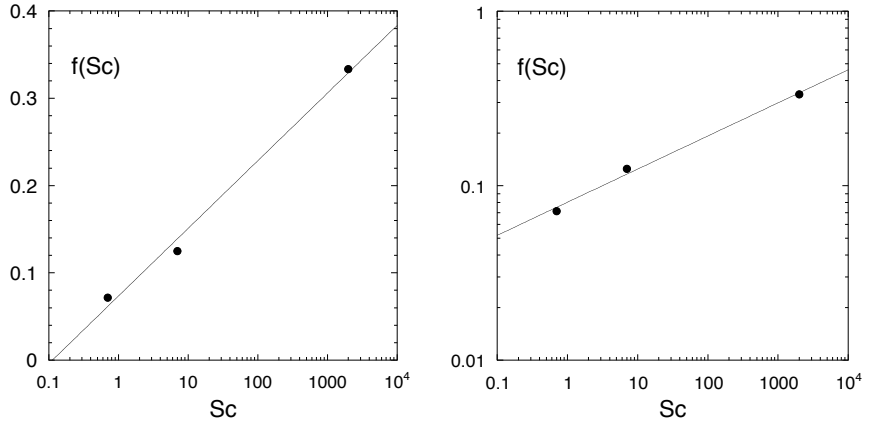

Figure 22. Dependence on the Schmidt number $f(Sc)$ of the argument α in the exponential wings at the inflexion point of the distributions $P(C)$ for the ever dispersing mixture (section 3.1). Left: Logarithmic adjustment. Right: Power law adjustment. The line has a slope equal to 1/5.

has thus experienced roughly $(L/u)/t_s \approx 5$ mixing times during its transit within a local integral scale L. The mixture has thus appreciably decayed within a stationary stirring field.

For the confined mixture, the residence time of the mixture in the channel spans many stirring times L/u and thus $\sigma \sim u/L$ providing $t_s \sim (L/u)Sc^{1/5}$, consistently with the observations of figures 5 and 8. These are fully compatible with Yeung [2001] who finds from Direct Numerical Simulations that the Lagrangian correlation time of the scalar is of the order of the integral timescale, independently of the Reynolds number.

7.1 Power law versus exponential

Although the flow is turbulent in both the channel and the free jet experiment, material lines grow in proportion to time instead of exponentially. This apparent power law has several causes, and may be interpreted as a transient effect reflecting the birth of an ultimate, genuine exponential regime.

In addition, the essentially identical description between the exponential and the power law stretchings is further assessed by the Schmidt number dependence of the mixing time revealed, for instance, by the slopes α of the histograms $P(C)$ of the ever dispersing mixture (figure 5). The exponen-

tial stretching anticipates $\alpha \sim \ln(Sc)$ while the linear stretching in three dimensions rather predicts $\alpha \sim Sc^{1/5}$, as shown in section 5. As can be seen from figure 22, deciding between the two trends is a matter of mood, although the Schmidt number varies on three orders of magnitude. The indecidability comes from the fact that a weak power law (in the present case 1/5) mimics a logarithmic behavior.

8 Lengthscales and Spectra

We describe some geometric aspects of the mixture and comment on their relationship with the mechanisms building the concentration field itself.

8.1 Scalar support lengthscales

The concentration signal recorded at one point downstream of the source in the ever dispersing mixture is organized as a succession of blobs and voids (see figure 3). These blobs are the trace of bundles of merged sheets. Let $P(r)$ be the distribution of the blobs transverse thickness, and $Q(r)$ that of the voids. Those two distributions are extracted from the temporal traces of the concentration signal owing to Taylor hypothesis in this advected flow. It is observed from figure 23 that $P(r)$ is well represented by

$$P(r) \approx \frac{1}{r} \exp\left(-\alpha \frac{C_s t}{d/u'} \frac{r}{L}\right), \tag{60}$$

where α depends on the Schmidt number. The physical content of equation (60) is readily understood as a Poisson process. Denote by $f = \int_{C_s}^{\infty} P(C)\mathrm{d}C$ the probability to find a concentration level larger than C_s at that location in the flow. Let η be the smallest size of the scalar field (i.e. spectrum cut-off or minimum coarse grained scale). The probability that a blob has a size $r + \delta r$ is obviously

$$P(r+\delta r) = P(r) f^{\frac{\delta r}{\eta}} \xrightarrow{\frac{\delta r}{\eta} \ll 1} P(r)\left(1 + \frac{\delta r}{\eta} \ln f\right). \tag{61}$$

Therefore $P(r) \sim \exp(\frac{r}{\eta} \ln f)$ and with $f \sim \exp(-\frac{t}{t_s} C_s)$ characteristic of the ever dispersing mixture, one expects

$$P(r) \sim \exp\left(-\frac{t}{t_s} C_s \frac{r}{\eta}\right) \tag{62}$$

which, with $\eta \sim LSc^{-2/5}$ (see the coarse grained scale in Duplat and Villermaux [2008]), reproduces the tails of the experimental distributions adequately in shape, and parameter dependences.

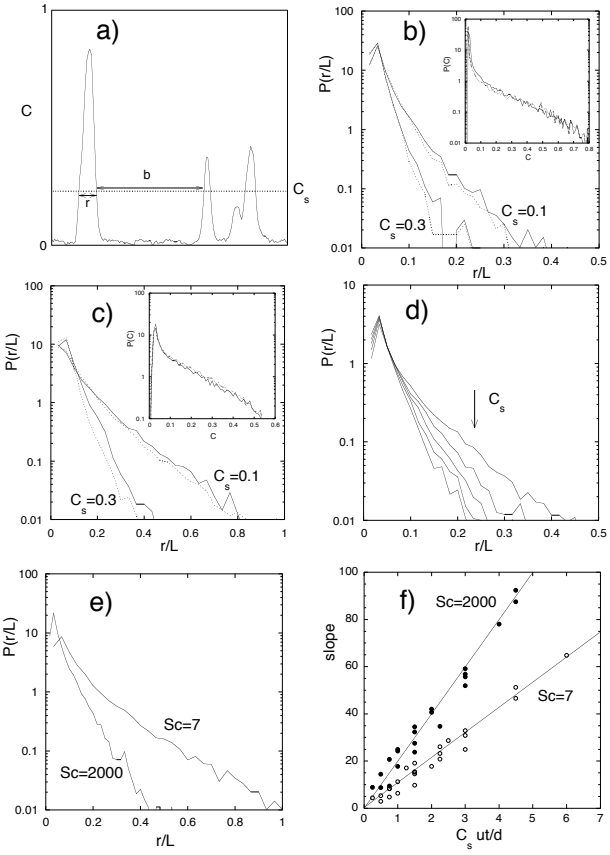

Figure 23. Distribution of the blobs widths $P(r)$ and its sensivity to the experimental parameters. a) definition sketch of the width r and void b between two adjacent blobs. b) Distribution $P(r)$ at $ut/d = 10$ and corresponding concentration distributions (insert) for $d = 3$ mm (dashed line) and $d = 6$ mm (continuous line) and for two values of the concentration threshold at $Sc = 2000$. c) Distribution $P(r)$ at $ut/d = 7.5$ and corresponding concentration distributions (insert) for $d = 3$ mm (dashed line) and $d = 6$ mm (continuous line) and for two values of the concentration threshold at $Sc = 7$. d) Distribution $P(r)$ at $ut/d = 5$ for $d = 6$ mm for increasing values of the concentration threshold ($C_s = 0.1, 0.2, 0.3, 0.4, 0.5$ in the direction of the arrow) at $Sc = 2000$. e) Distribution $P(r)$ at $ut/d = 5$ for $d = 6$ mm for two values of the Schmidt number at fixed concentration threshold $C_s = 0.2$. f) Argument of the tail of $P(r)$ in equation (60) for various d and C_s and two values of Sc.

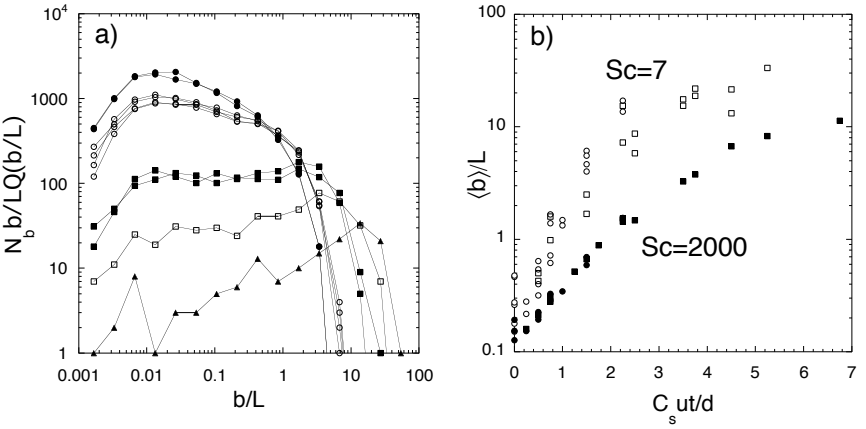

Figure 24. Distribution of the voids lengths and average void size. a) inter-blobs voids widths distribution $Q(b/L)$ multiplied by b/L and by the total number of voids N_b in the signal for the corresponding conditions: $C_s ut/d = 0.25$, •; $C_s ut/d = 0.75$, ◯; $C_s ut/d = 2.25$, ■; $C_s ut/d = 3.75$, □; $C_s ut/d = 4.25$ ▲ for both $d = 3$ mm and $d = 6$ mm and for $0.1 < C_s < 0.3$. $Sc = 2000$. The number of voids diminishes with downstream distance and small voids disappear at the expense of the formation of larger and larger voids. b) Average void size $\langle b \rangle$ as a function of downstream distance for two Schmidt numbers.

The distribution of the voids $Q(b)$ has a power-law like shape up to a sharp cut-off $\mathcal{C}(b/b^*)$ at a void size b^* increasing exponentially with downstream distance.

$$Q(b) \sim \left(\frac{b}{L}\right)^{-\zeta} \mathcal{C}\left(\frac{b}{b^*}\right), \tag{63}$$

The apparent exponent ζ is of order unity, slightly decreasing, and

$$b^* \sim \langle b \rangle \sim \exp\left(\frac{t}{t_s} C_s\right), \tag{64}$$

as shown on figure 24. The average void size increase follows the dependence of the cut-off void size b^* with downstream distance. The number of voids diminishes with downstream distance and small voids disappear at the expense of the formation of larger and larger voids. Note that the average void can be as large as 10 local integral scale L.

8.2 Spectra

It is a notorious fact that a scalar mixture with concentration field $C(\mathbf{r}, t)$ stirred in a turbulent fashion ($Re = u'L/\nu \gg 10^4$) displays a power spectrum

$$F(k,t) \sim \left\langle \left(\int C(\mathbf{r},t) e^{i\mathbf{k}.\mathbf{r}} \mathrm{d}\mathbf{r} \right)^2 \right\rangle \tag{65}$$

proportional to $k^{-5/3}$ in the well-mixed limit that is far from the sources and for $t \gg t_s$ (Onsager [1949], Obukhov [1949], Corrsin [1951]). An example can be seen on figure 25.

It is conversely also known that for a very intermittent scalar field for which the fluctuations of concentration are of the order of the mean, as for instance in the near field of a spatially localized scalar injection, the spectral signature is essentially k^{-1} in the inertial range of scales (Villermaux et al. [2001]). Some measurements also report an intermediate, power law-like spectrum whose exponent depends on the Reynolds number, increasing in absolute value from 1 towards 5/3 for increasing Reynolds number (Miller and Dimotakis [1996], Sreenivasan [1996], Mydlarski and Warhaft [1998], Warhaft [2000]). It has been suggested that this crossover, notably observed in shear flows, is a sign of a large scale persistent shear which alters the pair dispersion law (Celani et al. [2005]).

As outlined above, the blobs and voids widths are broadly distributed in the ever dispersing mixture. The concentration within each blob is itself variable, and its statistics is the concentration distribution $P(C)$ at that location in the flow. We show below how the knowledge of the distributions of the blobs $P(r)$ and that of the voids $Q(b)$ fully determine the shape of the concentration power spectrum $F(k)$.

Spectrum of a random square wave signal We schematically represent the concentration signal (i.e. a one-dimensional cut through the scalar field) as a set of consecutive blobs starting at x_i, ending at y_i with amplitude C_i for the blob number i. The concentration signal thus writes formally

$$C(x) = \sum_i C_i \left(H(x - x_i) - H(x - y_i) \right) \tag{66}$$

where H is a Heavyside function (figure 3). The signal spectrum $F(k)$ is the square of its Fourier transform

$$F(k) = \int e^{ikr} \langle C(x) C(x+r) \rangle dr = \hat{C}(k) \hat{C}^*(k) \tag{67}$$

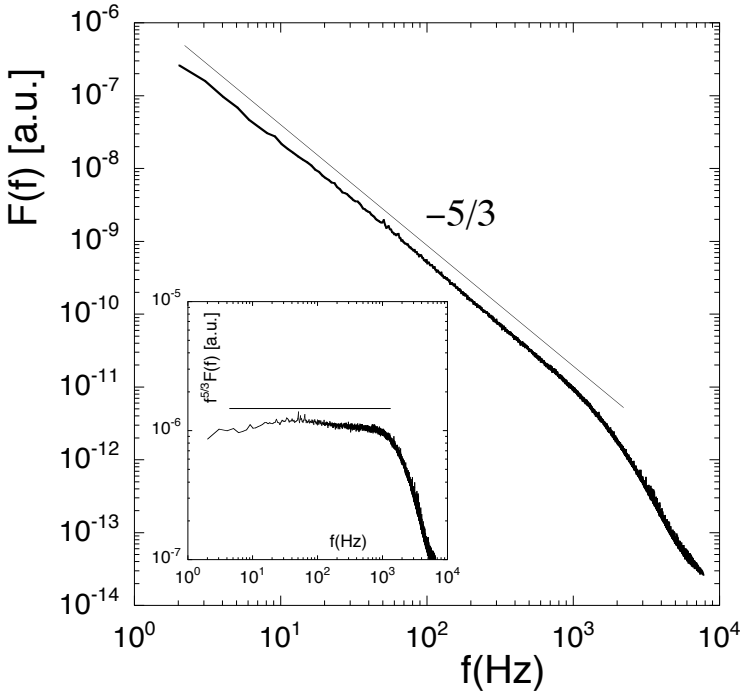

Figure 25. Spectrum of temperature temporal fluctuations recorded at one point in the Modane wind tunnel. Frequencies actually mean wavenumbers through a constant convection velocity of the order of 30 m/s. The Taylor scale based Reynolds number is $R_\lambda = \sqrt{Re} \approx 3000$ (adapted from Gagne et al. [1999]).

where $\hat{C}$ is the Fourier transform of C and $\hat{C}^*$ its complex conjugate. With

$$\hat{C}(k) = \sum_i C_i \frac{1}{k} \left(e^{iky_i} - e^{ikx_i} \right) \tag{68}$$

one has

$$F(k) = \sum_{i,i'} C_i C_{i'} \frac{1}{k^2} \left(e^{ik(y_i - y_{i'})} + e^{ik(x_i - x_{i'})} - e^{ik(y_i - x_{i'})} - e^{ik(x_i - y_{i'})} \right) \tag{69}$$

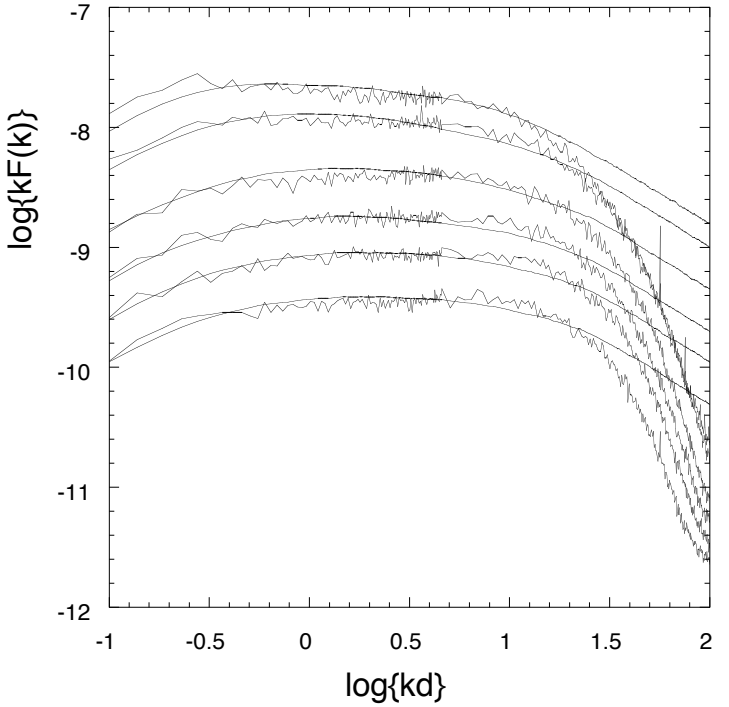

Figure 26. Compensated power spectra $kF(k)$ of the scalar fluctuations at different successive times compared to the expected shape ($kd = d/r$). $Sc = 2000$, $d/L = 0.1$, $L = 6$ cm, $u = 0.4$ m/s. In the direction of the arrow, $x = ut = 1.5$, 3, 4.5, 6, 7.5 and 9 cm.

The change of indices $j = i' - i$ leads to

$$F(k) = \sum_{i,j} \frac{C_i C_{i+j}}{k^2} \left(e^{ik(y_i - y_{i+j})} + e^{ik(x_i - x_{i+j})} - e^{ik(y_i - x_{i+j})} - e^{ik(x_i - y_{i+j})} \right) \tag{70}$$

We proceed with the two following assumptions, well verified in practice:

- The distributions of the blobs $P(r)$ and of the voids $Q(r)$ are statistically independent. In particular, there is no correlation between the sizes of two neighboring blobs.
- The amplitude C_i is independent of the blob size.

Thus for a given index j,

$$\sum_i C_i C_{i+j} \frac{1}{k^2} \left(e^{ik(y_i - y_{i+j})} \right) \tag{71}$$

is given by the Fourier transform of the probability to find two blobs of concentrations C_i and C_{i+j} and whose ends are at a distance $\delta = (y_i - y_{i+j})$ apart. The sum over all i ensures that all combinations have been accounted for. The trivial case $j = 0$ leads to

$$\frac{N}{k^2} \langle C^2 \rangle \tag{72}$$

where N is the number of blobs, and $\langle C^2 \rangle$ is the average of the C_i^2. When $j > 0$ in the interval $[y_i \; y_{i+j}]$, one finds j voids and j blobs. The probability $\mathcal{P}_j$ that $\delta = y_{i+j} - y_i$ is thus, since no correlation is assumed between neighbors is the probability that j voids and j blobs put together have a total length δ. This probability is given by the convolution of j times the probability P times the convolution of j times the probability Q

$$\mathcal{P}_j = P^{\otimes j} \otimes Q^{\otimes j}. \tag{73}$$

which translates in the Fourier domain in

$$\hat{\mathcal{P}}_j = \hat{P}^j \hat{Q}^j. \tag{74}$$

The weighting factor $C_i C_{i+j}$ is independent of j and is $\langle C^2 \rangle$, thus

$$\sum_i C_i C_{i+j} \frac{1}{k^2} \left(e^{ik(y_i - y_{i+j})} \right) = \frac{N}{k^2} \langle C \rangle^2 \hat{P}^{*j} \hat{Q}^{*j}. \tag{75}$$

and for $j < 0$ one has equivalently

$$\sum_i C_i C_{i+j} \frac{1}{k^2} \left(e^{ik(y_i - y_{i+j})} \right) = \frac{N}{k^2} \langle C \rangle^2 \hat{P}^{-j} \hat{Q}^{-j}. \tag{76}$$

A similar treatment of the other terms in equation (69) leads finally to

$$F(k) = \frac{N}{k^2} \left(\begin{array}{l} \langle C^2 \rangle (2 - \hat{P}(k) - \hat{P}^*(k)) \\ + \langle C \rangle^2 (-\hat{Q}(k) - \hat{Q}^*(k)) \\ + \langle C \rangle^2 \sum_{j \geq 0} (2 - \hat{P}(k) - \hat{Q}(k)) (\hat{P}(k) \hat{Q}(k))^j \\ + \langle C \rangle^2 \sum_{j \geq 0} (2 - \hat{P}^*(k) - \hat{Q}^*(k)) (\hat{P}^*(k) \hat{Q}^*(k))^j \end{array} \right) \tag{77}$$

that is

$$F(k) = \frac{2N}{k^2}\left((\langle C^2\rangle - \langle C\rangle^2)Re\left(1-\hat{P}\right) + \langle C\rangle^2 Re\left(\frac{(1-\hat{P})(1-\hat{Q})}{(1-\hat{P}\hat{Q})}\right)\right) \tag{78}$$

or

$$F(k) = \frac{2N}{k^2}\left((\langle C^2\rangle - \langle C\rangle^2)Re(1-\hat{P}) + \langle C\rangle^2 Re(S)\right) \tag{79}$$

with

$$\frac{1}{S} = \frac{1}{1-\hat{P}} + \frac{1}{1-\hat{Q}} - 1. \tag{80}$$

Note finally that $\frac{1-\hat{P}}{ik} = \hat{\mathcal{P}}$ if $\mathcal{P}(r) = \int_r^\infty P(r')dr'$ denotes the probability that a blob has a size larger than r. One thus has

$$F(k) = \frac{2N}{k}\left((\langle C^2\rangle - \langle C\rangle^2)Im(\hat{\mathcal{P}}) + \langle C\rangle^2 Re(S')\right) \tag{81}$$

with

$$\frac{1}{S'} = -k - \frac{i}{\hat{\mathcal{P}}} - \frac{i}{\hat{\mathcal{Q}}}. \tag{82}$$

The comparison of the calculated and experimental spectra is shown on figure 26. The knowledge of the statistics of the blobs and of the voids sizes implies the shape of the spectrum. Precisely, since $\mathcal{P}$ decays faster than $\mathcal{Q}$, the shape of the spectrum is essentially fixed by the distribution of the voids $\mathcal{Q}$, by contrast with usual interpretations of the Batchelor regime in scalar turbulence (Batchelor [1959], Kraichnan [1974]). The slow decay of the theoretical spectrum at large k is an artifact of the discontinuous edges of the blobs (square wave signal). In reality, the edges are smooth (with a width given by the Batchelor scale), and the spectrum fall-off is steeper, as the experiment shows.

9 Conclusion

The evolution of the concentration level C of a fluid particle in a deforming substrate results from the balance between the substrate rate of deformation and molecular diffusion. The microscopic associated problem is solved in closed form (section 5), illustrating the central concept of the *mixing time* t_s.

The natural randomness among the fluid particles net elongation at a given instant of time induces a distribution of the mixing times from which molecular diffusion becomes effective in erasing the concentration differences. This ingredient, analyzed in section 6 has been found to represent

very accurately the evolution of the concentration distribution of $P(C,t)$ in an ever dispersing mixture. Its shape and rate of deformation is found to depend on a single, Schmidt number dependent timescale $\langle t_s \rangle$ (section 3.1).

The analysis suggests that the mixture composition results from a one step lengthening process distributed among the sheets, as opposed to a sequential cascade of uncorrelated stretchings. It infers a prediction for the corresponding distribution of the mixing times (equation (47)) consistent with earlier predictions (Shraiman and Siggia [1994], Chertkov et al. [1995], Villermaux et al. [1998], Balkovsky and Fouxon [1999]) and finally a detailed analytic description of $P(C,t)$ (equation (51)).

The ever dispersing limit reveals the distribution of individual trajectories within the mixture inherent to turbulent motions among fluid particles evolving essentially independently of each other. This is no more true when the spatial density of particles is increased so that their mutual interaction is enforced. The composition $P(C,t)$ given in equation (51) is only valid for a single plume dispersing in a large scale stirring field. As soon as multiple sources are present, the picture is different. More generally, a set of constantly overlapping and merging sheets selects a different route towards uniformity, which is examined in Duplat and Villermaux [2008].

Bibliography

M. Abramowitz and A. Stegun, I. *Handbook of Mathematical Functions.* Dover Publications, Inc., New York., 1964.

C. J. Allègre and D. L. Turcotte. Implications of a two-component marble-cake mantle. *Nature*, 323:123–127, 1986.

E. Balkovsky and A. Fouxon. Universal long-time properties of lagrangian statistics in the batchelor regime and their application to the passive scalr problem. *Phys. Rev. E.*, 60((4)):4164–4174, 1999.

G. K. Batchelor. Small-scale variation of convected quantities like temperature in a turbulent fluid. part 1. general discussion and the case of small conductivity. *J. Fluid Mech.*, 5:113–133, 1959.

D. Beigie, A. Leonard, and S. Wiggins. A global study of enhanced stretching and diffusion in cahotic tangles. *Phys. Fluids A*, 3((5)):1039–1050, 1991.

R. Betchov. An inequality concerning the production of vorticity in isotropic turbulence. *J. Fluid Mech.*, 1:497–504, 1956.

G. Boffetta and I. M. Sokolov. Statistics of two-particle dispersion in two-dimensional turbulence. *Phys. Fluids*, 14((9)):3224–3232, 2002.

J.-P. Bouchaud and M. Potters. *Theory of Financial Risks and Derivative Pricing.* Cambridge University Press., 2003.

B. Castaing, G. Gunaratne, F. Heslot, L. Kadanoff, A. Libchaber, S. Thomae, X. Z. Wu, S. Zaleski, and G. Zanetti. Scaling of hard thermal turbulence in rayleigh-benard convection. *J. Fluid Mech.*, 204:1–30, 1989.

H. J. Catrakis and P. E. Dimotakis. Mixing in turbulent jets: scalar measures and isosurface geometry. *J. Fluid Mech.*, 317:369–406, 1996.

A. Celani, M. Cencini, M. Vergassola, E. Villermaux, and D. Vincenzi. Shear effects on passive scalar spectra. *J. Fluid Mech.*, 523:99–108, 2005.

M. Chertkov, G. Falkovich, I. Kolokolov, and V. Lebedev. Statistics of a passive scalar advected by a large scale two-dimensional velocity field: Analytic solution. *Physical Review E*, 51(6):5609, 1995.

W. J. Cocke. Turbulent hydrodynamic line-stretching: The random walk limit. *Phys. Fluids*, 14((8)):1624–1628, 1971.

S. N. Coppersmith, C. h. Liu, S. Majumdar, O. Narayan, and T. A. Witten. Model for force fluctuations in bead packs. *Phys. Rev. E*, 53((5)):4673–4685, 1996.

S. Corrsin. On the spectrum of isotropic temperature fluctuations in an isotropic turbulence. *J. Appl. Phys.*, 22:469–473, 1951.

R. L. Curl. Dispersed phase mixing: I. theory and effect in simple reactors. *AIChE J.*, 9((2)):175–181, 1963.

P. E. Dimotakis. Turbulent mixing. *Annu. Rev. Fluid Mech.*, 37:329–356, 2005.

P. E. Dimotakis and H. J. Catrakis. Turbulence, fractals and mixing. In H. Chaté, E. Villermaux, and J. M. Chomaz, editors, *Mixing Chaos and Turbulence*. Kluwer Academic/Plenum Publishers, New York., 1999.

C. Dopazo. Recent developments in pdf methods. In P. A. Libby and F. A. Williams, editors, *Turbulent Reacting Flows*, chapter 7. Academic Press, 1994.

J. Duplat and E. Villermaux. Persistency of material element deformation in isotropic flows and growth rate of lines and surfaces. *Eur. Phys. J. B*, 18:353–361, 2000.

J. Duplat and E. Villermaux. Mixing by random stirring in confined mixtures. *J. Fluid Mech.*, 617:51–86, 2008.

C. Eckart. An analysis of the stirring and mixing processes in incompressible fluids. *J. Mar. Res.*, 7:265–275, 1948.

G. Falkovich, K. Gawedzki, and M. Vergassola. Particles and fields in fluid turbulence. *Rev. Mod. Phys.*, 73((4)):913–975, 2001.

A. Fannjiang, S. Nonnenmacher, and L. Wolonski. Dissipation time and decay of correlations. *Nonlinearity*, 17:1481–1508, 2004.

D. R. Fereday and P. H. Haynes. Scalar decay in two-dimensional chaotic advection and batchelor-regime turbulence. *Phys. Fluids*, 16(12):4359–4370, 2004.

J. Fourier. *Théorie analytique de la chaleur*. Firmin Didot, Paris., 1822.
R. O. Fox. *Computational Models for Turbulent Reacting Flows*. Cambridge University Press., 2004.
Y. Gagne, E. Villermaux, J. Duplat, and C. Auriault. Etude expérimentale du scalaire passif et du mélange en turbulence. *DGA Report, DGA/DSP*, 97/1045, 1999.
J. W. Gibbs. *Elementary Principles in Statistical Mechanics*. Reprint Ox Bow Press, Woodbridge, 1981., 1901.
S. S. Girimaji and S. B. Pope. Material-element deformation in isotropic turbulence. *J. Fluid Mech.*, 220:427–458, 1990.
A. Groisman and V. Steinberg. Efficient mixing at low reynolds numbers using polymer additives. *Nature*, 410:905–908, 2001.
E. J. Hinch. Mixing, turbulence and chaos–an introduction. In H. Chaté, E. Villermaux, and J. M. Chomaz, editors, *Mixing Chaos and Turbulence*. Kluwer Academic/Plenum Publishers, New York., 1999.
M. Holzer and E. D. Siggia. Turbulent mixing of a passive scalar. *Phys. Fluids*, 6((5)):1820–1837, 1994.
Jayesh and Z. Warhaft. Probability distributions of a passive scalar in grid-generated turbulence. *Phys. Rev. Letters*, 67((25)):3503–3506, 1991.
Jayesh and Z. Warhaft. Probability distributions, conditional dissipation, and transport of passive temperature fluctuations in grid-generated turbulence. *Phys. Fluids A*, 4((10)):2292–2307, 1992.
M. C. Jullien, P. Castiglione, and P. Tabeling. Experimental observation of batchelor dispersion of passive tracers. *Phys. Rev. Letters*, 85((17)): 3636–3639, 1980.
J. Kalda. Simple model of intermittent passive scalar turbulence. *Phys. Rev. Letters*, 84:471–474, 2000.
S. Kida and S. Goto. Line statistics: Stretching rate of passive lines in turbulence. *Phys. Fluids*, 14((1)):352–361, 2002.
R. H. Kraichnan. Convection of a passive scalar by a quasi-uniform random field. *J. Fluid Mech.*, 64(4):737–762, 1974.
A. Lavertu and L. Mydlarski. Scalar mixing from a concentrated source in a turbulent channel flow. *J. Fluid Mech.*, 528:135–172, 2005.
M. A. Levèque. Les lois de la transmission de la chaleur par convection. *Ann. Mines*, 13:201–239, 1928.
F. E. Marble. Mixing, diffusion and chemical reaction of liquids in a vortex field. In M. Moreau and P. Turq, editors, *Chemical Reactivity in Liquids: Fundamental Aspects*. Plenum Press., 1988.
F. E. Marble and J. E. Broadwell. The coherent flame model for turbulent chemical reactions. *Project SQUID, Tech. Rep. TRW-9-PU*, 1977.
P. Meunier and E. Villermaux. How vortices mix. *J. Fluid Mech.*, 476: 213–222, 2003.

P. L. Miller and P. E. Dimotakis. Measurements of scalar power spectra in high schmidt number turbulent jets. *J. Fluid Mech.*, 308:129–146, 1996.
W. D. Mohr, R. L. Saxton, and C. H. Jepson. Mixing in laminar-flow systems. *Industrial and Engineering technology*, 49((11)):1855–1856, 1957.
L. Mydlarski and Z. Warhaft. Passive scalar statistics in high peclet number grid turbulence. *J. Fluid Mech.*, 358:135–175, 1998.
S. Nagata. *Mixing, Principles and Applications*. John Wiley & sons, New York., 1975.
A. M. Obukhov. Structure of the temperature field in a turbulent flow. *Izv. Acad. Nauk SSSR, Geogr. i Geofiz*, 13:58–69, 1949.
L. Onsager. Statistical hydrodynamics. *Nuovo Cimento*, VI((IX)):279–287, 1949.
J. M. Ottino. *The Kinematics of Mixing: Stretching, Chaos, and Transport*. Cambridge University Press., 1989.
J.M. Ottino. Mixing, chaotic advection and turbulence. *Annu. Rev. Fluid Mech.*, 22:207–253, 1990.
S. B. Pope. *Turbulent Flows*. Cambridge University Press., 2000.
S. B. Pope. Pdf methods for turbulent reacting flows. *Prog. Energy Combust. Sci.*, 11:119–192, 1985.
A. Pumir, B. I. Shraiman, and E. D. Siggia. Exponential tails and random advection. *Phys. Rev. Letters*, 66((23)):2984–2987, 1991.
W. E. Ranz. Application of a stretch model to mixing, diffusion and reaction in laminar and turbulent flows. *AIChE Journal*, 25((1)):41–47, 1979.
L. F. Richardson. Atmospheric diffusion shown on a distance-neighbour graph. *Proc. R. Soc. Lond. A*, 110:709–737, 1926.
M. K. Rivera and R. E. Ecke. Pair dispersion and doubling time statistics in two-dimensional turbulence. *Phys. Rev. Letters*, 95:194503., 2005.
H. Schlichting. *Boundary Layer Theory*. McGraw-Hill, Inc., New York., 1987.
B. I. Shraiman and E. D. Siggia. Scalar turbulence. *Nature*, 405:639–646, 2000.
B. I. Shraiman and E. D. Siggia. Lagrangian path integrals and fluctuations in random flows. *Phys. Rev. E*, 49:2912–2927, 1994.
C. Simonet and A. Groisman. Chaotic mixing in a steady flow in a microchannel. *Phys. Rev. Letters*, 94:134501., 2005.
D. T. Son. Turbulence decay of a passive scalar in the batchelor limit: Exact results from a quantum-mechanical approach. *Phys. Rev. E.*, 59 ((4)):R3811–R3814., 1999.
K. R. Sreenivasan. Fractals and multifractals in fluid turbulence. *Annu. Rev. Fluid Mech.*, 23:539–600, 1991.
K. R. Sreenivasan. The passive scalar spectrum and the obukhov-corrsin constant. *Phys. Fluids*, 8((1)):189–196, 1996.

A. D. Stroock, S. K.W. Dertinger, A. Adjari, I. Mezic, H. A. Stone, and G. M. Whitesides. Chaotic mixer for microchannels. *Science*, 295:647–651, 2002.

J. Sukhatme and R. T. Pierrehumbert. Decay of passive scalars under the action of single scale smooth velocity fields in bounded two-dimensional domains: From non-self-similar probability distribution functions to self-similar eigenmodes. *Phys. Rev. E*, 66:056302, 2002.

E. S. Szalai and F. J. Muzzio. Predicting microstructure in three-dimensional chaotic systems. *Phys. Fluids*, 15((11)):3274–3279, 2003.

G. I. Taylor. Diffusion by continuous movements. *Proc. Lond. Math. Soc.*, 20:196–212., 1921.

G. I. Taylor. Statistical theory of turbulence, part i. *Proc. Roy. Soc. A*, CLI:421–444, 1935.

S. T. Thoroddsen and C. W. Van Atta. Exponential tails and skewness of density-gradient probability density functions in stably stratified turbulence. *J. Fluid Mech.*, 244:547–566, 1992.

E. Villermaux and J. Duplat. Mixing as an aggregation process. *Phys. Rev. Letters*, 91((18)):184501., 2003.

E. Villermaux and Y. Gagne. Line dispersion in homogeneous turbulence: Stretching, fractal dimensions and micromixing. *Phys. Rev. Letters*, 73 ((2)):252–255, 1994.

E. Villermaux and C. Innocenti. On the geometry of turbulent mixing. *J. Fluid Mech.*, 393:123–145, 1999.

E. Villermaux and H. Rehab. Mixing in coaxial jets. *J. Fluid Mech.*, 425: 161–185, 2000.

E. Villermaux, C. Innocenti, and J. Duplat. Histogramme des fluctuations scalaire dans le mélange turbulent transitoire. *C. R. Acad. Sci. Paris*, 326(Série IIb):21–26, 1998.

E. Villermaux, H. Chaté, and J. M. Chomaz. Why mixing ? In H. Chaté, E. Villermaux, and J. M. Chomaz, editors, *Mixing Chaos and Turbulence*. Kluwer Academic/Plenum Publishers, New York., 1999.

E. Villermaux, C. Innocenti, and J. Duplat. Short circuits in the corrsinoboukhov cascade. *Phys. Fluids*, 13(1):284–289, 2001.

E. Villermaux, A. D. Stroock, and H. A. Stone. Bridging kinematics and concentration content in a chaotic micromixer. *Phys. Rev. E*, 77(1, Part 2), JAN 2008. ISSN 1539-3755. doi: 10.1103/PhysRevE.77.015301.

M. von Smoluchowski. Versuch einer mathematischen theorie der koagulationskinetik kolloider losungen. *Z. Phys. Chem.*, 92:129–168, 1917.

G. A. Voth, G. Haller, and J. P. Gollub. Experimental measurements of stretching fields in fluids. *Phys. Rev. Letters*, 88((25)):254501, 2002.

Z. Warhaft. Passive scalars in turbulent flows. *Annu. Rev. Fluid Mech.*, 32: 203–240, 2000.

Z. Warhaft. Probability distributions of a passive scalar in grid-generated turbulence. *Phys. Rev. Letters*, 67:3503–3506, 1991.

P. Welander. Studies on the general development of motion in a two-dimensional, ideal fluid. *Tellus*, 7((2)):141–156, 1955.

B. S. Williams, D. Marteau, and J. P. Gollub. Mixing of a passive scalar in magnetically forced two-dimensional turbulence. *Phys. Fluids*, 9((7)): 2061–2080, 1997.

P. K. Yeung. Lagrangian characteristics of turbulence and scalar transport in direct numerical simulations. *J. Fluid Mech.*, 427:241–274, 2001.

Experimental Visualization of Lagrangian Coherent Structures Using Eulerian Averaging

Fotis Sotiropoulos

Saint Anthony Falls Laboratory, Department of Civil Engineering
University of Minnesota, Minneapolis, MN, USA

Abstract. Time-averaging of Eulerian light intensity measurements in flow visualization experiments is proposed as a powerful, non-intrusive technique for visualizing Lagrangian coherent structures in dynamically rich flows. For steady and time-periodic laminar flows a formal theory has been developed that explains the success of such technique by showing the equivalency between Eulerian and Lagrangian averages of quantities conserved along particle paths. Similar Eulerian averaging ideas, however, have been successfully used to visualize and extract the coherence time scale of Lagrangian coherent eddies in an aperiodic (turbulent) flow. Recent examples from the application of these ideas to visualize Lagrangian coherent structures in laminar and turbulent flows are presented.

1 Introduction

The term Lagrangian coherent structures (LCS) denotes large-scale, deterministic patterns that emerge and persist for sufficiently long times (relative to an appropriate Eulerian time scale of the flow) in the advection of a passive tracer in flows with rich Lagrangian dynamics. In chaotically advected laminar flows, for example, LCS are known as the invariant sets of the flow or more commonly as unmixed islands. These, often topologically complex, structures can trap tracers for very long times (comparable to the time scale of molecular diffusion) thereby reducing the portion of the flow domain that is occupied by chaotically advected trajectories and consequently diminishing the overall mixing efficiency. In turbulent, large-scale, geophysical flows, on the other hand, LCS emerge in the form of long-lived, coherent eddies, which dominate global transport and mixing (Provenzale, 1999). In spite of significant recent strides in theoretical and numerical studies of LCS (Haller and Yuan, 2000; Haller, 2002; Mezić and Wiggins, 1999; Poje et al. 1999; Mezić, 1994; etc.), however, experimental studies in this area remain relatively sparse. Thus, whether one is interested in optimizing mixing in low Reynolds number flows or in understanding global transport in geophysical and environmental flows, the development of experimental techniques for eluci-

dating the dynamics of LCS in laboratory and/or field experiments is a pacing research issue.

The first successful attempt to visualize unmixed island chains in a steady chaotically advected three-dimensional flow was reported by Fountain et al. (2000). They employed a series of injection needles to deliver small blobs of dye at various locations within the chaotically advected region of the flow they studied, thus, specifying a set of initial "particle" locations. The intersections of the resulting streaks of dye with a laser sheet constitute, by definition, the Poincaré map of the flow. Fountain et al. (2000) applied this technique to a creeping flow in a open cylindrical container driven by a rotating tilted disk and were able to construct experimental Poincaré maps that were in excellent agreement with numerical computations. In spite of their success, however, this technique is intrusive and very cumbersome to implement and, thus, it is not suitable for complex three-dimensional flows—see related discussion in Fountain et al. (2000).

In unsteady, aperiodic flows the concept of LCS is closely linked with that of finite-time stable and unstable manifolds (e.g. Haller and Yuan, 2000). A technique for extracting finite-time manifolds from PIV velocity measurements in a 2D time-periodic, chaotically advected flow was proposed by Voth et al. (2002). They carried out precision measurements of particle tracer trajectories to directly measure the time-dependent stretching field, whose local maxima have been shown to coincide with stable and unstable manifolds of LCS (Haller and Yuan, 2000). Their technique was applied to a time periodic flow but in principle is applicable to aperiodic flows as well.

In a series of papers, Sotiropoulos and co-workers (Sotiropoulos et al. 2002; Mezić and Sotiropoulos 2002; Chrisohoides and Sotiropoulos, 2003) introduced a novel, non-intrusive, simple to implement experimental technique that relies on averaging Eulerian scalar concentration measurements. Even though the relationship of Eulerian measurements and LCS is not readily apparent, Mezić and Sotiropoulos (2002) showed that a theoretically rigorous connection can be made for the case of steady and time-periodic chaotically advected flows via concepts of ergodic theory. In the case of aperiodic flows the theoretical link is not yet established but the technique has been adapted and successfully applied to visualize LCS in an aperiodic, turbulent free-surface flow (Chrisohoides and Sotiropoulos, 2003).

In this chapter I will first briefly review the concept of Lagrangian averaging and its relationship to invariant sets in chaotically advected flows. Subsequently I will discuss the link between Lagrangian and Eulerian averages and show how the latter, which can be readily constructed from laboratory measurements, can be used to visualize LCS experimentally. Results will be presented both for a chaotically advected, 3D steady flow and a turbulent, aperiodic flow. The section on the theory of Lagrangian averaging is based on the works of Mezić (1994) and Mezić and Wiggins (1999) while the discussion of the experimental implementation

reviews the works of Mezić and Sotiropoulos (2001), Sotiropoulos et al. (2002), Chrisohoides and Sotiropoulos (2003) and the recent computational work of Paik and Sotiropoulos (2005).

2 Lagrangian averaging and invariant sets

The concept of Lagrangian averaging and its relation to invariant sets in chaotically advected flows is central to the development of the subsequently discussed experimental techniques. For that reason in this section I will briefly discuss the concept of Lagrangian averaging and present an example of how it can be applied to numerically visualize the invariant sets of the Poincaré map of a 3D, steady, chaotically advected flow. The subsequent discussion is only intended to provide a summary of the key underlying ideas. For a more comprehensive and rigorous treatment the reader is referred to Mezić (1994) and Mezić and Wiggins (1999), and Mezić and Sotiropoulos (2002).

Consider a laminar, chaotically advected flow. The trajectory of a passive tracer $\underset{\sim}{x} = \underset{\sim}{x}(t)$ introduced into the flow at an initial location $\underset{\sim}{x}_o = (x_o, y_o, z_o)$ at time t_o and advected by the flow velocity field $\underset{\sim}{u} = \underset{\sim}{u}(\underset{\sim}{x}, t)$ is obtained by solving the following set of equations:

$$\frac{d}{dt}[\underset{\sim}{x}(t)] = \underset{\sim}{u}(\underset{\sim}{x}, t) \tag{1}$$

with initial conditions:

$$\underset{\sim}{x}(t_o) = \underset{\sim}{x}_o \tag{2}$$

The solution of the initial value problem (1) and (2) can be written as follows:

$$\underset{\sim}{x} = \underset{\sim}{x}(\underset{\sim}{x}_o, t) = (x(x_o, t), y(y_o, t), z(z_o, t)) \tag{3}$$

For the sake of brevity the specific particle whose trajectory is given by Eqn. (3) will be denoted by its initial location, i.e. as particle $\underset{\sim}{x}_o$.

Let now $f_{\underset{\sim}{x}}^{E}(t) = f(\underset{\sim}{x}, t)$ denote the Eulerian description of any property of the flow—e.g. velocity, pressure, vorticity, etc.—at a given point $\underset{\sim}{x} = (x, y, z)$. Property f can also be expressed in Lagrangian terms by considering the values of f sampled by particle $\underset{\sim}{x}_o$ as it moves through the flowfield along its trajectory given by Eqn. (3). We can, thus, formulate the Lagrangian description of f as follows:

$$f_{\underset{\sim}{x}_o}^{L}(t) = f(\underset{\sim}{x}(\underset{\sim}{x}_o, t)) \tag{4}$$

The Lagrangian average of property f associated with particle $\underset{\sim}{x}_o$ is readily defined as the average over all possible values of $f_{\underset{\sim}{x}_o}^{L}$ sampled by the particle as it moves along its trajectory and can be formally defined as follows:

$$\bar{f}^{L}(\vec{x}_o) = \lim_{t\to\infty} \frac{1}{t} \int_o^t f(\vec{x}(\vec{x}_o, t))dt \tag{5}$$

The fact that for an incompressible flow in a bounded domain the average in equation (5) exists follows directly from Birkhoff's ergodic theorem. Note that Birkhoff's ergodic theorem is valid for almost every initial condition (in the sense of measure theory) and thus its validity is not restricted only to chaotic or to regular regions of the flow.

Mezić (1994) and Mezić and Wiggins (1999) proposed an approach to visualize numerically the invariant sets of the Poincaré map of a chaotically advected flow using the concept of Lagrangian averaging. The overall procedure is summarized as follows:

1. Define a set of initial conditions $\vec{x}_o$;
2. Compute the Lagrangian time averages of a chosen function *f*, $\bar{f}^{L}(\vec{x}_o)$, over the fluid particle trajectories (streamlines in a steady flow) originating from the points $\vec{x}_o$;
3. Map the so computed $\bar{f}^{L}(\vec{x}_o)$ to $\vec{x}_o$ and plot the level sets of the resulting scalar field

Ergodic theory can be used to rigorously show that the iso-contours of $\bar{f}^{L}(\vec{x}_o)$ will indeed visualize the unmixed regions in the flow (invariant sets) (Petersen 1983)—see Mezić (1994) and Mezić and Wiggins (1999) for more details.

An important aspect of the above method concerns the integration time required for the averages to converge to their mean value. It is known that along chaotically advected trajectories convergence is extremely slow (Meiss 1994) and the trajectory integration needs to be carried out for millions of time steps. As shown in Mezić and Sotiropoulos (2002), however, along periodic trajectories convergence is very rapid, about t^{-1}. This property of periodic orbits suggest that Lagrangian averaging can be used to develop an efficient computational technique for identifying unmixed islands in complex, 3D flows.

The utility of Lagrangian averaging in numerical studies of chaotic advection was demonstrated in the recent study by Lackey (2004) and Lackey and Sotiropoulos (2006) who employed this approach to visualize invariant sets in a steady, chaotically advected flow in a cylindrical container with two exactly counter-rotating lids.

3 Experimental Visualization of LCS in Steady Laminar Flows

The fact that Lagrangian averaging can be used to visualize the invariant sets of a chaotically advected flow is useful in numerical studies (see Lackey and Sotiropoulos, 2006) but it is not at all clear how or if the same concept can be extended to laboratory studies as Lagrangian averages can not be constructed experimentally. Instead in laboratory experiments it is straightforward to obtain Eulerian time series of a flow quantity $f_{\vec{x}}^{E}(t) = f(\vec{x},t)$ (by carrying out measurements at fixed points $\vec{x}$) and, thus, only Eulerian averages are available:

$$\bar{f}^{E}(\vec{x}) = \lim_{t\to\infty} \frac{1}{t} \int_{o}^{t} f(\vec{x},t)dt \tag{6}$$

It has been rigorously shown by Mezić and Sotiropoulos (2002), however, that in a steady, incompressible flow *the Eulerian time average of a quantity conserved along particle paths at a point is equal to the Lagrangian average of the same quantity along the particle path that originates from that point*. That is, if the material derivative of f is zero:

$$\bar{f}^{E}(\vec{x}) = \bar{f}^{L}(\vec{x}) \tag{7}$$

In the context of the previous discussion on Lagrangian averaging, this important finding proves that the level sets of the Eulerian time-average field of a quantity that is conserved along particle paths will visualize unmixed regions in the flow.

The equivalence between Lagrangian and Eulerian averaging has been exploited to construct a very simple, non-intrusive experimental visualization technique (Mezić and Sotiropoulos 2002; Sotiropoulos et al. 2002). The technique relies on the standard laser-induced fluorescent (LIF) technique and consists of the following steps:

1) Introduce, within the chaotically advected region of the flow, a non-uniform concentration of fluorescent dye at the initial time.
2) Illuminate the surface of section for the Poincaré map using a laser sheet.
3) Time-average the instantaneous concentration of dye (quantified in terms of the intensity of the scattered light in LIF experiments—see Figure 2) at the surface.
4) Plot the level sets of the time-averaged concentration field.

The fact that contour plots of the time-averaged light intensity field will visualize the unmixed regions of the flow follows from the fact that, neglecting molecular diffusion, concentration is conserved along a particle trajectory.

It is important to emphasize that there are two prerequisites for successful application of this technique: 1) the initial spatial distribution of fluorescent dye within the chaotically advected region must be non-uniform; and 2) the averaging

time must be smaller than the molecular diffusion time scale of the flow but much larger than a characteristic time scale of the flow—see Mezić and Sotiropoulos (2002) for an extensive theoretical discussion of the various aspects of this technique.

The experimental technique described above was applied successfully to resolve the invariant sets of Poincaré maps in the interior of steady vortex breakdown bubbles by Sotiropoulos et al. (2002). Incompressible Newtonian fluid of kinematic viscosity ν fills a closed cylindrical container (see Figure 1). The bottom endwall is rotated at a constant angular velocity Ω while the top wall is held stationary. The two non-dimensional parameters that determine the various flow regimes are the aspect ratio, H/R, and the Reynolds number $Re=\Omega R^2/\nu$. Ekman suction and pumping drive a meridional flow and give rise to the formation of a columnar vortex along the container axis. Above a threshold Reynolds number the columnar vortex breaks down and forms one or more vortex breakdown (VB) bubbles, which remain steady for a wide range of Re (Escudier, 1984). Even though axisymmetric numerical simulations have successfully captured most Eulerian aspects of the flow (Lopez, 1990), laboratory visualization experiments have consistently revealed small, albeit clearly visible, asymmetries at the downstream end of the VB bubble, which in the experiments appears open and asymmetric (Escudier, 1984; Spohn et al., 1998; etc.). Sotiropoulos et al. (2002) studied the same problem numerically by solving the three-dimensional Navier-Stokes equations and showed that the flow within stationary vortex breakdown bubbles could exhibit chaotic particle paths. Consequently, very small three-dimensional perturbations, which are bound to be present in any experiment, could have a profound effect on the Lagrangian dynamics of the flow in the interior of a VB bubble. That is, even though the flow could be essentially axisymmetric from an Eulerian sense it can never be visualized as such in a real-life laboratory experiment in which disturbances can never be fully eliminated. Sotiropoulos et al. (2001) provided a detailed description of the topological aspects of vortex breakdown including a discussion of the specific chaos-inducing mechanism and numerically calculated Poincaré sections.

Sotiropoulos et al. (2002) reported a set of LIF experiments using the ergodic experimental technique described in this section, which confirmed all computational findings and reveal new insights into the dynamics of VB bubbles (see Sotiropoulos et al. (2002) for the details of the experiments). Figure 2 shows typical instantaneous LIF images (iso-contours of the instantaneous light intensity field) for the steady, vortex breakdown bubble for Re=1850 and H/R=1.75. Figure 3 compares the numerically calculated Poincaré map for the same flow (Sotiropoulos et al., 2001) with the invariant sets of the flow obtained by applying the ergodic experimental technique—i.e. by time-averaging a sufficiently long series of instantaneous LIF images such as those shown in Figure 2 and plotting

the level sets of the resulting time-average field. It is seen that the unmixed island chains that are present in the numerically constructed Poincaré map are in excellent agreement with those marked by the level sets of the time-averaged light intensity field obtained experimentally. Both numerical and experimental images reveal the presence of period two, three, and four islands (invariant sets) embedded within well stirred stochastic regions (uniform colored regions in the experimental map). This level of agreement validates the proposed visualization technique and underscores its potential as a powerful tool for experimental investigations of a variety of flows exhibiting chaotic advection.

4 Eulerian averaging and aperiodic flows

The formal theory developed by Mezić and Sotiropoulos (2001) has established the equivalence between Lagrangian and Eulerian averages of quantities conserved along particle paths both for steady and unsteady, time-periodic flows. Whether, however, the same ideas can be exploited to develop an experimental technique for visualizing LCS in aperiodic flows is far from obvious. The first evidence that an averaging-based technique could hold promise in numerical studies of aperiodic flows was reported by Poje et al. (1999). They showed that Lagrangian finite-time averaging can capture the finite-time geometry of LCS with remarkable clarity provided that an optimal averaging window is selected. Unlike steady or time-periodic flows, however, where Lagrangian averaging can be rigorously linked to Eulerian averaging, in aperiodic flows no such formal theoretical link has been established so far. Yet Chrisohoides and Sotiropoulos (2002) were able to develop and successfully apply a novel flow visualization technique for aperiodic flows that is based on finite-time averaging of Eulerian light intensity measurements. In this section we briefly describe this technique and present sample results from its application to visualize LCS in a turbulent, free-surface flow (Chrisohoides and Sotiropoulos, 2003). Recent computational results that confirm the validity of the experimental technique (Paik and Sotiropoulos, 2005) are also reported below.

The flowfield under consideration takes place in a straight rectangular open channel with a rectangular block mounted midway through the channel at one of its corners (see Figure 4). The general features of the flow at the free surface, as derived from experiments (Chrisohoides and Sotiropoulos, 2003) and numerical simulations (Paik and Sotiropoulos, 2005), are illustrated in the sketch shown in Figure 4. As the upstream flow approaches the obstacle, it encounters a strong transverse pressure gradient that diverts it around the obstacle. A large region of recirculating flow forms at the upstream junction between the obstacle and the channel side wall. The flow within this region is slowly evolving but very complex consisting of multiple, large-scale eddies, which appear and disappear in a

seemingly random manner. Paik and Sotiropoulos (2005) recently showed computationally that this region is energized continuously by vorticity from the shear layer forming at the interface with the fast moving outer fluid, which is entrained into the recirculation region at the saddle point of attachment on the obstacle upstream face. They also showed that the temporal dynamics in this region takes place on a quasi-periodic torus. A large recirculating zone is also present at the downstream end of the obstacle and a shear layer develops at the interface between the slow moving fluid within this zone and the flow diverted around the obstacle. The results presented in this section focus on the LCS emerging in the recirculating zone upstream of the obstacle. The Reynolds number (based on obstacle length and the average velocity) is $\mathrm{Re} = 4.2\times10^5$. A detailed description of the experimental flume and other experimental details can be found in Chrisohoides and Sotiropoulos (2003).

To visualize LCS, small tracer particles (paper pieces) are manually introduced on the free-surface upstream of the obstacle. A digital camera is mounted above the obstacle with the aid of an airlift and clamps so that it could be adjusted both vertically and transversely. The sampling rate of the camera is 30 frames per second. Instantaneous images collected with the digital camera suggest a general recirculating flow pattern but do not provide any information about the rich dynamics of LCS that dominate particle transport in this region. To extract LCS we employ a technique that is analogous to long-time exposure photography, which is commonly used for qualitative visualization of flow structures in laboratory experiments, as follows.

To construct time series of light intensity, we digitize instantaneous images by assigning to every pixel (x_p,y_p)—where x_p and y_p are the Cartesian coordinates of the pixel—an instantaneous brightness index $\Im(x_p,y_p,t)$, i.e., a number quantifying the intensity of light emitted by the pixel at that instant in time. Assume now that in a given region of the flow field a LCS forms and persists over a finite time interval τ_c—the *coherence time scale* of the LCS. In Chrisohoides and Sotiropoulos (2002) it was postulated that information about the finite-time geometry of such a LCS should be embedded within the chaotic light intensity time series and can be extracted if the dynamics of the time series is considered at the intermediate time scale $\tau=\tau_c$. A new time series, $\Im_\tau$, is thus constructed by averaging $\Im$ over a finite-time window τ as follows:

$$\Im_\tau\left(x_p,y_p,t\right)=\frac{1}{\tau}\int_{t-\tau/2}^{t+\tau/2}\Im\left(x_p,y_p,t'\right)dt'$$

Level sets of $\Im_\tau$ can visualize LCS and elucidate their dynamics with clarity provided that τ is selected to be close to the coherence time scale of the LCS, which can be defined as the time-scale at which the time series is dominated by

non-trivial, deterministic effects. Chrisohoides and Sotiropoulos (2003) further proposed a technique for extracting the coherence time scale from the light intensity time series. The technique is based on the fluctuation analysis approach presented in Rand and Wilson (1995) and Keeling et al. (1997). In these references, fluctuation analysis was proposed as the means for extracting the coherence length scale in spatio-temporally chaotic, artificial ecology models. For a given averaging window size τ, the standard deviation, E_τ, of $\mathfrak{I}_\tau$ about $\overline{\mathfrak{I}}$ (the long-term time average of $\mathfrak{I}_\tau$) is calculated to quantify the fluctuations of $\mathfrak{I}_\tau$ about $\overline{\mathfrak{I}}$ for various window sizes. For sufficiently large τ, adjacent windows would become independent and according to the central limit theorem E_τ should begin to scale as $\tau^{-1/2}$. The coherence time scale τ_c is thus defined as the window size for which the standard deviation begins to scale in accordance to the central limit theorem. The reader is referred to Chrisohoides and Sotiropoulos (2003) for further details on the implementation of this technique to actual experimental time series of light intensity.

In Figures 5 and 6 we compare the experimental results of Chrisohoides and Sotiropoulos (2003) with the recent computations of Paik and Sotiropoulos (2005), who employed the detached-eddy simulation approach to study the dynamics of coherent structures induced by the obstacle (see reference for details). The results in Figure 5 are shown for one instant in time when the flow in the core region of the recirculating region is dominated by two co-rotating eddies—see Paik and Sotiropoulos (2005) for a detailed discussion of the various states of the coherent structures in this region. The experimental image in Figure 5a corresponds to the raw experimental image depicting the instantaneous arrangement of paper particles. Figures 5b and c show the effect of successively increasing the averaging window τ, which for $\tau = 2$ sec ultimately leads to the emergence of two clearly defined eddies connected at a saddle. As shown in Chrisohoides and Sotiropoulos (2002) further increasing the averaging windows starts diminishing the clarity of the image ultimately causing the two-eddy structure to disappear. Chrisohoides and Sotiropoulos (2002) also applied the fluctuation analysis technique discussed above to verify that indeed the coherence time scale of the two-eddy structure is close to 2 sec. It is also worth noting that video animations of the finite-time averaged light intensity fields in this core region of the flow reveal complex coherent dynamics consisting of rotation of the two eddies, merging into a single eddy, subsequent splitting, etc., which are not visible in the raw visualization images.

To confirm the experimental results Paik and Sotiropoulos (2005) developed a numerical technique, which is the numerical equivalent of the experimental technique. At some instant in time t_o, a set of initial release locations for passive Lagrangian markers on the surface is distributed uniformly within the region of interest (see Figure 5a). The tracers are advected by the resolved DES flowfield by

performing time-accurate integration of the Lagrangian equations of motion to determine the trajectory $\vec{x}^k$ of the k^{th} tracer at time t. The numerical integration for each tracer is carried out say for N time steps to obtain the set of N discrete positions $\vec{x}_n^k$ (n=1,N) visited by the k^{th} tracer during the time interval [t_o, $t_o + N\Delta t$]:

$$\vec{x}_n^k \equiv \vec{x}_n^k(t_o + n\Delta t) = \vec{x}_n^k(t_o) + \int_{t_o}^{t_o+n\Delta t} \vec{u}\left[\vec{x}^k(t), t\right] dt$$

where $\vec{u}$ is the resolved velocity field. For each k, a streak is drawn on the plane connecting all consecutive $(\vec{x}_n^k, \vec{x}_{n-1}^k)$ pairs. The resulting numerical images are essentially equivalent to the experimental images obtained by Chrisohoides and Sotiropoulos (2003) by superimposing instantaneous digital images of particle locations collected over the same time interval.

As seen in Figures 5 (a)-(c) the progression of the clarity level of the computed images is remarkably similar to that in the experiments. Note for instance that for τ=0.5s, both in the experiments and simulations only the lower left eddy has begun to emerge while the second eddy is not visible yet. For τ=2.0s, on the other hand, both eddies have appeared clearly in the experimental and simulated images. It is also worth noting that as seen in Figure 5(c) the spatial heterogeneity in the distribution of length and brightness of the streaks is very similar in the experimental and computed images. Given the procedure we adopted to construct these streaks, this finding is very important as it implicitly suggests reasonable agreement between the laboratory and simulated velocity fields in this region of the flow. This conclusion is further reinforced in the comparisons shown in Figure 6, which depicts experimental and computational results for the upper corner of the recirculation region—i.e. near the saddle of separation. The experiments reveal very complex eddy structure in this region, which evolves at time scales slower than in the core region. Both experiments and calculations start yielding similar structures with similar level for clarity for τ =4.0sec.

5 Summary and Conclusions

In this chapter, I reviewed recent progress toward the development of averaging-based experimental techniques for visualizing LCS in flows with rich large-scale dynamics. The lack of a simple and easy to implement in real-life flows experimental technique for studying LCS has been a pacing item in the areas of chaotically advected steady and time-periodic flows as well as in turbulent flows where transport is dominated by coherent structures. The techniques reviewed here have shown significant promise to fill this void and evolve into powerful experimental research tools to supplement theoretical and numerical studies.

The unifying element of the techniques for visualizing LCS in chaotically advected laminar flows and aperiodic flows is the use of averaging of Eulerian

measurements of light intensity. This quantity is directly proportional to scalar concentration and when considered at time scales much shorter than that of the molecular diffusion it can be assumed that it is conserved along particle paths. For steady and time-periodic chaotically advected flows this property of light intensity can be exploited to rigorously link its Eulerian average at a point to its Lagrangian average along the particle path passing through that point using the theory of Mezić and Sotiropoulos (2002). This key finding places the concept of Eulerian averaging firmly within the context of the ergodic theory of Mezić (1994) and Mezić and Wiggins (1999), which established that mapping Lagrangian averages to initial release locations and plotting the level sets of the resulting field will visualize the invariant sets of the flow. Therefore, in the context of steady and time-periodic flows the technique is well established and the reasons for its success are well understood. Future work in this area should focus on the demonstration of its applicability to time-periodic flows and applications to other chaotically advected flows to further establish its capabilities and versatility.

In the context of aperiodic flows the results of finite-time Eulerian averaging have been very promising so far but many issues remain to be resolved both theoretical and practical. The recent computations of Paik and Sotiropoulos (2003) provided striking evidence establishing the capabilities of the finite-time averaging approach as well as the fluctuation analysis approach for determining the coherence time-scale of LCS proposed by Chrisohoides and Sotiropoulos (2003). Yet the precise link between the level-sets of the finite-time averaged light intensity field and the finite-time geometry of the LCS is not understood and theoretical work is needed to fill this fundamental knowledge gap. Another important issue that needs to be resolved for the technique to evolve into a powerful experimental tool is with regard to determination of the temporal variation of the coherent time scale of the LCS in a given region of the flow. As discussed in Chrisohoides and Sotiropoulos (2005) it is reasonable to expect that τ_c will vary in time for a given region of the flow. The fluctuation analysis technique in its current form, however, can not be used to detect such temporal variability and needs to be modified. Working to address these issues, however, could be proven very useful because the finite-time averaging approach is inherently suited for experimental investigations of LCS at field scale experiments for a broad range of geophysical and environmental flows.

References

Chrisohoides, A., and Sotiropoulos, F. (2003). Experimental visualization of Lagrangian coherent structures in aperiodic flows. *Phys. Fluids* 15(13).

Escudier, M. P. (1984) Observations of the flow produced in a cylindrical container by a rotating endwall. *Exp. Fluids* 2 4, pp. 189-196.

Fountain, G. O., Khakhar, D. V., Mezić, I., and Ottino, J. M. (2000), Chaotic mixing in a bounded 3D flow. *J. Fluid Mech* **417**, 265 (2000).

Haller, G. (2002). Lagrangian Coherent Structures from Approximate Velocity Data, *Phys. Fluids* 14(6), 1851-1861.

Haller, G. and Yuan, G. (2000). Lagrangian Coherent Structures and Mixing in Two-Dimensional Turbulence. *Physica D* 147, 352-370.

Keeling, M. J., Mezić, I., Henry, R. J., McGlade, J., and Rand, D. A. (1997). Characteristic Length Scales of Spatial Models in Ecology via Fluctuation Analysis. *Proc. R. Soc. Lond*. B 352, 1589-1601, 1997.

Lackey, T. C., and Sotiropoulos, F. (2006). The Relationship between Stirring Rate and Reynolds Number in the Chaotically Advected Steady Flow in a Container with Exactly Counter-Rotating Lids. *Phys. Fluids* (submitted).

Lopez, J. M. (1990) Axisymmetric vortex breakdown. Part 1: Confined swirling flow. *J. Fluid Mech*. 221, pp. 533-552.

Meiss, J. D. (1994) Transient measures in the standard map. *Physica D* 74, 254.

Mezić, I. (1994). On geometrical and statistical properties of dynamical systems: theory and applications. PhD. Thesis, California Institute of Technology.

Mezić, I. (1997). FKG Inequalities in Cellular Automata and Coupled Map Lattices. *Physica D* 103, 491-504.

Mezić, I and Wiggins, S. (1999). A method for visualization of invariant sets of dynamical systems based on the ergodic partition. *Chaos* 9 (1), 213-218.

Mezić, I. and Sotiropoulos, F. (2002). Ergodic Theory and Experimental Visualization of Invariant Sets in Chaotically Advected Flows. *Phys. Fluids* 14(7).

Nore, C., Tartar, M., Daube, O. and Tuckerman, L. S. (2004). Survey of instability thresholds of flow between exactly counter-rotating disks. *J. Fluid Mech*. 511, 45-65.

Paik. J., and Sotiropoulos, F. (2005). Coherent structure dynamics upstream of a long rectangular block at the side of a large aspect ratio channel. *Phys. Fluids* 17(11).

Petersen, K. (1983). Ergodic Theory. Cambridge University Press. Cambridge, UK.

Poje, A. C., Haller, G., and Mezić, I. (1999)**.** The geometry and statistics of mixing in aperiodic flows. *Phys. of Fluids* 11, 2963.

Provenzale, A. (1999). Transport by Coherent Barotropic Vortices, *Annu. Rev. Fluid Mech*. 31:55-93.

Rand D. A., and Wilson, H. B. (1995). Using Spatio-Temporal Chaos and Intermediate-Scale Determinism to Quantify Extended Ecosystem. *Proc. R. Soc. Lond*. B 259, 111-117.

Sotiropoulos, F., Ventikos, Y., and Lackey, T. C. (2001). Chaotic advection in three-dimensional stationary vortex-breakdown bubbles: Sil'nikov's chaos and the devil's staircase. *J. Fluid Mech.* 444: 257-297.

Sotiropoulos, F., Webster, D. R., and Lackey, T. C. (2002). Experimental Studies of Lagrangian Transport in Steady Vortex Breakdown Bubbles in a Confined Flow. *J. Fluid. Mech*., **466** , 215 – 248.

Spohn, A., Mory, Y. M., and Hopfinger, E.J. (1998) Experiments on vortex breakdown in a confined flow generated by a rotating disk. *J. Fluid Mech*. 370, pp. 73-99.

Voth, G. A., Haller, G., and Gollub, J. P. (2002). Experimental Measurements of Stretching Fields in Fluid Mixing. *Phys. Rev. Letters* 88(25), 254501(4).

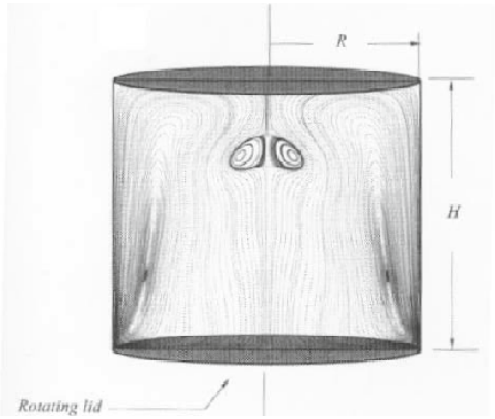

Figure 1. Schematic of the container with meridional streamlines for (Re=1850; H/R=1.75).

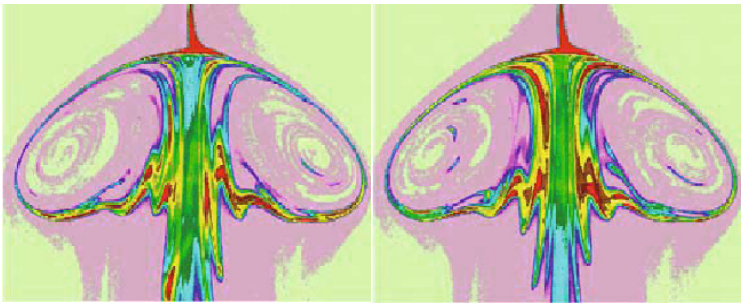

Figure 2. Typical instantaneous iso-contours of light intensity for a steady vortex breakdown bubble (Re=1850; H/R=1.75). From Sotiropoulos et al. (2002).

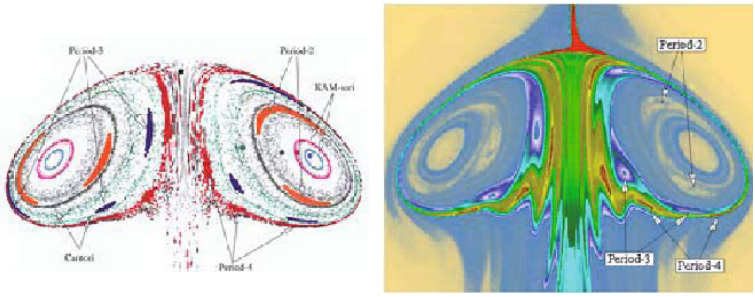

Figure 3. Left: Calculated Poincare map for the steady vortex breakdown bubble (Re=1850; H/R=1.75); Right: Invariant sets of the Poincare map for the same vortex breakdown bubble visualized by time-averaging a sufficiently long series of LIF images as those shown in Figure 2. From Sotiropoulos et al. (2002).

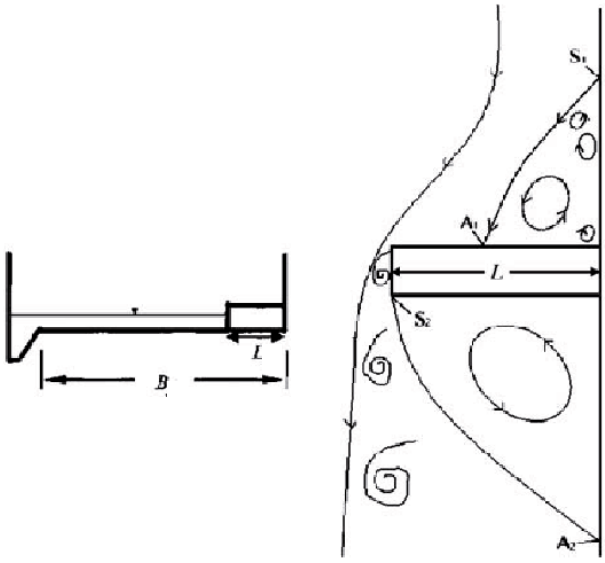

Figure 4. Schematic of the flume and obstacle geometry with representative flow patterns. Left: cross-sectional view; Right: top

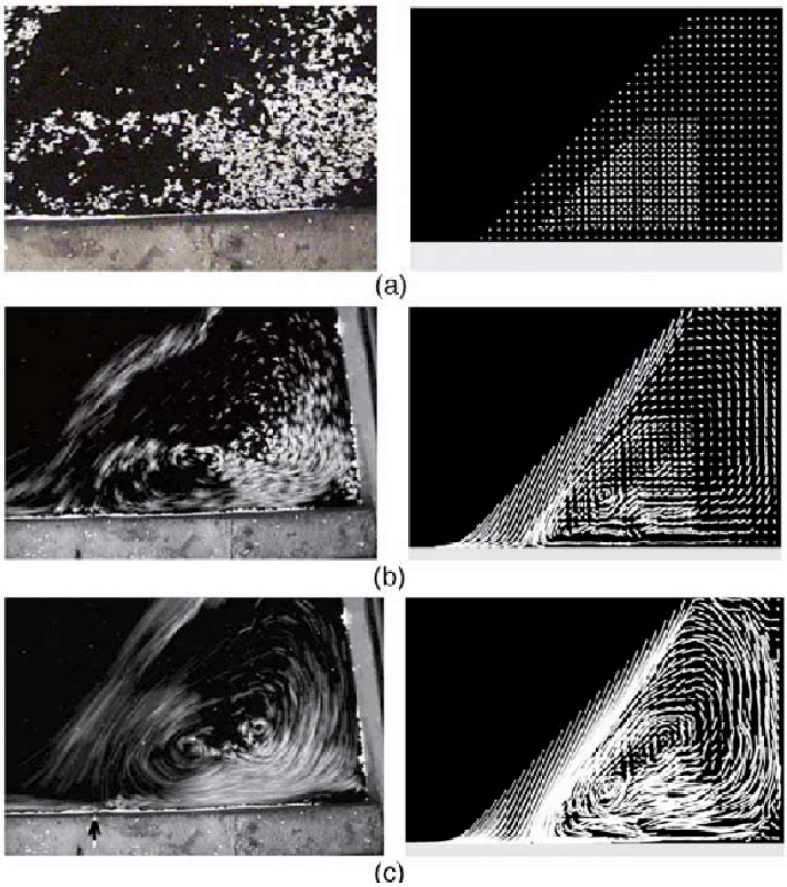

Figure 5. Effect of the size of the time-averaging window on the clarity of the Lagrangian coherent structures in the central area of the upstream recirculating region. Left: finite-time averaging experimental technique; Right: numerical simulation. a) Raw image ($\tau = 0$s); b) $\tau = 0.5$ s; c) $\tau = 2.0$ s. From Paik and Sotiropoulos (2005).

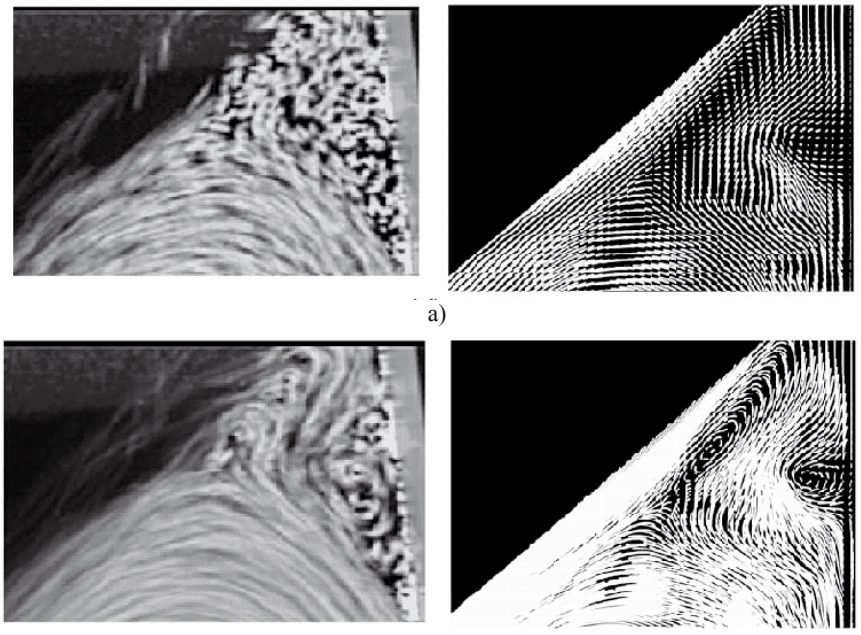

Figure 6. Effect of the size of the time-averaging window on the clarity of the Lagrangian coherent structures in the upper corner of the upstream recirculating region. Left: finite-time averaging experimental technique; Right: numerical simulation. a) τ = 2.0 s); b) τ = 4.0 s. From Paik and Sotiropoulos (2005).

Quality Measures and Transport Properties

Tatyana Krasnopolskaya * and Vyatcheslav Meleshko †

* Department of Vortex Motion, Institute of Hydromechanics, Kiev, Ukraine
† Department of Theoretical Mechanics, Taras Shevchenko University, Kiev, Ukraine

Abstract Three criteria for estimating the quality of mixing are developed. The idea of our approach traces back to the fundamental works of Gibbs, Danckwerts and Welander and consists of using the concept of a 'coarse grained' density of the mixed component. Numerical data are presented showing the change in time of the statistical values of the square density and the intensity of segregation for Gibbs' classical example of fluid mixing. Computation of the measures shows a complete reversibility in spite of irreversibility of some individual points. The coarse-grained representations over an investigation area show a 'residence place' for the dyed material at any instant. For study of transport properties of materials in chaotic two-dimensional stirring Spencer and Wiley (1951) matrix method is suggested. The exchange matrix can show transport of patches or particles from any place in the area under consideration to an arbitrary location and time if it happens.

1 Introduction

Mixing operations are widely used in polymer, chemical and food processing and are the subject of considerable study and research for several decades – see for detail review articles by Irving and Saxton (1967), Edwards (1985), Ottino (1990), Aref (2002) and separate chapters in the textbooks by Brodkey (1967), Middleman (1977), Ottino (1989). Despite these efforts, a proper definition of mixing quality is not in common use (see Krasnopolskaya et al., 1999, and Krasnopolskaya and Meleshko, 2004).

The study of distributive mixing (i.e. stirring) is based on the description of the paths of the individual particles of dyed fluid. The dyed particle is supposed to be inertialess, it is not subjected to diffusion, and no interfacial tension is operative. The idea of such an approach, connecting the Eulerian and Lagrangian representations of fluid flow, was laid down already by Maxwell (1870) and developed later by Riecke (1879), Morton (1913) and

first put forward by Aref (1984) in investigation of chaotic advection (in this pioneering paper it was shown that chaotic mixing of a passive tracer may occur even in deceptively simple flow systems).

A formal mathematical definition of mixing was first introduced by Poincaré and developed in the mid–thirties by Birkhoff, von Neumann and Hopf (see, for example, Hopf, 1934, for a general discussion). This definition reads (Arnold and Avez, 1968) as follows: the process is called the mixing process if for any given non-intersecting at initial moment regions A and B with measures $\mu(A)$ and $\mu(B)$, respectively, in a space V with measure $\mu(V)$, the measure $\mu(A \cap B)$ of the image of the region A, which is contained in the region B, after a sufficiently long time will have the value $\mu(A)\,\mu(B)/\mu(V)$.

The problem of mechanical mixing, which we deal with in this paper differs essentially from the mathematical mixing systems. We restrict our consideration to finite times and are mainly interested in how to optimize mixing.

In his book Gibbs (1902), while considering ensembles in phase space going to statistical equilibrium (by the process which he called 'stirring'), suggested an analogy for this process the mixing of an insoluble coloured fluid in water. He derived that the 'colour' density (of value 0 or 1) at any point remains unchanged, while with fixed box sizes of the spatial elements the mean square density decreases to minimum, provided that mixing is continued indefinitely long. In order to sharpen this distinction the Ehrenfests (1911) introduced the terms 'fine-grained density' and 'coarse-grained density' for these two conceptions. Gibbs' statement of irreversibility, when going to an uniform state, has led to vast and active discussion (see, for example, Tolman, 1938; Krylov, 1979; Sklar, 1993). It was argued by Zermelo (1906), reviewing on his own German translation of Gibbs' book, that for any mechanical (Hamiltonian) system one cannot properly approach equilibrium because of Poincaré's theorem (Poincaré, 1890) that every such a system eventually returns arbitrary close to its initial state. This theorem, however, refers to a trajectory of one individual point in the phase space. When considering an ensemble of points (e.g. a coloured blob) this return will happen at different times for different points. Consequently, at any instant only a fraction of points of the ensemble is close to its initial positions.

2 Evaluation of Mixture Quality

The purpose of mixing is to achieve a uniform distribution of the components. But the main practical question is, however, not whether the system

will eventually approach this uniform distribution, but much more how far, at any moment in time, the mixing state deviates from a uniform state. For this we need a measure. We will adopt Gibbs' approach and use the 'coarse-grained density' of the distribution as a basic measure for the three criteria of the mixed state: averaged square density (Welander, 1955), entropy (Gibbs, 1902) and intensity of segregation (Danckwerts, 1952). All three criteria show the dynamics of mixing in their own scales and may be used descriptively but never causatively, which was explained by Ben-Naim (1986). By using these criteria we can estimate the time necessary for the mixed state to be uniform within some specified range, for a given volume element size (the 'grain'). The larger the element size, the faster this desired mixed state is reached. At any moment in time the different current values, given the criteria chosen and their values in a perfectly mixed state (which are known from the beginning) can be calculated. It is important to notice that the three criteria are not independent and that they are statistical measures of the first order (Tucker, 1993). For more a complete description of a mixture, we will also introduce the 'scale of segregation' (Danckwerts, 1952) which is a statistical measure of the second order. It represents an average of the size of the clumps of the mixed component.

Let us consider in details how the course-grained density is applied to quantify mixing on an example two-dimensional problem of stirring when initial state of black blob is located in the center of cavity as shown in Figure 1. Cover the cavity by the grid of square cells with the side δ and with the area $S_\delta = \delta^2$ each. Let N_δ is the number of cells which cover the cavity, then the area of the cavity is equal to $S = N_\delta\, S_\delta$. In Figure 1 the cavity as the square container (with each side equals to 32 selected units and the total area $S = 32\text{x}32 = 1024$) has the black blob in the center (with the side of 16 units and area $S_b = 256$) and is covered by two types of cells. In Figure 1 (a) $S_\delta = 16$, $N_\delta = 64$, and in Figure 1 (b) $S_\delta = 1$, $N_\delta = 32\text{x}32 = 1024$.

We consider the process of stirring, when the area of coloured blob S_b should be conserved. The property of conservation of the black area during deformation of the blob gives the possibility to introduce a probability function of the dyed material distribution inside a phase space cell with number n as proportional to value of the area occupied by coloured matter $S_b^{(n)}$ in this cell. A ratio of $S_b^{(n)}$ and S_δ denoted as $D_n = S_b^{(n)}/S_\delta$ may be called as a probability density. If we simply averaged this value over the cavity space S, i.e. calculate the sum (keeping the cell area constant, so we could not use integration procedure)

$$\frac{1}{N_\delta}\sum_{n=1}^{N_\delta} D_n = \frac{1}{N_\delta S_\delta}\sum_{n=1}^{N_\delta} S_b^{(n)},$$

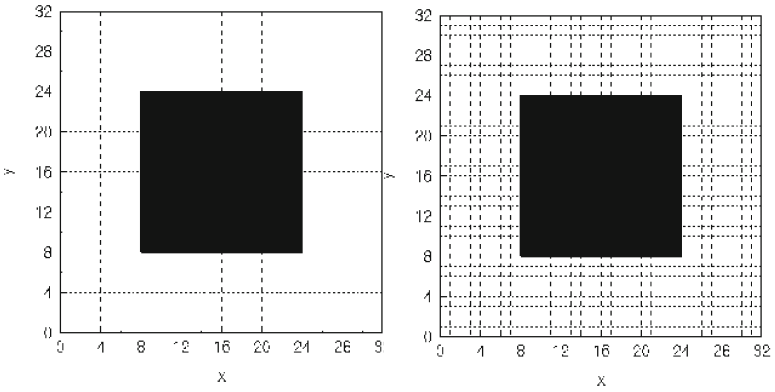

Figure 1. Square cavity with black blob in the center: (a) – covering by cells with $\delta = 4$ and (b) – with $\delta = 1$.

we get the ratio S_b/S, i.e. the ratio of the area of the coloured matter S_b and the total area of the cavity S. This value does not change in the course of stirring and is the mean or uniform density of the coloured blob in the cavity $\langle D \rangle$

$$\langle D \rangle = \frac{1}{N_\delta} \sum_{n=1}^{N_\delta} D_n = \frac{S_b}{S} \,. \tag{1}$$

The angle brackets here and later denote an average over the cavity.

However, using the square density defined by

$$D_n^2 = (S_b^{(n)}/S_\delta)^2$$

and averaging over the area of the cavity, keeping the cell area constant as before, we get the inequality:

$$\langle D^2 \rangle = \frac{1}{N_\delta} \sum_{n=1}^{N_\delta} D_n^2 = \frac{1}{S} \sum_{n=1}^{N_\delta} D_n S_b^{(n)} \leq \frac{S_b}{S} \,. \tag{2}$$

because $D_n \leq 1$.

In Figure 1 for two types of cell grid all cells with the black matter are covered by dye completely, i.e. for those cells $D_n = 1$, and for cells without the black dye $D_n = 0$. So, we may get for both patterns in Figure 1 (a) and (b)

$$\langle D \rangle = 256/1024 = 1/4,$$

$$\langle D^2 \rangle = 256/1024 = 1/4. \tag{3}$$

Let the stirring of the blob is such that the mixture has the pattern at some moment in time as shown in Figures 2. Let use the same covering by two different grids of cells as in Figure 1. In the case shown in Figure 2 (a),

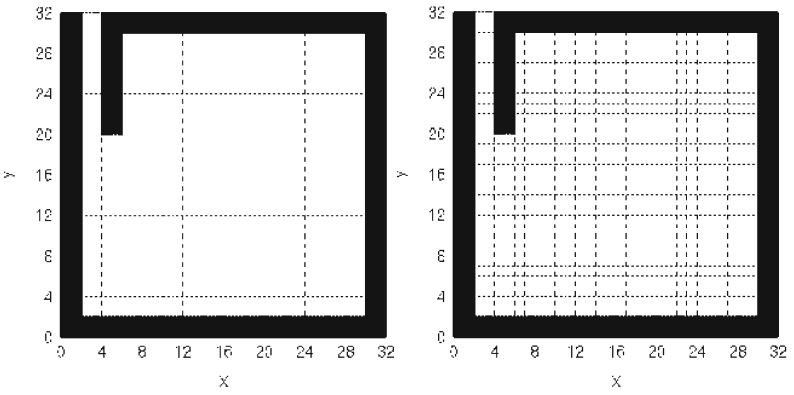

Figure 2. Mixing pattern: (a) – with covering by cells with $\delta = 4$ and (b) – covering by cells with $\delta = 1$.

when $\delta = 4$, each cell which has some black dye covered either by half (i.e. $D_n = 1/2$) or by three quatre (i.e. $D_n = 3/4$). Then as could be calculated using Figure 2 (a)

$$\langle D \rangle = 1/64[26/2 + 12/4] = 1/4;$$

$$\langle D^2 \rangle = 1/64[26(1/2)^2 + 4(3/4)^2] = 35/256 = 0.14 < 1/4. \tag{4}$$

In Figure 2 (b) the same mixture is covering by cells with $\delta = 1$ and all cells with dye are covered completely, i.e. $D_n^* = 1$ and

$$\langle D^* \rangle = 256/1024 = 1/4,$$

$$\langle D^{*2} \rangle = 256/1024 = 1/4. \tag{5}$$

Therefore, using the cells with $\delta = 4$ the value of $\langle D^2 \rangle$ is changed comparatively to its value for the initial situation in Figure 1 (a) and calculated in (2.3), namely is decreasing with decreasing a width of the black filament. And the value of $\langle D^2 \rangle$ calculated in the cell grid with $\delta = 1$ is constant and does not change if dye matter occupied the whole cell or does not occupied at all (for the "empty" cell). In terms of statistical mechanics, D_n is the 'coarse-grained density', which is different from the 'fine-grained density' f_d of the infinitesimal, super-differential elements dS_f, which are always assumed to be small compared to the width of the area of the coloured matter. Moreover, dS_f is always so small that it either is located inside the coloured matter and f_d equals to one or it is outside the coloured matter and f_d equals to zero. Thus, behaviour of f_d is similar to D_n^* in Figure 2 (b), where it is either one for black cells or zero for "empty" cells.

It was shown by Gibbs (for the special case, considered in the next section, of mixing two fluids which approaches statistical equilibrium, i.e. the perfect mixed state), that the final state of mixing is characterized by a minimum statistical square density, i.e. for the variation it holds

$$\langle (D_n - \langle D \rangle)^2 \rangle \equiv \langle D^2 \rangle - \langle D \rangle^2 \to 0. \tag{6}$$

Thus, going to a uniform mixture in time, the mean square density $\langle D^2 \rangle$ will approach its minimum $\langle D \rangle^2$. The rate of decrease of these values is not only time dependent but also depends on the cell sizes.

It is also possible to use the analogy of entropy, $-D_n \log D_n$, instead of D_n^2 as a statistical measure. If the dyed material occupies a box completely or is absent $-D_n \log D_n$ equals to zero. The entropy measure changes only in those boxes, where $0 < D_n < 1$. Moreover, for $0 < D_n < 1$, $-\log D_n$ is always positive, so the more boxes the dyed material covers the bigger is $-\sum_{n=1}^{N_\delta} D_n \log D_n$. As a result, for a good mixing process, the entropy of the mixture

$$e = -\langle D \log D \rangle \tag{7}$$

will grow in time to its maximum

$$e_0 = -\langle D \rangle \log \langle D \rangle, \tag{8}$$

The entropy measure is not independent of the square density measure, both of them have a first-order statistics (one element of area at a time).

Danckwerts (1952) has defined two properties that are useful in evaluating the quality of mixing with diffusion and chemical reactions: the 'scale of segregation' L_C and the 'intensity of segregation' I_C. The scale of segregation is a measure of a size of clumps in a mixture, while the intensity of segregation refers to the variance in composition. For the intensity of segregation he introduced the formula

$$I_C = \frac{\int_S (C - \langle C \rangle)^2 \, dS}{\langle C \rangle (1 - \langle C \rangle) S} = \frac{\langle (C - \langle C \rangle)^2 \rangle}{\langle C \rangle (1 - \langle C \rangle)} \tag{9}$$

where C is the local concentration, which is in Gibbs's and Welander's definitions equal to the fine-grained density f_d (i.e. behaviour is similar to D_n^* in Figure 2 (b) or in the equations (5)). It is easy to see that for the fine-grained density $\langle (f_d - \langle f_d \rangle)^2 \rangle = \langle f_d \rangle - \langle f_d \rangle^2$ and in that case I_C always equals to one. Consequently, for mixing without diffusion and chemical reactions the intensity of segregation I_C is not decreasing, but equals the constant, initial value.

Therefore, we suggest a modification of the intensity of segregation, by making the Gibbs' mean square density (6) dimensionless by dividing by $\langle D \rangle (1 - \langle D \rangle)$, namely

$$I = \frac{\langle (D_n - \langle D \rangle)^2 \rangle}{\langle D \rangle (1 - \langle D \rangle)} \tag{10}$$

For good mixing $\langle (D - \langle D \rangle)^2 \rangle$ tends to zero, which means that I also tends to zero.

Our definition of I is different from a similar mixing measure I_O used by Ottino (1989). I_O is defined as the square root of the mean square density divided by $\langle D \rangle^2$, so $I_O^2 = \langle (D - \langle D \rangle)^2 \rangle / \langle D \rangle^2$. For calculation of I, as is proposed in (10) and what is the coarse grain modification of I_C, it is necessary to use an additional assumption in investigation of mixing by set of N points. This assumption should say that every of N points (which together represent the dyed blob behaviour) carries undeformed under mixing process a small area equals to S_b/N, what can be correct approximation for continiuos mixing flow with large stretching and folding.

The scale of segregation L_C was defined by Danckwerts (1952) by means of the correlation function

$$K_C(\boldsymbol{\eta}) = \langle (C_1 - \langle C \rangle)(C_2 - \langle C \rangle) \rangle \tag{11}$$

which shows how the concentration fluctuations $C - \langle C \rangle$ at points 1 and 2, separated by the vector $\boldsymbol{\eta}$, differ from each other. The normalized correlation function is called the correlation coefficient

$$\rho_c(\boldsymbol{\eta}) = \frac{\langle (C_1 - \langle C \rangle)(C_2 - \langle C \rangle) \rangle}{\langle (C - \langle C \rangle)^2 \rangle} \tag{12}$$

It is obvious that $\rho(\mathbf{0})= 1$. When $|\eta|$ exceeds a certain value, the relationship between the concentrations in points may become random and $K_C(\eta)$ (11) drops to zero. If a mixture consists of clumps, $|\eta|$ at which $K_C(\eta)$ (11) is equal to zero (say, $|\eta| = \xi$) is approximately an average size of the clumps in the direction $\boldsymbol{\eta}$. More precisely, the average radius of clump in the direction of $\boldsymbol{\eta}$. is

$$L_C(\boldsymbol{\eta}) = \int_0^{\xi} \rho_c(\boldsymbol{\eta}) d|\boldsymbol{\eta}| \tag{13}$$

The mixing patterns which we are going to discuss do not consist of a random distribution of clumps, but of layered structures. However, the coarse grain representations of these patterns may look like clumps. If we cover area by cells for which the density D_n is larger than $\langle D\rangle$ with black, the cells, where D_n equals to $\langle D\rangle$ with grey, and cells where $0 \le D_n < \langle D\rangle$ with white colour, then such representation can be considered as white and black clumps with grey clumps that serve as transitional ones. Moreover, with the coarse-grained correlation function defined as

$$K(\boldsymbol{\eta}) = \langle (D_1 - \langle D\rangle)(D_2 - \langle D\rangle)\rangle, \tag{14}$$

(where D_1 and D_2 correspond to coarse-grained density in the boxes 1 and 2 separated by vector $\boldsymbol{\eta}$) the short term regularity (when $K > 0$) of it in the interval (0,ξ) gives important information about the mixture pattern and can be examined. Short term regularity means that in average in two boxes at any distance $|\eta| < \xi$ the fluctuations $D_n - \langle D\rangle$ have the same sign (i.e. the same colour) and thus $K > 0$. For $|\eta| = \xi$ the fluctuations become uncorrelated and therefore $K = 0$. Thus, the distance $|\eta| = \xi$ in the direction $\boldsymbol{\eta}$ is related to the size of average clump in this direction, and the value

$$L(\boldsymbol{\eta}) = \int_0^{\xi} \frac{\langle (D_1 - \langle D\rangle)(D_2 - \langle D\rangle)\rangle}{\langle (D - \langle D\rangle)^2\rangle}\, d|\boldsymbol{\eta}| \tag{15}$$

gives the average radius of the clump. Complementary to intensity of segregation I, the scale of segregation L can be used as a measure of clump sizes of the coarse-grained description of mixing patterns. The dynamics of such scales should reflect the changes of sizes of unmixed regions, where D_n is always larger than $\langle D\rangle$.

3 Gibbs' Classical Example of Fluid Stirring

Here we consider the famous Gibbs' example of fluid stirring. Gibbs (1902) described the case when black fluid differs only by colour and occupied the

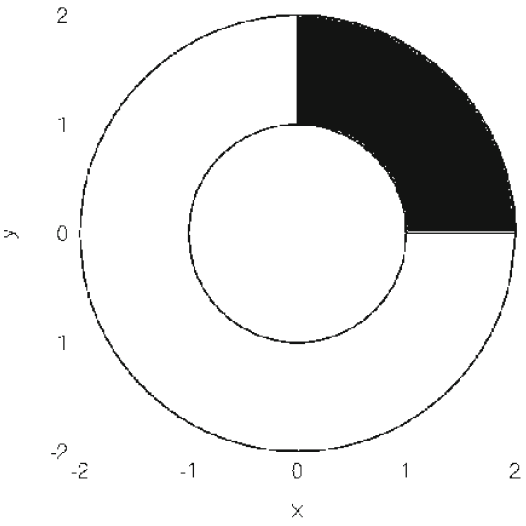

Figure 3. Initial distribution of black dye.

sector of 90° between two infinite cylinders. The cross section of area between two cylinders is shown in Figure 3. Consider two-dimensional flow of incompressible viscous fluid in an annular cavity between the two cylinders of the radius $r = 1$ and $r = 2$, coursed by tangential constant in time velocity external cylinder V_2. The inner cylinder is motionless, $V_1 = 0$ when $r = 1$. The radial component of velocity u_r is equal to zero for the whole process, so there is only the azimuthal u_θ component which can be written in the form (see Krasnoposlaya and Meleshko, 2004)

$$u_\theta = Ar + \frac{B}{r}, \qquad A = \frac{V_2 b}{b^2 - a^2}, \qquad B = -\frac{V_2 a^2 b}{b^2 - a^2}, \tag{16}$$

For the case under consideration $a = 1$ and $b = 2$, therefore, $A = 2/3V_2$ and $B = -2/3V_2$. Advection equations can be presented as

$$\frac{dr}{dt} = 0, \qquad \frac{d\theta}{dt} = u_\theta, \tag{17}$$

and with initial conditions $r = r_{in},\ \theta = \theta_{in}\ \ t = 0$ describe motion of passive Lagrangian particle occupied point (r, θ) in time t in the known Eulerian velocity field.

The system (17) can be written in rectangular coordinates $x = r\sin\theta$, $y = r\cos\theta$ as

$$\frac{dx}{dt} = -Ay - \frac{By}{x^2+y^2}, \qquad \frac{dy}{dt} = Ax + \frac{Bx}{x^2+y^2}, \tag{18}$$

where A and B are as in (16).

For obtaining mixing pattern we follow deformation of interface between black and white fluids. Every point of the interface moves according to advection equations (17)-(18). At the initial moment the interface is described by relations: $1 \le r \le 2$ and $\theta = 0$ (horizontal part of the boundary), $0 \le \theta \le \pi/2$ and $r = 2$ (upper curved part), $2 \ge r \ge 1$ $\theta = \pi/2$ (vertical part), $\pi/2 \ge \theta \ge 0$ $r = 1$ (lower part of the boundary).

After 12 complete turns of the external cylinder mixture has pattern shown in Figure 4 (a). The black fluid is now in the whole area between the cylinders. In the course of time black windings will be more and more. Under infinite number of turns number of windings becomes infinite and mixture is uniform. Let us apply such measures as square density and intensity of segregation to quantify mixing quality. In Figure 4 (b) mixture pattern corresponding to Figure 4 (a) is shown as square density D_n distribution when cell size is $\delta = 0.2$. In Figure 4 (c) the same pattern is presented in the cells with $\delta = 0.1$. From comparison of graphs we may conclude that in bigger cells the mixture looks as uniform and in smaller is nonuniform (having some empty cells without black fluid).

Dynamics of measure criteria such as intensity I (10), calculated with $\delta = 0.1$, when t/T is the number of half turns and function of square density $\langle D^2\rangle/\langle D\rangle^2 - 1$ are shown in Figure 5. We may see that mixture becomes more uniform with increasing turn number. The intensity of segregation is more convenient as criterion because it is changing between two number: from one to zero.

We used the special numerical algorithm for two-dimensional contour line tracking for representation of the interface between the black and white fluids which provides an area-preservation mapping in the flow and conserves all topological properties of black fluid enclosed inside the boundaries of interface (see Krasnopolskaya et al., 1999, and Krasnopolskaya and Meleshko, 2004). In our algorithm the key idea is the use of a non-uniform distribution of points at the initial contour to present this interface in such a way that: (i) the distance between neighbouring points remains between some chosen values (for that points are added when the distance becomes long enough and points are removed when it becomes too short) and (ii) the angle between any neighbouring straight lines is larger than some prescribed value. The principal advantage of our algorithm is that area preservation of the blob enclosed by the contour is guaranteed even after high stretch-

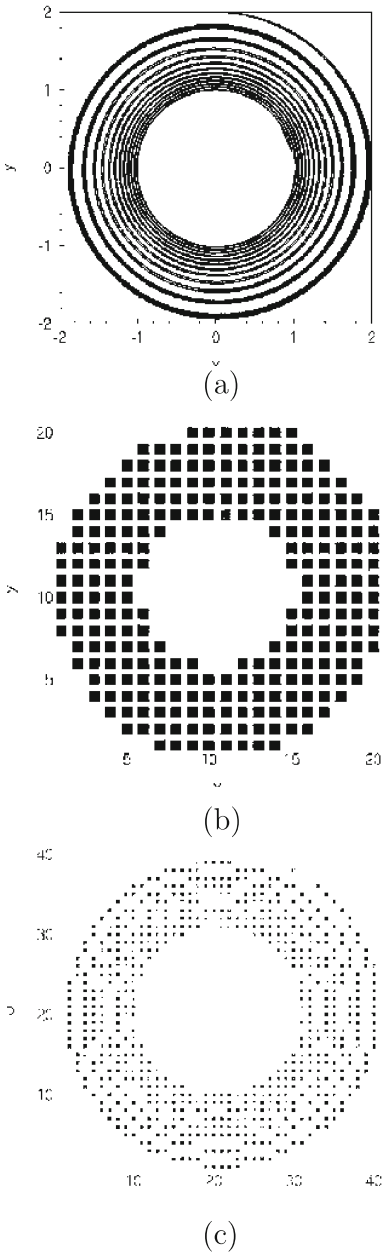

Figure 4. Mixture pattern – (a), square density distribution with $\delta = 0.02$ – (b) and with $\delta = 0.01$ – (c).

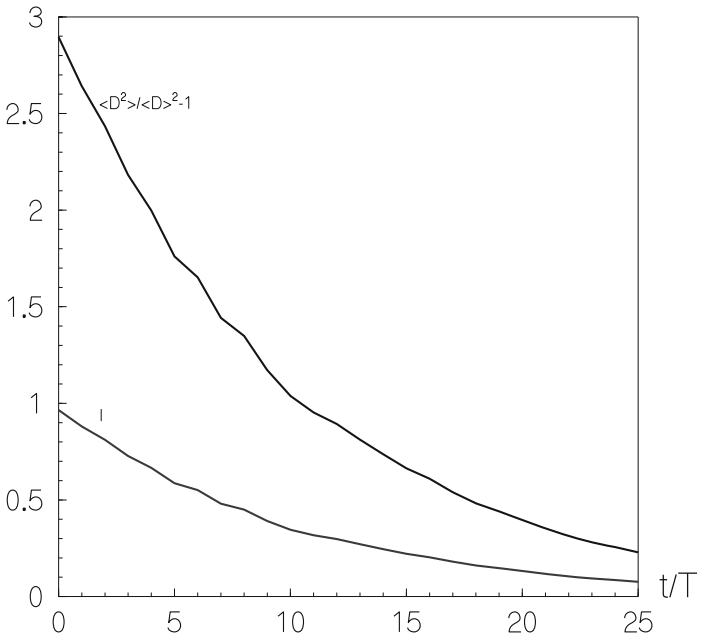

Figure 5. Dependence of criterions on number of half turns.

ing and complicated folding. Knowing the position of the contour line (the boundary of the black fluid) we can construct an Eulerian description of the mixing process, giving an opportunity to quantify mixing at any moment of time.

It is worth noting that the more traditional approach, based upon the presentation of the blob as a collection of N points uniformly distributed over the area S_b of the dyed material, can provide a reasonable treatment of mixing with excellent correspondence with the experiments, even in complex domains (Jana, Metcalfe and Ottino, 1994). For long time evolutions, however, this approach provides only a quantitative general picture of mixing (see, Liu, Muzzio and Peskin, 1994; Blake and Otto, 1996, for several examples). Fine details, especially the question if an 'empty' space surrounded by

a cluster of points really means the absence of the to be mixed component, remain unclear. Basically, the uniformly distributed multipoint approach can not provide a valid description of dyed blob stretching and folding, if the thickness of filaments becomes less than $(S_b/N)^{1/2}$, or if the length of the contour line becomes more than $2(NS_b)^{1/2}$. Besides, being distributed uniformly at the initial moment, the points tend to spread out nonuniformly and, sometimes, collect into dense clusters. Any 'box-counting' calculations based upon the preservation of a Lebesgue measure of the set of N points (with an 'area' related to each point S_b/N), can provide only qualitative estimates for quality of mixing (Ottino, 1989).

An important issue is connected with the time reversibility of all measures. There are two questions in this issue. One concerns the reversibility of individual points, representing the contour line after some time T_R, to their initial positions at time $2T_R$. The second question is connected with the conservation of the dyed area and, therefore, reversibility of all measures. Our calculations with 100000 points uniformly distributed along the initial circular contour line , for example, have shown the accurate reversibility after ten periods of periodical distributive stirring in the wedge cavity (for details see Krasnopolskaya et. al., 1999). In spite of the accurate calculations of the individual point positions already after the two first periods the blob area was not conserved, the relative error after the nine periods was, for example, 70% (meaning that 70% of the original blob area has been 'lost'). The calculations based on our algorithm with nonuniform distribution of points conserved the blob area for twelve periods of forward and twelve periods of backward motions of periodical distributive stirring in the wedge cavity (a check on area conservation leaned that even after 12 periods of forward motion less than 1% of the dyed material was lost). In this case the computations of all coarse grained measures based on the value of the blob area are reliable. Nevertheless, for such computations not all points come back to their initial positions. After the reverse process some of the points are located along pieces of the unstable manifold for the backward motion (which coincides with the stable manifold for the forward motion). The contribution of these spurious lines to the blob area equals zero. Thus, we can conclude that computation of the measures shows a complete reversibility in spite of irreversibility of some individual points.

4 Evaluation of Transport Properties by Exchange Matrix Method

The study of transport properties is an important issue. This part of the paper deals with exchange matrix method described by Spencer and Wiley

(1951). In general chaotic dynamics of particles motion in efficient mixing could be studied in different ways, for example, by means of Poincaré sections. However, we are interested in the short term history of fluid transport. Poincaré sections present the history of motion of points in some area during a long time interval, say, during a thousand periods of flow. On the contrary, we need to know which part of the Eulerian space will be mixed in a short time and, more importantly, how much dyed matter will leak to some specific part of the area under consideration. The orbit expansion method developed by Beerens, Ridderinkhof and Zimmerman (1995) for a quantification of the chaotic transport does not give answers to those questions. In our case, it is important to know not the mixing region (where presumably mixing is instantaneous) obtained by the long time tool - Poincaré sections, – or the rate of material exchange (which could be high in a very narrow domain), but how uniformly this mixing region is distributed over the whole area during a specific finite interval of time. We suggest a different approach for an estimation and quantification of transport properties. Here we briefly present a methodology for the quantification of the chaotic transport based on the matrix method.

First step is to divide the whole area of investigating by cell grid in the square boxes with the side size δ and the area $S_\delta = \delta^2$. We may number all cells starting from 1 to N. The next step is to compute the exchange matrix coefficients D_{ij} using Spencer and Wiley (1951) method.

Coefficient D_{ij} is equal to the fraction of the material (say, dyed matter) originally occupying completely the j box which is moving by flow field to the i cell. This is the basic step in the matrix method. In order to compute the value of coefficient D_{ij} we put dyed patch as a square blob continuously occupying the j cell. Then we use a contour tracking algorithm that conserves both area and topological properties (connectedness and non-self-intersection) to find the blob's boundary in Eulerian space under investigation at the moment of time which we called as the end of cycle in flow field (end of period for periodical flows and end tidal for tidal flow). Then we project the found blob's boundary in to the i cell. The ration of dyed material in that i cell $S_b^{(i)end}$ to the area of initial dyed blob $S_b^{(j)start}$ in the j box is equal D_{ij}, namely

$$D_{ij} = \frac{S_b^{(i)end}}{S_b^{(j)start}} = \frac{S_b^{(i)end}}{S_\delta} \tag{19}$$

Then using this matrix we can predict transport of dyed matter from any place (any box) in the area to an arbitrary location and determine the time when it happens. If $a_j^{(0)}$ is the initial course grained density in the j

cell, the density in the i cell after n operations are given by the elements of the matrix

$$[a_i^{(n)}] = [a_j^{(0)}][D_{ij}]^n = [a_j^{(0)}][D_{ij}^{(n)}] \tag{20}$$

If $a_i^{(n)}$ is not zero then dyed material polluted the i cell and n number shows after how many operations it is happened. For zero $a_i^{(n)}$ it is necessary to have either zero value of the $a_j^{(0)}$ or $D_{ij}^{(n)}$. We want to stress that for computing of $D_{ij}^{(n)}$ we need to know flow field. It could be done by analytical presentation or by numerical approximation or even by experimental observations.

Bibliography

H. Aref. *Stirring by chaotic advection. J. Fluid Mech.*, 143:1–24, 1984.

H. Aref. The development of chaotic advection. *Phys. Fluids* A, 14:1315-1325, 2002.

V. I. Arnold and A. Avez. *Ergodic Problems of Statistical Mechanics*. Benjamin, New York, 1968.

S. Beerens, H. Ridderinkhof and J.T.F. Zimmerman. *An analytical study of chaotic stirring in tidal areas.* In H. Aref and M.S.El Naschie, editors, *Chaos Applied to Fluid Mixing*. Pergamon Press, 267–285, 1995.

A. Ben-Naim. *Is mixing a thermodynamic process? Amer. J. Phys.*, 58:725–733, 1987.

J. R. Blake and S. R. Otto. *Ciliary propulsion, chaotic filtration and a 'blinking' stokeslet. J. Engng Math.*, 30:151–168, 1996.

R. S. Brodkey. *T*he Phenomena of Fluid Motions. Addison-Wesley, San Diego, 1967.

P. V. Danckwerts. *The definition and measurement of some characteristics of mixtures. Appl. Sci. Res. A.*, 3:279–296, 1952.

M. F. Edwards. *Laminar flow and distributive mixing.* In N. Hardy, M. F. Edwards and A. W. Nienow, editors, *Mixing in the Process Industries*. Butterworth, Boston, 202–225,1985.

P. and T. Ehrenfest. *Begriffliche Grundlagen der statistischen Auffassung in der Mechanik.* In *Encyklopädie der mathematischen Wissenschaften*. Teubner, Berlin, 4, Art. 32, 3–90, 1911.

J. W. Gibbs. *Elementary Principles in Statistical Mechanics*. Scribner, New Haven, 1902.

E. Hopf. *On causality, statistics and probability. J. Mathematics Phys.*, 13:51–102, 1934.

H. F. Irving and R. L. Saxton. *Mixing of high viscosity materials.* In V. W. Uhl and J. B. Gray, editors, *Mixing. Theory and Practice, II*. Academic, Palo Alto, 169–224, 1967.

S. C. Jana, G. Metcalfe and J. M. Ottino. *Experimental and computational studies of mixing in complex Stokes flows: the vortex mixing flow and multicellular cavity flows. J. Fluid Mech.*, 269:199–246, 1994.

T. S. Krasnopolskaya, V. V. Meleshko, G. W. M. Peters and H. E. H. Meijer. *Mixing in Stokes flow in an annular wedge cavity. Eur.J. Mech.B/Fluids*, 18:793–822, 1999).

T. S. Krasnopolskaya and V. V. Meleshko. *Laminar stirring of fluids. Part 1. Methodology aspects. Applied Hydromechanics*, 6:28–40, 2004.

N. S. Krylov. *The process of relaxation of statistical systems and the criterion of mechanical instability.* In *Works on the Foundations of Statistical Physics by Nikolai Sergeevich Krylov*. Princeton University Press, Princeton, 193–238, 1979.

M. Liu, F. J. Muzzio and R. L. Peskin. *Quantification of mixing in apereodic chaotic flows. Chaos, Solitons & Fractals*, 4:869–893, 1994.

J. C. Maxwell. *On the displacement in a case of fluid motion. Proc. Lond. Math. Soc.*, 3:82-87, 1870.

S. Middleman. *Fundamentals of Polymer Processing* . McGraw-Hill, New York, 1977.

W. B. Morton. *On the displacements of the particles and their paths in some cases of two-dimensional motion of a frictionless liquid. Proc. R. Soc. Lond. A,* 89:106–124, 1913.

J. M. Ottino. *The Kinematics of Mixing: Stretching, Chaos and Transport*. Cambridge University Press, Cambridge, 1989.

J. M. Ottino. *Mixing, chaotic advection, and turbulence. Ann. Rev. Fluid Mech.*, 22:207–253, 1990.

H. Poincaré. *Sur le problème des trois corps et les équations de la dinamique. Acta Mathem.*, 13:1–270, 1890.

L. Sklar. *Physics and Chance*. Cambridge University Press, Cambridge, 1993.

R. S. Spencer and R. M. Wiley. *The mixing of very viscous liquids. J. Colloid Sci.* 6:133–145, 1951.

R. C. Tolman. *The Principle of Statistical Mechanics*. Oxford University Press, Oxford, 1938.

C. L. Tucker. *Principles of mixing measurements.* In C. Rauwendaal, editor, *Mixing in Polymer Processing*. Dekker, Boston, 101–127, 1991.

P. Welander. *Studies of the general development of motion in a two-dimentional ideal fluid. Tellus*, 7:141–156, 1955.

E. Zermelo. *Referat über Gibbs "statistische Mechanik". Jahresber. deutsch. Math.-Ver.* 15:232-242, 1906.

Reactions in chaotic flows

Tamás Tél [*] and György Károlyi [†]

[*] Institute for Theoretical Physics, Eötvös University, P.O. Box 32, H-1518 Budapest, Hungary

[†] Center for Applied Mathematics and Computational Physics, and Department of Structural Mechanics, Budapest University of Technology and Economics, Műegyetem rkp. 3., H-1111 Budapest, Hungary

Abstract In this pedagogical review we summarize recent results on reactivity in chaotic hydrodynamical flows, in both open regimes and closed containers. In open flows, reaction is concentrated on the fractal filaments of the unstable manifold of a chaotic saddle. In closed flows, the product does not show a well-defined fractal property, nevertheless, there is a transient filamentary structure present. We derive a rate equation both for frontal (autocatalytic-like) and acid-base reactions in both types of flows. In open flows, this equation indicates that reactions are enhanced by the unstable manifold, which serves as a fractal catalyst. In closed flows, the effect of transient filamentary patterns can be taken into account by the coupling of the reactive dynamics to a time-dependent effective dimension.

1 Introduction

We are witnessing an increasing interest in the properties of chemical reactions taking place in time-dependent two-dimensional flows whose advection dynamics is chaotic. After a strong theoretical approach of the last decade (for a review, see Tél *et al.* (2005)), and an early attempt (Paireau and Tabeling, 1997), there is a series of experimental works currently appearing. Recent studies investigate reactions in the blinking vortex flow (Nugent *et al.*, 2004), in cellular flows (Paoletti and Solomon, 2005; Schwartz and Solomon, 2008), in an electrolytic flow (Arratia and Gollub, 2006; Paoletti *et al.*, 2006), in vortex rings (Rogers and Morris, 2005; Rogers *et al.*, 2008), and in vertically oasillating fluids (Fernández-García *et al.*, 2008). The type of reactions ranges from excitable media, via autocatalytic, to acid-base reactions.

A relevant field of application of these studies is in microfluidics (Stroock *et al.*, 2002; Bottausci *et al.*, 2004; Müller *et al.*, 2004; Ottino and Wiggins,

2004; Stremler *et al.*, 2004) (see also the lecture by Mezić (2008)) since there is an industrial demand for micromixers in which efficient and controlled reactions can take place. The problem of reactive chaotic flows is important for other fields as well, ranging from chemical engineering and combustion (Menzinger and Dutt, 1990; Kiss *et al.*, 2004) to environmental aspects, like the spreading of reactive pollutants, the ozone loss in the stratosphere (Wonhas and Vassilicos, 2002; Grooß *et al.*, 2005), and the plankton blooming in the ocean (Abraham *et al.*, 2000; Bracco *et al.*, 2000; Martin, 2003; Sandulescu *et al.*, 2006, 2007, 2008).

Although the experiments have been done in closed containers, the theoretical understanding indicates that some features appear in a much cleaner form in open flows (for a review see Tél *et al.* (2005)). In open flows there is a fluid current flowing through the region of observation to which particles, once escaped downstreams, cannot return within the observation time. For simplicity, we concentrate on two-dimensional, smooth, icompressible flows.

Based on detailed studies of passive chaotic advection (see Aref (2002, 2008)), we can see that there is a basic dichotomy between the advection dynamics in open and closed flows, as shown in Table 1. In the open case there is a very clean and time-independent fractal dimension associated to the chaotic advection dynamics. The chaotic advection dynamics itself is, however, unavoidably transient, i.e., of finite lifetime. In the closed case, chaos is permanent, but produces structures whose degree of filamentarity changes in time. Hence filamentarity is of transient character. This dichotomy is also reflected in the reaction outcome in these different types of flows.

Table 1. Properties of passive advection in open and closed flows.

	open flow	closed flow
chaos	transient	permanent
filamentarity	permanent	transient

In open flows, there exists a fractal set of particle trajectories that never escape the region of observation, this is called the chaotic set. The set of these trajectories is unstable in the sense that though typical trajectories might approach it for a transient time, but eventually they leave it along its unstable manifold. This unstable manifold is a filamentary fractal of zero measure in two-dimensional flows, and it becomes the skeleton of active processes (Toroczkai *et al.*, 1998) (see Fig. 1).

In closed flows, however, the unstable filamentation is dense over the full domain, and there is no invariant set which had a well-defined dimension

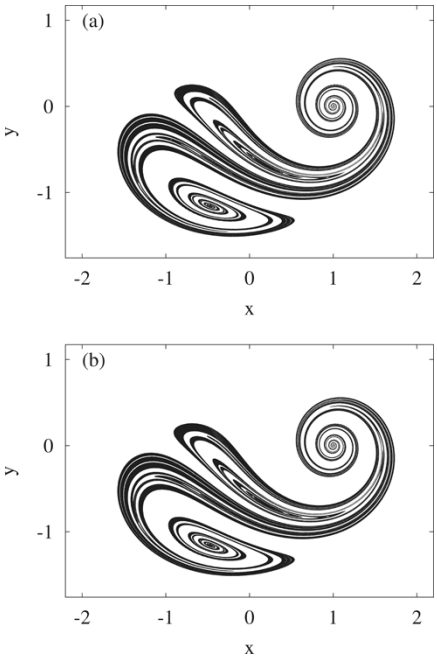

Figure 1. Distribution of product C of the autocatalytic reaction A+C $\rightarrow$ 2C (A: white, C: black) in the plane of the blinking vortex-sink system. The flow, introduced by Aref *et al.* (1989) and studied in detail by Károlyi and Tél (1997), is a combination of the blinking vortex (Aref, 1984) and the pulsed sink system (Jones and Aref (1988), see also Stremler (2008)). The flow is open since particles leaving via the sinks never return. The sinks are situated at $(x = \pm 1, y = 0)$, and a period starts with the opening of the left sink. Panel a (b) shows the distribution after 4 (6) periods. The initial condition is a small square of C particles in a sea of A. The distribution becomes periodic with the same period as the flow after about 2 periods: a steady state sets in due to a balance between the chemical production and the hydrodynamical outflow.

strictly lower than 2, the dimension of the flow. In the absence of fluid transport barriers in closed flows, autocatalytic (Neufeld *et al.*, 2002a) or excitable reactions (Neufeld, 2001; Neufeld *et al.*, 2002b) or even acid-base reactions lead to a steady state in which the full fluid domain is either occupied by the product or no product is present at all. The asymptotic state is thus homogeneous, and hence much less interesting than in the open case. This is fully consistent with the observation that the product is distributed along the unstable manifolds (Metcalfe and Ottino, 1994; Cartwright *et al.*, 2004). Before reaching the asymptotic state, the chemical product appears, however, to have filamentary features (Neufeld *et al.*, 2002a,b; Neufeld, 2001; Wonhas and Vassilicos, 2002) (see Fig. 2).

2 Local chemical dynamics across the stretching direction of the flow

Much insight can be gained into any kind of reaction dynamics by analyzing the concentration dynamics across the unstable filamentation (Clifford *et al.*, 1999; Vikhansky, 2004; Vikhansky and Cox, 2006). A particularly useful approach is the so-called Lagrangian filament slice model (Neufeld, 2001). The idea is to investigate a long, straight segment of the unstable manifold and follow the reaction perpendicular to this segment only, since due to a fast stretching, the concentration distribution can be assumed to be homogeneous along the manifold. Consider a reaction, assumed to be governed by a single relevant component, of dimensionless concentration c according to the rate equation $\dot{c} = kR(c)$, in a medium at rest, where k is the rate constant, and function $R(c)$ specifies the reaction. The effect of the flow transversal to the manifold is a local exponential contraction governed by the contracting Lyapunov exponent. Taking the x coordinate as the one measuring the distance from the unstable manifold, the typical flow field can be written as $-\overline{\lambda}x$, since in incompressible two-dimensional flows the average contracting Lyapunov exponent coincides with the expanding one $\overline{\lambda}$ (in modulus). The Lagrangian filament slice model is thus a one-dimensional approximation, a partial differential equation for the dimensionless concentration distribution $c(x,t)$ in the form of

$$\frac{\partial c}{\partial t} - \overline{\lambda}x\frac{\partial c}{\partial x} = kR(c) + D_{\mathrm{diff}}\frac{\partial^2}{\partial x^2}c, \tag{1}$$

with D_{diff} as the diffusion coefficient. Note that this is a generalization of the reduced convection-diffusion equation (the limit of $k = 0$ of (1)) investigated in the lectures of Leonard (2008), see also Villermaux and Rehab (2000); Villermaux and Duplat (2003) for the reactive case.

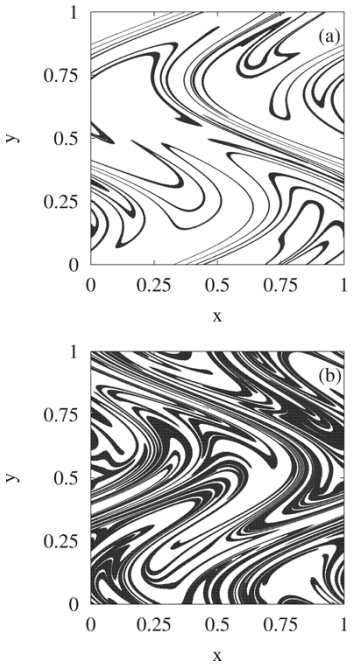

Figure 2. Distribution of product C of the autocatalytic reaction A+C → 2C (A: white, C: black) in the double sine flow, introduced by Franjione and Ottino (1992); Liu *et al.* (1994); Pierrehumbert (1994). The flow is double periodic over the unit square and is periodic in time. It is closed since there is no outflow: particles leaving across one edge re-enter across the opposite one. Panel a (b) shows the distribution after 4 (6) periods. The initial condition is a narrow band of C particles in a sea of A. There is a drastical difference in the pattern. The chemical product is gradually accumulating in the system: the filaments (of approximately the same width) cover an increasing area, and appear therefore to have a fractal dimension increasing in time. The asymptotic steady state is a macroscopically homogeneous distribution of C which sets in after about 15 periods.

By measuring time in units of $1/\overline{\lambda}$ and length in units of some linear scale L, the equation becomes

$$\frac{\partial c}{\partial t} - x\frac{\partial c}{\partial x} = \mathrm{Da}\ R(c) + \frac{1}{\mathrm{Pe}}\frac{\partial^2}{\partial x^2}c, \tag{2}$$

where two dimensionless parameters remain (Tél *et al.*, 2005):

$$\mathrm{Da} = \frac{k}{\overline{\lambda}}, \quad \text{and} \quad \mathrm{Pe} = \frac{\overline{\lambda}L^2}{D_{\mathrm{diff}}}, \tag{3}$$

The first one is the Lagrangian Damköhler number (Tél *et al.*, 2005) which is the ratio of the time scale of the chaotic advection ($1/\overline{\lambda}$, the Lyapunov time) to the time scale of the reaction. The other dimensionless quantity is the Lagrangian Péclet number which characterizes the relative strength of the advection and diffusion, and is typically large: $Pe \gg 1$.

In what follows we consider a simplified version of this model where the distribution is sharp so that it can be modelled by a step function on which the concentration value is the constant $\bar{c}$, and whose support is of width $\delta(t)$. For a pictorial view see Fig. 3 Such sharp transitions are expected to be present for fast rections: $Da \gg 1$ (Giona *et al.*, 2002; Straube *et al.*, 2005; Giona, 2008). The problem reduces then to the bandwidth dynamics of δ which can be described by ordinary differential equations (Tél *et al.*, 2000,2004).

Consider first reactions with front propagation, e.g., an autocatalytic reaction A + C → 2C. In such cases material C is spreading into the medium of material A with a constant front velocity v (see left panel of Fig. 3).. The width of the band in which material C is distributed along the unstable manifold increases therefore with the speed of $2v$, but in a chaotic flow it is also shrinking with the rate $-\bar{\lambda}\delta$. In a domain of linear size L, the dynamics of the relative width $d = \delta/L$ is thus

$$\dot{d} = -\bar{\lambda}d + 2v/L. \tag{4}$$

This equation is expected to be valid for *any* reaction with frontal propagation. According to Luther's law (Cross and Hohenberg, 1993), the front velocity is proportional to the square root of the reaction rate k and of the diffusion coefficient D_{diff}:

$$v = \alpha(kD_{\mathrm{diff}})^{1/2}. \tag{5}$$

With α of order unity, this law holds for an amazing variety of reactions ranging from bistable and excitable ones to flames (Cross and Hohenberg, 1993).

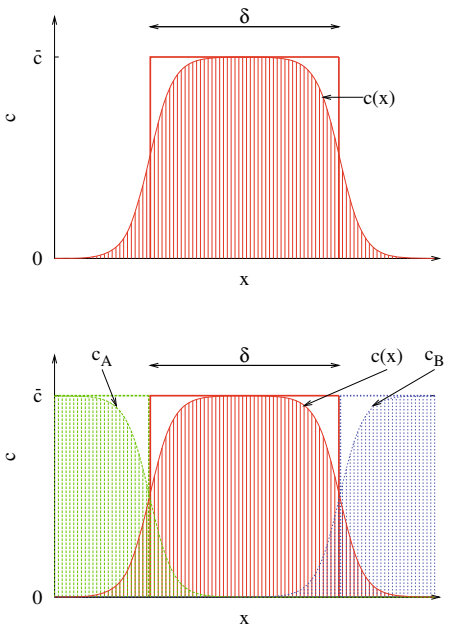

Figure 3. Concentration distribution $c(x)$ along the contracting direction x of the flow and the definition of the bandwidth $\delta(t)$. Left panel: autocatalytic reaction, material A is in abundance outside of C. The transition region, the reaction front, is propagating with a fixed velocity v relative to the fluid. Right panel: acid-base reaction. The motion of the transition region, relative to the flow, is due to diffusion; there is no intrinsic front velocity v in this problem. If the transition region between material C and the other components is narrow enough, the concentration of material C can be well approximated by a function which is constant (of value $\bar{c}$) over an interval of length $\delta(t)$, and zero outside. Concentrations are considered here as number densities. Each band of width δ is imagined to surround a filament of the unstable manifold.

In the case of an acid-base type reaction A+B $\rightarrow$ 2C, we imagine that components A and B are distributed uniformly on the two sides of the manifold and reaction takes place within bands of average width $\delta(t)$. Inside this band the C-concentration is assumed to be a constant $\bar{c}$ (see right panel of Fig. 3.). The width is changing due to diffusion with a rate $D_{\rm diff}/\delta$. Note that $\dot{\delta} = D_{\rm diff}/\delta$ has the usual $\delta = \sqrt{\delta_0^2 + 2D_{\rm diff}t}$ solution. This δ is thus proportional to the quantity σ treated in the lecture by Leonard (2008): $\sigma = \sqrt{2}\delta$. In a chaotic flow, this diffusive spreading is counteracted by the simultaneous presence of exponential contraction. The full dynamics of the dimensionless bandwidth $d = \delta/L$ is now governed by

$$\dot{d} = -\bar{\lambda}d + D_{\rm diff}/(L^2 d). \tag{6}$$

We can unify and generalize these cases by writing the bandwidth dynamics as

$$\dot{d} = -\bar{\lambda}dg(d), \tag{7}$$

where function $g(d)$ is dimensionless. Based on the examples, we assume that there is a steady state solution $d^* > 0$ for which

$$g(d^*) \equiv 0, \tag{8}$$

and the steady state is stable ($g'(d^*) > 0$).

The steady state bandwidth for the particular reactions (4) and (6) is

$$d^* = 2U \quad \text{and} \quad d^* = {\rm Pe}^{-1/2}, \tag{9}$$

respectively. Here $U = v/(\bar{\lambda}L)$ is a dimensionless front velocity, which can be written in view of (5), as $U = \alpha({\rm Da}/{\rm Pe})^{1/2}$ (see (3)). Equations (9) show that acid-base type reactions are essentially diffusion limited, while in the frontal case the reaction rate also plays an important role.

3 Global dynamics due to fractality in open flows

As mentioned earlier, the product is concentrating along the unstable manifold of the chaotic set present in the open flow, whose filaments are complicatedly folded. After some finite transient time, t_c, we can assume that the product has spread along all the branches of the unstable manifold with a more or less uniform width $\delta(t)$, whose dynamics is governed by the filament slice model (7). Due to the foldings, however, several manifold filaments come arbitrarily close. Consequently, many bands filled with product concentration $\bar{c}$ do *overlap*. Such bands cannot be resolved one-by-one. The smaller the bandwidth, the better the separation. The effect of foldings and

overlaps can thus be taken into account by applying the rule of fractal geometry (Mandelbrot, 1982), according to which the number $N(\varepsilon)$ of boxes needed to cover a set with linear size ε depends on the size, the resolution, as

$$N(\varepsilon) \sim \varepsilon^{-D}, \tag{10}$$

with a non-integer power, the fractal dimension, D. Accordingly, with boxes of linear size $\delta(t)/L = d$, the number of boxes needed to cover all the bands occupied with product of width $\delta(t)$ around the fractal manifold of dimension D is proportional to d^{-D}. Since the area of a box is δ^2, the total area of the bands in a square of size L is therefore, $d^{2-D}L^2$ (for simplicity, the prefactor has been taken to be unity). The product content is $C(t) = \bar{c}d(t)^{2-D}L^2$, and the average dimensionless concentration is then $c(t) = C(t)/(\bar{c}L^2)$, i.e.,

$$c(t) = d(t)^{2-D}. \tag{11}$$

By taking the time derivative of this concentration, using (7), and expressing d with c, we find

$$\dot{c} = -(2-D)\bar{\lambda}g(c^{1/(2-D)})c. \tag{12}$$

According to a general rule of the theory of transient chaos (Tél, 1990; Tél and Gruiz, 2006), the combination $(2-D)\bar{\lambda}$ is precisely the escape rate κ from the chaotic saddle. This quantity tells us how rapidly the number of non-reactive particles decays in any preselected region with time, due to the outflow. The decay follows the rule $N(t) \sim \exp(-\kappa t)$. With the escape rate, we find

$$\dot{c} = -\kappa g(c^{1/(2-D)})c. \tag{13}$$

This is a rate equation for the overall concentration in a square-shaped region of the fluid, in which a chemical reaction, specified with the local width dynamics (7), takes place superimposed on an open flow. It is remarkable that the flow's properties are reflected in two parameters of the passive advection process: the escape rate and the dimension. Moreover, the dimension appears in the exponent $1/(2-D)$ which is always larger then unity, since D is between 1 and 2 in two-dimensional flows. By taking into account that function g contains a negative power of its argument (cf. (4), (6), (7)), we see that a *negative* power of the concentration appears. In particular, for the frontal and acid-base reactions governed by (4) and (6) we obtain

$$\dot{c} = -\kappa c + 2U\kappa c^{-\beta}, \quad \text{and} \quad \dot{c} = -\kappa c + \frac{2\kappa}{\mathrm{Pe}}c^{-(1+2\beta)}, \tag{14}$$

respectively, with

$$\beta = \frac{D-1}{2-D} > 0. \tag{15}$$

The powers of c are negative in both cases, leading to a singularity of the product terms due to the underlying fractal pattern. This shows that having only a small amount of product in the region of observation, the rate of reaction is enhanced. This is a consequence of the *fractal catalyst* property of the unstable manifold: if there is less reacting material present the bands become more finely resolved, and the activity becomes faster. On the contrary, when the product is abundant, material flows out rapidly from the region of observation.

Equations (14) illustrate that a steady state can set in with a finite amount of concentration $c^* < 1$, in which the production is compensating the loss due to the outflow from the region of interest. In the general setting we find that this concentration is expressed as a non-integer power of the steady state bandwidth:

$$c^* = {d^*}^{2-D}. \tag{16}$$

Using the particular forms of (4) and (6) we find

$$c^* \sim (\mathrm{Da}/\mathrm{Pe})^{1-D/2}, \quad \text{and} \quad c^* \sim \mathrm{Pe}^{-1+D/2}, \tag{17}$$

respectively. This implies an anomalous scaling with the reaction rate and the diffusion coefficient.

4 Global dynamics due to temporally changing filamentarity in closed flows

The case of closed flows can be considered as the limit of vanishing escape of open flows: $\kappa \to 0$. Equation (13) is said to hold after a transient time, t_c, needed for the product material to be distributed roughly uniformly along the filaments of the unstable manifold. Approaching the limit of closed flows, the filaments becomes denser and denser, the dimension tends towards 2. Consequently, the transient time t_c becomes very large. This is consistent with the fact that for $\kappa \to 0$ Equation (13) leads to the trivial statement $\dot{c} = 0$. For closed flows (13) is thus only valid in the limit of very long times.

To understand the interesting part of the dynamics, preceding the approach towards the steady state, we observe that in closed flows a patch of product is quickly stretched in filaments, but the length of this filament is *growing* over a long period of time. We are applying therefore the width dynamics to an unstable manifold segment whose length is growing in time. Due to area preservation (incompressibility) the typical rate of contraction ($\overline{\lambda}$ in (4)) towards the unstable manifold must be the same as the stretching rate of typical line segments, which should grow initially as $\exp(\overline{\lambda}t)$.

The increase of the length $\mathcal{L}$ of a material line *of finite width* $\delta(t)$ is exponential over short times only, later saturation sets in at some $\mathcal{L}^*$ since the width dynamics reaches a steady state δ^*. In a square-shaped container of area L^2, the total length is $\mathcal{L}^* = L/d^*$. As a simple, though general, form we write the equation for the dimensionless length $l = \mathcal{L}/L$ as

$$\dot{l} = \bar{\lambda} l \left(1 - f(ld^*)\right). \tag{18}$$

We do not specify the functional form of $f\left(\mathcal{L}/\mathcal{L}^*\right) > 0$, but require $f(0) = 0$ and $f(1) = 1$ to ensure an initial exponential growth and a saturation.

Fractal dimension of curves can be considered as a measure of their foldedness. Since a long line can fit into a finite area only if it is strongly folded, we *define* an instantaneous effective dimension $D(t)$ (Villermaux and Gagne, 1994; Károlyi, 2005) by counting the number N of boxes needed to cover all the bands containing product C with boxes of size $d(t)$, and requiring that N scales as a power of d: $N(d(t)) = d(t)^{-D(t)}$ $(1 \leq D_{\text{eff}} \leq 2)$. To total length can then be written as

$$l(t) = d(t)^{1-D(t)}. \tag{19}$$

The product content in the container is $C(t) = \bar{c}\mathcal{L}\delta = \bar{c}L^2 d(t)^{2-D(t)}$, where $\bar{c}$ is the concentration inside the bands. The average dimensionless concentration is then $c(t) = C(t)/(\bar{c}L^2)$, and we find from (19) that

$$c(t) = d(t)l(t) = d(t)^{2-D(t)}, \tag{20}$$

which is a generalization of (11).

By taking the time derivative of the left equality and using (7) and (18), we obtain

$$\dot{c} = c\bar{\lambda}[1 - g(c^{1+\beta}) - f(c^{-\beta}d^*)], \tag{21}$$

where

$$\beta(t) = \frac{D(t) - 1}{2 - D(t)}. \tag{22}$$

It is remarkable that a negative power $(-\beta(t))$ of the average concentration occurs in the chemical rate equation, just like in open flows (c.f. (14)).

Differentiating the right equality of (20), and using (7), (21) and (22), an equation for the effective dimension follows:

$$\dot{\beta} = \frac{\dot{D}}{(2-D)^2} = \frac{\bar{\lambda}}{\ln c}\left\{\beta g(c^{1+\beta}) + (1+\beta)\left[f(c^{-\beta}d^*) - 1\right]\right\}. \tag{23}$$

Equations (21) and (23) form a coupled set of equations for the concentration c and the dimension-dependent exponent β.

For short times, $t \ll 1/\bar{\lambda}$, we can assume that $f \approx 0$ since saturation is not yet in effect. If the product is distributed along a line initially, so that the effective dimension is $D(0) = 1$, implying $\beta(0) = 0$, we find from (21)

$$\dot{c} = \bar{\lambda} c[1 - g(c)]. \tag{24}$$

Substituting here (4) and (6), we find for frontal and acid-base reactions

$$c(t) = c_0 + 2U\bar{\lambda}t, \quad \text{and} \quad c(t) = \sqrt{c_0^2 + 2\bar{\lambda}t/\mathrm{Pe}} \approx c_0 + \frac{\bar{\lambda}t}{c_0 \cdot \mathrm{Pe}}, \tag{25}$$

respectively, implying a linear initial growth. Note that an exponential growth would only follow from (24) if g were constant, which is not the case.

In order to see how the trivial $c \to 1$, $D \to 2$, $d \to d^*$ final state is reached, we take into account that $c^{1+\beta} \equiv d$ and $c^{-\beta} d^* \equiv c d^*/d$, and linearize Eqs. (7), (21) and (23) as

$$\dot{d} = -b\bar{\lambda} d^* (d - d^*) \tag{26}$$

$$\dot{c} = -a\bar{\lambda}(c - 1) - \bar{\lambda}(b - a/d^*)(d - d^*), \tag{27}$$

$$\dot{D} = \frac{a\bar{\lambda}}{\ln d^*}(c - 1) + \frac{\bar{\lambda}}{\ln d^*}(b - a/d^*)(d - d^*), \tag{28}$$

respectively, where $D(t)$ is used instead of $\beta(t)$, and notations $a \equiv f'(1)$ and $b \equiv g'(d^*)$ have been introduced. We immediately observe that the dynamics of the dimension $D(t)$ simply follows the dynamics of the concentration c, as we approach the steady state: comparing (27) and (28) we see that $\dot{D} = -\dot{c}/\ln d^*$. The convergence $c \to 1$ is governed by the largest of the eigenvalues of the Jacobian in Eqs. (26,27). The eigenvalues turn out to be $-a\overline{\lambda}$ and $-bd^*\overline{\lambda}$, hence we have

$$c - 1 \sim \exp(-\sigma t), \quad D_{\mathrm{eff}} - 2 \sim \exp(-\sigma t), \tag{29}$$

with

$$\sigma = \min\{a\overline{\lambda}, bd^*\overline{\lambda}\}. \tag{30}$$

It is easy to check from the definition of $g(d)$ that for frontal and acid-base reactions $bd^* = 1$, and $bd^* = 2$, implying

$$\sigma = \min\{a\overline{\lambda}, \overline{\lambda}\}, \quad \text{and} \quad \sigma = \min\{a\overline{\lambda}, 2\overline{\lambda}\}, \tag{31}$$

respectively. Finally, we mention that for very long times, $t \gg 1/\sigma$, close to the fully homogeneous state, the rule (29) might break down since if the

distance between neighbouring C-bands is smaller than the bandwidth (9), the bands might desintegrate into drops and the basic assumption of the theory is then no longer valid.

It is worth pointing out that, in contrast to the open case, the (time-dependent) dimension is different in the passive and in the active cases. When both diffusion and reaction are absent, we have $g \equiv 1$ and $f \equiv 0$, since there is no saturation in filament length. From (21) $\dot{c} \equiv 0$ follows, as should be in a closed container. From (23) we find that $\dot{\beta} = -\overline{\lambda}/\ln c = \text{const}$, consequently $\beta(t) = \beta(0) - (\overline{\lambda}/\ln c)t$. From (22) $D = (1+2\beta)/(1+\beta)$, i.e.,

$$D(t) = 2 - \frac{2 - D(0)}{1 - (2 - D(0))\bar{\lambda}t/\ln c}. \tag{32}$$

The time evolution of the effective dimension is much slower in passive advection than in reacting cases, since the decay is governed by a power law.

5 Discussion

The behavior indicated by these arguments has been verified by a number of numerical experiments both in open (Toroczkai *et al.*, 1998; Tél *et al.*, 2005) and closed flows (Károlyi and Tél, 2005, 2007). The anomalous scaling of the overall product with the diffusion coefficient, as indicated by (17), has been found in a model of atmospheric chemical reactions based on realistic wind data Wonhas and Vassilicos (2002). Recent experiments (Arratia and Gollub, 2006) are in agreement with both the initial non-exponential growth (25) of the chemical product in closed containers, and the exponential convergence towards to homogeneous distribution (29).

As a conclusion, we augment the qualitative comparison of Table 1. with quantitative relations, including features characterizing the chemical product (see Table 2.).

Table 2. Properties of open and closed reactive chaotic flows.

	open flow	closed flow
chaos	transient	permanent
remaining particles	$N(t) \sim e^{-\kappa t}$, $\kappa = \text{const}$	$N = \text{const}$, $\kappa = 0$
filamentarity	permanent	transient
dimension	$D = \text{const} < 2$	$D(t) - 2 \sim e^{-\sigma t}$
concentration	$\dot{c}$ determined by κ, D	$\dot{c}$ coupled to $\dot{D}$
asymptotics in c	$c^* = d^{*2-D}$	$c(t) - 1 \sim e^{-\sigma t}, c^* = 1$

The theory presented here has been shown (Tél *et al.*, 2005) to be extendable in the open case to temporally non-periodic, e.g., chaotically time dependent flows, to flows with transport barriers, and to three-dimensional flows. In the last case, the unstable manifold might be a fractal surface, implying that the products are distributed along curtains in three-dimensional flows. The theory can also be extended to other types of chemical reactivity (Benczik *et al.* (2005); Benczik (2005); Cox (2006); Menon and Gottwald (2007); Pérez-Muñuzuri and Fernández-García (2007); Straube and Pikovsky (2007)), and in particular to biological activity. In this respect, notable examples are, besides the plankton problem (Abraham *et al.*, 2000; Bracco *et al.*, 2000; Martin, 2003; Sandulescu *et al.*, 2006, 2007, 2008), the competition of populations (Scheuring *et al.*, 2003a; Károlyi *et al.*, 2005), the problem of early evolution (Károlyi *et al.*, 2000; Scheuring *et al.*, 2003b), and metabolic networks (Károlyi *et al.*, 2002) in flows.

The essential observation of our arguments has been the presence of some kind of fractality in all these cases, which leads to a singular enhancement of the reactivity. Since this fractal feature is universal in chaotic advection, on which the reactivity is superimposed, we expect that our treatment of closed flows, and the essence of the features summarized in Table 2., remain valid in all the cases mentioned above.

Acknowledgments

Useful discussion with P. Arratia, I. Benczik, J. Gollub, C. Grebogi, A.P.S. de Moura, Z. Neufeld, I. Scheuring, T. Solomon and E. Villermaux are acknowledged. This research has been supported by OTKA grants T72037, F042476, T046646. Gy. K. has been supported by a Bolyai grant.

Bibliography

E.R. Abraham *et al.*, Nature **407**, 727 2000
H. Aref, J. Fluid Mech. **143**, 1 (1984)
H. Aref, Phys. Fluids **14**, 1315 (2002)
H. Aref, this volume (2008)
H. Aref *et al.*, Physica D **37**, 423 (1989)
P.E. Arratia and J.P. Gollub, Phys. Rev. Lett. **96**, 024501 (2006); see also C. Day, Physics Today **59**, 15 (2006)
I.J. Benczik, Phys. Rev. **E 71**, 066205 (2005)
I.J. Benczik, Z. Neufeld and T. Tél, Phys. Rev. **E 71**, 016205 (2005)
F. Bottausci *et al.*, Phil. Trans. Roy. Soc. (London) **A 362**, 1001 (2004)
A. Bracco, A. Provenzale, and I. Scheuring, Proc. Roy. Soc. B **276**, 1795 (2000)

J. Cartwright *et al.*, Phys. Rev. Lett. **93**, 035502 (2004)
M.J. Clifford, S.M. Cox and E.P.L. Roberts, Physica **A 262** 294 (1999)
S.M. Cox, Phys. Rev. **E 74**, 056206 (2006)
M.C. Cross and P.C. Hohenberg, Rev. Mod. Phys. **65**, 851 (1993)
G. Fernández-García *et al.*, Phys. Rev. **E 77**, 026204 (2008)
J.G. Franjione and J.M. Ottino, Phil. Trans. Royal Soc. **A 338**, 301 (1992)
M. Giona, this volume (2008)
M. Giona, S. Cerbelli, and A. Adrover, Phys. Rev. Lett. **88**, 024501 (2002); J. Phys. Chem. **A 106**, 5722 (2002)
J.-U. Grooß, P. Konopka and R.M. Müller, J. Atmos. Sci. **62**, 860 (2005)
S.W. Jones and H. Aref, Phys. Fluids **31**, 469 (1988)
G. Károlyi, Phys. Rev. **E 71**, 031915 (2005)
G. Károlyi *et al.*, Proceedings of the National Academy of Sciences **97**, 13661 (2000)
G. Károlyi, Z. Neufeld and I. Scheuring, J. Theor. Biol. **236**, 12 (2005)
G. Károlyi, I. Scheuring, and T. Czárán, Chaos **12**, 460 (2002)
G. Károlyi and T. Tél, Phys. Rep. **290**, 125 (1997)
G. Károlyi and T. Tél, Phys. Rev. Lett. **95**, 264501 (2005)
G. Károlyi and T. Tél, Phys. Rev. **E76**, 046315 (2007)
I.Z. Kiss, J.H. Merkin, and Z. Neufeld, Phys. Rev. **E 79**, 026216 (2004)
A. Leonard, this volume (2008)
M. Liu, F.J. Muzzio and R.L. Peskin, Chaos. Sol. Fract. **4**, 869 (1994)
B.B. Mandelbrot, *The Fractal Geometry of Nature* (Freeman, San Francisco, 1982)
A.P. Martin, Prog. Oceanography **57**, 125 (2003)
S.N. Menon and G.A. Gottwald, Phys. Rev. **E 75**, 016209 (2007)
M. Menzinger and A.K. Dutt, J. Phys. Chem. **94**, 4510 (1990)
G. Metcalfe and J.M. Ottino, Phys. Rev. Lett. **72**, 2875 (1994)
I. Mezić, this volume (2008)
S.D. Müller, I. Mezić, J.H. Walter, and P. Koumoutsakos, Comp. Fluids **32**, 521 (2004)
Z. Neufeld, Phys. Rev. Lett. **87**, 108301 (2001)
Z. Neufeld, P. Haynes, and T. Tél, Chaos **12**, 426 (2002a)
Z. Neufeld et al., Phys. Rev. **E66**, 066208 (2002b)
C.R. Nugent, W.M. Quarles, and T.H. Solomon, Phys. Rev. Lett **93**, 218301 (2004)
J.M. Ottino and S. Wiggins, Science **305**, 485 (2004); Phil. Trans. Royal Soc. **A 362**, 923 (2004)
O. Paireau and P. Tabeling, Phys. Rev. **E 56**, 2287 (1997)
M.S. Paoletti and T.H. Solomon, Europhys. Lett. **69**, 819 (2005); M.S. Paoletti and T.H. Solomon, Phys. Rev. **E 72**, 046204 (2005)

M.S. Paoletti, C.R. Nugent and T.H. Solomon, Phys. Rev. Lett. **96**, 124101 (2006)
V. Pérez-Muñuzuri and G. Fernández-García, Phys. Rev. **E 75**, 046209 (2007)
R. Pierrehumbert, Chaos. Sol. Fract. **4**, 1091 (1994)
M.C. Rogers and S. W. Morris, Phys. Rev. Lett. **95**, 024505 (2005);
M.C. Rogers *et al.*, Phys. Rev. **E 77**, 026105 (2008)
M. Sandulescu *et al.*, Tellus **A58**, 605 (2006)
M. Sandulescu *et al.*, Nonlin. Proc. Geophys. **14**, 334 (2007)
M. Sandulescu *et al.*, Ecol. Complexity **5**, 228 (2008)
I. Scheuring *et al.*, Theoretical Population Biology **63**, 77 (2003a)
I. Scheuring *et al.*, Origins Life Evol. B. **33**, 319 (2003b)
M.E. Schwartz and T.H. Solomon, Phys. Rev. Lett. **100**, 028302 (2008)
A.V. Straube, M. Abel, and A. Pikovsky, Phys. Rev. Lett. **93**, 174501 (2005)
A.V. Straube and A. Pikovsky, Phys. Rev. Lett. **99**, 184503 (2007)
M.A. Stremler, this volume (2008)
M.A. Stremler, F.R. Haselton and H. Aref, Phil. Trans. Royal Soc. **A 362**, 1019 (2004)
A.D. Stroock *et al.*, Science **295**, 647 (2002)
T. Tél, in: Directions in Chaos, ed.: H. Bai-Lin (World Scientific, Singapore, 1990) pp. 149-211
T. Tél and M. Gruiz: *Chaotic Dynamics: An Introduction Based on Classical Mechanics*, (Cambridge University Press, Cambridge, 2006)
T. Tél, A.M. de Moura, C. Grebogi, and G. Károlyi, Phys. Reports **413**, 91 (2005)
T. Tél et al., Chaos **10**, 89 (2000); Chaos **14**, 72 (2004)
Z. Toroczkai et al., Phys. Rev. Lett. **80**, 500 (1998)
A. Vikhansky, Phys. Fluids **16**, 4738 (2004)
A. Vikhansky and S.M. Cox, Phys. Fluids **18**, 037102 (2006)
E. Villermaux and J. Duplat, Phys. Rev. Lett. **91**, 184501 (2003)
E. Villermaux and Y. Gagne, Phys. Rev. Lett. **73**, 252 (1994)
E. Villermaux and H. Rehab, J. Fluid Mech **425**, 161 (2000)
A. Wonhas and J.C. Vassilicos, Phys. Rev. **E 65**, 051111 (2002)

Fluid Mixing, Chaotic Advection, and Microarray Analysis

Mark A. Stremler

Department of Engineering Science and Mechanics
Virginia Polytechnic and State University, Blacksburg, VA 24061, U.S.A.

Abstract Chaotic advection has developed into one of the primary tools for analyzing stirring and estimating mixing in laminar flows. Much of the current interest in laminar mixing is focused on small-scale systems, and many of the key applications are in biomedical systems. Here I discuss the use of chaotic advection in designing a mixing protocol to improve DNA microarray analysis. The accuracy and sensitivity of the results can be improved by mixing the solution of unknown DNA across the microarray surface by periodically operating an arrangments of sources and sinks. Optimal operating parameters are predicted using an investigation of chaotic advection in a mathematical model of the system. The findings of the chaos analysis are consistent with experimental mixing results, supporting the use of chaotic advection for predicting and optimizing mixing when designing fluid-based biomedical devices.

1 Introduction

Microarray analysis is a massively parallel biomolecule screening technique that is used widely in genomic and proteomic research (Heller, 2002; Ng and Ilag, 2003; Stoll et al., 2004). In a standard implementation, the microarray is a glass slide with 'probe' molecules immobilized on one surface. Probes are arranged in an array of circular 'spots', with each spot containing thousands of probe molecules of a single sequence or type. Depending on the complexity of the genome being analyzed, for example, the microarray may contain 10,000 or more unique probe spots. Unknown 'target' molecules are analyzed by distributing them across the microarray in a fluid solution and observing which probe spot(s) capture these molecules. A target molecule is captured by a probe molecule when a sufficient number of binding events have occurred to overcome the energy of disassociation. With DNA analysis,

binding, or *hybridization*, occurs as a result of ionic bonding between the nucleotide bases of the respective molecules, and probe DNA hybridize specifically with complementary target DNA. Thus, a target DNA molecule is captured by a specific spot on the microarray surface based on its sequence. Similar behavior can be achieved with protein–protein, protein–DNA, and protein–drug interactions (Stoll et al., 2004). The resulting distribution of target molecules then gives a profile of the types and relative quantities of target in the original sample. This technology has been established as an important tool for gene expression profiling (Schena et al., 1995), disease diagnosis (Mohr et al., 2002), and drug discovery (Debouck and Goodfellow, 1999), and its use is spreading to other areas such as forensic DNA 'fingerprinting' (Willse et al., 2005).

A typical microarray analysis involves covering a centimeter-scale microarray surface with a volume of fluid roughly 10–100 μm thick. The (relatively) large surface area is required to accommodate the thousands of probe spots needed for massively-parallel screening, and the sample volume is kept small in order to minimize the necessary quantity of unknown target and facilitate interaction of these molecules with the probe molecules. Bond distances between hybridized nucleotides are sub-nanometer, so the complementary probe and target DNA must be quite close together for hybridization to occur. In a standard implementation, diffusion is the primary mechanism for achieving this proximity. Since the DNA targets are large macromolecules, transport by molecular diffusion is slow. For those target molecules that are initially close to a complementary probe, diffusion is sufficient. However, effective use of the microarray requires that every probe spot interact with as many target molecules as possible from the entire fluid volume. Thus, reliance on diffusive transport has severely restricted the speed and reliability of this technique; consistent results require tests to be run for as long as three days, with typical tests lasting 12–14 hours (Sartor et al., 2004), and as much as 94% of the resulting data is considered statistically unreliable (Iyer et al., 1999).

A number of researchers have demonstrated that improvements in the speed and reliability of microarray analysis can be achieved by flowing the hybridization solution across the microarray (McQuain et al., 2004; Adey et al., 2002; Liu et al., 2003; Cheek et al., 2001; van Beuningen et al., 2001; Erickson et al., 2004; Vanderhoeven et al., 2004, 2005; Benoit et al., 2001). One approach has been to modify the geometry of the microarray itself (van Beuningen et al., 2001; Benoit et al., 2001). This present work is focused instead on improving conventional glass-based microarray analysis; leveraging the existing infrastructure should greatly increase the potential for truly impacting current and emerging microarray applications.

The microarray community recognizes that the 'appropriate' fluid motion is one that mixes targets across the microarray. The size and geometry of the microarray system restricts practical operation to well within the range of laminar flow (Sharp and Adrian, 2004), and achieving efficient mixing is typically difficult as a result. Viscous forces dominate the fluid motion, limiting the options for driving the flow. Even with motion, many laminar flows will naturally tend to segregate different regions of the fluid. Diffusion will, of course, cause mixing between these regions, but, as noted above, the diffusive time scale is too long to provide adequate levels of mixing across the large microarray surface. Optimizing the performance of a microarray system thus involves establishing a flow protocol that efficiently mixes target molecules across the entire microarray surface.

The most popular approach to mixing across standard microarrays has been to periodically drive the fluid with a combination of flow sources and sinks. The first device of this type in the literature uses a flexible membrane at each end of the top surface to push fluid back and forth across the microarray surface (Adey et al., 2002). A commercial version of this system is available (MAUI from BioMicro Systems, Inc., Salt Lake City, UT), and other vendors have developed similar systems (*e.g.*, Lucidea SlidePro Hybridizer, Amersham Biosciences, Buckinghamshire, UK). Each of these devices uses a single source–sink pair, which tends to push a target molecule back and forth between (roughly) the same two points on the microarray. Other mixing approaches include the 'planetary centrifugal mixer' (Bynum and Gordon, 2004), which overcomes the dominance of viscous forces by subjecting the microarray to approximately $100\,g$ of acceleration. Shear mixing (Vanderhoeven et al., 2004, 2005), in contrast, relies on viscosity to move the fluid as one of the parallel surfaces is moved. Finally, mixing has also been produced by acoustically oscillating bubbles placed strategically throughout the fluid volume (Liu et al., 2003). Operation of these systems is based primarily on empirical observations of mixing or DNA hybridization.

One tool for systematic evaluation of mixing in laminar flow systems is the theory of *chaotic advection*, a phenomenon in which passive particles advected by a periodic velocity field exhibit chaotic trajectories. This mathematical approach has been used to predict rapid mixing in a large number of laminar flows; see, *e.g.*, Ottino (1989); Aref (1990, 2002); Ottino and Wiggins (2004b). A previous investigation of chaotic advection in a simple pulsed source–sink system (Jones and Aref, 1988) suggests that this approach can be used to enhance microarray operation, but there is not yet a clear connection between a theoretical analysis and a practical optimization. The work I review here is aimed at accomplishing this connection.

In the following sections I discuss a system for enhancing microarray

analysis that uses *two* pulsed source–sink pairs, as described in §2. This approach can result in efficient mixing across the entire microarray surface. In §3, I review an experimental analysis (Cola et al., 2006) that indicates this device can be optimized for mixing. Optimal performance of a model system has been determined using an analysis of chaotic advection (Stremler and Cola, 2006), and I review these results in §4. Good correspondence between the experimental and modeling results support the (careful) use of chaotic advection for identifying optimal mixing performance. New modeling results in §4 show that improved mixing should be obtained simply by interchanging the connectivity of the sources and sinks. Finally, in §5 I conclude by discussing the application of this system to DNA microarray analysis (McQuain et al., 2004).

2 The pulsed source–sink system

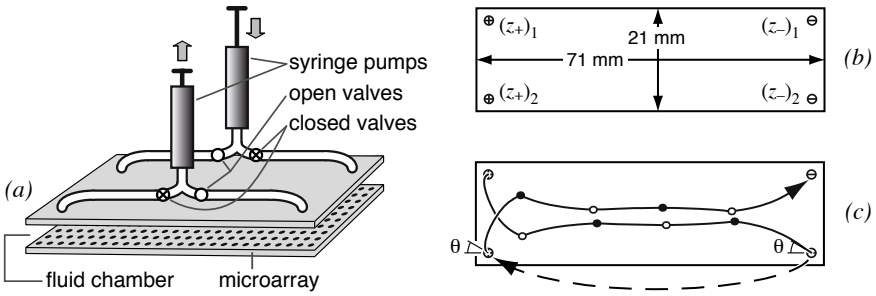

Figure 1. (*a*) Schematic of the pulsed source–sink system in configuration *A*. (*b*) Two-dimensional representation of the fluid chamber in configuration *A*. Source locations are indicated by $\oplus$ and labeled $(z_+)_i$ and sink locations by $\ominus$ and $(z_-)_i$. Source $(z_+)_1$ and sink $(z_-)_1$ are operated together as a pair, as are $(z_+)_2$ and $(z_-)_2$. For configuration *B*, $(z_-)_1$ and $(z_-)_2$ switch locations. (*c*) Computed trajectory of a particle leaving $(z_+)_1$ at $t = 0$ for $\alpha = 20\%$ in the mathematical model of configuration *A*. Circles show the locations of the particle after each pulse. This particle is extracted through $(z_-)_1$ during the 5th pulse and reinjected through $(z_+)_2$ during the 6th pulse. From Stremler and Cola (2006).

The device in Figure 1 uses two interconnected source–sink pairs to mix fluid across a microarray surface. This system is based on the microfluidic mixer introduced by Evans et al. (1997). The sources and sinks are generated by driving fluid through four small holes in the top surface with two syringe pumps. These holes are located near the corners of the fluid chamber as shown, and they are connected to the pumps with, for example,

flexible tubing (McQuain et al., 2004) or microfabricated channels (Cola et al., 2006). For the configuration illustrated in Figure 1, $(z_+)_1$ and $(z_-)_1$ are operated together as a source and a sink, respectively, while $(z_+)_2$ and $(z_-)_2$ are 'turned off' by pinching closed the corresponding channels. The active source and sink each have strength Q, which is the volumetric flowrate injected or extracted through each hole. The system is operated steadily in the configuration shown for a *pulse time*, T_p. During this pulse, the source (or sink) will inject (or extract) a *pulse volume* $V_p = Q/T_p$. Valve states then switch and the pumps reverse direction, and the system is operated steadily for T_p with $(z_+)_2$ and $(z_-)_2$ as the source–sink pair with strength Q. Operation proceeds by periodically switching between these two configurations. In order to minimize the needed volume of working fluid and to enhance mixing, any fluid extracted from the chamber through a sink is later reinjected through the connected source; *e.g.*, fluid extracted through $(z_-)_1$ is reinjected through $(z_+)_2$, as illustrated in Figure 1(*c*). The diameters of the channels are chosen small enough that generally at least 90% of the extracted fluid is reinjected during the next pulse.

With the domain geometry and hole locations fixed as shown in Figure 1, the mixing capabilities of this system depend primarily on the connectivity of the sources and sinks and on the magnitude of the pulse volume. I will refer to the source–sink connectivity shown in Figure 1 as *configuration A*. For *configuration B*, the locations of $(z_-)_1$ and $(z_-)_2$ are switched, so that holes in opposite corners are connected and, for example, the top two holes in Figure 1(*b*) are operated together as a source–sink pair. Fluid is periodically relocated from sink to source in both *A* and *B*.

Raynal et al. (2004) have independently considered a variation of configuration *A*. Their device is square, but otherwise has essentially the same geometry and hole locations as in Figure 1. However, in their approach each hole acts alternately as a source *and* a sink, with any fluid extracted from the chamber subsequently reinjected through the *same* hole. That is, Raynal et al. (2004) use reinjection without relocation, as in the systems mentioned in §1 that use a single source–sink pair. I discuss the impact of this operating procedure on chaos and mixing in §4.

When operated at low Reynolds numbers and high Peclet numbers as intended, the mixing characteristics of this system should not depend on the scale of the fluid chamber or the magnitude of Q. It is convenient then to work in terms of the dimensionless pulse volume $\alpha = V_p/V_c$, where V_c is the volume of the fluid chamber, and the dimensionless time $\tau = Qt/V_c$. With this scaling, the dimensionless pulse time, QT_p/V_c, is equal to α; that is, the dimensionless pulse volume α can also be viewed as the time it takes to complete one pulse relative to the time it would take to inject (and extract)

a fluid volume V_c. Since the depth of the fluid chamber is constant, α is also the fraction of the microarray surface that is covered by injected fluid during a single pulse.

3 Mixing experiments

Cola et al. (2006) present mixing experiments for the pulsed source–sink system in configuration A. Mixing is evaluated by initially injecting a small amount of dye at $(z_+)_1$ and monitoring the distribution of that dye during device operation. Digital images of the fluid domain, such as those in Figure 2, are recorded after each pulse of the system, and it is assumed that the signal intensity at each pixel is proportional to the local dye concentration. The quality of mixing can be quantified by the coefficient of variation in intensity for each image,

$$\mathrm{COV} = \sigma / I_{\mathrm{ave}}, \tag{1a}$$

where I_{ave} is the average intensity in the image and σ is the standard deviation of the intensity. Normalizing the COV to account for variations in initial conditions gives as a measure of mixing the *mixing index*

$$\eta = \mathrm{COV}/\mathrm{COV}_{\max}, \tag{1b}$$

where $\mathrm{COV}_{\max}$ is the maximum coefficient of variation in intensity for a

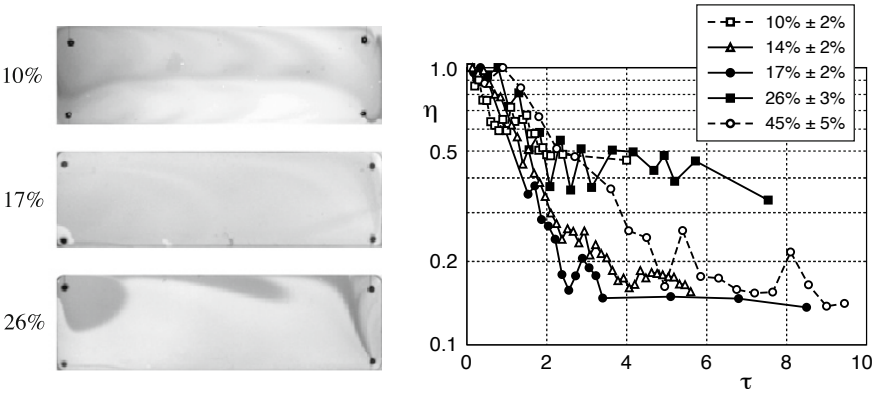

Figure 2. *(left)* Dye distribution after 19 pulses in configuration A for three values of α. *(right)* Evolution of the mixing index η in the experiment. Curves are labeled according to the value of α. Estimated error in η is ± 0.05. From Cola et al. (2006).

given experimental run. Thus, the most poorly mixing image in a single experimental run gives $\eta = 1$, and as the fluid is mixed η decreases.

Temporal evolution of the mixing index is shown in Figure 2 for five different values of α. For the three cases that mix well (*i.e.* for $\alpha \approx 14, 17$, and 45%), the limiting value of η is roughly 0.14. Assuming an error in η of ± 0.05, both $\alpha \approx 14$ and 17% are well mixed (*i.e.* $\eta \leq 0.19$) by $\tau \approx 4$. This dimensionless time does not account for any delay that may occur between sequential pulses, which is neglected for this discussion; comments on the impact of a 'delay time' can be found in either Cola et al. (2006) or Stremler and Cola (2006). The system also mixes well for $\alpha \approx 45\%$, but in this case it takes roughly twice as long to achieve $\eta \leq 0.19$ as for $\alpha \approx 17\%$. For $\alpha \approx 10$ and 26%, mixing initially proceeds at a rate similar to the other cases, but for $\tau > 2$ mixing (temporarily) plateaus with $\eta \approx 0.4$–0.5. This delay in the mixing is caused by segregation of the fluid domain, which is evident in the experimental images in Figure 2. For $\alpha \approx 10\%$, dye that starts in the top (or bottom) half of the domain remains in the top (or bottom) half for a large number of pulses. For $\alpha \approx 26\%$, repeating patterns appear in the dye distribution, with significant portions of the fluid being consistently extracted and reinjected together.

These experiments suggest that optimal mixing in the pulsed source–sink configuration A can be achieved through appropriate selection of the pulse volume. The parameter space for this optimization is quite large, as there are an infinite number of choices for α. It would also be useful to include options such as configuration B in the consideration. The scale of the problem motivates considering transport and mixing in a model of the flow.

4 Chaotic advection analysis

As first noted by Hele-Shaw (1898), low-Reynolds-number flow in a thin planar gap (with depth δ) can be represented by a velocity potential that is proportional to the local pressure. This analogy between Hele-Shaw flow and potential flow has long been used to experimentally visualize inviscid flows, and sources and sinks are commonly used to generate various flow structures. Jones and Aref (1988) document chaotic advection due to pulsed operation of one source and one sink in the unbounded plane. The analytical solution for steady, simultaneous operation of one source and one sink with equal strength $q = Q/\delta$ in the unbounded plane is given by Lamb (1932). For a source and a sink located at z_+ $(= x_+ + \mathrm{i}\, y_+)$ and z_-, respectively, in the complex plane, the complex potential for flow in a rectangular domain

is (Stremler and Cola, 2006)

$$F(z) = \frac{q}{2\pi}\Big\{\log\big[\sigma(z)-\sigma(z_+)\big] + \log\big[\sigma(z)-\sigma^*(z_+)\big] \\ - \log\big[\sigma(z)-\sigma(z_-)\big] - \log\big[\sigma(z)-\sigma^*(z_-)\big]\Big\} \quad (2a)$$

with $\sigma(x) = \mathrm{sn}\big[(x/L+\mathrm{i}\,a)\,K(k), k\big]$, where the asterisk denotes complex conjugation, $\mathrm{sn}(z,k)$ is the Jacobian elliptic sine, $K(k)$ is the complete elliptic integral of the first kind, L is the width of the domain, and k is determined from the aspect ratio of the domain, a, via

$$a = K(\sqrt{1-k^2})/2\,K(k). \quad (2b)$$

Consider, then, potential flow due to piecewise continuous operation of two alternating source–sink pairs as a model of the device operation described in §2. Chaotic advection in this system can be quantified by applying numerous tools from dynamical systems theory. The tools considered here, namely Poincaré sections, Lyapunov exponents, and Kolmogorov-Sinai entropy, rely on tracking passive particles in the flow. Streamlines generated by steady operation of one source–sink pair are given by the imaginary part of F in (2), and the motions of passive particles are obtained by integrating numerically along these streamlines. During the operation of several pulses, a particle will follow a zig-zag trajectory across the microarray surface, as illustrated in Figure 1(c) for configuration A. This zig-zag trajectory is caused by the periodic crossing of streamlines (Ottino and Wiggins, 2004a), which plays an important role in mixing while fluid is transported across the domain.

In the model representation it is necessary to specify the method by which particles extracted through a sink are reinjected through a source. The device operation outlined in §2 uses a 'first in, last out' reinjection procedure; that is, the first particle extracted from the chamber is the last to be reinjected. Other reinjection procedures could be considered (Jones and Aref, 1988), but the experimental system is best represented by this 'first in, last out' procedure. The present model analysis also assumes that any fluid extracted during a single pulse is reinjected during a single (but later) pulse, and that a particle leaves the source with the same angle θ at which it entered the sink. In reality, the reinjection angle is likely to be somewhat random, but a stochastic model precludes the use of standard dynamical systems tools. One of the interesting results of this work is the finding that this ideal model does a reasonable job of predicting optimal mixing despite the underlying assumptions.

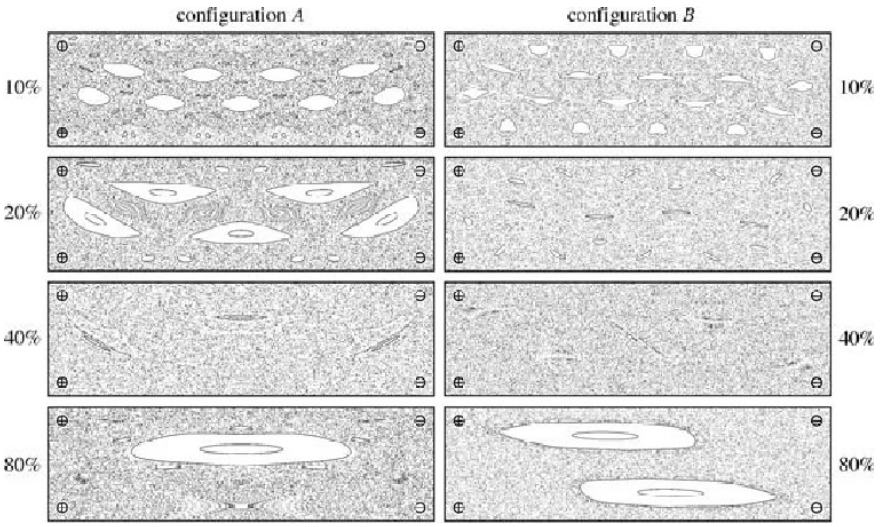

Figure 3. Poincaré sections for the model flow in *(left)* configuration A and *(right)* configuration B. Panels are labeled according to the value of α. Initial particle locations vary between panels and are chosen to highlight island structure. The Poincaré sections for $\alpha = 20$ and 40% in configuration A are from Stremler and Cola (2006).

Poincaré sections such as those in Figure 3 are generated for this system by recording the position of a passive particle in the domain after every period of operation, *i.e.* after every 2α. For the trajectory in Figure 1(c), the solid circles contribute to the Poincaré section. This system exhibits periodic points of various order for different values of α, which is reflected in the *elliptic island* structure in the Poincaré sections. The fluid contained within an elliptic island is isolated from the remainder of the fluid, is stretched only linearly in time, and is thus 'not well mixed'. In contrast, fluid in the surrounding *chaotic sea* is rapidly and repeatedly stretched and folded and is thus, by some measure, 'well mixed'.

The fraction of a Poincaré section that is covered by chaotic sea, μ_s, is quantified in Figure 4(a) for configuration A. Some of the existing work on optimal mixing focuses exclusively on maximizing μ_s (which occurs for $\alpha \approx 40\%$ in configuration A) or on systems that exhibit mixing in the ergodic theory sense (*i.e.* that always have $\mu_s = 100\%$). The presence of large elliptic islands will, of course, have a negative impact on global mixing; fluid in the chaotic sea may be rapidly mixed, but fluid trapped in an elliptic island will

remain separate from the mixed fluid. However, non-ideal behavior such as diffusion tends to quickly 'smear out' the effects of small elliptic islands in most, if not all, practical implementations. This pulsed source–sink work suggests that focusing exclusively on flow protocols with minimal, or no, elliptic islands may be inappropriate when attempting to predict optimal mixing in a practical system.

The exponential stretching rate of fluid in the domain is related to the maximum Lyapunov exponent for the flow, σ_τ. Within the chaotic sea, the length l of a material line will grow exponentially in time as $l \sim l_o \exp(\sigma_\tau \tau)$, where l_o is the initial (infinitesimal) length. The maximum Lyapunov exponent can also be defined for the Poincaré map as $\sigma_n = 2\alpha\,\sigma_\tau$, in which case it quantifies the stretching rate per period of operation. Both σ_τ and σ_n for configuration A are shown in Figure 4(b, c). The stretching rate per period, or σ_n, generally increases with increasing α. However, larger pulse volumes require more time to complete, and as a result σ_τ generally decreases with increasing α. Within an elliptic island, in contrast, fluid experiences only linear stretching in time, and the corresponding Lyapunov exponents are zero.

The net effect of stretching and folding in the flow can be quantified by the Kolmogorov–Sinai, or KS, entropy (Lichtenberg and Lieberman, 1992),

$$h_k = \mu_s\,\sigma_\tau, \tag{3}$$

which can be viewed as an area-weighted average of the Lyapunov expo-

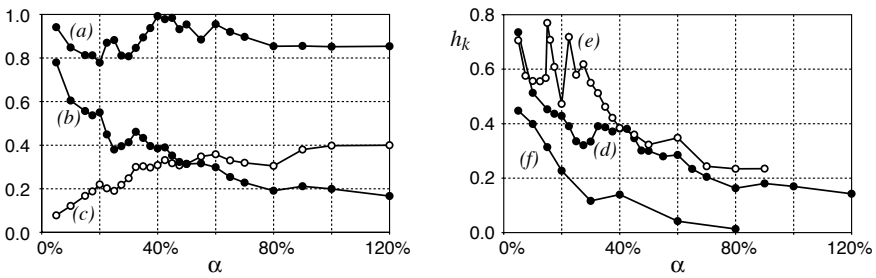

Figure 4. Chaos diagnostics from the model analysis, including, for configuration A, (a) μ_s, the fraction of a Poincaré section covered by the chaotic sea; (b) σ_τ, the maximum Lyapunov exponent for the flow; and (c) σ_n, the maximum Lyapunov exponent for the map. KS entropy, h_k, is shown for (d) configuration A with fluid relocation; (e) configuration B with fluid relocation; and (f) configuration A without fluid relocation, as in Raynal et al. (2004). Curves (a)–(d) are from Stremler and Cola (2006).

nents in the chaotic sea and the elliptic islands. Large KS entropy thus generally indicates rapid stretching and folding over a large fraction of the flow domain, and the conditions that maximize entropy are also likely to mix well. Ideally, the theoretical determination of maximum entropy will predict optimal mixing; this study is aimed, in part, at testing this connection between theory and practice. KS entropy has been used to examine a model system that exhibits mixing in the ergodic theory sense (D'Alessandro et al., 1999), and Stremler and Cola (2006) introduced its use for examining decomposable systems, which contain both regular and chaotic regions.

The KS entropy is shown in Figure 4(d) for source–sink configuration A with fluid relocation from sink to source. The trend in KS entropy suggests that very small pulse volumes optimize mixing. For these cases, however, particles remains trapped in either the top or bottom half of the domain for a large number of periods. This division, or segregation, of the domain is observed in the model analysis of configuration A for $\alpha \leq 10\%$, which is consistent with the experimental results discussed in §3. Fluid within each half of the domain is rapidly stretched and folded, but this fluid is not mixed well throughout the entire domain. Thus, for $\alpha \leq 10\%$ the KS entropy does not accurately predict mixing in configuration A. However, comparison with the mixing experiments shows that KS entropy gives a reasonable prediction of the mixing rate for $\alpha > 10\%$. Optimal mixing is achieved for $\alpha \approx 15\%$, mixing is relatively poor for $23\% \lesssim \alpha \lesssim 32\%$, and mixing improves for $32\% \lesssim \alpha \lesssim 45\%$.

One approach to eliminating the domain segregation for small α in configuration A is to switch the identification of $(z_-)_1$ and $(z_-)_2$, which leads to consideration of configuration B. Fluid extracted from the top half of the domain is now reinjected into the bottom half, for example. The KS entropy for this configuration is shown in Figure 4(e). Maximum entropy is (interestingly) achieved for $\alpha \approx 15\%$ without neglecting $5\% \leq \alpha < 15\%$. This maximum value for h_k is roughly 1.7 times that for configuration A at $\alpha \approx 15\%$! The KS entropy for configuration B is quite sensitive to changes in α, so it is not clear that a such a significant improvement over configuration A would be seen in practice. However, h_k is greater for configuration B than for A at almost every value of α, so these model results predict that configuration B is the better choice even if it is difficult to pinpoint optimal performance.

Finally, consider the device operation examined by Raynal et al. (2004), which corresponds to using configuration A *without* relocating the fluid. That is, fluid is driven between opposite corners during a given pulse, and each hole operates alternately as a source and a sink. The KS entropy for this case is shown in Figure 4(f). The stretching per period (*i.e.* σ_n) is sim-

ilar to that shown in Figure 4(*c*), but each period of operation requires four pulses instead of two. Furthermore, for $\alpha \geq 60\%$ the domain is dominated by regular transport, with $\mu_s < 45\%$. The net result is a KS entropy that is significantly lower than that for configuration A with fluid relocation.

5 Conclusions

Fluid in a rectangular Hele-Shaw cell can be mixed effectively by pulsing two source–sink pairs that are placed at the corners of the domain. Maximum KS entropy is found to occur in a model of the flow when the sources and sinks are connected in configuration B, extracted fluid is relocated from sink to source, and the system is operated with a pulse volume $\alpha \approx 15\%$. For almost every pulse volume examined, the KS entropy for configuration B is greater than that for configuration A, on which our research had previously focused (McQuain et al., 2004; Stremler and Cola, 2006; Cola et al., 2006). Relocating the fluid from sink to source always produces a higher KS entropy than when the fluid is simply reinjected at the location from which it was extracted, as in Raynal et al. (2004).

Comparison of the chaotic advection analysis with the experimental mixing results for configuration A shows that, when interpreted carefully, relative values of KS entropy can predict mixing performance in a pulsed source–sink system. In the case of configuration A, this approach incorrectly identifies small α as optimal. However, this same analysis clearly shows segregation between the two halves of the domain for $\alpha \leq 10\%$, as observed in the experiments. When this segregation does not occur (*i.e.* for $\alpha > 10\%$), the experimentally observed mixing performance corresponds well with KS entropy. This segregation does not appear in configuration B, and I expect that in this case the KS entropy provides a reliable prediction of mixing performace over all of the pulse volumes examined.

Configuration A has been applied to microarray analysis for the case $\alpha \approx 30\%$, and the details are reported in McQuain et al. (2004). This application was actually conducted before any of the work in §3 and §4, and it has served as motivation for the detailed study I review here. Thus, the microarray application remains, at this point, a preliminary study. Mixing the fluid solution during the analysis resulted in higher overall levels of hybridization, more uniform hybridization across an array, and significantly shorter analysis times relative to a standard analysis with no fluid motion. It is my expectation that noticeable improvement over these results can be achieved by mixing the hybridization fluid with configuration B using $\alpha \approx 15\%$.

I would like to thank my colleagues F.R. Haselton, who has willingly

shared with me his expertise in microarray analysis, and T.S. Fisher, who initiated this collaborative effort and provided crucial experimental expertise. A significant portion of the work reviewed here was performed by B.A. Cola, E. Graybill, D.S. Schaffer, and P. Sheppard, whom I thank for their assistance. This publication was made possible by grant number 1-R43-CA94601-01 from the NIH National Cancer Institute and by contract/grant number W911NF0410349 from the U. S. Army Research Laboratory and the U. S. Army Research Office.

Bibliography

N. B. Adey, M. Lei, M. T. Howard, J. D. Jensen, D. A. Mayo, D. L. Butel, S. C. Coffin, T. C. Moyer, D. E. Slade, M. K. Spute, A. M. Hancock, G. T. Eisenhoffer, B. K. Dalley, and M. R. McNeely. Gains in sensitivity with a device that mixes microarray hybridization solution in a 25-μm-thick chamber. *Anal. Chem.*, 74:6413–6417, 2002.

H. Aref. Chaotic advection of fluid particles. *Proc. R. Soc. London* A, 434: 273–289, 1990.

H. Aref. The development of chaotic advection. *Phys. Fluids*, 14(4):1315–1325, 2002.

V. Benoit, A. Steel, M. Torres, Y.-Y. Yu, H. Yang, and J. Cooper. Evaluation of three-dimensional microchannel glass biochips for multiplexed nucleic acid fluorescence hybridization assays. *Anal. Chem.*, 73(11):2412–2420, 2001.

M. A. Bynum and G. B. Gordon. Hybridization enhancement using microfluidic planetary centrifugal mixing. *Anal. Chem.*, 76:7039–7044, 2004.

B. J. Cheek, A. B. Steel, M. P. Torres, Y. Y. Yu, and H. Yang. Chemiluminescence detection for hybridization assays on the flow-thru chip, a three-dimensional microchannel biochip. *Anal. Chem.*, 73:5777–5783, 2001.

B. A. Cola, D. K. Schaffer, T. S. Fisher, and M. A. Stremler. A pulsed source–sink fluid mixing device. *J. Microelectromech. Sys.*, 15(1), 2006. In press.

D. D'Alessandro, M. Dahleh, and I. Mezić. Control of mixing in fluid flow: a maximum entropy approach. *IEEE Trans. Auto. Control*, 44(10):1852–1863, 1999.

C. Debouck and P. N. Goodfellow. DNA microarrays in drug discovery and development. *Nature Genetics*, 21(1 Suppl.):48–50, 1999.

D. Erickson, X. Liu, U. Krull, and D. Li. Electrokinetically controlled DNA hybridization microfluidic chip enabling rapid target analysis. *Anal. Chem.*, 76:7269–7277, 2004.

J. Evans, D. Liepmann, and A. P. Pisano. Planar laminar mixer. In *Proc. 10th Ann. Int. Wrkshp Microelectromech. Sys. (MEMS '97)*, pages 96–101. IEEE, 1997.

H. S. Hele-Shaw. The flow of water. *Nature*, 58:34–36, 1898.

M. J. Heller. DNA microarray technology: Devices, systems, and applications. *Ann. Rev. Biomed. Eng.*, 4:129–153, 2002.

V. R. Iyer, M. B. Eisen, D. T. Ross, G. Schuler, T. Moore, J. C. F. Lee, J. M. Trent, L. M. Staudt, J. Hudson Jr., M. S. Boguski, D. Lashkari, D. Shalon, D. Botstein, and P. O. Brown. The transcriptional program in the response of human fibroblasts to serum. *Science*, 283(5398):83–87, 1999.

S. W. Jones and H. Aref. Chaotic advection in pulsed source-sink systems. *Phys. Fluids*, 31(3):469–485, 1988.

H. Lamb. *Hydrodynamics*. Cambridge University Press, 6th edition, 1932.

A. J. Lichtenberg and M. A. Lieberman. *Regular and chaotic dynamics*. Springer–Verlag, New York, 2nd edition, 1992.

R. H. Liu, R. Lenigk, R. L. Druyor-Sanchez, J. Yang, and P. Grodzinski. Hybridization enhancement using cavitation microstreaming. *Anal. Chem.*, 75(8):1911–1917, 2003.

M. K. McQuain, K. Seale, J. Peek, T. Fisher, S. Levy, M. A. Stremler, and F. R. Haselton. Chaotic mixer improves microarray hybridization. *Anal. Biochem.*, 325:215–226, 2004.

S. Mohr, G. D. Leikauf, G. Keith, and B. H. Rihn. Microarrays as cancer keys: An array of possibilities. *J. Clinical Oncology*, 20:3165–3175, 2002.

J. H. Ng and L. L. Ilag. Biochips beyond DNA: technologies and applications. *Biotech. Ann. Rev.*, 9:1–149, 2003.

J. M. Ottino. *The Kinematics of Mixing: Stretching, Chaos, and Transport*. Cambridge University Press, 1989.

J. M. Ottino and S. Wiggins. Designing optimal micromixers. *Science*, 305 (5683):485–486, 2004a.

J. M. Ottino and S. R. Wiggins. (eds). A theme issue on "Transport and mixing at the microscale". *Phil. Trans. Roy. Soc. London* A, 362(1818): 923–1129, 2004b.

F. Raynal, F. Plaza, A. Beuf, P. Carrière, E. Souteyrand, J.-R. Martin, J.-P. Cloarec, and M. Cabrera. Study of a chaotic mixing system for DNA chip hybridization chambers. *Phys. Fluids*, 16(9):L63–L66, 2004.

M. Sartor, J. Schwanekamp, D. Halbleib, I. Mohamed, S. Karyala, M. Medvedovic, and C. R. Tomlinson. Microarray results improve significantly as hybridization approaches equilibrium. *Biotechniques*, 36: 790–796, 2004.

M. Schena, D. Shalon, R. W. Davis, and P. O. Brown. Quantitative monitoring of gene expression patterns with a complementary DNA microarray. *Science*, 270(5235):467–470, 1995.

K. V. Sharp and R. J. Adrian. Transition from laminar to turbulent flow in liquid filled microtubes. *Exp. Fluids*, 36:741–747, 2004.

D. Stoll, J. Bachmann, M. F. Templin, and T. O. Joos. Microarray technology: an increasing variety of screening tools for proteomic research. *Drug Disc. Today: Targets*, 3(1):24–31, 2004.

M. A. Stremler and B. A. Cola. A maximum entropy approach to optimal mixing in a pulsed source–sink flow. *Phys. Fluids*, 18(011701):4pp., 2006.

R. van Beuningen, H. van Damme, P. Boender, N. Bastiaensen, A. Chan, and T. Kievits. Fast and specific hybridization using flow-through microarrays on porous metal oxide. *Clin. Chem.*, 47:1931–1933, 2001.

J. Vanderhoeven, K. Pappaert, B. Dutta, G. Baron, and G. Desmet. Exploiting the benefits of miniaturization for the enhancement of DNA microarrays. *Electrophoresis*, 25:3677–3686, 2004.

J. Vanderhoeven, K. Pappaert, B. Dutta, P. Van Hummelen, and G. Desmet. Comparison of a pump-around, a diffusion-driven, and a shear-driven system for the hybridization of mouse lung and testis total RNA on microarrays. *Electrophoresis*, 26:3773–3779, 2005.

A. Willse, D. P. Chandler, A. White, M. Protic, D. S. Daly, and S. Wunschel. Comparing bacterial DNA microarray fingerprints. *Stat. App. Genetics Molecular Bio.*, 4(1):art. 19, 36 pp, 2005.

The Size of Ghost Rods

Jean-Luc Thiffeault,[*] Emmanuelle Gouillart,[†] and Matthew D. Finn[‡]

[*] Department of Mathematics, University of Wisconsin – Madison, Madison, WI 53706, USA

[†] Surface du Verre et Interfaces, UMR 125 CNRS/Saint-Gobain, 93303 Aubervilliers, France

[‡] School of Mathematical Sciences, University of Adelaide, Adelaide SA 5005, Australia

Abstract "Ghost Rods" are periodic structures in a two-dimensional flow that have an effect on material lines that is similar to real stirring rods. An example is a periodic island: material lines exterior to it must wrap around such an island, because determinism forbids them from crossing through it. Hence, islands act as topological obstacles to material lines, just like physical rods, and lower bounds on the rate of stretching of material lines can be deduced from the motion of islands and rods. Here, we show that unstable periodic orbits can also act as ghost rods, as long as material lines can "fold" around the orbit, which requires the orbit to be parabolic. We investigate the factors that determine the effective size of ghost rods, that is, the magnitude of their impact on material lines.

1 Introduction

Topological kinematics is the application of topology to chaotic advection in fluids. In two dimensions, braids are the natural mathematical construct to use for a topological analysis. Boyland et al. used braids very effectively to analyse the motion of stirring rods in viscous flow (Boyland et al., 2000) and point vortices in ideal flow (Boyland et al., 2003). A braid is associated with the motion of the rods or vortices by plotting their trajectory in a space-time diagram: the resulting "spaghetti plot" is obviously a braid. Here, we shall not be too concerned with the precise mathematical properties of braids—the intuitive, capillary notion of what a braid resembles will suffice.

Rods and points vortices share the common feature that they are topological obstacles to material lines in two dimensions. Of course, any fluid particle is such an obstacle, and recently one of us analysed braids formed by particle trajectories (Thiffeault, 2005). The fact that particle orbits are

topological obstacles puts a lower bound on the *topological entropy*—the growth rate of material lines (Boyland et al., 2000; Newhouse and Pignataro, 1993). Imagine a material line that is initially linked around the topological obstacles under consideration (rods or fluid particles). Then as the position of these obstacles evolves the material line is dragged along, and as the particles braid around each other the material line must grow by at least a certain amount. The properties of the braid thus imply a lower bound on the growth rate of material lines in the fluid.

For time-periodic flows, the natural topological obstacles to study are fluid parcels associated with particular periodic orbits. Recently, we introduced to fluid mechanics the concept of "ghost rods" (Gouillart et al., 2006). We analysed the motion of material rods, stable periodic orbits (islands), and unstable periodic orbits from a topological perspective. We showed that periodic orbits associated with islands behave very similarly to material rods: they are large topological obstacles ploughing through the fluid, and material lines must get out of their way or else wrap around them. Periodic islands have the advantage of being easily identifiable visually, and can clearly be regarded as "rods." Figure 1 illustrates this: there is only one physical rod stirring the flow, but a ghostly second rod is clearly visible in the centre-left portion of the plot, around which material lines are wrapped. Indeed, there is a regular island in that region (Gouillart et al., 2006).

Figure 1. A material line being stirred by a moving rod in a viscous fluid. The rod is the circle visible in the centre-right portion of the fluid, but observe that there is a rod-like structure in the centre-left portion. This is a periodic island that acts like a rod—a ghost rod.

The foregoing description is topological in nature. The size of the rods is immaterial to the topological entropy (Boyland et al., 2000; Finn et al., 2003). Of course, in practice their size matters a lot: if the rods are made smaller, so does the region of the fluid for which the topological entropy lower bound applies. In the limit of infinitely small rods, one might expect this region to shrink to zero. This is certainly true of physical rods: if they were made infinitely small, the fluid would not even notice their presence and nothing would happen, except in a vanishingly small region. There is currently no theory that gives the size of the affected region given the size of the rods and their path, but in practice it is observed (in viscous flows) that it is of the order of the size of the rods and the size of the region swept by their motion.

So much for physical rods. But what about ghost rods? As their name indicates, they have no material existence. However, since they behave much like physical rods, we may ask what is their effective size. That is, topologically a ghost rod is supposed to mimic a real physical rod, but how much of an impact does it effectively have on the surrounding fluid? For periodic islands, the answer is clear: the effective size of the ghost rod is the size of the island. Figure 1 convincingly illustrates that, as far as material lines are concerned, there is a stirring rod of the size of the periodic island in the centre-left portion of the flow.

For unstable periodic orbits, the answer is much less clear, since in principle ghost rods of this type have zero size. In this paper, we shall investigate the effective size of ghost rods associated with unstable periodic orbits. In fact, as we shall see, not all unstable periodic orbits can even be said to be ghost rods. Rather, only unstable periodic orbits of parabolic (as opposed to hyperbolic) type can hope to qualify as ghost rods. The local linear structure near an hyperbolic orbit prevents material lines from "wrapping" around the periodic point, so that it does not appear as a rod at all. For parabolic orbits of a certain type, the unstable manifold terminates at the periodic orbit, allowing material lines to wrap around the point without encountering the invariant manifold. Thus, the periodic orbit appears *visually* as a tiny rod, which is our criterion for considering periodic orbits to be ghost rods.

2 Unstable Periodic Orbits

In an incompressible flow, the linearised flow around an unstable periodic orbit can be one of two types. Figure 2 depicts the most common, called a hyperbolic orbit, or hyperbolic point if one is speaking of the Poincaré section (stroboscopic map) of the time-periodic flow. There are two distin-

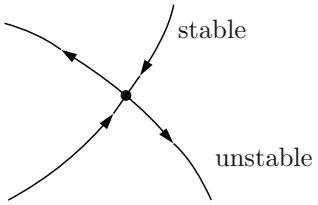

Figure 2. The stable and unstable manifolds of a hyperbolic point.

guished directions along which points respectively get away from or converge to the periodic orbit. These directions can be nonlinearly extended into the unstable and stable manifolds of the periodic orbit. A sufficient condition for the periodic orbit to be hyperbolic is that its Floquet matrix have non-degenerate eigenvalues. (The Floquet matrix is obtained by linearising the system about the periodic orbit and integrating over a full period of the orbit, as we will do in Section 3 for a specific flow.) Even though they are topological obstacles to material lines in the flow, such orbits can hardly be called ghost rods. This is because material lines must align with the unstable manifold of the periodic orbit, a phenomenon sometimes referred to as asymptotic directionality (Giona et al., 1998; Thiffeault, 2004). A material line cannot possibly fold around such a periodic orbit, since the unstable manifold goes straight through the orbit and appears linear in its neighbourhood. Hence, the periodic orbit does not "look" like a tiny little rod to the naked eye: it looks like any other point on the material line, and only a detailed knowledge of the velocity field allows its detection, usually by numerical means. We conclude that hyperbolic periodic orbits do not form "proper" ghost rods, since they cannot be detected visually.

That leaves the second type of unstable periodic orbit: parabolic orbits. In that case the Floquet matrix has degenerate eigenvalue that must both be equal to unity, by incompressibility of the fluid. For parabolic points, we cannot deduce the behaviour of points near the periodic orbit by examining only the linearised system—nonlinear terms must be considered. As we shall see in the following section, a particular type of nonlinear structure gives rise to parabolic points that exhibit the appropriate behaviour for a ghost rod.

3 Case Study: The Sine Flow

We shall now illustrate the type of unstable periodic orbit that gives rise to ghost rods by examining a specific system, namely the Zeldovich sine

flow (Pierrehumbert, 1994). This is a nice system to work with because its Poincaré map can be obtained analytically, and for special parameter values we can also determine some periodic orbits analytically. These orbits were exploited by Finn et al. (2006) to show the presence of chaos. The sine flow is given by the velocity field

$$\boldsymbol{u}(\boldsymbol{x},t) = \begin{cases} (0\,,\,\sin 2\pi x), & n\tau \le t < (n+\frac{1}{2})\tau; \\ (\sin 2\pi y\,,\,0), & (n+\frac{1}{2})\tau \le t < (n+1)\tau, \end{cases} \tag{1}$$

where n is an integer. The equation $\dot{\boldsymbol{x}} = \boldsymbol{u}(\boldsymbol{x},t)$ can then be integrated over one period to give the sine map

$$\begin{aligned} x_{n+1} &= x_n + \tfrac{1}{2}\,\tau\,\sin 2\pi y_{n+1}\,; \\ y_{n+1} &= y_n + \tfrac{1}{2}\,\tau\,\sin 2\pi x_n\,, \end{aligned} \tag{2}$$

with $\boldsymbol{x}_n := \boldsymbol{x}(n\tau)$. As an example, we will take $\tau = 1$, because then we can determine many periodic orbits analytically. For instance, there is a period-4 orbit starting at $\boldsymbol{x}_0 = (1/12, 1/2)$, with iterates

$$(1/12,1/2) \to (7/12,3/4) \to (7/12,1/2) \to (1/12,1/4) \to (1/12,1/2). \tag{3}$$

The initial location of this orbit is inside the small square in Fig. 3(a), which also shows a material line advected for a few periods of the sine flow. Figure 3(b) is a blow-up of the material line near this periodic orbit. Notice how the material line is sharply folded around the periodic orbit. In fact, Fig. 3(a) contains several such sharp folds. They are quite generic in chaotic flows, and are associated with regions of anomalously low stretching (Liu and Muzzio, 1996; Thiffeault, 2004).

We are interested in the behaviour of the map (2) in the neighbourhood of this periodic orbit, so we define a variable $\widetilde{\boldsymbol{X}} := \boldsymbol{x} - \boldsymbol{x}_0$. Then, we can expand the map to second order in $\widetilde{\boldsymbol{X}}$,

$$\begin{aligned} \widetilde{X}' &= \widetilde{X} - 2\pi\widetilde{Y} + \alpha_{\widetilde{X}}\,\widetilde{X}^2 + \beta_{\widetilde{X}}\,\widetilde{Y}^2 + \gamma_{\widetilde{X}}\,\widetilde{X}\widetilde{Y}, \\ \widetilde{Y}' &= \widetilde{Y} \qquad\qquad + \alpha_{\widetilde{Y}}\,\widetilde{X}^2 + \beta_{\widetilde{Y}}\,\widetilde{Y}^2 + \gamma_{\widetilde{Y}}\,\widetilde{X}\widetilde{Y}, \end{aligned} \tag{4}$$

where the primes denote four iterations of the sine map, so that the periodic orbit has become a fixed point of the map (4) at $\widetilde{\boldsymbol{X}} = (0,0)$. The periodic orbit is parabolic, as can easily be seen from the fact that the linear part of (4) (the Floquet matrix) has matrix representation

$$\mathcal{J} = \begin{pmatrix} 1 & -2\pi \\ 0 & 1 \end{pmatrix}, \tag{5}$$

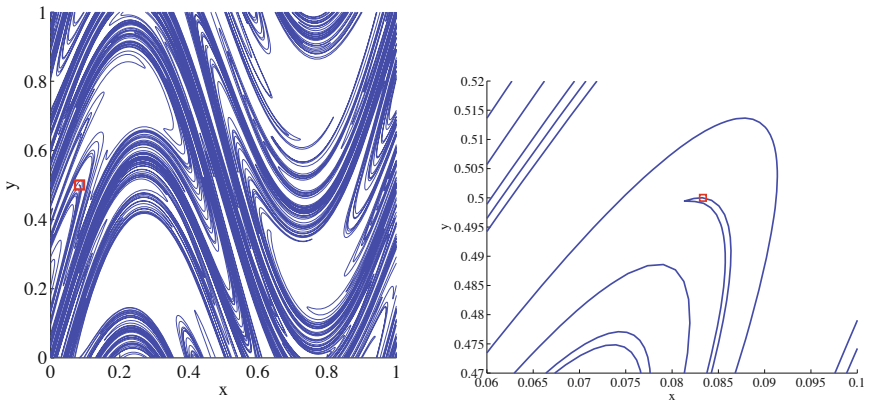

(a) (b)

Figure 3. (a) A material line stretched and folded by the sine flow. The parabolic periodic point at $(x, y) = (1/12, 1/2)$ is shown boxed. (b) Blow-up of the periodic point. Note that the material line is folded near, but not quite tightly around, the parabolic fixed point.

which implies unit eigenvalues for the map. However, this matrix is not diagonalisable: it only has one eigenvector, $(0 \quad 1)^T$ (this can only occur for a parabolic point). We will see that it is this nondiagonalisable nature that allows the "folding" of material lines around the periodic point. In general, a matrix $\mathcal{J}$ has this property if $(\mathcal{J} - \mathbb{I})^2 = 0$, for $\mathcal{J} \neq \mathbb{I}$, which given that $\det \mathcal{J} = 1$ is equivalent to $\operatorname{tr} \mathcal{J} = 2$, with $\mathcal{J} \neq \mathbb{I}$.

After a linear transformation and a near-identity area-preserving quadratic transformation, Eq. 4 can be brought into the form

$$\begin{aligned} X' &= X + Y + \alpha XY\,, \\ Y' &= Y + \alpha\left(\tfrac{1}{2}X^2 + XY\right), \end{aligned} \tag{6}$$

where the coefficients are such that the map is area-preserving to linear order. (The transformation used to get to (6) is not generally orientation-preserving.) As long as the linear part of the system is a Jordan block of the form (5), we can transform the system to Eq. (6). We have thus reduced the dynamics near the parabolic point to a one-parameter map (basically a Hénon map), which we proceed to analyse.

3.1 Invariant Manifolds and Dynamics Near the Origin

We now want to find the shape of the unstable and stable manifolds of the fixed point of (6) at the origin. Unlike hyperbolic fixed points, for a parabolic point the invariant manifolds cannot be determined solely from the linear part. Rather, we use the invariance property of the manifold: we parametrise the invariant manifold by $(X, Y_{\text{inv}}(X))$ and iterate the map,

$$X' = X + Y_{\text{inv}}(X) + \alpha\, XY_{\text{inv}}(X)\,, \tag{7a}$$

$$Y_{\text{inv}}(X') = Y_{\text{inv}}(X) + \alpha\left(\tfrac{1}{2}X^2 + XY_{\text{inv}}(X)\right), \tag{7b}$$

where we wrote $Y' = Y_{\text{inv}}(X')$ since, by the invariance property, the iterated point must still belong to the invariant manifold. We can then substitute (7a) into (7b),

$$Y_{\text{inv}}(X + Y_{\text{inv}}(X) + \alpha\, XY_{\text{inv}}(X)) = Y_{\text{inv}}(X) + \alpha\left(\tfrac{1}{2}X^2 + XY_{\text{inv}}(X)\right), \tag{8}$$

which is an equation that must be solved for $Y_{\text{inv}}(X)$. We are interested in the small X form of the manifold, so we assume $Y_{\text{inv}}(X) = \sigma X^\delta$ and try to balance the leading order terms:

$$\sigma\,(X + \sigma X^\delta + \alpha\,\sigma X^{1+\delta})^\delta = \sigma X^\delta + \alpha\left(\tfrac{1}{2}X^2 + \sigma X^{1+\delta}\right). \tag{9}$$

Where we go next depends on the magnitude of δ. If $\delta = 1$, we get the equation $\sigma(1+\sigma) = \sigma$ for the coefficients of the linear terms, which implies $\sigma = 0$, an unacceptable state of affairs since then the quadratic term is unbalanced. If $\delta < 1$, we get the leading-order balance

$$\sigma\,(\sigma X^\delta)^\delta = \sigma X^\delta. \tag{10}$$

This can only be satisfied for $\delta = 1$, a contradiction, or $\delta = 0$, which again leads to an unbalanced quadratic term. Hence, our only choice is to take $\delta > 1$, which gives the leading-order balance

$$\sigma\,(X + \sigma X^\delta)^\delta = \sigma X^\delta + \tfrac{1}{2}\alpha X^2, \tag{11}$$

where we have kept an extra order, because the leading terms cancel after expanding the exponent,

$$\sigma X^\delta\,(1 + \sigma\delta X^{\delta-1}) = \sigma X^\delta + \tfrac{1}{2}\alpha X^2, \tag{12}$$

and we get finally

$$\sigma^2\,\delta X^{2\delta-1} = \tfrac{1}{2}\alpha X^2, \tag{13}$$

yielding $\delta = 3/2$, $\sigma = \pm\sqrt{\alpha/3}$. We can thus write the shape of the invariant manifolds as

$$Y_{\mathrm{inv}}(X) = \pm\sqrt{\tfrac{1}{3}\,\alpha X}X\,, \tag{14}$$

to leading order, where we have written αX under the square root to show that X and α must have the same sign. Note an important fact: for a parabolic point of this type, the manifolds exist only on one side of the X axis, in contrast to a hyperbolic point (Fig. 2) where the manifolds must radiate from the fixed point in four directions.

The two solutions for σ correspond to the stable and unstable manifolds. We can determine which sign goes with which manifold by looking at an iterate of X in Eq. (7a),

$$X' = X \pm \sqrt{\tfrac{1}{3}\,\alpha X}X\,, \tag{15}$$

where we neglected higher-order terms ($X^{5/2}$). Thus, for $\alpha > 0$, which implies $X > 0$, the '+' solution takes X farther from the origin (unstable manifold), whilst the '$-$' solutions takes the point closer to the origin (stable manifold). The situation is reversed for $\alpha < 0$.

Figure 4 shows a few iterates of horizontal lines under the action of the map (6). The linear part of the map acts as a "shear flow" that sweeps the line around the origin, but the nonlinear terms prevent the line from crossing the unstable manifold. The net result is a line folded around the unstable manifold. This is why it is appropriate to refer to (6) as the 'folding normal form': inside every sharp fold of the flow lurks such a map.[1] Since nearby material lines align with the unstable manifold of the periodic orbit, the folding is made possible by the one-sidedness of the unstable manifold: unlike hyperbolic points (Fig. 2), the manifold does not traverse the parabolic periodic point, but instead terminates there. This allows material lines to wrap around the periodic point without encountering the invariant unstable manifold, which cannot be crossed.

3.2 Curvature

As time progresses the folds in the material lines in Fig. 4 come closer and closer to the periodic orbit. There seems to be no limit to how close they can come, which is consistent with the ghost rod having zero effective size. The best we can do is to characterise the effective size of the ghost rod by how quickly the curvature of the folds evolve. We shall now examine how the curvature of a material line evolves near the parabolic orbit.

[1] At the workshop, Stefano Cerbelli and Massimiliano Giona pointed out that their research also seems to support this.

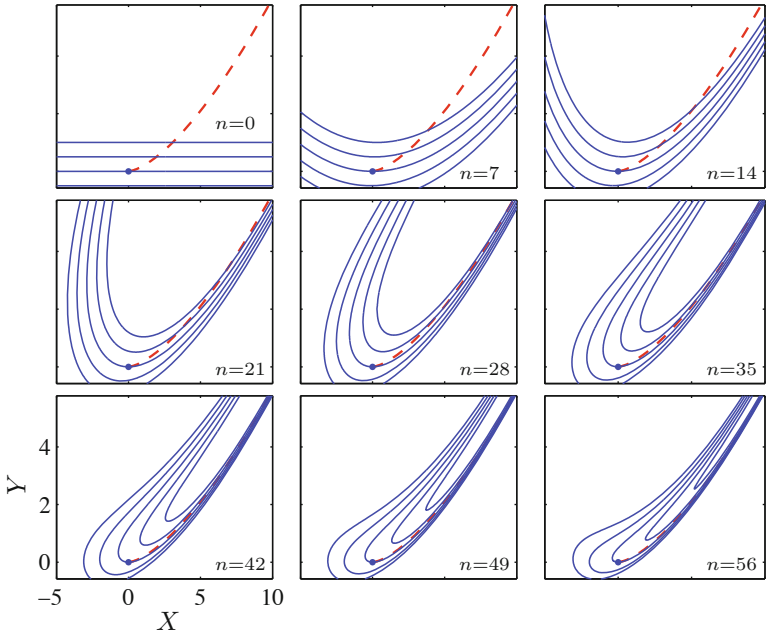

Figure 4. Iteration of a few material lines by the map (6) for $\alpha = 1$. The lines fold around the unstable manifold (dashed curve). The X axis has been rescaled by 10^{-3}, the Y axis by 10^{-4}.

Consider a material line going through the origin of (6), as depicted in Fig. 4. The tangent map of (6) at the origin tells us how the tangent to the curve evolves,

$$\begin{pmatrix} \delta X' \\ \delta Y' \end{pmatrix} = \begin{pmatrix} 1 & 1 \\ 0 & 1 \end{pmatrix} \begin{pmatrix} \delta X \\ \delta Y \end{pmatrix}, \tag{16}$$

where $(\delta X \;\; \delta Y)^T$ is the tangent. The second variation of (6) is

$$\begin{pmatrix} \delta^2 X' \\ \delta^2 Y' \end{pmatrix} = \begin{pmatrix} 1 & 1 \\ 0 & 1 \end{pmatrix} \begin{pmatrix} \delta^2 X \\ \delta^2 Y \end{pmatrix} + \alpha \begin{pmatrix} \delta X \delta Y \\ (\delta X)^2 + \delta X \delta Y \end{pmatrix}. \tag{17}$$

For the case shown in Fig. 4, the initial tangent is parallel to $(1 \;\; 0)^T$, which is an eigenvector of the matrix in (16): the tangent doesn't change. Given that $\delta^2 X$ and $\delta^2 Y$ are zero initially (the line is straight), we can solve (17) for $\delta^2 Y$,

$$\delta^2 Y = n\, \alpha (\delta X)^2, \tag{18}$$

where n is the number of iterations. The curvature of the line is given by (Liu and Muzzio, 1996)

$$\kappa = \frac{\delta X \delta^2 Y - \delta Y \delta^2 X}{\|\delta \boldsymbol{X}\|^3}\,. \tag{19}$$

Now given the solution (18) and the fact that $\delta Y = 0$ for all time, the curvature evolves as

$$\kappa = n\,\alpha\,, \tag{20}$$

so the curvature of the material line grows linearly with time. This is verified by a calculation with the sine flow, for the periodic orbit (3): Figure 5 shows that the curvature of a material line anchored at the periodic orbit

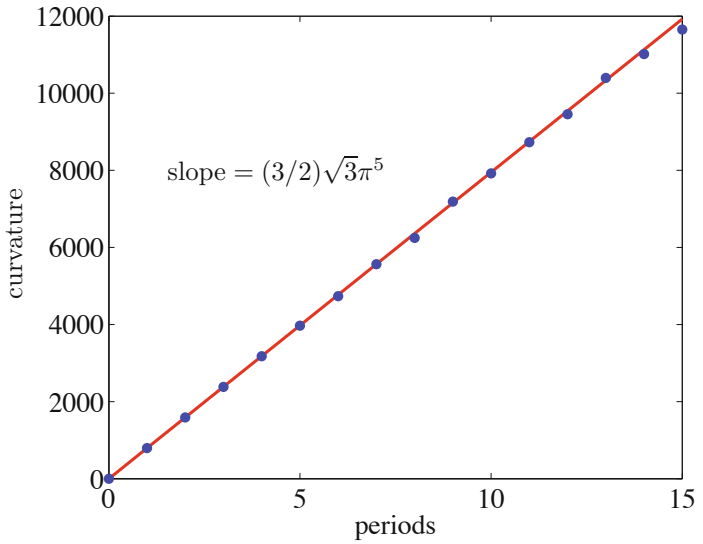

Figure 5. The evolution of the curvature of a material line passing through the periodic point shown in Fig. 3, with orbit given by Eq. (3). The curvature at the point increases linearly with the number of periods, showing that the line is getting more tightly folded around the parabolic point.

does indeed grow linearly with the number of iterations, and the slope is in perfect agreement with the results from the folding normal form.

Note that this linear evolution of the curvature is not an artefact of our choice of orientation of the material line. If we choose the line to be orthogonal to the one in Fig. 4, we find that the tangent evolves as $(\delta X \;\; \delta Y)^T =$

$(n \;\; 1)^T \delta Y_0$, which means that the tangent aligns with the direction of the unstable manifold for large n. The curvature will then grow asymptotically at the rate given by (20).

It is clear from Fig. 4 that the point of highest curvature is not at origin. Nevertheless, the increase in curvature is linear in the neighbourhood of the periodic orbit, and all material lines near the orbit eventually wrap around it, so the orbit can still be said to be acting as a ghost rod.

We conclude that α measures the "size" of the rod: a higher α means that material lines converge towards the periodic orbit more rapidly, so that the ghost rod has a smaller apparent impact on the flow. Visually, α could be estimated by looking at the rate at which material lines "bunch up" near a periodic orbit, as in Fig. 4, but in practice this is quite difficult.

4 Discussion

Of course, this paper is just a sketch of a theory for the size of ghost rods: a comprehensive theory remains to be developed. Rather, we tried to give an indication of the factors that influence a ghost rod's apparent size.

The motivation behind this study, and the ghost rod framework in general, is to try to determine some stirring properties of a flow from visual cues. It is obvious that we can determine the size of physical rods by just looking at them. The effective size of ghost rods that are elliptic islands can also be determined visually, as is apparent in Fig. 1. Ghost rods associated with parabolic points are harder to identify: they typically occur inside sharp folds in material lines, as in Fig. 3. Even if they are identified, measuring their effective impact on the flow is far from trivial: one can attempt to measure the evolution of curvature near the point, in the same spirit as in Section 3.2, or see how rapidly material lines bunch-up near the periodic orbit, effectively a measure of the coefficient α.

The sharp folds observed in material lines are the spots where the stretching is weakest, because there is usually a competition between stretching and curvature (Liu and Muzzio, 1996; Thiffeault, 2004). Hence, folds are associated with inhomogeneities in the stretching field, and thus typically decrease the efficiency of stirring since uniformity is desirable. Knowing how fast the curvature grows (as measured by α) gives a hint of how much inhomogeneity a fold introduces, and thus quantifies its impact on the quality of mixing.

The parabolic points may be the "relevant" ghost rods, *i.e.* the ones on which one can construct a braid that captures exactly the topological entropy of the flow (Gouillart et al., 2006). We have no proof of this assertion yet; however, since the folds determine the skeleton around which a material

line will wrap, these points certainly play a distinguished role.

Acknowledgments

We thank the organisers, Luca Cortelezzi and Igor Mezić, as well as Stefano Cerbelli and Massimiliano Giona for helpful discussions during the workshop. We also point out that two excellent papers on ghost rods (Stremler and Chen, 2007; Binder and Cox, 2008) have appeared since the workshop, after this report was written. This work was funded by the UK Engineering and Physical Sciences Research Council grant GR/S72931/01, when all the authors were based at Imperial College London.

Bibliography

B. J. Binder and S. M. Cox. A mixer design for the pigtail braid. *Fluid Dyn. Res.*, 49:34-44, 2008.

P. L. Boyland, H. Aref, and M. A. Stremler. Topological fluid mechanics of stirring. *J. Fluid Mech.*, 403:277–304, 2000.

P. L. Boyland, M. A. Stremler, and H. Aref. Topological fluid mechanics of point vortex motions. *Physica D*, 175:69–95, 2003.

M. D. Finn, S. M. Cox, and H. M. Byrne. Topological chaos in inviscid and viscous mixers. *J. Fluid Mech.*, 493:345–361, 2003.

M. D. Finn, J.-L. Thiffeault, and E. Gouillart. Topological chaos in spatially periodic mixers. *Physica D*, 221:92–100, 2006.

M. Giona, S. Cerbelli, F. J. Muzzio, and A. Adrover. Non-uniform stationary measure properties of chaotic area-preserving dynamical systems. *Physica A*, 254:451–465, 1998.

E. Gouillart, J.-L. Thiffeault, and M. D. Finn. Topological Mixing with ghost rods. *Phys. Rev. E*, 73:036311 2006.

M. Liu and F. J. Muzzio. The curvature of material lines in chaotic cavity flows. *Phys. Fluids*, 8:75–83, 1996.

S. Newhouse and T. Pignataro, On the estimation of topological entropy. *J. Stat. Phys.*, 72:1331, 1993.

R. T. Pierrehumbert. Tracer microstructure in the large-eddy dominated regime. *Chaos Solitons Fractals*, 4:1091–1110, 1994.

M. A. Stremler and J. Chen. Generating topological chaos in lid-driven cavity flow. *Phys. Fluids*, 19:103602, 2007.

J.-L. Thiffeault. Stretching and curvature along material lines in chaotic flows. *Physica D*, 198:169–181, 2004.

J.-L. Thiffeault. Measuring topological chaos. *Phys. Rev. Lett.*, 94:084502, 2005.

Nonlinear Preconditioning in Problems of Optimal Control for Fluid Systems

Bartosz Protas [*]

[*] Department of Mathematics & Statistics, McMaster University, Hamilton, Ontario, Canada

Abstract This note discusses certain aspects of computational solution of optimal control problems for fluid systems. We focus on approaches in which the steepest descent direction of the cost functional is determined using the adjoint equations. In the first part we review the classical formulation by presenting it in the context of Nonlinear Programming. In the second part we show some new results concerning determination of descent directions in general Banach spaces without Hilbert structure. The proposed approach is illustrated with computational examples concerning a state estimation problem for the 1D Kuramoto–Sivashinsky equation.

1 Introduction

Problems of optimal control arise in very many areas of science and engineering. Given a (possibly nonlinear) system $\mathbf{u}(\mathbf{x},\boldsymbol{\phi}) = 0$, where $\mathbf{x}$ is the state of the system and $\boldsymbol{\phi}$ is an actuation, control problems consist in determining the control $\boldsymbol{\phi}$, so that this control and the corresponding state minimize some performance criterion, i.e.,

$$\min_{\mathbf{x}\in\mathcal{X},\boldsymbol{\phi}\in\mathcal{U}} \tilde{\mathcal{J}}(\mathbf{x},\boldsymbol{\phi}) \tag{1a}$$

$$\text{subject to } \mathbf{u}(\mathbf{x},\boldsymbol{\phi}) = 0, \tag{1b}$$

where $\mathcal{U}$ represents the set of admissible controls, whereas $\mathcal{X}$ is the space of system states. Applications of such problems in Fluid Mechanics are ubiquitous. Here we mention just some of the most important examples, admitting that this list is far from being exhaustive:

- shape optimization with application to aircraft design, e.g., Mohammadi and Pironneau (2001); Martins et al. (2004),
- flow control for drag reduction, e.g., Bewley et al. (2001); Protas and Styczek (2002),
- variational data assimilation in dynamic meteorology, e.g., Kalnay (2003),

- mixing enhancement.

In the above examples the performance criterion $\tilde{J}$ and the control $\boldsymbol{\phi}$ may take different forms reflecting the structure of the problem at hand. The equation (1b) governing the state of the system is usually some form of the Navier–Stokes equation. In fact, from the formal point of view, optimal control problems are examples of *inverse problems* [see, e.g., Isakov (1997)].

In practice, problems of the type (1) involving minimization of a cost functional subject to some constraints are solved using optimization methods. Since the constraint is a partial differential equation (PDE), such problems are examples of *PDE–constrained optimization*. One of the first studies to analyze systematically such problems was the seminal work by Lions (1968). In the context of Fluid Mechanics these problems were further investigated by Abergel and Temam (1990) and Gunzburger (2002). When such infinite–dimensional problems are solved in practice, suitable discretization is used to obtain a corresponding finite–dimensional problem which, at least in principle, can be solved using methods of Nonlinear Programming (NLP). There are, however, some aspects of the problem that make this approach quite challenging. First of all, since the discrete systems are obtained from discretizations of PDEs, the dimension of the discrete state vector $\mathbf{x}$ can be extremely large. Consequently, it is impossible to store the linear operators involved in the solution process as matrices. Consequently, many existing software packages designed to solve finite–dimensional NLP problems cannot be used and "matrix–free" alternatives have to be developed. Secondly, given the size of the discrete system and difficulties involved in calculating second–order derivatives of the cost functional, the Hessian information is usually unavailable and Newton's method can rarely be used. Consequently, one needs to use first–order (gradient) approaches such as, for instance, the Conjugate Gradient (CG) method. Moreover, the physical systems of interest to us are often characterized by a broad range of interacting length– and time–scales and, as a result, the optimization problem is very poorly conditioned. The purpose of the present paper is to discuss some recent ideas useful for accelerating convergence of iterative solution to such optimization problems. In particular, we will focus on nonlinear preconditioning strategies which, by performing locally a nonlinear change of the metric, attempt to increase the range of validity of the tangent linear approximation which is crucial to the present approach.

The structure of the paper is as follows: in the next Section we introduce a simple, yet relevant from the Fluid Mechanics perspective, optimization problem based on the Kuramoto–Sivashinsky equation that we will use as our "toy model", then we present a standard adjoint–based optimization approach typically used to solve such problems; in Section 3 we will introduce the idea of nonlinear preconditioning and show how it can be formulated in terms of gradient extraction in spaces without Hilbert structure; in Section 4 we will present some computational

results indicating the utility of the proposed method; conclusions and discussion of further perspectives are deferred to Section 5. The present report is of a rather exploratory nature, and more complete results concerning this problem are already available in Protas (2008).

2 Adjoint–Based Optimization

Here we show how problem (1) can be efficiently solved using methods of Nonlinear Programming. In its initial formulation this is a *constrained* optimization problem in which both the state $\mathbf{x}$ and the control $\boldsymbol{\phi}$ are variables to be optimized. This is a rather inconvenient situation, since $\mathbf{x}$ is a solution of a (time–dependent) PDE and its discretization may contain a very large number of degrees of freedom in space and in time. On the other hand, the state $\mathbf{x}$ may be considered a function of the control, i.e., $\mathbf{x} = \mathbf{x}(\boldsymbol{\phi})$, which allows us to express problem (1) in the corresponding *unconstrained* form

$$\min_{\boldsymbol{\phi}\in\mathcal{U}} \tilde{\mathcal{J}}(\mathbf{x}(\boldsymbol{\phi}),\boldsymbol{\phi}) = \min_{\boldsymbol{\phi}\in\mathcal{U}} \mathcal{J}(\boldsymbol{\phi}), \tag{2}$$

where $\mathcal{J} : \mathcal{U} \to \mathbb{R}$ is called the *reduced cost functional*[1]. An advantage of this formulation over (1) is that now optimization is carried out with respect to one variable only with discretization usually involving much fewer degrees of freedom. Moreover, problem (2) is unconstrained so that optimization methods required to solve it are simpler, however, the price to be paid for this is that the functional dependence of $\mathcal{J}$ on $\boldsymbol{\phi}$ is now much more involved.

As mention in Introduction, we are concerned here with situations where calculation of the Hessian of (2) is impossible or impractical. We will therefore focus on first–order gradient–based methods. The necessary condition characterizing the minimum of the cost functional $\mathcal{J}(\boldsymbol{\phi})$ is the vanishing of its Gâteaux differential $\mathcal{J}' : \mathcal{U}\times\mathcal{U} \to \mathbb{R}$, i.e.

$$\mathcal{J}'(\boldsymbol{\phi}_{opt};\boldsymbol{\phi}') = 0, \quad \forall \boldsymbol{\phi}' \in \mathcal{U}, \tag{3}$$

where the Gâteaux differential is defined as $\mathcal{J}'(\boldsymbol{\phi};\boldsymbol{\phi}') = \lim_{\varepsilon\to 0} \frac{\mathcal{J}(\boldsymbol{\phi}+\varepsilon\boldsymbol{\phi}')-\mathcal{J}(\boldsymbol{\phi})}{\varepsilon}$ and $\boldsymbol{\phi}_{opt}$ is the minimizer. In most applications, and also in the case considered here, the cost functional $\tilde{\mathcal{J}}$ is quadratic in both $\mathbf{x}$ and $\boldsymbol{\phi}$, however, $\mathbf{x} = \mathbf{x}(\boldsymbol{\phi})$ is often a nonlinear mapping and the optimization problem (2) may be therefore nonconvex. As a result, it may admit nonunique solutions and (3) will characterize only a local minimizer $\boldsymbol{\phi}_{opt}$. Given some initial guess $\boldsymbol{\phi}^{(0)}$, such a minimizer can be found using gradient–based descent method of the general form

$$\boldsymbol{\phi}^{(k+1)} = \boldsymbol{\phi}^{(k)} + \mathbf{d}^{(k)}, \quad k = 1,2,\ldots, \tag{4}$$

[1] Since this is the formulation we will focus on below, hereafter we will skip the adjective "reduced", unless needed for clarity.

such that $\lim_{k\to\infty}\boldsymbol{\phi}^{(k)}=\boldsymbol{\phi}_{opt}$, where k is the iteration count. At every iteration k the descent direction $\mathbf{d}^{(k)}$ is determined based on the gradient $\boldsymbol{\nabla}\mathcal{J}$ of the cost functional calculated at $\boldsymbol{\phi}^{(k)}$. As will be shown below, this gradient can be extracted from $\mathcal{J}'(\boldsymbol{\phi}^{(k)};\boldsymbol{\phi}')$. A convenient expression for $\mathcal{J}'(\boldsymbol{\phi}^{(k)};\boldsymbol{\phi}')$ can be found using methods of Nonlinear Programming [see Lewis (2001) for a discussion of NLP techniques in the context of PDE–constrained optimization]

$$\mathcal{J}'(\boldsymbol{\phi};\boldsymbol{\phi}')=\left\langle D_{\boldsymbol{\phi}}\mathcal{J},\boldsymbol{\phi}'\right\rangle_{\mathcal{U}\times\mathcal{U}^*}=\left\langle D_{\boldsymbol{\phi}}\tilde{\mathcal{J}},\boldsymbol{\phi}'\right\rangle_{\mathcal{U}\times\mathcal{U}^*}+\left\langle D_{\mathbf{x}}\tilde{\mathcal{J}},(D_{\boldsymbol{\phi}}x)\boldsymbol{\phi}'\right\rangle_{\mathcal{X}\times\mathcal{X}^*}, \tag{5}$$

where D_aF denotes the Fréchet derivative of the mapping $F=F(a)$ [see Berger (1977)]. In (5) $\mathcal{U}^*$ is the dual space with respect to $\mathcal{U}$ and $\langle\cdot,\cdot\rangle_{\mathcal{U}\times\mathcal{U}^*}$ represents the standard duality pairing between the spaces $\mathcal{U}$ and $\mathcal{U}^*$. Below we will show how the cost functional differential in (5), and in particular the term $D_{\boldsymbol{\phi}}\mathcal{J}$, can be expressed using an appropriately–defined *adjoint state*. Using the implicit function theorem, the term $D_{\boldsymbol{\phi}}\mathbf{x}$ can be expressed as

$$D_{\boldsymbol{\phi}}\mathbf{x}=-(D_{\mathbf{x}}u)^{-1}D_{\boldsymbol{\phi}}u, \tag{6}$$

so that the second term on the RHS in (5) can be transformed as follows

$$\begin{aligned}\left\langle D_{\mathbf{x}}\tilde{\mathcal{J}},(D_{\boldsymbol{\phi}}x)\boldsymbol{\phi}'\right\rangle_{\mathcal{X}\times\mathcal{X}^*}&=-\left\langle D_{\mathbf{x}}\tilde{\mathcal{J}},(D_{\mathbf{x}}u)^{-1}D_{\boldsymbol{\phi}}u\boldsymbol{\phi}'\right\rangle_{\mathcal{X}\times\mathcal{X}^*}\\&=-\left\langle D^*_{\boldsymbol{\phi}}u\,(D_{\mathbf{x}}u)^{-*}D_{\mathbf{x}}\tilde{\mathcal{J}},\boldsymbol{\phi}'\right\rangle_{\mathcal{U}\times\mathcal{U}^*}\triangleq\left\langle D^*_{\boldsymbol{\phi}}\mathbf{x}D_{\mathbf{x}}\tilde{\mathcal{J}},\boldsymbol{\phi}'\right\rangle_{\mathcal{U}\times\mathcal{U}^*},\end{aligned} \tag{7}$$

where an asterisk denotes a Banach space adjoint. Putting together (5) and (7) we see that the adjoint operator $D^*_{\boldsymbol{\phi}}\mathbf{x}:\mathcal{X}^*\to\mathcal{U}^*$ can be used to express the differential of the cost functional (5) in a convenient form as

$$\mathcal{J}'(\boldsymbol{\phi};\boldsymbol{\phi}')=\left\langle D_{\boldsymbol{\phi}}\tilde{\mathcal{J}}+D^*_{\boldsymbol{\phi}}\mathbf{x}D_{\mathbf{x}}\tilde{\mathcal{J}},\boldsymbol{\phi}'\right\rangle_{\mathcal{U}\times\mathcal{U}^*}=\left\langle D_{\boldsymbol{\phi}}\mathcal{J},\boldsymbol{\phi}'\right\rangle_{\mathcal{U}\times\mathcal{U}^*}. \tag{8}$$

As is evident from the above relationship, the first argument in the duality pairing can be identified with the *gradient* of the reduced cost functional $\mathcal{J}:\mathcal{U}\to\mathbb{R}$ in the metric induced by the space $\mathcal{U}$. It must be emphasized that the gradient in fact belongs to the dual space $D_{\boldsymbol{\phi}}\mathcal{J}\in\mathcal{U}^*$ and, since in most infinite–dimensional cases the dual space $\mathcal{U}^*$ *is not* contained in the original space $\mathcal{U}$, this gradient may not be used as a descent direction in $\mathcal{U}$. In the special case when $\mathcal{U}$ is a Hilbert space we can invoke Riesz' representation theorem [Berger (1977)] which allows us to map $D_{\boldsymbol{\phi}}\mathcal{J}\in\mathcal{U}^*$ to the corresponding element $\boldsymbol{\nabla}\mathcal{J}\in\mathcal{U}$ as

$$\mathcal{J}'(\boldsymbol{\phi};\boldsymbol{\phi}')=\left\langle D_{\boldsymbol{\phi}}\mathcal{J},\boldsymbol{\phi}'\right\rangle_{\mathcal{U}\times\mathcal{U}^*}=\left(\boldsymbol{\nabla}\mathcal{J},\boldsymbol{\phi}'\right)_{\mathcal{U}}, \tag{9}$$

where $(\cdot,\cdot)_{\mathcal{U}}$ represents the inner product on the Hilbert space $\mathcal{U}$, so that now $\nabla\mathcal{J} \in \mathcal{U}$ can be used to construct a descent direction in $\mathcal{U}$. On the other hand, when $\mathcal{U}$ is not a Hilbert space, Riesz' theorem does not apply and identification (9) is not possible. However, in Section 3 we will present a method for constructing an equivalent of $\nabla\mathcal{J}$ in the space $\mathcal{U}$ in such a general case.

Now we illustrate these somewhat abstract considerations by analyzing a concrete example of PDE–constrained optimization. We will focus on a model problem introduced in Protas et al. (2004) which concerns estimation of the initial condition for the 1D Kuramoto–Sivashinsky equation. This particular problem is selected as it models the variational data assimilation, known as 4DVAR, in Dynamic Meteorology [see Kalnay (2003)]. The Kuramoto–Sivashinsky equation is chosen, since it is endowed with chaotic and multiscale behavior and as such is an attractive model for the Navier–Stokes system. We follow here Protas et al. (2004) as regards the set–up of this problem and below highlight only the main points of the derivation, while the Reader is referred to the original source for further details.

For simplicity, we will consider the 1D Kuramoto–Sivashinsky equation on a periodic spatial domain $\Omega = [0, 2\pi]$ and a time interval $[0, T]$

$$\begin{cases} \partial_t v + 4\partial_x^4 v + \kappa\left(\partial_x^2 v + v\partial_x v\right) = 0, & x \in \Omega,\ \ t \in [0,T], \\ \partial_x^i v(0,t) = \partial_x^i v(2\pi,t), & t \in [0,T],\ \ i = 0,\ldots,3,. \\ v(x,0) = \phi, & x \in \Omega. \end{cases} \tag{10}$$

Given incomplete and possibly noisy measurements $y = \mathcal{H}v_{act} + \eta \in \mathcal{Y}$, where $v_{act}(\cdot,t) \in \mathcal{X}$ is the actual system trajectory, $\mathcal{H} : \mathcal{X} \to \mathcal{Y}$ is an observation operator and η is (Gaussian) noise, our optimization problem consists in finding an initial condition ϕ in (10) such that the corresponding system trajectory best matches the available measurements y. In other words, we minimize the following cost functional

$$\mathcal{J}(\phi) = \frac{1}{2}\left\|\mathcal{H}v(\phi) - y\right\|^2_{L_2(0,T;L_2(\Omega))} = \frac{1}{2}\int_0^T (\mathcal{H}v(\phi) - y)^2\, d\tau. \tag{11}$$

Consistently with the properties of system (10), we will assume that $\phi \in \mathcal{U} = L_2(\Omega)$. Since $\mathcal{J}$ depends on the control variable ϕ implicitly through the state equation (10), expression (11) represents in fact the reduced cost functional [cf. (2)]. We will assume that the observation operator $\mathcal{H}$ has the form of projection on a set of cosine modes with the wavenumbers in some set Λ_r, i.e.

$$\mathcal{H} = \sum_{r\in\Lambda_r} \mathcal{P}_r, \quad \text{where} \quad \mathcal{P}_r z = \left[\frac{1}{\pi}\int_0^{2\pi} \cos(rx')z(x')dx'\right]\cos(rx). \tag{12}$$

The Gâteaux differential of (11) is given by [cf. (5)]

$$\mathcal{J}'(\phi;\phi') = \int_0^T \int_0^{2\pi} (\mathcal{H}v - y)\mathcal{H}v'\, dx\, dt, \tag{13}$$

where the perturbation $v'(\phi;\phi')$ is obtained by solving the Kuramoto–Sivashinsky equation linearized around the state ϕ, i.e.

$$\begin{cases} \mathcal{L}v' = \partial_t v' + 4\partial_x^4 v' + \kappa\left[\partial_x^2 v' + v\,\partial_x v' + (\partial_x v)\,v'\right] = 0, & x \in \Omega,\ t \in [0,T], \\ \partial_x^i v'(0,t) = \partial_x^i v'(2\pi,t), & t \in [0,T],\ \ i = 0,\ldots,3, \\ v'(x,0) = \phi', & x \in \Omega, \end{cases} \tag{14}$$

with the operator $\mathcal{L} : \mathcal{X} \to \mathcal{X}^*$ understood in the weak sense. Relation (13) can now be transformed to a form consistent with (8) by introducing an adjoint operator $\mathcal{L}^* : \mathcal{X} \to \mathcal{X}^*$ and the corresponding adjoint state $v^* \in \mathcal{X}^*$ via the following identity

$$\left\langle v^*, \mathcal{L}v' \right\rangle_{\mathcal{X}\times\mathcal{X}^*} = \left\langle \mathcal{L}^* v^*, v' \right\rangle_{\mathcal{X}\times\mathcal{X}^*} + b_{\mathcal{L}}. \tag{15}$$

Using integration by parts and the definition of $\mathcal{L}$ in (14), we obtain

$$\begin{aligned} &\mathcal{L}^* v^* = -\partial_t v^* + 4\partial_x^4 v^* + \kappa\left(\partial_x^2 v^* - v\,\partial_x v^*\right), \qquad \text{and} \\ &b_{\mathcal{L}} = \left[\int_0^{2\pi} v^*\, v'\, dx\right]_{t=0}^{t=T}. \end{aligned} \tag{16}$$

We remark that $b_{\mathcal{L}}$ does not contain any boundary terms (resulting from integration by parts), since all of them vanish due to periodicity. Defining an adjoint system as

$$\begin{cases} \mathcal{L}^* v^* = \mathcal{H}^*(\mathcal{H}v - y), & x \in \Omega,\ \ t \in [0,T], \\ \partial_x^i v^*(0,t) = \partial_x^i v^*(2\pi,t), & t \in [0,T],\ \ i = 0,\ldots,3, \\ v^*(x,T) = 0, & x \in \Omega, \end{cases} \tag{17}$$

and using (14), (15) and (16) we can now express the Gâteaux differential (13) in the desired form (5)

$$\mathcal{J}'(\phi;\phi') = \int_0^{2\pi} v^*\Big|_{t=0} \phi'\, dx. \tag{18}$$

Thus, this differential (i.e., the sensitivity of the cost functional $\mathcal{J}$ with respect to perturbations of the initial condition) can be expressed using the solution of the adjoint system (17).

Relationship (18) can now be employed to extract the gradient required in a descent optimization algorithm. Since $\mathcal{U} = L_2(0,2\pi)$, we immediately obtain

$$\mathcal{J}'(\phi;\phi') = \int_0^{2\pi} v^*\Big|_{t=0} \phi'\, dx = \left(\boldsymbol{\nabla}^{L_2}\mathcal{J}, \boldsymbol{\phi}'\right)_{L_2(\Omega)} \implies \boldsymbol{\nabla}^{L_2}\mathcal{J} = v^*\Big|_{t=0}. \tag{19}$$

Despite its simplicity, in many cases this is not an optimal choice, as it may result in poor conditioning of the corresponding discrete optimization problem. In Protas

et al. (2004) a set of regularization options was identified which can, at least partially, alleviate some of such difficulties. In relation to gradient extraction it was shown that it can be beneficial to extract the cost functional gradient in a more general Hilbert space, Sobolev spaces being natural candidates [see also Neuberger (1997)]. In particular, gradient extraction was considered in the Sobolev space $H^1(\Omega)$ characterized by the inner product

$$\Big(z_1, z_2\Big)_{H^1(\Omega)} = \frac{1}{(1+l_2^2)} \int_0^{2\pi} \Big[z_1 z_2 + l_2^2 (\partial_x z_1)(\partial_x z_2)\Big]\, dx, \tag{20}$$

where l_2 is an adjustable length–scale. Identification $\mathcal{J}'(\phi;\phi') = \Big(\nabla^{H^1}\mathcal{J}, \phi'\Big)_{H^1(\Omega)}$ yields, after integration by parts, the gradient $\nabla^{H^1}\mathcal{J}$ defined via solutions of the following Helmholtz boundary value problem

$$\begin{cases} \dfrac{1}{1+l_2^2}\big[1 - l_2^2\partial_x^2\big]\nabla^{H^1}\mathcal{J} = \bar{v}^*\Big|_{t=0}, \\ \nabla^{H^1}\mathcal{J}(0) = \nabla^{H^1} J(2\pi). \end{cases} \tag{21}$$

Thus, the Sobolev space gradient $\nabla^{H^1}\mathcal{J}$ is obtained by applying the inverse Helmholtz operator to the classical L_2 gradient. Interestingly, when regarded in Fourier space, the inverse Helmholtz operator is equivalent to a low–pass filter with the cut–off given by the inverse of the length–scale l_2 parametrizing the inner product (20). Consequently, extracting gradients in Sobolev spaces with inner products given by (20) has the effect of de–emphasizing components with characteristic length–scales smaller than l_2. As was shown in Protas et al. (2004), adjusting this length–scale during solution of an optimization problem can accelerate convergence of iterations. In particular, starting with l_2 large and then progressively decreasing it to zero results in a multiscale procedure targeting first the large–scale structures and then homing in on smaller scale components of the solution ϕ_{opt}.

3 Nonlinear Preconditioning using Descent Directions in General Banach Spaces

In this Section we address the issue of gradient extraction in general Banach spaces and the potential advantage this technique may offer as a method of nonlinear preconditioning. Similar ideas were already discussed by Lewis (2001) and elaborated in greater detail by Neuberger (1997), however, they were not concerned with preconditioning nonlinear optimization problems. The present approach relies on the assumption that the Banach space $\mathcal{U}$, where the descent direction is to be identified, be *reflexive*, i.e., that $\mathcal{U}^{**} = \mathcal{U}$. As already mentioned in Section 2 in relation

to formula (9), the gradient is a linear functional on the space $\mathcal{U}$ and therefore belongs to the dual space $\mathcal{U}^*$. For example, if $\mathcal{U}$ is the Sobolev space $W_0^{1,p}$, $p \neq 2$, defined as

$$W_0^{1,p}(\Omega) = \{u : \Omega \to \mathbb{R}, \|u\|_{W^{1,p}} < \infty,\ v|_{\partial\Omega} = 0\},$$
$$\text{where } \|u\|_{W^{1,p}} = \left[\int_\Omega (|v|^p + l_p^p |\partial_x v|^p)\, d\Omega\right]^{1/p}, \tag{22}$$

where $l_p \in \mathbb{R}^+$ is a weight, then the dual space $\mathcal{U}^* = W^{-1,q}$, where $\frac{1}{p} + \frac{1}{q} = 1$ [see Adams and Fournier (2005)]. Since a dual space is usually "larger", its elements do not necessarily belong to the original space $\mathcal{U}$ and therefore cannot be used to represent descent directions in that space. Consequently, it is necessary to propose a different approach which allows one to extract a descent direction $\tilde{\mathbf{g}}$ from $\mathcal{J}'(\boldsymbol{\phi};\boldsymbol{\phi}')$ such that $\tilde{\mathbf{g}} \in \mathcal{U}$. As shown by Lewis (2001) and Neuberger (1997), this can be done defining $\tilde{\mathbf{g}}$ as a unit–norm element of $\mathcal{U}$ which minimizes expression (9). In other words, we postulate to find $\tilde{\mathbf{g}}$ as a solution of the following constrained minimization problem

$$\min_{\|\mathbf{g}\|_{\mathcal{U}}=1} \left\langle D_{\boldsymbol{\phi}}\mathcal{J}, \mathbf{g} \right\rangle_{\mathcal{U}^*\times\mathcal{U}} \tag{23}$$

which can be converted to the more convenient unconstrained form

$$\min_{\mathbf{g}\in\mathcal{U}} \left[\left\langle D_{\boldsymbol{\phi}}\mathcal{J}, \mathbf{g} \right\rangle_{\mathcal{U}^*\times\mathcal{U}} + \frac{\mu}{p}\|\mathbf{g}\|_{\mathcal{U}}^p \right] = \min_{\mathbf{g}\in\mathcal{U}} \mathcal{G}(\mathbf{g}), \tag{24}$$

where p is an integer, μ is the Lagrange multiplier and $\mathcal{G} : \mathcal{U} \to \mathbb{R}$. This problem can be solved with a method analogous to the approach described earlier in Section 2. Thus, the descent direction $\tilde{\mathbf{g}}$ is characterized by the vanishing of the Gâteaux differential of (24), i.e.

$$\forall_{\mathbf{g}'\in\mathcal{U}} \quad \mathcal{G}'(\tilde{\mathbf{g}};\mathbf{g}') = \left\langle D_{\mathbf{g}}\mathcal{G}(\tilde{\mathbf{g}}), \mathbf{g}' \right\rangle_{\mathcal{U}^*\times\mathcal{U}} = 0, \tag{25}$$

where $D_{\mathbf{g}}\mathcal{G} : \mathcal{U} \to \mathcal{U}^*$. Thus, we obtain

$$D_{\mathbf{g}}\mathcal{G}(\tilde{\mathbf{g}}) = 0 \quad \text{in } U^* \tag{26}$$

as an equation determining the direction $\tilde{\mathbf{g}} \in \mathcal{U}$. Below we will show how this direction can be determined when $\mathcal{U}$ is one of the Banach spaces commonly arising in the analysis on nonlinear PDEs. This analysis will be carried out in the setting of the optimization problem for the Kuramoto–Sivashinsky equation introduced in Section 2. We begin with the Lebesgue spaces $L_p(\Omega)$ with norms defined as [Adams and Fournier (2005)]

$$\|u\|_{L_p(\Omega)} = \begin{cases} \left(\displaystyle\int_\Omega |u|^p\, d\Omega\right)^{1/p} & 1 \le p < \infty, \\ \text{ess sup}_{x\in\Omega}\, |u| & p = \infty. \end{cases} \tag{27}$$

Considering for the moment the case with $1 \leq p < \infty$, the unconstrained cost functional (24) and its Gâteaux differential (25) take the form

$$\mathcal{G}(g) = \int_\Omega (v^*\big|_{t=0} g + \frac{\mu}{p}|g|^p)\, d\Omega, \tag{28a}$$

$$\forall_{g' \in L_p(\Omega)} \;\; G'(g;g') = \int_\Omega (v^*\big|_{t=0} g + \mu g|g|^{(p-2)}) g'\, d\Omega, \tag{28b}$$

so that the descent direction $\tilde{g}_{L_p}$ is characterized by the algebraic relation

$$\tilde{g}|\tilde{g}|^{(p-2)} = -\frac{1}{\mu} v^*\big|_{t=0}. \tag{29}$$

The solution of (29) is

$$\tilde{\mathbf{g}}_{L_p} = \begin{cases} \sqrt[p-1]{-\frac{1}{\mu} v^*\big|_{t=0}}, & p \text{ — even}, \\ -\operatorname{sgn}(v^*\big|_{t=0}) \sqrt[p-1]{\frac{1}{\mu}\left|v^*\big|_{t=0}\right|}, & p \text{ — odd}. \end{cases} \tag{30}$$

We thus see that when $p \neq 2$, the descent direction in $L_p(\Omega)$ is obtained by applying a *nonlinear* transformation to the original gradient $\nabla^{L_2} \mathcal{J} = v^*|_{t=0}$. In the special case $p = 2$ we immediately obtain

$$\tilde{\mathbf{g}}_{L_2} = -\frac{1}{\mu} v^*\big|_{t=0} \tag{31}$$

which is the classical expression obtained in Section 2. As regards the constant μ, which serves as a Lagrange multiplier in the unconstrained formulation (24), it is chosen to normalize $\tilde{g}$ to unit norm $\|\tilde{g}\|_{\mathcal{U}} = 1$. In the second special case $p = \infty$, it can be shown that

$$\tilde{\mathbf{g}}_{L_\infty} = -\operatorname{sgn}(v^*\big|_{t=0}) \tag{32}$$

consistently with taking the limit $p \to \infty$ in expressions (30). We also remark that in the case $p = 1$ the descent direction $\tilde{g}_{L_1}$ cannot be defined, since the space $L_1(\Omega)$ is not reflexive.

We now proceed to discuss the problem of determining the descent direction when $\mathcal{U} = W^{1,p}$, where $W^{1,p}$ is the Sobolev space defined in (22). Considering the case $1 \leq p < \infty$, the unconstrained cost functional and its Gâteaux differential take the form

$$\mathcal{G}(g) = \int_\Omega \left[v^*\big|_{t=0} g + \frac{\mu}{p}(|g|^p + l_p^p |\partial_x g|^p) \right] d\Omega, \tag{33a}$$

$$\mathcal{G}'(g;g') = \int_\Omega \left\{ v^*\big|_{t=0} g' + \frac{\mu}{p} \left[g|g|^{(p-2)} g' - l_p^p \partial_x (\partial_x g |\partial_x g|^{(p-2)}) g' \right] \right\} d\Omega. \tag{33b}$$

As before, the boundary terms due to integration by parts vanish because of periodicity of $\tilde{g}$ and g'. Since the descent direction $\tilde{g}$ is characterized by $\mathcal{G}'(\tilde{g};g') = 0$, $\forall_{g'\in\mathcal{U}}$, it can be obtained as a solution of the following problem in $\mathcal{U}^*$ (due to nondifferentiability of the absolute value function $|\cdot|$, this equations is formulated in the weak sense)

$$\begin{cases} \tilde{g}|\tilde{g}|^{(p-2)} - l_p^p \partial_x \left[(\partial_x \tilde{g}) |\partial_x \tilde{g}|^{(p-2)} \right] = -\dfrac{1}{\mu} v^*\big|_{t=0}, \\ \tilde{g}(0) = \tilde{g}(2\pi). \end{cases} \tag{34}$$

The second term on the LHS in the first equation in (34) is usually referred to as the *p–Laplacian* [Neuberger (1997)], as it represents a nonlinear generalization of the familiar Laplace operator. Evidently, in the case $p = 2$, $W^{1,2}(\Omega) = H^1(\Omega)$ is a Hilbert space and the p–Laplacian reduces to the classical Laplace operator. As a result, (34) simplifies to (21) and we recover the Hilbert space framework discussed in Section 2. The Lagrange multiplier μ can be adjusted in order to normalize the descent direction to the unit norm. We can conclude that identification of descent directions in Banach spaces (such as $L_p(\Omega)$, or $W^{1,p}(\Omega)$, when $p \neq 2$) results in *nonlinear* transformations of the adjoint field $v^*|_{t=0}$. As regards equations with the p–Laplacian operator such as (34), a variety of their interesting properties is discussed by Ishii and Loreti (2005) (see also references contained therein).

We now comment briefly on the utility of extraction descent directions in general Banach spaces as a nonlinear preconditioning technique. The purpose of preconditioning is to modify the metric in which a given iterative process takes place, so as to accelerate convergence. For linear problems with quadratic functionals this can also be regarded as decreasing the condition number of the Hessian of the reduced cost functional. In such cases linear preconditioning techniques are efficient enough (in fact, in many situations there exist specific guidelines regarding the choice of an optimal preconditioner). However, for nonlinear problems linear preconditioning may not be sufficient and a nonlinear change of the metric may lead to better results. In the framework proposed here, choosing a preconditioner is in fact equivalent to choosing a Banach space $\mathcal{U}$ in which the descent direction is identified. The question of how to choose this space is important. Unlike certain linear problems, most nonlinear PDEs result in optimization problems with structure that is too complicated to allow for a thorough analysis. In such situations finding the most suitable preconditioning strategy is a matter of experimentation. There are, however, certain general conditions that need to be satisfied. In general, for the evolution equation (10) to be well–posed, the control ϕ must belong to some appropriate space $\mathcal{U}$ (identical with $L_2(\Omega)$ in the present case). Therefore, if at the k–th iteration we want to precondition the gradient by extracting it in some Banach space $\mathcal{U}^{(k)}$, it must be ensured that this gradient $\boldsymbol{\nabla}^{\mathcal{U}^{(k)}} \mathcal{J}$ will still

belong to the original space $\mathcal{U}$, in other words $\mathcal{U}^{(k)} \subseteq \mathcal{U}$, $\forall_{k\in\mathbb{Z}}$. Such preconditioning is equivalent to restricting the iterates to a family of subspaces nested in $\mathcal{U}$. Computational results concerning linear preconditioning reported by Protas et al. (2004) indicate that the best results were obtained when the subspaces formed the following hierarchy

$$\mathcal{U}^{(0)} \subseteq \mathcal{U}^{(1)} \subseteq \cdots \subseteq \mathcal{U}^{(k)} \subseteq \cdots \subseteq L_2(\Omega). \tag{35}$$

When considering general Banach spaces, additional guidance for constructing hierarchies like (35) can be obtained by considering the family of *Sobolev Imbedding Theorems* [Adams and Fournier (2005)]. Imbedding Theorems provide criteria that allow one to determine whether or not one Sobolev (or Lebesgue) space is "contained" in another one. In the following Section we present computational results that address some of these issues.

4 Computational Results

In this Section we show some computational results illustrating the utility of the nonlinear preconditioning techniques developed in Section 3. We treat the results from Protas et al. (2004) as our point of reference, so we consider here precisely the same problem of state estimation for the Kuramoto–Sivashinsky equation. The observation operator in (12) uses projections on the first $r = 50$ cosine modes (i.e., $\Lambda_r = \{1,\ldots,50\}$) and we set $\kappa = 4000$ in equation (10). Both equation (10) and its adjoint (17) are solved using a dealiased pseudo–spectral Fourier–Galerkin method with $N = 1024$ grid points. The Reader is referred to Protas et al. (2004) for further numerical details. The nonlinear equation (34) involving the p–Laplacian operator is solved using Newton's method applied to the system of nonlinear algebraic equations obtained after discretization.

In order to see the effect of nonlinear preconditioning we will present results obtained for two optimization horizons (given in terms of the time step $\Delta t = 10^{-8}$) $T = 300$ and $T = 500$. Since the effect of nonlinear preconditioning appears most pronounced for the longer optimization horizon $T = 500$, some of the results will be presented for that case only. We begin presentation of the results by examining the shape of the descent directions $\tilde{g}$ obtained in different Banach spaces. To fix attention, we consider the first iteration in the problem with $T = 500$ with a zero initial guess $\phi^{(0)} \equiv 0$. In Figure 1 we compare the descent directions $\tilde{g}$ extracted in the Banach spaces $L_2(\Omega)$, $L_\infty(\Omega)$ and $W^{1,4}(\Omega)$ with $l_4 = 10.0$ [cf. (22)] with the standard gradient $\nabla^{L_2}\mathcal{J}$ extracted in the space $L_2(\Omega)$. We observe that for increasing p the descent directions obtained in the spaces $L_p(\Omega)$ approach a square wave.

In computational solution of our optimization problem we found the preconditioning involving descent directions in the Sobolev spaces $W^{1,p}(\Omega)$, where $p \geq 3$,

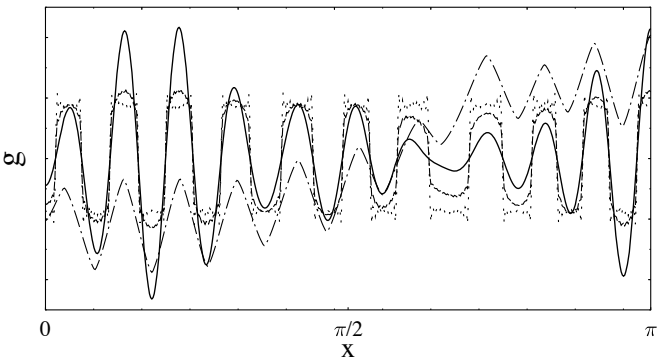

Figure 1. Shapes of the descent directions obtained at the first iteration in the data assimilation problem with $T = 500$ and determined in: (solid line) $L_2(\Omega)$, (dashed line) $L_5(\Omega)$, (dotted line) $L_\infty(\Omega)$ and (dash–dotted line) $W^{1,4}(\Omega)$. For clarity, only half of the domain Ω is shown.

to be more efficient than the preconditioning using descent directions in $L_p(\Omega)$. This is the case we will focus on exclusively below. In Figures 2a and 2b, corresponding to optimization with $T = 300$ and $T = 500$, we study the effect that the quantity l_p, the characteristic "length–scale" parametrizing the definitions of the norm $\|u\|_{W^{1,p}}$, has on optimization efficiency. Given that the value of the cost function (11) before optimization (i.e., for $\phi^{(0)} \equiv 0$) is normalized to unity, Figures 2a and 2b show the decrease of the cost functional at the first iteration for the descent directions obtained in the spaces $W^{1,3}(\Omega)$ and $W^{1,4}(\Omega)$ with values of l_3 and l_4 indicated on the abscissa. For comparison, we also show the results obtained with the gradient extracted in L_2. We note that the decrease of the cost functional significantly depends on the choice of l_p ($p = 3,4$). For $T = 300$ the window of l_p giving improvement over optimization with the L_2 gradients exists for descent directions in $W^{1,3}(\Omega)$ only and is rather narrow. The advantage of determining descent directions in a Banach space becomes much more evident for $T = 500$, where the windows of l_p giving improvement over gradients in L_2 are unbounded.

Now we proceed to analyze the effect of nonlinear preconditioning on the whole optimization process involving many iterations. As regards optimization with the descent directions obtained in the Banach spaces $W^{1,p}(\Omega)$ we follow the strategy outlined in Section 3: for a given choice of the space $W^{1,p}(\Omega)$ we start with the value of l_p which was determined to give the best results at the first iter-

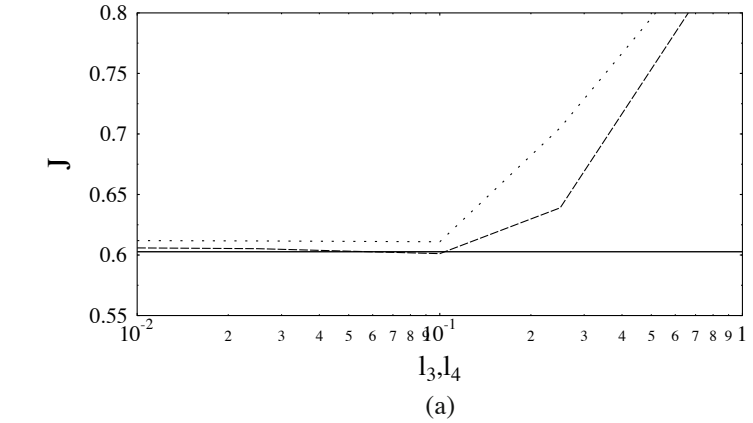

(a)

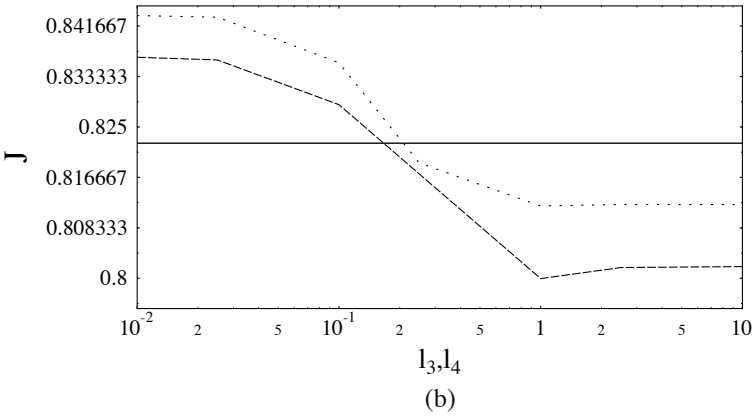

(b)

Figure 2. Decrease of the cost functional (11) at the first iteration in optimization with (a) $T = 300$ and (b) $T = 500$. The descent directions are extracted in the spaces (solid line) $L_2(\Omega)$, (dashed line) $W^{1,3}(\Omega)$ and (dotted line) $W^{1,4}(\Omega)$ for values of l_3 and l_4 indicated on the abscissa.

ation and then progressively decrease it to zero, so that the corresponding descent directions approach the L_p descent direction. As a result, our preconditioning strategy is equivalent to extracting the descent directions in a sequence of nested spaces $W^{1,p}(\Omega)$, all contained in the "master" space $L_2(\Omega)$. This strategy, initially investigated by Protas et al. (2004) for the case of gradient extraction in the Sobolev space $H^1(\Omega) = W^{1,2}(\Omega)$, was found to give good results. In Figures 3a and 3b we show the decrease of the cost functional $\mathcal{J}(\phi^{(k)})$ as a function of the iteration count k for $T = 300$ and $T = 500$, respectively. In both cases the descent directions are extracted in the spaces $W^{1,4}(\Omega)$ with the initial values of l_4 equal to 10^{-1} and 10 in the two cases, respectively. For comparison, in the two Figures we also show the decrease of the cost functional obtained with gradients obtained in the space $L_2(\Omega)$. We note that when $T = 300$ nonlinear preconditioning offers little advantage over the unpreconditioned case, in contrast to the case with $T = 500$ where a significant convergence acceleration is observed. In order to further emphasize this point in Figures 4a and 4b we show the data for the error in the reconstruction of the initial condition, i.e., $\|\phi^{(k)} - \phi_{act}\|_{L_2(\Omega)}$ corresponding to the same cases as in Figure 3. We note that these results provide further evidence for the trends already shown in Figure 3. We also examined nonlinear preconditioning in the case of shorter optimization horizons $T \ll 300$, however, no acceleration of convergence comparing to the optimization with the L_2 gradients was observed. Hence, we do not show these results here.

5 Conclusions and Outlook

In this paper we first reviewed the formulation of an optimal control problem for a fluid system using the language of Nonlinear Programming. We focused on a particular aspect relevant from the computational point of view, namely, determination of well–preconditioned descent directions for the cost functional. We extended an earlier approach and showed how a descent direction can be determined in a general Banach space without Hilbert structure. In particular, we showed that extracting this descent direction in a Sobolev space $W^{1,p}(\Omega)$ leads to solution of an elliptic problem with a p–Laplacian. Such a preconditioning strategy has the effect of a nonlinear change of the metric in the space where optimization is performed. When employed judiciously, this approach may have the potential to mitigate the effect of nonlinearities present in the system. Indeed, our computational results indicate that such a nonlinear preconditioning can accelerate convergence of iterations in an optimization problem for a nonlinear PDE. Interestingly, effectiveness of the proposed approach increases with the length of the optimization interval $[0,T]$ and becomes more evident for problems with large T, i.e., in situations when nonlinear effects play a more significant role. Research is underway to apply a similar approach to precondition optimization of more realistic problems,

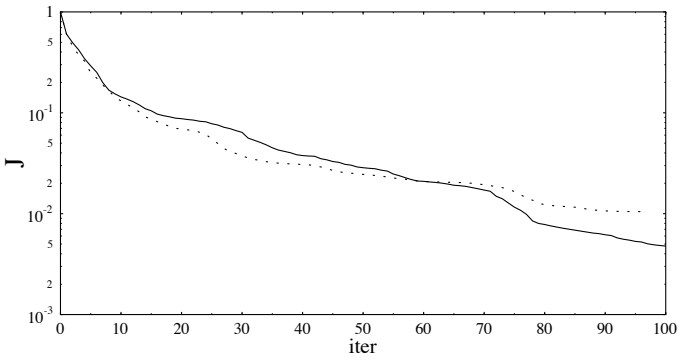

(a)

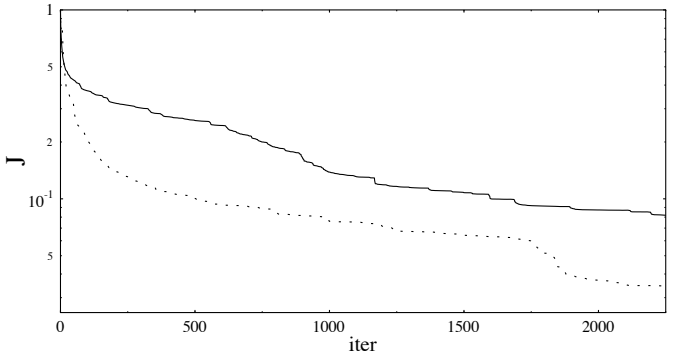

(b)

Figure 3. Decrease of the cost functional $\mathcal{J}(\phi^{(k)})$ in function of iterations for optimizations with (a) $T = 300$ and (b) $T = 500$. The results are obtained with the descent directions in (solid line) L_2 and (dotted line) $W^{1,4}(\Omega)$ where the parameter l_4 progressively decreases with iterations.

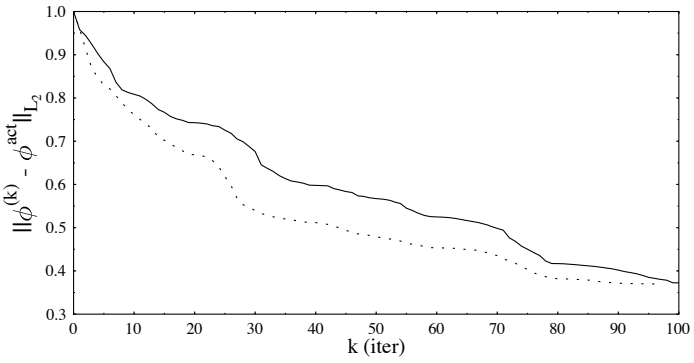

(a)

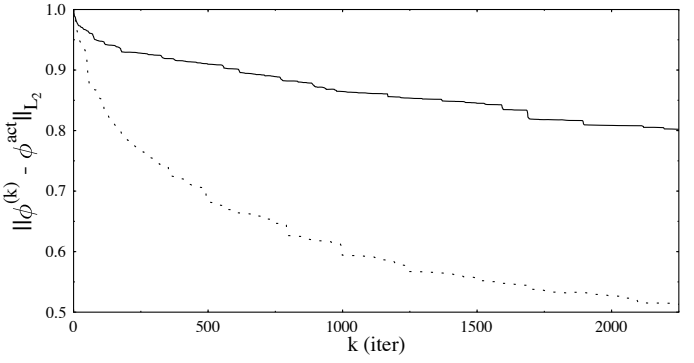

(b)

Figure 4. Decrease of the error of the reconstruction of the initial condition $\|\phi^{(k)} - \phi_{act}\|_{L_2(\Omega)}$ in function of iterations for optimizations with (a) $T = 300$ and (b) $T = 500$. The results are obtained with the descent directions in (solid line) L_2 and (dotted line) $W^{1,4}(\Omega)$ where the parameter l_4 progressively decreases with iterations.

such as the state estimation in a 3D turbulent channel flow already investigated by Bewley and Protas (2004). Another possibility is to investigate descent directions in more general Banach spaces and here Besov spaces [see, e.g., Adams and Fournier (2005)] are attractive candidates. A thorough treatment of this subject is given in Protas (2008).

In the present investigation the space giving "optimal" preconditioning was chosen by trial and error. A very challenging theoretical question is to develop a rigorous procedure that will determine guidelines for choosing such an optimal space. Such procedures are in fact available for certain optimization problems formulated for some linear PDEs, however, no such results appear available for nonlinear PDEs. Encouraging computational results reported in the present paper may therefore serve to motivate further theoretical research in this direction.

6 Acknowledgments

This research has been supported by an NSERC (Canada) Discovery Grant.

Bibliography

F. Abergel and R. Temam. On some control problems in fluid mechanics. *Theoretical and Computational Fluid Dynamics*, 1:303–325, 1990.

R. A. Adams and J. J. F. Fournier. *Sobolev Spaces*. Elsevier, second edition edition, 2005.

M. S. Berger. *Nonlinearity and Functional Analysis*. Academic Press, 1977.

T. R. Bewley and B. Protas. Skin friction and pressure: the "footprints" of turbulence. *Physica D*, 196:28–44, 2004.

T. R. Bewley, P. Moin, and R. Temam. DNS–based predictive control of turbulence: an optimal benchmark for feedback algorithms. *Journal of Fluid Mechanics*, 447:179–225, 2001.

M. Gunzburger. *Perspectives in Flow Control*. SIAM, 2002.

V. Isakov. *Inverse Problems for Partial Differential Equations*. Springer, 1997.

H. Ishii and P. Loreti. Limits of solutions if p–laplace equations as p goes to infinity and related variational prblems. *SIAM J. Math. Anal.*, 37:411–437, 2005.

E. Kalnay. *Atmospheric modeling, data assimilation and predictability*. Cambridge University Press, 2003.

R. M. Lewis. A nonlinear programming perspective on sensitivity calculations for systems goverened by state equations. Technical report, ICASE, 2001.

J. L. Lions. *Contrôle optimal de systèmes gouvernés pas des équations aux dérivées partielles*. Dunod, 1968.

J. R. R. A. Martins, J. J. Alonso, and J. J. Reuther. High–fidelity aerostructural design optimization of a supersonic business jet. *Journal of Aircraft*, 41:523–530, 2004.

B. Mohammadi and O. Pironneau. *Applied Shape Optimization for Fluids*. Oxford University Press, 2001.

J. Neuberger. *Sobolev Gradients and Differential Equations*. Springer, 1997.

B. Protas. Adjoint–based optimization of pde systems with alternative gradients. *Journal of Computational Physics*, 227:6490–6510, 2008.

B. Protas and A. Styczek. Optimal rotary control of the cylinder wake in the laminar regime. *Physics of Fluids*, 14:2073–2087,, 2002.

B. Protas, T. Bewley, and G. Hagen. A comprehensive framework for the regularization of adjoint analysis in multiscale pde systems. *Journal of Computational Physics*, 195:49–89, 2004.

Sensitivity of mixing optimization to the geometry of the initial scalar field.

Oleg Gubanov and Luca Cortelezzi
Department of Mechanical Engineering, McGill University, Montreal, Canada.

Abstract. In this study, we address the conceptual problem of designing a mixing device able to maintain a uniform mixing quality for different initial configurations of the mixture. As a case study, we consider as a mixing device a two-dimensional, piecewise steady, nonlinear flow, the sine flow. To promote mixing in the sine flow, we generate an optimized stirring protocol using the short time horizon procedure. We use the mix-norm as a measure of the mixing efficiency and as the cost function of the optimization. We assess the sensitivity to the geometry of the initial configuration of the short-time-horizon optimal protocols in terms of their mixing efficiency. We use the periodic and recursive symmetry-breaking protocols as benchmarks for our assessment. We show that the optimized protocols are generally quite insensitive to the geometry of the initial scalar field when compared to the periodic and recursive symmetry-breaking protocols. We show that the on-line optimization is essential for achieving a uniform mixing efficiency. We characterize the effect of the switching time horizon on the sensitivity of the optimized protocols to the geometry of the initial configuration. Our results indicate that the optimization over very short time horizons could be in principle used as an on-line procedure for maintaining a uniformly high quality of mixing for different initial configurations of the mixture.

1 Introduction

Many industrial applications involve mixing of two or more different fluids. For example, mixing is encountered in pharmaceutical, food, polymer, and biotechnological processes, to name a few. Often, it is desirable to promote mixing at low speed to prevent damage to shear-sensitive materials or reduce energy consumption, especially for highly viscous substances. In many applications, the ones targeted by this study, it is impractical and often impossible to promote turbulence to enhance mixing, consequently mixing should be induced in a laminar flow regime. In general, laminar

mixing is poor because fluid motion is dominated by viscous forces. In laminar regimes, severe manufacturing problems such as insufficient product yield or quality, or excessive generation of byproducts often require costly corrections in the apparatus. Thus, the problem of optimization and control of laminar fluid mixing is of great practical importance.

Often, the quality of mixing induced by a mixing device in a laminar flow regime depends on the initial geometrical configuration of the mixture. The effect of the initial configuration is particularly evident on the performance of industrially-relevant static mixers. A static mixer is a mixing device which consists, for example, of a series of motionless elements installed in a pipe. These elements promote mixing of two or more fluids which flow through the pipe due to a pressure gradient. For more details on static mixers, the reader is referred to a comprehensive review by Thakur et al. (2003). Hobbs and Muzzio (1997) investigated the sensitivity of the mixing efficiency induced by the Kenics static mixer to the injection location of a small stream of a passive tracer. They evaluated mixing qualitatively by examining the spread of the tracer on cross-sectional slices of the mixer and quantitatively by computing the variation coefficient as a function of the axial position. The authors found that the mixing efficiency of the Kenics mixer is highly sensitive to the injection location over the first few elements of the mixer. In particular, they found that the least effective injection location requires up to four additional mixing elements to achieve the same target value of the variation coefficient as the most effective injection location. The authors noted that the sensitivity of the mixing efficiency induced by the Kenics mixer to the injection location can be reduced by adding extra mixing elements. Hobbs and Muzzio (1997) concluded that for a typical industrial application using a 6- or 12-element Kenics mixer, the sensitivity to the injection location could have a significant impact on the product quality. Zalc et al. (2003) investigated the effect of injection location on the mixing efficiency induced by a four-element SMX static mixer. They measured mixing qualitatively by examining mixing patterns on cross-sectional slices of the mixer and quantitatively by computing the variation coefficient and the average rate of stretching. The authors found that the off-center injection location considerably reduces the homogeneity of the mixture when compared to the centerline injection location. Zalc et al. (2003) conclude that a poorly chosen injection location can substantially affect the performance of the SMX mixer. The authors noted that reducing the sensitivity to the injection location by adding extra mixing elements may be impractical because this also increases the required pressure gradient and, consequently, the cost of operation.

The above examples indicate that in industrial applications the initial ge-

ometrical configuration of the mixture could vary with time. Consequently, the product quality generated by current industrial mixers could also change with time. Therefore, the design of a novel mixer able to maintain a uniform product quality for a time-dependent injection configuration is of great practical importance. A possible solution is a mixer which implements an on-line optimization, i.e. a mixer which is able to measure on-line the geometrical configuration of the mixture and, in response, induce the most efficient mixing action. Thus motivated, we consider, as a case study, laminar mixing optimization in a simplified mixer. Our goal is to assess the sensitivity of the mixing efficiency obtained with this optimization to the geometry of the initial configuration of the mixture.

Laminar mixing has become a subject of study over the past twenty years. The concept of chaotic advection was introduced in the pioneering work by Aref (1984); then, laminar mixing became a subject of numerous studies (Ottino, 1989; Aref and El Naschie, 1995; Alvarez et al., 1998; Zalc and Muzzio, 1999; Aref, 2002; Szalai et al., 2003; Gleeson, 2005; Gouillart et al., 2006; Phelps and Tucker, 2006; Vikhansky and Cox, 2007, to name a few). A sufficiently general mathematical theory of laminar mixing has only started emerging over the past decade (Sturmap et al., 2006, and references therein).

Under laminar mixing conditions, one could expect that an initial concentration field could be homogenized by intelligently coordinating the action of two mixing mechanisms: advection (mechanical stirring) and diffusion (mixing at molecular level). Advection dominates during the early stages of the homogenization process, its purpose is to maximize the gradients of the concentration field. Large concentration gradients stimulate diffusion, which prevails during the final stages of the homogenization process, fading away remaining concentration gradients (Eckart, 1948; Aref, 2002). The quality of the resulting mixture strongly depends on a how effectively and uniformly the initial concentration field has been stirred. The time sequence of actuations used to stir a given mixture is referred to as a *stirring protocol*. In the absence of advection, or with a poor choice of a stirring protocol, fluid homogenization can be achieved mainly by sole means of diffusion, which takes much longer than demanded by practical applications (Ottino and Wiggins, 2004; Sturmap et al., 2006).

Early studies of laminar mixing and chaotic advection have characterized the effects induced on a given concentration field by *periodic* stirring protocols. For this class of protocols, in the absence of diffusion, mixing efficiency can be conveniently analyzed using dynamical systems tools such as Poincaré maps and Lyapunov exponents. However, the analysis of different mixing devices showed that periodic protocols often create mixtures

where islands of regular motion are surrounded by a chaotic sea (Aref, 2002; Finn et al., 2004; Paul et al., 2004, and references therein). Islands of regular motion emerge around elliptic fixed points and greatly reduce mixing efficiency. In order to overcome this difficulty, Liu et al. (1994) suggested to enhance mixing by using *aperiodic* protocols, which have no elliptic fixed points and thus are more likely to induce mixtures free of islands of regular motion. An interesting example of an aperiodic protocol is the *recursive symmetry-breaking protocol*. This non-random, self-similar stirring protocol was initially derived by Franjione et al. (1989), who analyzed a periodic flow in terms of its symmetries. The authors suggested to break the symmetries of the flow in a systematic way so as to destroy the islands of regular motion. The recursive symmetry-breaking protocol, as well as several other, random protocols considered by Liu et al. (1994) was found to induce chaotic advection over the entire mixing domain under conditions for which the corresponding periodic protocols induced regular motion almost everywhere.

Unfortunately, mixing efficiency of aperiodic protocols cannot be evaluated using Poincaré sections nor Lyapunov exponents. Hence, Liu et al. (1994) introduced other diagnostics such as the stretching field statistics and the spreading rate of passive tracers. Several other useful measures were reported in literature. Finn et al. (2004) summarized and investigated correlations between various mixing diagnostic emerging from statistical, physical and dynamical systems contexts. Recently, Mathew et al. (2005) introduced the *mix-norm*, a new indicator of mixing. The mix-norm is defined as the root mean square of the average values of the concentration field over a dense set of subsets contained in the flow domain. The mix-norm is capable of quantify the mixing efficiency of periodic and aperiodic protocols when applied to purely advective or advective-diffusive flows. Unlike some other diagnostics, such as Lyapunov exponents, the mix-norm can be used to evaluate mixing efficiency of a stirring protocol in the context of a given concentration field.

In general, the performance of a stirring protocol depends on the initial geometrical configuration of the mixture. Particularly affected are the protocols that generate islands of regular motion, because the portion of mixture initially lying within an insland is eventually poorly mixed (Tucker and Peters, 2003). For globally chaotic protocols, the choice of initial condition affects the mixing efficiency during the early stages of mixing but does not affect the asymptotic efficiency of the protocol (Muzzio et al., 2000; Tucker and Peters, 2003). Hence, the geometrical configuration of the initial concentration field should be taken into consideration when optimizing mixing over a finite period of time.

An ideal mixing device should be able to produce an homogenized mixture in the shortest time possible using the least amount of work. To this basic requirements one could add, for example, the requirement that the stirring field should generate shear-stresses as uniform as possible over the entire mixing domain and with intensity below a given threshold. The first step towards the design of such devices is to derive robust optimization or control procedures able to generate optimal or sub-optimal mixing protocol for a given mixing device.

Fluid mixing in a prototypical mixing device was formulated as a control problem by D'Alessandro et al. (1999). The authors consider the *egg-beater flow* (Franjione and Ottino, 1992), in which a fluid constrained on a two-dimensional torus is stirred by two velocity fields v_0 and v_1 acting orthogonally. The control problem is stated as follows: given the shapes of the stirring velocity profiles and a measure of mixing, find a stirring protocol which minimizes this measure by intelligently blinking v_0 and v_1. Using entropy as a measure of mixing and simple shear velocity profiles $v_0(y) = ay,\ v_1(x) = bx,\ ab > 0$, D'Alessandro et al. (1999) derived a periodic protocol which maximizes entropy among all admissible periodic protocols.

The control approach to fluid mixing suggested by D'Alessandro et al. (1999) has been applied in recent studies by Gibout et al. (2006), Mathew et al. (2007), Cortelezzi et al. (2008) and Thiffeault and Pavliotis (2008). Gibout et al. (2006) studied optimization of mixing in a steady, three-dimensional flow in a curved pipe equipped with motionless mixing elements of four different types. The authors obtained numerically the concentration field in the cross-section of the outlet applying a mapping method to an anisotropic unstructured mesh. As a measure of mixing efficiency and as the cost function of optimization, Gibout et al. (2006) used the discrete intensity of segregation of the concentration field. As a stirring protocol, the authors defined a sequence of the types of mixing elements. By evaluating the mixing efficiency of all possible stirring protocols of a given length, Gibout et al. (2006) showed that the most of the stirring protocols induce a poor mixing. The authors showed that mixing-efficient protocols can be obtained at low computational cost applying the genetic algorithm approach. Mathew et al. (2007) considered as an actuator the fluid flow induced on a two-dimensional torus by a finite set of prescribed force fields modulated in time. They considered as a control problem the problem of finding a protocol which minimizes a weighted sum of the degree of mixedness and the stirring action per unit mass. As the measure of mixing, the authors used the mix-norm. Mathew et al. (2007) solved the control problem numerically using a conjugate gradient descent algorithm and obtained a sub-optimal

protocol. Thiffeault and Pavliotis (2008) considered optimization of mixing in a perturbed uniform flow and a simple cellular flow. The optimization problem was to find the source distribution that maximizes mixing for a given velocity field. As a measure of mixing, the authors used a generalized variance of the concentration field, which is a parameterized quantity closely related to the mix-norm for a specific value of the parameter. Thiffeault and Pavliotis (2008) solved the optimization problem using a variational approach. They summarized common features exhibited by the optimal source distributions and described how these distributions change with the value of the diffusivity and the value of the parameter that governs the measure of mixing.

Cortelezzi et al. (2008) considered the eggbeater model stirred by two orthogonal, sinusoidal velocity profiles $v_0(y) = \sin(2\pi y)$ and $v_1(x) = \sin(2\pi x)$. This model, which is also known as the *sine flow* (Liu et al., 1994), has been a popular playground for investigation of laminar mixing (Liu et al., 1994; Pierrehumbert, 1994; Antonsen et al., 1996; Alvarez et al., 1998; Muzzio et al., 2000; Szalai et al., 2003; Thiffeault et al., 2004; Phelps and Tucker, 2006). Cortelezzi et al. (2008) considered the problem of finding the optimal protocol able to induce the lowest value of the mix-norm at a given final time. The authors showed that the cost function, i.e. the mix-norm, associated with optimization in time has a complex structure with many nearly equal local minima making conventional optimization algorithms ineffective. In order to overcome this difficulty, Cortelezzi et al. (2008) introduced a *short time horizon optimization procedure*. This procedure considers all admissible stirring subprotocols for a given time horizon and, among these subprotocols, it selects an optimal stirring subprotocol which minimizes the mix-norm. The selected subprotocol is then used to stir the mixture up to the beginning of the next time horizon. These steps are repeated until a given final time is reached. The selected subprotocols are concatenated together to compose a sub-optimal stirring protocol, the *short time horizon optimal protocol*. Cortelezzi et al. (2008) drew two important conclusions from their results. First, among all possible stirring protocols, the short time horizon optimization procedure is able to find a suboptimal protocol which is nearly as mixing efficient as the optimal protocol. Second, protocols obtained using a less expensive optimization over very short time horizons are competitively mixing efficient with respect to protocols optimized over longer time horizons. These conclusions indicate that the short time horizon optimization procedure could be used to optimize and control mixing in engineering applications.

In this study we model homogenization of two fluids in a static mixer using the sine flow model. We restrict our study to purely advective flows as

we focus on mixing over times which are small with respect to the characteristic diffusion times. The sine flow is suitable for our study because this model captures the complex behavior of industrially-relevant mixing devices such as Kenics static mixer. The laminar flow in a static mixer is closely related to the Poiseuille flow, which is a laminar flow driven by a pressure gradient in an unobstructed pipe. However, mixing elements installed within a static mixer are able to efficiently redistribute flow in the radial direction. As the result, the velocity profile in a static mixer approaches the velocity profile of the plug flow rather than the parabolic velocity profile of the Poiseuille flow (Thakur et al., 2003). In other words, the flow velocity in a static mixer is nearly constant across any cross-section orthogonal to the main flow direction. Therefore, the dynamics induced in a cross-section of a three-dimensional flow in a static mixer can be represented qualitatively by the dynamics induced in the two-dimensional sine flow (Hobbs et al., 1997). In this study we consider, as a hyphothetical enhancement of a static mixer, a continuous-injection mixing device able to optimize mixing on-line. We model this device using the sine flow in which mixing is enhanced with the short time horizon procedure by Cortelezzi et al. (2008).

The goal of this study is to assess how sensitive is the mixing efficiency induced by the stirring protocols obtained with the short time horizon optimization procedure to the geometry of the initial concentration field. To perform this assessment, we consider five different configurations of the initial concentration field. For each configuration, we use the short time horizon optimization procedure to obtain an optimized protocol. We quantify the mixing efficiency of the optimized protocols by comparing the time-evolution of the mix-norm induced by them. Subsequently, we quantify the sensitivity of the optimized protocols by computing the time evolution of the spreading of the mix-norm induced by these protocols for the five initial configurations. We use the periodic and recursive symmetry-breaking protocols as benchmarks for our assessment. We show that the short time horizon optimization procedure generates protocols of nearly the same mixing efficiency regardless of the initial configuration. In other words, we show that the performance of the protocols obtained with this optimization procedure is generally quite insensitive to the geometry of the initial scalar field when compared to the performance of the periodic and recursive symmetry-breaking protocol.

The remainder of the article is organized as follows. In section 2, we define the sine flow system and review the solution to the purely advective problem. In the same section, we also define the mix-norm and sketch its computation. In section 3, we provide the definition of the recursive symmetry-breaking protocol and review the short time horizon optimization

procedure by Cortelezzi et al. (2008). In section 4, we present, discuss and compare the mixing efficiency and its sensitivity to the geometry of the initial configuration for the protocols obtained with the short time horizon optimization procedure as well as for the periodic and recursive symmetry-breaking protocols. We summarize our findings in section 5.

2 Mathematical description of the problem

In this section, we define the sine flow system and review the numerical solution to the purely advective sine flow problem. We also sketch the computation of the mix-norm and discuss the choice of the computational grid which is used to obtain the numerical solution.

2.1 The sine flow system

In this study we adopt the sine flow (Liu et al., 1994) as a model mixer to develop and test our optimization procedures. In the sine flow model, a passive scalar field (e.g., concentration field) is stirred iteratively by a pair of orthogonal, sinusoidal velocity fields

$$\mathbf{v}_0(x,y) = [\sin(2\pi y), 0]^T, \qquad \mathbf{v}_1(x,y) = [0, \sin(2\pi x)]^T, \tag{1}$$

inside a unit square domain with periodic boundaries. During each iteration, the concentration field is advected by one of the two velocity fields over a switching time τ. A *stirring protocol* is defined as a sequence of N binary digits $\{\alpha_k\}_{k=1}^N$, where N is the total number of iterations to be performed. Entries α_k set to zero and one are associated with velocity fields $\mathbf{v}_0$ and $\mathbf{v}_1$, respectively. The set of 2^N binary strings of length N represents all admissible protocols that can be used to stir the mixture by a given final time $T = \tau N$.

2.2 Solution to the purely advective sine flow problem

Pure advection of a scalar concentration field $\varphi(x,y,t)$ is governed by the dimensionless equation

$$\frac{\partial \varphi}{\partial t} = -\mathbf{v} \cdot \nabla \varphi. \tag{2}$$

Characteristic velocity and length chosen for nondimensionalization are the maximum absolute value of the stirring velocity field and the length of the square domain, respectively. Equation (2) states that in the absence of diffusion the concentration associated with any fluid particle is preserved in time. Hence, the time evolution of the concentration field can be obtained

from the time evolution of fluid particles moving under the action of the stirring velocity fields (1).

The time evolution of a fluid particle $(X(t), Y(t))$ under the action of the stirring velocity field $\mathbf{v}_0$ is described by the system of ordinary differential equations

$$\frac{dX}{dt} = \sin(2\pi Y), \quad \frac{dY}{dt} = 0 \tag{3}$$

with initial conditions

$$X(t_0) = X_0, \quad Y(t_0) = Y_0. \tag{4}$$

Integrating this system and applying initial conditions, we obtain the coordinates of the particle at time $t = t_0 + \tau$:

$$\begin{aligned} X(t_0 + \tau) &= X_0 + \tau \sin(2\pi Y_0) && \mod 1, \\ Y(t_0 + \tau) &= Y_0 && \mod 1. \end{aligned} \tag{5}$$

Note that the module one on the right hand side of (5) enforces periodic boundary conditions, i.e. it restricts the motion of the particle to lie within the unit square domain. Similarly, the time evolution of a fluid particle under the action of $\mathbf{v}_1$ is given by

$$\begin{aligned} X(t_0 + \tau) &= X_0 && \mod 1, \\ Y(t_0 + \tau) &= Y_0 + \tau \sin(2\pi X_0) && \mod 1. \end{aligned} \tag{6}$$

Consequently, the time evolution of a fluid particle under the action of the stirring protocol $\{\alpha_k\}_{k=1}^N$ with switching time τ can be obtained combining (5) and (6). In particular, the coordinates of the particle at time $t_{k+1} = \tau(k+1)$, $k = 1, \ldots, N$, are given by the map

$$\begin{pmatrix} X_{k+1} \\ Y_{k+1} \end{pmatrix} = \begin{cases} \begin{pmatrix} X_k + \tau \sin(2\pi Y_k) \\ Y_k \end{pmatrix} \mod 1, & \text{if} \quad \alpha_k = 0, \\ \begin{pmatrix} X_k \\ Y_k + \tau \sin(2\pi X_k) \end{pmatrix} \mod 1, & \text{if} \quad \alpha_k = 1. \end{cases} \tag{7}$$

Hence, the solution of the advection equation (2) is obtained leveraging the fact that in a purely advective flow the initial concentration associated with a fluid particle remains constant in time. Thus, in order to obtain the concentration $\varphi(X_k, Y_k, t_k)$ for $k = 1, \ldots, N$, it is sufficient to consider a particle located at (X_k, Y_k) at $t = t_k$, track the particle position backward

in time to its initial position (X_0, Y_0) at $t = 0$, and determine the initial concentration field $\varphi(X_0, Y_0, 0)$, i.e.

$$\varphi(x, y, t_k) = \varphi(X_0, Y_0, 0). \tag{8}$$

The initial position of the particle, (X_0, Y_0), is obtained from its position $(X_k, Y_k) = (x, y)$ at time $t = t_k$ using the inverse of the map (7),

$$\begin{pmatrix} X_{m-1} \\ Y_{m-1} \end{pmatrix} = \begin{cases} \begin{pmatrix} X_m - \tau \sin(2\pi Y_m) \\ Y_m \end{pmatrix} \bmod 1, & \text{if} \quad \alpha_m = 0, \\ \\ \begin{pmatrix} X_m \\ Y_m - \tau \sin(2\pi X_m) \end{pmatrix} \bmod 1, & \text{if} \quad \alpha_m = 1, \end{cases} \tag{9}$$

for $m = k, \ldots, 1$.

To compute numerically the concentration field at time $t = t_k$, the unit square domain is discretized into $M \times M$ nonoverlapping equal square cells, where M, the *grid resolution*, is an integer number. The concentration within the $(i, j)^{\text{th}}$ cell is approximated by the concentration of the fluid particle $(X^{i,j}(t), Y^{i,j}(t))$ located at time $t = t_k$ in the center of the cell, i.e.

$$\begin{aligned} X_k^{i,j} &\equiv X^{i,j}(t_k) = \frac{i - 1/2}{M}, \\ Y_k^{i,j} &\equiv Y^{i,j}(t_k) = \frac{j - 1/2}{M}, \end{aligned} \qquad i, j = 1, \ldots, M. \tag{10}$$

The concentration $\varphi(X_k^{i,j}, Y_k^{i,j}, t_k)$ at time $t = t_k$ in the $(i, j)^{\text{th}}$ cell is obtained by tracking the position of the $(i, j)^{\text{th}}$ particle backwards in time using (9) and then substituting the initial position of the particle, $(X_0^{i,j}, Y_0^{i,j})$, into (8).

2.3 Computation of the mix-norm

The optimization procedures considered in this study generate optimal mixing protocols by minimizing a cost function, the mix-norm. Consequently, it is important to compute the mix-norm efficiently and accurately. The mix-norm is a multi-scale measure of the mixedness of a scalar concentration field. It was introduced by Mathew et al. (2005) and is defined as the root mean square of the average values of the concentration field over a dense set of subsets contained in the flow domain. The mix-norm μ_φ of the scalar concentration field $\varphi(x, y, t)$ with zero mean can be computed as

follows (Mathew et al., 2005)

$$\mu_\varphi = \sqrt{\sum_{\mathbf{k}\in\mathbb{Z}^2} \frac{|\Phi_{\mathbf{k}}|^2}{\sqrt{1+4\pi^2||\mathbf{k}||^2}}}, \tag{11}$$

where $\{\Phi_{\mathbf{k}}\}_{\mathbf{k}\in\mathbb{Z}^2}$ is the spectral representation of the concentration field. For more details on computation of the mix-norm, the reader is referred to Mathew et al. (2007).

An approximate spectral representation of the concentration field $\varphi(x, y, t_k)$ can be obtained by computing the Fast Fourier Transform (FFT) of the concentration matrix $\{\varphi_{i,j}(t_k)\}_{i,j=1}^{M}$. Obviously, the mix-norm of the concentration matrix depends on the grid resolution M. As the grid resolution increases, the concentration matrix approximates the concentration field more precisely. At the same time, the computational cost of computing the mix-norm, which is of order $O(M^2)$, becomes more expensive when the grid resolution is increased. To find the optimal grid resolution, we computed the time evolution of the mix-norm induced by a periodic protocol at switching time $\tau = 0.8$ for $M^2 = 512^2$, 1024^2, 2048^2, 4096^2 and 8192^2. Note that for this value of τ the periodic protocol induces a globally chaotic flow. Consequently, we test the mix-norm under the worst possible conditions. For the above resolutions, the wall-clock time needed to compute the mix-norm of a concentration field on a computer with a 3.4GHz Pentium-4 processor with 1Mb L2 cache and 2Gb of RAM is 17, 71, 320, 1576 and 27633 milliseconds, respectively. At the same time, the relative errors between the mix-norm at time $t = 6$ computed for $M^2 = 8192^2$ and the mix-norms at time $t = 6$ computed for $M^2 = 512^2$, 1024^2, 2048^2 and 4096^2 are 38%, 17%, 7% and 2.5%, respectively. Based on these data, we found the grid resolution $M = 2048$ to be acceptable. This resolution was used to obtain the results presented in this study.

3 Stirring protocols

As it was mentioned in the introduction, the goal of this study is to assess the sensitivity of the short time horizon optimal protocols to the geometry of the initial configuration. We use the periodic and the recursive symmetry-breaking protocols as benchmarks for this assessment. In this section, we review the definitions of the periodic, recursive symmetry-breaking and short-time-horizon optimal protocols.

3.1 Periodic protocol

The periodic protocol is the traditional protocol used in the sine flow system. This protocol is defined by the alternating sequence $\{0, 1, 0, 1, \ldots\}$. Although the periodic protocol is simple, it is known to induce an unsteady flow which exhibits a chaotic dynamics for a range of the switching time values (Zalc and Muzzio, 1999).

3.2 Recursive symmetry-breaking protocol

The recursive symmetry-breaking protocol (Franjione et al., 1989) can be defined as follows: The first two iterations of this protocol are $\{0, 1\}$. Then, the protocol of a desired length can be obtained by iterative concatenation of existing protocol with its inverse. The inverse of a given protocol $\{\alpha_1, \ldots, \alpha_N\}$ is the protocol $\{\beta_1, \ldots, \beta_N\}$ in which $\beta_i = 0$ if $\alpha_i = 1$, and $\beta_i = 1$ when $\alpha_i = 0$, $i = 1, \ldots, N$. For example, the first four entries of the recursive symmetry-breaking protocol are $\{0, 1, 1, 0\}$, the first eight entries are $\{0, 1, 1, 0, 1, 0, 0, 1\}$, and so on. For a detailed derivation of this protocol the reader is referred to Franjione et al. (1989). As it was shown by Liu et al. (1994), the recursive symmetry-breaking protocol enhances mixing efficiency in the sine flow when compared to the periodic protocol because it does not generate islands of regular motion.

3.3 Short time horizon optimal protocols

A procedure for generating short time horizon optimal protocols has been proposed by Cortelezzi et al. (2008). For a given switching time τ and a total number of iterations N, a short time horizon optimal protocol is obtained through a sequence of optimizations. Each optimization in this sequence identifies a subprotocol that minimizes the mix-norm over a given time horizon $t = \tau\nu$. The parameter ν, the *switching time horizon*, a submultiple of N, defines the number of short time horizon optimizations, m, needed to reach the final time $T = \tau N = \tau m \nu$. Starting at $t = 0$, the short time horizon optimization considers all possible subprotocols $\{\alpha_1, \alpha_2, \ldots, \alpha_\nu\}$. For each of these protocols, the solution to the purely advective equation is computed using a given initial condition, $\varphi(x, y, 0)$, up to one time horizon, $t = \nu\tau$. The mix-norms of each solution, $\varphi(x, y, \nu\tau)$, are then evaluated, and the protocol which induced the lowest mix-norm is selected. The concentration field $\varphi(x, y, \nu\tau)$ induced by the selected subprotocol is used as the initial condition for optimization over the next time horizon, $\nu\tau \leqslant t < 2\nu\tau$. The m subprotocols selected by the short time horizon optimizations are concatenated together to compose a suboptimal stirring protocol, which is referred to as a short time horizon optimal protocol.

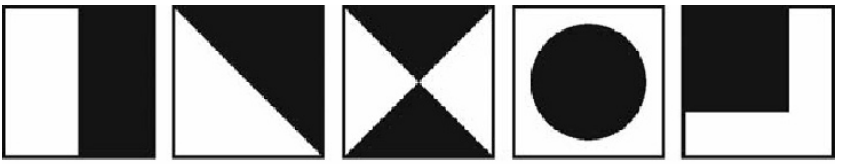

Figure 1. The 'vertical' (**V**), the 'diagonal' (**D**), the 'envelope' (**E**), the 'circle' (**C**) and the 'cornersquare' (**CS**) initial conditions. The initial concentration $\varphi(x, y, 0)$ is equal to -1 and $+1$ inside the black and white regions, respectively.

4 Results

In this section, we compare the mixing efficiency and sensitivity to the geometry of the initial concentration field of the periodic, recursive symmetry-breaking and short time horizon optimal protocols. In order to characterize the performance of these protocols, we consider five initial concentration fields, see figure 1, 'vertical', 'diagonal', 'envelope', 'circle' and 'cornersquare'. We consider the 'vertical' initial concentration field to model a continuous injection mixing device with injection streams that feed the black and white fluids from the right and left side, respectively. We model a possible distortion of this injection configuration by considering the 'diagonal' initial concentration field, see figure 1. As another possible injection configuration, we consider configuration in which the black and white fluids are separated in the radial direction, i.e. when the black fluid is surrounded by the white fluid. We model this injection configuration with the 'circle' initial concentration field. We model a possible distortion of this injection configuration by considering the 'cornersquare' initial concentration field, see figure 1. Finally, we consider the 'envelope' initial concentration field to model the injection configuration in which the black fluid is injected from the top and bottom sides, and the white fluid is injected from the left and right sides. Hence, we investigate how the geometry of the initial concentration field affects the mixing efficiency of the protocols generated by the short time horizon optimization procedure in comparison with the periodic and recursive symmetry-breaking protocol.

We restrict our study to the final optimization time $T = 6$ because this final time is sufficiently large for the structure in the mixture to be fully developed. We consider three values of the switching time $\tau = 0.1$, 0.4 and

0.8 because for these switching times the periodic protocol, which we use as a benchmark for optimization procedures, induces in the mixture, by time T, three well-defined flow structures (Zalc and Muzzio, 1999). For $\tau = 0.1$, the mixture is dominated by two islands of regular motion occupying the entire flow domain. For $\tau = 0.4$, the mixture presents four islands of regular motion are surrounded by a chaotic sea. For $\tau = 0.8$, the chaotic sea invades the entire flow domain and there are no detectable islands of regular motion in the mixture.

In order to clearly discuss the mixing efficiency of different stirring protocols with respect to given initial conditions, we introduce the following notation: The short time horizon optimization procedures with switching time horizons $\nu = 1$, 4 and 8 are identified by ν_1, ν_4 and ν_8, respectively. The five initial conditions 'vertical', 'diagonal', 'envelope', 'circle' and 'cornersquare' are identified by the symbols **V**, **D**, **E**, **C** and **CS** (see figure 1). Hence, a particular stirring protocol is identified by an abbreviation identifying the optimization procedure and the initial condition used. For example, $\nu_8(\mathbf{CS})$ identifies a protocol obtained with the short time horizon optimization procedure with switching time horizon $\nu = 8$ applied to the 'cornersquare' initial concentration field.

4.1 Optimization for $\tau = 0.1$

We consider first the switching time $\tau = 0.1$ because for this value of switching time the flow induced by the periodic protocol is laminar and presents two islands of regular motion occupying the entire flow domain. Figure 2(a) shows the time evolutions of the mix-norm induced by the periodic protocol applied to the five initial concentration fields shown in figure 1. The lines with the filled circle markers, the square markers, the triangle markers, the circle markers, and the filled square markers correspond to the 'circle', the 'cornersquare', the 'diagonal', the 'envelope' and the 'vertical' initial concentration fields, respectively. As it is shown by the spread of the curves in the lin-log plot (see figure 2(a)), the mixing efficiency of the periodic protocol depends greatly on the geometry of the initial concentration field. In particular, the periodic protocol applied to the 'circle' initial configuration is the most mixing efficient, while the same protocol applied to the 'envelope' initial configuration is the least mixing efficient. Towards the final time $T = 6$, the time evolution of the mix-norm induced by the periodic protocol when applied to the 'cornersquare', 'vertical' and 'diagonal' initial configurations approaches the time evolution of the mix-norm induced by the periodic protocol when applied to the 'circle' initial configuration, see figure 2(a). The final value of the mix-norm induced in these

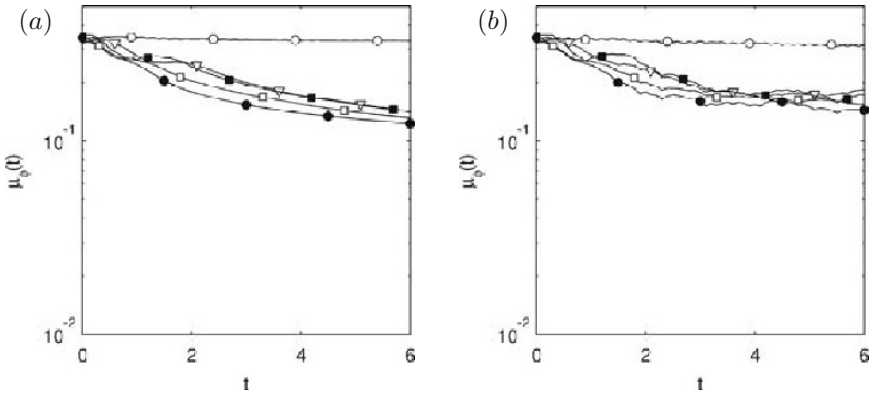

Figure 2. Time evolutions of the mix-norm induced by the periodic (a) and recursive symmetry-breaking (b) protocols applied to the 'circle' (—●—), the 'cornersquare' (—□—), the 'diagonal' (—▽—), the 'envelope' (—○—) and the 'vertical' (—■—) initial concentration fields for $\tau = 0.1$.

cases is about 1.3×10^{-1}, which is considerably less than the final value of mix-norm 3.3×10^{-1} induced by the periodic protocol when applied to the 'envelope' case.

To quantify the sensitivity of the periodic protocol to the geometry of the initial configuration, we compute the time evolution of the spreading of the mix-norm curves presented in figure 2(a). In other words, we consider, at any given time t, the relative difference $\delta(t)$ between the extreme values of the mix-norm induced by this protocol for the five initial configurations shown in figure 1. We compute the relative difference as follows

$$\delta(t) = \frac{\mu_{\max}(t) - \mu_{\min}(t)}{\left[\dfrac{\mu_{\max}(t) + \mu_{\min}(t)}{2}\right]}, \tag{12}$$

where $\mu_{\max}(t)$ and $\mu_{\min}(t)$ are the extreme values of the mix-norm. The time evolution of the relative difference δ induced by the periodic protocol for $\tau = 0.1$ is shown by the line with empty triangle markers in figure 3. Note that the initial value of the spreading, $\delta(t = 0)$, is already nonzero since the initial configurations shown in figure 1 have different values of the mix-norm. Under the stirring action induced by the periodic protocol, the initial relative difference increases with time, see the line with empty triangle markers in figure 3. Therefore, the periodic protocol is highly sensitive to the geometry of the initial configuration.

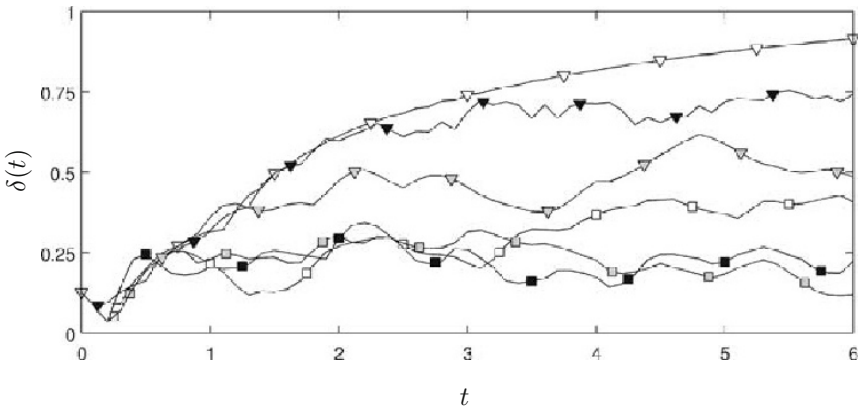

Figure 3. Time evolutions of the relative difference between the extreme values of the mix-norm, $\delta(t)$, for the periodic protocol (—▽—), the recursive symmetry-breaking protocol (—▼—), the protocols obtained with optimization procedures ν_1 (—□—), ν_4 (—▣—), ν_8 (—■—), and protocol $\nu_8(\mathbf{V})$ (—▽—) for switching time $\tau = 0.1$.

Figure 2(b) shows the time evolutions of the mix-norm induced by the recursive symmetry-breaking protocol applied to the five initial conditions (see figure 1) for $\tau = 0.1$. Surprisingly, the overall performance of this protocol is similar to the performance of the periodic protocol, as it can be seen by comparing figures 2(a) and 2(b). As for the periodic protocol, the recursive symmetry-breaking protocol applied to the 'circle' initial configuration is the most mixing efficient, while the same protocol applied to the 'envelope' initial configuration is the least mixing efficient. The latter fact indicates that the symmetry-breaking protocol is not effective in destroying the islands of regular motion in the early stages of stirring. The spreading of the mix-norm values induced by the recursive symmetry-breaking protocol is shown by the line with filled triangle markers in figure 3. The relative difference between the extreme values of the mix-norm induced by the recursive symmetry-breaking protocol increases with time and approaches the value of about 0.75 towards the final time $T = 6$. Surprisingly, this indicates that the recursive symmetry-breaking protocol is also highly sensitive to the geometry of the initial configuration, although not as sensitive as the periodic protocol.

The poor performance of the periodic protocol when applied to the 'envelope' initial condition is not surprising because the lines separating the

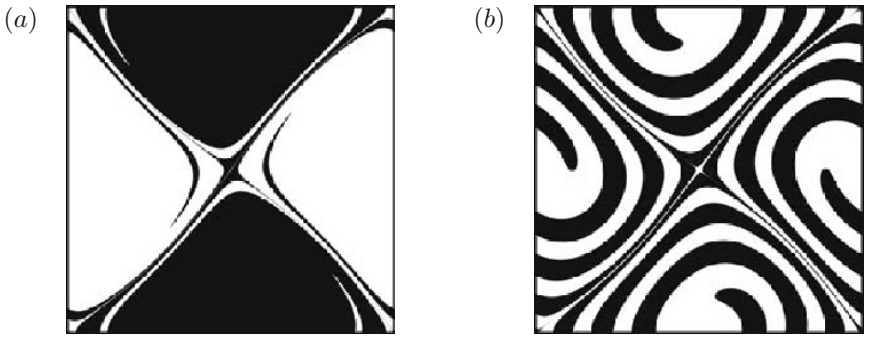

Figure 4. Snapshots at time $t = 4$ of the concentration field $\varphi(x, y, t)$ stirred by the periodic protocol applied to the 'envelope' (a) and the 'circle' (b) initial conditions for switching time $\tau = 0.1$.

white and black fluids nearly coincide with the stable and unstable manifolds of the flow induced by the periodic protocol. In other words, this initial configuration segregates nearly all white fluid in one island, while the black fluid is nearly segregated in the other. Hence, very little mixing is obtained by the periodic protocol because the stable and unstable manifolds act as barriers to mass transport. This is illustrated in figure 4(a), which presents the instantaneous snapshot of the concentration field at time $t = 4$. On the other hand, the good performace of the periodic protocol when applied to the 'circle' initial condition can be explained with a similar argument. In this case in fact, the initial configuration guarantees that there is the same amount of black and white fluids in each island. Furthermore, the stripe of white fluid in the center of the island separates two pockets of black fluid located in the corners. Hence, in each island the black and white fluids can be mixed by the swirling motion induced by the periodic protocol. This is illustrated in figure 4(b), which presents the instantaneous snapshot of the concentration field at time $t = 4$.

The similarity between the performance of the periodic and recursive symmetry-breaking protocol can also be seen by comparing the concentration fields induced by these protocols, i.e. by comparing figures 4 and 5. Figures 5(a) and 5(b) show the instantaneous snapshots of the concentration field induced by the recursive symmetry-breaking protocol applied to the 'envelope' and 'circle' initial conditions at time $t = 4$. Clearly, the location and size of islands of regular motion presented in figure 5 are similar to those presented in figure 4. However, the structure of the mixtures presents

(*a*) (*b*)

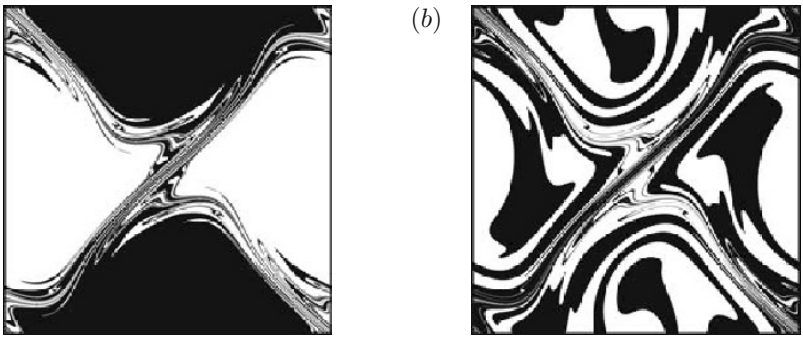

Figure 5. Snapshots at time $t = 4$ of the concentration field $\varphi(x, y, t)$ stirred by the recursive symmetry-breaking protocol applied to the 'envelope' (a) and 'circle' (b) initial conditions for switching time $\tau = 0.1$.

some peculiarities. On the one hand, for the 'envelope' initial condition, the recursive symmetry-breaking protocol is moderately more mixing efficient than the periodic protocol because the former induces finer lamellae in vicinity of stable and unstable manifolds, see figures 4(a) and 5(a). The corresponding values of the mix-norm, 3.34×10^{-1} and 3.25×10^{-1}, can be read from the curves with empty circle markers in figures 2(a) and 2(b), respectively. On the other hand, for the 'circle' initial condition the recursive symmetry-breaking protocol induces thicker lamellae inside the islands of regular motion than the periodic protocol, as it can be seen from figures 4(b) and 5(b). Consequently, for this initial condition the recursive symmetry-breaking protocol is moderately less mixing efficient than the periodic protocol. This is reflected by the values of the mix-norm 1.41×10^{-1} and 1.54×10^{-1} corresponding to the snapshots in figures 4(b) and 5(b). These mix-norm values can be read from the curves with filled circle markers in figures 2(a) and 2(b), respectively.

Figure 6(a) shows the time evolutions of the mix-norm induced by the protocols $\nu_1(\mathbf{C})$, $\nu_1(\mathbf{CS})$, $\nu_1(\mathbf{D})$, $\nu_1(\mathbf{E})$ and $\nu_1(\mathbf{V})$ obtained with the simplest optimization procedure ν_1 for $\tau = 0.1$. Note that in general these protocols are all different because the short time horizon optimization procedure generates an optimal sequence which depends on the initial condition. The overall performance of these protocols is much better than the performance of the periodic and recursive symmetry-breaking protocols as it is shown by figures 2(a), 2(b) and 6(a). The protocols $\nu_1(\mathbf{V})$ and $\nu_1(\mathbf{D})$ are more mixing efficient than $\nu_1(\mathbf{CS})$, which, in turn, is more mixing effi-

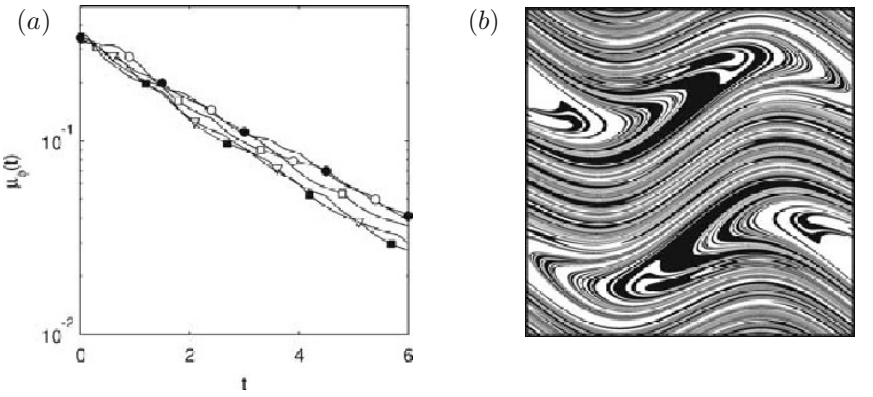

Figure 6. Panel (a): Time evolutions of the mix-norm induced by the protocols obtained with optimization procedure ν_1 applied to the 'circle' (—●—), the 'cornersquare' (—□—), the 'diagonal' (—▽—), the 'envelope' (—○—) and the 'vertical' (—■—) initial concentration fields for $\tau = 0.1$. Panel (b): Snapshot at time $t = 4$ of the concentration field $\varphi(x, y, t)$ stirred by the protocol $\nu_1(\mathbf{C})$ for switching time $\tau = 0.1$.

cient than the protocols $\nu_1(\mathbf{C})$ and $\nu_1(\mathbf{E})$. The spreading of the mix-norm values induced by the protocols obtained with optimization procedure ν_1 is shown by the line with empty square markers in figure 3. In this case, the initial spreading tends to increase with time but does not exceed the value of about 0.428. Therefore, the protocols obtained with optimization procedure ν_1 are considerably less sensitive to the geometry of the initial configuration than the periodic and recursive symmetry-breaking protocols.

It is interesting to relate the value of the mix-norm to the geometry of the partially mixed concentration field induced by the periodic and optimized protocols. Figure 6(b) shows the snapshot at time $t = 4$ of the structure of the concentration field generated by protocol $\nu_1(\mathbf{C})$. The stirring action of this protocol induces fine lamellar structures by recursively stretching and folding the concentration field. The corresponding value of the mix-norm, 8.6×10^{-2}, can be read from the curve with filled circle markers in figure 6(a). Figure 4(b) shows the snapshot at time $t = 4$ of the structure of the concentration field generated by the periodic protocol when applied to the 'circle' initial configuration. In contrast with $\nu_1(\mathbf{C})$, the stirring action of the periodic protocol applied to the 'circle' initial condition for $\tau = 0.1$ induces the swirling flow structure with relatively thick lamellae.

The corresponding value of the mix-norm, 1.4×10^{-1}, can be read from the curve with filled circle markers in figure 2(a). The protocol $\nu_1(\mathbf{C})$ is substantially more mixing efficient than the periodic protocol because under its stirring action the average lamellae thickness decreases exponentially in time, whereas the stirring action of the periodic protocol is able to decrease the average lamellae thickness only linearly in time.

Figure 7 shows the time evolutions of the mix-norm induced by the protocols obtained with optimization procedures ν_4 and ν_8 when applied to the five initial configurations (see figure 1) for $\tau = 0.1$. Figure 7 shows that the protocols generated by ν_4 and ν_8 have similar mixing efficiency and induce a final value of the mix-norm of about 3×10^{-2}. The overall performance of these protocols is much better than the performance of the periodic and recursive symmetry-breaking protocols, as it is shown by figures 2 and 7. Figure 7(a) shows that the protocols $\nu_4(\mathbf{V})$ and $\nu_4(\mathbf{D})$ are more mixing efficient than $\nu_4(\mathbf{CS})$, which, in turn, is more mixing efficient than $\nu_4(\mathbf{C})$ and $\nu_4(\mathbf{E})$. However, towards the final time $T = 6$, the time evolutions of the mix-norm induced by these protocols approach each other. Figure 7(b) shows that the protocol $\nu_8(\mathbf{V})$ is more mixing efficient than $\nu_8(\mathbf{C})$, $\nu_8(\mathbf{CS})$, $\nu_8(\mathbf{D})$ and $\nu_8(\mathbf{E})$. The spreading of the mix-norm induced by the protocols obtained with optimization procedures ν_4 and ν_8 is shown in figure 3 by the lines with grey square markers and filled square markers, respectively. The protocols obtained with procedures ν_1, ν_4 and ν_8 induce similar relative difference within the interval $0 \leqslant t \leqslant 3.3$. For times $t > 3.3$ the spreading induced by the protocols obtained with ν_4 and ν_8 is substantially less than the spreading in the case of ν_1. Thus, the computationally expensive protocols obtained with optimization procedures ν_4 and ν_8 are less sensitive to the geometry of the initial configuration than the protocols obtained with optimization procedure ν_1.

Finally, we characterize the sensitivity to initial concentration field of the stirring protocol $\nu_8(\mathbf{V})$ obtained with optimization procedure ν_8 for the 'vertical' initial configuration. We choose a protocol optimized for the 'vertical' initial configuration because this configuration is widely used in literature. Figure 8 shows the time evolutions of the mix-norm induced by the protocol $\nu_8(\mathbf{V})$ applied to the five initial concentration fields (see figure 1) for $\tau = 0.1$. As it is shown by the spread of the curves presented in figure 8, the protocol $\nu_8(\mathbf{V})$ is quite sensitive to the geometry of the initial concentration field. In particular, the protocol $\nu_8(\mathbf{V})$ applied to the 'vertical' initial configuration is the most mixing efficient, while the same protocol applied to the 'envelope' initial configuration is the least mixing efficient. The spreading of the mix-norm induced by the protocol $\nu_8(\mathbf{V})$ is shown by the line with gray triangle markers in figure 3. This figure shows

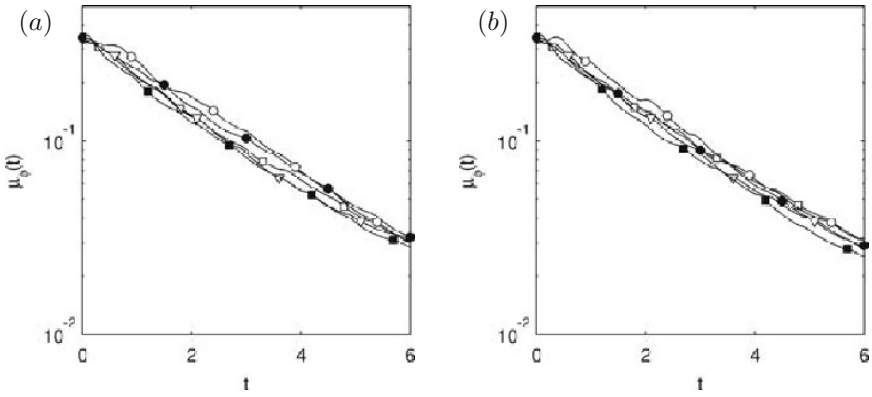

Figure 7. Time evolutions of the mix-norm induced by the protocols obtained with optimization procedures ν_4 (a) and ν_8 (b) applied to the 'circle' (—●—), the 'cornersquare' (—□—), the 'diagonal' (—▽—), the 'envelope' (—○—) and the 'vertical' (—■—) initial concentration fields for $\tau = 0.1$.

that the relative difference tends to increase during the interval $0 \leqslant t \leqslant 4.8$, reaches its peak value of about 0.62 at $t = 4.8$ and then decreases during the interval $4.8 < t \leqslant 6.0$. Clearly, the protocol $\nu_8(\mathbf{V})$ is less sensitive to the geometry of the initial configuration than the periodic and recursive symmetry-breaking protocols but is more sensitive than the protocols obtained with optimization procedures ν_1, ν_4 and ν_8, see figure 3.

4.2 Optimization for $\tau = 0.4$

We consider next the switching time $\tau = 0.4$. For this value of switching time the flow induced by the periodic protocol is partly chaotic and presents four islands of regular motion surrounded by a chaotic sea. Figure 9(a) shows the time evolutions of the mix-norm induced by the periodic protocol applied to the five initial concentration fields shown in figure 1. As it is shown by the spread of the curves in figure 9(a), the mixing efficiency of the periodic protocol is greatly sensitive to the geometry of the initial concentration field. The periodic protocol applied to the 'circle' initial configuration is the most mixing efficient, while the same protocol applied to the 'envelope' configuration is the least mixing efficient. On the other hand, the periodic protocol has similar mixing efficiency when applied to the 'cornersquare', 'vertical' and 'diagonal' initial configurations. The spreading of the mix-norm induced by the periodic protocol is shown by the line with

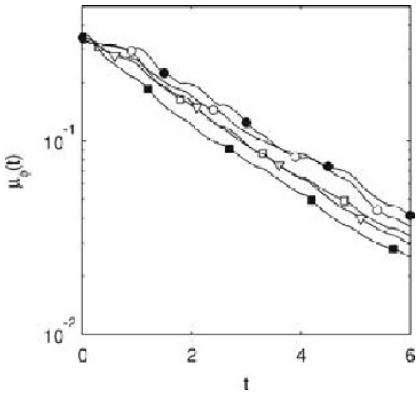

Figure 8. Time evolutions of the mix-norm induced by the protocol $\nu_8(\mathbf{V})$ applied to the 'circle' (—●—), the 'cornersquare' (—□—), the 'diagonal' (—▽—), the 'envelope' (—○—) and the 'vertical' (—■—) initial concentration fields for $\tau = 0.1$.

empty triangle markers in figure 10. As for the switching time $\tau = 0.1$, the relative difference increases with time under the stirring action of the periodic protocol. Thus, the periodic protocol is highly sensitive to the geometry of the initial configuration.

Figure 9(b) shows the time evolutions of the mix-norm induced by the recursive symmetry-breaking protocol applied to the five initial conditions (see figure 1) for $\tau = 0.4$. Unlike the case of $\tau = 0.1$, the overall mixing efficiency of this protocol is much better than the mixing efficiency of the periodic protocol, as it can be seen by comparing figures 9(a) and 9(b). In particular, the recursive symmetry-breaking protocol applied to the 'vertical' initial configuration is the most mixing efficient, while the same protocol applied to the 'envelope' configuration is the least mixing efficient. The spreading of the mix-norm induced by the recursive symmetry-breaking protocol is shown by the line with filled triangle markers in figure 10. The recursive symmetry-breaking and periodic protocols induce similar spreading within the interval $0 \leqslant t \leqslant 4.8$. In particular, the relative difference induced by these protocols increases with time and reaches the value of about 0.68 at $t = 4.8$. However, for $t > 4.8$ the relative difference tends to decrease in the case of the recursive symmetry-breaking protocol, whereas it continues to increase in the case of the periodic protocol. Thus, the recursive symmetry-breaking protocol is, over time, less sensitive to the geometry of the initial configuration than the periodic protocol.

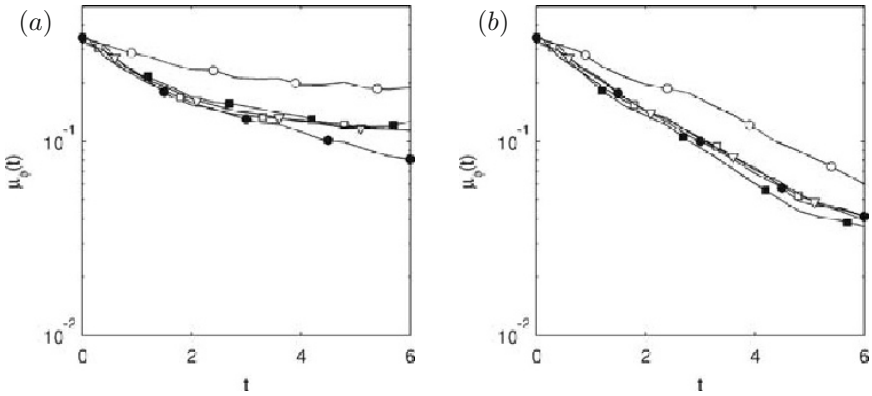

Figure 9. Time evolutions of the mix-norm induced by the periodic (a) and recursive symmetry-breaking protocol (b) applied to the 'circle' (—●—), the 'cornersquare' (—□—), the 'diagonal' (—▽—), the 'envelope' (—○—) and the 'vertical' (—■—) initial concentration fields for $\tau = 0.4$.

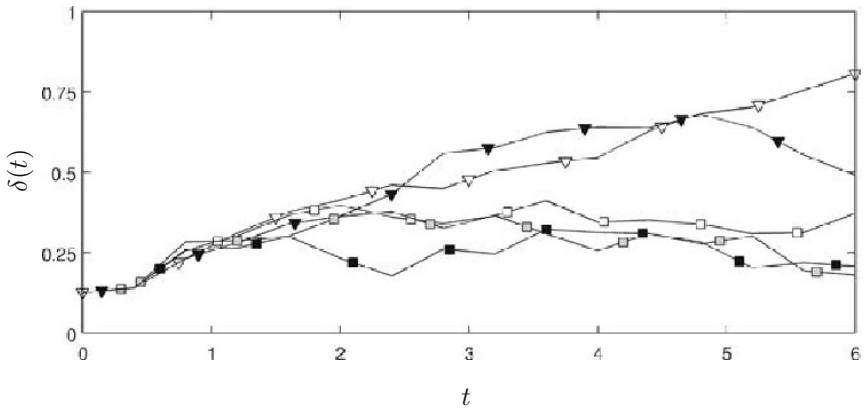

Figure 10. Time evolutions of the relative difference between the extreme values of the mix-norm, $\delta(t)$, for the periodic protocol (—▽—), the recursive symmetry-breaking protocol (—▼—) and the protocols obtained with optimization procedures ν_1 (—□—), ν_4 (—▩—) and ν_8 (—■—) for switching time $\tau = 0.4$.

(*a*)  (*b*) 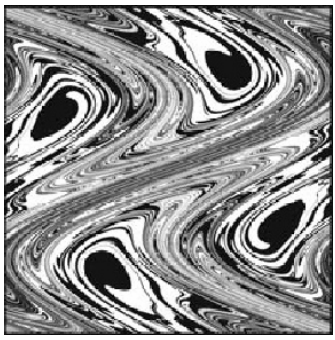

Figure 11. Snapshots at time $T = 6$ of the concentration field $\varphi(x, y, t)$ stirred by the periodic protocol applied to the 'envelope' (a) and the 'circle' (b) initial conditions for switching time $\tau = 0.4$.

The poor performance of the periodic protocol when applied to the 'envelope' initial condition is not surprising because this initial configuration segregates black fluid in two of the four islands of regular motion induced by this protocol, while white fluid is segregated in the other two islands. Hence, mixing is poor within the island of regular motion because the boundaries of the islands act as barriers to mass transport. This is illustrated in figure 11(a), which presents the instantaneous snapshot of the concentration field at time $T = 6$. On the other hand, the good performance of the periodic protocol when applied to the 'circle' initial condition can be explained with a similar argument. In this case, the initial configuration guarantees that there is comparable amount of black and white fluids in each island. Hence, the black and white fluids can be mixed by the swirling motion induced in each island by the periodic protocol. This is illustrated in figure 11(b), which presents the instantaneous snapshot of the concentration field at time $T = 6$.

The difference in performance between the periodic and recursive symmetry-breaking protocol for $\tau = 0.4$ can be seen by comparing the concentration fields induced by these protocols. Figure 12 shows the instantaneous snapshots of the concentration field induced by the recursive symmetry-breaking protocol applied to the 'envelope' and 'circle' initial conditions at time $T = 6$. As it can be seen from this figure, the recursive symmetry-breaking protocol induces no islands of regular motion. This protocol is more mixing efficient for the 'circle' initial configuration than for the 'envelope' configuration. The corresponding values of the mix-norm,

(a) 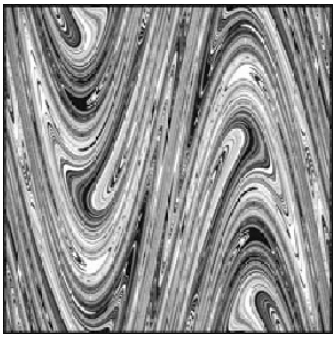 (b) 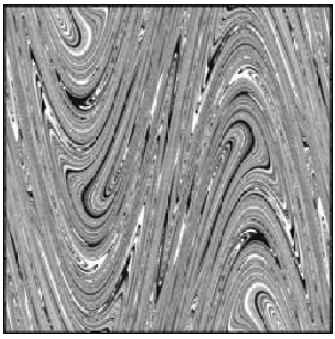

Figure 12. Snapshots at time $T = 6$ of the concentration field $\varphi(x, y, t)$ stirred by the recursive symmetry-breaking protocol applied to the 'envelope' (a) and the 'circle' (b) initial conditions for switching time $\tau = 0.4$.

4.1×10^{-2} and 6.0×10^{-2}, can be read from the curves with filled circle and empty circle markers in figure 9(b). These mix-norm values are smaller than the values 1.9×10^{-1} and 8.0×10^{-2} induced by the periodic protocol at time $T = 6$. The above values of the mix-norm induced by the periodic protocol correspond to the snapshots of the concentration field shown in figure 11 and can be read from the curves with filled circle and empty circle markers in figure 9(a).

Figure 13(a) shows the time evolutions of the mix-norm induced by the protocols $\nu_1(\mathbf{C})$, $\nu_1(\mathbf{CS})$, $\nu_1(\mathbf{D})$, $\nu_1(\mathbf{E})$ and $\nu_1(\mathbf{V})$ obtained with the simplest optimization procedure ν_1 for $\tau = 0.4$. The overall performance of these protocols is much better than the performance of the periodic protocol and slightly better than the performance of the recursive symmetry-breaking protocol, as it can be seen from figures 9(a), 9(b) and 13(a). The protocol $\nu_1(\mathbf{E})$ is visibly less mixing efficient than the other protocols obtained with ν_1. The protocols $\nu_1(\mathbf{C})$, $\nu_1(\mathbf{CS})$, $\nu_1(\mathbf{D})$ and $\nu_1(\mathbf{V})$ are similarly mixing efficient. The stirring action of the protocols obtained with optimization procedure ν_1 is illustrated in figure 13(b), which presents the instantaneous snapshot of the concentration field induced by the protocol $\nu_1(\mathbf{E})$ at time $T = 6$. As it can be seen from figure 13(b), this protocol induces no islands of regular motion. The stirring action of $\nu_1(\mathbf{E})$ seems to be similar to the stirring action of the recursive symmetry-breaking protocol, as it can be seen by comparing figures 12(a) and 13(b). The spreading of the mix-norm induced by the protocols obtained with optimization procedure ν_1 is shown by the line with empty square markers in figure 10. For these protocols, the

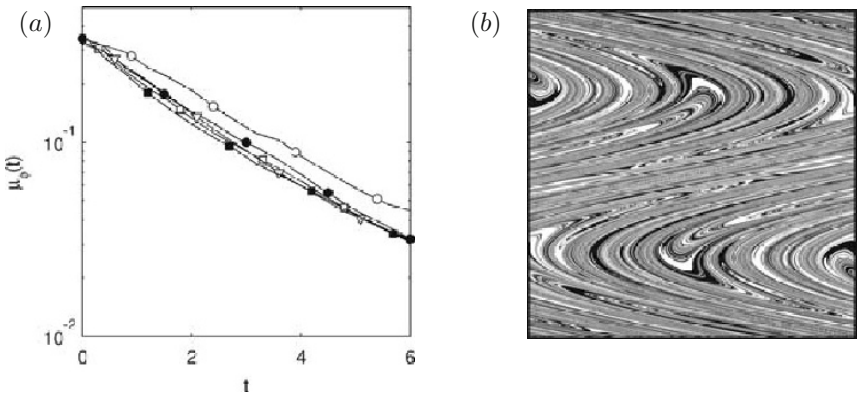

Figure 13. Panel (a): Time evolutions of the mix-norm induced by the protocols obtained with optimization procedure ν_1 applied to the 'circle' (—●—), the 'cornersquare' (—□—), the 'diagonal' (—▽—), the 'envelope' (—○—) and the 'vertical' (—■—) initial concentration fields for $\tau = 0.4$. Panel (b): Snapshot at time $T = 6$ of the concentration field $\varphi(x, y, t)$ stirred by the protocol $\nu_1(\mathbf{E})$ for switching time $\tau = 0.4$.

relative difference increases within the interval $0 \leqslant t \leqslant 2$ where reaches the value of about 0.4, and then it fluctuates near this value. Thus, the protocols obtained with optimization procedure ν_1 are considerably less sensitive to the geometry of the initial configuration than the periodic and recursive symmetry-breaking protocols.

Figure 14 shows the time evolutions of the mix-norm induced by the protocols obtained with optimization procedures ν_4 and ν_8 when applied to the five initial configurations (see figure 1) for $\tau = 0.4$. Figure 14 shows that these protocols have similar mixing efficiency and induce a final value of the mix-norm of about 3×10^{-2}. The overall performance of the protocols obtained with ν_4 and ν_8 is quite similar and much better than the performance of the periodic protocol, as it is shown by figures 9(a) and 14. Figure 14(a) shows that the protocol $\nu_4(\mathbf{E})$ is clearly less mixing efficient than the four other protocols. Figure 14(b) shows that the protocol $\nu_8(\mathbf{V})$ is more mixing efficient than protocols $\nu_8(\mathbf{C})$, $\nu_8(\mathbf{CS})$ and $\nu_8(\mathbf{D})$, which, in turn, are more mixing efficient than $\nu_8(\mathbf{E})$. The spreading of the mix-norm induced by the protocols obtained with optimization procedures ν_4 and ν_8 is shown in figure 10 by the lines with grey square markers and filled square markers, respectively. The relative difference does not exceed the value of about 0.38 in the case of ν_4 and the value of about 0.32 in the case of ν_8.

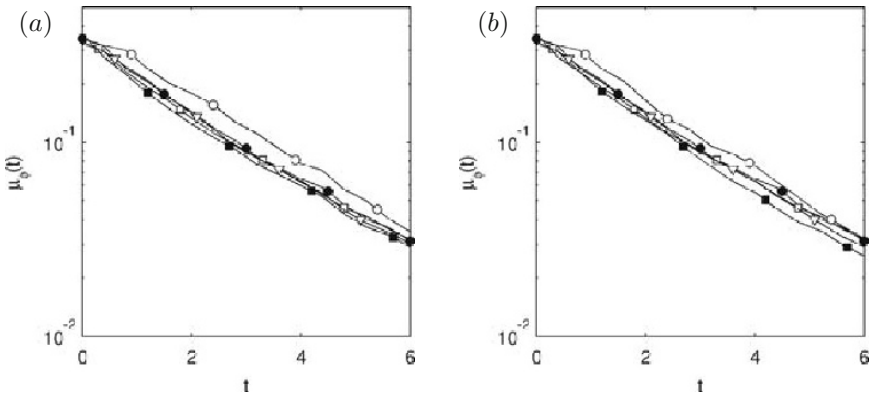

Figure 14. Time evolutions of the mix-norm induced by the protocols obtained with optimization procedures ν_4 (a) and ν_8 (b) applied to the 'circle' (—●—), the 'cornersquare' (—□—), the 'diagonal' (—▽—), the 'envelope' (—○—) and the 'vertical' (—■—) initial concentration fields for $\tau = 0.4$.

Thus, the protocols obtained with these optimization procedures are a little less sensitive to the geometry of the initial configuration than the protocols obtained with optimization procedure ν_1 and are considerably less sensitive than the periodic and recursive symmetry-breaking protocols.

4.3 Optimization for $\tau = 0.8$

We consider next the switching time $\tau = 0.8$. For this value of switching time the periodic protocol induces a globally chaotic flow, i.e. a flow without detectable islands of regular motion. Obviously, this case poses a challenge for the short time horizon optimization procedure. Figure 15(a) shows the time evolutions of the mix-norm induced by the periodic protocol applied to the five initial concentration fields shown in figure 1. The periodic protocol applied to the 'circle' and 'envelope' initial conditions is less mixing efficient than this protocol applied to the 'cornersquare', 'diagonal' and 'vertical' initial conditions. By comparing the spread of the curves presented in the figures 2(a), 9(a) and 15(a), one can see that the mixing efficiency of the periodic protocol for $\tau = 0.8$ is considerably less sensitive to the initial concentration field than the mixing efficiency of the periodic protocol for switching times $\tau = 0.4$ and 0.1. The spreading of the mix-norm induced by the periodic protocol is shown in figure 16 by the line with empty triangle markers. The relative difference increases within the interval $0 \leqslant t \leqslant 2.4$,

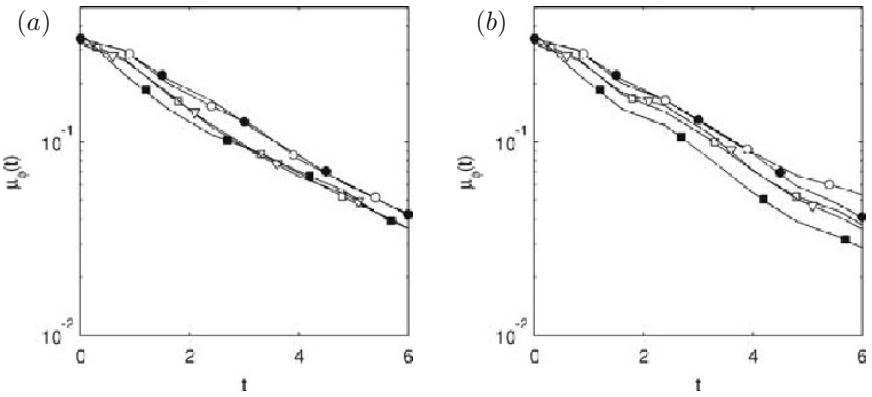

Figure 15. Time evolutions of the mix-norm induced by the periodic (a) and recursive symmetry-breaking (b) protocols applied to the 'circle' (—●—), the 'cornersquare' (—□—), the 'diagonal' (—▽—), the 'envelope' (—○—) and the 'vertical' (—■—) initial concentration fields for $\tau = 0.8$.

reaches the value of about 0.4 at $t = 2.4$ and then decreases to the value of about 0.17 towards the final time $T = 6$. Not surprisingly, the periodic protocol for $\tau = 0.8$ is considerably less sensitive to the geometry of the initial configuration than for $\tau = 0.1$ and 0.4 since for $\tau = 0.8$ this protocol induces a globally chaotic flow.

Figure 15(b) shows the time evolutions of the mix-norm induced by the recursive symmetry-breaking protocol applied to the five initial conditions (see figure 1) for $\tau = 0.8$. This protocol applied to the 'vertical' initial configuration is the most mixing efficient, while it is the least mixing efficient when applied to the 'envelope' initial configuration. The spreading of the mix-norm induced by the recursive symmetry-breaking protocol is shown in figure 16 by the line with filled triangle markers. The recursive symmetry-breaking and periodic protocols induce similar spreading within the interval $0 \leqslant t \leqslant 2.4$. Surprisingly, for $t > 2.4$, the relative difference induced by the periodic protocol starts to decrease whereas the relative difference induced by the recursive symmetry-breaking protocol starts to increase and reaches the value of about 0.62 at $T = 6$. Thus, the recursive symmetry-breaking protocol is considerably more sensitive to the geometry of the initial configuration than the periodic protocol.

Figure 17 shows the time evolutions of the mix-norm induced by the protocols $\nu_1(\mathbf{C})$, $\nu_1(\mathbf{CS})$, $\nu_1(\mathbf{D})$, $\nu_1(\mathbf{E})$ and $\nu_1(\mathbf{V})$ obtained with the simplest optimization procedure ν_1 for $\tau = 0.8$. The protocol $\nu_1(\mathbf{V})$ is more

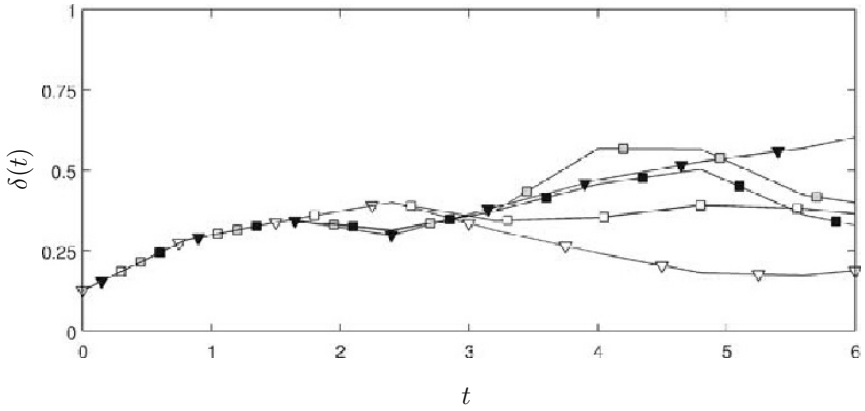

Figure 16. Time evolutions of the relative difference between the extreme values of the mix-norm, $\delta(t)$, for the periodic protocol (—▽—), the recursive symmetry-breaking protocol (—▼—) and the protocols obtained with optimization procedures ν_1 (—□—), ν_4 (—▨—) and ν_8 (—■—) for switching time $\tau = 0.8$.

mixing efficient than $\nu_1(\mathbf{CS})$ and $\nu_1(\mathbf{D})$, which, in turn, are more mixing efficient than $\nu_1(\mathbf{C})$ and $\nu_1(\mathbf{E})$. The spreading of the mix-norm induced by the protocols obtained with optimization procedure ν_1 is shown in figure 16 by the line with empty square markers. Within the interval $0 \leqslant t \leqslant 2.4$, these protocols and the periodic protocol induce similar relative difference. For $t > 2.4$, the relative difference induced by the optimized protocols fluctuates near the value of about 0.38. Therefore, the protocols obtained with optimization procedure ν_1 are more sensitive to the geometry of the initial concentration field than the periodic protocol and are less sensitive than the recursive symmetry-breaking protocol.

Figure 18 shows the time evolutions of the mix-norm induced by the protocols obtained with optimization procedures ν_4 and ν_8 when applied to the five initial configurations (see figure 1) for $\tau = 0.8$. Figure 18(a) shows that the protocol $\nu_4(\mathbf{V})$ is more mixing efficient than protocols $\nu_4(\mathbf{D})$ and $\nu_4(\mathbf{CS})$, which, in turn, are more mixing efficient than protocols $\nu_4(\mathbf{E})$ and $\nu_4(\mathbf{C})$. Figure 18(b) shows that the protocol $\nu_8(\mathbf{V})$ is more mixing efficient than protocols $\nu_8(\mathbf{CS})$ and $\nu_8(\mathbf{D})$, which, in turn, are more mixing efficient than protocols $\nu_8(\mathbf{C})$ and $\nu_8(\mathbf{E})$. The spreading of the mix-norm induced by the protocols obtained with optimization procedures ν_4 and ν_8 is shown in figure 16 by the lines with grey square markers and filled square markers,

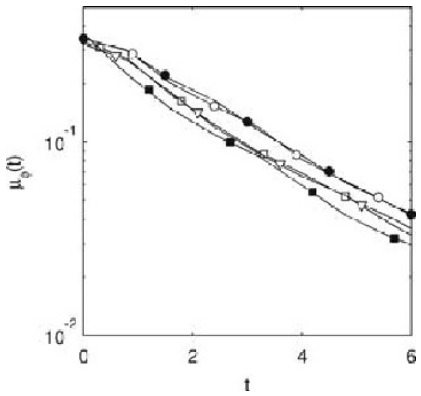

Figure 17. Time evolutions of the mix-norm induced by the protocols obtained with optimization procedure ν_1 applied to the 'circle' (—●—), the 'cornersquare' (—□—), the 'diagonal' (—▽—), the 'envelope' (—○—) and the 'vertical' (—■—) initial concentration fields for $\tau = 0.8$.

respectively. Within the interval $0 \leqslant t \leqslant 3$, the protocols obtained with optimization procedures ν_1, ν_4 and ν_8 induce similar relative difference. Surprisingly, within the interval $3 < t \leqslant 5.6$, the relative difference induced by the protocols obtained with ν_4 and ν_8 is greater than in the case of ν_1. Thus, the protocols obtained with ν_4 and ν_8 are more sensitive to the geometry of the initial configuration than the protocols obtained with ν_1. At the same time, the protocols obtained with ν_4 and ν_8 and the recursive symmetry-breaking protocol induce similar relative difference within the interval $0 \leqslant t \leqslant 5$, see figure 16. For $t > 5$, the relative difference induced by the optimized protocols decreases and becomes considerably less than in the case of the recursive symmetry-breaking protocol. Therefore, the protocols obtained with optimization procedures ν_4 and ν_8 are a little less sensitive to the geometry of the initial configuration than the recursive symmetry-breaking protocol.

4.4 Analysis of the structure of stirring protocols

In this subsection, we investigate the correlation between the structure of the optimized protocols and the geometry of the initial scalar filed. For this reason we visualize the structure of a stirring protocol $\{\alpha_1, \ldots, \alpha_N\}$ with N black or white squares arranged in a column from top to bottom. Black and white squares identify velocity fields $\mathbf{v}_1$ and $\mathbf{v}_0$, respectively. The i^{th}

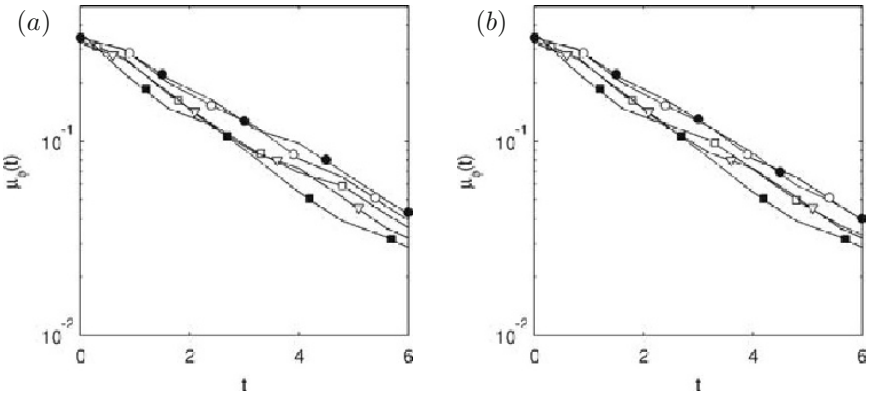

Figure 18. Time evolutions of the mix-norm induced by the protocols obtained with optimization procedure ν_4 (a) and ν_8 (b) applied to the 'circle' (—●—), the 'cornersquare' (—□—), the 'diagonal' (—▽—), the 'envelope' (—○—) and the 'vertical' (—■—) initial concentration fields for $\tau = 0.8$.

square represents velocity field $\mathbf{v}_{\alpha_i}$ which is active during the i^{th} iteration of the sine flow, $i = 1, \ldots, N$.

Figure 19 shows the structure of the protocols obtained with optimization procedures ν_1, ν_4 and ν_8 when applied to the five initial configurations (see figure 1) for $\tau = 0.1$. We choose this switching time because it allows an easier identification of the structure of stirring protocols. As mentioned before, the protocols are all different because each optimization procedure generates protocol which depends on the initial condition. Protocols present the difference in the sequence during the first 10–15 iterations, see figure 19. For example, protocol $\nu_1(\mathbf{V})$ applies the velocity field $\mathbf{v}_0$ during the first 14 iterations, whereas protocol $\nu_1(\mathbf{C})$ prescribes alternately the velocity fields $\mathbf{v}_0$ and $\mathbf{v}_1$ during the first 6 iterations and then applies velocity field $\mathbf{v}_1$ during the next 5 iterations, as it is shown in figure 19(a). Hence, we refer to the first 10–15 iterations of a stirring protocol as the *transient* part of the protocol. On the other hand, the remaining 45–50 iterations of the protocols shown in figure 19 share similar structures. Specifically, during these iterations the protocols are nearly periodic, see figure 19. We refer to the last 45–50 iterations of a stirring protocol obtained for $\tau = 0.1$ as the *quasi-periodic* part of the protocol.

The quasi-periodic parts of the protocols obtained with optimization procedure ν_1 consist of series of 5–16 iterations with on average 10 iterations in a series, see figure 19(a). For optimization procedure ν_4, the quasi-

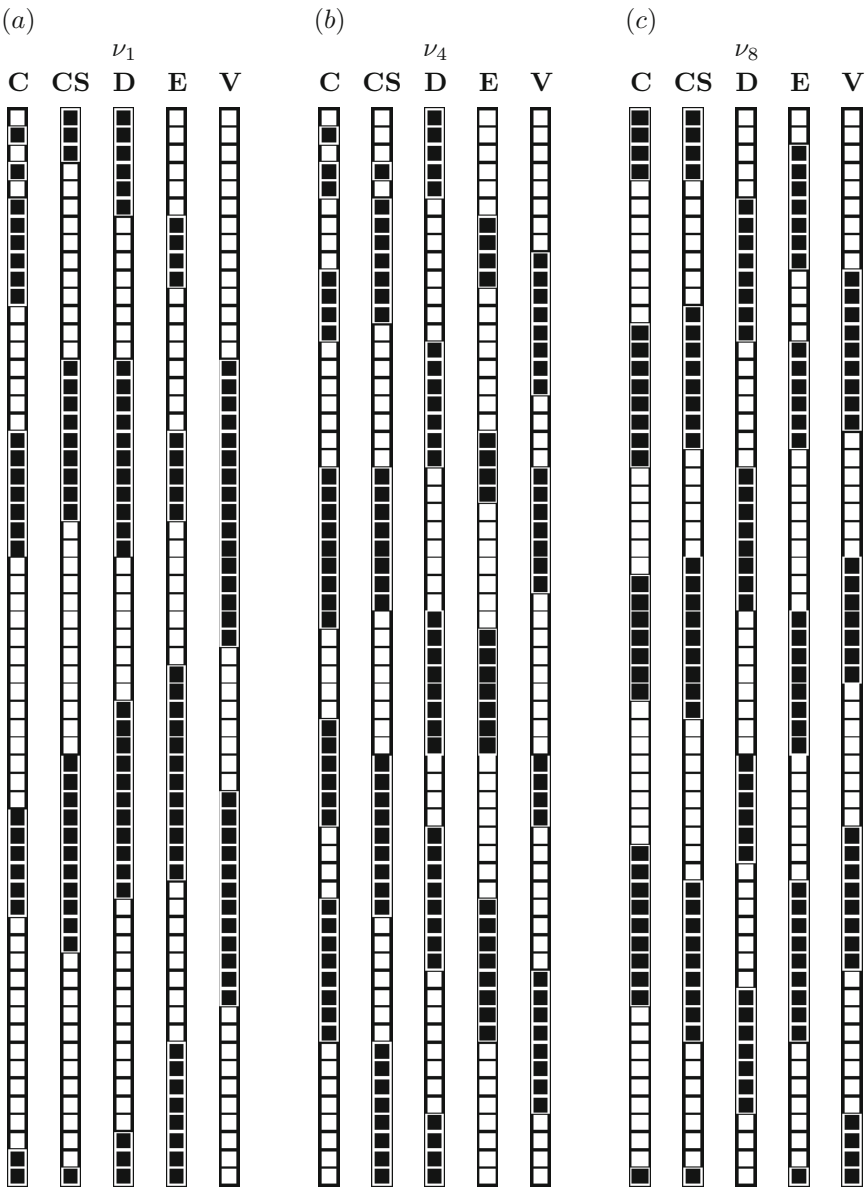

Figure 19. Visualizations of the stirring protocols obtained with optimization procedures ν_1 (a), ν_4 (b) and ν_8 (c) for $\tau = 0.1$. Abbreviations above the protocol visualizations indicate the geometry of the initial condition chosen: 'circle' (**C**), 'cornersquare' (**CS**), 'diagonal' (**D**), 'envelope' (**E**) and 'vertical' (**V**).

periodic part of the protocols consist of series of only 4–9 iterations with on average 8 iterations in a series, see figure 19(b). For optimization procedure ν_8, the quasi-periodic part of the protocols consist of series of 6–9 iterations with on average 8 iterations in a series, see figure 19(c). We conclude that the quasi-periodic part of the protocols obtained with optimization procedure ν_1 resemble the periodic protocol at the switching time $\tau = 1.0$, whereas the quasi-periodic parts of the protocols obtained with optimization procedures ν_4 and ν_8 resemble the periodic protocol at switching time $\tau = 0.8$.

In contrast with the case of $\tau = 0.1$, the protocols obtained with optimization procedures ν_1, ν_4 and ν_8 when applied to the five initial configurations shown in figure 1 for the switching times $\tau = 0.4$ and 0.8 have no transient parts. For $\tau = 0.4$, these protocols consist of series of 1–3 iterations with on average 2 iterations in a series. For $\tau = 0.8$, these protocols consist of series of 1–2 iterations with on average 1 iteration in a series. As a result, the optimized protocols obtained for $\tau = 0.4$ and 0.8 resemble the periodic protocol at $\tau = 0.8$, which induces a globally chaotic dynamics.

5 Summary and conclusions

In this study, we considered the conceptual problem of designing a mixing device able to maintain a uniform quality of mixing for different initial configurations of the mixture. As a case study, we considered as a model device a two-dimensional, piecewise steady, nonlinear flow, the sine flow. To promote mixing in this device, we optimized on-line a stirring protocol using the short time horizon procedure. This procedure considers all admissible stirring subprotocols over a sequence of time horizons and selects a suboptimal stirring protocol which maximizes the quality of mixing at a given final time. As a measure of the quality of mixing and as the cost function of the optimization, we used the mix-norm, an average multi-scale measure of the scalar variance over different coarse graining of the mixing domain.

We assessed the sensitivity of the short-time-horizon optimal protocols to the geometry of the initial configuration by considering five different configurations of the initial concentration field. For each configuration, we used the short time horizon procedure to obtain an optimized protocol. We quantified the mixing efficiency of the optimized protocols by comparing the time evolutions of the mix-norm induced by them. Subsequently, we quantified the sensitivity of the optimized protocols by computing the time evolution of the spreading of the mix-norm induced by these protocols for the five initial configurations. We used the performance of the periodic and recursive symmetry-breaking protocols as benchmarks for our assessment.

We showed that for the small values of the switching time, such as $\tau = 0.1$ and 0.4, the performance of the optimized protocols is quite insensitive to the geometry of the initial configuration when compared to the performance of the periodic and recursive symmetry-breaking protocols. For these values of τ, the recursive symmetry-breaking protocol is only a little less sensitive than the periodic protocol. Surprisingly, we found that for large values of the switching time, such as $\tau = 0.8$, optimized protocols are more sensitive to the geometry of the initial configuration than the periodic protocol. On the one hand, the sensitivity of the periodic protocol is expected to be quite small for $\tau = 0.8$ because for this value of the switching time this protocol induces a globally chaotic dynamics. On the other hand, it is not clear why for $\tau = 0.8$ the periodic protocol is even less sensitive than the optimized protocols.

We hypothesized that on-line optimization of mixing is essential to achieve a uniform mixing efficiency for different initial configurations of the mixture. To corroborate this hypothesis, we applied the stirring protocol optimized for one initial configuration to the four other initial configurations. We found that this protocol is considerably more sensitive to the geometry of the initial configuration than the protocols optimized for the five initial configurations.

We characterized the effect of the switching time horizon ν and the switching time τ on the sensitivity of the optimized protocols to the geometry of the initial configuration. For switching times $\tau = 0.1$ and 0.4, the protocols optimized over the shortest time horizon, $\nu = 1$, are competitively sensitive to the geometry of the initial configuration with respect to the protocols optimized over longer time horizons, $\nu = 4$ and 8. For the switching time $\tau = 0.8$, the protocols optimized over $\nu = 1$ are even less sensitive than the protocols optimized over $\nu = 4$ and 8. In addition, for all of the above values of the switching time the protocols optimized over $\nu = 1$ are competitively mixing efficient with respect to the protocols optimized over $\nu = 4$ and $\nu = 8$. Consequently, the simplest optimization, $\nu = 1$, is more suitable for practical applications than the more complex optimizations, $\nu = 4$ and $\nu = 8$.

We observed that the structure of the optimized protocols strongly depends on the initial configuration for which the protocols were generated. For the small switching time, $\tau = 0.1$, the protocols have different structure within the transient part, the first 10–15 iterations. The structure of the remaining part of these protocols, the last 45-50 iterations, is quasi-periodic. The period is about 1.0 for the protocols optimized over $\nu = 1$ and about 0.8 for the protocols optimized over $\nu = 4$ and $\nu = 8$. For large switching times, $\tau = 0.4$ and 0.8, the optimized protocols have no transient parts and

are quasi-periodic with the period of about 0.8. Therefore, for all the values of the switching time, $\tau = 0.1$, 0.4 and 0.8, the optimized protocols generally resemble the periodic protocol at $\tau = 0.8$, a protocol which is known to induce a globally chaotic dynamics.

The results obtained in this study indicate that the optimization over very short time horizons could be in principle used as an on-line procedure for maintaining a uniformly high quality of mixing for a time-dependent initial configuration.

6 Acknowledgments

Funding was provided by NSERC under a Postgraduate Scholarship and under Contract No. RGPIN217169.

Bibliography

M. M. Alvarez, F. J. Muzzio, S. Cerbelli, A. Adrover, and M. Giona. Self-similar spatiotemporal structure of intermaterial boundaries in chaotic flows. *Physical Review Letters*, 81:3395, 1998.

T. M. Antonsen, Jr., Z. Fan, E. Ott, and E. Garcia-Lopez. The role of chaotic orbits in the determination of power spectra of passive scalars. *Physics of Fluids*, 8:3094–3104, November 1996.

H. Aref. Stirring by chaotic advection. *Journal of Fluid Mechanics*, 143: 1–21, 1984.

H. Aref. The development of chaotic advection. *Physics of Fluids*, 14: 1315–1325, 2002.

H. Aref and M. S. El Naschie, editors. *Chaos Applied to Fluid Mixing*. Pergamon, New York, 1995.

L. Cortelezzi, A. Adrover, and M. Giona. Feasibility, efficiency and transportability of short horizon optimal mixing protocols. *Journal of Fluid Mechanics*, 597:199–231, 2008.

D. D'Alessandro, M. Dahleh, and I. Mezić. Control of mixing in fluid flow: a maximum entropy approach. *IEEE Transactions on Automatic Control*, 44:1852–1863, 1999.

C. Eckart. An analysis of the stirring and mixing processes in incompressible fluids. *Journal of Marine Research*, 7:265, 1948.

M.D. Finn, S. M. Cox, and H. M. Byrne. Mixing measures for a two-dimensional chaotic stokes flow. *Journal of Engineering Mathematics*, 48:129–155, 2004.

J.G. Franjione and J.M. Ottino. Symmetry concepts for the geometric analysis of mixing flows. *Philosophical Transactions of the Royal Society of London, Series A*, 338:301–323, 1992.

J.G. Franjione, C.W. Leong, and J.M. Ottino. Symmetries within chaos: A route to effective mixing. *Physics of Fluids A*, 1:1772–1783, 1989.

S. Gibout, Y. L. Guer, and E. Schall. Coupling of a mapping method and a genetic algoritm to optimize mixing efficiency in periodic chaotic flows. *Communications in Nonlinear Science and Numerical Simulation*, 11: 413–423, 2006.

J. P. Gleeson. Transient micromixing: examples of laminar and chaotic stirring. *Physics of Fluids*, 17:100614, 2005.

E. Gouillart, J.-L. Thiffeault, and M. D. Finn. Topological mixing with ghost rods. *Physical Review E*, 73:036311, 2006.

D. M. Hobbs and F. J. Muzzio. Effects of injection location, flow ratio and geometry on kenics mixer performance. *American Institute of Chemical Engineers Journal*, 43:3121–3132, 1997.

D. M. Hobbs, M. M. Alvarez, and F. J. Muzzio. Mixing in globally chaotic flows: a self-simila process. *Fractals*, 5:395–425, 1997.

M. Liu, F.J. Muzzio, and R.L. Peskin. Quantification of mixing in aperiodic chaotic flows. *ChaosSolFrac*, 4:869–893, 1994.

G. Mathew, I. Mezic, and L. Petzold. A multiscale measure for mixing and its applications. *Physica D*, 211:23–46, 2005.

G. Mathew, I. Mezic, S. Grivopoulos, U. Vaidya, and L. Petzold. Optimal control of mixing in stokes fluid flows. *Journal of Fluid Mechanics*, 580: 261–281, 2007.

F. J. Muzzio, M. M. Alvarez, S. Cerbelli, M. Giona, and A. Adrover. The intermaterial area density generated by time- and spatially periodic 2d chaotic flows. *Chemical Engineering Science*, 55:1497–1508, 2000.

J. M. Ottino. *The Kinematics of Mixing: Stretching, Chaos, and Transport*. Cambridge University Press, New York, 1989.

J. M. Ottino and S. Wiggins. Introduction: mixing in microfluidics: One contribution of 11 to a Theme 'Transport and mixing at the microscale'. *Royal Society of London Philosophical Transactions Series A*, 362:923–935, May 2004.

E. L. Paul, V. A. Atiemo-Obeng, and S. M. Kresta, editors. *Handbook of Industrial Mixing : Science and Practice*. Wiley-Interscience, 2004.

J. H. Phelps and C. L. Tucker. Lagrangian particle calculations of distributive mixing: limitations and applications. *Chemical Engineering Science*, 61:6826–6836, 2006.

R. T. Pierrehumbert. Tracer microstructure in the large-eddy dominated regime. *Chaos, Solitons and Fractals*, 4:1091–1110, 1994.

R. Sturmap, J.M. Ottino, and S. Wiggins. *The Mathematical Foundations of Mixing: The Linked Twist Map as a Paradigm in Applications: Micro to Macro, Fluids to Solids*. Cambridge University Press, 2006.

E. S. Szalai, J. Kukura, P. E. Arratia, and F. J. Muzzio. Effect of hydrodynamics on reactive mixing in laminar flows. *American Institute of Chemical Engineers Journal*, 49:168–179, 2003.

R. K. Thakur, Ch. Vial, D. P. Nigam, E. B. Nauman, and G. Djelveh. Static mixers in the process industries – a review. *Chemical Engineering Research and Design*, 81:878–826, 2003.

J.-L. Thiffeault and G. A. Pavliotis. Optimizing the source distribution in fluid mixing. *Physica D*, 237:918–929, 2008.

J.-L. Thiffeault, C. R. Doering, and J. D. Gibbon. A bound on mixing efficiency for the advection-diffusion equation. *Journal of Fluid Mechanics*, 521:105–114, 2004.

C. L. Tucker and G. W. M. Peters. Global measures of distributive mixing and their behavior in chaotic flows. *Korea-Australia Rheology Journal*, 15:197–208, 2003.

A. Vikhansky and S. M. Cox. Conditional moment closure for chemical reactions in laminar chaotic flows. *American Institute of Chemical Engineers Journal*, 53:19–27, 2007.

J. M. Zalc, E. S. Szalai, and F. J. Muzzio. Mixing dynamics in the smx static mixer as a function of injection location and flow ratio. *Polymer Engineering and Science*, 43:875–890, 2003.

J.M. Zalc and F.J. Muzzio. Parallel-competitive reactions in a two-dimensional chaotic flow. *Chemical Engineering Science*, 54:1053–1069, 1999.